Springer Optimization and Its Applications 66

Giuseppe Buttazzo
Aldo Frediani *Editors*

Variational Analysis and Aerospace Engineering: Mathematical Challenges for Aerospace Design

Contributions from a Workshop held at the School of Mathematics in Erice, Italy

Springer

Springer Optimization and Its Applications

Springer Optimization and Its Applications

VOLUME 66

Aims and Scope

Optimization has been expanding in all directions at an astonishing rate during the last few decades. New algorithmic and theoretical techniques have been developed, the diffusion into other disciplines has proceeded at a rapid pace, and our knowledge of all aspects of the field has grown evenmore profound. At the same time, one of the most striking trends in optimization is the constantly increasing emphasis on the interdisciplinary nature of the field. Optimization has been a basic tool in all areas of applied mathematics, engineering, medicine, economics, and other sciences.

The series *Springer Optimization and Its Applications* publishes undergraduate and graduate textbooks, monographs and state-of-the-art expository work that focus on algorithms for solving optimization problems and also study applications involving such problems. Some of the topics covered include nonlinear optimization (convex and nonconvex), network flow problems, stochastic optimization, optimal control, discrete optimization, multiobjective programming, description of software packages, approximation techniques and heuristic approaches.

For further volumes:
www.springer.com/series/7393

Giuseppe Buttazzo • Aldo Frediani
Editors

Variational Analysis and Aerospace Engineering: Mathematical Challenges for Aerospace Design

Contributions from a Workshop held at the School of Mathematics in Erice, Italy

Springer

Editors
Giuseppe Buttazzo
Department of Mathematics "L. Tonelli"
University of Pisa
Pisa
Italy

Aldo Frediani
Department of Aerospace Engineering
University of Pisa
Pisa
Italy

ISSN 1931-6828 Springer Optimization and Its Applications
ISBN 978-1-4614-2434-5 e-ISBN 978-1-4614-2435-2
DOI 10.1007/978-1-4614-2435-2
Springer New York Dordrecht Heidelberg London

Library of Congress Control Number: 2012933756

Mathematics Subject Classification (2010): 49J15, 49J20, 35Q93, 47N10, 65K10, 65N30, 65N38, 74R20, 76M10, 76N25

This book is dedicated to
Professor Franco Giannessi
on the occasion of his 75th birthday.

Preface

The new challenges in Aerospace Sciences and Engineering are not limited to partial improvement of the systems available today, but the ambition is to design innovative machines with a jump forward of efficiency to reduce fuel consumption and noxious emissions or, in synthesis, to fly cleaner and quieter. Mathematics is fundamental in this respect. The series of the workshops held at the "*Ettore Majorana Foundation and Centre for Scientific Culture*" of Erice continues bringing together mathematicians and aerospace engineers coming from both Academia and Industry. Erice is a place where the dialog is easy and fruitful and young research fellows can interact and discuss in a pleasant and sophisticated scientific atmosphere.

The present volume collects most of the papers presented at the workshop "*Variational Analysis and Aerospace Engineering II*" held on 8–16 September 2010; some papers, dealing with new challenges in Aeronautics, were added in order to present a set of new problems requiring an extensive application of mathematical tools.

The editors wish to continue this series and are confident, as written in the volume published on 2009, "to capture the interest of people, ..., particularly, young researchers working on new frontiers of mathematical application to engineering".

This volume is dedicated to Franco Giannessi, eminent professor of Mathematics at the University of Pisa and Director of the School of Mathematics "G. Stampacchia" of the Erice Centre, on the occasion of his 75th birthday. Franco continues to be a guide to the new generations of scientists.

Pisa, Italy

Giuseppe Buttazzo
Aldo Frediani

Acknowledgements

This volume collects contributions presented in the workshop "*Variational Analysis and Aerospace Engineering II*" held at the School of Mathematics of the E. Majorana Centre in Erice on 8–16 September 2010.

The workshop has been possible thanks to the contributions of the following organizations:

- University of Pisa (Italy),
- Department of Aerospace Engineering "L. Lazzarino", University of Pisa (Italy),
- Department of Mathematics "L. Tonelli", University of Pisa (Italy),
- Technical University of Technology, Delft (Holland),
- IDS Company, Pisa (Italy),
- GNAMPA (Gruppo Nazionale per l'Analisi Matematica, la Probabilità e le loro Applicazioni).

We gratefully acknowledge the E. Majorana Centre and Foundation for Scientific Culture and the precious help by Franco Giannessi and Vittorio Cipolla.

Contents

Contributors

Frédéric Alauzet INRIA, Le Chesnay, France

Nicola Beccasio Cascina Costa di Samarate (VA), Italy

Giovanni Bernardini University Roma Tre, Rome, Italy

Vincenzo Binante Mechanics of Materials and Structures Laboratory, ISTI-CNR, Pisa, Italy

Giuseppe Buttazzo Dipartimento di Matematica, Università di Pisa, Pisa, Italy

Rauno Cavallaro Department of Aerospace Engineering, San Diego State University, San Diego, USA

Vittorio Cipolla Department of Aerospace Engineering, University of Pisa, Pisa, Italy

Francesco Contini Carbench International S.p.A., Massa, Italy

Dario Dal Canto Department of Aerospace Engineering, University of Pisa, Pisa, Italy

Jan de Klerk Faculty of Aerospace Engineering, Delft University of Technology, Delft, The Netherlands

Boris Desmorat Institut Jean Le Rond d'Alembert, Université Paris Sud, UMR7190, Université Paris 6 – CNRS, 4, Paris, France

N. Divoux Delft University of Technology, Delft, The Netherlands

Aldo Frediani Department of Aerospace Engineering, University of Pisa, Pisa, Italy; Dipartimento di Ingegneria Aerospaziale "L. Lazzarino", Università di Pisa, Pisa, Italy

Massimo Gennaretti University Roma Tre, Rome, Italy

Gian Luca Ghiringhelli Department of Aerospace Engineering, Polytechnic of Milano, Milano, Italy

Matteo Lombardi MATHICSE, CMCS Chair of Modelling and Scientific Computing, EPFL, Lausanne, Switzerland

Francesco Maddalena Dipartimento di Matematica Politecnico di Bari, Bari, Italy

Bijan Mohammadi CERFACS, Toulouse, France

Sergey A. Nazarov Institute of Mechanical Engineering, Russian Academy of Sciences, St. Petersburg, Russia

Fabrizio Oliviero Department of Aerospace Engineering, University of Pisa, Pisa, Italy

Nicola Parolini MOX, Politecnico di Milano, Milano, Italy

Danilo Percivale Dipartimento di Ingegneria della Produzione Termoenergetica e Modelli Matematici, Università di Genova, Genova, Italy

Olivier Pironneau Laboratoire J-L. Lions, University of Paris VI, Paris, France

Alfio Quarteroni MATHICSE, CMCS Chair of Modelling and Scientific Computing, EPFL, Lausanne, Switzerland; MOX, Politecnico di Milano, Milano, Italy

Flavio Quattrone Departement Physique et Mecanique des Materiaux, ENSMA – Teleport 21, Futuroscope Chasseneuil Cedex, France

Emanuele Rizzo SkyBox Engineering S.r.l., Pisa, Italy

Gianluigi Rozza MATHICSE, CMCS Chair of Modelling and Scientific Computing, EPFL, Lausanne, Switzerland

Dieter Schmitt Aeronautical Consultant, Frankfurt am Main, Germany

Mauro Terraneo Department of Aerospace Engineering, Polytechnic of Milano, Milano, Italy

Marco Tesconi Massa (MS), Italy

Franco Tomarelli Dipartimento di Matematica "Francesco Brioschi", Politecnico di Milano, Milano, Italy

Daan van Ginneken Faculty of Aerospace Engineering, Delft University of Technology, Delft, The Netherlands

Paolo Vannucci Institut Jean Le Rond d'Alembert, Université Versailles Saint Quentin, UMR7190, Université Paris 6 – CNRS, 4, Paris, France

Piero Villaggio Department of Structures, University of Pisa, Pisa, Italy

Angela Vincenti Institut Jean Le Rond d'Alembert, UMR7190, Université Paris 6 – CNRS, 4, Paris, France

Mark Voskuijl Faculty of Aerospace Engineering, Delft University of Technology, Delft, The Netherlands

PrandtlPlane Propelled with Liquid Hydrogen: A Preliminary Study

Nicola Beccasio, Marco Tesconi, and Aldo Frediani

1 Introduction

In 1998, the world's airlines transported more than 1600 million of passengers and 29 million tons of freight, generating an annual turnover of US$ 307 billion. These numbers have raised up and, in the future, are supposed to improve with a predicted growth of revenue passengers-km of 4–5% every year.

Today transport aviation is supposed to produce about 2.5% of the total CO_2 emissions, and, considering its growth, this is a problem for the future of aviation industry [13].

The document "*A Vision for 2020*", published by the Advisory Council for Aeronautics Research in Europe, October 2002, summarizes the main guidelines to make Aircraft and Air Transport System responding to society's needs, despite a threefold increase in air transporting. The main points of interest are Quality and Affordability, Safety, and Environment; Environment is the starting point of this paper. The main exhausts of aircraft engines are Carbon Nitride CO_2, Water vapour, Nitride Oxides NO_x, non-combusted fuels, and particulates. CO_2 has a long-term permanence in the atmosphere (about 100 years), and the impact on climate is independent of the height of flight. It can be reduced by reducing the engine specific consumption and improving the efficiency of the kerosene propelled aircraft; the other possibility is to

N. Beccasio
Agusta Westland Via Giovanni Agusta 520, 21017 Cascina Costa di Samarate (VA), Italy
e-mail: nicola.beccasio@agustawestland.com

M. Tesconi
Astec Tongiani Srl Via Acquale 16, 54100 Massa (MS), Italy
e-mail: marco.tesconi@gmail.com

A. Frediani (✉)
Dipartimento di Ingegneria Aerospaziale "L. Lazzarino", Universitá di Pisa, Via G. Caruso 8, 56122 Pisa, Italy
e-mail: a.frediani@dia.unipi.it

G. Buttazzo, A. Frediani (eds.), *Variational Analysis and Aerospace Engineering: Mathematical Challenges for Aerospace Design*, Springer Optimization and Its Applications 66,
DOI 10.1007/978-1-4614-2435-2_1,

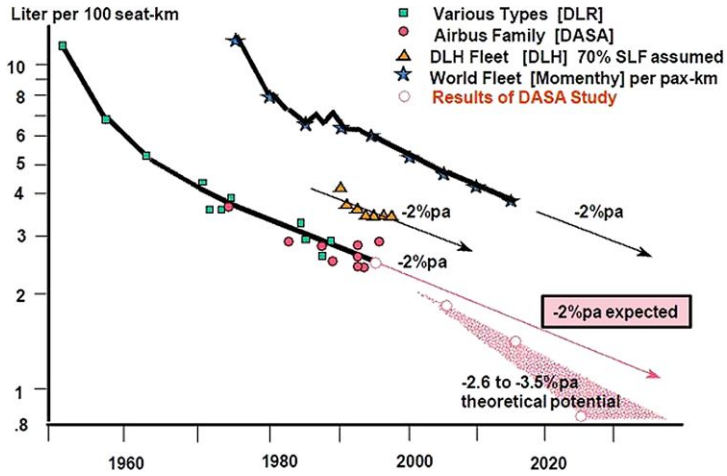

Fig. 1 Efficiency trend of aircraft engines

eliminate the kerosene by introducing new fuels. The water vapour effect vanishes soon at low altitudes but is persistent at high altitudes and produces some greenhouse effect due to the contrails formation [1]. The result of the engine combustion is NO, and, then, NO_2 is produced by oxidation of NO into the atmosphere; these products are dangerous for human health. Other noxious products are UHC and CO deriving from incomplete combustion, which generally occurs at low regimes of the engines. Particulate is made of small flying particles of carbon and hydrogen; it is not toxic but produces smog. The efficiency of civil transport aircraft has improved constantly in the past. The increase of efficiency has invested new materials, new engines and on-board systems. In 2000 the material used for the main structures were the following: Aluminum alloys 65%, composites 15%, Titanium 5% and steel 15%; in 2020 the following is forecast: 65% composites, 15% Aluminum, 5% Titanium and 15% steel. The fuel consumed per 100 seat-km have been reduced constantly as shown in Fig. 1 [6].

The new requirements on environment are a reduction in perceived noise to one half of the current average levels, noise nuisance outside the airport boundary eliminated by quieter aircraft, CO_2 emissions per passenger kilometer cutted by 50% (i.e. a cut of 50% in specific fuel consumption) and NO_x cutted by 80%.

To achieve these goals in the medium term, it is necessary to change the way to design airplanes, introducing innovative configurations; in the long-term perspective, the fuel needs to be changed in addition. In this paper, both aircraft configuration and a new fuel are indicated; the new configuration is the PrandtlPlane, and the candidate fuel is Hydrogen.

The PrandtlPlane is potentially the most efficient aircraft configuration and, also, permits an easy integration of different types of engines, including the hydrogen ones. When passing from kerosene to Hydrogen, the general architecture of the aeronautical engines does not change apart from the combustion chambers; because the

Table 1 Comparative characteristics of some fuels

	H_2	CH_4	$CH_{1.93}$
Molecular mass	2.016	16.04	≈168
Heat of combustion [kJ/g]	120	50	42.08.00
Density [g/cm^3]	0.071	0.29375	≈0.811
Boiling point, 1 atm [K]	20.27	112	440–539
Freezing point [K]	14.04	91	233
Specific heat capacity [J/g K]	0.422917	3.05	0.109722
Heat of vapourization [J/g]	446	510	360

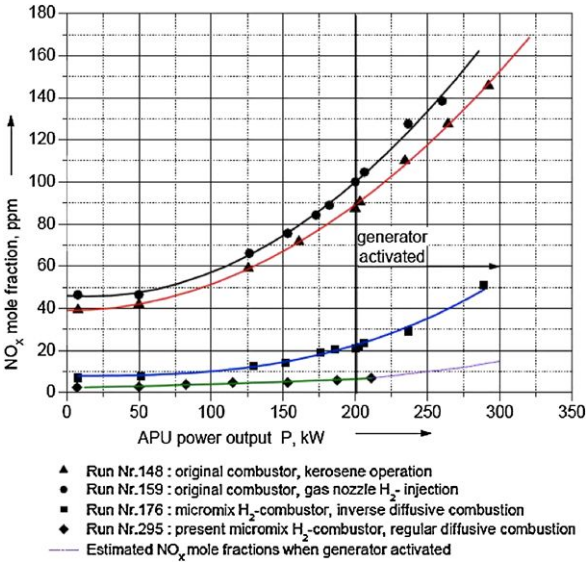

Fig. 2 NO_x production with different combustors

flame speed of Hydrogen is eight times higher than for the kerosene, the chambers are smaller and shorter, with the consequences of a lower permanence of fuel into the chambers (and a lower probability of NO_x formation) and lower refrigeration temperature. A comparison between the characteristics of Hydrogen and Kerosene, taken from the literature, are presented in Table 1.

Liquid Hydrogen reduces significantly NO_x emissions (from 30% to 50% compared to a kerosene propelled aircraft). Recent progresses in the combustor design (Micromix) have produced a further reduction of NO_x; a comparison of the kerosene and hydrogen NO_x emissions vs. power of an APU unit is presented in Fig. 2, which shows that a reduction of about 85% compared with a standard combustor of kerosene is obtained.

Hydrogen engines eliminate totally CO_2, reduce the fuel mass by a factor of 2.8 but improve the water vapour by a factor 2.6 compared to kerosene for completing the same mission (Fig. 3).

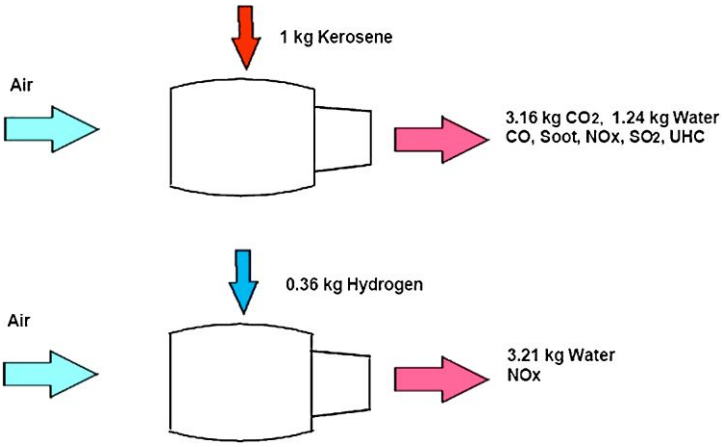

Fig. 3 Emissions of kerosene and Hydrogen propelled engines

Fig. 4 Example of LH_2 propelled aircraft [18]

The noxious emissions and water vapour productions indicated before are related to a conventional cruise altitude, but the conclusions could be different when changing it. So, if the generation of pollution (including water vapour) is the objective function to be minimized, the cruise altitude becomes a main parameter, and, in addition, in order to define a compromise with aerodynamic efficiency, the second main parameter is the aspect ratio. There are also undesired properties connected to liquid Hydrogen as, for example, low energy required for ignition, hide range of flammability, high volatility, high flame speed, etc.; these aspects are well known and discussed in the literature [6, 9, 12, 14–16]. In addition, because of its low density, about $4\times$ fuel volume is required in comparison to conventional fuel; consequently, very large pressurized fuel tanks are needed, and new concepts in Aerodynamics and overall architecture become the main challenges. The liquid hydrogen configurations proposed so far have, fundamentally, conventional layout apart from the positioning of the LH_2 tanks into the fuselage; in Fig. 4, a model of LH_2 aircraft developed in the CryoPlane Project [6] is illustrated.

Table 2 Technical specifications of the PrandtlPlane

Design payload	250 pax.
Range	2500 nm
Flight crew	2
Cabin crew	8
Standard pax weight	75 kg
Luggage	20 kg
Fuel	Liquid Hydrogen
Unusuable fuel	5% of fuel weight
Propulsion	2 engines
Cruise speed	0.75 Mach
Approach speed	<150 kts
Max take off field length	7000 ft
Max landing field length	6000 ft
Airport altitude	0 m
Landing performance	WLA = 0.95WTO
N° of external tanks	2
Tank differential pressure	1.4 bar

The most serious disadvantage of this solution are tanks positioned over the heads of passengers, and safety could be dramatically reduced.

In this paper a new PrandtlPlane configuration is proposed with the aim of proving that the Hydrogen tanks could be fully separated from the passenger cabin contrary to a conventional aircraft.

2 Preliminary Design

The application of liquid Hydrogen propulsion to a PrandtlPlane configuration [7] is proposed in the case of a 250-seat medium-size aircraft, designed for continental flights (max 2500 nm) and for a reduced cruise speed (0.75 Mach). The complete list of design requirements is reported in Table 2.

As said before, a cut to pollution and, at the same time, an efficient air transport system inside continental routes are the main scopes of the project. Wing aspect ratios ($AR = b^2/S$, where S is the sum of front and rear wing surfaces) and cruise altitudes (h_{cruise}) are assumed as variables in convenient ranges of variation; the aspect ratio varies in the interval 4–11, and the cruise altitude between 27.000 and 35.000 ft.

The present optimization procedure of the lifting system is affected by more approximations than the ones introduced in [8], due to the very preliminary design using Hydrogen as a fuel and, also, the lack of previous experience; thus, forward and rear wing reference surfaces are fixed as 45% and 55% of total one, respectively. The design process is summarized in Fig. 5.

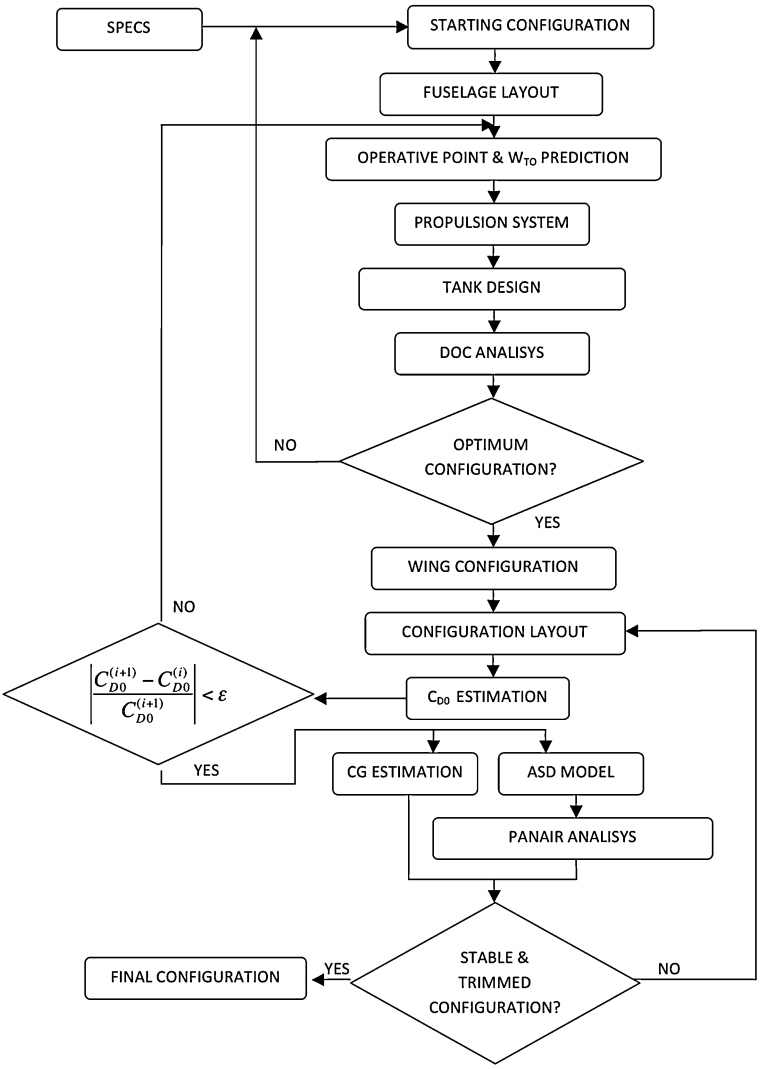

Fig. 5 Design procedure of the aircraft [2]

Starting from an initial layout, the efficiency during cruise is optimized meanwhile the aircraft is trimmed and stable in flight.

The fuselage layout is designed in order to minimize the wetted area; in this analysis the fuselage is assigned and not subjected to any modification during the design process. The passenger deck is the same of the other PrandtlPlane configurations, where about 250 passengers in 2 classes or 300 passengers in one single class are embarked; a typical solution is depicted in Fig. 6, in the case of two classes.

The cargo deck allocates two containers abreast (Fig. 7) for a total of 22 LD1 containers. A central axial support connects the passenger beam to the bottom fuse-

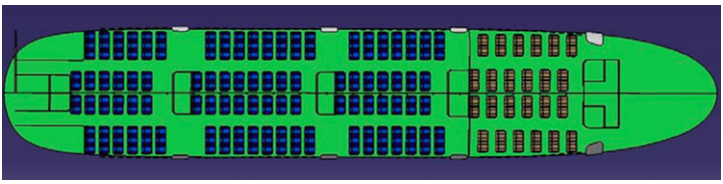

Fig. 6 General overview of the seats' disposition

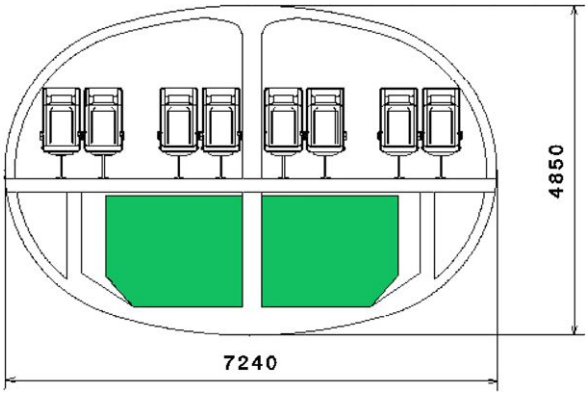

Fig. 7 General fuselage cross section (business class, 250-pax. version)

Fig. 8 General fuselage layout

lage in order to save weight and improve the stiffness; a truss loaded in traction (due to pressurization) is mounted between the top and bottom central fuselage.

As said before, due to the low density of hydrogen, we must provide a four times fuel volume of an equivalent aircraft propelled with Kerosene; for this reason, a part of the fuselage after the rear bulkhead could be used to allocate a fraction of total fuel. The presence of this tank could be avoided by reducing the range to about 1800 nm; in the case of a long route where the rear cabin tank is necessary, the relative positions of the Centre of gravity and the neutral point can be changed by a proper translation of the lifting system along the fuselage direction. The main part of fuel is set on two pressurized cylindrical tanks at the wing tips, insulated with Polymethacrylamide and all contained into an exterior aluminium case. In this paper, we do not discuss about the fuel tank detail design, but only their external layout is defined; the tank weight is predicted by means of statistic formulas.

In the center fuselage, two sponsons contain the main undercarriage (Fig. 8); previous experience have shown that the sponsons are not critical as far as transonic Aerodynamics is concerned; even more so, when the cruise speed has been reduced.

Once the external fuselage layout is fixed, preliminary wing layout and engine integration are necessary to determine the operative point. In particular, consid-

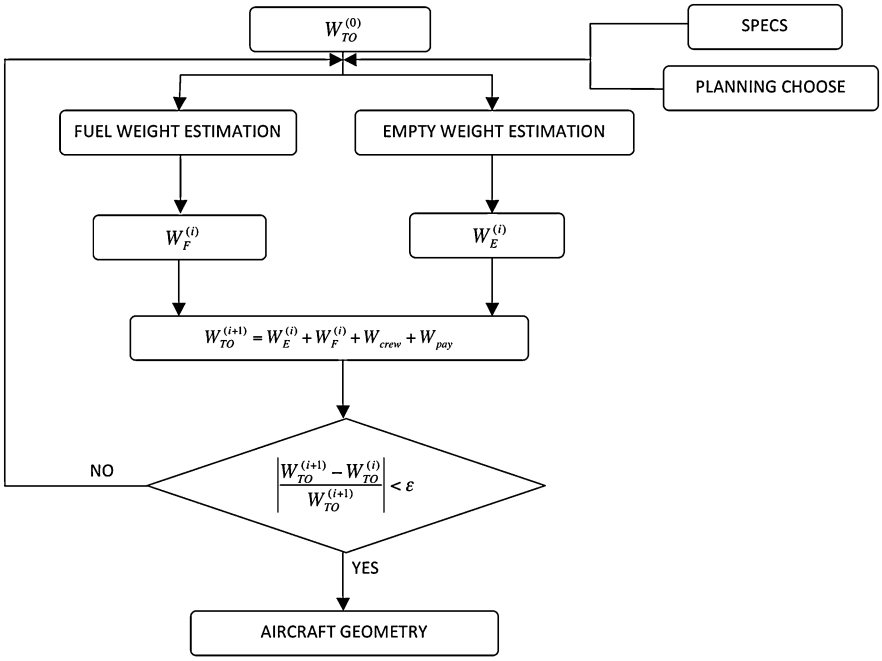

Fig. 9 Logic diagram used to predict take-off weight

ering FAR25 Regulations and the technical specifications in terms of Max Take Off/Landing field length, the minimum value of thrust required is selected together with the maximum wing load.

To predict the takeoff weight, the standard procedure indicated in the logic scheme in Fig. 9 is adopted.

Fuel weight is first estimated by fuel fraction method, where a typical mission is divided into steps, and fuel burnt is evaluated step by step using predictions taken from the literature and modified with proper corrective coefficients.

Semi-empirical expressions from NASA CR-151970 [3], adapted to take the specific configuration into account, are used to evaluate the empty weight of the single components of the aircraft.

Once Thrust/Weight (T/W) and Takeoff weight (W_{TO}) are calculated, the necessary thrust is given, and the engine features can be established. Many engine integrations are possible so avoiding to mix the presence of passengers in the cabin with hydrogen pipelines; the engines could be positioned at the rear fuselage, under the front wing or under the rear wing, depending on the layout of the hydrogen pipelines connecting the engines and the tanks. The configuration with the engines positioned on the lateral fuselage is typical of the propulsion with Kerosene, but, in the case of hydrogen propulsion, it is not allowed for safety reasons with the fuselage tank, and, in the case of tip tanks only, the pipeline layout along the vertical and rear wings is too long and unsafe.

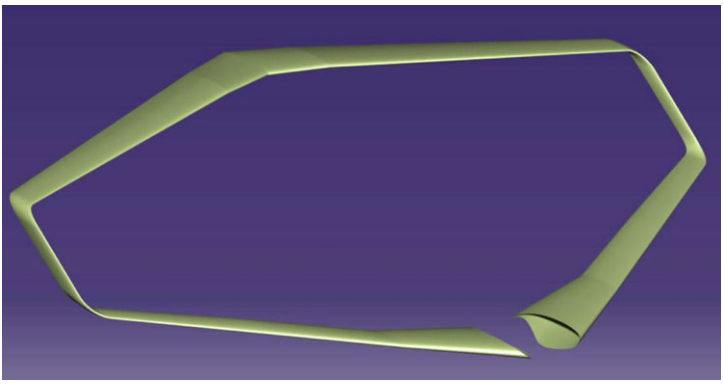

Fig. 10 The box wing system of the present PrandtlPlane

Table 3 Airfoils

1	SC 20714
2	SC 20714
3	GRUMMAR K2
4	GRUMMAR K2
5	GRUMMAR K2
6	SC 20412
7	GRUMMAR K2

The solution with two engines under the front wing is convenient when hydrogen is contained in the tip tanks only. The solution with the engines under the rear wings is always valid and safe, both with tip tanks and rear fuselage tank [5].

In analogy with others aircraft, a reference engine is fixed, and the final choice is obtained using the so called Engine Scale Factor method; the Engine Scale Factor method used here is based on ESF factor, defined as

$$ESF = \frac{T_{\text{des}}}{T_{\text{ref}}}, \tag{1.1}$$

where T_{ref} is the reference engine static thrust, and T_{des} is the actual engine static thrust. Once ESF is obtained, the reference engine can be scaled to be adapted to the configuration studied; this method is valid in the range $0.8 < ESF < 1.2$. After having fixed the wing load, W/S, we can define the wing shape; a typical PrandtlPlane wing system is illustrated in Fig. 10.

Airfoils are fixed in analogy with others 250-pax (Table 3). PrandtlPlane configurations; a typical aerodynamic solution is shown in Fig. 11: hereinafter, sweep angle, wing system condition and other wing geometrical characteristics will be fixed to make the aircraft stable and trimmed longitudinally.

The dihedral angles are set according to other PrandtlPlane configurations, The optimization procedure allows us to obtain the following quantities (functions of cruise altitude and Aspect Ratio): Maximum Take Off Weight, Empty Operating

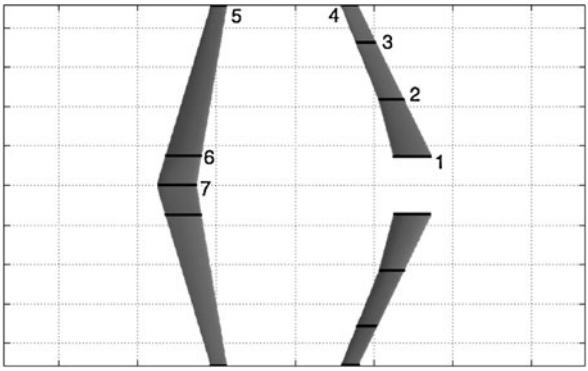

Fig. 11 Airfoil definition

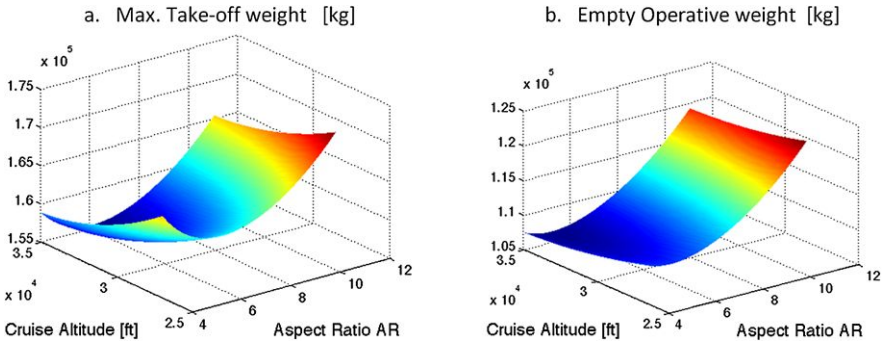

Fig. 12 Results a and b

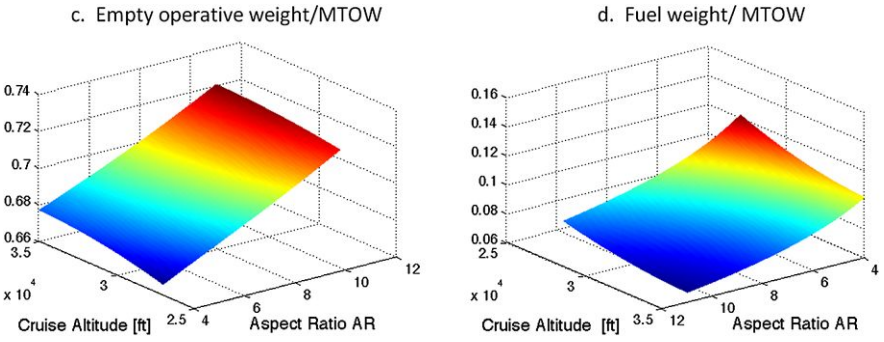

Fig. 13 Results c and d

Weight, Empty Operating Rate/Maximum Take Off Weight, Fuel Weight/Maximum Take Off Weight, Wing Span, ESF, Wing Surface, Fuel Weight, Landing Weight/ Maximum Take Off Weight, Wing Tank Weight including fuel inside. The results obtained are summarized in Figs. 12, 13, 14, 15 and 16.

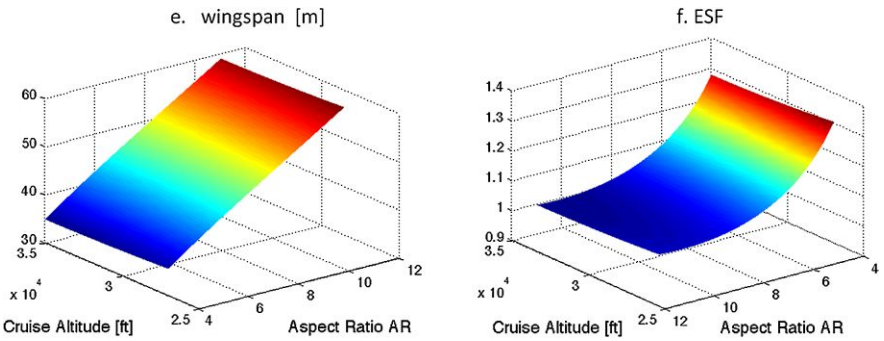

Fig. 14 Results e and f

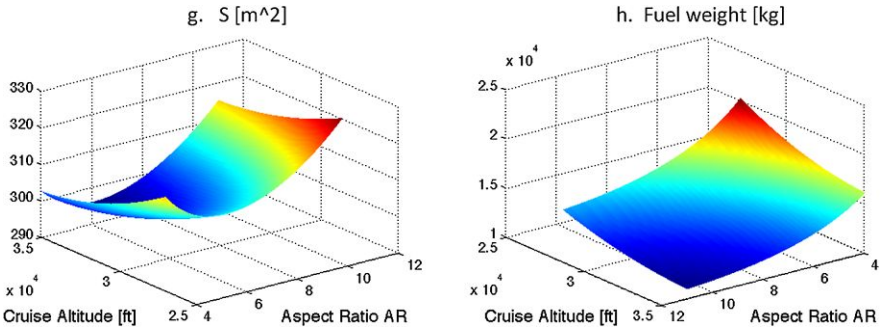

Fig. 15 Results g and h

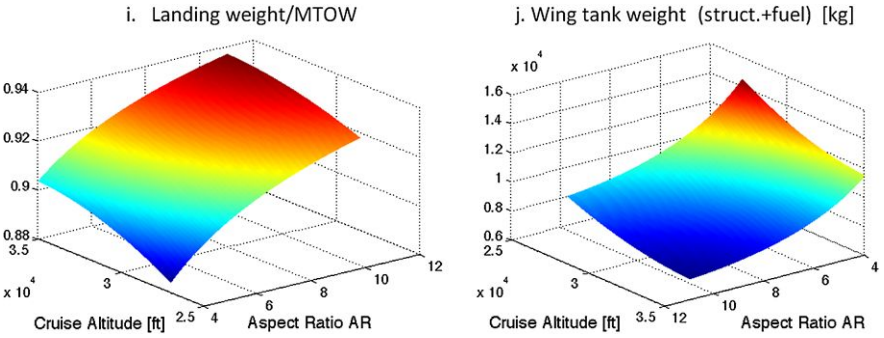

Fig. 16 Results i and j

Figure 12a shows how the maximum take-off weight depends on both cruise altitude and aspect ratio. The results confirm that fuel consumption is reduced when flying at high altitudes and also that, given a cruise altitude, maximum take off weight is a parabolic function of the Aspect Ratio: a low AR corresponds to a low efficiency, and, as AR increases, the efficiency will raise with the same law of the

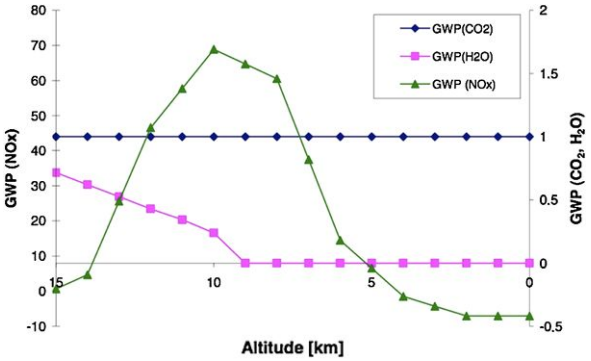

Fig. 17 GWP for CO_2, NO_x and water vapour emissions of a typical aircraft

empty operative weight (Fig. 12b). It is worth noting that operative weight is very high (about 68%–70% of take-off weight) because of the low density of liquid hydrogen; this conclusion is confirmed by Fig. 12d, where the fuel weight is small (about 7%–9% of take-off weight). If only aircraft performances are considered, the optimum cruise altitude is the maximum one, but, when noxious emissions and environmental impact are considered, the optimum altitude is different. In this respect, we make reference to some results in the literature to establish the cruise flight altitude as a compromise between a high aerodynamic efficiency and a low environmental impact.

3 The Choice of Flight Altitude

The cruise flight altitude of minimum fuel consumption is the maximum one (35.000 ft), but it corresponds to an unacceptable level of noxious emissions. The influence of the emissions on the global warming is conventionally considered through the so-called Global Warming Parameter (GWP). Figure 17 [16] shows the effect on heart heating of the main emissions in terms of GWP for a typical Kerosene propelled aircraft. The effects of CO_2 are nearly independent of flight altitude, the contrary for NO_x, and no warming effect due to contrails is produced under about 9-km altitude. Under 4000 m, NO_x produces a refrigeration, and the maximum warming effect occurs at 10000 m due the interactions of NO_x with other gases (e.g. Ozone, Methane, etc.); the global effect is the superposition of the partial ones. It appears that, should CO_2 be eliminated by an Hydrogen propelled aircraft, we could obtain a good compromise between performances and pollution at altitudes lower than 9000 m, with no effect of contrails.

Figures 18 and 19 show the GWP concentrations at the altitudes of interest in the case of kerosene and hydrogen propelled aircraft, respectively [16].

Figures 20 and 21 show the effects of Hearth warming in terms of change of fuel burnt and MTOW for the two engines. This results that a kerosene engine has no benefit to reduce the cruise altitude; when passing, for example, from FL390 to FL310 the fuel burnt increases by 20%, the MTOW increases by 2% and the GWD

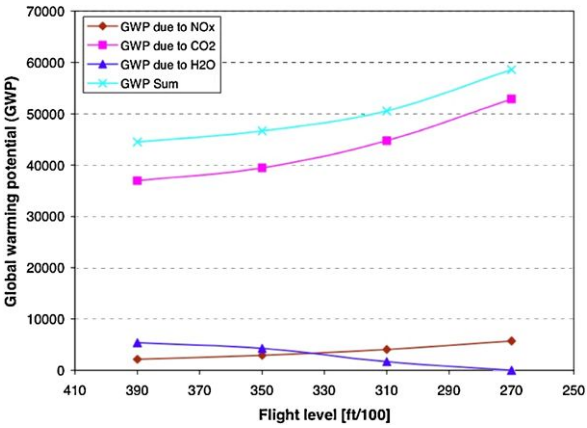

Fig. 18 GWP for a typical Kerosene propelled aircraft

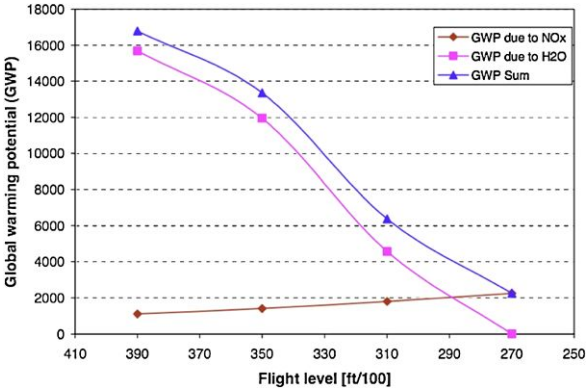

Fig. 19 GWP for a Hydrogen propelled aircraft

by 10%; under the same conditions, a hydrogen propelled aircraft experiences an increase of MTOW of 2%, a specific consumption of 10% and a reduction of GWD (or NO_x) of 60%.

In the present analysis, the attention is focused on the reduction of noxious emissions, and, thus, we assume a flight altitude of 29000 ft (8.840 m). After that the cruise level has been stated, it is possible to reduce all figures from Figs. 12 to 16 to the simple curves shown in the figures from Figs. 22 to 26.

Now the aircraft configuration is obtained by means of the optimization procedure presented before; the starting configuration is defined with the following characteristics: 50-m maximum wing span, maximum value of $AR = 8$ and best value of $AR = 6.5$ (with these values, the take-off weight is minimized, and reasonable tank weights and dimensions result).

When the optimization procedure converges, the aerodynamic drag is minimized (the relevant parameter is the friction drag coefficient CD_0). The results of the optimization procedure are presented in the next section. Given the aerodynamic configuration, the range of positions of the Centre of Gravity is defined consequently in

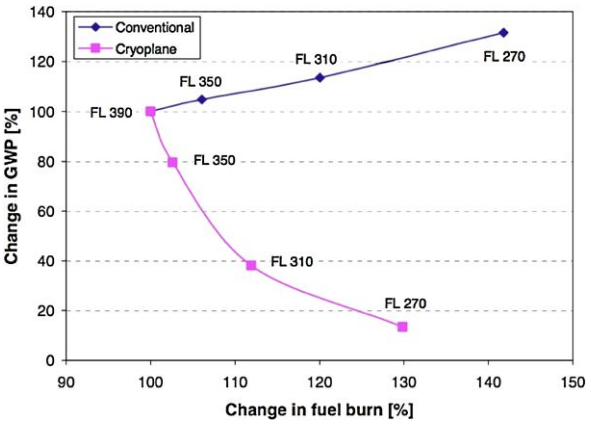

Fig. 20 GWP vs change in fuel burn

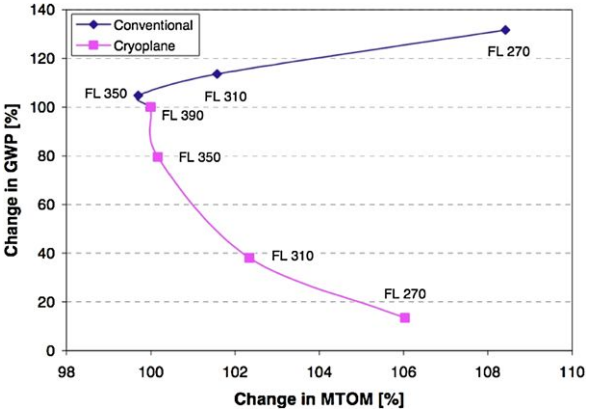

Fig. 21 GWP vs change in fuel burn

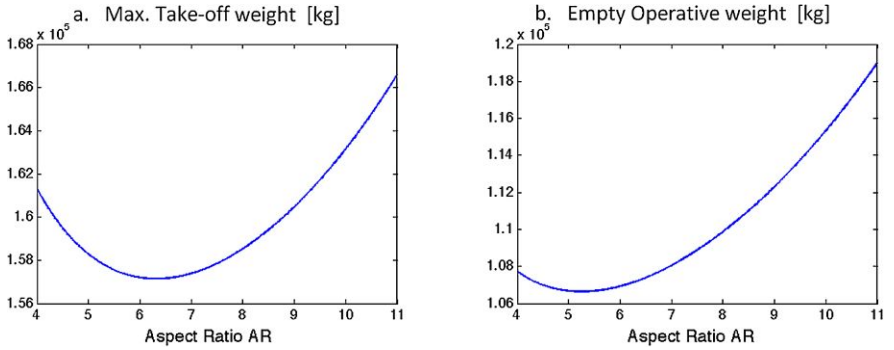

Fig. 22 The effect of the aspect ratio on the aircraft performances, a and b

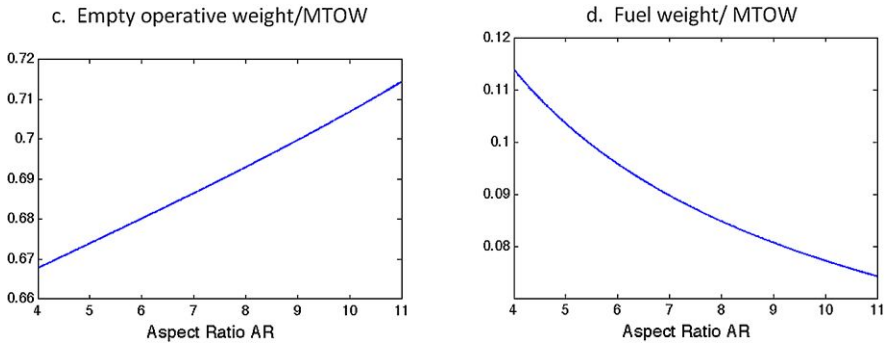

Fig. 23 The effect of the aspect ratio on the aircraft performances, c and d

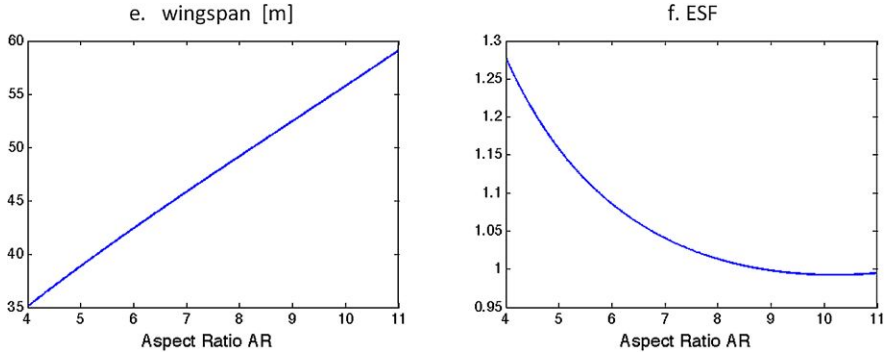

Fig. 24 The effect of the aspect ratio on the aircraft performances, e and f

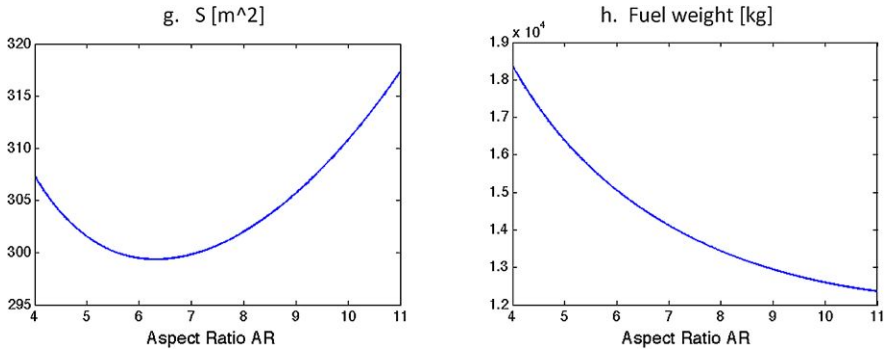

Fig. 25 The effect of the aspect ratio on the aircraft performances, g and h

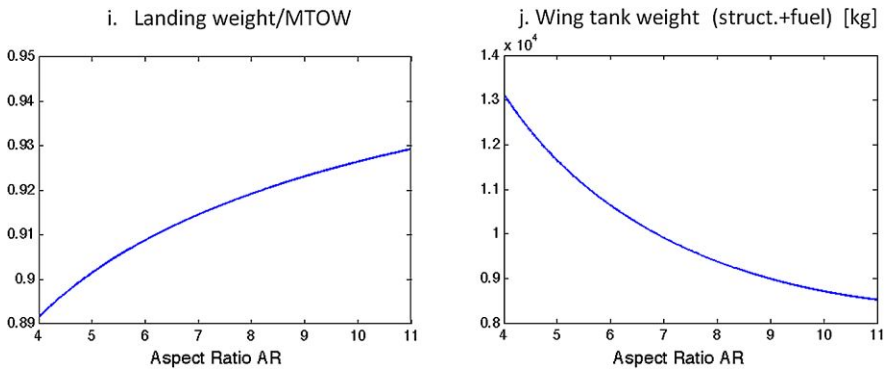

Fig. 26 The effect of the aspect ratio on the aircraft performances, i and j

such a way to obtain the static stability of flight in all the flight envelope; different operative conditions are considered, namely:

- full loaded aircraft (design condition);
- empty wing tanks;
- empty fuselage tank;
- empty tanks (wing and fuselage);
- no freight;
- no passengers, luggage and fuel;
- no passengers, luggage, fuel and freight.

Excursions of CG have been also examined in order to avoid any possible failure for "off design" conditions. Finally, the aerodynamic shape is constructed using [4], and the aerodynamic analysis is performed.

4 Final Configuration of the Aircraft

An artistic view of the final baseline configuration is illustrated in Fig. 27 in the case of a range of 2500 nm, with three tanks (at wing tips and inside rear fuselage).

All main characteristics of the final configuration have been calculated starting the formulas reported in the iterative loops illustrated in Figs. 5 and 9, using the commercial software Matlab. In Fig. 28 below it is possible to find out the iterative cycles necessary to have final values regarding the main aircraft weights.

In Tables 4–9 all the main data of the aircraft are summarized.

The aerodynamic chord is the average of the mean aerodynamic chords of the two horizontal wings; the results are relevant to 250 passengers with their luggage without any additional cargo. The empty weight has been obtained with standard statistical methods; corrections have been introduced to take the influence of the large fuel tanks, plants, etc., into account.

The total length of the fuselage becomes 51.64 m, resulting from the passenger accommodation and the presence of the rear fuselage Hydrogen tank. The wing span

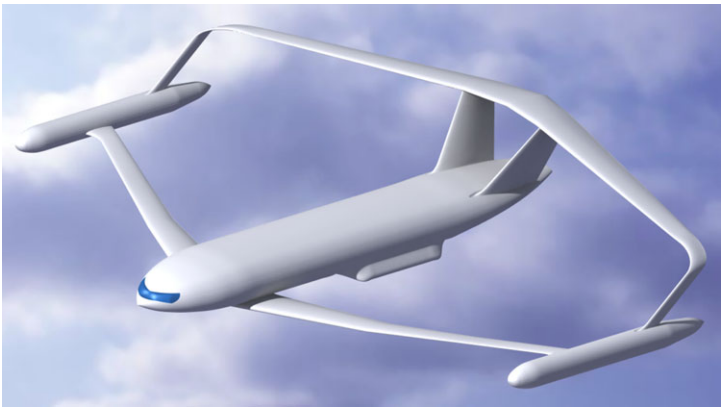

Fig. 27 Configuration resulting from a preliminary optimization

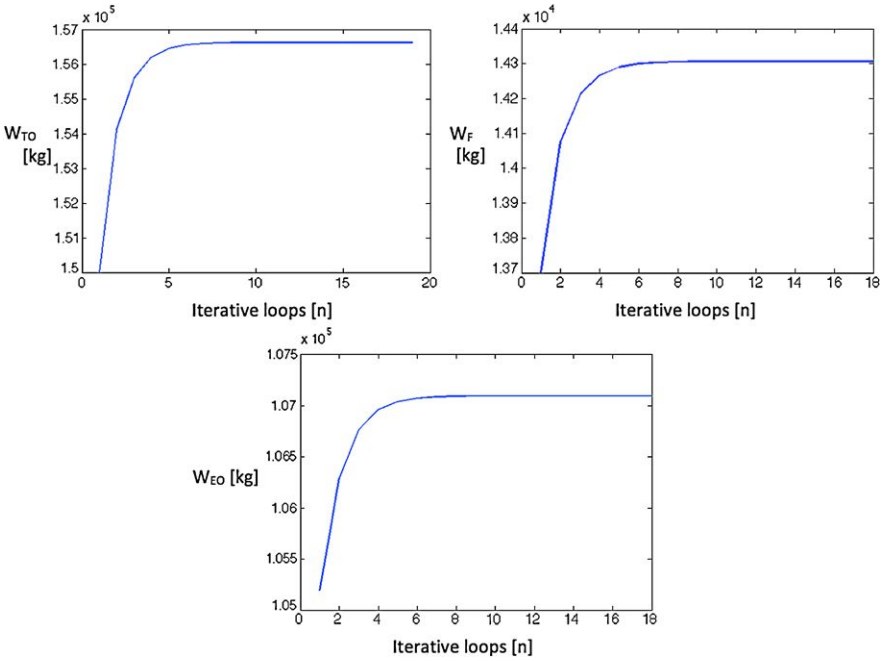

Fig. 28 Configuration resulting from a preliminary optimization

results from the optimization process; the final span of the optimized wing is 44 m, including the rounds to connect horizontal wings to the vertical ones (for a total of 3.24 m).

The preliminary weight estimation of this paper was conducted by using statistical formulas (see [10, 11, 17]), properly modified. For example, according to [8],

Table 4 Main LH2 PrandtlPlane characteristics

Max take-off weight [kg]	W_{TO}	156627
Empty operative weight [kg]	W_{EO}	107098
Fuel weight [kg]	W_{FUEL}	14306
Payload weight [kg]	W_{PAY}	23750
Thrust/max. take-off weight	T/W	0.32
Wing load [kg/m^2]	W/S	525
Cruise efficiency	$(L/D)_{CR}$	14.26
Maximum efficiency	$(L/D)_{MAX}$	16.47
Total fuselage length [m]	L_{TOT}	51.64
Wing span [m]	b	44
Reference surface [m^2]	S	298.4
Main aerodynamic chord [m]	MAC	3.6

Table 5 Forward wing geometry

Wing surface [m^2]	S_{FOR}	134.27
Wing span [m]	b	44.04
Main aerodynamic chord [m]	MAC_{FOR}	3.56
Aspect ratio	AR_{FOR}	11.8
Taper ratio	$(CT/CR)_{FOR}$	0.45
Relative average thickness	$(t/c)_{FOR}$	0.12
Sweep angle 25% [deg]	$\Lambda 25_{FOR}$	35
Sweep angle LE [deg]	ΛLE_{FOR}	35.94
Sweep angle TE [deg]	ΛTE_{FOR}	32.12
Root choord [m]	Cr_{FOR}	5.08
Kink choord [m]	Ck_{FOR}	3.37
Tip choord [m]	Ct_{FOR}	2.28
Dihedral angle [deg], Bay n°1	$\Gamma 1_{FOR}$	0
Dihedral angle [deg], Bay n°2	$\Gamma 2_{FOR}$	5

the empty weight of a PrandtlPlane wing system is nearly the same of that of a conventional aircraft; thus, we start from the statistical evaluation of the wing weight of a conventional aircraft to be improved in order to take the position of the tip tanks, heat exchangers and the tip local reinforcements into account and to be reduced because the present wings are free of the engines.

Figures 29 and 30 show some aerodynamic results obtained from a BEM analysis using Panair, even though, in these figures, vertical tail is single and not double as the final configuration (the reason is that only longitudinal stability has been studied). The figures give just an indication that the aerodynamic behaviour of the aircraft is not critical.

The aircraft is stable during trimmed cruise flight, as shown in Fig. 31, where the main longitudinal aerodynamic derivatives are reported.

Table 6 Backward wing geometry

Wing surface [m^2]	S_{AFT}	164.11
Wing span [m]	b	44.04
Main aerodynamic chord [m]	MAC_{AFT}	3.63
Aspect ratio	AR_{AFT}	11.82
Taper ratio	$(CT/CR)_{\mathrm{AFT}}$	0.45
Relative average thickness	$(t/c)_{\mathrm{AFT}}$	0.12
Sweep angle 25% [deg]	$\Lambda 25_{\mathrm{AFT}}$	20
Sweep angle LE [deg]	$\Lambda LE_{\mathrm{AFT}}$	21.79
Sweep angle TE [deg]	$\Lambda TE_{\mathrm{AFT}}$	14.04
Longitudinal axis choord [m]	Ccl_{AFT}	5.3
Root choord [m]	Cr_{AFT}	4.78
Kink choord [m]	Ck_{AFT}	3.75
Tip choord [m]	Ct_{AFT}	2.15
Dihedral angle [deg], Bay n°1	$\Gamma 1_{\mathrm{AFT}}$	0
Dihedral angle [deg], Bay n°2	$\Gamma 2_{\mathrm{AFT}}$	−5
Dihedral angle [deg], Bay n°3	$\Gamma 3_{\mathrm{AFT}}$	−5

Table 7 Fin geometry

Surface [m^2]	S_{FIN}	34.4
Wing span [m]	b	5.6
Aspect ratio	AR_{FIN}	0.9
Taper ratio	$(CT/CR)_{FIN}$	0.6
Relative average thickness	$(t/c)_{\mathrm{FIN}}$	0.1
Sweep angle 25% [deg]	$\Lambda 25_{\mathrm{FIN}}$	35
Root choord [m]	Cr_{FIN}	7.2
Tip choord [m]	Ct_{FIN}	4.3
Dihedral angle [deg]	$\Gamma 3_{\mathrm{FIN}}$	15

Table 8 Engine characteristics

Engine (Ref.)		GE CF6 80C2-B2
Thrust [kg]	Thrust	25062
Bypass ratio	BPR	5.31
Fan diameter [m]	D_{FAN}	2.4
Length [m]	L_{ENG}	4.2
Cruise specific fuel consumption [1/h]	SFC_{CR}	0.2021
Loiter specific fuel consumption [1/h]	SFC_{LOI}	0.1819

Table 9 Wing tank

Length [m]	L_{TANK}	22.7
Diameter [m]	D_{TANK}	2.1
Aspect ratio	$(L/D)_{\text{TANK}}$	10.8
Total volume [m^3]	V_{TANK}	67.8
Insulator thickness [mm]	δ_{TANK}	61.0
Insulator (mat.)		Polyvinyl chloride

Table 10 DOC parameter

Block time [h]	0.269444
Utilization [h/yr]	3456
Commercial speed [km/h]	787
Aircraft delivery price [MUSD]	124.210
DOC [$/(km pax)]	0.07148

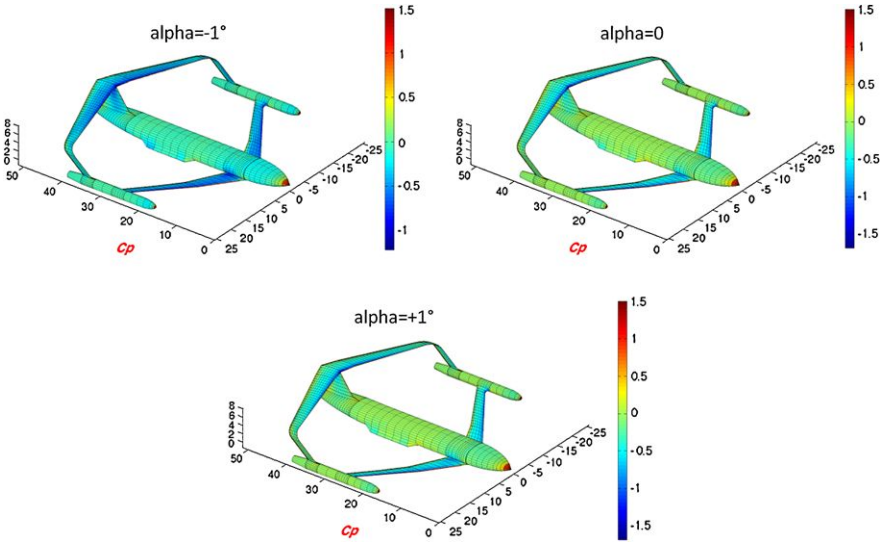

Fig. 29 Pressure coefficients

A preliminary economic analysis has been carried out, in order to investigate the real economical feasibility of an LH2 PrandtlPlane; the main data are summarized in Table 10.

The DOC (Direct Operating Costs) represent the cost (in USD) to be supported to carry a passenger for one kilometer; in general, DOC can be written as

$$DOC = \frac{CA + CM + CV}{U \cdot N_{\text{pax}} \cdot V_s}, \tag{1.2}$$

where

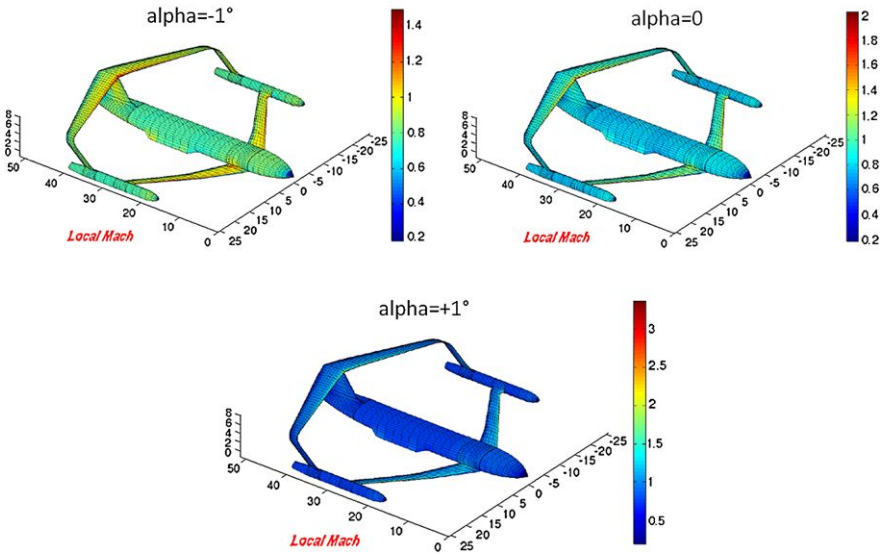

Fig. 30 Local mach number

Fig. 31 Trim conditions

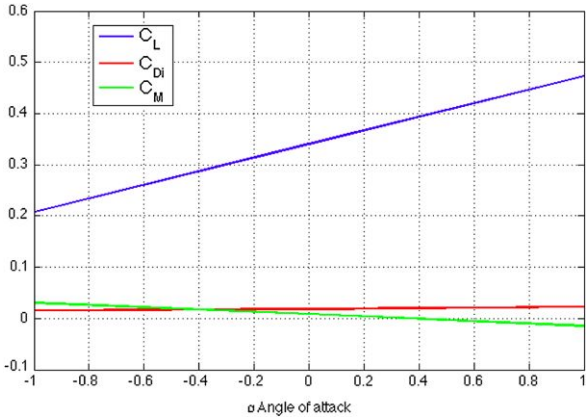

- CA represent the annual costs (fixed costs as taxes, aircraft depreciation, insurance costs). In order to estimate this costs, it is necessary to have the ADP (Aircraft Delivery Price), or MSSP (Manufacturer's Standard Study Price): to perform this analysis, statistic model DAPCA IV has been used;
- CM: maintenance cost;
- CV is the cost of flight (crew and fuel costs);
- N_{pax} is the total passengers number;
- U is the use in each year and is expressed in [h/yr];
- VB = Range/BT is the speed of the plane (or block speed), and BT is the block time (typical mission time).

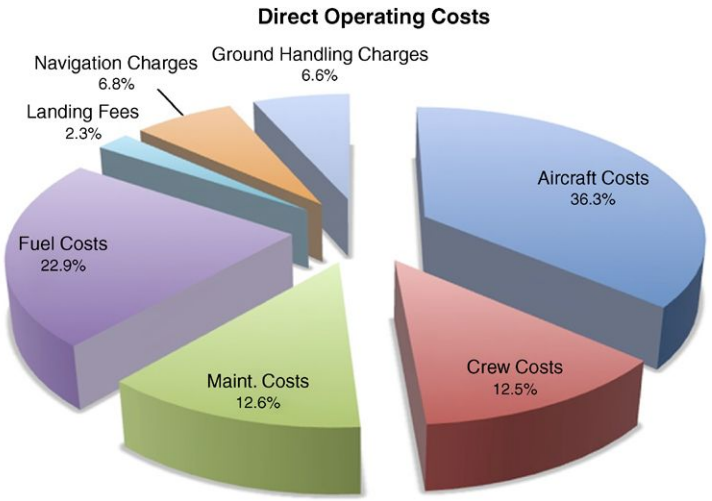

Fig. 32 Direct operating cost breakdown

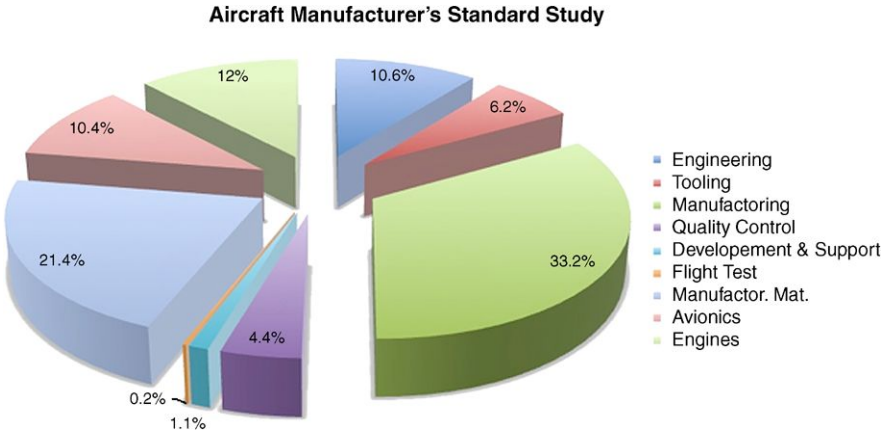

Fig. 33 Manufacturer study price breakdown

In Figs. 32 and 33 details about the composition of the DOC and MSSP costs are represented.

Fuel costs represent about a quarter of total DOC for an LH2 configuration, higher than that of kerosene aircraft because the present cost of liquid Hydrogen is much higher than the cost of kerosene; for this reason, the direct operating costs of LH2 propelled airplanes are higher than conventional airplanes. The prize of liquid Hydrogen could decrease in the future when other applications (e.g. car industry) could be introduced or new energetic scenarios may happen.

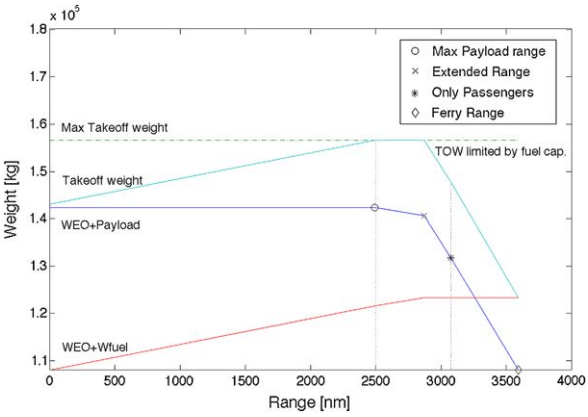

Fig. 34 Payload-range diagram

Table 11 Feasibility results

Max payload range (project condition)	Take-off weight, [kg]	W_{TO}	156627
	Range, [nm]	R	2500
	Fuel, [kg]	W_{FUEL}	14306
	DOC [$/(km pax)]		0.07148
Extended range	Take-off weight, [kg]	W_{TOEXT}	156627
	Range, [nm]	R_{EXT}	2871
	Fuel, [kg]	W_{FUEL}	15838
	DOC [$/(km pax)]		0.06246
Only passengers range	Take-off weight, [kg]	$W_{TO\ PAX}$	147771
	Range, [nm]	R_{PAX}	3075
	Fuel, [kg]	W_{FUEL}	16022
	DOC [$/(km pax)]		0.05976
Ferry range	Take-off weight, [kg]	$W_{TO\ ferry}$	123300
	Range, [nm]	R_{ferry}	3593
	Fuel, [kg]	W_{FUEL}	16022

Finally, the possibility of changing the operating conditions has been investigated to make the aircraft more adaptable to many different conditions of use. In particular, the following quantities are considered:

- Max Payload Range: maximum range covered with a fully loaded aircraft;
- Extended Range: maximum range covered with all tanks fully loaded;
- Only Passengers Range: the maximum range covered excluding freight (only passengers and luggage);
- Ferry Range: the maximum range covered with an empty aircraft.

The results are summarized in Fig. 34 and Table 11.

5 Conclusions

This paper shows that a civil transport PrandtlPlane with liquid hydrogen propulsion can be designed in order to fully separate the hydrogen tanks from the passengers. Liquid hydrogen tanks can be positioned at the front wing tips of a PrandtlPlane, after that structural optimization and aeroelastic analysis have shown that the wing system allows this solution. In order to improve the aerodynamic performances, the tanks volume must be reduced; this is attained by limiting the cruise speed to 0.75 Mach and limiting the range to continental flights with a maximum of 2500 nm. With these requirements, the fuel tanks are compatible with aerodynamic performances and structural and aeroelastic requirements, including flutter, even though a more specific analysis is needed. A design procedure has implemented to define the best configuration by making use of in house software properly set up to design PrandtlPlane aircraft. Thanks to these tools, the computation time is so reduced that several aerodynamic analyses on 3d configurations have been conducted.

Preliminary economic analysis shows that, nowadays, it is not affordable the real production and marketing of an LH2 configuration: in fact, DOC cost is higher in regard to kerosene-propelled aircraft because of the high costs of liquid hydrogen production.

References

1. Air Travel—Greener by design: The challenge. www.greenerbydesign.org.uk
2. Beccasio, N., Tesconi, M.: Progetto preliminare di un velivolo non convenzionale prandlplane propulso ad idrogeno liquido. Master's thesis, University of Pisa (2009)
3. Beltramo, M.N., Trapp, D.L., Kimoto, B., Daniel, P.: Parametric study of transport aircraft systems cost and weights. Technical report, NASA (1977)
4. Cavallaro, R., Frediani, A.: A code for shape generation and aerodynamic design of aircraft. In: Buttazzo, G., Frediani, A. (eds.) Variational Analysis and Aerospace Engineering II: Mathematical Challenges for Aerospace Design. Springer, Berlin (2012)
5. Divoux, N., Frediani, A.: The lifting system of a PrandtlPlane, Part 2: preliminary study on flutter characteristics. In: Buttazzo, G., Frediani, A. (eds.) Variational Analysis and Aerospace Engineering II: Mathematical Challenges for Aerospace Design. Springer, Berlin (2012)
6. Fass, R.: Cryoplane, Flugzeuge mit Wasserstoffantrieb. In: Airbus Deutschland Cryoplane presentation (2001)
7. Frediani, A., Cipolla, V., Rizzo, E.: The PrandtlPlane configuration: overview on possible applications to civil aviation. In: Buttazzo, G., Frediani, A. (eds.) Variational Analysis and Aerospace Engineering II: Mathematical Challenges for Aerospace Design. Springer, Berlin (2012)
8. Frediani, A., Ghiringhelli, G.L., Terraneo, M., Dal Canto, D.: The lifting system of a PrandtlPlane, Part I: design and analysis of a light alloy structural solution. In: Buttazzo, G., Frediani, A. (eds.) Variational Analysis and Aerospace Engineering II: Mathematical Challenges for Aerospace Design. Springer, Berlin (2012)
9. Pohl, H., Malychev, V.: Hydrogen in future civil aviation. Int. J. Hydrog. Energy **22**, 1061–1069 (1997)
10. Raymer, D.P.: Aircraft Design: A Conceptual Approach. AIAA, Washington (1989)
11. Roskam, J.: Airplane Design. Roskam Aviation and Corporation (1987)

12. Sanchez, O.: Ground operations and airport facilities for a liquid hydrogen. Fuelled Aircraft—Cryoplane. Unpublished Thesis, Cranfield University
13. Sefain, M.: Hydrogen aircraft concepts and ground support. PhD thesis, Cranfield University (2006)
14. Sefain, M., Jones, R.: Cryoplane project. Technical report, Unconventional Aircraft Configurations. Task Final Report (2001)
15. Slingerland, R.: Aircraft with LH2 propulsion. In: Torenbeek, E., Deconinck, H. (eds.) Von Karman Institute of Fluid Dynamics, Innovative Configurations and Advanced Concepts for Future Civil Aircraft (2005)
16. Svensson, F.: Potential of reducing the environmental impact of civil subsonic aviation by using liquid hydrogen. PhD thesis, Cranfield University (2005)
17. Torenbeek, E.: Synthesis of Subsonic Airplane Design. Delft University Press, Rotterdam (1972)
18. Liquid hydrogen fuelled aircraft—system analysis. Technical report, Airbus Deutschland (2003)

Aeroacousto-Elastic Modeling for Response Analysis of Helicopter Rotors

Massimo Gennaretti and Giovanni Bernardini

1 Introduction

Helicopter rotors in steady flight are characterized by the generation of vibratory loads and acoustic disturbance. A passenger boarding a helicopter for the first time is undoubtedly struck with the level of vibrations (and noise) that arises within the cabin. It is much higher than that experienced within airplanes and makes helicopter rides significantly less comfortable. The fuselage vibrations caused by the vibratory loads from the main rotor also have a negative impact both on the fatigue-life of the structure and on the functionality of onboard instruments, making their reading difficult, too.

On the other hand, for an external observer, the passage of an helicopter is readily noticed because of the typical tonal noise emitted. It has characteristic frequencies that depend on the performed maneuver and in some flight conditions may produce high levels of acoustic annoyance, insomuch as to make the environmental and public acceptance of helicopters a critical issue.

All this explains why the reduction of both vibratory rotor hub loads and noise emission is one of the most critical (and challenging) goals in the design of new-generation helicopters. In this framework, the availability of reliable simulation tools for the prediction of helicopter rotor noise and vibrations is of primary importance.

The prediction of the vibratory loads transmitted by the main rotor to the fuselage requires the application of an accurate aeroelastic solver derived from coupling a blade structural dynamic model that takes into account both the strong coupling between bending and torsion degrees of freedom and the effect of the significant

M. Gennaretti (✉) · G. Bernardini
University Roma Tre, Via Vasca Navale 79, 00146 Rome, Italy
e-mail: m.gennaretti@uniroma3.it

G. Bernardini
e-mail: g.bernardini@uniroma3.it

G. Buttazzo, A. Frediani (eds.), *Variational Analysis and Aerospace Engineering: Mathematical Challenges for Aerospace Design*, Springer Optimization and Its Applications 66,
DOI 10.1007/978-1-4614-2435-2_2,

deformations usually experienced by slender structures, with an unsteady aerodynamics model that is able to take into account the complex interaction effects arising among the blades. It is a common solution procedure to make the rotor aeroelastic response analysis follow an initial evaluation of the control settings (blade collective and cyclic pitch, shaft angle) through a helicopter trimming process, although a simultaneous evaluation of helicopter trim state and rotor response could be achieved. Once the pressure over the rotor blades is determined from the aeroelastic solver, radiated noise may be computed through a pressure propagation formulation. It is strongly affected by the aerodynamic solution that, therefore, plays a fundamental role both for vibratory loads and acoustic analysis. This is particularly true for the analysis of those flight configurations where blade-vortex interactions, BVI, produce blade impulsive loads and corresponding extremely annoying acoustic effects.

In the last decades, the prediction of helicopter rotor aeroelastic response aimed at examining both emitted noise and vibratory hub loads has been the objective of many researchers operating in the field of rotorcraft. Typically, prediction tools developed to analyze rotor aeroelasticity are based on aerodynamic models that couple 2-D airfoil-theory loads with wake inflow from a 3-D free-wake solver. If blade pressures are needed for aeroacoustic computations, these are usually determined from a different aerodynamic tool that uses blade deformations as an input. An example of this kind of approach is the study aimed to aeroelastic applications presented in Ref. [1], where a multiple-trailer vortex model is used in the free-wake analysis that predicts the wake inflow to be coupled with an aerodynamic load model based on thin airfoil theories. A similar approach is considered in Ref. [2] for aeroacoustic purposes. The combined use of a dual vortex free-wake code with a 2-D aerodynamics code is applied in Refs. [3] and [4] for the aeroelastic and aeroacoustic analysis of rotors aimed to vibration and noise reduction. In Ref. [5] the aerodynamic analysis of rotors in BVI conditions consists of a four-step procedure. An initial rotor trim code based on 2-D aerodynamics is followed by a vortex-lattice free-wake analysis that is then coupled with a roll-up model in order to identify the higher-intensity vortex structures. In turn, these are considered as the interacting vortices in a pressure predictor code based on a 2-D solver. Predictions of vibratory hub loads through an aeroelastic tool combining unsteady 2-D section load models with wake inflow from free-wake analysis are presented in Ref. [6]. An extensive review on tools available for vibratory hub loads prediction is given in Ref. [7].

The aim of this chapter is the presentation of the aeroacousto-elastic simulation tool for helicopter rotors developed in the last years at the Department of Mechanical and Industrial Engineering of University Roma Tre. The models applied for the description of rotor structural dynamics, aerodynamics and aeroacoustics will be outlined in detail, along with the strategy used for their numerical integration. The importance of the role played by the unsteady aerodynamic model in such a kind of solvers will be examined by the numerical investigation. Aeroelastic solvers developed for helicopter and tiltrotor analysis have been presented in Refs. [8–10], the boundary integral equation approach for the velocity potential introduced to predict unsteady aerodynamics of rotors with significant interaction effects (like BVI) has

been described in Ref. [11], while reduced-order aerodynamic models developed for state-space aeroelasticity have been presented in Refs. [12–15]. Applications to rotor aeroacoustic analysis are given in Ref. [16], where the examination of the impact of the aeroelastic modelling on radiated noise prediction is discussed in details.

2 Blade Structural Modeling

A beam-like model is applied to describe the structural dynamics of rotor blades. It is based on the nonlinear bending-torsion formulation presented in Ref. [19] that is valid for straight, slender, homogeneous, isotropic, nonuniform, twisted blades, and undergoing moderate displacements. In this model, second-order terms are retained in the equations after application of an ordering scheme dropping third-order terms (with respect to bending slope) not contributing to damping. The radial displacement is eliminated from the set of equations by solving it in terms of local tension, and thus the resulting structural operator consists of a set of coupled nonlinear differential equations governing the bending of the elastic axis and the blade torsion [20]. Specifically, for $v(x,t)$ denoting the lead-lag bending (lying in the plane of rotation), $w(x,t)$ denoting the flapwise bending, and $\phi(x,t)$ denoting the cross-section torsion about the deformed elastic axis, the blade dynamics is governed by the following set of three dimensionless integro-differential equations [19]:

$$\begin{aligned}
&\left[\left(\Lambda_2 - \Lambda_{21}\sin^2\theta\right)v''\right]'' + \left[\frac{\Lambda_{21}}{2}w''\sin(2\theta)\right]'' \\
&\quad + \left[\Lambda_{21}\left(\phi w''\cos(2\theta) - \phi v''\sin(2\theta)\right)\right]'' - \left[e_A T\cos(\theta+\phi)\right]'' - (Tv')' \\
&\quad = L_v(\mathbf{x}) + p_y(\mathbf{x}) - q_z'(\mathbf{x}) \qquad (1)\\
&\left[\left(\Lambda_1 + \Lambda_{21}\sin^2\theta\right)w''\right]'' + \left[\frac{\Lambda_{21}}{2}v''\sin(2\theta)\right]'' \\
&\quad + \left[\Lambda_{21}\left(\phi v''\cos(2\theta) + \phi w''\sin(2\theta)\right)\right]'' - \left[e_A T\sin(\theta+\phi)\right]'' - (Tw')' \\
&\quad = L_w(\mathbf{x}) + p_z(\mathbf{x}) + q_y'(\mathbf{x}) \qquad (2)\\
&\Lambda_{21}\left[\left(w''^2 - v''^2\right)\sin\theta\cos\theta + v''w''\cos(2\theta)\right] - (\kappa\phi')' - \left[K^2T(\phi+\theta)'\right]' \\
&\quad - e_A T(w''\cos\theta - v''\sin\theta) \\
&\quad = M_\phi(\mathbf{x}) + q_x(\mathbf{x}) + v'q_y(\mathbf{x}) + w'q_z(\mathbf{x}) \qquad (3)
\end{aligned}$$

where the tension, T, is given by

$$T = \int_x^1 p_x(\mathbf{x})\,\mathrm{d}\bar{x} \qquad (4)$$

and $(\,)'$ denotes differentiation with respect to the dimensionless spanwise coordinate. In the equations above, dimensionless lengths are related to the blade radius, R,

while dimensionless time coincides with blade azimuth position. The bending equations (1) and (2) have been obtained by dividing by the factor $m_0\Omega^2 R$, while the torsion equation (3) is the result of division by the factor $m_0\Omega^2 R^2$, with m_0 denoting the reference blade mass per unit length, and Ω denoting the angular velocity of the blade. In addition, Λ_1 and Λ_2 are the dimensionless flap and lead-lag bending stiffnesses, respectively, $\Lambda_{21} = \Lambda_2 - \Lambda_1$, κ is the dimensionless torsion rigidity, K is the square of the ratio between the blade cross-section polar radius of gyration and the blade cross-section mass radius of gyration, while e_A denotes the distance between tensile axis and elastic axis [19, 20]. The blade loading terms due to section inertial forces, p_x, p_y, p_z, section inertial moments, q_x, q_y, q_z, and aerodynamic loads per unit length, L_v, L_w, M_ϕ, are functions of the blade section degrees of freedom, $\mathbf{x} = \{v, w, \phi\}$. Note that in (1)–(3) blade precone angle, hinge offset, torque offset, and mass offset, if present, would appear in the description of the distributed inertial and aerodynamic loads.

3 Rotor Aerodynamics Modeling

The aerodynamics of helicopters is significantly affected by the interactions among main rotor, fuselage, and tail rotor. However, in many configurations of interest, a crucial role is played by the interactions between rotor blades and rotor wake. These phenomena are known as blade-vortex interactions (BVI) and include blade passages close to the wake, as well as blade-wake impacts that produce impulsive pressures on the blade surface. They strongly contribute to the vibratory loads transmitted to the airframe and generate extremely annoying acoustic effects. Therefore, a simulation tool applied for the optimal design of a new-generation helicopter has to be able to predict BVI occurrence and corresponding aeroelastic and aeroacoustic effects. In view of this, a boundary integral formulation for potential flows suited for the prediction of strong aerodynamic interaction effects has been presented in Ref. [11]. It is a development of the formulation introduced in Ref. [17] and further extended to rotors in forward flight in Ref. [18]. A brief outline of the potential-flow formulation suited for BVI analysis is given in the following.

For the unsteady, incompressible flow around a helicopter rotor, the velocity potential field, φ, may be described through the following boundary integral representation [17, 18]:

$$\varphi(\mathbf{x}, t) = \int_{S_B} \left(G \frac{\partial \varphi}{\partial n} - \varphi \frac{\partial G}{\partial n} \right) \mathrm{d}S(\mathbf{y}) - \int_{S_W} \Delta\varphi \frac{\partial G}{\partial n} \, \mathrm{d}S(\mathbf{y}) \tag{5}$$

where S_B and S_W denote blades and wake surfaces, respectively, while $G = -1/4\pi r$ is the unit-source solution of the 3-D Laplace equation, with $r = \|\mathbf{y} - \mathbf{x}\|$. The impermeability boundary condition on S_B yields $\partial\varphi/\partial n = \mathbf{v} \cdot \mathbf{n}$, with $\mathbf{v}$ representing the body velocity and $\mathbf{n}$ its outward unit normal. In addition, $\Delta\varphi$ is the potential jump across the wake surface that is known from the past history of the potential discontinuity at the trailing edge of the corresponding body through the

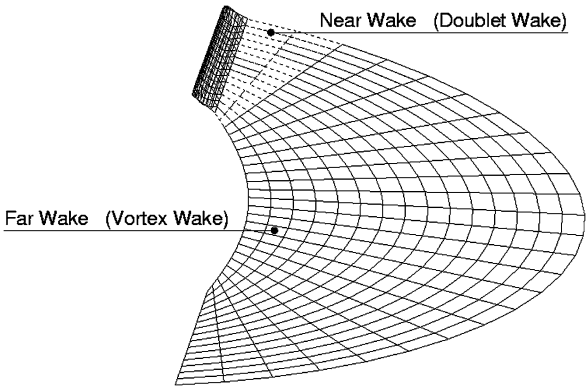

Fig. 1 Far-wake and near-wake decomposition

Kutta–Joukowski condition, i.e., $\Delta\varphi(\mathbf{x}_W, t) = \Delta\varphi(\mathbf{x}_W^{\mathrm{TE}}, t - \vartheta)$, with $t - \vartheta$ denoting the instant when the wake material point currently in $\mathbf{x}_W$ emanated from the trailing edge point $\mathbf{x}_W^{\mathrm{TE}}$ (see Refs. [17] and [18] for details). Equation (5) shows that the potential field is generated by a distribution of sources and doublets over the blades, along with distribution of doublets over the wake surface. However, using the boundary element method for the numerical solution of this equation causes instabilities to arise when wake panels come too close to or impinge on the body surfaces [11]. Thus, this formulation cannot be applied as it is to examine the problem under consideration.

The boundary integral approach proposed in Ref. [11] overcomes this limitation. It introduces the decomposition of the potential field into an incident field, φ_I, and a scattered field, φ_S. The scattered potential is generated by sources and doublets over the body surfaces and by doublets over the wake portion that is very close to the trailing edge from which emanated (near wake, S_W^N). The incident potential is generated by the doublets over the complementary wake region that compose the far wake, S_W^F (see Fig. 1). This is the wake portion that may come in contact with other blades. The scattered potential is discontinuous across S_W^N, whereas the incident potential is discontinuous across S_W^F. Hence, as demonstrated in Ref. [11], for $\varphi = \varphi_I + \varphi_S$, the scattered potential is obtained by

$$\varphi_S(\mathbf{x}, t) = \int_{S_B} \left[G(\chi - \chi_I) - \varphi_S \frac{\partial G}{\partial n} \right] \mathrm{d}S(\mathbf{y}) - \int_{S_W^N} \Delta\varphi_S \frac{\partial G}{\partial n} \, \mathrm{d}S(\mathbf{y}) \tag{6}$$

where $\chi = \mathbf{v} \cdot \mathbf{n}$ and $\chi_I = \mathbf{u}_I \cdot \mathbf{n}$, with the velocity induced by the far wake, $\mathbf{u}_I$, given by

$$\mathbf{u}_I(\mathbf{x}, t) = \nabla\varphi_I(\mathbf{x}, t) = -\nabla \int_{S_W^F} \Delta\varphi_S\left(\mathbf{y}_W^{\mathrm{TE}}, t - \vartheta\right) \frac{\partial G}{\partial n} \, \mathrm{d}S(\mathbf{y}) \tag{7}$$

The incident potential affects the scattered potential through the induced-velocity term, χ_I, and, in turn, the scattered potential affects the incident potential by its trailing-edge discontinuity that is convected along the wake and yields the intensity of the doublet distribution over the far wake.

Obtaining the discrete form of (7) by using N panels over the far wake and recalling the vortex-doublet equivalence, the incident velocity field may be evaluated through the following expression:

$$\mathbf{u}_I(\mathbf{x},t) \approx -\sum_{k=1}^{N} \Delta\varphi_S\left(\mathbf{y}_{W_k}^{\mathrm{TE}}, t-\vartheta_k\right) \int_{C_k} \nabla_{\mathbf{x}} G \times \mathrm{d}\mathbf{y} \tag{8}$$

where C_k denotes the contour line of the kth far wake panel, $\mathbf{y}_{W_k}^{\mathrm{TE}}$ is the trailing edge position where the wake material point currently in $\mathbf{y}_{W_k}$ emanated at time $t-\vartheta_k$, and $\nabla_{\mathbf{x}}$ denotes gradient operator with respect to the variable $\mathbf{x}$. This equation represents the velocity field given by the Biot–Savart law applied to the vortices having the shape of the far wake panel contours and intensity $\Delta\varphi_S(\mathbf{y}_{W_k}^{\mathrm{TE}}, t-\vartheta_k)$. Equation (8) is applied to evaluate both the term χ_I in (6) and, once extended to the whole wake, the velocity field in the free-wake distortion analysis, if required.

The final step of the formulation consists of introducing in (8) a finite-thickness vortex model that assures a regular distribution of the induced velocity within the vortex core, and thus a stable and regular solution even in body-vortex impact conditions [11]. The description of the wake influence through the use of finite-core vortices is a way to include also diffusivity and vortex-stretching effects that, otherwise, would not be taken into account in a potential-flow aerodynamic formulation (see Refs. [21] and [22] for details on this issue).

Equation (6) is solved numerically by boundary elements, i.e., by dividing S_B and S_W^N into quadrilateral panels, assuming φ_S, χ, χ_I, and $\Delta\varphi_S$ to be piecewise constant (zeroth-order boundary element method, BEM) and imposing that the equation be satisfied at the center of each body element (collocation method) [11].

Once the potential field is known, the Bernoulli theorem yields the pressure distribution (see Appendix A), and hence blade loads may be evaluated through integration.

3.1 Aerodynamic Loads From Airfoil Theories

In several aeroelastic prediction tools commonly used in rotorcraft applications, the blade aerodynamic forcing terms are obtained as radial integration of the loads given by sectional aerodynamics models. These are typically derived from airfoil unsteady aerodynamics theories, corrected with wake inflow to take into account the three-dimensional effects due to wake vortices.

For a thin, straight airfoil moving in an incompressible flow, following the Greenberg theory [23] (which is the extension of the Theodorsen theory [24] to pulsating airstream), it is possible to determine the aerodynamic force acting on it by combining the noncirculatory lift, L_{nc}, orthogonal to the chord with the circulatory lift, L_c, directed along the normal to the relative wind (see, for instance, Ref. [20]). Specifically, for ρ denoting the air density and b denoting the airfoil semi-chord length,

the noncirculatory lift is expressed as

$$L_{nc}(t) = \pi\, \rho\, b^2\, \dot{v}^n_{1/2} \tag{9}$$

where $\dot{v}^n_{1/2}$ denotes the time derivative of the normal component of the relative wind evaluated at the airfoil mid point (positive upwards). The circulatory lift, which in practical applications is the most relevant load contribution, is given by the expression

$$L_c(t) = 2\pi\, \rho\, b\, V\, \mathscr{F}^{-1}\left[C(k)\tilde{v}^n_{3/4}\right] \tag{10}$$

where V denotes the relative wind velocity, $\mathscr{F}$ denotes Fourier transformation, and $\tilde{v}^n_{3/4} = \mathscr{F}(v^n_{3/4})$ with $v^n_{3/4}$ representing the normal component of the relative wind evaluated at the airfoil 3/4-chord point. In addition, $C(k)$ is the lift deficiency (complex) function defined by Theodorsen [24] in terms of the reduced frequency, $k = \omega\, b/\bar{V}$, where ω is the variable in the Fourier domain, and $\bar{V}$ is the mean (or reference) value of V which is responsible for the shed vorticity convection (see Ref. [25] for a detailed analysis of the effects of nonuniform convection of the shed vorticity along the wake). For a harmonic $v^n_{3/4}$ input, $C(k)$ defines gain and phase shift of the L_c/V harmonic response. The set of the aerodynamic loads acting on the airfoil includes also the pitching moment about the 1/4-chord point (positive clockwise for the relative wind directed from left to right), which is given by [23]

$$M_{1/4}(t) = -\frac{b}{2}L_{nc} - \pi\rho\frac{b^3}{2}\left(V\omega_a + \frac{b}{4}\dot{\omega}_a\right) \tag{11}$$

where ω_a is the angular velocity of the airfoil. Once $v^n_{1/2}, v^n_{3/4}, \omega_a$, and V are expressed in terms of the blade degrees of freedom (a major elastic contribution from blade lag may appear also in V), Eqs. (9), (10), and (11), combined with a model to take into account drag effects, may be applied to develop an aeroelastic formulation for helicopter rotors. Note that a similar unsteady aerodynamics formulation has been developed by Loewy for the airfoil of a rotor blade in hovering or axial flow [26].

Some difficulties in the application of unsteady aerodynamics airfoil theories stem from the presence of the lift deficiency function. Indeed, it is a transcendental function of the reduced frequency and hence requires the introduction of a convolution integral for the evaluation of the circulatory lift (see (10)). Alternatively, it may be expressed through a Padè approximant (see, for instance, Ref. [27]), thus avoiding the computation of convolution integrals, at the cost of introducing some aerodynamic states in the state-space realization of the aeroelastic problem. However, this problem does not appear when the so-called quasi-steady approximation of the airfoil theory is applied. It consists of assuming that very low frequencies are involved in the aeroelastic process and observing that $C(k) \to 1$ as $k \to 0$. In this case the transcendent terms in the circulatory lift disappear, and the model is considerably simplified. In many research and industry applications, the inaccuracies introduced by the quasi-steady aerodynamic model are compensated by coupling it with dynamic wake inflow models taking into account the influence of shed and

trailed vorticity coming also from aeroelastic effects. Widely used dynamic wake inflow models are those introduced by Peters and his coworkers (see, for instance, Refs. [28–30]). When the wake inflow is evaluated without considering aeroelastic effects (i.e., it is assumed to be independent of the blade degrees of freedom), it is referred to as static inflow; coupled with the quasi-steady approximation of the airfoil theory, it yields a simplified but user-friendly aerodynamic model yet frequently applied in rotorcraft solvers.

Finally, note that for the analysis of helicopter rotors operating at high forward flight speeds, the unsteady aerodynamics modeling has to take into account also the effects of the reverse flow occurring at the blade root region in the retreating side, along with the influence of the phenomenon of dynamic stall caused by the onset of large torsional airloads and vibrations on the blade [22].

4 Harmonic Balance for Aeroelastic Response Analysis

Equations (1), (2), and (3) governing the blade structural dynamics coupled with the unsteady aerodynamic load modelling yield the aeroelastic integro-differential equations to be integrated. Here, the space integration is performed through the Galerkin approach, starting from the following description of the elastic axis deformation as a linear combination of shape functions

$$v(x,t) = \sum_n q_n^v(t)\Psi_n^v(x); \qquad w(x,t) = \sum_n q_n^w(t)\Psi_n^w(x);$$

$$\phi(x,t) = \sum_n q_n^\phi(t)\Psi_n^\phi(x)$$

For instance, considering a hingeless rotor, Ψ_n^v, Ψ_n^w, and Ψ_n^ϕ, might conveniently be chosen as the bending and torsion natural modes of vibration of a nonrotating cantilever beam [20]. The resulting aeroelastic system consists of a set of nonlinear ordinary differential equations of the type

$$\mathbf{M}(t)\ddot{\mathbf{q}} + \mathbf{C}(t)\,\dot{\mathbf{q}} + \mathbf{K}(t)\,\mathbf{q} = \mathbf{f}_{\rm str}^{\rm nl}(t,\mathbf{q}) + \mathbf{f}_{\rm aer}(t,\mathbf{q}) \tag{12}$$

where $\mathbf{q}$ denotes the vector of the Lagrangian coordinates, whereas $\mathbf{M}$, $\mathbf{C}$, and $\mathbf{K}$ are time-periodic, mass, damping, and stiffness structural matrices representing the linear structural terms (note that these matrices are time-variant because of the cyclic pitch contribution). Nonlinear structural contributions are collected in the forcing vector $\mathbf{f}_{\rm str}^{\rm nl}(t,\mathbf{q})$, whereas vector $\mathbf{f}_{\rm aer}(t,\mathbf{q})$ collects the generalized aerodynamic forces. Specifically, the generalized forces related to lead-lag, flap, and torsion equations are, respectively, given by

$$f_{{\rm aer}_j}^v = \int_{x_R}^1 L_v \Psi_j^v \,{\rm d}x; \qquad f_{{\rm aer}_j}^w = \int_{x_R}^1 L_w \Psi_j^w \,{\rm d}x; \qquad f_{{\rm aer}_j}^\phi = \int_{x_R}^1 M_\phi \Psi_j^\phi \,{\rm d}x$$

where x_R is the dimensionless aerodynamic root cutout, while L_v, L_w, and M_ϕ denote, respectively, sectional force components along the bending directions and sectional torsion moment about the elastic axis. Sectional aerodynamic loads may be obtained either by integration along the airfoil contour of the pressure distribution given by the BEM solver outlined above (or any other CFD tool available) or by using the expressions in (9)–(11) derived from the airfoil theory.

Since the aim is the prediction of the aeroelastic and aeroacoustic steady periodic response during forward flight, the aeroelastic system in (12) is solved by using the harmonic balance approach. It is a methodology suitable for the analysis of the asymptotic solution (as time goes to infinity) of differential equations forced by periodic terms, as in the present case. The harmonic balance solution consists of: (i) express LHS and RHS of the aeroelastic system (Eq. (12)) in terms of their Fourier series; (ii) equate the resulting coefficients; and (iii) solve the corresponding algebraic system in terms of the unknown Fourier coefficients of the Lagrangian coordinates of the problem. Specifically, expressing $\mathbf{q}$ and $\mathbf{f} = \mathbf{f}_{\text{str}}^{\text{nl}} + \mathbf{f}_{\text{aer}}$ in terms of the Fourier series

$$\mathbf{q}(t) = \mathbf{q}_0 + \sum_{n=1}^{N} \left[\mathbf{q}_n^c \cos(\Omega_n t) + \mathbf{q}_n^s \sin(\Omega_n t) \right]$$

$$\mathbf{f}(t) = \mathbf{f}_0 + \sum_{n=1}^{N} \left[\mathbf{f}_n^c \cos(\Omega_n t) + \mathbf{f}_n^s \sin(\Omega_n t) \right]$$

(where $\mathbf{q}_n^c$, $\mathbf{q}_n^s$, $\mathbf{f}_n^c$, and $\mathbf{f}_n^s$ denote the cosine and sine components of the nth harmonic of $\mathbf{q}$ and $\mathbf{f}$, whereas $\Omega_n = n\Omega$ with Ω representing the fundamental frequency, i.e., the rotor angular velocity) and then combining with (12) yields the following representation of the aeroelastic system harmonic components:

$$[\hat{\mathbf{M}} + \hat{\mathbf{C}} + \hat{\mathbf{K}}]\hat{\mathbf{q}} = \hat{\mathbf{f}} \tag{13}$$

where $\hat{\mathbf{q}}^T = \{\mathbf{q}_0^T \ \mathbf{q}_1^{cT} \ \mathbf{q}_1^{sT} \ \mathbf{q}_2^{cT} \ \mathbf{q}_2^{sT} \ \cdots\}$ and $\hat{\mathbf{f}}^T = \{\mathbf{f}_0^T \ \mathbf{f}_1^{cT} \ \mathbf{f}_1^{sT} \ \mathbf{f}_2^{cT} \ \mathbf{f}_2^{sT} \ \cdots\}$. The matrices $\hat{\mathbf{M}}$, $\hat{\mathbf{C}}$, and $\hat{\mathbf{K}}$ in (13) come out from (12) by combining the harmonics of the $\mathbf{q}$, $\dot{\mathbf{q}}$, and $\ddot{\mathbf{q}}$ terms with the harmonics of the matrices $\mathbf{M}$, $\mathbf{C}$, and $\mathbf{K}$. In particular, if $\mathbf{M}$, $\mathbf{C}$, and $\mathbf{K}$ were constant matrices, in (13) one would have block-diagonal matrices, and each harmonic of $\mathbf{q}$ would depend only on the same harmonic of $\mathbf{f}$ (the $\mathbf{q}$-harmonics equations would be uncoupled). Instead, in the problem under examination the structural matrices are periodic, and hence, once expressed in terms of the Fourier series and combined with the harmonics of $\mathbf{q}$, $\dot{\mathbf{q}}$, and $\ddot{\mathbf{q}}$, they yield fully populated $\hat{\mathbf{M}}$, $\hat{\mathbf{C}}$, and $\hat{\mathbf{K}}$ matrices, thus coupling the algebraic equations for the unknown harmonics in $\hat{\mathbf{q}}$ (as an example, in Appendix B the $\hat{\mathbf{K}}$ matrix is given in terms of the harmonics of $\mathbf{K}$).

Because of the presence of nonlinear structural terms and of aerodynamic contributions in $\hat{\mathbf{f}}$, (13) has to be solved using an iterative procedure. To this aim, the Newton–Raphson method with a simplified Jacobian matrix is applied. Specifically,

the harmonic aeroelastic solution is obtained from convergence of the following iterative procedure (with n indicating the iteration step number):

$$\hat{\mathbf{q}}_n = [\hat{\mathbf{M}} + \hat{\mathbf{C}} + \hat{\mathbf{K}} - \hat{\mathbf{J}}_{\text{aer}}]^{-1}[\hat{\mathbf{f}}_{n-1} - \hat{\mathbf{J}}_{\text{aer}}\hat{\mathbf{q}}_{n-1}] \tag{14}$$

where $\hat{\mathbf{J}}_{\text{aer}}$ is the aerodynamic Jacobian evaluated at $\hat{\mathbf{q}} = \mathbf{0}$, while $\hat{\mathbf{f}}_{n-1}$ denotes the nonlinear structural terms and aerodynamic loads evaluated at $\hat{\mathbf{q}} = \hat{\mathbf{q}}_{n-1}$ (i.e., through the Lagrangian coordinates given by the previous iteration step). Under this assumption, the aerodynamic portion of the forcing term is equivalent to $\hat{\mathbf{f}}^0_{\text{aer}} + \hat{\mathbf{f}}^{\text{nl}}_{\text{aer}}$, with $\hat{\mathbf{f}}^0_{\text{aer}}$ denoting the aerodynamic load portion that is not influenced by the structural deformation. The introduced approximation of the Jacobian is convenient in that it implies that the matrix inversion required in (14) has to be evaluated only one time. If convergence problems arise (because of large differences between the local aerodynamic gradient and $\hat{\mathbf{J}}_{\text{aer}}$), the aerodynamic Jacobian has to be re-evaluated during the iteration process (either analytically or numerically, depending on the aerodynamic solver applied), along with the inverted global Jacobian matrix.

5 Radiated Noise Modeling

Once the aeroelastic (and hence aerodynamic) response has been determined, it is possible to proceed with the evaluation of the noise radiated by the helicopter rotor. Indeed, it requires the knowledge of blade motion, blade surface pressure distribution, and, for transonic configurations, also the flow field around it. The aeroacoustic solver applied in the prediction tool developed by the authors is based on the well-known Ffowcs Williams–Hawkings equation, written for compressible flows undergoing transformations with negligible entropy changes [31]. In this case, the pressure-density relationship is approximated by the linear term of its series expansion, namely $p' = c_0^2\tilde{\rho}$, where p' denotes the acoustic pressure disturbance, c_0 is the speed of sound in the undisturbed medium, and $\tilde{\rho}$ denotes the density perturbation.

The Ffowcs Williams–Hawkings equation represents a rearrangement of the mass and momentum conservation laws into an inhomogeneous wave equation which extends to the presence of moving bodies the field of application of the Lighthill theory for the aerodynamically generated sound. In its more general form, for $f(\mathbf{x}, t) = 0$ describing an arbitrary moving surface, the Ffowcs Williams–Hawkings equation reads

$$\begin{aligned}
&\frac{1}{c_0^2}\frac{\bar{\partial}^2 p'}{\partial t^2} - \bar{\nabla}^2 p' \\
&\quad = \frac{\bar{\partial}}{\partial t}\Big\{\big[\rho_0 v_n + \rho(u_n - v_n)\big]\delta(f)\Big\} \\
&\qquad - \frac{\bar{\partial}}{\partial x_i}\Big\{\big[\Delta P_{ij}\, n_j + \rho u_i (u_n - v_n)\big]\delta(f)\Big\} + \frac{\bar{\partial}^2}{\partial x_i \partial x_j}\Big\{T_{ij} H(f)\Big\}
\end{aligned} \tag{15}$$

where $T_{ij} = \rho u_i u_j + P_{ij} - c_0^2 \tilde{\rho} \delta_{ij}$ denotes a component of the Lighthill tensor, P_{ij} is a component of the compressive stress tensor, $\Delta P_{ij} = P_{ij} - p_0 \delta_{ij}$ with δ_{ij} representing the Kronecker delta function, while p_0 is the pressure of the undisturbed medium. In addition, the overbar denotes generalized derivative, the fluid and body velocity components are indicated by u_i and v_i, respectively, whereas the subscript n denotes projection along the outward normal to the surface $f(\mathbf{x}, t) = 0$. The Dirac and Heaviside functions on the right-hand side point out the particular nature of the different source terms: two surface terms directly related to the effects of the discontinuity $f(\mathbf{x}, t) = 0$ in the flow field and a volume term accounting for all sources acting outside $f(\mathbf{x}, t) = 0$. Generally, $f(\mathbf{x}, t) = 0$ coincides with the body surface, S_B, so that the impermeability condition $u_n = v_n$ notably simplifies (15). Furthermore, the assumptions of an inviscid flow reduces the compressive stress tensor to the scalar pressure field upon the surface, i.e., $\Delta P_{ij} = (p - p_0)\delta_{ij} = \tilde{p}\delta_{ij}$.

The use of the standard Green function approach yields the solution of (15) in terms of a boundary integral form, suitable for numerical purposes. Specifically, the aeroacoustic computational tool is based on the widely used boundary integral representation known as formulation 1A, developed by Farassat [32, 33]. Note that the presence of three different terms in (15) gives rise to three separate integral contributions known as thickness, loading, and quadrupole noise, each related to a well-defined generating noise mechanism. The thickness terms only depends on the blade geometry and the kinematics of the problem, the loading term is related to the blade airload, whereas the quadrupole source contribution accounts for the possible nonlinear effects taking place in the flow field. Generally, this last term can be reasonably neglected, provided that the blade rotational velocity is far from the transonic/supersonic range. Within formulation 1A, the thickness and loading integral terms (identified as p'_T and p'_L, respectively) assume the following forms:

$$4\pi p'_T(\mathbf{x}, t) = \int_{S_B} \left[\frac{\rho_0 \dot{v}_n}{r|1 - M_r|^2} \right]_\tau \mathrm{d}S(\mathbf{y}) + \int_{S_B} \left[\frac{\rho_0 v_n (r \dot{M}_i \hat{r}_i + c_0 M_r - c_0 M^2)}{r^2 |1 - M_r|^3} \right]_\tau \mathrm{d}S(\mathbf{y})$$

$$4\pi p'_L(\mathbf{x}, t) = \frac{1}{c_0} \int_{S_B} \left[\frac{\dot{\tilde{p}} n_i \hat{r}_i + \tilde{p} \dot{n}_i \hat{r}_i}{r|1 - M_r|^2} \right]_\tau \mathrm{d}S(\mathbf{y}) + \int_{S_B} \left[\frac{\tilde{p} n_i \hat{r}_i - \tilde{p} M_n}{r^2 |1 - M_r|^2} \right]_\tau \mathrm{d}S(\mathbf{y}) + \frac{1}{c_0} \int_{S_B} \left[\frac{\tilde{p} n_i \hat{r}_i}{r^2 |1 - M_r|^3} (r \dot{M}_i \hat{r}_i + c_0 M_r - c_0 M^2) \right]_\tau \mathrm{d}S(\mathbf{y})$$

with $\mathbf{r}$ denoting the distance between $\mathbf{x}$ and $\mathbf{y}$, $r = |\mathbf{r}|$, and $\hat{\mathbf{r}} = \mathbf{r}/r$. In addition, $\mathbf{M} = \mathbf{v}/c_0$ is the local Mach vector, $M = |\mathbf{M}|$, and $M_r = \mathbf{M} \cdot \hat{\mathbf{r}}$.

Formulation 1A is classified as a retarded-time formulation, since it requires retarded functions to be integrated over a domain corresponding to the actual rotor blade surface [32, 33]. The integrals are computed through a simple zeroth-order formulation applied to the blade surface discretized through panels, where the integral kernels are assumed to be uniform and equal to the values at the centroids.

The notation $[\ldots]_\tau$ indicates that these quantities must be evaluated at the emission time τ. Indeed, a backward-in-time integration scheme is adopted, by fixing the observer time t and computing the corresponding emission time τ at each source point by solving the root-finding problem for the equation

$$\tau - t + \frac{r}{c_0} = \tau - t + \frac{|\mathbf{x}(t) - \mathbf{y}(\tau)|}{c_0} = 0$$

For given observer time t and location $\mathbf{x}$, τ represents the instant when the contribution to the noise signature was released from $\mathbf{y}$. Due to the rotational blade motion, the root-searching scheme requires an iterative process. Nonetheless, the overall computational effort of the integration procedure is quite limited (even for very fine meshes), and the acoustic pressure time history can be achieved at each point in a handful of seconds. The availability of the noise signature in time domain enables the evaluation of the corresponding spectrum in the frequency domain (via a discrete Fourier transform) and the noise level in dB. Thus, by accounting for a prescribed map of observer locations, it is possible to draw the noise level contour plot and to appreciate the main features of the acoustic pressure field, both in terms of noise level and directivity.

6 Numerical Investigation on Aeroelastic and Aeroacoustic Responses

Here, some results from the aeroelastic/aeroacoustic formulation for helicopter rotors outlined above are presented. First, a short overview of the validation analysis of the aeroelastic solver carried out in the past is illustrated, along with an examination of the impact of the aerodynamic modeling on the simulation of helicopter rotor aeroelastic response. Then, some correlations of aeroacoustic predictions with experimental measurements are shown.

6.1 Aeroelastic Responses

First, the validation analysis concerning the rotor model examined in Ref. [34] is considered. It is a four-bladed rotor with radius $R = 4.93$ m, constant chord $c = 0.395$ m, NACA 0012 section profile, and a linear twist angle of $-8°$. The sectional rotor structural properties considered in the analysis are $\Lambda_1 = 0.008345$, $\Lambda_2 = 0.023198$, $\kappa = 0.00225$, and blade mass per unit length $m = 6.462$ kg/m (see Ref. [34] for additional details). The rotor has been examined in level flight conditions with rotational speed $\Omega = 40$ rad/s, at advance ratios $\mu = 0.15$ and $\mu = 0.3$. For the two advance ratios investigated, rotor shaft angles, and collective and cyclic pitch angles of the blades considered are those determined in Ref. [34] with linear inflow trimming.

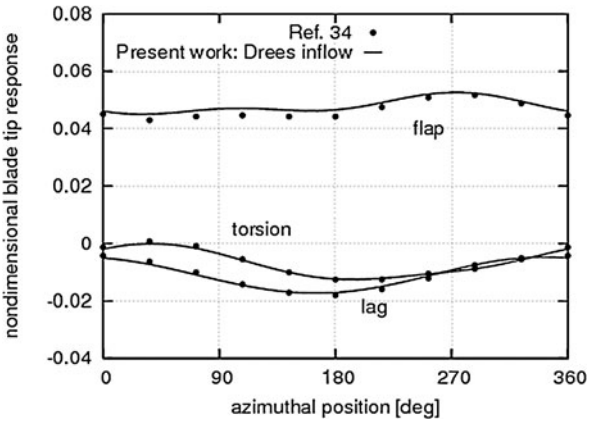

Fig. 2 Blade tip deformation for $\mu = 0.15$

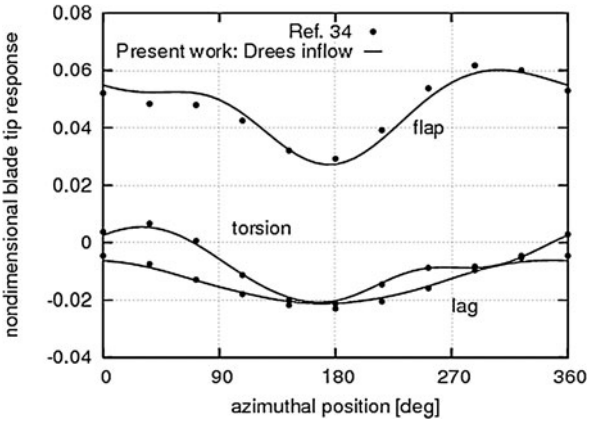

Fig. 3 Blade tip deformation for $\mu = 0.30$

Some results from the aeroelastic formulation presented here are compared with those given in Ref. [34], based on the rotor code UMARC [35] that is a well-known, widely used aeroelastic solver. It uses a nonlinear, finite-element approach for the structural analysis, whereas unsteady aerodynamic loads are given by combination of 2-D airfoil theory with wake inflow obtained either from analytical models or from free-wake analysis [6, 35]. In this case, in order to describe the aerodynamic loads similarly to Ref. [34], the sectional quasi-steady aerodynamic theory with linear Drees wake inflow is applied (see also Ref. [8]). Figures 2 and 3 show that, for both advance ratios, the blade tip deformations (namely, lag, flap, and torsion) predicted by the present formulation are in good agreement with those presented in Ref. [34]. The same level of agreement is shown in Fig. 4 in which, for $\mu = 0.3$, the comparison is presented in terms of the 4/rev vibrating loads calculated at the rotor hub (it is worth noting that the hub is forced by the combination of the loads transmitted by each rotor blade, and the harmonics of the resulting loads are multiples of the number of the rotor blades).

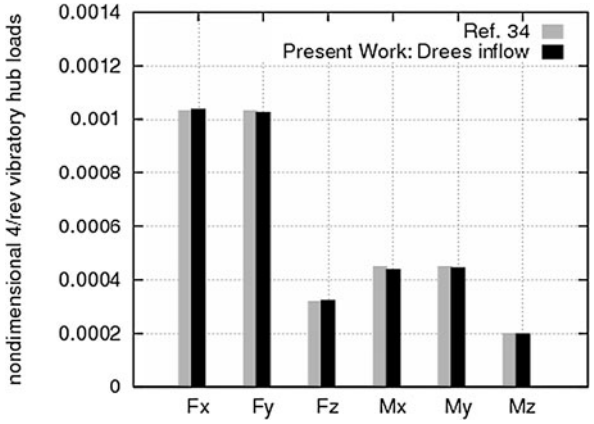

Fig. 4 4/rev hub loads for $\mu = 0.30$

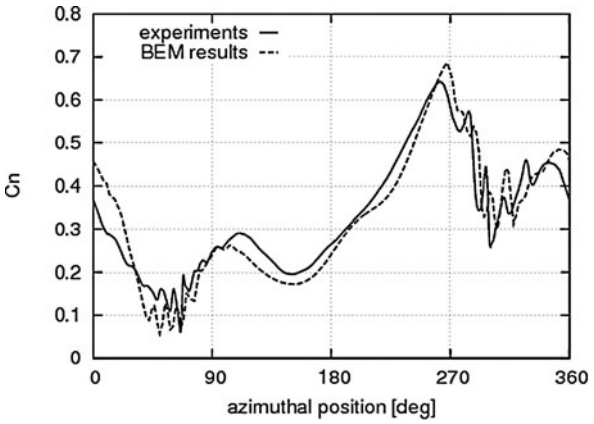

Fig. 5 C_n at blade section $r/R = 0.92$

Next, some results which concern the validation of the BEM solver outlined in Sect. 3 are shown. These have already been presented in Ref. [8] and correlate numerical predictions from the BEM tool with experimental results obtained within the European Project HELISHAPE [36]. The rotor considered is the four-bladed EC/ONERA 7A main rotor, tested at the DNW wind tunnel [36]. It has rectangular blades with aspect ratio equal to 15 and is examined in 6°-descent forward flight condition, with rotational speed $\Omega = 101$ rad/s, advance ratio $\mu = 0.166$, and rotational tip Mach number $M_\Omega = 0.615$ (related to HELISHAPE Datapoint 70). Figures 5 and 6 show the comparisons between measurements and free-wake BEM predictions in terms of the normal force coefficient, C_n, respectively at blade sections $r/R = 0.92$ and $r/R = 0.98$. These results demonstrate that the presented BEM solver has a good capability of predicting unsteady airloads, with inclusion of BVI effects that are well captured in terms of both oscillation amplitude and azimuth location occurrence.

Now, the assessment of the effects of the aerodynamic model on the aeroelastic response simulation is analyzed. Specifically, the attention is focused on the

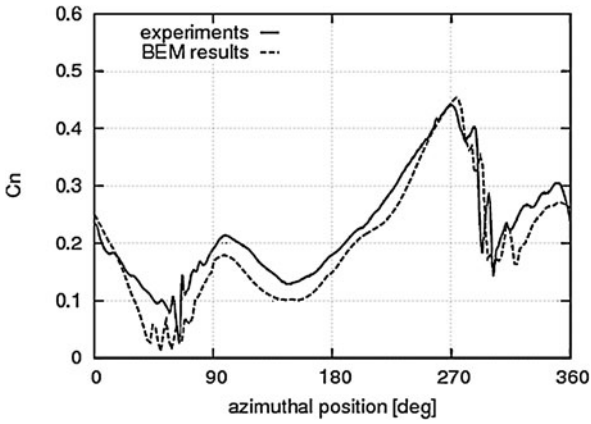

Fig. 6 C_n at blade section $r/R = 0.98$

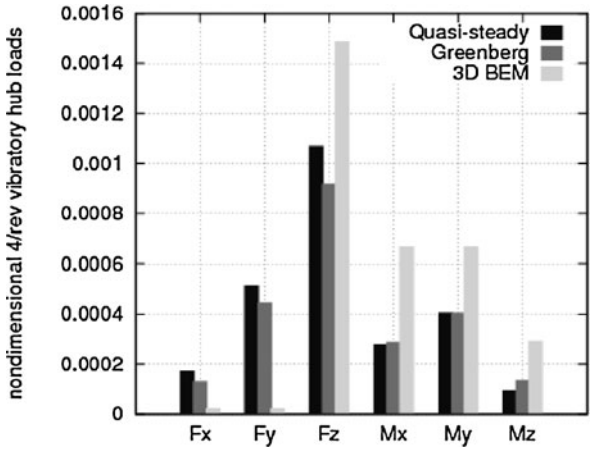

Fig. 7 4/rev hub loads for $\mu = 0.15$

prediction of the vibratory loads arising at the hub of the model rotor described in Ref. [34]. These have been carried out through: (i) sectional quasi-steady aerodynamics with wake inflow from the BEM solver with a prescribed wake shape, (ii) sectional unsteady aerodynamics (Greenberg's theory) with wake inflow from the BEM solver with a prescribed wake shape, and (iii) unsteady aerodynamic loads given directly from the 3-D BEM potential formulation with a prescribed wake shape. In these analyses, the prescribed wake consists of the surface swept by the trailing edges of the blades during their motion. Note that, using the expression in Eq. (8), the wake effect is equivalent to that of a vortex-lattice with the presence of both trailed and shed vortices: the effects of shed vorticity is not taken into account in the evaluation of the wake inflow used in Greenberg's theory.

For advance ratio $\mu = 0.15$, Fig. 7 depicts the comparison among the results from the three aerodynamic models considered in terms of vibratory hub loads, while the results for $\mu = 0.30$ are given in Fig. 8. These results demonstrate that, at least for the prediction of the vibratory hub loads, the aerodynamic quasi-steady approxima-

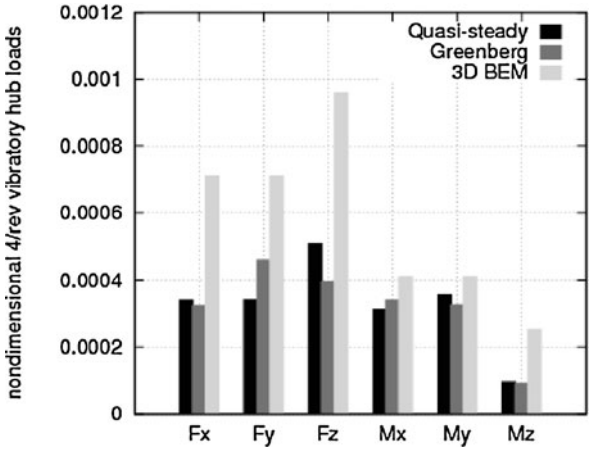

Fig. 8 4/rev hub loads for $\mu = 0.30$

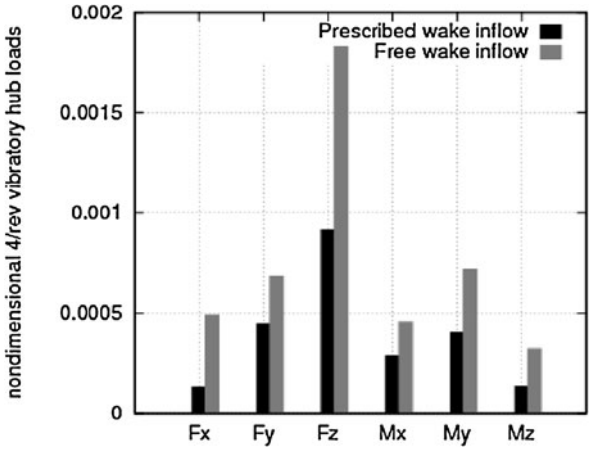

Fig. 9 4/rev hub loads for $\mu = 0.15$

tion combined with wake inflow from a 3-D solver gives results that are comparable with those from the application of the complete unsteady section theory (i.e., with inclusion of lift deficiency function effects). Rather, different results come from the evaluation of loads directly through the BEM solver, thus proving the relevant contribution due to 3-D and interaction effects.

Finally, fixing the sectional Greenberg aerodynamic model, Figs. 9 and 10 show the influence of the wake inflow model applied on the predicted hub loads. While for $\mu = 0.30$, wake inflows from prescribed wake shape and from free-wake analysis give different but comparable hub loads, for $\mu = 0.15$, they yield dramatically different hub loads predictions. This is due to the fact that the role of the wake is crucial when the wake remains in the vicinity of the rotor ($\mu = 0.15$ case), whereas it tends to decrease as the wake rapidly goes far from the rotor ($\mu = 0.30$ case). This confirms the great attention that has to be paid on the definition of the wake contribution in helicopter rotor aeroelastic analyses.

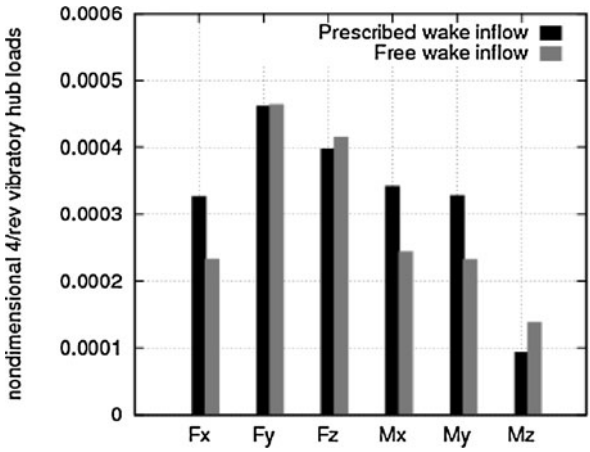

Fig. 10 4/rev hub loads for $\mu = 0.30$

6.2 Aeroacoustic Responses

Here, the present formulation is applied to the aeroacoustic analysis helicopter rotors in BVI conditions. The rotor considered is the above-mentioned four-bladed EC/ONERA 7A main rotor analyzed within the European Project HELISHAPE [36], and the flight condition examined is the 6°-descent forward flight (HELISHAPE Datapoint 70). The results discussed in the following have already been presented by the authors in Ref. [11]. The numerical analysis has been performed using the azimuthal step $\Delta\psi = 1.33°$ and including two wake spirals. In BVI conditions the aerodynamic field and the corresponding radiated noise are strongly dependent on the shape of the wake and on its distance from the rotor blades, and thus an accurate prediction of the distorted wake is essential. Figures 11 and 12 depict rear and side view, respectively, of the distorted wake geometry given by the present free-wake analysis. These figures show clearly that during the descent flight the wake remains close to the rotor disk, thus inducing severe blade/wake impingement. In addition, for the sake of clarity, Fig. 13 depicts the wake of only one blade and shows the impact between one rotor blade and the wake generated by the preceding blade. This figure concerns the azimuth position $\psi = 65°$ and indicates that the strongest BVI occurs at positions around $\psi = 60°$ in the advancing side, although close blade/wake interaction occurs also around $\psi = 310°$ in the retreating side. For this flight condition, the experimental measurements have detected strong BVI occurrence at azimuth positions around $\psi = 55°$ [36].

Once the blade pressure distribution has been obtained from the aeroelastic solver, the aeroacoustic formulation described in Sect. 5 has been applied to predict the noise emitted by the helicopter rotor. Figures 14, 15 and 16 present a comparison between the measured acoustic pressure and the acoustic time signature given by the numerical predictions concerning observers that are located 2.286 m below the rotor disk. The first one (Obs A) corresponds to the upstream microphone that is 2-m distant from the rotor hub (advancing rotor side), the second one (Obs B) corresponds to the upstream microphone located 3 m far from the rotor hub (advancing rotor

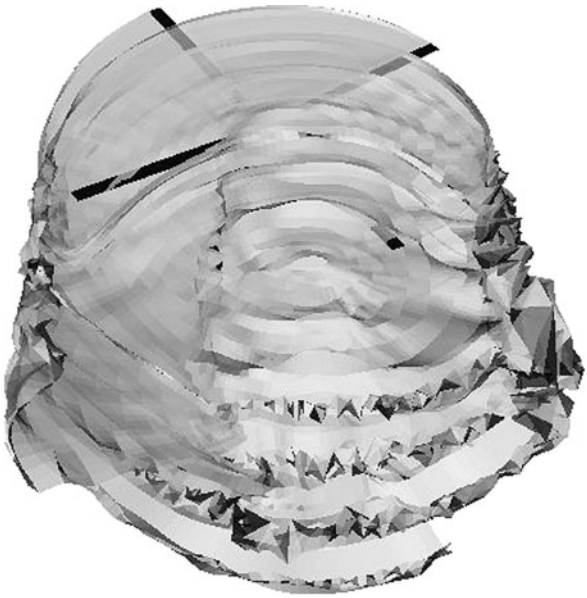

Fig. 11 Rotor 7A: rear view of computed wake geometry

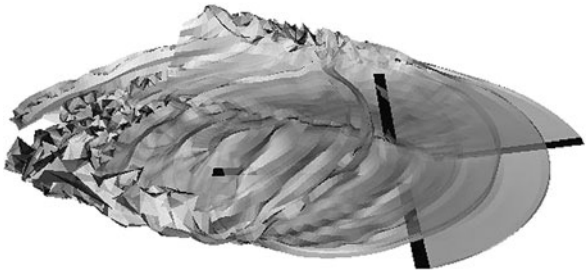

Fig. 12 Rotor 7A: side view of computed wake geometry

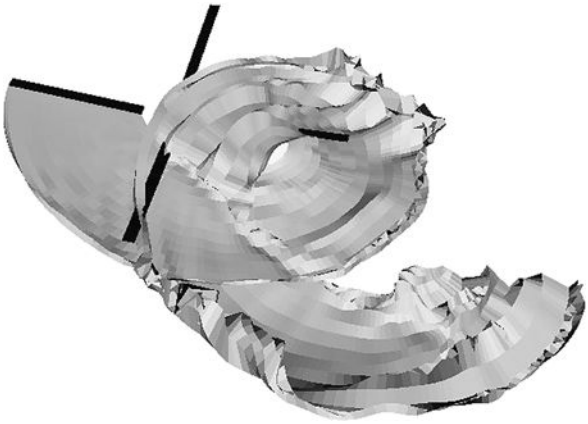

Fig. 13 Rotor 7A: blade/wake impingement

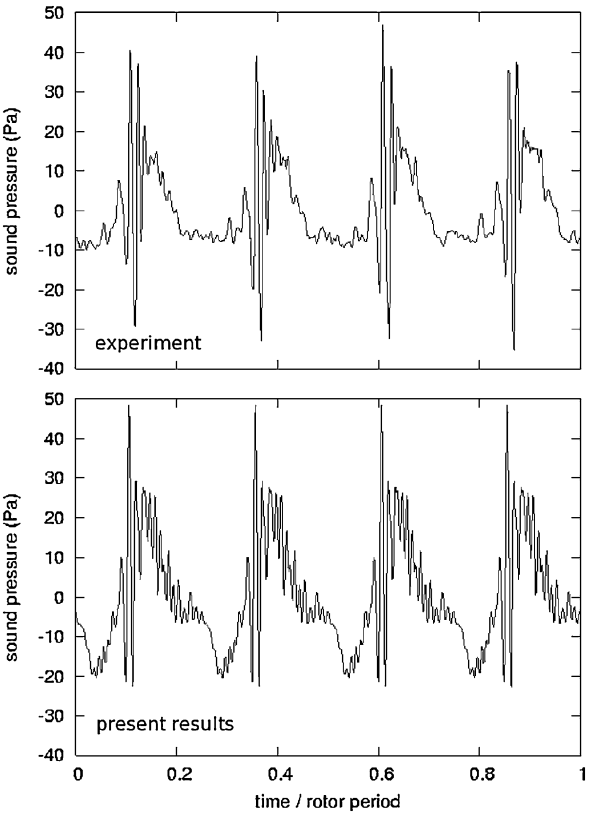

Fig. 14 Rotor 7A: experimental and numerical acoustic signature at Obs A

side), while the third one (Obs C) corresponds to the upstream microphone located 3.5 m far from the rotor hub (retreating rotor side). The acoustic correlations show that, although the numerical results present a bit more oscillating behavior with respect to the experimental data, the impulsiveness of the signal and the intensity of the peaks due to BVI are well captured by the aeroacousto-elastic solvers outlined here that, therefore, seem to be suitable tools for helicopter design applications.

Appendix A

From the decomposition of the potential field into a scattered component, φ_S, and an incident component, φ_I, introduced in Sect. 3, in a body-fixed frame of reference the Bernoulli theorem reads

$$\dot{\varphi}_S + \dot{\varphi}_I - \mathbf{v}_B \cdot (\nabla\varphi_S + \mathbf{u}_I) + \frac{\|\nabla\varphi_S + \mathbf{u}_I\|^2}{2} + \frac{p}{\rho} = \frac{p_0}{\rho} \tag{A.1}$$

where p_0 is the pressure of the undisturbed medium. In order to evaluate the pressure distribution, the expression above requires the determination of $\dot{\varphi}_I$, which is the only

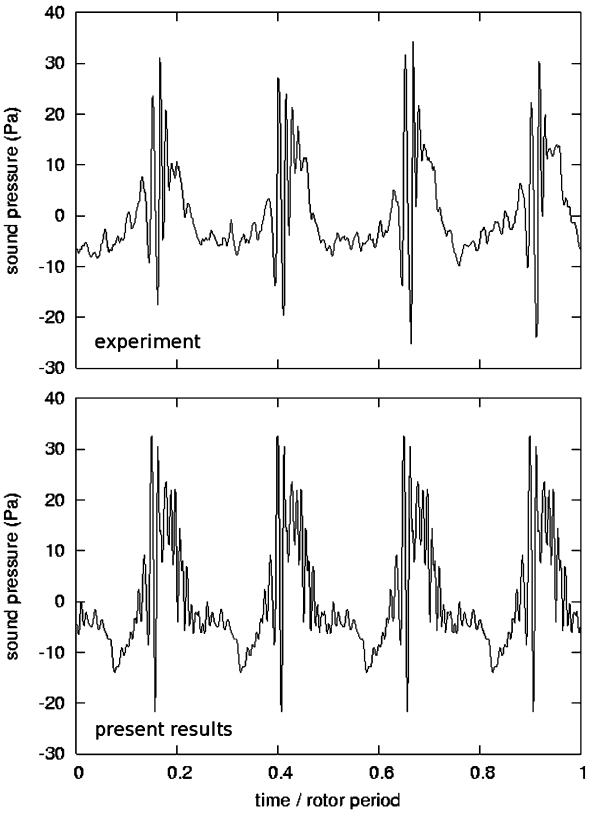

Fig. 15 Rotor 7A: experimental and numerical acoustic signature at Obs B

term not directly available from the aerodynamic formulation presented in Sect. 3. The incident potential (and the corresponding time derivative) could be obtained from the doublet distribution over the far wake, S_W^F, using the following integral expression (see also Eq. (7)):

$$\varphi_I(\mathbf{x},t) = -\int_{S_W^F} \Delta\varphi_S\big(\mathbf{y}_W^{\mathrm{TE}}, t-\vartheta\big)\frac{\partial G}{\partial n}\,\mathrm{d}S(\mathbf{y}) \tag{A.2}$$

that, dividing the wake into panels, $S_{W_k}^F$, is approximated as

$$\varphi_I(\mathbf{x},t) \approx -\sum_{k=1}^{N} -\Delta\varphi_S\big(\mathbf{y}_{W_k}^{\mathrm{TE}}, t-\vartheta_k\big)\int_{S_{W_k}^F}\frac{\partial G}{\partial n}\,\mathrm{d}S(\mathbf{y}) \tag{A.3}$$

However, as already mentioned in Sect. 3, the above expression cannot be applied to those wake panels coming in contact with the body or passing very close to it (BVI occurrence), in that they become numerically unstable and yield unrealistic potential distributions.

In order to avoid this problem, for the far wake panels, the contribution to $\dot{\varphi}_I$ is obtained in the following robust and accurate way. Consider the closed vortex at

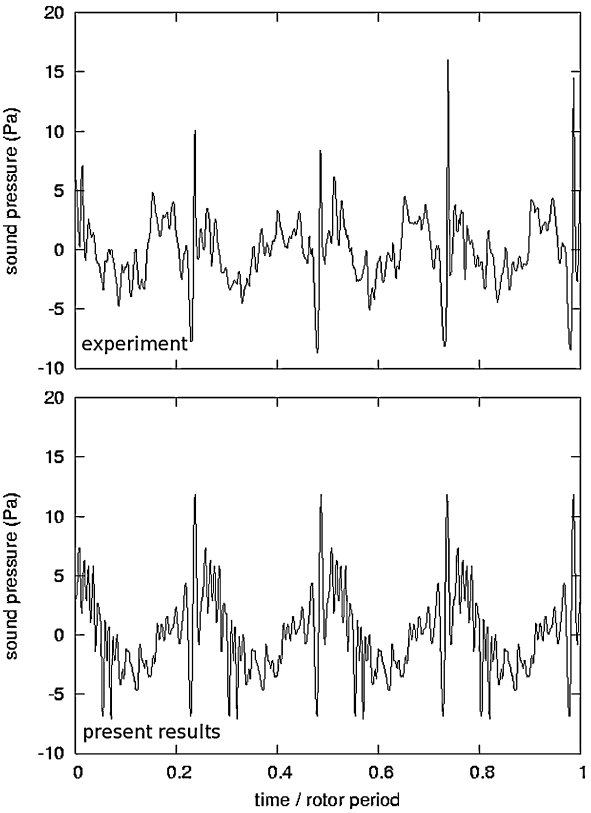

Fig. 16 Rotor 7A: experimental and numerical acoustic signature at Obs C

the contour of the kth panel of the far wake that might risk to come in contact with the body, $C_k = \partial S^F_{W_k}$, and introduce a frame of reference rigidly connected with it such that, under the assumption of undeformed wake panel, the incident potential induced by the vortex is constant in time on each point of it. Next consider a body surface point and a vortex frame point that at a given time coincide. Observing that for a generic function, $f = f(\mathbf{x}, t)$,

$$\left.\frac{\partial f}{\partial t}\right|_V = \left.\frac{\partial f}{\partial t}\right|_B + \mathbf{v}_{B-V} \cdot \nabla f$$

where $\partial f/\partial t|_V$ and $\partial f/\partial t|_B$ denote the time derivatives observed, respectively, in the vortex frame and in the body frame, while $\mathbf{v}_{B-V} = \mathbf{v}_V - \mathbf{v}_B$ is the relative velocity between the two frames at the considered point, for $f = \varphi^k_I$ (with φ^k_I denoting the incident potential due to the kth far wake vortex) and recalling that $\dot{\varphi}^k_I = 0$ in the vortex frame, it is possible to obtain, for the time derivative of the incident potential in the body frame,

$$\left.\frac{\partial \varphi^k_I}{\partial t}\right|_B = -\mathbf{v}_{B-V} \cdot \mathbf{u}^k_I \tag{A.4}$$

with $\mathbf{u}_I^k$ known from the (regularized) kth contribution in (8).

If the evaluation of the pressure is carried out within a free-wake solution, each far wake vortex is subject to deformation. In this case, the related (doublet) potential induced in the corresponding vortex frame yields an additional contribution in that it is no longer stationary, although the intensity of the doublet is time independent (indeed, it is given by the potential jump across the wake that is constant following a material point [17, 18]). Nevertheless, this contribution is not taken into account for the vortices that are close to the evaluation point, in that negligible with respect to the contribution from the term in (A.4), due to the very high induced velocity arising. Note that, a further contribution comes from the wake vortices entering the far wake region at each time step, in terms of the corresponding incident potential variation in the unit of time.

A procedure similar to that described above for the evaluation of the $\dot{\varphi}_I^k$ from a wake vortex has been applied in Ref. [37] for the evaluation of the pressure on a body induced by vortex filaments.

Appendix B

This Appendix yields the stiffness matrix appearing in the Fourier-transformed aeroelastic equations, namely (13) and (14).

It is obtained by expressing the stiffness matrix in terms of the Fourier series

$$\mathbf{K}(t) = \mathbf{K}_0 + \sum_{n=1}^{N} \left[\mathbf{K}_n^c \cos(\Omega_n t) + \mathbf{K}_n^s \sin(\Omega_n t) \right]$$

and combining it with the harmonics of $\mathbf{q}$. The result is that the harmonics of the term $\mathbf{K}(t)\mathbf{q}$ in (12) are given by $\hat{\mathbf{K}}\,\hat{\mathbf{q}}$ with

$$\hat{\mathbf{K}} = \begin{bmatrix} \mathbf{K}_0 & \frac{1}{2}\mathbf{K}_1^c & \frac{1}{2}\mathbf{K}_1^s & \frac{1}{2}\mathbf{K}_2^c & \frac{1}{2}\mathbf{K}_2^s & \cdots \\ \mathbf{K}_1^c & \mathbf{K}_0 + \frac{1}{2}\mathbf{K}_2^c & \frac{1}{2}\mathbf{K}_2^s & \frac{1}{2}(\mathbf{K}_1^c + \mathbf{K}_3^c) & \frac{1}{2}(\mathbf{K}_1^s + \mathbf{K}_3^s) & \cdots \\ \mathbf{K}_1^s & \frac{1}{2}\mathbf{K}_2^s & \mathbf{K}_0 - \frac{1}{2}\mathbf{K}_2^c & -\frac{1}{2}(\mathbf{K}_1^s - \mathbf{K}_3^s) & \frac{1}{2}(\mathbf{K}_1^c - \mathbf{K}_3^c) & \cdots \\ \mathbf{K}_2^c & \frac{1}{2}(\mathbf{K}_1^c + \mathbf{K}_3^c) & -\frac{1}{2}(\mathbf{K}_1^s - \mathbf{K}_3^s) & \mathbf{K}_0 + \frac{1}{2}\mathbf{K}_4^c & \frac{1}{2}\mathbf{K}_4^s & \cdots \\ \mathbf{K}_2^s & \frac{1}{2}(\mathbf{K}_1^s + \mathbf{K}_3^s) & \frac{1}{2}(\mathbf{K}_1^c - \mathbf{K}_3^c) & \frac{1}{2}\mathbf{K}_4^s & \mathbf{K}_0 - \frac{1}{2}\mathbf{K}_4^c & \cdots \\ \vdots & \vdots & \vdots & \vdots & \vdots & \cdots \end{bmatrix}$$

where only the contribution of the lowest two harmonics is explicitly expressed. Similar expressions are derivable for $\hat{\mathbf{M}}$ and $\hat{\mathbf{C}}$.

References

1. Lim, J.W., Yu, Y.H., Johnson, W.: Calculation of rotor blade-vortex interaction airloads using a multiple-trailer free-wake model. J. Aircr. **40**(6), 1123–1130 (2003)

2. Munsky, B., Gandhi, F., Tauszig, L.: An analysis of helicopter blade-vortex interaction noise with flight path or attitude modification. In: 58th Annual Forum of the American Helicopter Society, Montréal, Canada (2002)
3. Liu, L., Patt, D., Friedmann, P.P.: Simultaneous vibration and noise reduction in rotorcraft using aeroelastic simulation. In: 60th Annual Forum of the American Helicopter Society, Baltimore, MD (2004)
4. Patt, D., Liu, L., Friedmann, P.P.: Rotorcraft vibration reduction and noise predictions using a unified aeroelastic response simulation. J. Am. Helicopter Soc. **50**(1), 95–106 (2005)
5. Beaumier, P., Delrieux, Y.: Description and validation of the ONERA computational methods for the prediction of blade-vortex interaction noise. Aerosp. Sci. Technol. **9**, 31–43 (2005)
6. Datta, A., Chopra, I.: Validation and understanding of UH-60A vibratory loads in steady level flight. J. Am. Helicopter Soc. **49**(3), 271–287 (2004)
7. Hansford, R.E., Vorwald, J.: Dynamics workshop on rotor vibratory loads prediction. J. Am. Helicopter Soc. **31**(1), 76–87 (1998)
8. Gennaretti, M., Bernardini, G.: Aeroelastic response of helicopter rotors using a 3-D unsteady aerodynamic solver. Aeronaut. J. **110**(1114), 793–801 (2006)
9. Gennaretti, M., Molica Colella, M., Bernardini, G.: Analysis of helicopter vibratory hub loads alleviation by cyclic trailing-edge blade flap actuation. Aeronaut. J. **113**(1146), 549–556 (2009)
10. Gennaretti, M., Molica Colella, M., Bernardini, G.: Prediction of tiltrotor vibratory loads with inclusion of wing-proprotor aerodynamic interaction. J. Aircr. **47**(1), 71–79 (2010)
11. Gennaretti, M., Bernardini, G.: Novel boundary integral formulation for blade-vortex interaction aerodynamics of helicopter rotors. AIAA J. **45**(6), 1169–1176 (2007)
12. Gennaretti, M., Corbelli, A., Mastroddi, F.: A comparison among some aeroelastic models for the stability analysis of a flap-lag-torsion helicopter rotor in hover. In: 26th European Rotorcraft Forum, The Hague, The Netherlands, Sept. (2000)
13. Gennaretti, M., Greco, L.: Time-dependent coefficient reduced-order model for unsteady aerodynamics of proprotors. J. Aircr. **42**(1), 138–147 (2005)
14. Gennaretti, M., Greco, L.: Whirl flutter analysis of prop-rotors using unsteady aerodynamics reduced-order models. Aeronaut. J. **112**(1131), 233–242 (2008)
15. Gennaretti, M., Greco, L.: A multiblade aerodynamic reduced-order model for aeroelastic analysis of helicopter rotors in forward flight. In: 35th European Rotorcraft Forum, Paris, France, Sept. (2010)
16. Bernardini, G., Serafini, J., Ianniello, S., Gennaretti, M.: Assessment of computational models for the effect of aeroelasticity on BVI noise prediction. Int. J. Aeroacoust. **6**(3), 199–222 (2007)
17. Morino, L.: A general theory of unsteady compressible potential aerodynamics. NASA CR-2464 (1974)
18. Morino, L., Gennaretti, M.: Boundary integral equation methods for aerodynamics. In: Atluri, S.N. (ed.) Computational Nonlinear Mechanics in Aerospace Engineering. Progress in Astronautics & Aeronautics, vol. 146, pp. 279–320. AIAA, New York (1992)
19. Hodges, D.H., Dowell, E.H.: Nonlinear equation for the elastic bending and torsion of twisted nonuniform rotor blades. NASA TN D-7818, December (1974)
20. Hodges, D.H., Ormiston, R.A.: Stability of elastic bending and torsion of uniform cantilever rotor blades in hover with variable structural coupling. NASA TN D-8192, April (1976)
21. Morino, L., Bharadvaj, B.K.: A unified approach for the potential and viscous free-wake analysis of helicopter rotors. Vertica **12**, 147–154 (1988)
22. Leishman, J.G.: Principles of Helicopter Aerodynamics. Cambridge University Press, Cambridge (2000)
23. Greenberg, J.M.: Airfoil in sinusoidal motion in a pulsating stream. NACA TN-1326, June (1947)
24. Theodorsen, T.: General theory of aerodynamic instability and the mechanism of flutter. NACA report 496 (1935)
25. Van der Wall, B., Leishman, J.G.: The influence of variable flow velocity on unsteady airfoil behavior. J. Am. Helicopter Soc. **39**(4), 288–297 (1994)

26. Loewy, R.G.: A two-dimensional approximation of unsteady aerodynamics of rotary wings. J. Aeronaut. Sci. **24**(2), 81–92 (1957)
27. Venkatesan, C., Friedmann, P.P.: New approach to finite-state modeling of unsteady aerodynamics. AIAA J. **24**(12), 1889–1897 (1986)
28. Gaonkar, G.H., Peters, D.A.: Review of dynamic inflow modeling for rotorcraft flight dynamics. Vertica **12**(3), 213–242 (1988)
29. Peters, D.A., He, C.J.: Finite-state induced flow models, part II: three-dimensional rotor disk. J. Aircr. **32**(2), 323–333 (1995)
30. Peters, D.A.: How dynamic inflow survives in the competitive world of rotorcraft aerodynamics. J. Am. Helicopter Soc. **54**(1), 1–15 (2009)
31. Ffowcs Williams, J.E., Hawkings, D.L.: Sound generated by turbulence and surfaces in arbitrary motion. Philos. Trans. R. Soc. Lond. A **264**, 321–342 (1969)
32. Brentner, K.S.: Prediction of helicopter discrete frequency rotor noise—a computer program incorporating realistic blade motions and advanced acoustic formulation. NASA TM-87721 (1986)
33. Farassat, F.: Derivation of formulations 1 and 1A of Farassat. NASA TM-2007-214853 (2007) available at http://ntrs.nasa.gov
34. Zhang, J.: Active-passive hybrid optimization of rotor blades with trailing edge flaps. PhD thesis, Department of Aerospace Engineering, The Pennsylvania State University (2001)
35. Bir, G., Chopra, I., et al.: University of Maryland advanced rotor code (UMARC) theory manual. Technical report UM-AERO 94-18, Center for Rotorcraft Education and Research, University of Maryland, College Park, Maryland (1994)
36. Schultz, K.J., Splettstoesser, W., Junker, B., Wagner, W., Schoell, E., Arnaud, G., Mercker, E., Pengel, K., Fertis, D.: A parametric wind tunnel test on rotorcraft aerodynamics and aeroacoustics (HELISHAPE)—test documentation and representative results. In: 22nd European Rotorcraft Forum, Brighton, UK, Sept. (1996)
37. Bi, N.-P., Leishman, J.G., Crouse, G.L.: Investigation of rotor tip vortex interactions with a body. J. Aircr. **30**(6), 879–889 (1993)

Crack Extension Energy Rate and Energetic Approaches in Elastic–Plastic Fracture Mechanics

Vincenzo Binante

1 Introduction

The explanation of fracture in terms of the energy balance during the extension of a pre-existing crack began with the classic work of Griffith [9], by equating the decrease in potential energy caused by a crack extension in a linear elastic material to the surface energy of the newly created crack surfaces.

The Griffith fracture theory fails when applied to inelastic bodies. A generalization where surface energy includes crack tip plastic dissipation work was proposed by Irwin [12] in the case of small scale yielding, where the decrease in the potential energy resulting from crack extension equals the sum of the energy to create new crack surfaces and plastic work dissipation during crack extension.

Later on, Rice [21] proposed the J-integral as an extension of the Griffith's approach to inelastic solids. The starting point of Rice's considerations was the assumption that the inelastic material behavior can be treated as nonlinear elastic one; for such a material, he wrote the energy balance, during crack extension, in terms of a path-integral surrounding the crack tip, and, because the stresses can be derived from a potential, the strain energy density, which is a unique function of stresses or strains, he showed that the J-integral is path independent. In virtue of its path-independence, the J-integral is equivalent to the energy release rate.

For a cracked body $\mathscr{B}$, the J-integral represents the flow of the energy momentum tensor (also called *Eshelby tensor*) out of $\mathscr{B} - \Gamma$ across the path Γ moving with the crack tip; in [7] Eshelby gave the energy momentum tensor a physical interpretation of a generalized driving force acting on point defect (crack), and, for homogeneous elastic body, it is divergence free. This property was later used in [10] to show the path independence of the J-integral under the assumption of straight crack.

V. Binante (✉)
Mechanics of Materials and Structures Laboratory, ISTI-CNR, Via G. Moruzzi 1, 56124 Pisa, Italy
e-mail: vincenzo.binante@isti.cnr.it

G. Buttazzo, A. Frediani (eds.), *Variational Analysis and Aerospace Engineering: Mathematical Challenges for Aerospace Design*, Springer Optimization and Its Applications 66,
DOI 10.1007/978-1-4614-2435-2_3,

The path-independence made the J-integral the most used crack-tip integral in nonlinear fracture mechanics; with regard to numerical analyses of crack problems, the calculation of the energy release rate can be done by evaluating the J-integral over a path far away from crack tip, where numerical inaccuracy may occur.

Although the J-integral was derived in the context of nonlinear elasticity, its role of energy release rate is, approximately, valid for elastic–plastic material, under the assumptions that plastic zone size is small compared with a crack length and body dimension (*Small Scale Yielding*, SSY), and monotonic increasing loads are applied. In such case, Hutchinson [11] showed that the elastic J-integral controls the stress and strain fields in the plastic zone close to crack tip (J-dominance); in the framework of deformation theory of plasticity, he found asymptotic solutions for stress and strain fields in the vicinity of a crack (HRR fields) which depend on the J-integral. Hence, when SSY conditions are satisfied and proportional loading is applied, the J-integral can be considered a valid fracture parameter, providing a measure of singularity of stress and strain fields at a crack tip.

However, when applied loads are no longer growing monotonically or the plastic zone size is large, the J-integral is not path-independent, and, therefore, the meaning of energy release rate is lost. In a context of ductile fracture, many efforts were made to find new path-independent crack-tip integrals [1, 13, 19, 23].

In [1, 13], Kishimoto, Aoki, and Sakata argued that the mechanism of ductile fracture is accomplished by nucleation, growth and coalescence of voids or microcracks in a region near the crack tip called *Fracture Process Zone* (FPZ) and the energy release rate is associated with the evolution of the FPZ (translation, rotation, self-similar expansion, and distortion [1, 4]). In the case of a translation of the FPZ, the energy release rate is a new path-independent crack-tip integral $\hat{J}$, which is the sum of a line and an area integrals. Similar crack-tip integrals (denoted as $\hat{L}$, $\hat{M}$, and $\hat{I}$) had been obtained for the energy release rate associated with the rotation, self-similar expansion, and distortion of the FPZ, respectively. However, the evaluation of the crack-tip $\hat{J}$-integral (as well as $\hat{L}$, $\hat{M}$, and $\hat{I}$) requires the knowledge of the size and shape of the FPZ at each instant of the deformation process, and then the criterions appear useful only when the role of the FPZ vanishes.

In [19], Moran and Shih obtained several crack-tip integrals based on momentum and energy balances for elastic–plastic materials; furthermore, they examined the conditions under which these crack-tip integrals are (globally or locally) path-independent. In the case of bidimensional cracked bodies, they restated the energy release rate as integrals over finite domains around the crack tip (*domain integrals*); for elastic-plastic materials, the path-independence of a crack-tip integral was restored by introducing a weighting function q_1 defined over the domain of interest to be interpreted as the virtual translation of a material point due to a unit extension of the crack. In so doing, the energy release rate has been derived as a sum of a line and an area integrals and is independent on the size and shape of the domain where the weighting function is defined.

In [23], Schmitt and Kienzler extended the J-integral to materials described by an incremental theory of plasticity, by replacing the strain energy density with the

stress work density; path independence was restored by adding an area (or a volume in the case of 3-D problems) integral. So, the extended J-integral was identified as *work dissipation rate* and related to the energy release rate.

The idea to restate the crack-tip integral as sum of a path and area integrals was pursued by Chiarelli, Frediani, and Lucchesi [5, 6, 8] to extend the J-integral to elastic–plastic materials with work-hardening; from the stress-power theorem they derived an energy balance. In the framework of a general theory of plasticity for ductile materials, proposed by Lucchesi, Owen, and Podio-Guidugli [14, 16, 17], they defined a quantity named *Crack Extension Energy Rate* (CEER) and derived a closed-form expression of the stress work density [15], allowing a simpler evaluation of the CEER on numerical basis. The CEER represents the amount of the work done by the applied forces available to crack growth. The path-integral of CEER, even though the expression is similar, is totally different from the J-integral, because the J-integral depends on the current elastic state, while the path-integral of CEER depends on the whole deformation process. The area-integral of CEER takes dissipative effects due to a plastic zone near a crack tip into account. Both path and area integrals are domain-dependent, but their sum is independent of the domain.

Numerical evaluations of the CEER in 2-D cracked bodies [2, 5, 6, 8, 20] have been carried out under generic loading histories and work-hardening rules for stationary cracks; under monotonic increasing loads, the results of these studies show that the material behaves elastically and the CEER predicts the same value of the J-integral, confirming the J-dominance pointed-out in [11]. However, when a cyclic loading history is considered, the plasticity around the crack tip plays an important role even in SSY conditions; in such a case the CEER completely differs from the J-integral. The latter fails due to non-proportional stress at the crack-tip region, and the HRR fields are no longer valid; on the contrary, the CEER is able to detect some peculiar aspects of ductile fracture, such as elastic unloading, dependence on the amplitude of alternating and medium tensile stress, crack-closure effect, crack-tip constraint effect on fracture toughness.

Therefore, for elastic–plastic cracked bodies, undergoing quasi-static deformations with stationary cracks, the CEER can be considered a valid fracture criterion in Non-Linear Fracture Mechanics. Nevertheless, as shown in [2, 3], this criterion, as well as any energetic approach based on the Griffith criterion, fails to describe stable crack propagation in ductile materials.

2 Fundamentals of the Theory of Plasticity

This section introduces some results of the flow theory of infinitesimal plasticity, starting from the general theory of materials with elastic range proposed in [14] with regard to Von Mises materials under the assumption of small displacement gradient from a fixed reference configuration.

We begin with a number of indispensable definitions.

Definition 1 (History) Let $\widehat{\mathbf{E}} : [0, \overline{\tau}] \to Sym$ be a continuous and continuously piecewise differentiable mapping, defined on the closed real interval $[0, \overline{\tau}]$ with values in Sym and such that $\widehat{\mathbf{E}}(0) = \mathbf{0}$.

The value $\widehat{\mathbf{E}}(\tau)$ at the instant τ of a history $\widehat{\mathbf{E}}$ is the infinitesimal strain tensor, starting from a fixed reference configuration, in a fixed material point. At each instant τ in which $\widehat{\mathbf{E}}$ is differentiable, $\dot{\mathbf{E}}$ is the time derivative of $\widehat{\mathbf{E}}$ at the instant τ; for each instant τ in which $\dot{\mathbf{E}}$ is discontinuous, we shall denote by $\dot{\mathbf{E}}$ the right-hand derivative. All deformation processes are thought to begin at some fixed initial state.

We shall consider elastic–plastic isotropic materials whose mechanical response to deformation processes is described by a *frame-indifferent* and *rate-independent* constitutive functional. For each history $\widehat{\mathbf{E}}(\tau)$, $\widehat{\mathbf{T}}_E(\tau)$ is the Cauchy stress tensor at the instant τ associated with the history $\widehat{\mathbf{E}}$ by the constitutive functional.

The kind of constitutive response is further specified by the notions of *elastic range* and *plastic history*.

Definition 2 (Elastic range) The elastic range $\mathscr{E}_E(\tau)$ at time τ corresponding to the history $\widehat{\mathbf{E}}$ is the closure of an arcwise connected open subset of Sym, whose boundary is attainable from interior points only; it contains $\widehat{\mathbf{E}}$, and its points are infinitesimal strains from a reference configuration to configurations that are elastically accessible from the current one.

Definition 3 (Plastic history) Let $\widehat{\mathbf{E}}^P : [0, \overline{\tau}] \to Sym_0$ be a continuous and continuously piecewise differentiable mapping defined on the closed real interval $[0, \overline{\tau}]$ with values in Sym_0 and such that $\widehat{\mathbf{E}}^P(0) = \mathbf{0}$.

The value $\widehat{\mathbf{E}}^P(\tau)$ is the plastic history at time τ associated with the deformation process $\widehat{\mathbf{E}}$ and belongs to $\mathscr{E}_E(\tau)$. It corresponds to an unstressed configuration.

Definition 4 (Cauchy structural mapping) Let μ and λ be two material constants such that, if $\widehat{\mathbf{E}}$ and $\widehat{\mathbf{E}}^P$ are the infinitesimal total and plastic strains, we have, for each $\tau \in [0, \overline{\tau}]$:

$$\widehat{\mathbf{T}}_E(\tau) = \mathbb{T}\big[\widehat{\mathbf{E}}(\tau) - \widehat{\mathbf{E}}^P(\tau)\big] = 2\mu\big(\widehat{\mathbf{E}}(\tau) - \widehat{\mathbf{E}}^P(\tau)\big) + \big(\lambda \operatorname{tr} \widehat{E}(\tau)\big)\mathbf{I}. \tag{1}$$

Remark 1 In analogy with the theory of linear elasticity, μ and λ are identified as Lamè moduli. Equation (1) reflects the classical assumption that the stress response to a purely elastic strain starting from the unstressed configuration reached after unloading is both unaffected by the past deformation process and completely determined by $\widehat{\mathbf{E}}(\tau)$ and $\widehat{\mathbf{E}}^P(\tau)$.

Definition 5 (Odqvist parameter) For each history $\widehat{\mathbf{E}}$ and for each instant $\tau \in [0, \overline{\tau}]$,

$$\zeta_E(\tau) = \int_0^\tau \big\|\dot{\widehat{\mathbf{E}}}^P(\tau')\big\| \, d\tau' \tag{2}$$

is the *Odqvist parameter* which represents the length of the path described up to the instant τ by the plastic strain tensor.

According to the Von Mises criterion, for each history $\widehat{\mathbf{E}}$ and for each instant $\tau \in [0, \overline{\tau}]$, the elastic range is the cylinder

$$\mathscr{E}_E(\tau) = \left\{\widehat{\mathbf{E}} \in Sym : \left\|\widehat{\mathbf{E}}_0 - \widehat{\mathbf{C}}(\tau)\right\| \leq \rho\big(\zeta_E(\tau)\big)\right\}, \tag{3}$$

where

(i) $\rho : \mathbb{R}^+ \to \mathbb{R}^+$ is a nondecreasing differentiable function that depends on the material but is independent of the history.
(ii) for each history $\widehat{\mathbf{E}}$, $\widehat{\mathbf{C}}_E$ is a tensor at value in Sym_0 and represents the center of the elastic range.

Moreover, in order to take the Buaschinger effect into account, we consider the classic kinematic hardening rule, according to which, for each history $\widehat{\mathbf{E}}$ and for each instant $\tau \in [0, \overline{\tau}]$, we have

$$\widehat{\mathbf{C}_E}(\tau) = (1+\eta)\widehat{\mathbf{E}}^P(\tau), \quad \eta \geq 0. \tag{4}$$

Remark 2 The elastic range of Eq. (3), associated with a history $\widehat{\mathbf{E}}$, is univocally determined once the radius, $\rho(\zeta_E)$, and the center, $\widehat{\mathbf{C}_E}$, of the cylinder are known. They reflect a general combined work-hardening rule, in particular, a material for which $\rho(\zeta_E)$ is a constant function and $\eta = 0$ is *perfectly plastic*. If $\eta > 0$ and $\rho(\zeta_E)$ is a constant function, then a material undergoing the plastic history exhibits *kinematic work-hardening*, while if $\eta = 0$ and $\rho(\zeta_E)$ is a variable function, the material undergoing the plastic history exhibits *isotropic work-hardening*. The constant η is called the Melan modulus.

The set of the constitutive hypotheses is completed by the flow rule, according to which, when $\dot{\widehat{\mathbf{E}}}^P$ is not null, it is parallel to $\widehat{\mathbf{N}}_E(\tau)$, the outward unit normal to the elastic range at the point $\widehat{\mathbf{E}}(\tau)$:

$$\begin{aligned} &\dot{\mathbf{E}}^P = \dot{\zeta}_E(\tau)\widehat{\mathbf{N}}_E(\tau), \\ &\widehat{\mathbf{N}}_E(\tau) = \big[\rho\big(\zeta_E(\tau)\big)\big]^{-1}\big(\widehat{\mathbf{E}}(\tau) - \widehat{\mathbf{C}}_E(\tau)\big). \end{aligned} \tag{5}$$

The evolution of the Odqvist parameter is described by the following first-order differential equation [14]:

$$\dot{\zeta}_E = \begin{cases} 0, & \|\widehat{\mathbf{E}}_0 - \widehat{\mathbf{C}}_E\| < \rho(\zeta_E), \\ 0, & \|\widehat{\mathbf{E}}_0 - \widehat{\mathbf{C}}_E\| = \rho(\zeta_E), \quad \widehat{\mathbf{N}}_E \cdot \dot{\widehat{\mathbf{E}}}_0 \leq 0, \\ \dfrac{\widehat{\mathbf{N}}_E \cdot \dot{\widehat{\mathbf{E}}}_0}{[1+\eta+\rho'(\zeta_E)]}, & \|\widehat{\mathbf{E}}_0 - \widehat{\mathbf{C}}_E\| = \rho(\zeta_E), \quad \widehat{\mathbf{N}}_E \cdot \dot{\widehat{\mathbf{E}}}_0 > 0. \end{cases} \tag{6}$$

with $\rho' = \frac{d\rho}{d\zeta}$. In the first two cases the material behaves elastically, while the last one denotes a plastic loading condition.

For each history $\widehat{\mathbf{E}}$ and for each instant $\tau \in [0, \overline{\tau}]$, $\widehat{\mathbf{T}}_E(\tau) \cdot \dot{\widehat{\mathbf{E}}}(\tau)$ is the *stress power*. The work density done by the internal forces during the history $\widehat{\mathbf{E}}$ up to time τ is given by

$$\widehat{w}_E(\tau) = \int_0^\tau \widehat{\mathbf{T}}_E(\tau') \cdot \dot{\widehat{\mathbf{E}}}(\tau')\, d\tau'. \tag{7}$$

With the following proposition, for each history $\widehat{\mathbf{E}}$ and for each instant $\tau \in [0, \overline{\tau}]$, an explicit relation, expressing $\widehat{w}_E(\tau)$ as a function of the state $(\widehat{\mathbf{E}}(\tau), \widehat{\mathbf{E}}^P(\tau), \zeta_E(\tau))$, can be defined [15].

Proposition 1 *For each history* $\widehat{\mathbf{E}}$ *and for each instant* $\tau \in [0, \overline{\tau}]$, *one gets*

$$\begin{aligned}\widehat{w}_E(\tau) = {} & \frac{1}{2}\big(\widehat{\mathbf{E}}(\tau) - \widehat{\mathbf{E}}^P(\tau)\big) \cdot \mathbb{T}\big[\widehat{\mathbf{E}}(\tau) - \widehat{\mathbf{E}}^P(\tau)\big] + \mu\eta \big\|\widehat{\mathbf{E}}^P(\tau)\big\|^2 \\ & + 2\mu\omega\big(\zeta_E(\tau)\big),\end{aligned} \tag{8}$$

where ω *is the primitive of* ρ *such that* $\omega(0) = 0$.

Proof Bearing in mind that a plastic history $\widehat{\mathbf{E}}^P \in Sym_0$, from Eqs. (1) and (7) we have

$$\begin{aligned}\widehat{w}_E(\tau) &= \int_0^\tau \widehat{\mathbf{T}}_E(\tau') \cdot \dot{\widehat{\mathbf{E}}}(\tau')\, d\tau' = \int_0^\tau \dot{\widehat{\mathbf{E}}}(\tau') \cdot \mathbb{T}\big[\widehat{\mathbf{E}}(\tau) - \widehat{\mathbf{E}}^P(\tau)\big]\, d\tau' \\ &= \int_0^\tau \big(\dot{\widehat{\mathbf{E}}}(\tau') - \dot{\widehat{\mathbf{E}}}^P(\tau')\big) \cdot \mathbb{T}\big[\widehat{\mathbf{E}}(\tau) - \widehat{\mathbf{E}}^P(\tau)\big]\, d\tau' \\ &\quad + \int_0^\tau \dot{\widehat{\mathbf{E}}}^P(\tau') \cdot \mathbb{T}\big[\widehat{\mathbf{E}}(\tau) - \widehat{\mathbf{E}}^P(\tau)\big]\, d\tau' \\ &= \frac{1}{2}\big[\big(\widehat{\mathbf{E}}(\tau) - \widehat{\mathbf{E}}^P(\tau)\big) \cdot \mathbb{T}\big[\widehat{\mathbf{E}}(\tau) - \widehat{\mathbf{E}}^P(\tau)\big]\big]_0^\tau \\ &\quad + \int_0^\tau 2\mu\big(\widehat{\mathbf{E}}(\tau) - \widehat{\mathbf{E}}^P(\tau)\big) \cdot \dot{\widehat{\mathbf{E}}}^P(\tau')\, d\tau'.\end{aligned}$$

Moreover, from Eqs. (4)–(6) we get

$$\begin{aligned}&\int_0^\tau 2\mu\big(\widehat{\mathbf{E}}(\tau) - \widehat{\mathbf{E}}^P(\tau)\big) \cdot \dot{\widehat{\mathbf{E}}}^P(\tau')\, d\tau' \\ &= \int_0^\tau 2\mu\rho\big(\zeta_E(\tau')\big)\widehat{\mathbf{N}}_E(\tau') \cdot \dot{\widehat{\mathbf{E}}}^P(\tau')\, d\tau' + \int_0^\tau 2\mu\eta\widehat{\mathbf{E}}^P(\tau') \cdot \dot{\widehat{\mathbf{E}}}^P(\tau')\, d\tau' \\ &= \big[2\mu\omega\big(\zeta_E(\tau')\big) + \mu\eta\big\|\widehat{\mathbf{E}}^P(\tau')\big\|^2\big]_0^\tau.\end{aligned}$$

Finally, keeping in mind that $\widehat{\mathbf{E}}(0) = \widehat{\mathbf{E}}^P(0) = \mathbf{0}$ and $\omega(\zeta_E(0)) = 0$, we obtain the result. □

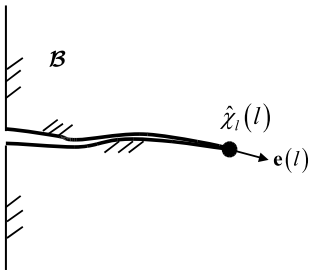

Fig. 1 Edge crack modeled as a smooth, nonintersecting curve $\widehat{\chi}_l(\alpha)$

3 The Energy Release Rate

In this section, the energy release rate (ERR) is obtained from a mechanical energy balance, under the classic assumptions of regularity of fracture fields (defined below), SSY conditions, quasi-static deformations and in the absence of body forces.

Let $\mathscr{B}$ is a regular homogeneous two-dimensional elastic–plastic body, whose mechanical response to deformation process is described by the set of the constitutive equations (1)–(7). We identify $\mathscr{B}$ with the particular region of $\mathbb{R}^2$ occupied by the body in the reference configuration; we consider a motion of $\mathscr{B}$ during the time interval $[0, \overline{\tau}]$, and for each material point $\mathbf{x} \in \mathscr{B}$, let us denote by $\widehat{\mathbf{E}}_x$ and $\widehat{\mathbf{E}}_x^P$ the infinitesimal total and plastic strains at the material point $\mathbf{x}$, respectively. We also assume that $\mathscr{B}$ contains an edge crack of negligible thickness. The crack is modeled as a smooth, nonintersecting curve

$$\widehat{\chi}_l : [0, l] \to \mathscr{B}, \quad \alpha \to \widehat{\chi}_l(\alpha),$$

which is parameterized by arc length $\alpha \in [0, l]$ (see Fig. 1).

The length $l = l(\tau)$ of the curve $\widehat{\chi}_l$ is a nondecreasing function of the time τ during the motion of $\mathscr{B}$; moreover, if $l_2 > l_1$, then $\widehat{\chi}_{l_2}$ is a continuation of $\widehat{\chi}_{l_1}$.

Let us define

$$\mathscr{C}(l) \triangleq \left\{ \mathbf{x} \in \mathscr{B} : \mathbf{x} = \widehat{\chi}_l(\alpha),\ \alpha \in [0, l] \right\} \tag{9}$$

as the set of points of $\mathscr{B}$ lying on the crack edges, where $\widehat{\chi}_l(l)$ is the current crack tip. The unit vector tangent to the crack is

$$\mathbf{e}(\alpha) = \frac{d\widehat{\chi}_l}{d\alpha}; \tag{10}$$

in particular, $\mathbf{e}(l)$ defines the direction of propagation.

Let us suppose that there is a time interval $[\tau_0, \tau_1] \subset [0, \overline{\tau}]$ such that

$$l(\tau_0) > 0 \quad \text{and} \quad \frac{dl}{d\tau} > 0 \quad \forall \tau \in [\tau_0, \tau_1];$$

then, in this time interval, l is a strictly increasing function of time, and, thus, it can be identified as a time scale. For $l \in [l(\tau_0), l(\tau_1)]$, the crack tip propagates in the direction $\mathbf{e}(l)$.

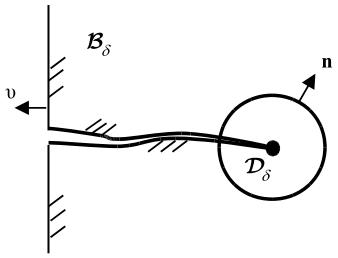

Fig. 2 Definition of the crack tip region

Definition 6 (Fracture field) Let $\varphi(\mathbf{x}, l)$ be a field defined at each material point $\mathbf{x} \in \mathscr{B} - \mathscr{C}(l)$ and for each $l \in [l_0, l_1)$. φ is a $\mathbb{C}^n$ *fracture field* ($n \geq 0$, integer) if

(i) the derivatives of φ of order $\leq n$ exist away from the crack;
(ii) φ and its derivatives of order $\leq n$ are continuous away from the crack and, except at the tip, are continuous up to both crack faces.

Thus, $\varphi(\mathbf{x}, l)$, as a function of $\mathbf{x}$, could admit a jump discontinuity when crossing the crack faces $\mathscr{C}(l) - \widehat{\chi}_l$; so, we can write:

$$\varphi^{\pm}(\alpha, l) = \lim_{\delta \to 0^+} \varphi\big(\widehat{\chi}_l(\alpha) \pm \delta \mathbf{m}(\alpha), l\big) \quad \alpha \in [0, l]$$

for the values of φ on the upper and lower faces of the crack, with $\mathbf{m}(\alpha)$ the outward unit normal to crack faces.

Remark 3 In the above definition, nothing is said about the behavior of φ at the crack tip. Generally, the total strain rate tensor is singular.

For all $l \in [l_0, l_1]$ and for each vanishing $\delta > 0$, $\mathscr{D}_\delta(l)$ denotes the disc of radius δ with center at the crack tip, and $\mathscr{B}_\delta(l) = \mathscr{B} - \mathscr{D}_\delta(l)$ is the complement of $\mathscr{D}_\delta(l)$ with respect to $\mathscr{B}$; ν and n are the outward unit normals to $\partial\mathscr{B}$ and $\mathscr{D}_\delta$, respectively (see Fig. 2).

For $\mathbf{x} \in \mathscr{B}$ and $l \in [l_0, l_1]$, $\mathbf{u}(\mathbf{x}, l)$ denotes the displacement field evaluated with respect to the reference configuration, and we put

$$\begin{aligned}
&\mathbf{E}(\mathbf{x}, l) \triangleq \widehat{\mathbf{E}}_x(\tau), \qquad \mathbf{E}^P(\mathbf{x}, l) \triangleq \widehat{\mathbf{E}}^P_x(\tau),\\
&\mathbf{T}(\mathbf{x}, l) \triangleq \mathbb{T}\big[\mathbf{E}(\mathbf{x}, l) - \mathbf{E}^P(\mathbf{x}, l)\big],\\
&\zeta(\mathbf{x}, l) \triangleq \zeta_{E_x}(\tau),\\
&w(\mathbf{x}, l) \triangleq \widehat{w}_{E_x}(\tau),
\end{aligned}$$

where ζ and $\widehat{w}$ are defined by Eqs. (6) and (7), and $l = l(\tau)$.

We are now in the position to state the main hypotheses regarding the fields $\mathbf{u}(\mathbf{x}, l)$, $T(\mathbf{x}, l)$, and $w(\mathbf{x}, l)$ [8, 10].

A1 $\mathbf{u}(\mathbf{x}, l)$ is a $\mathbb{C}^2$ fracture field, while $\mathbf{T}(\mathbf{x}, l)$ and $w(\mathbf{x}, l)$ are necessarily $\mathbb{C}^1$ fracture fields.

A2 For each l, $w(\mathbf{x}, l)$ and its derivative with respect to l are integrable in $\mathbf{x}$ over $\mathscr{B}$.

A3 $\int_{\mathscr{B}} w(\mathbf{x}, l)\, da$ is differentiable with respect to l, and furthermore

$$\lim_{\delta \to 0} \frac{d}{dl} \int_{\mathscr{B}_\delta} w(\mathbf{x}, l)\, da = \frac{d}{dl} \int_{\mathscr{B}} w(\mathbf{x}, l)\, da.$$

A4

$$\lim_{\delta \to 0} \int_{\partial \mathscr{D}_\delta} \mathbf{T}(\mathbf{x}, l)\mathbf{n} \cdot \dot{\mathbf{u}}(\mathbf{x}, l)\, ds = -\lim_{\delta \to 0} \mathbf{e}(l) \cdot \int_{\partial \mathscr{D}_\delta} \nabla \mathbf{u}^T(\mathbf{x}, l)\mathbf{T}(\mathbf{x}, l)\mathbf{n}\, ds.$$

A5 For each l, $\operatorname{div}(w(\mathbf{x}, l)\mathbf{I} - \nabla \mathbf{u}^T(\mathbf{x}, l)\mathbf{T}(\mathbf{x}, l))$ is integrable in $\mathbf{x}$ over $\mathscr{B}$.

A6 $\mathscr{B}$ undergoes to quasi-static deformations, and, in the absence of body forces,

$$\operatorname{div} \mathbf{T}(\mathbf{x}, l) = 0.$$

A7 The crack face are traction-free, i.e.,

$$\mathbf{T}^{\pm}(\alpha, l)\mathbf{m}(\alpha) = \mathbf{0}, \quad \alpha \in [0, l].$$

Remark 4 Assumption **A6** and the constitutive relations in Sect. 2 are not strictly necessary in order to obtain the ERR, i.e., it is possible to obtain an expression of the ERR in a similar way when large deformations occur and in the presence of body forces and inertial load. In such cases, assumptions **A1**–**A5** and **A7** are still valid.

We are now able to write a global energy balance for body $\mathscr{B}$ undergoing a quasi-static crack propagation in the time interval $[\tau_0, \tau_1]$. In analogy with the Griffith's criterion, the change in the work done by the external loads equals the sum of change in stored elastic energy and the energy dissipated into the material. Unlike the elastic material, the dissipation energy rate is related to the newly created crack surfaces and the plasticity arising around the crack tip; thus, the global energy balance is

$$\mathscr{E}(l) = \int_{\partial \mathscr{B}} \mathbf{T}\nu \cdot \dot{\mathbf{u}}\, ds - \frac{d}{dl} \int_{\mathscr{B}} w\, da, \tag{11}$$

where $\frac{d}{dl} \int_{\mathscr{B}} w\, da$ is the change in the internal energy (elastic plus plastic energy).

The function $\mathscr{E}(l)$ is called *Energy Release Rate*, and for each $l \in [l_0, l_1]$, the integral $\int_{l_0}^{l} \mathscr{E}(\xi)\, d\xi$ is interpreted as the work per unit thickness needed to increase the length of the crack from l_0 to l.

As a direct consequence of the previous assumptions, it is possible to evaluate the ERR from a local energy balance in the crack tip region [6, 8, 22].

Proposition 2 *For each* $l \in [l_0, l_1]$,

$$\mathscr{E}(l) = \lim_{\delta \to 0} \mathbf{e}(l) \cdot \int_{\partial \mathscr{D}_\delta} \left(w\mathbf{I} - \nabla \mathbf{u}^T \mathbf{T}\right)\mathbf{n}\, ds. \tag{12}$$

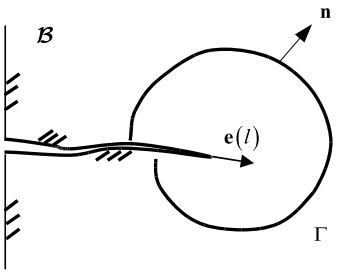

Fig. 3 Definition of the integration path around the crack tip

Proof From Eq. (7) and assumption **A6** we obtain

$$w' = \mathbf{T} \cdot \mathbf{E}' = \mathbf{T} \cdot \nabla \mathbf{u}' = \operatorname{div}(\mathbf{T}\mathbf{u}') - \mathbf{u}' \cdot \operatorname{div} \mathbf{T} = \operatorname{div}(\mathbf{T}\mathbf{u}').$$

Applying the divergence theorem to the set $\mathscr{B}_\delta$ and keeping assumption **A7** in mind, we have

$$\int_{\mathscr{B}_\delta} w' \, da = \int_{\partial \mathscr{B}} \mathbf{T}\nu \cdot \mathbf{u}' \, ds - \int_{\partial \mathscr{D}_\delta} \mathbf{T}\mathbf{n} \cdot \mathbf{u}' \, ds.$$

The transport theorem states that, for $\delta > 0$,

$$\frac{d}{dl} \int_{\mathscr{B}_\delta} w \, da = \int_{\mathscr{B}_\delta} w' \, da - \mathbf{e}(l) \cdot \int_{\partial \mathscr{D}_\delta} w\mathbf{n} \, ds;$$

therefore, it results in

$$-\frac{d}{dl} \int_{\mathscr{B}_\delta} w \, da + \int_{\partial \mathscr{B}} \mathbf{T}\nu \cdot \mathbf{u}' \, ds = \int_{\partial \mathscr{D}_\delta} (\mathbf{e} \cdot w\mathbf{n} + \mathbf{T}\mathbf{n} \cdot \mathbf{u}') \, ds.$$

Finally, with assumptions **A3** and **A4** we conclude the proof. □

Let Γ denote any smooth nonintersecting path which starts and ends on the crack and contains the crack tip; let $\mathbf{n}$ denote the outward unit normal on Γ (see Fig. 3). Let us denote by

$$\tilde{J}(\Gamma) = \mathbf{e}(l) \cdot \int_\Gamma \left(w\mathbf{I} - \nabla \mathbf{u}^T \mathbf{T} \right) \mathbf{n} \, ds \tag{13}$$

the *crack-tip integral* for the path Γ; thus, in view of Eqs. (12) and (13), we can write

$$\mathscr{E}(l) = \lim_{\delta \to 0} \tilde{J}(\partial \mathscr{D}_\delta). \tag{14}$$

This result expresses the concept that the energy release rate depends on the local stress and strain fields in a region close to the crack tip; this conclusion is due to the classical assumptions **A1**–**A7** of the continuum mechanics according to which singularities in stress and strain fields occur solely at the crack tip. As a consequence of the local nature of singularities in the fracture fields, nonsingular terms in Eq. (11) make no contribution, and, thus, a criterion of fracture is determined solely

by singularities in stress and strain fields. For this, the energy release rate evaluated through Eq. (11) is the same as calculated by Eq. (12).

For quasi-static propagation, this suggests the validity of Irwin's [12] proposal that fracture occurs when the crack tip SIF, as calculated from linear elasticity, attains a critical value. If the crack size and other geometric dimensions are sufficiently large so that the plastic zone size is small in comparison, one may expect that the linear elastic field is little disturbed and that the stress and strain field in the nonelastic zone is controlled by the SIF which determines the strength of the singularity in the linear elastic solution.

With the assumption of SSY and under some loading conditions in quasi-static crack growth problems, Eq. (14) can be simplified; this allows us to determine a criterion of fracture without evaluating the stress and strain fields at the crack tip. Under the conditions for which the nonlinear elastic solution controls the deformation process in the small plastic zone [11], the crack-tip integral of Eq. (13) reduces to the *Rice's J-integral*, which is path-independent.

In order to assess the path-independence of the J-integral, we begin with observing that the integrand of Eq. (13), $\mathbf{P} = w\mathbf{I} - \nabla\mathbf{u}^T\mathbf{T}$, is the energy momentum tensor which, for elastic bodies, is also known as *Eshelby's tensor*; Eshelby [7] showed that the energy momentum tensor can be interpreted as a generalized force acting on moving crack and established a connection with the J-integral. Furthermore, when an elastic body is also homogeneous, he proved that the elastic strain energy density, W, does not explicitly depend on the position of material points and, thus, its divergence vanishes,

$$\operatorname{div}\left(W\mathbf{I} - \nabla\mathbf{u}^T\mathbf{T}\right) = \mathbf{0}. \tag{15}$$

With assumption **A7**, assuming that the crack is straight, the solenoidal nature of the Eshelby's tensor shows the path independence of the J-integral.

Remark 5 The condition of homogeneous body, kept in this section, is not strictly necessary [10]; as claimed in [19], it is useful to assure the global path independence of the J-integral through the solenoidal nature of the Eshelby's tensor. When homogeneity is lost, the Eshelby's tensor is not solenoidal and its divergence is [7]

$$\operatorname{div}\left(W\mathbf{I} - \nabla\mathbf{u}^T\mathbf{T}\right) = \left.\frac{\partial W}{\partial \mathbf{X}}\right|_{\text{explicit}}.$$

In this case, the global path-independence of the J-integral is lost; however, a local path-independence can be restored with the assumption that the energy momentum tensor is singular at the crack tip [19], that is,

$$P_{1j} \approx \frac{A_j(\theta)}{r} + o(1/r) \quad \text{and} \quad \frac{\partial P_{1j}}{\partial x_j} = o\left(1/r^2\right) \quad \text{as } r \to 0^+,$$

where r is the radial distance from the moving crack tip, and θ is the angle formed with the direction of propagation. This result can be interpreted as a condition for locally steady-state behavior.

Because of the path-independence of the J-integral, we get

$$\mathscr{E}(l) = J(\Gamma) = \mathbf{e}(l) \cdot \int_{\Gamma} \left(W\mathbf{I} - \nabla\mathbf{u}^T\mathbf{T}\right)\mathbf{n}\, ds. \tag{16}$$

This result qualifies the J-integral as a crack driving force; from the point of view of the finite element method (FEM), the calculation of the energy release rate, during a quasi-static crack propagation, can be done by evaluating the integral of Eq. (13) around a path Γ sufficiently far away from the crack tip such that no knowledge of the stress and strain field is required here. This made the J-integral the most attractive tool of nonlinear fracture mechanics, widely used since 1970.

Generally for elastic–plastic bodies, the crack-tip integral of Eq. (13) differs from the Rice's J-integral because w is no longer the strain energy density but the stress work density which depends on the overall deformation process; furthermore, the crack-tip integral is not path-independent, and, then, it cannot be identified as the energy release rate. However, as already mentioned, there are some conditions for which Eq. (16) can be used even for elastic–plastic materials. When SSY condition is also satisfied for quasi-statically loaded body, if each material point is proportionally stressed, the crack-tip integral is globally path-independent [19]. Therefore, it is not necessary to shrink the radius δ onto the crack tip in order to evaluate the energy release rate and, thus, Eq. (16) provides a tool to predict the initiation of crack growth and subsequent quasi-static crack growth.

Under these conditions, using the deformation theory of plasticity, Hutchinson showed in [11] that there is an annular zone which surrounds a region of finite strain where the nonlinear elastic J-integral controls the deformation process in the small plastic zone; he established a correlation between the elastic J-integral and the stress, strain, and displacement fields near a crack tip, showing that the nonlinear elastic J-integral provides a measure of the crack-tip singularity fields (called HRR fields). While the asymptotic solutions for HRR fields are a good approximation in stationary crack problems, for quasi-static crack propagation, they are less accurate due, mainly, to elastic unloading and nonproportional plastic loading. However, if the amount of crack extension stays within certain limits and if nonproportional loading zones at the crack tip are surrounded by a much larger zone of proportional loading, then it is possible to describe stress, strain, and displacement fields here with the HRR fields.

For this, when the above conditions are met, it is still useful to evaluate the energy release rate from Eq. (16); this is the reason for which the Rice's J-integral is nowadays used.

When the conditions of HRR fields are not satisfied (elastic unloading and nonproportional plastic loading in cyclically loaded bodies), the elastic J-integral is no longer valid to estimate the energy release rate; in these cases, an appropriate evaluation of the ERR requires the determination of the crack tip-integral $\tilde{J}(\Gamma)$ with Γ shrinking onto the crack tip; with the application of the finite element method (from a point of view of numerical simulations of quasi-static crack propagation), Eq. (14) is no longer useful to assess a criterion of fracture.

Even when the effects of plastic flow at the crack tip are no longer negligible and loading histories are whatever (quasi-static or variable loading), it is possible to restore the path-independence of the crack-tip integral and then obtain a more advantageous expression of the equation.

In [1, 13], Kishimoto, Aoki, and Sakata have restated the crack-tip integral of Eq. (13) in terms of equivalent path and area integrals. They have considered a closed curve formed by an outer path, the crack faces, and an inner path, which surrounds the FPZ, where microstructural damage processes occur during crack extension, and continuum mechanics does not work. Applying an energy balance over the domain inside the closed curve, they have derived a crack-tip integral as sum of a contour integral over the outer path and the crack faces, a contour integral over the path delimiting the FPZ, and an area integral; in so doing, they have shown that, for a prescribed FPZ, the crack-tip integral is independent with respect to any arbitrary outer path. However, as they have pointed out, it depends on the dimensions and shape of the FPZ, which are influenced by loading conditions, crack length, and dimensions of microvoids; so, this approach is not so suitable for numerical evaluation of the energy release rate.

The idea to restate the crack-tip integral of Eq. (14) as sum of a path and an area integral have been later pursued by Schmitt and Kienzler [23], who showed that the path-independence of the crack-tip integral with respect to the size and shape of the domain can be recovered by introducing an additional volume integral, which receives nonzero contributions only from those plastically deformed regions that, due to crack propagation, suffer from nonproportional loading. Unlike the crack-tip integral proposed by Aoki et al. [1, 13], no knowledge of the shape and dimensions of the FPZ is required. They have given a physical interpretation of the crack-tip integral as *work dissipation rate*.

In a similar way, Chiarelli, Frediani, and Lucchesi [5, 6, 8], on the basis of the infinitesimal theory of plasticity of the previous section, have rewritten Eq. (14), making the crack-tip integral independent of the domain and extending it to elastic–plastic work-hardening materials undergoing general loading conditions. In so doing, they have considered, for each $l \in [l_0, l_1]$, the set $\mathscr{B}_\zeta \subset \mathscr{B}$ of material points in which plastic flow occurs,

$$\mathscr{B}_\zeta(l) = \big\{\mathbf{x} \in \mathscr{B} : \zeta(\mathbf{x}, l) \neq 0\big\}, \tag{17}$$

where $\zeta(\mathbf{x}, l)$ is defined by Eq. (6).

For each path Γ surrounding the crack tip, let $\mathscr{F}$ be the subset of $\mathscr{B}$ enclosed by Γ; let $\mathscr{L} = \mathscr{F} \cap \mathscr{B}_\zeta$ be the intersection between $\mathscr{F}$ and $\mathscr{B}_\zeta$ (see Fig. 4).

With the following proposition we can obtain an expression more useful than Eq. (14).

Proposition 3 *If the crack is straight, for each path Γ around the tip, we have*

$$\mathscr{E}(l) = \tilde{J}(\Gamma) - \mathbf{e} \cdot \int_{\mathscr{L}} \operatorname{div}\big(w\mathbf{I} - \nabla\mathbf{u}^T\mathbf{T}\big)\, da. \tag{18}$$

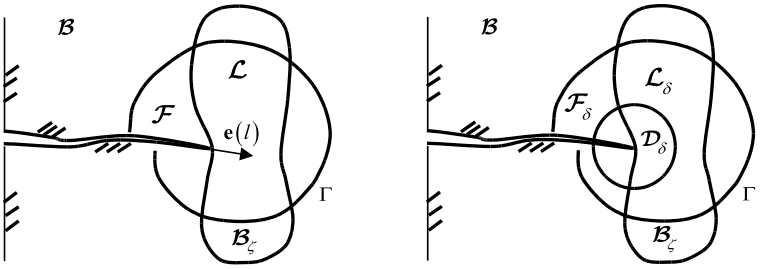

Fig. 4 Definition of the domain $\mathscr{L}$

Proof Let $\delta > 0$ be enough small so that the region $\mathscr{D}_\delta$ is enclosed by the path Γ (see Fig. 4); let $\mathscr{F}_\delta$ the subset bounded by the curve $\mathscr{C}_\delta = \Gamma + \partial\mathscr{D}_\delta + \Gamma^+ + \Gamma^-$ with Γ^+ and Γ^- denoting the upper and lower crack faces. Keeping assumption **A7** in mind, if the crack is straight, the divergence theorem applied to the subset $\mathscr{F}_\delta$ states

$$\tilde{J}(\partial\mathscr{D}_\delta) = \tilde{J}(\Gamma) - \mathbf{e}\cdot\int_{\mathscr{F}_\delta} \operatorname{div}\left(w\mathbf{I} - \nabla\mathbf{u}^T\mathbf{T}\right) da.$$

On the other hand, at all material points $\mathbf{x} \notin \mathscr{B}_\zeta$ the stress work density coincides with the strain energy density, and, then, the elastic–plastic energy momentum tensor reduces to the Eshelby tensor. Keeping Remark 5 on mind, by taking the limit for $\delta \to 0$ in the above equation, the nonvanishing contribution to the second term is given by all material points of the subset $\mathscr{L}_\delta = \mathscr{F}_\delta \cap \mathscr{B}_\zeta$; thus, Eq. (14) becomes

$$\mathscr{E}(l) = \tilde{J}(\Gamma) - \lim_{\delta\to 0} \mathbf{e}\cdot\int_{\mathscr{L}_\delta} \operatorname{div}\left(w\mathbf{I} - \nabla\mathbf{u}^T\mathbf{T}\right) da.$$

Finally, bearing assumptions **A3** and **A4** in mind, we conclude the proof. □

The quantity $\mathscr{E}(l)$ in Eq. (18) is known as *Crack Extension Energy Rate*; the second term of the CEER takes plastic effects near the crack tip into account and allows us to restore the path independence of CEER. For elastic bodies, the CEER coincides with the Rice's J-integral; so, CEER represents a generalization of the J-integral for elastic–plastic materials.

Numerical evaluation of the CEER [2, 6, 20] for elastic–plastic work-hardening materials in stationary crack problems and SSY conditions showed that, when monotonic increasing loading conditions are considered, the Rice's J-integral completely describes the fracture behavior of a ductile material; this agrees with what Hutchinson [11] discussed earlier. However, when variable loading histories are applied, the Rice's J-integral is no longer able to describe the fracture process. Unlike the Rice's J-integral, the CEER is able to take into account work-hardening effects, dissipative effects due to elastic unloading or effects due to residual stresses subsequent to an overload. In fact, as shown in [2, 6, 20], the occurrence of overloads gives rise to a reduction of the CEER, and then, the delay in crack growth can be

linked to the CEER vs load curves. For these considerations, we might conclude that the CEER is the crack driving force for ductile materials.

Remark 6 With applications to FEM, the evaluation of the area integral requires the calculations of the spatial derivative of the stress and strain tensor over the domain of interest, and, in proximity of the crack tip, numerical difficulties can arise; when they occur, path-independence of the CEER may be lost. In such cases, the *domain integral* method [18, 19] might be considered, which consists in evaluating the crack-tip integral of Eq. (14) as an integral over the finite domain $\mathscr{F}_\delta$ around the crack tip and considering any arbitrary smooth scalar-value weighting function $q(\mathbf{x})$ defined over $\mathscr{F}_\delta$. The weighting function may be interpreted as the virtual translation of the material point $\mathbf{x}$ due to a unit crack extension in the direction $\mathbf{e}(l)$; furthermore, $q(\mathbf{x}) = 1$ on $\partial\mathscr{D}_\delta$, $q(\mathbf{x}) = 0$ on Γ and $q(\mathbf{x}) \in [0, 1]$ in $\mathscr{F}_\delta$. Bearing assumption **A7** in mind and applying the divergence theorem to the subset $\mathscr{F}_\delta$, we get the finite following domain representation of the crack tip integral of Eq. (14):

$$\mathscr{E}(l) = -\mathbf{e} \cdot \int_{\mathscr{F}_\delta} (\mathbf{P}\nabla q + q\nabla \cdot \mathbf{P})\, da.$$

Although the domain integral method may circumvent the difficulties arising from near tip integration, it requires a greater effort in numerical implementation into a FEM code; the function q must be evaluated for each mesh element belonging to the domain of interest according to the integration scheme for the evaluation of the tangent stiffness matrix of the element. That means an additional degree of freedom for these elements and, as a direct consequence, a greater computational cost for the solution.

4 Conclusions

An overview on energetic approaches in Non-Linear Fracture Mechanics has been presented; starting from the original work of Griffith for brittle materials, several Griffith-like methods for ductile materials, available in the literature, have been discussed; a particular attention has been confined to the Crack Extension Energy Rate method, which has shown, in several works, to be a valid fracture criterion for applications to 2-D stationary crack problems.

References

1. Aoki, S., Kishimoto, K., Sakata, M.: Energy-release rate in elastic-plastic fracture problems. J. Appl. Mech. **48**, 825–829 (1981)
2. Binante, V.: A new energetic failure criterion and constitutive models of porous materials into the fracture process zone, in the framework of elastic-plastic fracture mechanics. Ph.D thesis in aerospace engineering, Universitá di Pisa, Faculty of Engineering (2010)

3. Binante, V., Frediani, A.: A criterion for ductile crack growth based on the energy momentum tensor. In: Buttazzo, G., Frediani, A. (eds.) Variational Analysis and Aerospace Engineering II: Mathematical Challenges for Aerospace Design. Springer, Berlin (2012)
4. Budiansky, B., Rice, J.R.: Conservation laws and energy-release rates. J. Appl. Mech. **40**, 201–203 (1973)
5. Chiarelli, M., Frediani, A., Lucchesi, M.: On the crack extension energy rate in elastic-plastic fracture mechanics. In: Blauel, J.B., Schwalbe, K.H. (eds.) Defect Assessment in Components: Fundamentals and Applications. Mechanical Engineering Publications, London (1991)
6. Chiarelli, M., Frediani, A., Lucchesi, M.: Computation of crack extension energy rate for elastic-plastic hardening materials under variable loading. Eng. Fract. Mech. **55**(5), 813–830 (1996)
7. Eshelby, J.D.: Energy relations and the energy–momentum tensor in continuum mechanics. In: Kanninen, M.F., Adler, W.F., Rosenfield, A.R., Jaffee, R.I. (eds.) Inelastic Behaviour of Solids, vol. 43, pp. 77–115. McGraw-Hill, New York (1970)
8. Frediani, A.: Effects of plasticity of metallic materials on fatigue and fracture mechanics. In: Miele, A., Salvetti, A. (eds.) Applied Mathematics in Aerospace Science and Engineering, Erice, Italy, 3–10 September. Mathematical Concepts and Methods in Science and Engineering, vol. 44, pp. 363–393. Plenum Press, New York (1994)
9. Griffith, A.A.: The phenomena of rupture and flow in solids. Philos. Trans. R. Soc. Lond. Ser. A **221**(582–593), 163–198 (1921). Containing Papers of a Mathematical or Physical Character
10. Gurtin, M.E.: On the energy release rate in quasi-static elastic crack propagation. J. Elast. **9**(2), 187–195 (1979)
11. Hutchinson, J.W.: Fundamentals of the phenomenological theory of nonlinear fracture mechanics. J. Appl. Mech. **50**, 1042–1051 (1983)
12. Irwin, G.R.: Analysis of stresses and strains near the end of a crack traversing a plate. J. Appl. Mech. **24**, 361–364 (1957)
13. Kishimoto, K., Aoki, S., Sakata, M.: On the path independent integral. J. Eng. Fract. Mech. **13**(4), 841–850 (1980)
14. Lucchesi, M., Owen, D.R., Podio-Guidugli, P.: Materials with elastic range: a theory with a view toward applications. Part III: Approximate constitutive relations. Arch. Ration. Mech. Anal. **117**(1), 53–96 (1992)
15. Lucchesi, M.: Free-energy functions for elastic-plastic material elements. Q. Appl. Math. **11**, 299–318 (1993)
16. Lucchesi, M., Podio-Guidugli, P.: Materials with elastic range: a theory with a view toward applications. Part I. Arch. Ration. Mech. Anal. **102**(1), 23–43 (1988)
17. Lucchesi, M., Podio-Guidugli, P.: Materials with elastic range: a theory with a view toward applications. Part II. Arch. Ration. Mech. Anal. **110**(1), 9–42 (1990)
18. Meith, W.A., Hill, M.R.: Domain-independent values of the j-integral for cracks in three-dimensional residual stress bearing bodies. Eng. Fract. Mech. **69**(12), 1301–1314 (2002)
19. Moran, B., Shih, C.F.: Crack tip and associated domain integrals from momentum and energy balance. Eng. Fract. Mech. **27**(6), 615–642 (1987)
20. Oriunno, M.: Meccanica della frattura elasto-palstica: modelli costitutivi per lo studio del fenomeno di propagazione. Tesi di dottorato in ingegneria aeronautica, Universitá di Pisa-Facoltá di Ingegneria (1996)
21. Rice, J.R.: A path independent integral and the approximate analysis of strain concentration by notches and cracks. J. Appl. Mech. **35**, 379–386 (1968)
22. Rice, J.R.: An examination of the fracture mechanics energy balance from the point of view of continuum mechanics. In: Swedlow, J.L., Yokobori, T., Kawasaki, T (eds.) Proceedings of the First International Conference on Fracture, Sendai, Japan, 12–17 September, vol. 1, pp. 309–340 (1965)
23. Schmitt, W., Kienzler, R.: The j-integral concept for elastic-plastic material behavior. Eng. Fract. Mech. **32**(3), 409–418 (1989)

A Criterion for Ductile Crack Growth Based on the Energy–Momentum Tensor

Vincenzo Binante and Aldo Frediani

1 Introduction

Residual static strength and crack growth resistance curve in a cracked body can be evaluated by means of an energy balance, according to which the decrease in potential energy caused by a crack extension equals the surface energy of the newly created crack surfaces.

For an elastic–plastic bidimensional body with a straight crack, undergoing quasi-static deformations in the absence of body forces, the energy required to produce a unit crack extension can be defined as

$$\mathscr{E}(l) = \tilde{J}(\Gamma) - \mathbf{e} \cdot \int_{\mathscr{L}} \operatorname{div}\left(w\mathbf{I} - \nabla\mathbf{u}^T\mathbf{T}\right) da, \tag{1}$$

for each path Γ around the crack tip, with $\mathscr{L}$ the region enclosed by Γ where plastic strains occur (see Fig. 1). The first term of the right-hand side of Eq. (1) is defined as

$$\tilde{J}(\Gamma) = \mathbf{e}(l) \cdot \int_{\Gamma} \left(w\mathbf{I} - \nabla\mathbf{u}^T\mathbf{T}\right)\mathbf{n}\, ds, \tag{2}$$

where w is the work density done by the internal forces, $\mathbf{T}$ is the Cauchy stress tensor, $\nabla\mathbf{u}$ is the displacement gradient tensor, $\mathbf{e}(l)$ defines the direction of propagation, l is the crack length, and $\mathbf{n}$ is the outward unit normal to the path Γ.

V. Binante (✉)
Mechanics of Materials and Structures Laboratory, ISTI-CNR, Via G. Moruzzi 1, 56124 Pisa, Italy
e-mail: vincenzo.binante@isti.cnr.it

A. Frediani
Dipartimento di Ingegneria Aerospaziale "L. Lazzarino", Universitá di Pisa, Via G. Caruso 8, 56122 Pisa, Italy
e-mail: a.frediani@dia.unipi.it

G. Buttazzo, A. Frediani (eds.), *Variational Analysis and Aerospace Engineering: Mathematical Challenges for Aerospace Design*, Springer Optimization and Its Applications 66,
DOI 10.1007/978-1-4614-2435-2_4,

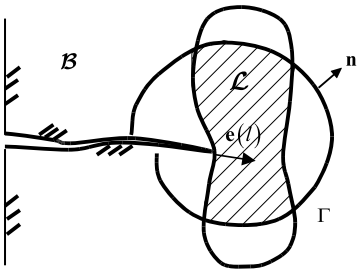

Fig. 1 Definition of the domain $\mathscr{L}$ for numerical evaluation of the CEER

Equation (1) is the *Crack Extension Energy Rate* (CEER) as proposed in [3, 4, 6]; the first term of CEER has the same formal expression of the Rice's J-integral [11] but denotes a different quantity. In fact, the J-integral depends only on the actual elastic state, while $\tilde{J}(\Gamma)$ depends on the whole deformation process. Furthermore, the Rice's J-integral is path-independent because of the solenoidal nature of its integrand (i.e., the elastic energy momentum tensor or *Eshelby tensor* [5]), while $\tilde{J}(\Gamma)$ is not. The path-independence of the CEER is restored with the addition of the surface integral of the divergence of the energy–momentum tensor, which denotes the dissipative contribution to the energy balance, due to plasticity arising around the crack tip. Nevertheless, for elastic materials, Eq. (1) reduces to the Rice's J-integral, and thus the CEER is an appropriate generalization of the J-integral for elastic–plastic materials.

Several studies of numerical evaluation of the CEER can be found in [1, 3, 4, 6, 10], relevant to stationary cracks in different specimens, under *small scale yielding* (SSY) conditions with different hardening rules. The results show that, under monotonic increasing load, the material behaves elastically and the plastic zone at the crack tip has small effects; in such a circumstance the fracture toughness predicted by both the Rice's J-integral and the CEER are equivalent.

However, when the specimens are subjected to cyclic loads, the effects of plasticity become important, even in SSY conditions, and the value of the CEER completely differs from the Rice's J-integral. In particular, at the end of the unloading phase the CEER assumes negative values and during the subsequent phase of increasing load applied the material behaves elastically again, and the CEER increases until a new peak lower than that corresponding to the previous one; this process continues at any cycle of applied load, but the difference between the peaks reduces until a quasi-constant value of the CEER is achieved [1, 4]. The effects on CEER of the amplitude and average tensile stress applied become clearly detectable, and certain phenomena as, for example, the delay of crack growth after a peak of tensile load applied could be qualitatively explained. The effect of hardening rules is mainly important at the end of the unloading phase; then the delay in increasing CEER, during the loading phase subsequent to unloading, can be identified as a closure effect of crack faces.

The aforementioned numerical studies seem to indicate that the CEER can be considered a generalized crack driving force for elastic–plastic materials and, thus, a valid tool of nonlinear Fracture Mechanics.

However, in quasi-static crack propagation under monotonic increasing load, the CEER or, more generally, any Griffith-like energy balance supplies vanishing value of the energy release rate; this results is commonly accepted in literature and known as the *paradox of Rice* [1, 8, 12, 15, 16].

In [12], Rice examined the fracture energy balance for a growing crack in an elastic–perfectly plastic body, under a constant load applied and the assumption of infinitesimal strain; in the case of quasi-static deformations, Rice showed that, from the point of view of the continuum mechanics, the rate of change of the work of applied forces during crack extension equals the rate of change in the stored energy plus the dissipated energy. Consequently, no energy surplus is available to extend the crack. Rice argued that the paradox is a direct consequence of the assumption of perfect plasticity and the classical hypotheses of continuum mechanics (according to which the stress and strain are bounded and change continuously with crack length everywhere in the body except almost at the crack tip). Under these conditions, a Griffith-like energy balance is unable to describe a crack extension, and, therefore, a fracture criterion should be based on the assumption of surface energy from microstructural considerations regarding the separation of material surfaces. In addition, Rice argued that for an elastic-plastic material with work-hardening, a Griffith-like energy balance could predict a nonzero value of the surface energy; this conclusion was based on the assumption that an elastic–plastic material with a high degree of hardening can be treated as an elastic one for which finite energy release rate is found.

In [8], Moran and Shih argued that a nonzero value of the energy release rate can be obtained only if the energy momentum tensor (denoted in their paper as $\mathbf{H}$) is of order r^{-1} as $r \to 0$, with r a radial distance from the crack tip; for material response which can be characterized as highly nonlinear, the energy–momentum tensor is less singular than r^{-1}, and therefore the energy flow to the crack tip is necessarily zero. More precisely, for elastic–plastic materials they argued that, while for a stationary crack in a quasi-statically loaded body, it is worth to assess the surface energy in terms of a Griffith-like energy balance, for growing cracks, this energy balance is zero; furthermore they raised the question whether a Griffith-like energy balance is properly formulated or not for such materials.

The fracture energy balance for elastic–perfectly plastic bodies was later examined using the finite element method by Sun and Wang in [16]; under the assumption of SSY conditions, the results of their simulations confirm the inadequacy of a Griffith-like criterion to predict stable crack growth for any assumed crack extension. They also argued that, at the onset of fracture, a critical value of the plastic dissipation work rate (denoted in their paper as G_p) might be regarded as critical condition for crack extension, and then a relationship between critical plastic dissipation work rate and surface energy of fracture might be stated. However, when finite plastic strains occur, this relationship cannot be established, and, then, the surface energy of fracture must be evaluated on the basis of continuum micromechanics.

In a similar way, Sumpter [13–15] oriented his studies to find a fracture criterion on the basis of a critical value of the energy dissipation rate (denoted in his works as D and representing the derivative of the plastic dissipation with respect to a crack length). The starting point is supplied by a Griffith-like energy balance in which the term due to surface energy is suppressed (that means a zero value of the energy release rate). With such an energy balance, Sumpter identified a condition for stable crack growth in SSY conditions by matching the energy input rate (denoted as C_p or C_{RL}, depending on whether applied loads are constant or increasing during crack extension) to the energy dissipation rate, the latter assumed as a material constant, representing a measurement of fracture toughness.

In [1], Binante raised the question whether the Sumpter's dissipation rate criterion is adequate or not; as it will be shown later on in this paper, the method based on the energy dissipation rate does not represent a fracture criterion, rather it is a direct consequence of the constitutive model of the continuum mechanics considered. The numerical results of this work show that during the whole loading-crack growth process the rate of the work of applied forces is converted into stored energy rate and plastic dissipation rate; therefore, this situation is not an intrinsic feature of crack extension. Furthermore, the plastic dissipation rate cannot be regarded as a material constant (or equivalently as a measurement of fracture toughness), but, as shown in [1] and in this paper, it depends on the applied load, crack length, and specimen shape. It is clearly difficult to identify a critical value of the energy dissipation rate at fracture.

In the literature the paradox of Rice has been assumed to depend on the hypothesis of perfect plasticity and infinitesimal strain; in this paper we show that the paradox is valid even for isotropic-hardening rule under finite deformation. Numerical simulations conduced on compact tension (CT) specimens show both the inadequacy of an energy balance based on the Griffith criterion to describe the stable crack propagation and the impossibility to identify in the plastic dissipation rate a critical condition for crack extension. The results obtained also show that during all crack extension steps the trace of the energy–momentum tensor, P_H, evaluated at the current crack tip, assumes a constant value which is independent of applied load, crack length, and specimen size. If we assume this value as a critical condition for crack propagation, we obtain a load versus crack extension curve which is in excellent agreement with experimental data.

The paper is organized into two main parts. First, we show the results of the finite element analyses of quasi-static growing crack in CT specimens under the assumption of monotonic increasing load; then, we introduce a proposal of crack growth criterion based on the energy–momentum tensor (and called *P-approach*).

2 Numerical Studies of Crack Growth in CT Specimens

In this section, the results obtained from numerical analyses of quasi-static crack propagation under monotonic increasing load are presented. Numerical studies have

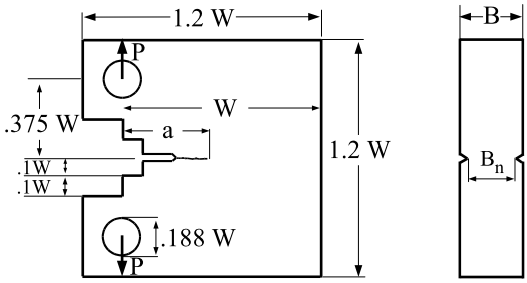

Fig. 2 CT specimen geometries

Table 1 Dimensions of the fracture specimens used in numerical studies

Sample	Sample size in mm			$\frac{a}{W}$
	W	B	a	
CT2	51	12.5	25.5	0.5
CT3	102	12.5	51	0.5

Table 2 Material properties and hardening parameters

Sample	Elastic–plastic properties			Hardening parameters		
	E [GPa]	n	σ_Y [MPa]	β	n	ρ_0 [MPa]
CT2-CT3	71	0.33	315	185.78	0.15	257.31

been restricted to 2-D bodies in plane strain conditions. Two compact tension (CT) samples have been used (see Fig. 2), whose sizes are shown in Table 1.

Elastic–plastic isotropic hardening material have been used for both samples, with mechanical properties shown in Table 2.

The isotropic hardening function can be written in the following way:

$$\rho(\zeta) = \rho_0(1 + \beta\zeta)^n$$

with $n \leq 1$; for $n = 0$, the material is perfectly plastic, while $n = 1$ expresses a linear isotropic hardening function. At each instant τ of a deformation process, $\rho(\zeta(\tau))$ determines the radius of the yield locus, and $\zeta(\tau)$ is the Odqvist parameter, representing the amount of plastic strain [2].

The uniaxial true stress-strain curve is depicted in Fig. 3, relevant to Al2024-T3 aluminium alloy.

Depending on the step-wise approximation of the experimental load-crack extension curve, which have been used to describe the whole process of crack growth, two numerical simulations have been carried out for CT2 samples.

The finite element mesh of a half CT2 specimen have been setup with the following procedure: first, we choose to split the continuous crack growth into a finite number of extension steps Δa, during which the applied load is kept constant; thus, a step-wise approximation of the load-crack extension experimental curve is made (see Fig. 4). During a crack extension from a point A to a point B, it is necessary to

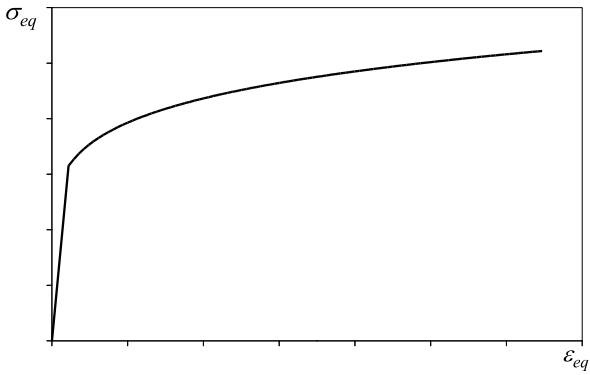

Fig. 3 Uniaxial stress-strain curve of Al2024-T3 alloy, whose mechanical properties are shown in Table 2

use a large number (N) of extension substeps (see Fig. 5). In other words, each extension substep $\delta a = \Delta a/N$ must be sufficiently small in order to capture the work done during the continuous advance of the plastic zone ahead of the crack tip. If the extension substep is not small enough, the plastic dissipation work might be under estimated.

Sun and Wang [16] propose a relationship between the number N of extension substeps and the plastic zone size, which ensures converged solutions; they assert that, for values of the ratio $\delta a/r_p \leq 0.01$, with r_p the plastic zone size, it is possible to capture the small plastic zone, and, then, the plastic dissipation work is accurately calculated. Therefore, in all simulations of crack growth we have maintained $\delta a/r_p = 0.01$. We remark that δa determines the characteristic length of the element on crack front ahead of the current crack tip.

To estimate the plastic zone size, the Irwin's plane strain formula has been used, namely,

$$r_p = \frac{K_I^2(a)}{6\pi\sigma_Y^2},$$

where σ_Y is the uniaxial tensile yielding stress, and $K_I(a)$ is the *Stress Intensity Factor* (SIF), as evaluated from SIF handbook for CT specimen

$$K_I = \frac{P}{B \cdot W}\sqrt{a} \cdot \left(29.6 - 185.5 \cdot \left(\frac{a}{W}\right) + 655.7 \cdot \left(\frac{a}{W}\right)^2 - 1017 \cdot \left(\frac{a}{W}\right)^3 + 638.9 \cdot \left(\frac{a}{W}\right)^4\right).$$

This expression is valid for $a/W \leq 0.7$; in the above formula, P is the applied load taken from the experimental curve ("P" versus "a"), corresponding to the current crack length a.

With this procedure, a finite element mesh of 46066 plane strain isoparametric four-node elements with 46613 nodes has been used. The characteristic length of the elements immediately ahead the crack tip is about 0.005 mm.

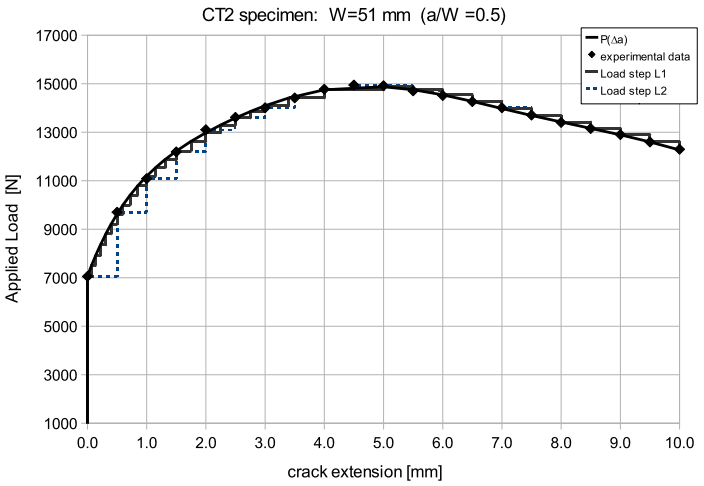

Fig. 4 Load versus crack extension curve used in numerical simulation of crack growth for CT2 specimens. Experimental curve from [7]

The separation of crack surfaces during crack growth has been simulated using the nodal release technique in which the crack tip nodal reaction force is decreased to zero by M steps, where M should be large enough to ensure numerical convergence (see Fig. 6(a)). As proposed in [16], a value of $M = 50$ debonding steps has been chosen. Figure 6(b) shows the crack length as a piecewise linear function of time, which has been considered for the crack growth in any extension substep.

The experimental load versus crack extension curves used in all numerical simulations are taken from [7, 9, 17].

As shown in Fig. 4, two stepwise approximations of the experimental curve have been used: the first loading history L1 consists of 29 loading steps and 384 debonding steps, each realized by 50 release steps. Thus, a total of 413 loading–debonding steps have been used to simulate 8.5 mm of crack extension. At the first stages of the crack growth process, small extension steps Δa (typically $\Delta a = 0.07$ mm), in which load is kept constant, were used; later on, when crack growth resistance curve decreases, larger values of Δa have been used, up to a maximum value of $\Delta a = 0.5$ mm. The maximum experimental load is about 15 kN corresponding to about 4.5 mm of crack extension. Loading history L2 differs from L1 as far as loading steps are concerned; a total of 17 loading steps have been applied up to 8.5-mm crack length and, for any applied load, the crack has been extended for $\Delta a = 0.5$ mm (see Fig. 4).

Now, before discussing the numerical results, we need to correlate the *Crack Extension Energy Rate* (CEER) and global energy rate during a crack growth [2].

Let t_0 and t_1 be the initial and final time in which crack grows from a length a_0 to a_1, respectively. In all numerical simulations, assumptions **A1**–**A7** in [2] have been kept, together with the condition of a constant applied load during crack increments;

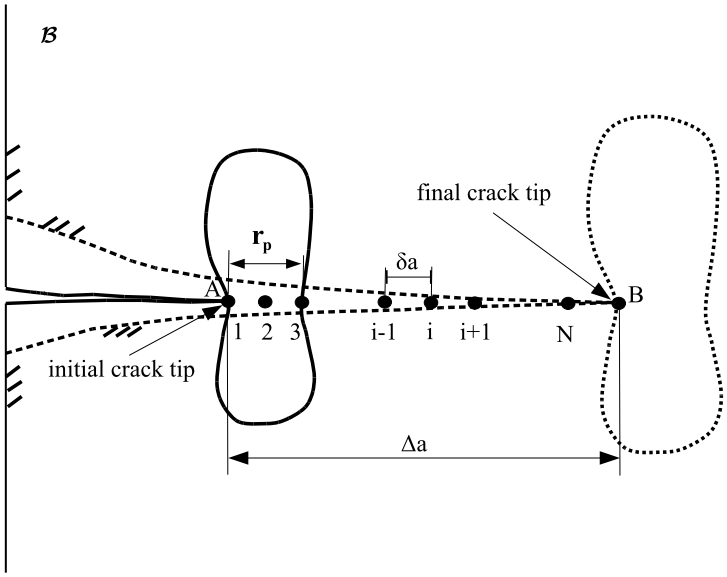

Fig. 5 Partition of an extension step Δa into N substeps δa

furthermore, finite strains may occur in the crack tip region. For convenience, some of the assumptions in [2] are reported below.

1. $P = \text{const}\ \forall t \in [t_0, t_1]$;
2. $a(t_0) > 0$, $\frac{da}{dt} > 0\ \forall t \in [t_0, t_1]$;
3. $\mathbf{Tm} = \mathbf{0}$ *on* A'.

The second assumption identifies the crack length as a time scale so that $\partial(\cdot)/\partial a \propto \partial(\cdot)/\partial t$; the third assumption implies that the newly created crack surfaces, A', are stress-free.

Let V be the volume of a region occupied by the body whose boundary ∂V consists of a region A_T, where a constant stress tensor $\mathbf{T}_0$ is applied, a region A_U, where fixed displacements are imposed, and the newly created crack surface A' (see Fig. 7). During a crack growth process in the time interval $[t_0, t_1]$, because the new crack surface is stress-free and $\dot{\mathbf{u}} = \mathbf{0}$ on A_U, the work done by the external loads is

$$W = \int_{\partial V} \left[\int_{t_0}^{t_1} \mathbf{T}_0 \mathbf{n} \cdot \dot{\mathbf{u}}\, d\tau \right] dA = \int_{\partial V} \mathbf{T}_0 \Delta \mathbf{u} \cdot \mathbf{n}\, dA.$$

Applying the divergence theorem to volume V and bearing in mind that body forces are null, we get

$$W = \int_V \left[\int_{t_0}^{t_1} \mathbf{T}_0 \cdot \nabla \dot{\mathbf{u}}\, d\tau \right] dV = \int_V w_0\, dV;$$

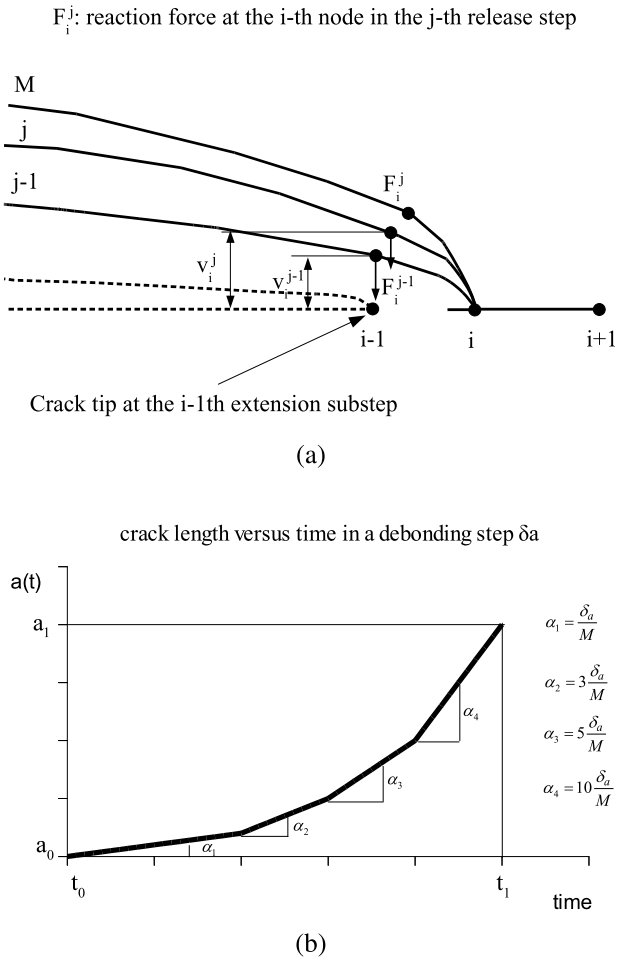

Fig. 6 A process of crack growth: (**a**) nodal release technique; (**b**) piecewise linear function of crack length versus time used in an extension substep δa (Fig. 5)

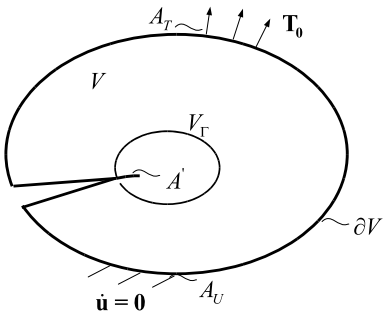

Fig. 7 Schematic representation of the crack-tip region

the work done by the internal forces during a crack extension is

$$U = \int_V w\, dV = \int_V \left[\int_{t_0}^{t_1} \mathbf{T} \cdot \nabla \dot{\mathbf{u}}\, d\tau \right] dV.$$

With reference to Fig. 7, we consider a finite volume V_Γ which completely surrounds the crack-tip region at the time t_0 and such that the newly created crack surface A' at time t_1 is inside V_Γ. Let Γ be the bounding surface of V_Γ.

The external work can be rewritten as

$$W = \int_{V_\Gamma} w_0\, dV + \int_{V - V_\Gamma} w_0\, dV;$$

the derivative with respect to crack length is

$$\frac{\partial W}{\partial a} = \frac{\partial}{\partial a} \int_{V_\Gamma} w_0\, dV + \frac{\partial}{\partial a} \int_{V - V_\Gamma} w_0\, dV.$$

By applying the classical transport theorem to the integral over $V - V_\Gamma$, we obtain [2]

$$\frac{\partial}{\partial a} \int_{V - V_\Gamma} w_0\, dV = \int_{V - V_\Gamma} \frac{\partial w_0}{\partial a}\, dV - \mathbf{e} \cdot \int_\Gamma w_0 \mathbf{n}\, ds;$$

bearing in mind Assumption 2 and applying the divergence theorem to the integral over $V - V_\Gamma$ on the right-hand side of the above equation, we can rewrite the rate of the external work as

$$\frac{\partial W}{\partial a} = \frac{\partial}{\partial a} \int_{V_\Gamma} w_0\, dV + \int_{A_T} \mathbf{T}_0 \nu \cdot \dot{\mathbf{u}}\, ds - \int_\Gamma \mathbf{T}_0 \mathbf{n} \cdot \dot{\mathbf{u}}\, ds - \mathbf{e} \cdot \int_\Gamma w_0 \mathbf{n}\, ds.$$

Finally, taking the limit for $\Gamma \to 0$ of the above expression and keeping assumptions **A3** and **A4** in mind, we get:

$$\frac{\partial W}{\partial a} - \int_{A_T} \mathbf{T}_0 \nu \cdot \dot{\mathbf{u}}\, ds = -\mathbf{e} \cdot \lim_{\Gamma \to 0} \int_\Gamma \left(w_0 \mathbf{I} - \nabla \mathbf{u}^T \mathbf{T}_0 \right) \mathbf{n}\, ds = -CEER(a_0), \quad (3)$$

where $CEER(a_0)$ is the value of the energy release rate at the onset of the crack extension.

Similarly, the rate of the work done by the internal forces, during the crack extension, is obtained by

$$\frac{\partial U}{\partial a} - \int_{A_T} \mathbf{T} \nu \cdot \dot{\mathbf{u}}\, ds = -\mathbf{e} \cdot \lim_{\Gamma \to 0} \int_\Gamma \left(w \mathbf{I} - \nabla \mathbf{u}^T \mathbf{T} \right) \mathbf{n}\, ds = -CEER(a), \quad (4)$$

which is equivalent to Eq. (11) of [2]; subtracting Eq. (4) from Eq. (3), we get

$$\frac{\partial W}{\partial a}(a) - \frac{\partial U}{\partial a}(a) = \Delta \mathscr{E}(a) = CEER(a) - CEER(a_0); \quad (5)$$

thus, during the crack extension from a_0 to a_1, the energy release rate is evaluated as the change in CEER between the current crack length and that at the onset crack growth.

The energy release rate may also be evaluated from the global energy balance as the difference between the rate of the external work and the rate of change in internal energy.

Figure 8 shows a numerical evaluation of a global energy balance per unit thickness for the CT2 specimen undergoing the loading history L1 during the first 3.5 mm of crack growth. The work done by the internal forces, U, is split into a stored elastic energy, U_{el}, and a dissipated plastic energy, U_{pl}; the bulk energy, E_{bulk}, is evaluated as the difference between the external work and the internal energy. Thus, in Fig. 8(a) we show all the energy terms as functions of crack extension during the whole loading-crack growth process; due to the approximation of the loading history, each energy is described as a step-wise function $f(P, \Delta a)$ of the applied load, P, and the crack growth, Δa, in which the step represents the loading application. Figure 8(b) shows the rate of the energy terms, and Fig. 8(c) depicts the ratio of elastic, plastic, and bulk energy rates to the external work rate.

The result is that, during a crack extension under constant load, the external work is converted into a stored elastic energy and a dissipated plastic energy and the bulk energy is negligible; this occurs for every crack extension step.

Furthermore, with reference to Eq. (5), we obtain that the rate of the bulk energy represents the energy release rate during a crack extension; for each extension step, the bulk energy is negligible, or, equivalently, no energy surplus is available during the extension of a crack length from a_0 to a_1, and the crack extension is unreal.

Similar results have been obtained for loading history L2 (Fig. 9 relevant to 5.5 mm of crack extension); contrary to loading history L1, the energy rates during the crack extension are not constant. This is due to the step-wise approximation of the loading history; in fact, the loading history L1 better fits the experimental curve than L2, and, therefore, we can expect that the energy rates, during a crack extension previous to the achievement of the maximum applied load, assume a quasi-constant value. Thus, it is reasonable to assume that the external work rate and the rate of change in internal energy depend only on the current applied load for values of the cumulative crack growth Δa less than a critical value, in correspondence of which unstable crack growth occurs. This critical value can be determined from the slope of the experimental curve $\frac{dP}{d(\Delta a)}$ (similar to tearing resistance curve); when $\frac{dP}{d(\Delta a)}$ decreases more quickly until negative values, the rate of all energy terms are no longer constant with respect to crack length (see Fig. 9(b)). In this circumstance, the plastic dissipation rate becomes larger than the elastic strain rate and, furthermore, shows a more marked dependence on crack length. Anyway, the most important feature shown in Fig. 9(b) is a negligible value of the bulk energy rate during the whole crack growth process, as we have found for the loading history L1.

The result of a vanishing energy surplus is known as the paradox of Rice. As shown in [12], the inadequacy of a Griffith-like energy balance to assess a fracture criterion for crack propagation is due to limits of continuum mechanics, on the basis of which the energy balance is formulated. Relative to small scale yielding conditions and for elastic–perfectly plastic materials, Rice showed that the paradoxical

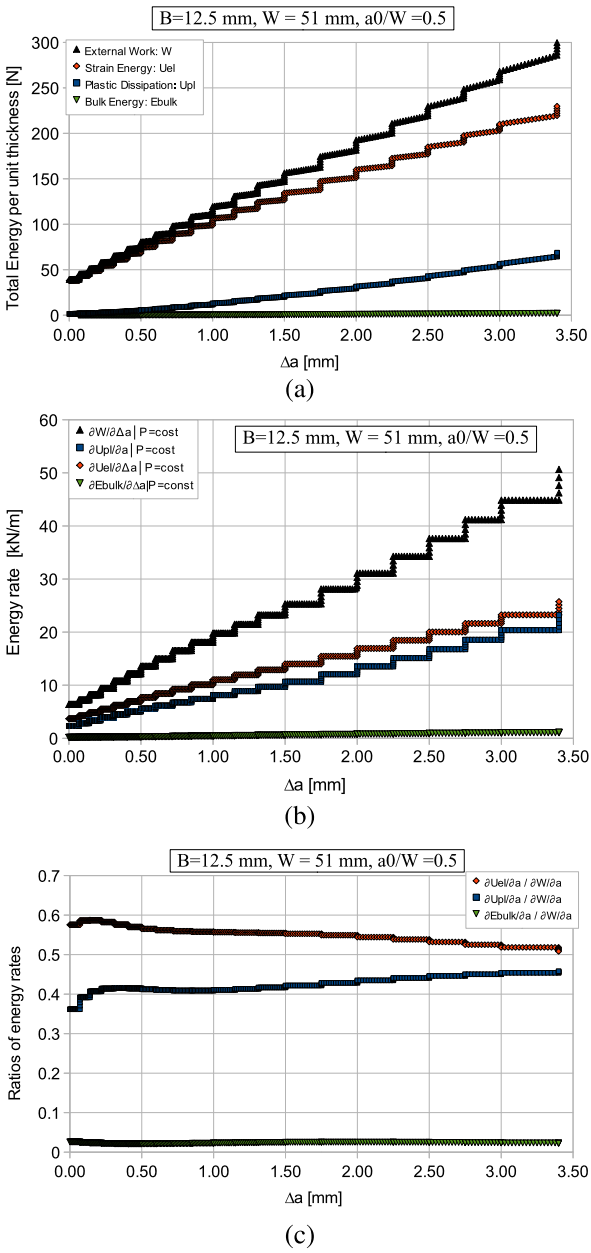

Fig. 8 Energy rates versus crack extension in the first 3.5 mm of crack growth for CT2 sample undergoing the loading history L1

conclusion is due to the classical assumptions of smoothness in stress and strain fields, with respect to which stress and strain fields may be singular only at the crack tip. Furthermore, Rice argued that, when an elastic–plastic material exhibits a work-hardening behavior, a nonnull value of the energy surplus might be achieved.

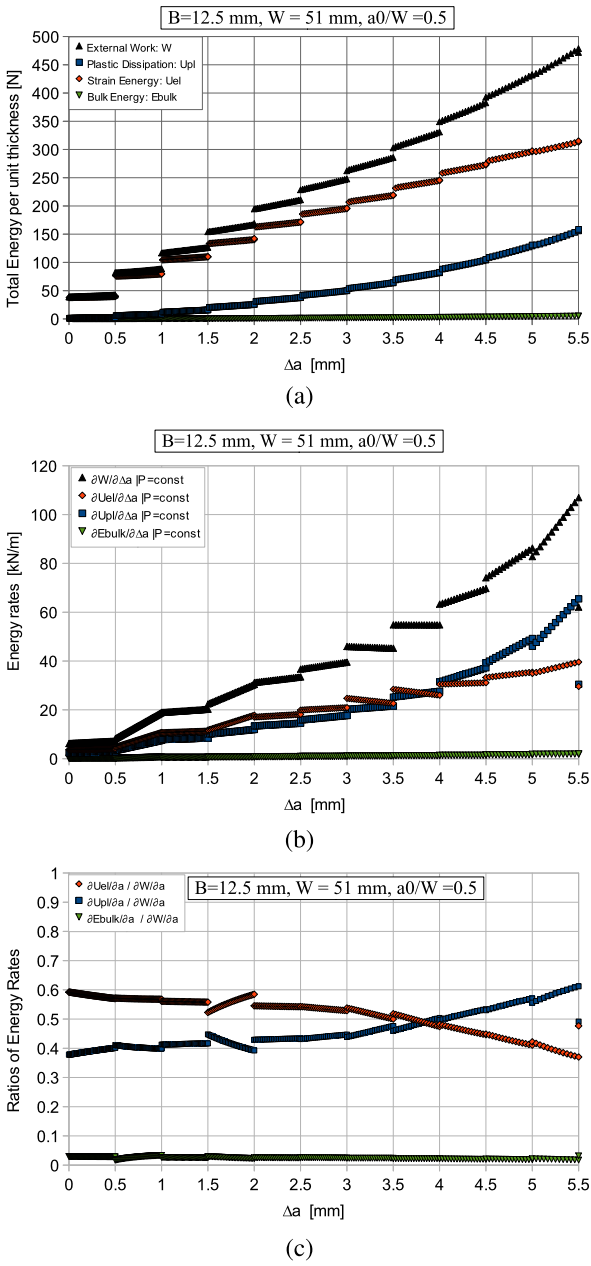

Fig. 9 Energy rates versus crack extension in 5.5 mm of crack growth for CT2 sample undergoing the loading history L2

This consideration is justified considering that, when the level of work-hardening is sufficiently high to have an elastic behavior of material, the energy release rate is finite; on the contrary, a very small work-hardening level is equivalent to a perfectly plastic material; in this case the energy release rate is zero.

The results of Figs. 8–9, however, show that the energy release rate is null, even when work-hardening behavior is taken into account, regardless of small or finite strain conditions; in fact, the global energy balance states that

$$W - U = \int_V \left[\int_{t_0}^{t_1} (\mathbf{T}_0 - \mathbf{T}) \cdot \nabla \dot{\mathbf{u}} \, d\tau \right] dV = \int_V (w_0 - w) \, dV \approx 0,$$

and, because it is valid for any finite volume V, we get

$$\int_{t_0}^{t_1} (\mathbf{T}_0 - \mathbf{T}) \cdot \nabla \dot{\mathbf{u}} \, d\tau \approx 0.$$

The above relationship states that, during the crack extension, the stress and strain fields vary continuously everywhere in V, except, almost, just at the crack tip. Furthermore, the changes in stress field for $t \in [t_0, t_1]$ are negligible. From the Eqs. (3)–(5), this implies

$$\begin{aligned} \Delta \mathscr{E}(a) &= -\mathbf{e} \cdot \lim_{\Gamma \to 0} \int_\Gamma \left[(w_0 - w)\mathbf{I} - \nabla \mathbf{u}^T (\mathbf{T}_0 - \mathbf{T}) \right] \mathbf{n} \, ds \\ &\approx \mathbf{e} \cdot \lim_{\Gamma \to 0} \int_\Gamma \left[\nabla \mathbf{u}^T (\mathbf{T}_0 - \mathbf{T}) \right] \mathbf{n} \, ds \approx 0, \end{aligned}$$

and, thus, irrespective of small or finite conditions on the displacement field, the energy release rate during the crack extension is null.

Therefore, for elastic–plastic materials an energy balance according to the Griffith's criterion cannot be formulated; in the case of stationary crack and/or quasi-static crack propagation in an elastic body, the only dissipative mechanism is due to a crack (extension), and, then, the energy surplus in Griffith's criterion, representing the energy dissipated into the body, can be identified as energy available to extend a crack. For elastic–plastic materials, there are essentially two dissipative mechanisms: one is due to the creation of a plastic zone close to the crack-tip region with increasing load; the other is due to the spread of plastic flow on the crack front as the crack advances. In the case of stationary crack in an elastic–plastic body, a Griffith-like energy balance can yet be formulated, with the plastic work rate expressing the effect of arising plastic zone at the crack tip with increasing load. In the case of crack propagation in elastic–plastic materials, the plastic work rate takes the loading and crack growth effects on plastic flow into account, and, thus, no other energy rate term into an energy balance should be considered. This is true whether infinitesimal or finite strain conditions are used. In other words, in order to assess a fracture criterion, the energy required for extending a crack (called surface energy of fracture) may be correlated to some critical condition of the plastic dissipation rate. In such a sense, Rice argued that, from a point of view of continuum mechanics, the fracture criterion might be restated in the following way:

$$\frac{\partial W}{\partial a}(P_f) - \frac{\partial U_{\mathrm{el}}}{\partial a}(P_f) = \frac{\partial U_{\mathrm{pl}}}{\partial a}(P_f), \tag{6}$$

where in his paper the left-hand side of the above relationship was denoted as $\mathscr{G}$ and $\frac{\partial U_{\mathrm{pl}}}{\partial a}$ as p; P_f is the load at fracture. However, the value of the plastic dissipation rate at fracture cannot be considered as a material constant; rather it should be related to the surface energy (denoted in his paper as 2Γ), the latter being evaluated from microstructural considerations of the separation of material surfaces. This concept has been later resumed by Sun and Wang [16], who stated that under small scale yielding conditions for elastic-perfectly plastic materials the plastic dissipation rate (denoted in their paper as plastic dissipation work rate G_p) at the onset of fracture might be regarded as a fracture criterion, even though it cannot be identified as the surface energy of fracture which must be evaluated on the basis of continuum micromechanics. Furthermore, they argued that, when finite plastic strains occur, a relation between plastic dissipation rate and surface energy of fracture cannot be established, and then this approach is no longer adequate. Along the same line, Sumpter oriented his works [13–15] to find a fracture criterion on the basis of a critical value of the energy dissipation rate. The starting point is supplied by Eq. (6) (in his papers, $\frac{\partial U_{\mathrm{pl}}}{\partial a}$ is the dissipation energy rate denoted as D, while the left-hand side of the equation is identified as the input energy rate and denoted as C); he confined his attention to identify in this relation a condition to predict stable crack growth and tearing instability in small scale yielding conditions. According to his approach, stable crack growth occurs when the value of the energy input rate C_{RL} under increasing load matches the value of the energy dissipation rate D, while the unstable tearing, occurring when the crack propagates under constant load, is predicted by the matching of C_p to D. In this approach, the input energy rate C depends on specimen geometry, crack length, stress, and load path during crack advance and can be evaluated from numerical analyses. The energy dissipation rate D is considered as a constant material and represents a measure of material toughness.

Some conclusions concerning the use of the plastic dissipation rate as a fracture criterion are questionable: (1) is this approach adequate? In our opinion, it does not represent a fracture criterion, rather it is a direct consequence of the constitutive model considered, based on continuum mechanics. As the present numerical results show, during the whole loading-crack growth process, the external work is quasi-completely converted into stored elastic energy and plastic dissipation energy; therefore, this situation is not an intrinsic feature of fracture. Furthermore, even if the effect of the crack extension on the plastic flow can be regarded as some critical condition of fracture, generally, it is difficult to identify this condition, even with the support of finite element analyses. A relation between critical value of the plastic dissipation rate and surface energy of fracture, as Rice suggested, requires the knowledge of the latter, which, generally, cannot be regarded as a material constant, but it should be evaluated from continuum micromechanics. (2) Should we take the total or local plastic dissipation rate into account, as a fracture criterion? In the literature this is yet an open question. In our opinion, a local form of the fracture criterion is preferable for two considerations; first, from a point of view of the correlation between fracture process zone and plastic dissipation rate, it is preferable to discard the work due to plastic flow at material points away from the crack surface. Secondly, we should consider only the contribution of plastic flow due to

crack extension. (3) On what basis can a critical condition of the plastic dissipation rate be established? As we already said, it is difficult to identify a fracture condition from a critical value of the plastic dissipation rate because, generally, the latter depends on the applied load, crack length, and specimen geometry. Therefore, it cannot be considered as a material constant. Sumpter assumed a constant value of the energy dissipation rate D as a material toughness, however, this is not correct, according to our opinion. To better understand this concept, we look at the results of Fig. 8(b); they show that, during the crack extension, $\frac{\partial U_{\text{pl}}}{\partial a}$ assumes a constant value with respect to crack growth Δa but depends on the current fixed value of the applied load P, that is, $\frac{\partial U_{\text{pl}}}{\partial a} = \frac{\partial U_{\text{pl}}}{\partial a}(P)$. Furthermore, if we consider the results of Fig. 9(b), we can see that, during a crack extension step, the plastic dissipation rate can vary linearly with respect to crack growth, and then $\frac{\partial U_{\text{pl}}}{\partial a} = \frac{\partial U_{\text{pl}}}{\partial a}(P, a)$. Clearly, these results depend on step-wise approximation of the experimental curve load versus crack length and that the loading history L1, for which a constant value of the plastic dissipation rate is found during crack growth, better fits the experimental curve than the loading history L2. However, for large values of Δa, L1 and L2 are identical, and we can see from Fig. 9(b) that there is a trend in plastic dissipation rate and elastic strain rate, which is inverse with respect to small values of Δa. That is, for values of Δa in correspondence of which $\frac{dP}{d(\Delta a)}$ decreases or becomes negative (tearing instability), the plastic dissipation rate increases with increasing crack length more quickly than the elastic strain rate. Thus, if it is reasonable to assume a constant value of the plastic dissipation rate with respect to a crack length, for values of Δa previous to the tearing instability, this is no longer valid as the tearing instability is approached. Finally, it is known in the literature that a geometry dependence of the plastic dissipation rate is envisaged. Therefore, we can conclude that a critical value of the plastic dissipation rate cannot be considered as a measure of material toughness.

From the above considerations we can conclude that the energy release rate, as evaluated from continuum mechanics according to Griffith's criterion, does not correspond to the surface energy of fracture because the former predicts zero value during crack extension. The plastic dissipation rate, as evaluated from continuum mechanics, is not a valid approach to predict crack growth because if it admits a critical value, this cannot be regarded as a characteristic parameter of fracture. Therefore, it is not possible to derive a fracture criterion by using an energetic approach based on continuum mechanics.

The surface energy of fracture represents the rate of work done by surface fractions on A' as the new crack surface is created:

$$\mathscr{G}\left(l^j_{FPZ}, T\right) = -\lim_{A' \to 0} \frac{1}{A'} \int_{A'} \left[\int_{t_0}^{t_1} \mathbf{T}\mathbf{n} \cdot \dot{\mathbf{u}}\, d\tau \right] da, \tag{7}$$

which is negative since the surfaces are pulled apart under opposing stresses; the work should be evaluated by microstructural considerations of the separation of material surfaces. Thus, it depends on some characteristic parameters of the *Fracture Process Zone* (FPZ) l^j_{FPZ} (such as void volume ratio f, void aspect ratio S, void distribution λ, which are tied to material microstructure) and stress triaxiality T.

When a mechanism of fracture is quasi-brittle or in the case of stationary crack in small scale yielding, a Griffith-like energy balance can be expressed by Eq. (7), and, thus, the continuum estimate of the surface energy agrees with microstructural one. When this is no longer valid (mechanism of fracture involves large plastic deformations in the FPZ, outside of which small scale yielding conditions are still valid), the continuum estimate predicts zero value of the energy release rate, while a crack grows from a length a_0 to a_1.

Experimental investigation of fracture surfaces, associated with a ductile-type mechanism of fracture, suggests that crack extension is a result of large plastic flow causing a large void to coalesce with smaller voids nearby, the latter being either preexisting or created by deformation around inhomogeneities. In such a case, the fracture propagation is a consequence of large deformations causing a crack extension by the flowing together of voids. One may define a surface energy $\mathscr{G}$ by considering the work required to coalesce a row of voids with the proper mean spacing λ, and proceed to obtain a fracture criterion through the energy balance. Some researchers state that fracture occurs when local stresses in a region close to crack tip overcomes cohesive forces acting on the crack surface; in such a context, the surface energy $\mathscr{G}$ is interpreted as the work per unit area done by cohesive forces in a small region near the crack tip to push crack surfaces. Anyway, the cohesive forces should be evaluated on microstructural sound, and, then, they may be correlated to the FPZ.

The evaluation of surface energy for elastic–plastic materials requires the knowledge of some phenomena occurring in the FPZ such as void nucleation, void growth, and void coalescence. In order to derive a fracture criterion based on energetic approach, it is opportune to leave the classical assumptions of continuum mechanics and adopt constitutive model more suitable to describe the microstructural phenomena in FPZ.

Concerning to the role of the FPZ on ductile-type fracture mechanism, here, we want to conclude showing that, if we adopt a constitutive model which incorporates damage phenomena such as those aforementioned, a nonnull value of the energy release rate may be achieved, and a relation with the surface energy can be restored. In so doing, we rewrite Eq. (5) as

$$\Delta\mathscr{E} = \lim_{A'\to 0} \frac{1}{A'} \int_V \left[\int_{t_0}^{t_1} (\mathbf{T}_0 - \mathbf{T}) \cdot \nabla \dot{\mathbf{u}} \, d\tau \right] dV;$$

as already done, we split the volume V into two parts: a small volume V_{FPZ} surrounding the FPZ in the crack tip region and the volume $V - V_{FPZ}$, where the material behavior can be described according to continuum mechanics. As we have previously seen, the changes in strain and stress fields in $V - V_{FPZ}$ during the crack extension are negligible, and then the integral over $V - V_{FPZ}$ is infinitesimal of order two in A' and disappears as $A' \to 0$. Thus Eq. (5) reduces to

$$\Delta\mathscr{E} = \lim_{A'\to 0} \frac{1}{A'} \int_{V_{FPZ}} \left[\int_{t_0}^{t_1} (\mathbf{T}_0 - \mathbf{T}) \cdot \nabla \dot{\mathbf{u}} \, d\tau \right] dV.$$

As known, the void coalescence represents the final stage of ductile fracture process and implies a localization of plastic flow in narrow bands of coalescing voids,

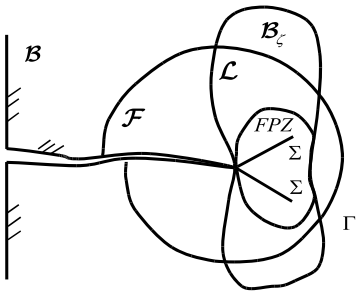

Fig. 10 Discontinuity surfaces inside of the FPZ

outside of which the material undergoes elastic unloading. The different mechanism of deformation between the outside region and inside of the narrow-band triggers off the creation of discontinuity surfaces Σ of the total strain rate $\nabla\dot{\mathbf{u}}$ (see Fig. 10). In such a case, we have

$$\Delta\mathscr{E} = \int_{\Sigma}\left[\int_{t_0}^{t_1}(\mathbf{T}_0 - \mathbf{T})\mathbf{n}\cdot\dot{\mathbf{u}}\,d\tau\right]da,$$

which allows us to overcome the paradox of Rice.

3 A Proposal of a New Criterion of Quasi-static Crack Propagation

Although a continuum treatment of the energy release rate predicts paradoxical results and the plastic dissipation rate seems to be not a valid approach, it seems to be still possible to use the framework of continuum mechanics in order to find some critical conditions at fracture. A new approach to describe quasi-static crack growth is proposed here, based on the numerical studies of the previous section. This approach is, currently, supported by only numerical results, and, thus, more research activity is needed to validate it on a theoretical basis and more numerical studies must be carried out concerning different structures and materials.

The stress and strain fields at the current crack tip are investigated, and, in particular, the energy–momentum tensor $\mathbf{P}$ is examined; as we have discussed in [2], $\mathbf{P}$ represents the generalized force acting on defect (crack). In the absence of a more refined theoretical basis, the present proposal starts from the assumption that the energy–momentum tensor stores the whole history of deformation, plastic region expansion, elastic unloading when the crack advances, and so on. We consider the hydrostatic component of the energy–momentum tensor P_H,

$$P_H = \mathbf{P}\cdot\mathbf{I} = \sum_i P_i. \tag{8}$$

Figure 11 shows the distribution of P_H along the crack front, in the presence of the loading history L2 for a CT2 specimen; the trace of the energy–momentum tensor is evaluated at the centroid of each element positioned into the plane of fracture,

including also the elements positioned along the crack faces. The profile of P_H is shown for some loading steps (at the last increment of them) before a crack extension. Thus, Fig. 11(a) depicts the value of P_H at the end of the load step of 7 kN at the incipient propagation ($\Delta a = 0$) for all bonded elements of the crack front; the maximum value of P_H is at the current crack tip and, quickly, decreases with increasing distance from crack tip. The same occurs for the other considered loading steps during the crack-growth process; in particular, for a given loading step of the deformation process, P_H is maximum at the current crack tip and in correspondence of those underwent the previous load increments. Ahead of the current crack tip, P_H decreases quickly to negligible values, while, all elements behind it, which did not have to undergo a load increment, assume a quasi-constant value of P_H. The over-peaks of P_H depend on the magnitude of the load increment, ΔF; with reference to Fig. 4, the step-wise loading function L2 provides a maximum value of $\Delta F \approx 2.6$ kN in correspondence with the second loading step. In such a case, the element undergoing this load increment exhibits larger strains than the others and, then, a higher value of P_H. Therefore, we can deduce that the over-peaks depend on the particular step-wise approximation of the loading history considered. If a step-wise approximation is made of small values of ΔF, the magnitude of the over-peaks of P_H is correspondingly reduced; this occurs for the loading history L1 (see Fig. 12), which is characterized by more loading steps than L2 with smaller ΔF. As a limiting case in which ΔF is infinitesimal, a crack growth history with continuous loading applications should be characterized by a constant value of P_H for all elements behind the current crack tip.

By comparing the two step-wise loading functions, we can see that, irrespective of the over-peaks and the level of the applied load, all elements which do not have to undergo a load increment show, approximatively, the same value of P_H, suggesting that the force acting on the crack during its propagation is quasi-constant.

Therefore, confining our attention at the current crack tip only, we are interested in knowing the value of P_H at the onset of fracture; thus, Figs. 13(b) and 13(a) show that, irrespective of the considered loading history, during crack growth, the trace of the energy–momentum tensor assume a constant value, with a high degree of approximation. This remark suggests us to identify this constant value as the critical condition for crack growth. In particular, the constant value of P_H is about $\bar{P} = 40$ MPa in the case considered. We conclude that, for a given shape of the specimen, $\bar{P}$ is independent of the current applied load and crack length, unlike the value of plastic dissipation rate which, as already discussed, shows a dependence on them.

In order to candidate this critical condition as a criterion of crack growth, we should verify that $\bar{P}$ is independent of the specimen size. In such a context, we have considered the CT specimen, CT3, whose dimensions are shown in Table 1, and the value $\bar{P} = 40$ MPa has been kept. The finite element mesh of a half CT3 has been made according to the procedure shown in Sect. 2; the numerical simulation requires an iterative procedure for the load application, because a priori knowledge of the boundary conditions which imply P_H to be equal to $\bar{P}$ is not possible. The flowchart of the iterative procedure is shown in Fig. 14; regarding the loading history to

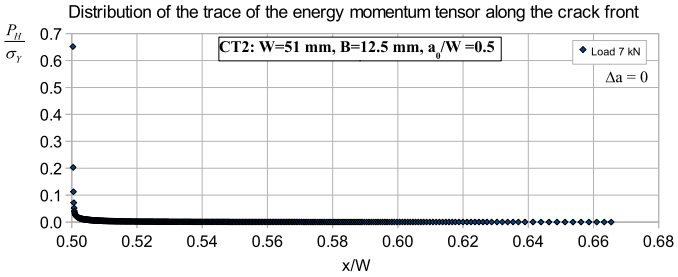

(a)

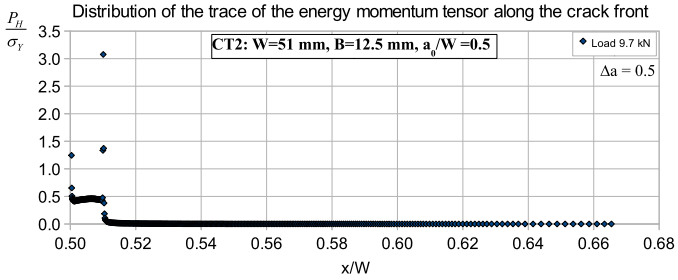

(b)

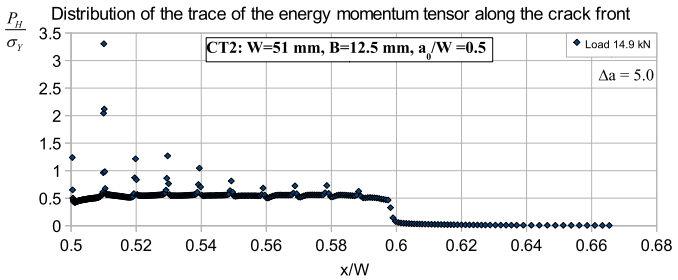

(c)

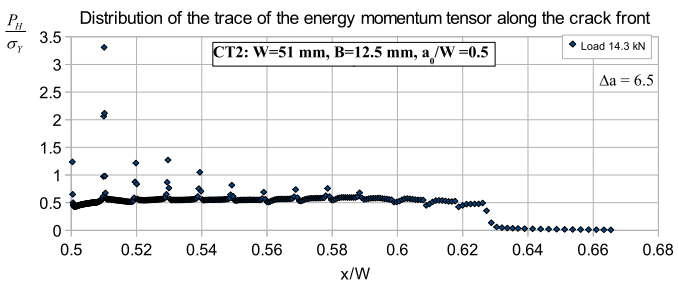

(d)

Fig. 11 Trace of the energy–momentum tensor along the crack front at several load increments. Loading history L2

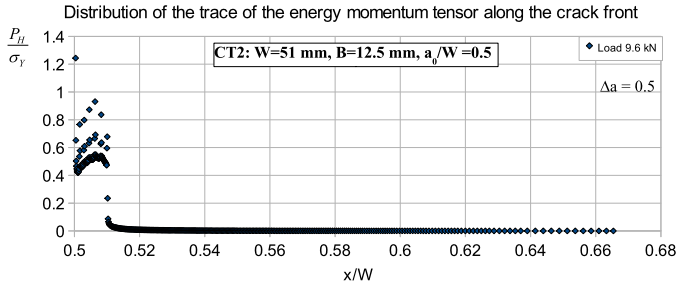

(a)

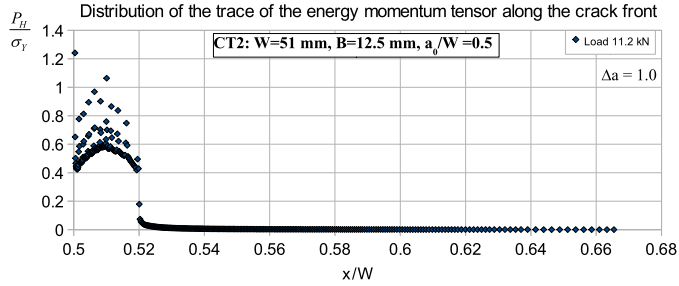

(b)

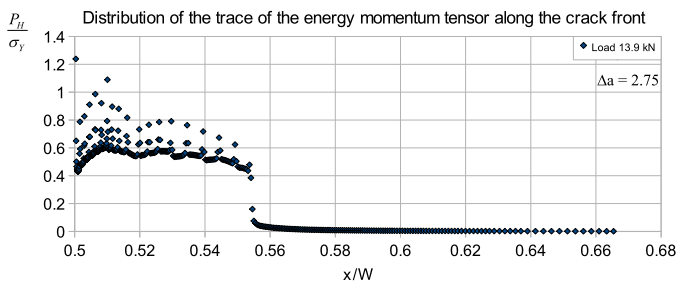

(c)

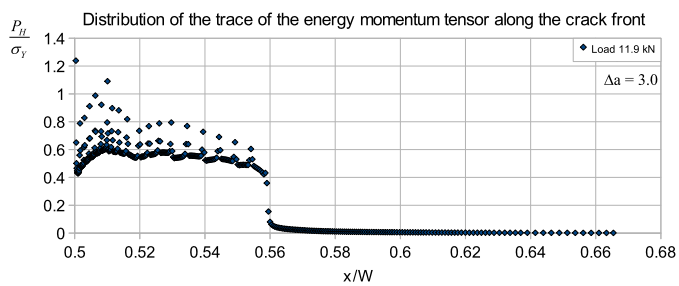

(d)

Fig. 12 Trace of the energy–momentum tensor along the crack front at several load increments. Loading history L1

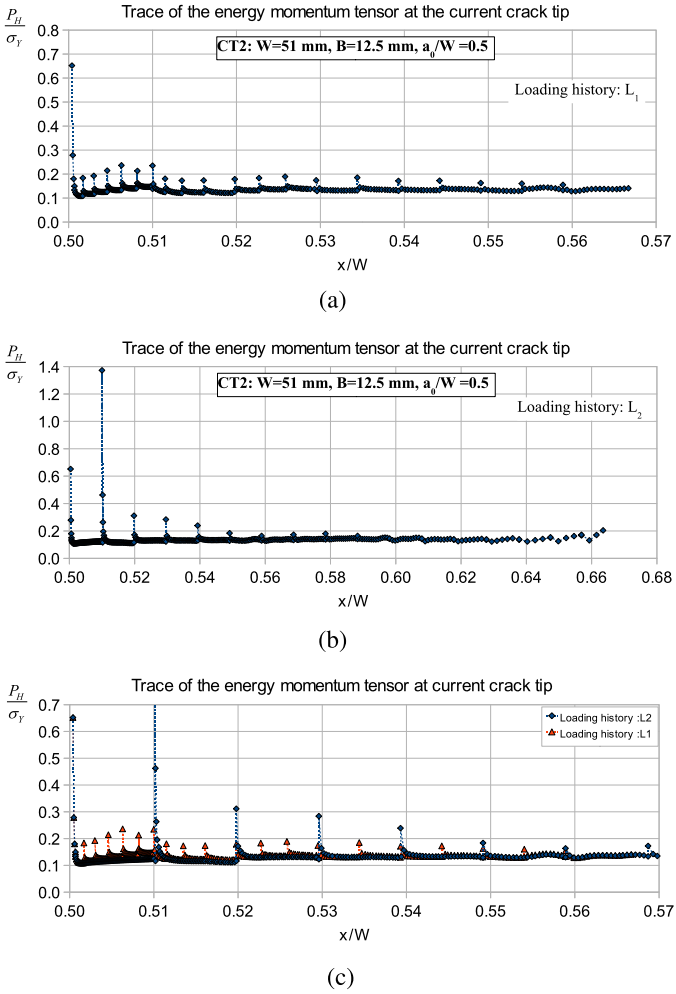

Fig. 13 Trace of the energy–momentum tensor at the current crack tip for two loading histories

be reproduced, we have used only the value of the load applied, F_{IC}, at the onset of crack growth, taken from experimental data [7]. This is necessary because the fracture criterion proposed might predict crack-growth conditions, but not fracture toughness. The iterative procedure in Fig. 14 is based on the application of small extension steps Δa_i (then δa_i) in which the unknown load $F_i = F_{i-1} + \Delta F_i$ is kept constant. As far as the influence of the applied load on P_H is concerned, a large applied load produces high peaks of P_H, and, then, more steps of computation are needed to verify that P_H equals $\bar{P}$. Thus, a choice of small Δa_i is more suitable; in particular, the first check on P_H has been carried out after $N^* = 4$ extension substeps δa_i subsequent to the load application.

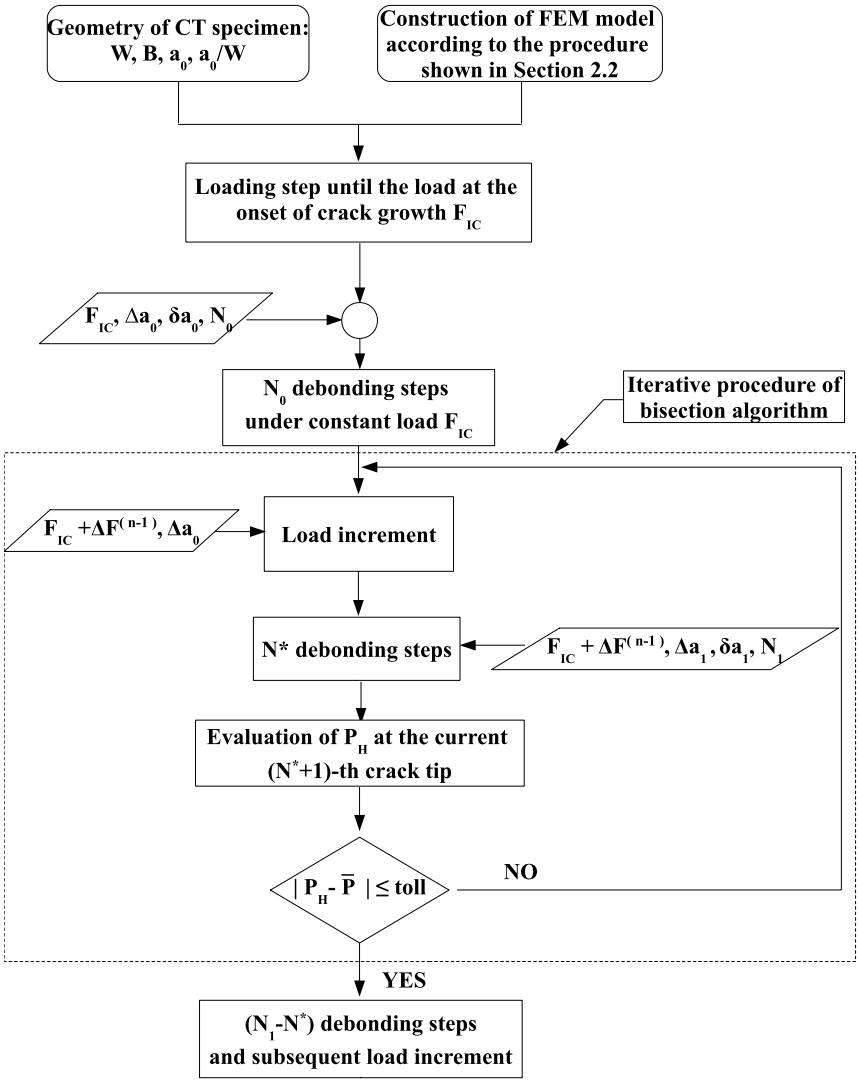

Fig. 14 Flow-chart of iterative procedure for load applications in CT3 sample

Figure 15 shows the experimental load versus crack extension curve together with that obtained by the above iterative procedure. As we can see, they are in a good agreement (see also Table 3); therefore, on the basis of the independence from the applied load, specimen size, and crack length, the condition $P_H = \text{const}$ may be a valid approach to describe the crack growth process in ductile materials; we define it as *P-approach*.

Some comments could be useful when comparing P-approach with K_R, J_R criterions and energy dissipation rate. The energy dissipation rate approach is geometry

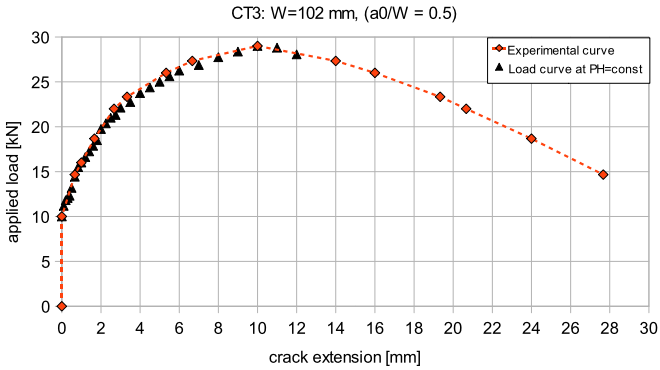

Fig. 15 Load versus crack extension curve for CT3 sample. Experimental data from [7]

Table 3 Load versus crack extension curve for CT3 sample

Experimental curve from [7]		Load curve at $P_H = 40$ MPa	
F [kN]	Δa [mm]	F [kN]	Δa [mm]
10.0	0.0	10.0	0.0
14.7	0.7	14.4	0.7
16.0	1.0	16.0	1.0
18.7	1.7	17.9	1.6
22.0	2.7	21.3	2.8
23.3	3.3	22.8	3.5
26.0	5.3	25.6	5.5
27.3	6.7	26.9	7.0
29.0	10.0	29.0	10.0
27.3	14.0	28.0	12.0

dependent, and it depends also on applied load and crack length and, above all, is not a critical condition at fracture, because Eq. (6) is always valid, also when the load is applied and no crack propagation occurs; the K_R criterion is based on the elastic solution of the near crack tip fields, and it is applicable only when the plastic zone size is small and plastic effects are negligible. Similarly, the J_R crack growth resistance curve is based on the J-dominance (HRR-dominance) concept, according to which an outer region of material with elastic behavior, undergoing proportional stress, controls a small plastic zone close to a crack tip. Furthermore, the J_R-based methods show a dependence on specimen size, specimen geometry, and crack length.

On the contrary, the P-approach is independent of the applied load, crack length, and specimen size.

4 Conclusions

The results of this work show that:

- the paradox of Rice is also valid when isotropic hardening behavior and large scale yielding are considered; thus, a Griffith-like energy balance is no longer valid to predict stable crack growth in a material when the mechanism of fracture is ductile;
- a criterion based on the plastic dissipation rate, as proposed in [15], cannot be properly identified as a fracture criterion, because plastic dissipation rate depends on a crack length and loading history;
- the proposed P-approach model represents a valid alternative to the classical approaches; the numerical studies of this work show that the P-approach expresses a characteristic condition of crack growth and is independent of the applied load, crack length, and specimen size. In addition, it is based on a more suitable theoretical framework because the energy–momentum tensor represents the generalized force acting on a defect.

Future works will be confined to assess the proposed criterion on the basis of both theoretical ground and numerical investigations on a wide range of materials with different hardening rules and fracture specimens.

References

1. Binante, V.: A new energetic failure criterion and constitutive models of porous materials into the fracture process zone, in the framework of elastic–plastic fracture mechanics. Ph.D. thesis in aerospace engineering, Universitá di Pisa, Faculty of Engineering, 2010
2. Binante, V., Crack extension energy rate and energetic approaches in elastic–plastic fracture mechanics. In: Buttazzo, G., Frediani, A. (eds.) Variational Analysis and Aerospace Engineering II: Mathematical Challenges for Aerospace Design. Springer, Berlin (2012)
3. Chiarelli, M., Frediani, A., Lucchesi, M.: On the crack extension energy rate in elastic-plastic fracture mechanics. In: Blauel, J.B., Schwalbe, K.H. (eds.) Defect Assessment in Components: Fundamentals and Applications. Mechanical Engineering Publications, London (1991)
4. Chiarelli, M., Frediani, A., Lucchesi, M.: Computation of crack extension energy rate for elastic-plastic hardening materials under variable loading. Eng. Fract. Mech. **55**(5), 813–830 (1996)
5. Eshelby, J.D.: Energy relations and the energy–momentum tensor in continuum mechanics. In: Kanninen, M.F., Adler, W.F., Rosenfield, A.R., Jaffee, R.I. (eds.) Inelastic Behaviour of Solids, vol. 43, pp. 77–115. McGraw-Hill, New York (1970)
6. Frediani, A.: Effects of plasticity of metallic materials on fatigue and fracture mechanics. In: Miele, A., Salvetti, A. (eds.) Applied Mathematics in Aerospace Science and Engineering. Erice, Italy, 3–10 September 1994. Mathematical Concepts and Methods in Science and Engineering, vol. 44, pp. 363–393. Plenum Press, New York (1994)
7. Gu, I.: A CTOD approach to predicting crack extensions in aluminum alloys. J. Test. Eval. **27**, 143–149 (1999)
8. Moran, B., Shih, C.F.: Crack tip and associated domain integrals from momentum and energy balance. Eng. Fract. Mech. **27**(6), 615–642 (1987)
9. Nikishkov, G., Heerens, J., Hellmann, D.: Comparison of finite element results and experimental measurements of CTOD $\delta 5$ in CT specimens. J. Test. Eval. **27**, 307–311 (1999)

10. Oriunno, M.: Meccanica della Frattura elasto-plastica: modelli costitutivi per lo studio del fenomeno di propagazione. Tesi di dottorato in ingegneria aeronautica, Universitá di Pisa, Facoltá di Ingegneria (1996)
11. Rice, J.R.: A path independent integral and the approximate analysis of strain concentration by notches and cracks. J. Appl. Mech. **35**, 379–386 (1968)
12. Rice, J.R.: An examination of the fracture mechanics energy balance from the point of view of continuum mechanics. In: Swedlow, J.L., Yokobori, T., Kawasaki, T. (eds.) Proceedings of the First International Conference on Fracture, vol. 1, pp. 309–340. Sendai, Japan, 12–17 September (1965)
13. Sumpter, J.D.G.: Energy dissipation rate analysis of a low upper shelf data set. Eng. Fract. Mech. **71**(1), 39–56 (2004)
14. Sumpter, J.D.G.: The energy dissipation rate approach to tearing instability. Eng. Fract. Mech. **71**(1), 17–37 (2004)
15. Sumpter, J.D.G.: Energy rates and crack stability in small scale yielding. Int. J. Fract. **130**(3), 667–681 (2004)
16. Sun, C.T., Wang, C.Y.: A new look at energy release rate in fracture mechanics. Int. J. Fract. **113**(4), 295–307 (2002)
17. Wilson, C., Landes, J.: Inconsistencies between CTOD and J calculations. J. Test. Eval. **22**, 505–511 (1994)

Optimal Location of Support Points in the Kirchhoff Plate

Giuseppe Buttazzo and Sergey A. Nazarov

1 Introduction

1.1 The Kirchhoff Plate with a Clamped Edge

Let Ω be a domain in the plane $\mathscr{R}^2$ with a smooth (of class C^∞ for simplicity) boundary $\Gamma = \partial\Omega$ and the compact closure $\overline{\Omega} = \Omega \cup \partial\Omega$. The bi-harmonic equation

$$\Delta_x^2 w(x) = f(x), \quad x \in \Omega, \tag{1}$$

with the Laplacian Δ_x in the Cartesian coordinates $x = (x_1, x_2)$ is known as an adequate model to describe the deflexion $w(x)$ of a thin isotropic elastic plate under a transversal loading proportional to the right-hand side $f(x)$ of (1) (the proportionality coefficient is not important for our purposes).

Equation (1) is called the *plate equation* after S. Germain, who, for the first time in 1815 [13],[1] discovered a relationship between a fourth-order differential operator and a bent plate. A consistent method to infer equations of type (1) together with concomitant boundary conditions in the theory of plates was developed by Kirch-

[1] For this work, Mademoiselle Sophie Germain was awarded with a prize by French Academy of Sciences. Actually, the original manuscript contained a mistake corrected by Poisson [25] in 1829.

G. Buttazzo (✉)
Dipartimento di Matematica, Università di Pisa, Largo B. Pontecorvo 5, 56127 Pisa, Italy
e-mail: buttazzo@dm.unipi.it

S.A. Nazarov
Institute of Mechanical Engineering, Russian Academy of Sciences, V.O. Bol'shoy pr. 61, St. Petersburg 199178, Russia
e-mail: srgnazarov@yahoo.co.uk

G. Buttazzo, A. Frediani (eds.), *Variational Analysis and Aerospace Engineering: Mathematical Challenges for Aerospace Design*, Springer Optimization and Its Applications 66,
DOI 10.1007/978-1-4614-2435-2_5,

hoff [14] in 1850–1859 under suitable hypotheses,[2] i.e. by means of an intuitive asymptotic analysis.

A rigorous mathematical derivation of two-dimensional thin plate equations from three-dimensional elasticity problem, together with asymptotically sharp error estimates, has been performed in many publications in the last century by various methods and with miscellaneous formulations of the problem. Mentioning a few of works [6, 22, 24, 27] only, we refer to books [5, 10, 23] for a much more complete list.

The bi-harmonic equation can be considered with the simplest boundary conditions

$$w(x) = 0, \qquad \partial_n w(x) = 0, \quad x \in \Gamma, \tag{2}$$

where ∂_n stands for differentiation along the outward normal. These conditions correspond to clamping the plate edge, and we call (2) the Dirichlet conditions because they are fully inherited by the energy space in the variational formulation of the boundary-value problem (1), (2), namely $w \in H_0^2(\Omega)$ and

$$(\Delta_x w, \Delta_x v)_\Omega = (f, v)_\Omega \quad \forall v \in H_0^2(\Omega), \tag{3}$$

where $(\cdot,\cdot)_\Omega$ is the natural scalar product in the Lebesgue space $L^2(\Omega)$, and $H_0^2(\Omega)$ is the completion of the linear set $C_c^\infty(\Omega)$ (infinitely differentiable functions with compact supports) with respect to the standard norm in the Sobolev space $H^2(\Omega)$. We also refer to [18] for a couple of known facts formulated below.

For any functional $f \in (H_0^2(\Omega))'$ linear and continuous in the space $H_0^2(\Omega)$, the variational problem (3) admits a unique (generalized) solution $w \in H_0^2(\Omega)$, and the estimate

$$\|w\|_{H^2(\Omega)} \le c\|f\|_{(H_0^2(\Omega))'}$$

is valid. If $f \in L^2(\Omega)$, the generalized solution becomes classical, falls into the Sobolev space $H^4(\Omega)$, and satisfies the estimate

$$\|w\|_{H^4(\Omega)} \le c\|f\|_{L^2(\Omega)}. \tag{4}$$

We emphasize that the bilinear form on the left of (3) is coercive in $H_0^2(\Omega)$ due to the second fundamental inequality [17] which needs, at least, one Dirichlet condition $w = 0$ on Γ (cf. Sect. 3.3).

Remark 1 The integral identity (3) extended over the whole Sobolev space $H^2(\Omega)$ cannot be well posed: the bi-linear form on the left of (3) degenerates on the infinite-dimensional linear space of harmonic functions in Ω, while the corresponding Neumann boundary conditions (intrinsic, in the terminology of [18])

$$\Delta_x w(x) = \partial_n \Delta_x w(x) = 0, \quad x \in \Gamma, \tag{5}$$

[2] Two Kirchhoff hypotheses contradict to each other and must be used in a proper order and at an appropriate moment of the analysis. An example of the erroneous usage of the hypotheses leading to a wrong conclusion is explained and discussed in [28] (see also [23, Mistake 4.2.5]).

do not satisfy the Shapiro–Lopatinsky requirement, i.e., the boundary-value problem (1), (5) is not elliptic in any sense. In this way, a plate with a free edge must be supplied with another bi-linear form, namely the plate elastic energy (45), and a couple of second- and third-order boundary conditions (48), which are different from (5) (see, e.g., [21]). The fact that the quadratic form $\frac{1}{2}(\Delta_x u, \Delta_x u)_\Omega$ coincides with the elastic energy (45) of the Kirchhoff plate is exclusively due to the full family of the Dirichlet conditions (2) and can be verified using an integration by parts (see, e.g., [21] and cf. the Green formula (47)).

As mentioned, the Dirichlet conditions (2) correspond to a three-dimensional thin plate with a clamped edge. This conclusion can be made along the construction of boundary layers, i.e., asymptotic components of elastic fields which manifest themselves only in the vicinity of the plate edge and decay exponentially in the plate body, see [9, 28] for thin solids and [20, Chaps. 15, 16] for a general procedure to study the boundary layer phenomenon. Notice that the boundary conditions at the contour Γ appear as a decay condition of the boundary layer and result from the boundary conditions at the lateral side of the thin plate in the three-dimensional elasticity problem.

1.2 The Sobolev Conditions at Support Points

Let $\mathscr{P} = \{P^1, \dots, P^J\}$ be a finite family of points inside of Ω with $P^j \neq P^k$ as $j \neq k$. Since we are in a two-dimensional domain, according to the Sobolev embedding $H^2 \subset C^{0,\alpha}$ ($C^{0,\alpha}$ is the Hölder class of exponent $\alpha \in (0, 1)$), the linear set

$$H_0^2(\Omega; \mathscr{P}) = \big\{w \in H_0^2(\Omega) \,:\, w\big(P^1\big) = \cdots = w\big(P^J\big) = 0\big\} \tag{6}$$

is a closed subspace of $H^2(\Omega)$. Hence, the variational problem

$$(\Delta_x u, \Delta_x v)_\Omega = (f, v)_\Omega \quad \forall v \in H_0^2(\Omega; \mathscr{P}) \tag{7}$$

is well posed in the space (6). We call it the Sobolev problem, while

$$u\big(P^1\big) = \cdots = u\big(P^J\big) = 0 \tag{8}$$

are called either point or Sobolev conditions at the support set $\mathscr{P}$. The following assertion is a direct consequence of the Riesz representation theorem.

Lemma 1 *The Sobolev problem* (7) *has a unique solution* $u \in H_0^2(\Omega; \mathscr{P})$ *for any right-hand side* $f \in (H_0^2(\Omega; \mathscr{P}))'$, *and the following estimate holds*:

$$\|u\|_{H^2(\Omega)} \leq c \|f\|_{(H_0^2(\Omega; \mathscr{P}))'}. \tag{9}$$

The differential formulation of the variational problem (7) relies on the equation

$$\Delta_x^2 u = f \quad \text{on } \Omega \setminus \mathscr{P} \tag{10}$$

with the point conditions (8) and the boundary conditions (2).

Notice that the differential equation (10) is posed in the punctured domain $\Omega \setminus \mathscr{P}$. As a result, solutions of the Sobolev problem with the right-hand side $f \in L^2(\Omega)$ do not belong to $H^4(\Omega)$ due to their possible singularities at the points $P^1, \dots, P^J$. However, u belongs to $H^4_{\mathrm{loc}}(\overline{\Omega} \setminus \mathscr{P})$ and, together with its derivatives, is Hölder continuous, so that the point conditions can be understood properly. Moreover, u lives in the Kondratiev space $V^4_0(\Omega; \mathscr{P})$ [15]. The space $V^l_\beta(\Omega; \mathscr{P})$ is defined as the completion of the linear space $C^\infty_c(\overline{\Omega} \setminus \mathscr{P})$ with respect to the weighted norm

$$\|v\|_{V^l_\beta(\Omega;\mathscr{P})} = \left(\sum_{p=0}^{l} \left\| \rho^{\beta-l+p} \nabla_x^p v \right\|^2_{L^2(\Omega)} \right)^{1/2}, \tag{11}$$

where $l \in \{0, 1, 2, \dots\}$ and $\beta \in \mathscr{R}$ are the smoothness and weight indices, $\nabla_x^p v$ is the family of all pth-order derivatives of the function v, and $\rho(x) = \min_j\{|x - P^j|\}$. Note that $V^l_\beta(\Omega; \mathscr{P})$ consists of all functions $v \in H^l_{\mathrm{loc}}(\overline{\Omega} \setminus \mathscr{P})$ such that the norm (11) is finite. The Kondratiev theory [15] of elliptic problems in domains with conical singularities of the boundary applies to the Steklov problem because any isolated point P^j of the boundary $\partial\Omega \cup \mathscr{P}$ can be treated as the top of the "complete" angle $\mathscr{R}^2 \setminus P^j$.

The next lemma delivering asymptotic representations of solutions as $x \to P^j$ is fully analyzed in [20, § 5.5.2], and here we only sketch its proof.

Lemma 2 *In the case $f \in L^2(\Omega)$, the solution $u \in H^2_0(\Omega; \mathscr{P})$ takes the asymptotic form*

$$u(x) = \sum_{j=1}^{J} \chi_j(x) \left(\sum_{i=1,2} a^i_j \big(x_i - P^j_i\big) + \frac{a^0_j}{8\pi} \big|x - P^j\big|^2 \ln\big|x - P^j\big| \right.$$
$$\left. + \frac{1}{2} \sum_{i,q=1,2} a^{iq}_j \big(x_i - P^j_i\big)\big(x_q - P^j_q\big) \right) + \tilde{u}(x), \tag{12}$$

where a^i_j, a^0_j, a^{iq}_j are some coefficients, χ_j is a smooth cut-off function such that $\chi_j = 1$ in a neighborhood $\mathscr{V}^j \subset \Omega$ of the point P^j and $\chi_j(x) = 0$ for $x \in \overline{\mathscr{V}^k}$ with $k \neq j$, and the remainder $\tilde{u} \in H^4(\Omega)$ belongs to the Kondratiev space $V^4_\beta(\Omega; \mathscr{P})$ with any $\beta > 0$. The estimate

$$\|\tilde{u}\|_{V^4_\beta(\Omega;\mathscr{P})} + \sum_{j=1}^{J} \left(\big|a^0_j\big| + \sum_{i=1,2} \left(\big|a^i_j\big| + \sum_{q=1,2} \big|a^{iq}_j\big| \right) \right) \le c_\beta \|f\|_{L^2(\Omega)} \tag{13}$$

holds, where the factor c_β is independent of f, with $c_\beta \to \infty$ as $\beta \to +0$.

Proof Generally speaking, decomposition (12) and estimate (13) follow from the relation $f \in L^2(\Omega) = V^0_0(\Omega; \mathscr{P})$ and the theorem on asymptotics [15] (see also, e.g., monograph [20, § 5.2]). Let us outline the scheme of application of general results. First of all, we need a variant of the one-dimensional Hardy inequality

$$\int_0^\rho r^{-4} \left|\ln \frac{r}{\rho}\right|^{-2} \left|V(r)\right|^2 r\,dr \le c \int_0^\rho r^{-2} \left|\ln \frac{r}{\rho}\right|^{-2} \left|\frac{dV}{dr}(r)\right|^2 r\,dr$$
$$\le C \int_0^\rho \left|\frac{d^2V}{dr^2}(r)\right|^2 r\,dr,$$

which is valid for any $V \in C_c^\infty[0, \rho)$. This inequality uses the radial variable $r_j = |x - P^j|$ (the factor r stands on dr for the Jacobian) and must be additionally integrated over the angular variable $\varphi_j \in [0, 2\pi)$. As a result, we conclude that, with any $\beta > 0$,

$$\|u\|_{V^2_\beta(\Omega;\mathscr{P})} \le c\big(\big\|\rho^{-2}\big(1 + |\ln \rho|\big)^{-1} u\big\|_{L^2(\Omega)}$$
$$+ \big\|\rho^{-1}\big(1 + |\ln \rho|\big)^{-1} \nabla_x u\big\|_{L^2(\Omega)} + \big\|\nabla_x^2 u\big\|_{L^2(\Omega)}\big)$$
$$\le C\|u\|_{H^2_0(\Omega;\mathscr{P})}. \tag{14}$$

Furthermore, $u \in V^4_{\beta+2}(\Omega; \mathscr{P})$ due to the theorem on lifting the smoothness [15]; notice that $V^4_{\beta+2}(\Omega; \mathscr{P}) \subset V^2_\beta(\Omega; \mathscr{P})$ by virtue of (11). Applying the theorem on asymptotics [15] ([20, Theorem 3.2.9]) to the problem (10), (8), (2) with the right-hand side $f \in L^2(\Omega) \subset V^0_\beta(\Omega; \mathscr{P})$, we arrive at expansion (12) with any small $\beta > 0$ (the weight index $\beta = 0$ is not available due to logarithmic weights, see the middle of (14)) and at the detached asymptotic terms that live in $V^4_{\beta+2}(\Omega; \mathscr{P})$ and in $H^2(\Omega)$ but stay outside the smaller space $V^4_\beta(\Omega; \mathscr{P})$. □

Lemma 2 describes the smoothness of the Sobolev problem solution u and defines the coefficients in its expansions at the points P^j. Notice that the embedding $H^2 \subset C^{0,\alpha}$ is only able to ensure the equalities, while, by the embedding $\widetilde{u} \in H^4(\Omega) \subset C^{2,\alpha}(\Omega)$ and the inclusion $|x - P^j| \ln |x - P^j| \in C^{1,\alpha}(\Omega)$, Lemma 2 shows that $u \in C^{1,\alpha}(\Omega)$ and

$$a^i_j = \frac{\partial u}{\partial x_i}\big(P^j\big) =: u_{,i}\big(P^j\big).$$

Although the theory of three-dimensional boundary layers in thin elastic plates is not completed yet, the Sobolev conditions (8) ought to be interpreted as a model for small supports of the plate. One may think about clamped zones of infinitesimal diameter on the plate bases, however error estimates for such a model do not yet exist in the literature.

1.3 The Minimization Problem

Problems (3) and (7) can be formulated as minimization problems for the functional

$$E(v;f)=\frac{1}{2}(\Delta_x v,\Delta_x v)_\Omega-(f,v)_\Omega \tag{15}$$

in the function spaces $H_0^2(\Omega)$ and $H_0^2(\Omega;\mathscr{P})$, respectively, and with the loading f in the corresponding dual space. A solution of the problem gives the minimum of the functional (15) which is nothing but the potential energy of the plate (elastic energy minus work of external forces).

Since $H_0^2(\Omega)\subset H_0^2(\Omega;\mathscr{P})$, the solutions w and u of the Dirichlet and Sobolev problems respectively, provide the relationship

$$E(w;f)\le E(u;f), \tag{16}$$

which mechanically means that supporting the plate at the points $P^1,\dots,P^J$ increases concurrently the potential energy stored.

1.4 The Optimization Problems

For a fixed integer N, we are interested in the optimal location of N points $\mathscr{P}=\{P_1,\dots,P_N\}$ in Ω in order to minimize the total *compliance* functional. As usual, the compliance is defined as

$$C(\mathscr{P};f)=\int_\Omega u(x)f(x)\,dx, \tag{17}$$

where u minimizes the potential energy (15). An integration by parts readily shows that

$$C(\mathscr{P};f)=-2\min\big\{E(v;f)\ :\ v\in H_0^2(\Omega;\mathscr{P})\big\}=(\Delta_x u,\Delta_x u)_\Omega\ge 0. \tag{18}$$

The optimization problem we deal with is then

$$\min\big\{C(\mathscr{P};f)\ :\ \mathscr{P}\subset\overline{\Omega},\ \#\mathscr{P}\le N\big\}, \tag{19}$$

where $\#\mathscr{P}$ is the number of points in $\mathscr{P}$. If it is proved that the compliance functional varies continuously when the points $P^1,\dots,P^J$ move in $\overline{\Omega}$, then the existence theorem, formulated below, is straightforward. However, the following situation can hypothetically happen: caused by a singularity of the right-hand side f, the potential energy (15), calculated for the solution $u^{\mathscr{P}}$ of the Sobolev problem (10), (2), (8), grows indefinitely when one point P^j in the set $\mathscr{P}$ approaches another point $P^k\in\mathscr{P}$. In Appendix we verify that the assumption $f\in L^2(\Omega)$ is sufficient to confirm the continuity of the function

$$\overline{\Omega}^{\#\mathscr{P}}\ni\mathscr{P}\mapsto E\big(u^{\mathscr{P}};f\big), \tag{20}$$

where $u^{\mathscr{P}}$ denotes the solution to problem (7) with the point conditions (8) at $\mathscr{P}$.

Theorem 1 *In the case $f \in L^2(\Omega)$, the optimization problem (19) admits a solution for every N.*

As remarked in Sect. 1.3, the Sobolev space $H_0^2(\Omega;\mathscr{P})$ shrinks when $\mathscr{P}$ expands, and therefore the corresponding energy increases, and, by formulas (18) and (15), (16), we immediately deduce the following result.

Proposition 1 *If $f \in L^2(\Omega)$ and $\mathscr{P}^{\rm opt}$ is an optimal solution, then $\#\mathscr{P}^{\rm opt} = N$.*

The inclusion $u^{\mathscr{P}} \in H^2(\Omega) \subset C^{0,\alpha}(\Omega)$ suggests to consider also the minimization of the deflexion functional

$$\mathscr{W}(\mathscr{P};f) = \max\left\{\left|u^{\mathscr{P}}(x)\right| \,:\, x \in \overline{\Omega}\right\}, \tag{21}$$

which is much more relevant to the engineering practice than the compliance functional. The optimization problem

$$\min\left\{\mathscr{W}(\mathscr{P};f) \,:\, \mathscr{P} \subset \overline{\Omega},\ \#\mathscr{P} \le N\right\} \tag{22}$$

is discussed in Sect. 2.5.

When the number N of points that have to be located becomes large, since the cost functions $C(\mathscr{P};f)$ and $\mathscr{W}(\mathscr{P};f)$ are highly nonconvex, the numerical computations necessary to determine the set $\mathscr{P}_N^{\rm opt}$ are very heavy. On the other hand, problems of this type appear in many practical situations (think, for instance, of the problem of supporting a big roof by a large number of columns). This is why, instead of determining $\mathscr{P}_N^{\rm opt}$, it is much simpler to find its *asymptotic density*, defined as the probability measure

$$\overline{\mu} = \lim_{N\to\infty} \frac{1}{N} \sum_{P \in \mathscr{P}_N^{\rm opt}} \delta_P.$$

In Sect. 2.6 we address this interesting point of view that has been fruitfully developed for various kinds of problems but, as far as we know, still remains open for the case of plates.

1.5 The Structure of the Paper

We start the next section by introducing the Green function $G(x,y)$ of the problem (1), (2) and detecting a relation between solutions of the Dirichlet and Sobolev problems in terms of G that leads to an "almost explicit" representation formula for the energy (33) and compliance (17) functionals. Based on this formula, a simple approach is realized in Sect. 2.3 to get a necessary condition for the optimal location

of the support points $P^1, \dots, P^J$ (Theorem 2). At the first sight, the logarithmic singularities of second derivatives of G do not permit to derive a sufficient condition, however the representation formula contains only twice differentiable functions, and therefore a sufficient conditions is straightforward as well (Theorem 3). In Sect. 2.5 we discuss the minimization of the deflexion functional (21), and in Sect. 2.6 we point out the questions related to determining the asymptotic density, as $N \to \infty$, of the optimal set $\mathscr{P}_N^{\rm opt}$.

In Sect. 3 we remark that the optimization problem (19) with $\#\mathscr{P} = 1$ requires to locate the only support point P^1 at an extremal point of the function

$$\Omega \ni x \mapsto G(x,x)^{-1/2} w(x) \tag{23}$$

(note that $G(x,x) > 0$ inside Ω, see (28)). We also give an example and discuss several open optimization problems for linear and nonlinear plate models.

In Appendix we confirm the continuity of the function (20).

2 Optimizing the Location of Support Points

2.1 The Green Function

Let us introduce the Green function $G(x,y)$, i.e., a solution of the problem

$$\begin{aligned} &\Delta_x^2 G(x,y) = \delta(x-y), \quad x \in \Omega, \\ &G(x,y) = \partial_{n(x)} G(x,y) = 0, \quad x \in \Gamma, \end{aligned} \tag{24}$$

where $\delta(x-y)$ is the Dirac mass concentrated at the point $y \in \Omega$. Since a fundamental solution of the bi-harmonic operator in the plane $\mathscr{R}^2$ takes the form

$$\Phi(x) = (8\pi)^{-1} |x|^2 \ln |x|$$

and, therefore, belongs to $H^2_{\rm loc}(\mathscr{R}^2)$, the distributional solution G of problem (24) becomes a generalized solution in $H^2_0(\Omega)$ and satisfies the integral identity

$$(\Delta_x G, \Delta_x v)_\Omega = v(y) \quad \forall v \in H^2_0(\Omega). \tag{25}$$

Notice that $H^2_0(\Omega) \ni v \mapsto v(y)$ is a continuous functional due to the Sobolev embedding theorem. Furthermore, the difference $\mathscr{G}(x,y) = G(x,y) - \Phi(x-y)$, which is the regular part of the Green function, is an infinitely differentiable function in $x, y \in \Omega$. The symmetry property

$$G(x,y) = G(y,x) \tag{26}$$

is known as well.

The function $\overline{\Omega} \setminus P^j \ni x \mapsto G_j(x) = G(x, P^j)$ with the fixed second argument admits the expansions, as $x \to P^k$,

$$G_j(x) = \Phi\big(x - P^j\big)\delta_{j,k} + \mathscr{G}^0_{jk} + \sum_{i=1,2} \mathscr{G}^i_{jk}\big(x_i - P^k_i\big) + \frac{1}{2} \sum_{i,q=1,2} \mathscr{G}^{iq}_{jk}\big(x_i - P^k_i\big)\big(x_q - P^k_q\big) + O\big(\big|x - P^k\big|^3\big), \tag{27}$$

where the coefficients $\mathscr{G}^0_{jk}$, $\mathscr{G}^i_{jk}$, and $\mathscr{G}^{iq}_{jk} = \mathscr{G}^{qi}_{jk}$ are given by the Taylor coefficients of the regular part $\mathscr{G}_j$ of the Green function G_j. Thus $\mathscr{G}^0_{jk} = \mathscr{G}(P^k, P^j)$ depends smoothly on the points P^j and P^k inside Ω.

Inserting $v = G_k$ into (25) and changing G for G_j, we see that the $(J \times J)$-matrix $\mathscr{G}^0$ with the entries

$$\mathscr{G}^0_{jk} = G_j\big(P^k\big) = G\big(P^k, P^j\big) = (\Delta_x G_j, \Delta_x G_k)_\Omega \tag{28}$$

is symmetric and positive definite since it is the Gram matrix constructed from linearly independent functions $G_1, \dots, G_J$ with the help of a specific scalar product in $H^2_0(\Omega)$.

2.2 Relating the Solutions of the Dirichlet and Sobolev Problems

We set

$$u(x) = w(x) + G(x, \mathscr{P})A, \tag{29}$$

where $A = (A_1, \dots, A_J)^\top$ is a column in $\mathscr{R}^J$, $\top$ stands for transposition, and

$$G(x, \mathscr{P}) = \big(G_1(x), \dots, G_J(x)\big).$$

Evidently, $G(P^1, \mathscr{P}), \dots, G(P^J, \mathscr{P})$ are lines in the matrix $\mathscr{G}^0 = \mathscr{G}(\mathscr{P}, \mathscr{P})$. Thus, to satisfy the point conditions (8), we write

$$\mathscr{R}^J \ni 0 = u(\mathscr{P}) = w(\mathscr{P}) + \mathscr{G}(\mathscr{P}, \mathscr{P})A,$$

where $u(\mathscr{P}) = (u(P^1), \dots, u(P^J))^\top$, and obtain

$$A = -\mathscr{G}(\mathscr{P}, \mathscr{P})^{-1} w(\mathscr{P}) = -\mathscr{G}(\mathscr{P}, \mathscr{P})^{-1}\big(w(P^1), \dots, w(P^J)\big)^\top, \tag{30}$$

so that

$$u(x) = w(x) - G(x, \mathscr{P})\mathscr{G}(\mathscr{P}, \mathscr{P})^{-1} w(\mathscr{P}). \tag{31}$$

Remark 2 Estimate (4), the Sobolev embedding $H^4 \subset C^{2,\alpha}$, and the Taylor formula yield

$$w(x) = \sum_{j=1}^{J} \chi_j(x) \Big(b_j^0 + \sum_{i=1,2} b_j^i \big(x_i - P_i^j\big) + \frac{1}{2} \sum_{i,q=1,2} b_j^{iq} \big(x_i - P_i^j\big)\big(x_q - P_q^j\big) \Big) + \widetilde{w}^j(x), \tag{32}$$

where $w \in V_\beta^4(\Omega; \mathscr{P})$ with any $\beta > 0$, and

$$b_j^0 = w\big(P^j\big), \qquad b_j^i = w_{,i}\big(P^j\big), \qquad b_j^{iq} = w_{,iq}\big(P^j\big).$$

Comparing formulas (32) and (31), (12), (27), we find out the relations

$$a^0 = -\big(\mathscr{G}^0\big)^{-1} b^0, \qquad a^i = b^i - \mathscr{G}^i \big(\mathscr{G}^0\big)^{-1} b^0, \qquad a^{iq} = b^{iq} - \mathscr{G}^{iq} \big(\mathscr{G}^0\big)^{-1} b^0,$$

where $b^p = (b_1^p, \dots, b_j^p)^\top$, $a^p = (a_1^p, \dots, a_j^p)^\top$, and so on are coefficient columns, and $\mathscr{G}^i$, $\mathscr{G}^{iq}$ coefficient matrices from (27).

Furthermore, using (3) with $v = G_j$ and (25) with $v = w$, we calculate the potential energy

$$\begin{aligned} E(u, f) &= -\frac{1}{2}(f, u)_\Omega = -\frac{1}{2}(f, w)_\Omega + \frac{1}{2}\big(f, G(\cdot, \mathscr{P})\big)_\Omega \big(\mathscr{G}^0\big)^{-1} w(\mathscr{P}) \\ &= E(w; f) + \frac{1}{2} w(\mathscr{P})^\top \big(\mathscr{G}^0\big)^{-1} w(\mathscr{P}) \\ &= E(w; f) + \frac{1}{2} \sum_{j,k=1}^{J} \big(\big(\mathscr{G}^0\big)^{-1}\big)_{j,k} w\big(P^j\big) w\big(P^k\big). \end{aligned} \tag{33}$$

Here $((\mathscr{G}^0)^{-1})_{j,k}$ denotes an entry of the inverse matrix $(\mathscr{G}^0)^{-1}$, symmetric and positive definite. Hence, the energy increment $E(w; f) - E(u; f)$ caused by imposing supports at the points $P^1, \dots, P^J$ is negative that is in accord with Sect. 3, Chap. *PrandtlPlane Propelled with Liquid Hydrogen: A Preliminary Study*.

Clearly, the quantity (33) depends continuously on the points $P^1, \dots, P^J$ in the set when $P^j \neq P^k$ for $j \neq k$ and $P^j \notin \partial\Omega$ (the matrix $\mathscr{G}^0$ is then nonsingular). In Appendix, under the assumption $f \in L^2(\Omega)$, we shall verify that both exceptional cases are not optimal, so that the problem on the maximization of the energy functional (33) with respect to the location of the points $P^1, \dots, P^J \in \Omega$ has a solution (see Theorem 1).

2.3 The Necessary Condition for the Optimal Location of Support Points

Let us perturb one of the points in $\mathscr{P}$, namely $P^{j\varepsilon} = P^j + \varepsilon e_{(i)}$; here $e_{(i)}$ is the unit vector of the x_i-axis, and ε is a small parameter. By u^ε we denote the solution of the Sobolev problem with $\mathscr{P}^\varepsilon = \{P^1, \dots, P^{j-1}, P^{j\varepsilon}, P^{j+1}, \dots, P^J\}$.

We assume that $f \in L^2(\Omega)$ and, therefore, $w \in H^4(\Omega)$ due to (4). Since $w \in C^{2,\alpha}(\Omega)$ by the Sobolev embedding theorem, we have

$$w\big(P^{j\varepsilon}\big) = w\big(P^j\big) + \varepsilon w_{,i}\big(P^j\big) + O\big(\varepsilon^2\big)$$

with the traditional notation $w_{,i} = \partial w/\partial x_i$. Hence,

$$w\big(\mathscr{P}^\varepsilon\big) = w(\mathscr{P}) + \varepsilon \mathbf{e}_{(j)} w_{,i}\big(P^j\big) + O\big(\varepsilon^2\big), \tag{34}$$

where $\mathbf{e}_{(j)} = (\delta_{j,1}, \dots, \delta_{j,J})^\top$ is a basis vector in $\mathscr{R}^J$.

Owing to (27), the Green function $G(x, y)$ satisfies

$$G\big(P^{j\varepsilon}, P^k\big) = G\big(P^j, P^k\big) + \varepsilon \frac{\partial}{\partial x_i} G\big(P^j, P^k\big) + O\big(\varepsilon^2 |\ln \varepsilon|\big),$$

$$G\big(P^k, P^{j\varepsilon}\big) = G\big(P^k, P^j\big) + \varepsilon \frac{\partial}{\partial y_i} G\big(P^k, P^j\big) + O\big(\varepsilon^2 |\ln \varepsilon|\big),$$

$$G\big(P^{j\varepsilon}, P^{j\varepsilon}\big) = G\big(P^j, P^j\big) + \varepsilon \frac{\partial}{\partial x_i} G\big(P^j, P^j\big) + \varepsilon \frac{\partial}{\partial y_i} G\big(P^j, P^j\big) + O\big(\varepsilon^2 |\ln \varepsilon|\big),$$

where $k = 1, \dots, J$ and $k \neq j$. In view of (26), we have

$$\frac{\partial G}{\partial x_i}\big(P^j, P^k\big) = \frac{\partial G}{\partial y_j}\big(P^k, P^j\big),$$

and, therefore, the matrix $\mathscr{G}^{0\varepsilon}$ corresponding to the support set $\mathscr{P}^\varepsilon$ takes the form

$$\mathscr{G}^0 + \varepsilon\big(\mathbf{e}_{(j)} G_{j,i}(\mathscr{P})^\top + G_{j,i}(\mathscr{P}) \mathbf{e}_{(j)}^\top\big) + O\big(\varepsilon^2 |\ln \varepsilon|\big),$$

where, according to (27),

$$G_{j,i}(\mathscr{P}) = \big(G_{j,i}\big(P^1\big), \dots, G_{j,i}\big(P^J\big)\big)^\top = \big(\mathscr{G}^i_{j1}, \dots, \mathscr{G}^i_{jJ}\big)^\top. \tag{35}$$

Applying the Neumann decomposition, we conclude that

$$\begin{aligned}\big(\mathscr{G}^{0\varepsilon}\big)^{-1} = \big(\mathscr{G}^0\big)^{-1} - \varepsilon\big(\mathscr{G}^0\big)^{-1}\big(\mathbf{e}_{(j)} G_{j,i}(\mathscr{P})^\top + G_{j,i}(\mathscr{P}) \mathbf{e}_{(j)}^\top\big)\big(\mathscr{G}^0\big)^{-1} \\ + O\big(\varepsilon^2 |\ln \varepsilon|\big).\end{aligned} \tag{36}$$

According to (33) and (34), (36), we now obtain

$$\begin{aligned} E\big(u^\varepsilon; f\big) &= E(w; f) + \frac{1}{2} w\big(\mathscr{P}^\varepsilon\big)^\top \big(\mathscr{G}^{0\varepsilon}\big)^{-1} w\big(\mathscr{P}^\varepsilon\big) \\ &= E(w; f) + \frac{1}{2} w(\mathscr{P})^\top \big(\mathscr{G}^0\big)^{-1} w(\mathscr{P}) + \frac{1}{2}\varepsilon\big(w(\mathscr{P})^\top \big(\mathscr{G}^0\big)^{-1} \mathbf{e}_{(j)} w_{,i}\big(P^j\big) \\ &\quad + \big(\mathbf{e}_{(j)} w_{,i}\big(P^j\big)\big)^\top \big(\mathscr{G}^0\big)^{-1} w(\mathscr{P}) - w(\mathscr{P})^\top \big(\mathscr{G}^0\big)^{-1} \big(\mathbf{e}_{(j)} G_{j,i}(\mathscr{P})^\top \\ &\quad + G_{j,i}(\mathscr{P}) \mathbf{e}_{(j)}^\top\big)\big(\mathscr{G}^0\big)^{-1} w(\mathscr{P})\big) + O\big(\varepsilon^2 |\ln \varepsilon|\big) \\ &= E(u; f) + \varepsilon\big(\big(\mathscr{G}^0\big)^{-1} w(\mathscr{P})\big)^\top \mathbf{e}_{(j)} \big(w_{,i}\big(P^j\big) - G_{j,i}(\mathscr{P})^\top \big(\mathscr{G}^0\big)^{-1} w(\mathscr{P})\big) \\ &\quad + O\big(\varepsilon^2 |\ln \varepsilon|\big). \end{aligned}$$

Thus, the necessary condition for the optimal location of J support points implies the following $2J$ equations ($j = 1, \dots, J$, $i = 1, 2$):

$$\big(\big(\mathscr{G}^0\big)^{-1} w(\mathscr{P})\big)^\top \mathbf{e}_{(j)} \big(w_{,i}\big(P^j\big) - G_{j,i}(\mathscr{P})^\top \big(\mathscr{G}^0\big)^{-1} w(\mathscr{P})\big) = 0. \tag{37}$$

If the scalars

$$\mathbf{e}_{(j)}^\top \big(\mathscr{G}^0\big)^{-1} w(\mathscr{P}), \quad j = 1, \dots, J, \tag{38}$$

do not vanish, then, in view of representation (31), conditions (37) lead to the equalities

$$\nabla_x u^{\mathscr{P}}\big(P^j\big) = 0, \quad j = 1, \dots, J,$$

which means that the first-order derivatives of the solution $u^{\mathscr{P}}$ to the Sobolev problem (10), (8), (2) with the optimal location of the support points vanish at the points $P^1, \dots, P^J$.

Remark 3 Since the matrix $(\mathscr{G}^0)^{-1}$ is symmetric and positive definite, all the scalars (38) can vanish only in the case $w(\mathscr{P}) = 0 \in \mathscr{R}^J$.

Theorem 2 *If $f \in L^2(\Omega)$ and $\mathscr{P}^{\mathrm{opt}}$ is an optimal solution of* (19), *then relations* (37) *are equivalent to*

$$\big(\big(\mathscr{G}^0\big)^{-1} w^{\mathscr{P}^{\mathrm{opt}}}\big(\mathscr{P}^{\mathrm{opt}}\big)\big)^\top \mathbf{e}_{(j)} u_{,i}^{\mathscr{P}^{\mathrm{opt}}}\big(P^{j\,\mathrm{opt}}\big) = 0, \quad j = 1, \dots, J, \ i = 1, 2. \tag{39}$$

2.4 A Sufficient Condition for a Local Extremum of the Compliance

Although the second-order derivatives of the Green function G have logarithmic singularities, the matrix $\mathscr{G}^0$ in (35) depends smoothly on the support points $P^1, \dots, P^J$

since it involves the values $\mathscr{G}^0_{jk} = G(P^k, P^j) = \mathscr{G}(P^k, P^j)$ of the regular part $\mathscr{G}$ which is C^∞-smooth inside $\Omega \times \Omega$. Moreover, $w \in C^{2,\alpha}(\Omega)$. Hence, the function

$$\Omega^J \ni \mathscr{P} \mapsto M(\mathscr{P}) = w(\mathscr{P})^\top \big(\mathscr{G}^0\big)^{-1} w(\mathscr{P}),$$

together with its second-order derivatives, is Hölder continuous. Furthermore, for the perturbed support set $\mathscr{P}^\varepsilon$ composed from the points $P^{j\varepsilon} = P^j + \varepsilon X^j$ where $j = 1, \dots, J$, $X^j \in \mathscr{R}^2$, and $\varepsilon > 0$ is a small parameter, we have

$$M\big(\mathscr{P}^\varepsilon\big) = M(\mathscr{P}) + \varepsilon \sum_{j=1}^{J} \sum_{i=1}^{2} \frac{\partial M}{\partial X^j_i}(\mathscr{P}) X^j_i + \frac{\varepsilon^2}{2} \sum_{j,k=1}^{J} \sum_{i,q=1}^{2} \mathscr{M}^{iq}_{jk}(\mathscr{P}) X^j_i X^k_q + O\big(\varepsilon^{2+\alpha}\big),$$

where

$$\mathscr{M}^{iq}_{jk}(\mathscr{P}) = \frac{\partial^2 M}{\partial X^j_i \partial X^k_q}(\mathscr{P}). \tag{40}$$

Note that the derivative $\partial M / \partial X^j_i$ has been computed in the previous section. Therefore a sufficient condition for a local minimum of the compliance functional is the following.

Theorem 3 *Let conditions* (37)–(39) *be satisfied for a support set* $\mathscr{P} = \{P^1, \dots, P^J\}$, *and let the matrix* $\mathscr{M}$ *with entries* (40) *be negative definite. Then the compliance* (17) *attains a local minimum at the support set* $\mathscr{P}$.

2.5 The Minimal Deflexion Functional

If the optimization problem (22) gets the supplementary restrictions

$$\operatorname{dist}\big(P^j, \Gamma\big) \geq \rho, \qquad \big|P^j - P^k\big| \geq \delta, \quad j = 1, \dots, J, \ P^k \neq P^j, \tag{41}$$

with $\rho > 0$ and $\delta > 0$, the matrix $\mathscr{G}^0$ in the representation formula (33) for the solution $u^{\mathscr{P}}$ of the Sobolev problem stays uniformly positive definite. Thus, problem (22), (41) admits a solution, and $\#\mathscr{P}^{\mathrm{opt}}_\rho = J$. In Appendix we prove (cf. estimate (65)) that the minimal deflexion functional (21) remains continuous in both the cases $P^j \to P^k$ and $P^j \to \Gamma$. This means that the optimization problem (22) itself has a solution, even if it may happen that $\#\mathscr{P}^{\mathrm{opt}} < J$.

2.6 The Asymptotic Analysis

Locating in an optimal way a given number J of support points for a clamped plate could be a very hard numerical problem when the number J is not small. Thus it becomes interesting to investigate the *asymptotic density* of $\mathscr{P}^{\rm opt}$ in Ω instead of the precise location of every point of $\mathscr{P}^{\rm opt}$. This density is defined in the following way: for every $J \in \mathbb{N}$, consider the optimal set $\mathscr{P}_J^{\rm opt} = \{P_1^J, \dots, P_J^J\}$ and the probability measure

$$\mu^J = \frac{1}{J} \sum_{j=1}^{J} \delta_{P_j^J};$$

the measures μ^J will converge (at least for a subsequence) to a measure $\overline{\mu}$ that we call the *asymptotic density* of $\mathscr{P}_J^{\rm opt}$.

In many situations the measure $\overline{\mu}$ can be recovered through a very simple minimization problem of the form

$$\min\left\{ \int_\Omega j\big(x, \mu(x)\big)\, dx \ : \ \int_\Omega d\mu = 1 \right\}, \tag{42}$$

where the integrand $j(x, s)$ depends on the nature of the problem and on the right-hand side f. Once reduced to (42), the determination of $\overline{\mu}$ is straightforward and comes out from the equation

$$\frac{\partial j}{\partial s}\big(x, \overline{\mu}(x)\big) = \text{constant}.$$

For instance, this happens in the Monge location problem (see [2, 3]) and in the location of supports for a membrane (see [4]), while for the case of plates, this problem is, as far as we know, still open.

3 An Example and Open Questions

3.1 One Support Point

If $J = 1$, the support set $\mathscr{P}$ is made by only one point P, and we have

$$E(u; f) = E(w; f) + \frac{1}{2} G(P, P)^{-1} \big|w(P)\big|^2.$$

Hence, the point P must be an extremum point of the function (23). This simple conclusion is in accord with conditions (37), which in the case $\mathscr{P} = \{P\}$ read

$$G(P, P)^{-1} w(P) \left(\frac{\partial w}{\partial x_i}(P) - G(P, P)^{-1} w(P) \frac{\partial G}{\partial x_i}(P, P) \right) = 0, \quad i = 1, 2. \tag{43}$$

Indeed, the left-hand side of (43) is equal to

$$G(P,P)^{-1/2}w(P)\frac{\partial}{\partial x_i}\big(G(x,x)^{-1/2}w(x)\big)\big|_{x=P}.$$

Let us present results of a simple calculation for the unit disk $\Omega=\{x\ :\ r=|x|<1\}$. The solution w of the Dirichlet problem (1), (2) with the right-hand side $f(x)=1$ (a horizontal cylindrical plate is bent by gravity) takes the form

$$w(x)=\frac{1}{64}\big(r^4-2r^2+1\big).$$

The solution u of the Sobolev problem with the support point at the center of the disk is given by

$$u(x)=\frac{1}{64}\big(r^4-2r^2\ln r-r^2\big).$$

Then

$$\begin{aligned} &C(w;1)=\frac{\pi}{192}, \qquad C(u;1)=\frac{\pi}{768}=\frac{1}{4}\frac{\pi}{192},\\ &\mathscr{W}(w;1)=\frac{1}{64}, \qquad \mathscr{W}(u;1)=\frac{1}{64}r_*^2\big(1-r_*^2\big)=\frac{1}{64}0.16190\ldots, \end{aligned} \tag{44}$$

while the maxima of w and u are attained at the point $r=0$ and the circle $r=r_*$, respectively, and $r_*=0.45076\ldots$ is the only root of the transcendent function $1-r^2-\ln r$ in the interval $(0,1)$. Formulas (44) show how the functionals (17) and (21) decrease due to the presence of the support point, that is, 4 and 6.17665… times, respectively. Since the Green function in the unit disk is known explicitly [1],

$$G(x,y)=\frac{1}{8\pi}|x-y|^2\big(\ln|x-y|-\ln\sqrt{|x|^2|y|^2-2x^\top y+1}\,\big)+\big(1-|x|^2\big)\big(1-|y|^2\big),$$

the solution of the optimization problems (19) and (22) using formulas derived in Sect. 2 needs computer resources only.

3.2 The Kirchhoff Plate with a Free Edge

In this subsection we continue the discussion started in Remark 1. To formulate the correct Neumann boundary-value problem in the Kirchhoff theory, we ought to consider the functional

$$a(w,w;\Omega)=\int_\Omega\Big(\big|\Delta_x w(x)\big|^2+2(1-\sigma)\big(\big|w_{,12}(x)\big|^2-w_{,11}(x)w_{,22}(x)\big)\Big)\,dx, \tag{45}$$

which involves all second-order derivatives $w_{,iq}=\partial^2 w/\partial y_i\partial y_q$ of the deflexion w, depends on the Poisson ratio σ, one of physical characteristics of the elastic

material, and implies the main asymptotic term of the elastic energy kept by the three-dimensional thin plate. From definition (45) one readily derives the inequality

$$a(w,w;\Omega) \geq (1-\sigma)\sum_{i,q=1}^{2} \|w_{,iq}\|^2_{L^2(\Omega)}$$

and, on the base of the Riesz representation theorem, concludes that the variational problem

$$a(w,v;\Omega) = (f,v)_\Omega, \quad v \in H^2(\Omega), \tag{46}$$

is well posed with the bilinear form

$$\begin{aligned} a(w,v;\Omega) &= \frac{1}{4}\big(a(w+v,w+v;\Omega) - a(w-v,w-v;\Omega)\big) \\ &= (\Delta_x w, \Delta_x v)_\Omega \\ &\quad + (1-\sigma)\big((w_{,12}, v_{,12})_\Omega - (w_{,11}, v_{,11})_\Omega - (w_{,22}, v_{,22})_\Omega\big). \end{aligned}$$

The following Green formula is valid (cf. [21]):

$$a(w,v;\Omega) = \big(\Delta_x^2 w, v\big)_\Omega + \big(N^1 w, \partial_n v\big)_\Gamma + \big(N^0 w, v\big)_\Gamma, \tag{47}$$

where $w \in H^4(\Omega)$, $v \in H^2(\Omega)$, and

$$\begin{aligned} N^1(x,\nabla_x)w(x) &= \sigma\,\Delta_x w(x) + (1-\sigma)\partial_n^2 w(x), \\ N^0(x,\nabla_x)w(x) &= \partial_n \Delta_x w(x) + (1-\sigma)\partial_s \partial_s \partial_n w(x), \end{aligned} \tag{48}$$

while ∂_s stands for differentiation along the contour Γ. In other words, the (intrinsic) Neumann boundary conditions read

$$N^1(x,\nabla_x)w(x) = 0, \qquad N^0(x,\nabla_x)w(x) = 0, \quad s \in \Gamma. \tag{49}$$

We refer to [18] for the following solvability and smoothness results. If the functional $f \in (H^2(\Omega))'$ fulfills the compatibility conditions

$$(f,\ell)_\Omega = 0, \quad \ell \in \mathscr{R} = \{a_0 + a_1 x_1 + a_2 x_2 \,:\, a_m \in \mathscr{R}\}, \tag{50}$$

then the variational problem (46) has a (generalized) solution $w \in H^2(\Omega)$ which is determined up to an addendum in $\mathscr{R}$ and, under the orthogonality condition

$$(w,\ell)_\Omega = 0, \quad \ell \in \mathscr{R}, \tag{51}$$

becomes unique and satisfies the estimate

$$\|w\|_{H^2(\Omega)} \leq c\|f\|_{(H^2(\Omega))'}.$$

Let the right-hand side $f \in L^2(\Omega)$ be subject to (50). Then a solution $w \in H^2(\Omega)$ of (46) becomes a classical solution to the Neumann problem (1), (49) and enjoys estimate (4) in the case (51).

The problem, composed by the differential equation (10), the boundary conditions (49), and the point conditions (8), is called the Neumann Sobolev problem (in contrast to the Dirichlet Sobolev problem (10), (8), (2)). The integral identity

$$a(w, v; \Omega) = (f, v)_\Omega, \quad v \in H^2(\Omega; \mathscr{P}), \tag{52}$$

gives the variational formulation of this problem, where we denoted by $H^2(\Omega; \mathscr{P})$ the subspace of functions in $H^2(\Omega)$ satisfying the point conditions (8).

Lemma 3 *The Neumann Sobolev problem* (52) *has a solution* $u \in H^2(\Omega; \mathscr{P})$ *if and only if the functional* $f \in (H^2(\Omega; \mathscr{P}))'$ *verifies the orthogonality conditions*

$$(f, \ell)_\Omega = 0, \quad \ell \in \mathscr{R}(\mathscr{P}),$$

where

$$\mathscr{R}(\mathscr{P}) = \left\{\ell \in \mathscr{R} \,:\, \ell\left(P^1\right) = \cdots = \ell\left(P^J\right) = 0\right\}. \tag{53}$$

This solution is determined up to an addendum in $\mathscr{R}(\mathscr{P})$ *but, under the orthogonality condition*

$$(u, \ell)_\Omega = 0, \quad \ell \in \mathscr{R}(\mathscr{P}),$$

becomes unique and verifies estimate (9).

Corollary 1 *The Neumann Sobolev problem with* $f \in (H^2(\Omega; \mathscr{P}))'$ *is uniquely solvable, provided that the family* $\mathscr{P}$ *satisfies the condition*

$$\mathscr{P} \quad \text{contains three points not lying on a same line.} \tag{54}$$

Remark 4 If $J = 1$ and $\mathscr{P}$ consists of the only point P^1, then $\mathscr{R}(P^1) = \{a_1(x_1 - P_1^1) + a_2(x_2 - P_2^1) \,:\, a_i \in \mathscr{R}\}$ and, therefore, $\dim \mathscr{R}(P^1) = 2$. If $\mathscr{P} \subset \mathscr{L}$, that is, all the points lie in a line $\mathscr{L} \subset \mathscr{R}^2$, then the subspace (53) is of dimension 1 and is spanned over the linear function $\ell \in \mathscr{R}$ such that $|\ell(x)| = \operatorname{dist}(x, \mathscr{L})$.

In the present paper we do not consider the optimization problem for the plate with the free edge $\partial\Omega$ and the support points $P^1, \ldots, P^J$. Notice that in the case where relation (50) is violated, the disposition of these points must take into account the necessity to satisfy condition (54) of the unique solvability, and, therefore, the assumption $J \geq 3$ is needed.

The furniture industry has been focusing upon the problem on optimizing, for the functional (21), the support set $\mathscr{P}$ in the rectangular or circular domain Ω with $\#\mathscr{P} = 4$ and $\#\mathscr{P} = 3$ (cf. Sect. 3.1). No mathematically rigorous result has been obtained yet.

3.3 The Simply Supported Plate

If Eq. (1) is supplied with one stable and one intrinsic boundary conditions, chosen from the groups (2) and (48) in coordination with the Green formula (47), the problem still admits a variational formulation (see [18] for the terminology and general procedures). For example, the boundary conditions of the simple support

$$w(x) = 0, \qquad N^1(x, \nabla_x) w(x) = 0, \quad x \in \Gamma, \tag{55}$$

lead to the problem

$$a(w, v; \Omega) = (f, v)_\Omega, \quad v \in H^2(\Omega) \cap H_0^1(\Omega).$$

Since this problem enjoys all properties of the Dirichlet problem (3), we avoid here a repetition of inferences and mention only that, owing to the first (stable) condition in (55), the second (intrinsic) condition is equivalent [21] to

$$\Delta_x w(s) + \sigma \varkappa(s) \partial_n w(s) = 0, \quad s \in \Gamma,$$

where $\varkappa(s)$ is the curvature of the contour Γ at the point s.

3.4 The von Kármán Plate

The nonlinear system of the von Kármán equations, which, in the framework of the nonlinear elasticity, takes into account an interaction of the deflexion and longitudinal deformation of a thin plate (see, e.g., [7]), reads

$$\begin{aligned} &\Delta_x^2 u(x) - \mu \langle F, u \rangle(x) = f(x), \quad x \in \Omega, \\ &\Delta_x^2 F(x) + \lambda \langle u, u \rangle(x) = 0, \quad x \in \Omega, \end{aligned} \tag{56}$$

where $\mu = \frac{E}{2(1+\sigma)}$ and $\lambda = \frac{\sigma E}{(1+\sigma)(1-2\sigma)}$ are the Lamé constants, $E > 0$ is the Young modulus, and σ is the Poisson ratio. Furthermore, u is the deflexion of the plate, and F the Airy function, a potential for the longitudinal two-dimensional stress field in the plate Ω. The bi-linear form $\langle F, u \rangle$ is given by the formula

$$\langle F, u \rangle = F_{,11}\, u_{,22} + F_{,22}\, u_{,11} - 2F_{,12}\, u_{,12}.$$

System (56) can be enclosed by the Dirichlet boundary conditions

$$u(x) = \partial_n u(x) = 0, \qquad F(x) = \partial_n F(x) = 0, \quad x \in \partial\Omega. \tag{57}$$

Note that the second couple of the boundary conditions requires that Ω is a simply connected domain (cf. [16]). It is known (see [7]) that problem (56), (57) with any right-hand side $f \in L^2(\Omega)$ has a (generalized) solution $\{u, F\} \in H_0^2(\Omega)^2$; moreover, it is classical, and w, $F \in H^4(\Omega)$. Owing to the embedding $H^2(\Omega) \subset C(\Omega)$,

system (56) can additionally be supplied with the point conditions (8), while repeating a standard argument proves the existence of a generalized solution to the obtained nonlinear Sobolev problem (see [19] for the asymptotic behavior of the solution near the support point). The point conditions on the Airy function F have no physical sense, but the point conditions for the deflexion u can be readily interpreted as supporting the plate at the points $P^1, \dots, P^J$ without prohibiting the longitudinal sliding. Optimization of the location of support points for the von Kármán plate is a fully open problem.

3.5 Increasing the Dimension and the Differentiation Order

One may consider the Dirichlet problem (1), (2) in a multidimensional domain $\Omega \subset \mathscr{R}^d$ with $d \geq 3$. Since the fundamental solution of the bi-harmonic operator Δ_x^2 in $\mathscr{R}^d$ takes the form

$$\Phi(x) = \begin{cases} C_3|x| & \text{for } d = 3, \\ C_4 \ln|x| & \text{for } d = 4, \\ C_d|x|^{4-d} & \text{for } d \geq 5, \end{cases}$$

where C_d are some constants, the Sobolev conditions (8) can be imposed in the case $d = 3$ only. The problem (10), (8), (2) may be examined in the same way as it has been done for $d = 2$; however the authors do not know a three-dimensional model in the mathematical physics which utilizes a fourth-order equation.

Certain mathematical models, like the Reissner–Mindtin plates [24, 26] and the micro-polar elasticity [8], invoke the polyharmonic operator $(-\Delta_x)^m$ for a potential U of some kind. Considering the case $m = 3$ and $d = 2$ only, we write the boundary-value problem as follows:

$$\begin{aligned} &-\Delta_x^3 U(x) + \mathscr{B}(\nabla_x)U(x) = F(x), \quad x \in \Omega \subset \mathscr{R}^2, \\ &U(x) = \partial_n U(x) = \partial_n^2 U(x) = 0, \quad x \in \partial\Omega. \end{aligned} \tag{58}$$

Here, $\mathscr{B}(\nabla_x)$ stays for formally self-adjoint fourth-order differential operator. For any $F \in (H_0^2(\Omega))'$, the Dirichlet problem (58) admits a unique generalized solution $U \in H_0^3(\Omega)$. By the Sobolev embedding $H^3(\Omega) \subset C^1(\Omega)$, one may assign point conditions, as either the triple

$$U\big(P^j\big) = U_{,1}\big(P^j\big) = U_{,2}\big(P^j\big) = 0 \tag{59}$$

or any subset of (59) at each point in $\mathscr{P}$. Of course, any point condition for a potential needs a clear physical interpretation. No result is known for an optimal design of these point conditions. Green functions of the Dirichlet problem for a polyharmonic operator in a ball have an explicit form (see [1]).

3.6 One-Side Conditions

The Sobolev condition (8) corresponds to the case where the point supports are double sided, i.e., they prohibit from both the up- and down-deflexions of the plate. It is quite natural to consider one-sided conditions. In this case the minimization problem for the energy functional (15) must be posed in the closed cone

$$H_0^2(\Omega;\mathscr{P})^+ = \big\{u \in H_0^2(\Omega;\mathscr{P}) \,:\, u\big(P^j\big) \ge 0\big\}.$$

Such a minimization problem can be treated as a variational inequality, and it is known that it has a unique solution for any right-hand side $f \in L^2(\Omega)$ (see, e.g., [12]). This solution may verify the Sobolev condition on a subset $\mathscr{P}_+$ of $\mathscr{P}$, while points in $\mathscr{P} \setminus \mathscr{P}_+$ do not support the plate being not in the contact with it. Since the Dirichlet problem for the bi-harmonic equation in general is not sign-preserving (see [11] and others), for a general set $\mathscr{P}$, some points can be removed without any change in the energy, and only the optimality conditions may give again that $\#\mathscr{P} = J$. In general, however, our results for the linear Sobolev problem do not apply to problems with one-sided conditions.

Acknowledgements The work of Giuseppe Buttazzo is part of the project 2008K7Z249 *Trasporto ottimo di massa, disuguaglianze geometriche e funzionali e applicazioni* financed by the Italian Ministry of Research. The work of Sergey A. Nazarov has been supported by the Russian Foundation of Basic Research, Grant 09-01-00759.

Appendix

Let us assume that the points $P^1, \dots, P^J$ in $\mathscr{P}$ are different, i.e., $|P^j - P^k| \ge c_{\mathscr{P}} > 0$ for $j \ne k$, but the additional points $P_\varepsilon^{J+1}, \dots, P_\varepsilon^N$ are situated close to P^J which is put at the coordinate origin $\mathscr{O}$. In other words,

$$P_\varepsilon^j = \varepsilon X^j, \quad j = J+1, \dots, N,$$

where $X^j \ne X^k$ for $j \ne k$, $|X^j| \le 1$, and $\varepsilon > 0$ is a small parameter. We denote by $\mathscr{P}^\varepsilon$ the set

$$\big\{P^1, \dots, P^J, P_\varepsilon^{J+1}, \dots, P_\varepsilon^N\big\}$$

and by u^ε the solution to the Sobolev problem (10), (8), (2) with the support points listed above, i.e., with $\mathscr{P}^\varepsilon$ replacing $\mathscr{P}$. The notation u is kept for the solution of the Sobolev problem with $\mathscr{P}$.

By representation (29), (30) of u and estimate (4) for w, we recall the smoothness of the regular part $\mathscr{G}$ of the Green function G and observe that (compare Lemma 2)

$$u(x) = -a|x|^2 \ln|x| + \tilde{u}(x), \quad \tilde{u} \in H^4(\mathscr{V}),$$

where a is a constant, and $\mathscr{V} \subset \Omega$ a neighborhood of the point $\mathscr{O} = P^J$ which is free of the points $P^1, \dots, P^{J-1}$. Hence, the Sobolev theorem on embedding $H^4 \subset C^2$ ensures the pointwise estimates

$$\big|u(x)\big| \le b|x|, \qquad \big|\nabla_x u(x)\big| \le b, \qquad \big|\Delta_x u(x)\big| \le b\big(1 + \big|\ln|x|\big|\big), \quad x \in \mathscr{V}. \tag{60}$$

Notice that the quantities $|a|$, b, and $\|\tilde{u}\|_{H^4(\mathscr{V}_j)}$ do not exceed $c\|f\|_{L^2(\Omega)}$ with some constant c (cf. (13)).

The function $u^\varepsilon \in H^2_0(\Omega; \mathscr{P}^\varepsilon)$ vanishes at all points $P^1, \dots, P^J$, and, therefore, the difference $u - u^\varepsilon$ can be taken as the test function in the integral identity for u, that is,

$$\big(\Delta_x u, \Delta_x\big(u - u^\varepsilon\big)\big)_\Omega = \big(f, u - u^\varepsilon\big)_\Omega. \tag{61}$$

The function $u \in H^2_0(\Omega; \mathscr{P})$ may not belong to $H^2(\Omega; \mathscr{P}^\varepsilon)$, and we multiply it by $\chi(|\ln\varepsilon|^{-1}|\ln|x||)$, where χ is a smooth cut-off function such that

$$0 \le \chi \le 1, \qquad \chi(t) = 0 \quad \text{for } t \ge 1, \quad \chi(t) = 1 \quad \text{for } t \le 1/2.$$

Notice that

$$\begin{aligned} &\chi\big(|\ln\varepsilon|^{-1}\big|\ln|x|\big|\big) = 0 \quad \text{for } |x| \le \varepsilon, \\ &\chi\big(|\ln\varepsilon|^{-1}\big|\ln|x|\big|\big) = 1 \quad \text{for } |x| > \varepsilon^{1/2}, \end{aligned} \tag{62}$$

and, therefore, the product χu vanishes at the points $P^{J+1}_\varepsilon, \dots, P^N_\varepsilon$ which live in the ε-neighborhood of $\mathscr{O}$. Here and further, the argument $|\ln\varepsilon|^{-1}|\ln|x||$ is assumed for χ.

We insert $u^\varepsilon - \chi u$ into the integral identity for u^ε and, after a simple transformation, obtain

$$\begin{aligned} \big(\Delta_x u^\varepsilon, \Delta_x\big(u^\varepsilon - u\big)\big)_\Omega = \big(f, u^\varepsilon - \chi u\big)_\Omega - \big(\Delta_x u^\varepsilon, (1-\chi)\Delta_x u\big)_\Omega \\ + \big(\Delta_x u^\varepsilon, [\Delta_x, \chi]u\big)_\Omega, \end{aligned} \tag{63}$$

where $[\Delta_x, \chi]$ is the commutator of the Laplace operator and the multiplication operator, i.e.,

$$[\Delta_x, \chi]u = 2(\nabla_x u)^\top \nabla_x \chi + u\Delta_x \chi, \tag{64}$$

while, in view of (62), expression (64) differs from zero in the annulus $\Theta(\varepsilon) = \{x : \varepsilon < |x| < \varepsilon^{1/2}\}$ only.

Applying estimates (60) and differentiating the cut-off function, we observe that

$$\begin{aligned} \big\|[\Delta_x, \chi]u\big\|^2_{L^2(\Omega)} &\le \frac{c}{|\ln\varepsilon|^2} \int_{\Theta(\varepsilon)} \left(\frac{1}{|x|^2}\big|\nabla_x u(x)\big|^2 + \frac{1}{|x|^4}\left(1 + \frac{1}{|\ln\varepsilon|^2}\right)\big|u(x)\big|^2 \right) dx \\ &\le \frac{cb^2}{|\ln\varepsilon|^2} \int_\varepsilon^{\varepsilon^{1/2}} \frac{1}{\rho^2}\, \rho\, d\rho \le \frac{c}{|\ln\varepsilon|}\|f\|^2_{L^2(\Omega)}. \end{aligned}$$

Using a similar but simpler argument and taking the first and third estimates (60) into account yield

$$\big\|(1-\chi)u\big\|^2_{L^2(\Omega)} \le cb^2 \int_0^{\varepsilon^{1/2}} \rho^2\,\rho\,d\rho \le c\varepsilon^2 \|f\|^2_{L^2(\Omega)},$$

$$\big\|(1-\chi)\Delta_x u\big\|^2_{L^2(\Omega)} \le cb^2 \int_0^{\varepsilon^{1/2}} |\ln\rho|^2\,\rho\,d\rho \le c\varepsilon|\ln\varepsilon|^2 \|f\|^2_{L^2(\Omega)}.$$

Thus, adding (63) to (61) and using the second fundamental inequality, we derive the relation

$$\begin{aligned} c_\Omega \big\|u-u^\varepsilon\big\|^2_{H^2(\Omega)} &\le \big\|\Delta_x\big(u-u^\varepsilon\big)\big\|_{L^2(\Omega)} \\ &= \big(f,(1-\chi)u\big)_\Omega - \big(\Delta_x u^\varepsilon,(1-\chi)\Delta_x u\big)_\Omega \\ &\quad + \big(\Delta_x u^\varepsilon,[\Delta_x,\chi]u\big)_\Omega \\ &\le c|\ln\varepsilon|^{-1}\big(\|f\|_{L^2(\Omega)} + \|\Delta_x u^\varepsilon\|_{L^2(\Omega)}\big)\,\|f\|_{L^2(\Omega)} \\ &\le c|\ln\varepsilon|^{-1}\|f\|^2_{L^2(\Omega)}, \end{aligned}$$

where $c_\Omega > 0$, and hence

$$\big\|u-u^\varepsilon\big\|_{H^2(\Omega)} \le c|\ln\varepsilon|^{-1/2}\|f\|_{L^2(\Omega)}. \tag{65}$$

The following assertion becomes trivial.

Lemma 4 *Under the above restriction on the location of the points $P^1,\dots P^J$ and $P^{J+1}_\varepsilon,\dots,P^N_\varepsilon$, there holds estimate (65) and the relationship*

$$E(u;f) \le E\big(u^\varepsilon;f\big) \le E(u;f) + c|\ln\varepsilon|^{-1/2}\|f\|^2_{L^2(\Omega)}. \tag{66}$$

A formula of type (31) relates the solutions of the Sobolev problems with supports at $P^1,\dots,P^J$ and $P^1,\dots,P^J,P^{J+1},\dots,P^N$. Thus, locating the additional points $P^{J+1},\dots,P^N$ at a small distance from $P^1,\dots,P^J$ gives a small increment to the energy functional, due to estimate (66). This means that placing new support points near the old ones $P^1,\dots,P^J$ is surely not profitable.

If the point P^{J+1} stays near a point Q on the boundary $\partial\omega$, i.e., $|P^{J+1}-Q| = \varepsilon \ll 1$, then by virtue of the conditions (2), estimates (60) turn into

$$\big|u(x)\big| \le bd(x)^2, \qquad \big|\nabla_x u(x)\big| \le bd(x), \qquad |\Delta_x u(x)| \le b, \quad x \in \Omega\cap\mathscr{V},$$

where $b = c\|f\|_{L^2(\Omega)}$, $d(x) = \operatorname{dist}(x,\partial\omega)$, and $\mathscr{V}$ is a neighborhood of Q. This modification brings the small factor ε instead of $|\ln\varepsilon|^{-1/2}$ into inequalities (65) and (66). In other words, putting a new support point near the clamped boundary is not advantageous as well.

References

1. Boggio, T.: Sulle funzioni di Green d'ordine m. Rend. Circ. Mat. Palermo **20**, 97–135 (1905)
2. Bouchitté, G., Jimenez, C., Mahadevan, R.: Asymptotic analysis of a class of optimal location problems. J. Math. Pures Appl. **95**(4), 382–419 (2011)
3. Buttazzo, G., Oudet, E., Stepanov, E.: Optimal transportation problems with free Dirichlet regions. In: Variational Methods for Discontinuous Structures, Cernobbio 2001. Progress in Nonlinear Differential Equations, vol. 51, pp. 41–65. Birkhäuser, Basel (2002)
4. Buttazzo, G., Santambrogio, F., Varchon, N.: Asymptotics of an optimal compliance-location problem. ESAIM Control Optim. Calc. Var. **12**, 752–769 (2006)
5. Ciarlet, P.G.: Mathematical Elasticity, II: Theory of Plates. North-Holland, Amsterdam (1997)
6. Ciarlet, P.G., Destuynder, P.: A justification of the two-dimensional plate model. J. Méc. **18**, 315–344 (1979)
7. Ciarlet, P.G., Rabier, P.: The von Kármán Equations. Lecture Notes in Mathematics, vol. 826. Springer, Berlin (1980)
8. Cosserat, E., Cosserat, F.: Théorie des Corps Déformables. Hermann, Paris (1909)
9. Dauge, M., Gruais, I.: Edge layers in thin elastic plates. Comput. Methods Appl. Mech. Eng. **157**(3–4), 335–347 (1998)
10. Destuynder, P.: Une Théorie Asymptotique des Plaques Minces en Elasticité Linéaire. Masson, Paris (1986)
11. Duffin, R.J.: On a question of Hadamard concerning super-bi-harmonic functions. J. Math. Phys. **27**, 253–258 (1949)
12. Duvaut, G., Lions, J.L.: Inequalities in Mechanics and Physics. Springer, Berlin (1976)
13. Germain, S.: Recherches sur la Théorie des Surfaces Élastiques. Courcier, Paris (1821)
14. Kirchhoff, G.R.: Über das Gleichgewicht und die Bewegung einer elastischen Scheibe. J. Reine Angew. Math. **40**, 51–88 (1850) and **56**, 285–313 (1859)
15. Kondratiev, V.A.: Boundary problems for elliptic equations in domains with conical or angular points. Tr. Mosk. Mat. Obŝ. **16**, 209–292 (1967). English transl.: Trans. Moscow Math. Soc. **16**, 227–313 (1967)
16. Kulikov, A., Nazarov, S.A., Sweers, G.: On Airy functions and stresses in nonisotropic heterogeneous 2d-elasticity. Z. Angew. Math. Mech. **88**, 955–981 (2008)
17. Ladyzhenskaya, O.A.: Boundary Value Problems of Mathematical Physics. Applied Math. Sciences, vol. 49. Springer, New York (1985)
18. Lions, J.L., Magenes, E.: Non-Homogeneous Boundary Value Problems and Applications, vol. I. Springer, New York (1972)
19. Maz'ja, V.G., Morozov, N.F., Plamenevskii, B.A.: On nonlinear bending of a plate with a crack. Differential and integral equations. Boundary value problems. In: I.N. Vekua Memorial Collection, Tbilisi, pp. 145–163 (1979). Engl. transl.: Amer. Math. Soc. Transl. **123**, 125–139 (1984)
20. Maz'ya, W.G., Nazarov, S.A., Plamenevskii, B.: Asymptotische Theorie Elliptischer Randwertaufgaben in Singulär Gestörten Gebieten, vol. 1. Akademie-Verlag, Berlin (1991). English transl.: Asymptotic Theory of Elliptic Boundary Value Problems in Singularly Perturbed Domains. Vol. I. Birkhäuser, Basel (2000)
21. Mikhlin, S.G.: Variational Methods in Mathematical Physics. Nauka, Moscow (1970). English transl.: Pergamon Press, Oxford (1964)
22. Morgenstern, D.: Herleitung der Plattentheorie aus der dreidimensionallen Elastozitätstheorie. Arch. Ration. Mech. Anal. **3**, 145–152 (1959)
23. Nazarov, S.A.: Asymptotic Theory of Thin Plates and Rods. Dimension Reduction and Integral Estimates, vol. 1. Nauchnaya Kniga, Novosibirsk (2002)
24. Percivale, D., Podio-Guidugli, P.: A general linear theory of elastic plates and its variational validation. Boll. Unione Mat. Ital. **2**, 321–341 (2009)
25. Poisson, S.D.: Mémoire sur l'équilibre et le mouvement des corps élastiques. Mém. Acad. Sci. Inst. Fr. **8**, 357–570 (1929)

26. Reissner, E.: On the theory of bending of elastic plates. J. Math. Phys. **23**, 184–191 (1944)
27. Shoikhet, B.A.: On asymptotically exact equations of thin plates of complex structure. Prikl. Mat. Meh. **37**, 914–924 (1973). English transl.: J. Appl. Math. Mech. **37**, 867–877 (1974)
28. Zorin, I.S., Nazarov, S.A.: Edge effect in the bending of a thin three-dimensional plate. Prikl. Mat. Meh. **53**, 642–650 (1989). English transl.: J. Appl. Math. Mech. **53**, 500–507 (1989)

A Code for Shape Generation and Aerodynamic Design of Aircraft

Rauno Cavallaro and Aldo Frediani

1 Introduction

The preliminary design optimization holds an important role in the aircraft design process. To be efficient, optimization needs a high degree of automation, leaving to the designer only minor tasks. The efficiency would be enhanced if the different modules required to the overall process of optimization are part of an unique integrated framework.

The preliminary aerodynamic property estimation represents the basis of a design procedure. Although theoretical prediction or lower-order aerodynamic solver, like vortex lattice codes, may be enough accurate for an early preliminary design, when investigating innovative configurations, the order of approximation may be unacceptable [4], mainly because its effect can lead to unreliable results. For example, blended wing body or PrandtlPlane stability of flight are highly sensitive to small aerodynamic load variations, and, hence, an efficient and fast code for preliminary aerodynamic design is needed. Moreover, the gained experience with the traditional configurations in aeronautics, which drives many design choices in the preliminary stages, may not directly carry-over to the new configuration to design.

The steps for obtaining an aerodynamic analysis consist into a geometrical configuration definition, a grid generation, and an aerodynamic solution; an integrated framework where preliminary aerodynamic design is easily undertaken is presented in this paper.

R. Cavallaro (✉)
Department of Aerospace Engineering, San Diego State University, Campanile Drive, 92120 San Diego, USA
e-mail: rcavalla@rohan.sdsu.edu

A. Frediani
Department of Aerospace Engineering, University of Pisa, via G. Caruso, 56100 Pisa, Italy
e-mail: a.frediani.dia@unipi.it

G. Buttazzo, A. Frediani (eds.), *Variational Analysis and Aerospace Engineering: Mathematical Challenges for Aerospace Design*, Springer Optimization and Its Applications 66,
DOI 10.1007/978-1-4614-2435-2_6,

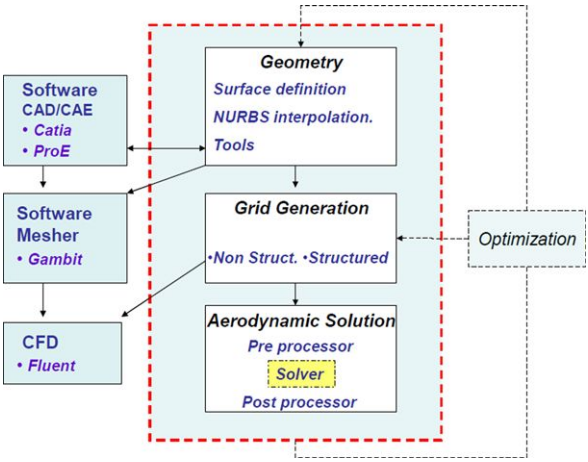

Fig. 1 Logical layout of the code

The logical layout of the code is illustrated in Fig. 1. The three main modules are depicted: geometric modeling, grid generation, and aerodynamic solver; possible interactions with external codes are also pointed together with an automated optimization tool.

The geometric modeling module provides the aerodynamic surface. This code is the result of research activities, carried out at Pisa University, with the aim of assessing a code for a quick, accurate, and flexible shape generation, Refs. [12, 15]; the code, named ASD (Aerodynamic Shape Design), indeed proved to be an excellent design tool, easily integrated into an aerodynamic design process, which allowed one to develop conventional and unconventional aircraft configurations. The geometric engine is based on a modern branch of Mathematics called NURBS (Non-Uniform Rational B-Spline), which received an enormous attention with the advent of CAD CAM tools. Some basic information on NURBS are given in the next paragraph, and, afterwards, a brief description of the shape generation module is presented; this module makes use of specific features; typical features for the wing surface generation are airfoil definition, their linear and angular position along span, fillets, curved wings or winglets, etc. A keypoint for the efficiency of the code is its user friendly approach. The GUIs enable one to easily set the parameters defining the design process; moreover, the parametric nature of the code is well suited for a fully automated optimization process.

The mesh generation module allows one to define both structured and unstructured meshes, provided with a mesh quality analyzer and a post-processing tool. The structured mesher is associated with a grid generation for different panel method codes. The aerodynamic mesh generation is fully automated to be coupled with the aerodynamic solvers, and the user can obtain the aerodynamic solution directly from the shape generation. Some examples of application are reported to show the performance of the present code. Now the code is available to produce an advancement into the aeronautical engineering field.

2 NURBS

NURBS is the acronym of *Non-Uniform Rational B-Spline*, Ref. [13]. It is a mathematical model commonly used in computer graphics for generating and representing curves and surfaces.

A NURBS curve is a vector-valued piecewise rational polynomial function of the form

$$\mathbf{C}(u) = \frac{\sum_{i=0}^{n} w_i \mathbf{P}_i N_{i,p}(u)}{\sum_{i=0}^{n} w_i N_{i,p}(u)}, \tag{1}$$

where the w_i are the so-called weights, the $\mathbf{P}_i$ are the control points (just as in the case of nonrational curves), and $N_{i,p}(u)$ are the normalized B-spline basis functions of degree p defined recursively as

$$N_{i,0}(u) = \begin{cases} 1 & \text{if } u_i \le u < u_{i+1}, \\ 0 & \text{otherwise,} \end{cases}$$

$$N_{i,p}(u) = \frac{u - u_i}{u_{i+p} - u_i} N_{i,p-1}(u) + \frac{u_{i+p+1} - u}{u_{i+p+1} - u_{i+1}} N_{i+1,p-1}(u), \tag{2}$$

where u_i are the knots, and the set of knots

$$U = \{u_0, u_1, \ldots, u_m\} \tag{3}$$

is the so-called knot vector. The degree, the number of knots, and the number of control points are related by the formula $m = n + p + 1$. For nonuniform and nonperiodic B-splines, the knot vector takes the form

$$U = \{\alpha, \alpha, \ldots, \alpha, u_{p+1}, \ldots, u_{m-p-1}, \beta, \beta, \ldots, \beta\}, \tag{4}$$

where the end knots α and β are repeated with multiplicity $p + 1$. In most practical applications $\alpha = 0$ and $\beta = 1$, as is assumed throughout this article.

A NURBS surface is the rational generalization of the tensor-product nonrational B-spline surface and is defined as follows:

$$\mathbf{S}(u, v) = \frac{\sum_{i=1}^{n} \sum_{j=0}^{m} w_{i,j} \mathbf{P}_{i,j} N_{i,p}(u) N_{j,q}(v)}{\sum_{i=1}^{n} \sum_{j=0}^{m} w_{i,j} N_{i,p}(u) N_{j,q}(v)}, \tag{5}$$

where $w_{i,j}$ are the weights, $\mathbf{P}_{i,j}$ form a control net, and $N_{i,p}(u)$ and $N_{j,q}(v)$ are the normalized B-spline basis functions of degree p and q in the u and v directions, respectively, defined over the knot vectors

$$U = \{0, 0, \ldots, 0, u_{p+1}, \ldots, u_{r-p-1}, 1, 1, \ldots, 1\}, \tag{6}$$

$$V = \{0, 0, \ldots, 0, v_{q+1}, \ldots, v_{s-q-1}, 1, 1, \ldots, 1\}, \tag{7}$$

where the end knots are repeated with multiplicities $p + 1$ and $q + 1$, respectively, and the relations $r = n + p + 1$ and $s = m + q + 1$ hold.

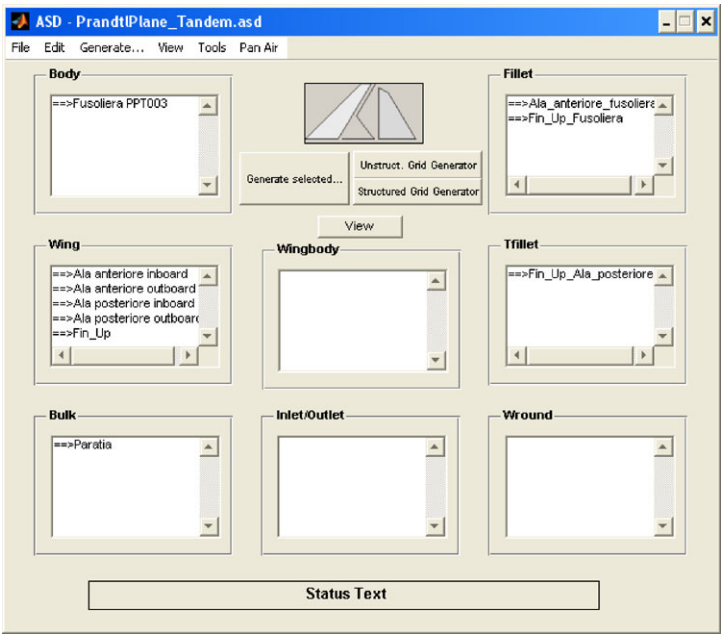

Fig. 2 The Main GUI

NURBS are very popular both in the academic and commercial geometric modeling world. They offer advantages which make them attractive for design applications:

- evaluation is straightforward, fast and computationally stable;
- they offer a common mathematical form for representing and designing both standard analytic shapes (conics, quadrics, surfaces of revolution, ...) and free-form curves and surfaces;
- by manipulating the control points and the weights, NURBS provide the flexibility to design a large variety of shapes;
- NURBS have clear geometric interpretations, making them particulary useful for designers;
- NURBS have a powerful geometric tool kit which can be used throughout to design, analyze, process, and interrogate objects;
- NURBS are invariant under scaling, rotation, translation and shear both parallel and perspective projections.

3 Surface Generation Module

In the surface generation module the user is guided through the definition of the configuration surfaces. The main graphical interface is depicted in Fig. 2. Surfaces

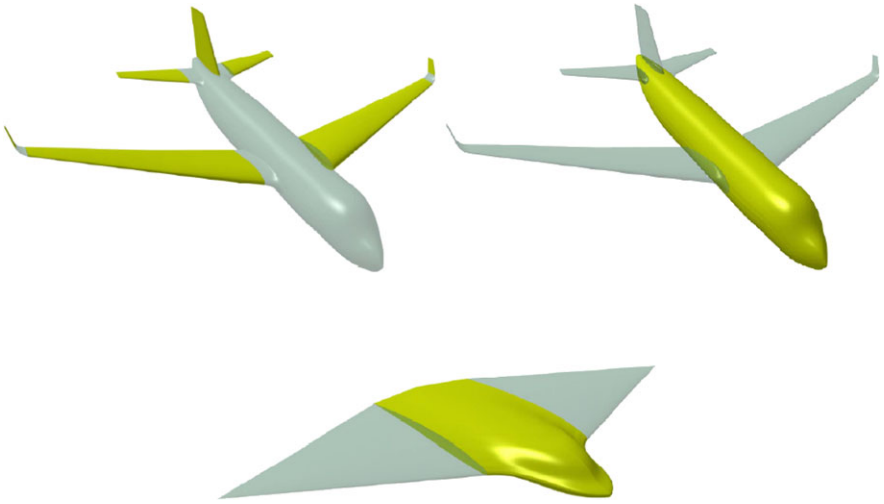

Fig. 3 Wing, body, and wing-body features (highlighted)

that belong to a configuration are classified in different features. Each box in Fig. 2 represents a feature, and the defined surfaces are listed in each box according to their nature. To outline a surface, a further intuitive GUI is displayed. This GUI asks the user to set the reference parameter and is fitted for the particular needs of the feature.

The three main features include wings, bodies, and wing-bodies. A configuration should contain at least one of these features. The remaining class of surfaces are defined starting from the main ones, basically as their intersections and connections. To be more precise, the wround and bulk class of surfaces are well suited for connecting different wings in an appropriate way. The fillet and tfillet connect a wing with a body or wing feature, respectively. The last class of feature, the inlet–outlet, is built specifically for drawing ducts inside a wing-body feature.

In order to support the user in the process of defining the reference parameters of the surfaces, a set of tools is also provided with the code.

As stated, the main features comprehend wings, bodies, and wing-bodies. The graphical interface asks for the reference parameters in order to build a *frame* (in terms of set of points) of the surface. Such parameters are appropriate for the feature to be generated and are explained through graphical examples in the GUI. The main features are depicted in Fig. 3.

In the *wing* feature the frame is obtained by the definition of the airfoils and by setting the parameters controlling the airfoil dimension and spatial positioning; it is also possible to position mobile surfaces or high-lift devices. The wing feature GUI is depicted in Fig. 4.

The *body* feature is well suited to describe fuselage-like surfaces. However, this feature is much more flexible and allows one to model more complicated shapes. The surfaces are defined mainly by sections shape definition and spacing, and top,

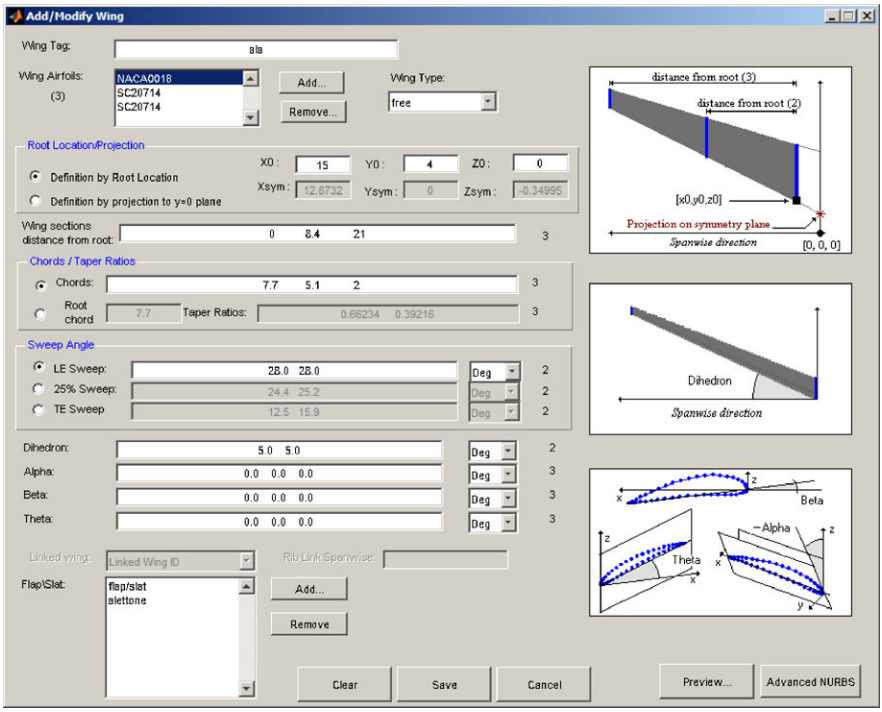

Fig. 4 The wing feature GUI

lower, center, and sideline curves which give the reference positioning of the sections.

The *wing-body* feature is wing-like surface to blend a generic root section to a wing. The result is a smoothly blended surface that extends the wing to the section specified by the user using different options to control section smoothness and generation.

When the parameters are set, the surface is ready to be generated by means of a NURBS interpolating algorithm, and, eventually, a continuous surface is obtained. However, the interpolation at this stage does not yet take intersections into account, such as the one between wing and fuselage.

3.1 The Connection/Intersection Features

These features define the surfaces which connect the main ones. The *bulk* and *wround* features connect wing edges, like the bulkhead in a box-wing system or a connecting surface between wing and winglet. The user should first specify which wings should be connected. For bulk surface, more parameters are required to better control the shape.

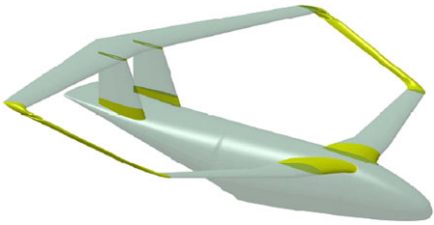

Fig. 5 Intersection features (highlighted): bulk, fillet, and tfillet

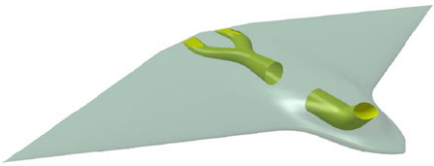

Fig. 6 Inlet–outlet feature (highlighted).

The *fillet* feature fills the gap between a wing and a fuselage with a connecting surface. According to some reference parameter, an algorithm computes the intersection between the selected body and a projection of the wing. The user controls the way this projection is carried out and, thus, the shape of the connection. Once the intersection has been calculated, the connecting surface is easily generated, and the pierced body is recalculated as a trimmed surface.

The *tfillet* feature is similar to the fillet one, with the exception that the intersection is between two wings. Compared to the fillet feature, the user could control a lower number of parameters. Examples of connection/intersection features are shown in Fig. 5.

3.2 The Internal Duct Feature

The *inlet–outlet* feature is specifically designed to generate the cavity of an inlet or outlet inside a wing-body like surface (an example in Fig. 6). The surface is generated by defining a set of sections and their spatial positions. The surface is finally given by interpolation of the section points.

As a final step, an intersection algorithm between the inlet/outlet and the involved wing-body leads to the definition of the final trimmed wing-body surface.

In order to support the user in the surface generation and exportation, some useful tools are provided within the geometric module.

3.3 Airfoil Tool

Airfoil Manager is a graphical user interface designed to manage airfoils. The layout is depicted in Fig. 7. A comprehensive database is given as part of the tool and is also possible to import external databases or wing sections.

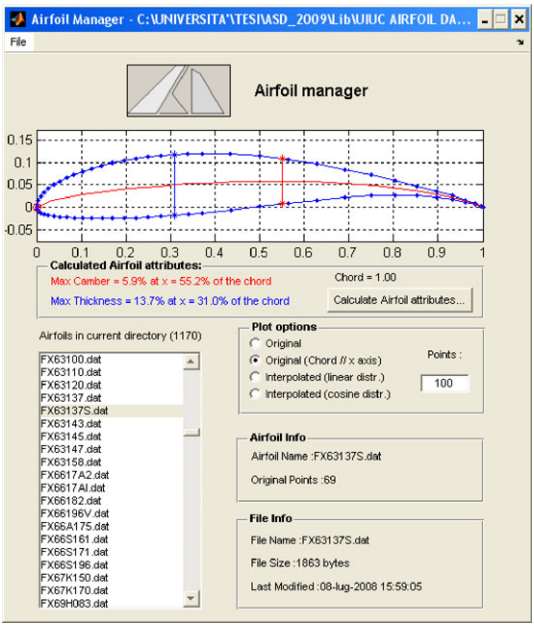

Fig. 7 The airfoil manager GUI

In the main window the airfoil is plotted, and some of its attributes such as camber or thickness are also estimated. The tools is particulary useful to define the airfoil when asked from the feature GUI. Other options are available, like coarser or finer airfoil points redistribution, and exportation tool.

The *NACA Airfoil Generator* is a graphical user interface designed to create NACA 4-digit and NACA 5-digit airfoil series. The interface asks the user the name of the airfoil and gives a plot of it. Simultaneously, thickness distribution and camber line are also plotted.

3.4 The Section Sketcher

With the aid of this tool the user is given the capability to create a section with any shape in an interactive way, adding or deleting points. A number of options are provided to assist the user to obtain the desired curve. The final product can be exported or used to define sections when asked from the feature GUI.

3.5 Flap Sketcher

Flap Sketcher is a graphical user interface designed to help defining two-dimensional mobile curves on different airfoils by means of NURBS. The tool layout is depicted in Fig. 8.

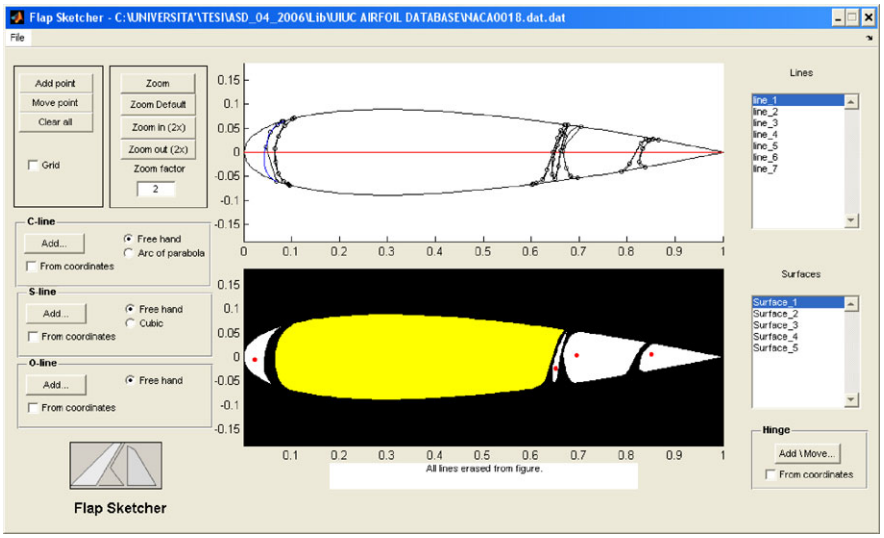

Fig. 8 The section Sketcher GUI

The interface gives the user the capability to create any flap/slat configuration starting from the base airfoil or to modify an existing configuration. The idea is to create a description of the mobile surfaces that is, to some extent, independent of the original airfoil it was created on. To achieve this, the mobile surfaces are saved in a parametric format and automatically adjusted to the loaded airfoil.

The flap/slat creation process consists of three basic steps:

- select the base airfoil,
- draw the flap/slat lines using the sketch assist tools of the flap sketcher,
- position the center of rotation of every surface.

In the first step, an airfoil is easily loaded by means of the menu. Once loaded, the airfoil is shown on both windows. The upper window shows the lines and should be used to sketch, while the lower window shows the results of the operations. Besides this, both windows can be used to enter points.

There are several methods to input the lines that define a flap/slat surface. Every line added modifies the flap configuration and the result is displayed on the lower window. There are many types of lines, that differ essentially for the end derivatives, each well suited for drawing a particular flap, slat, or mobile surface configuration.

Once a configuration of the mobile surface lines and the center of rotation is defined, it could be recalled within the wing feature GUI, together with its position and the motion law of the flap/slat elements so to complete the mobile surface definition on the wing. An example of an obtained flapped wing is depicted in Fig. 9.

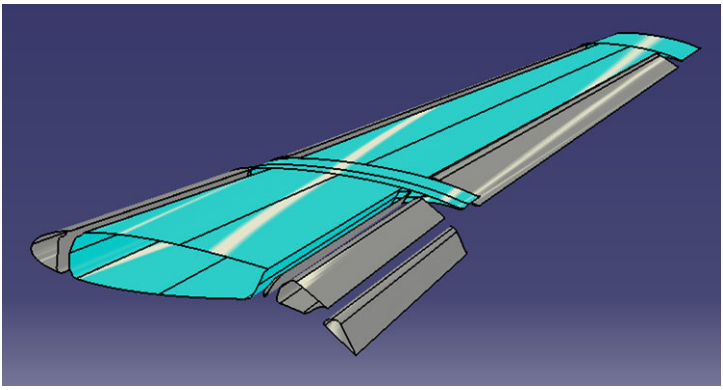

Fig. 9 A wing with flaps/slats and mobile surfaces

3.6 Advanced NURBS

This tool gives some control on the interpolating algorithm. As previously stated, the features are first defined by their typical parameters, leading to the definition of a set of points to be interpolated. Fitting of these points finally gives the NURBS description. Every feature has his own peculiarity, and the algorithm should be tuned for each situation. Even if this is done automatically, the user may need more control on the process.

One of the most important abilities of this GUI is the possibility to set the surface's level of quality. A C^1 (tangent continuous) or C^2 (curvature continuous) level of continuity for the surfaces are the available options. The second choice gives an high-quality surface, obtained through a minimization of a *fairness* functional related with the second- or third-order derivatives, depending on the user choice, Ref. [3]. If the choice is on the second derivatives, the functional Φ is expressed by

$$\Phi = \int_u \int_v \left\| \mathbf{S}^{(uu)}(u, v) \right\|^2 + \left\| \mathbf{S}^{(vv)}(u, v) \right\|^2, \tag{8}$$

where $\mathbf{S}(u, v)$ represents the surface in terms of the parameters u and v, and $\mathbf{S}^{(uu)}$ is the second-order derivative in respect of the parameter u.

The idea of fairing functional goes back to the observation that in nature a loaded flexible beam assumes a smooth deformed configuration according to the minimal energy principle. Since the stored energy mainly depends on the squared curvature, the minimization of the functional

$$\Phi = \int k^2 \, \mathrm{d}s, \tag{9}$$

where k represent the curvature, would lead to a smooth solution, accordingly with the external forces and constraints. Some articles and numerical experimentations have proposed also the variation of the curvature as a valuable choice, Ref. [10].

Whatever the choice, the minimization of a fairing functional is a widely used technique in the data fitting branch and results in smooth and aesthetical shapes, Refs. [14, 16].

In NURBS representation, due to its parametric nature, it is easier to refer to second-order derivative instead of directly to curvature, as the optimization problem becomes a linear one. In fact, for a B-spline[1] curve, it holds that

$$\mathbf{C}(u) = \sum_{i=0}^{n} \mathbf{P}_i N_{i,p}(u), \tag{10}$$

$$\mathbf{C}^{(u)}(u) = \sum_{i=0}^{n} \mathbf{P}_i N_{i,p}^{(u)} = \alpha \mathbf{e}_\mathrm{t}, \tag{11}$$

where $\mathbf{e}_\mathrm{t}$ is unitary vector tangent to the curve, α depends on the parameterization, and

$$\mathbf{C}^{(uu)}(u) = \sum_{i=0}^{n} \mathbf{P}_i N_{i,p}^{(uu)} = \alpha^{(u)} \mathbf{e}_\mathrm{t} + \alpha \mathbf{e}_\mathrm{n}^{(u)}. \tag{12}$$

By means of basic differential geometry and *Frenet–Serret* formulas, the last term could be rearranged as

$$\mathbf{e}_\mathrm{n}^{(u)} = \alpha \mathbf{k}, \tag{13}$$

where $\mathbf{k}$ is the curvature vector whose magnitude k is the curvature. The inverse of k is called the *radius of curvature*.

It is straightforward to realize that employing a functional as the one in Eq. (9) leads to a nonlinear minimization problem. This explains the choice of the functional of Eq. (8).

Considering for the sake of simplicity a curve, the functional could be written as

$$\Phi = \int_u \left\| \mathbf{C}^{(uu)}(u) \right\|^2 = \int_u \left\| \sum_{i=0}^{n} \mathbf{P}_i N_{i,p}^{(uu)} \right\|^2 \tag{14}$$

and, using a more comfortable matrix form,

$$\Phi = \int_u [P]^T \left[N^{(uu)}\right]^T \left[N^{(uu)}\right][P] = [P]^T \underbrace{\left(\int_u \left[N^{(uu)}\right]^T \left[N^{(uu)}\right] \right)}_{[K]} [P], \tag{15}$$

where $[K]$ is the stiffness matrix. The mathematical problem is a classic calculus of variation, widely used for finite element method. However, here the basis function are the B-Spline basis functions.

[1] B-Spline are particular cases of NURBS, where the weights w_i are set to unity.

The generic curve and surface have also to interpolate the given points. Moreover, constraints on the derivatives are also necessary for smoothly closed shapes, flat parts, and other situations where local control is needed. For a curve, the constraints can be expressed as

$$\mathbf{g}(\mathbf{P}) = 0 \rightarrow \begin{cases} \sum_{i=0}^{n} N_{i,p}(\bar{u}_k)\mathbf{P}_i - \mathbf{Q}_k = 0, & k = 1, \ldots, n_k, \\ \sum_{i=0}^{n} N^{(u)}_{i,p}(\bar{u}_l)\mathbf{P}_i - \mathbf{Q}'_l = 0, & l = 1, \ldots, n_l, \\ \sum_{i=0}^{n} N^{(uu)}_{i,p}(\bar{u}_m)\mathbf{P}_i - \mathbf{Q}''_m = 0, & m = 1, \ldots, n_m, \end{cases} \tag{16}$$

where $\bar{u}_k$, $\bar{u}_l$, $\bar{u}_m$ are the generic parameter values where the position, first derivative, and second derivative constraints are enforced, $\mathbf{Q}_k$, $\mathbf{Q}'_l$, $\mathbf{Q}''_m$ are the points to be interpolated, the first-order derivatives and second-order derivatives values respectively, and n_k, n_l, n_m are the numbers of respective constraints. In the matrix form,

$$[g] = [N_c][P] - [Q] = 0. \tag{17}$$

In order to enforce the constraints, a penalty or Lagrange multiplier method could be employed. In the last case, the constrained variational problem can be reduced to an unconstrained variational one with the following modified functional:

$$\tilde{\Phi} = \underbrace{\frac{1}{2}[P]^{\mathrm{T}}[K][P]}_{\Phi} + [\lambda]^{\mathrm{T}}[g], \tag{18}$$

where $[\lambda]$ is the *Lagrange multiplier* column vector and has the same dimension as the number of constraint equations. Differentiate Eq. (18) in order to find the stationary point:

$$\delta\tilde{\Phi} = [\delta P]^{\mathrm{T}}[K][P] + \delta\left([\lambda]^{\mathrm{T}}[g]\right) = 0, \tag{19}$$

which gives, with the aid of Eqs. (17), (18),

$$\begin{cases} \dfrac{\partial\tilde{\Phi}}{\partial P} = 0, \\ \dfrac{\partial\tilde{\Phi}}{\partial\lambda} = 0 \end{cases} \longrightarrow \begin{cases} [K][P] + [\lambda]^{\mathrm{T}}[N_c] = 0, \\ [N_c][P] - [Q] = 0. \end{cases} \tag{20}$$

The above is a linear system of $n + n_c$ equations, where $n_c = n_k + n_l + n_m$ is the number of total constraints, which can be represented in the form

$$\begin{bmatrix} [K] & [N^c]^T \\ [N^c] & [0] \end{bmatrix} \begin{Bmatrix} [P] \\ [\lambda] \end{Bmatrix} = \begin{Bmatrix} [0] \\ [Q] \end{Bmatrix}. \tag{21}$$

The linear system is defined as soon the matrices $[K]$ and $[N_c]$ are computed. Since B-spline basis $N_{i,p}$ is piecewise polynomial of order p, the Gaussian quadrature can be used to evaluate exactly the integral inside the stiffness matrix. The computation of the constraints matrix $[N_c]$ is easily achieved since it is nothing more than evaluation of the B-spline basis functions and their derivatives at the knot parameters associated with the constraints.

It is worth noting that, in the above matrix form, $[P]$ is intended as a column vector, even if its three spatial components require $[P]$ to be a matrix. Nonetheless, due to the constraints which set directly the derivatives, the development and resolution of the equations could be done separately for each of the three dimensions.

The generalization to the surface case is conceptually easy to do, but the notation would have been labored.

The tool offers much more control on the interpolating options, some of which are required a good knowledge of the subject. More details are reported in [3].

3.7 IGES Import/Export

It is possible to import and export NURBS surfaces or curves from/to a file written in *IGES* format. This capability enables to interface the code and other commercial softwares. The gained flexibility is of foremost value, as commercial softwares often represent a standard and offer powerful tools for further modifications and assessments.

Due to the way it has been arranged, this code meets the requirements of aeronautical shapes, providing an optimized tool in terms of efficiency and effort.

4 Grid Generation Module

NURBS representation is well suited for grid generation. In fact, with NURBS it is possible to maintain high level of accuracy, efficiency, and numerical stability during the grid generation, due also to its parametric nature.

The grid generation module routes the user through the meshing process. The mesh is intended as surface mesh and can be both structured or unstructured, depending on the objectives. It is worth noting that the aerodynamic solvers integrated within the code (PanAir, UPM, etc.) accept only structured meshes. However, in order to submit more rigorous analysis, the capability of exporting the grid in standard formats is also provided for both the structured and unstructured meshes, depending on which one is needed from the chosen solver. Within the grid generation module graphical tools for monitoring mesh quality are also integrated.

Since grid generation is an intermediate stage between the geometric definition and the mathematical solver, it should ideally be fast and automatic, requiring minimal user intervention. This requirements are nicely met with the GUI and arrangements of the grid generation module.

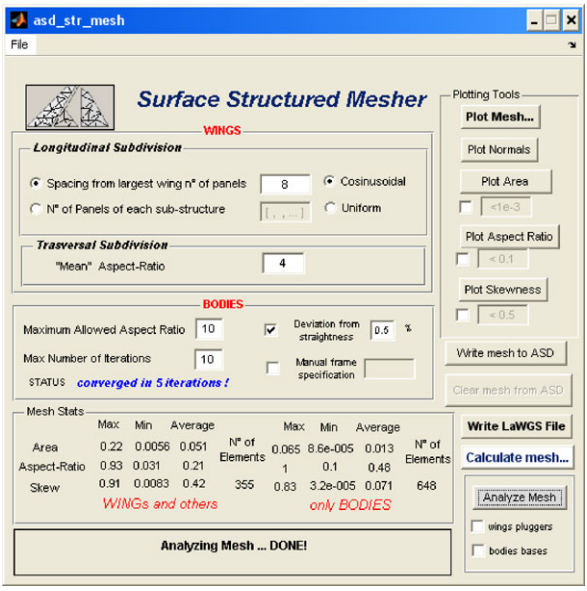

Fig. 10 The structured grid generation GUI

4.1 Structured Grid Generation

The structured grid requires a multiblock approach in order to overcome the topological limitations which arise when meshing complex geometries. Every block is meshed independently, but at the interfaces among two or more blocks the grid points should follow some basic rules, dictated from the solver requirements. For example, one of the integrated solver (PanAir) requires that no *gaps* exist at the common interfaces, where other solvers (UPM) do not. It is usually good practice to avoid such holes, and thus this has been set as a general rule. All the logical subdivision choices are done automatically by the code, without prompting and bothering the user. The structured grid generator GUI layout is depicted in Fig. 10.

In the first step the user is just asked to set the number of subdivisions in the chordwise direction for the largest wing of the configuration or the largest wings of each logical block. Also the distribution of the grid point, cosinusoidal or linear, can be set. The cosinusoidal distribution thickens the mesh at the leading and trailing edge of the wing, where bigger gradient of the aerodynamic flow properties are expected. Next, the number of subdivision should be set for the spanwise direction: this is done by defining the mean aspect ratio of the panels. All the features, except for the bodies, are meshed in such way. Now the user is asked to set parameters in order to build a grid for bodies. The first parameter is the maximum allowable aspect ratio for the panels, which is connected with the maximum number of iterations: it can happen, in fact, that the refinement process is unable to satisfy this parameter, thus a stop criterion is given. Moreover, the user can set some vertical mesh lines at the wished locations or obtain a grid that reproduces the original shape of the body at a desired level. An example of structured grid generated for a PrandtlPlane configuration is shown in Fig. 11.

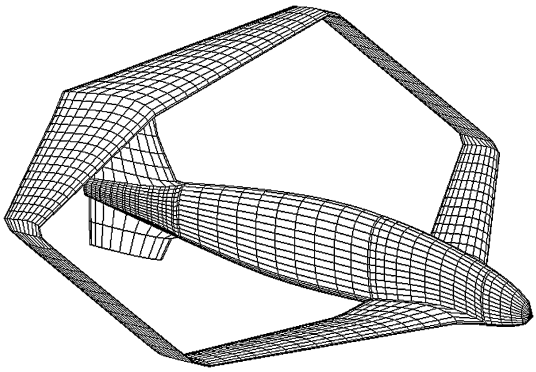

Fig. 11 A structured grid of a PrandtlPlane configuration

It is possible to export the obtained grid in the LaWGS format, Ref. [5]. The description follows precise rules in terms of grid point order which accords to the right-hand rule. It is important to notice that every panel is associated with an outgoing normal vector depending on the order of description of its vertices.

4.2 Unstructured Grid Generation

The unstructured grid typically provides great flexibility (highly required from complex configurations). As a first step, every feature is independently meshed accordingly to some basic parameters. After, it is possible to modify the grid in order to have a correct mesh connection or to satisfy other criteria. The unstructured grid generator GUI layout is depicted in Fig. 12.

The basic parameters for the unstructured grid specify the maximum distance from the real surface to the mesh, and the maximum element side length. The meshing process can also take a correct correspondence at the interfaces of different features into account. This builds a first grid on which some transformation can be done. A first modification to the grid bounds together triangles in order to obtain a mixed grid, according to user parameters which dictate when the bounding process can be undertaken. It is also possible to execute a Delaunay flip or to collapse points closer to a specified value into single points. An example of unstructured grid generated on a traditional configuration is shown in Fig. 13.

The obtained grid can be exported in different formats, in order to give a large flexibility. Between them, the STL format represents surely one of the most popular standards.

4.3 Mesh Analysis and Visualization

Once the grid has been created, it is possible to have a statistics about mesh elements. The statistics include the maximum, minimum, and average values of the

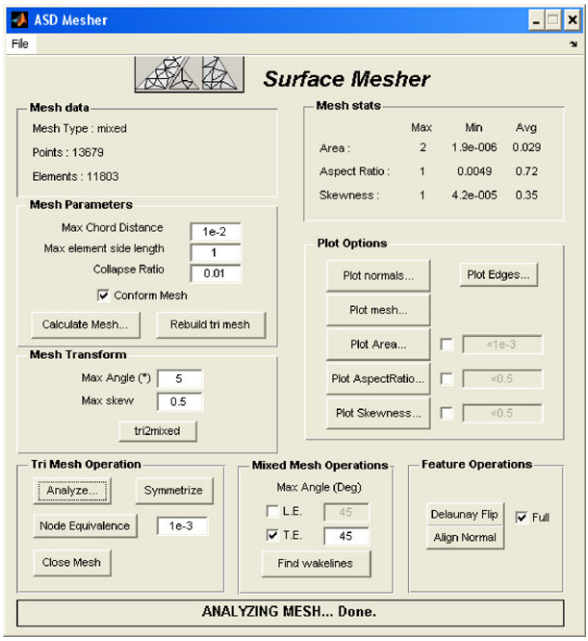

Fig. 12 The unstructured grid generation GUI

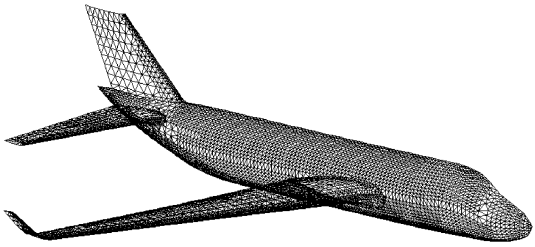

Fig. 13 An unstructured grid for a traditional configuration

mesh geometric parameters skew, aspect ratio, and area. Also the total number of elements is calculated. The statistics are reported in the main meshing GUI, as shown in Figs. 10 and 12.

From a visualization perspective, a three-dimensional plot of the mesh is given. A graphic visualization of the statistics is also provided, in order to have a direct knowledge of the areas where the quality parameters are more or less critical. This capability is further enhanced with a filter applicable to these plots, so as to look for mesh elements with a mesh geometric parameter value within a chosen range. Figure 14 shows an application of this capability.

5 Aerodynamic Solver Module

The aerodynamic module relies on a generic panel method code. In house unsteady panel code *UPM*, as well as *PanAir* have been used. The parameters are given to the

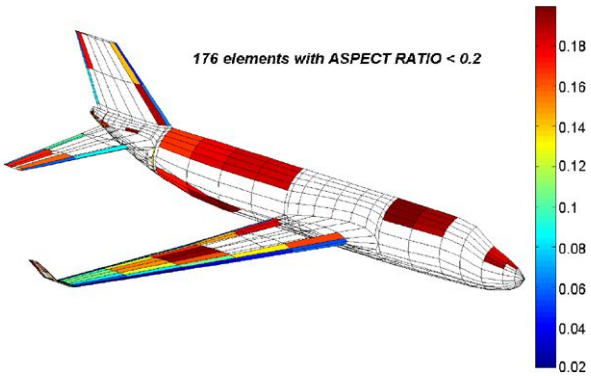

Fig. 14 Mesh elements with aspect ratio smaller than 0.2

solver by means of the preprocessor. Here the solver can be launched, and the solution parameters are graphically displayed with the aid of the postprocessor. Different panel solvers can theoretically be chosen, however, the pre- and post-processing tools have to be readapted in order to comply with the specific input and output formats.

PanAir (acronym of Panel Aerodynamics) is generally considered to be the first actual surface panel code with reliable numerics, even for supersonic flows, Refs. [2, 6]. Relative insensitivity and stability of computed results to paneling was a key for its success. In addition, the boundary condition flexibility allowed users to experiment with various types of modeling, leading to a wide variety of applications never entirely envisioned by the developers. Thus, within the limitations of linear potential flow theory, it could be used as an analytical wind tunnel for the analysis of completely arbitrary configurations. The code was first developed in the early 1970s at NASA and Boeing (were it was known as A502 code). Later, many featured were added. The code was successfully used in the project of big transport airplanes (Boeing 737, 707, 747) and military fighters, Ref. [7]. Sometimes it was used in conjunction with A598 code (a Boeing code for boundary layer analysis), even in fields like yacht design.

UPM (acronym of Unsteady Panel Method) is based on [9, 11] theory, with added unsteady capability. One of the advantages of such feature in steady regime is the so-called wake relaxation: the wake shape is been free to evolve from an initial prescribed to a more realistic one. Moreover, unsteady problems (rotor's blade, etc.) may be modeled. However, in such a case, only incompressible flow cases are supported.

Panel codes solve generally the Prandtl–Glauert equation

$$\left(1 - M_{\infty}^{2}\right)\phi_{xx} + \phi_{yy} + \phi_{zz} = 0, \tag{22}$$

where the free stream is aligned with the x direction, ϕ is the perturbation potential, M_{∞} is the freestream Mach number. To solve the equation, they use the classic approach adopted from boundary element method, that is, distributing singularities at the boundaries of the domain.

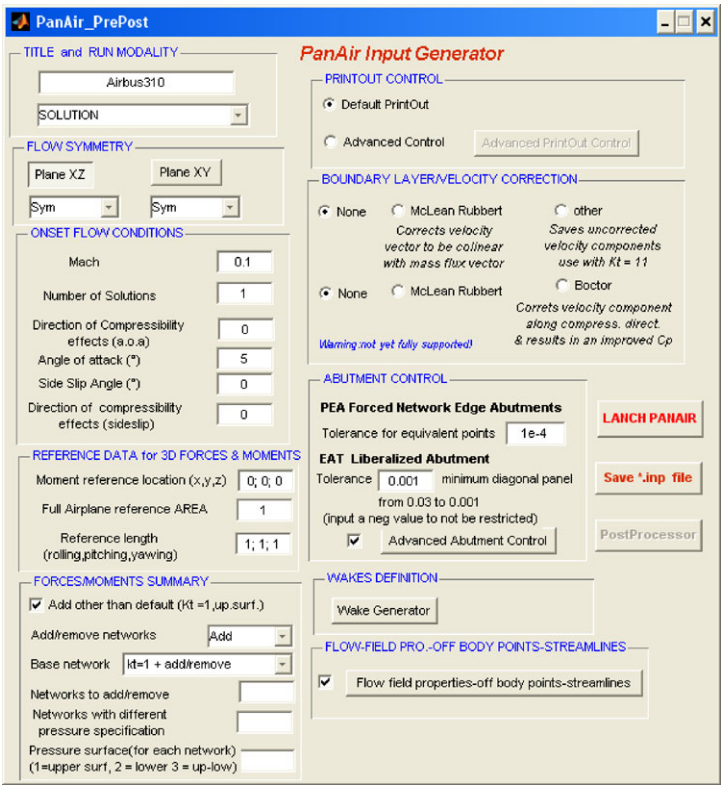

Fig. 15 Preprocessor GUI for PanAir

The used singularities are sources and doublets. To be more precise, UPM employs the classical flat panels with constant singularity distribution, where PanAir features a linear source and a quadratic doublet distribution on a triangular subpanel created starting from a rectangular one, in order to avoid numerical troubles in supersonic flows. This explains why PanAir is called an high-order panel method.

The issue on where higher- or lower-order panel methods are more efficient has been analyzed in [1, 6, 8]. It seems that, employing the so-called Morino's boundary condition, the lower-order panel methods perform significantly better in most cases, among which external flows. There are however situations where higher-order methods, such as internal flows, are necessary for reliable results.

5.1 Pre- and Postprocessors

The preprocessor aids the user to define mainly the flow conditions; moreover it helps in many other tasks like defining reference parameters for adimensionalization of the forces, setting the wakes shed from the surfaces, calculating the streamlines

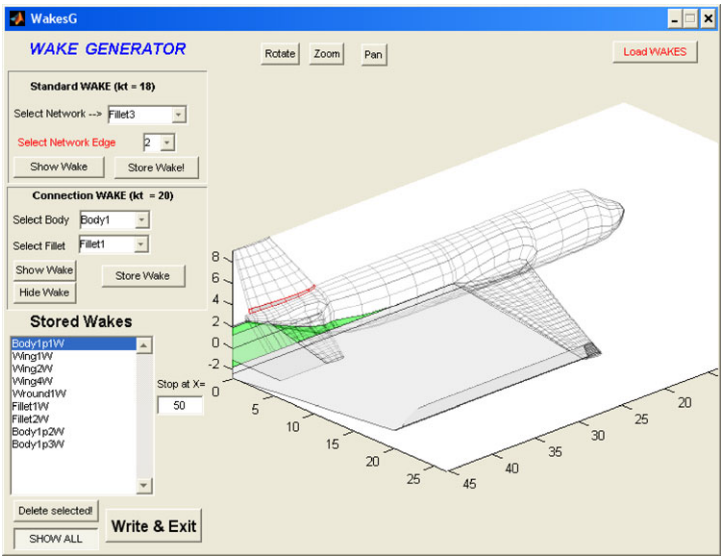

Fig. 16 The wake generator GUI

and the flow properties in off-body points, and other useful tools. The GUI is eloquent and saves the user from compiling manually a text input file specific for the aerodynamic solver, Fig. 15.

It is worth noting that the wake placement is aided by a further dedicated GUI, Fig. 16. Wake placements are of foremost importance in panel method, and an adequate knowledge of the theory is strongly required for reliable results. This is of even more importance for solvers that are not given wake relaxation capabilities (such as PanAir).

Once the input file is created, it is possible to submit the simulation launching the solver or to store the input file.

The main panel code output is a text file which stores the solution in a numerical format. Postprocessor permits a graphical visualization of the results. The main GUI is depicted in Fig. 17.

The window gives a brief resume of the onset flow condition, the reference parameters, and the force and moment coefficients. It is then possible to plot the force coefficient versus angle of attack/sideslip graphs. A window with the configuration networks is also automatically plotted when postprocessor is launched. In this same window it is possible to visualize, for the solution submitted and one at the time, the flow or singularity characteristics for points on the surface. The values of the solution are shown by means of coloration of the surface, and a color bar gives the relation between colors and solution values. Both the selected flow characteristic and the onset flow angles (angle of attack and yaw angle) are recalled directly in the window. An example of the pressure coefficient distribution for two different configuration is depicted in Figs. 18 and 19. The postprocessor enables also the visualization of the streamlines. In the proper listbox, all the streamlines defined at the

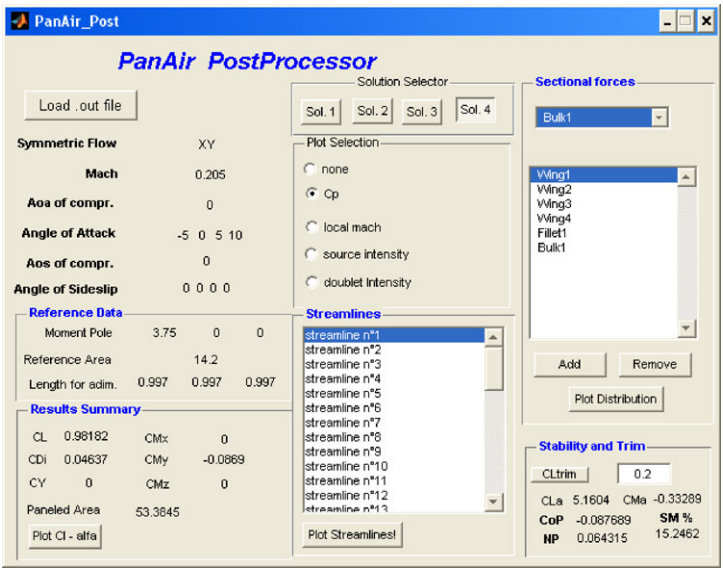

Fig. 17 Postprocessor GUI

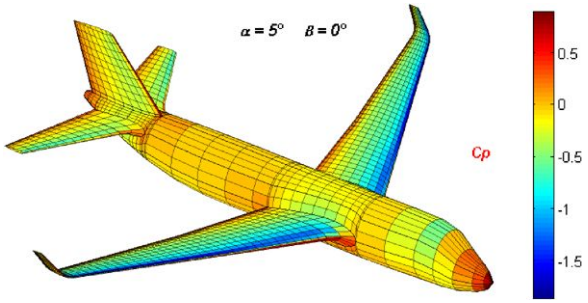

Fig. 18 Pressure coefficient distribution for a traditional configuration at 5° angle of attack

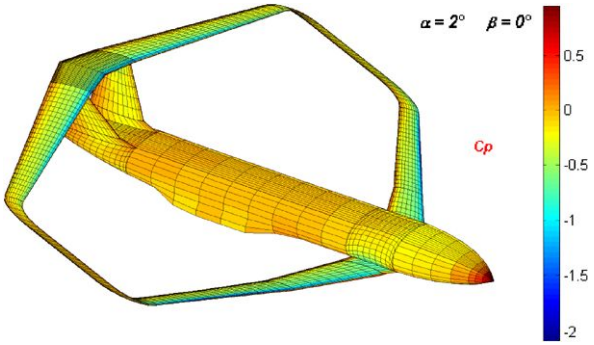

Fig. 19 Pressure coefficient distribution for a PrandtlPlane configuration at 2° angle of attack

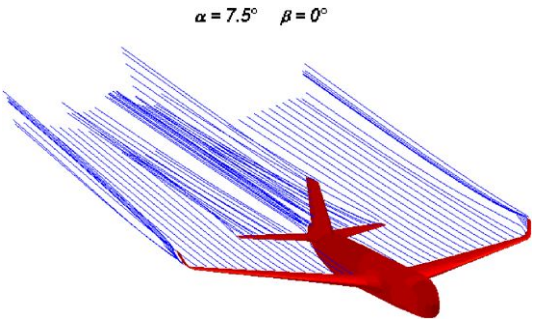

Fig. 20 Streamlines of a flow around a conventional configuration at 7.5° angle of attack

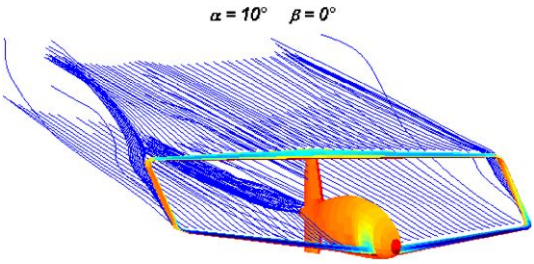

Fig. 21 Combined pressure coefficient and streamline visualization of a flow around a PrandtlPlane ULM configuration at 10° angle of attack

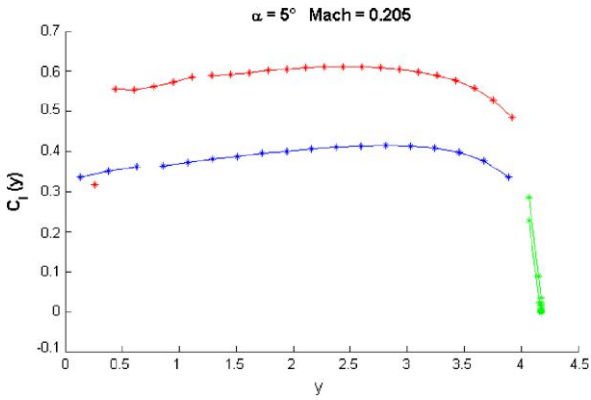

Fig. 22 Two-dimensional lift coefficient distribution along spanwise direction for a PrandtlPlane configuration

preprocessing stage are listed. It is possible then to select more of the elements of the list and plot them. An example of streamline visualization is depicted in Figs. 20 and 21.

Another useful tool implemented in the postprocessor is the ability to plot the two-dimensional lift coefficient along the spanwise direction for every selected network. In the *sectional forces* panel, just select the networks of interest and add them to the listbox; then, selecting the plot option, the lift coefficient versus the spanwise direction coordinate is plotted. An example is shown in Fig. 22 for a PrandtlPlane configuration. The wings and the bulk have been selected, and the plot shows the different behavior of upper and lower wings.

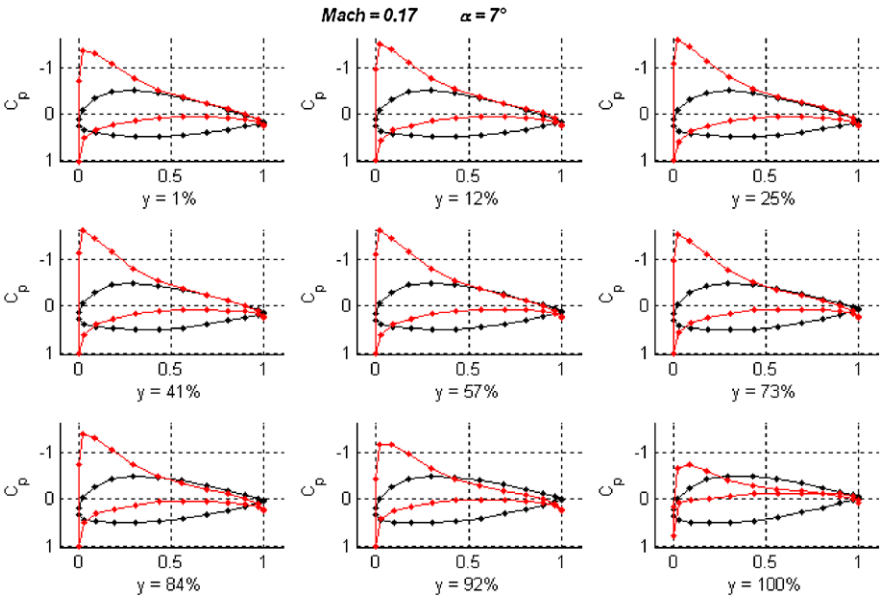

Fig. 23 Pressure coefficient distribution along chordwise direction, at different spanwise sections

To a more detailed knowledge of the flow, the possibility is given to plot the pressure coefficient along the chord at a fixed spanwise section, Fig. 23.

A Flight Mechanics tool providing information about the stability and trim of the configuration is also included at post processing level. Once the trim lift coefficient is set, the center of pressure and neutral point are automatically evaluated. A preliminary margin of stability calculation is then straightforward.

6 Conclusions

In this paper a code is presented featuring all the aspects related with a preliminary aerodynamic evaluation of complete aircraft configurations, from geometric modeling to aerodynamic flow solution. The output given by pressure distributions allows us to obtain immediate information on the trim and stability of flight; all the aerodynamic derivatives are made available including the aerodynamic controls. The use of external software resources is avoided as the main tools needed for the purpose are all integrated within a single framework. Capabilities of interface with commercial software is also guaranteed by exportation tools. The code is arranged in GUIs, so the user is easily routed through all the required steps. Moreover, the parametric nature is well suited for an eventual interface with an external optimization tool.

Acknowledgements Thanks to Andrea Rimondi and Fabrizio Petri for their efforts in writing most of the geometric module features. Thanks to Giovanni Bernardini, Roma 3 University, for his contribution and suggestions on panel method theory and practice.

References

1. Bernardini, G.: Problematiche Aerodinamiche Relative alla Progettazione di Configurationi Innovative. Ph.D. thesis, Politecnico di Milano, Italy, Novembre 1999
2. Carmichael, R.L., Erickson, L.L.: PAN AIR—a higher order panel method for predicting subsonic or supersonic linear potential flows about arbitrary configurations. In: American Institute of Aeronautics and Astronautics, Fluid and Plasma Dynamics Conference 14th, Palo Alto, CA, June 23–25, p. 35 (1981), Number AIAA-1981-1255
3. Cavallaro, R.: A code for surface modeling and grid generation coupled to a panel method for aerodynamic configuration design. Tesi di laurea specialistica, Università di Pisa, Italy (2009)
4. Chambers, J.R.: Innovation in flight: research of the NASA Langley Research Center on revolutionary advanced concepts for aeronautics. In: NASA SP. National Aeronautics and Space Administration (2005)
5. Craidon, C.B.: A description of the Langley Wireframe Geometry Standard (LaWGS) format. Technical Report TM 85767, NASA, February (1985)
6. Erickson, L.L.: Panel methods—an introduction. Technical Report NASA Technical Paper 2995, NASA (1990)
7. Johnson, F.T., Tinoco, E.N., Yu, N.J.: Thirty years of development and application of CFD at Boeing commercial airplanes. In: Seattle, O. (ed.) AIAA 16th CFD Conference, No. 2003-3439, Orlando, FL, 23–26 June (2003)
8. Katz, J., Plotkin, A.: Low-Speed Aerodynamics. Cambridge Aerospace Series. Cambridge University Press, Cambridge (2001)
9. Maskew, B.: Program VSAERO theory document. Technical Report Contractor Report 4023, NASA, September (1987)
10. Moreton, H.P.: Minimum curvature variation curves, networks, and surfaces for fair free-form shape design. Ph.D. thesis, Berkeley, CA, USA (1992)
11. Morino, L.: A finite-element formulation for subsonic flows around complex configurations. Technical Report NASA-CR-138142, NASA (1973)
12. Petri, F.: Sviluppo del codice ADS per la generazione parametrica di superfici aerodinamiche mediante NURBS. Tesi di laurea, Università di Pisa, Italy (2005)
13. Piegl, L., Tiller, W.: The NURBS Book. Springer, New York (1997)
14. Pourazady, M., Xu, X.: Direct manipulation of B-Spline and NURBS curves. Adv. Eng. Softw. **31**, 107–118 (2000)
15. Rimondi, A.: Generazione di configurazioni aerodinamiche mediante NURBS. Tesi di laurea, Università di Pisa, Italy (2005)
16. Welch, W., Witkin, A.: Variational surface modeling. In: SIG-GRAPH '92: Proceedings of the 19th Annual Conference on Computer Graphics and Interactive Techniques, New York, NY, USA (1992)

Design of Solar Powered Unmanned Biplanes for HALE Missions

Vittorio Cipolla and Aldo Frediani

Nomenclature

AM	Air Mass
AC_V	Aerodynamic centre of vertical surfaces
b	Wingspan
B	Balancing Mass Fraction
CG	Centre of gravity
CP	Centre of pressure
C_L	Lift coefficient
C_D	Drag coefficient
E	Energy
E_A	Aerodynamic efficiency
G_h	Non-dimensional horizontal distance between wings
G_v	Non-dimensional vertical distance between wings
H	Altitude
H_{cruise}	Cruise altitude
m	Pitch moment
mac	Mean aerodynamic chord
M	Mass
MoS	Margin of longitudinal stability
n_z	Vertical load factor
NP	Neutral point
N_V	Number of vertical wings
N_{wt}	Number of wing trunks on half wingspan
P	Power
$P_{\min}$	Minimum required power

V. Cipolla (✉) · A. Frediani
Department of Aerospace Engineering, University of Pisa, Via G. Caruso 8, 56122 Pisa, Italy
e-mail: vittorio.cipolla@for.unipi.it

A. Frediani
e-mail: a.frediani@ing.unipi.it

G. Buttazzo, A. Frediani (eds.), *Variational Analysis and Aerospace Engineering: Mathematical Challenges for Aerospace Design*, Springer Optimization and Its Applications 66,
DOI 10.1007/978-1-4614-2435-2_7,

P_{req}	Required power for cruise flight
Re	Reynolds number
S_H	Horizontal wing area
S_R	Ratio between rear wing and front wing areas
S_V	Vertical wing area
T	Mission endurance
V	Speed
V_{cruise}	Cruise speed
$V_{P_{\text{min}}}$	Minimum required power speed
V_V	Vertical tail volume

Greek Symbols

α	Angle of attack
β	Angle of sideslip
γ	Angle of climb
ΔT_{th}	Endurance variation threshold
ΔM_{th}	Mass variation threshold
ε_g	Energy Density
Φ	Latitude angle
η	Efficiency
ρ	Density

Subscripts

ac	Accumulator
st	Structure
lg	Landing gear
m	Motor
pay	Payload
ch	Charge (ref. to accumulators)
dis	Discharge (ref. to accumulators)
sa	Solar array
sc	Solar cell
p	Propeller
f	Flight
d	Devices
in	Input or initial
out	Output
th	Threshold

Acronyms

AFOV	Angular Field of View
DARPA	Defense Advanced Research Projects Agency
DIA	Department of Aerospace Engineering
ERAST	Environmental Research Aircraft and Sensor Technology
FEM	Finite Element Method

HALE	High Altitude Long Endurance
IFOV	Instantaneous Field of View
IRS	Intelligence, Reconnaissance and Surveillance
LE	Leading edge
NASA	National Aeronautics and Space Administration
SPB	Solar Powered Biplane
TE	Trailing edge
TLC	Telecommunication
UAV	Unmanned Aerial Vehicle
VLM	Vortex-Lattice Method

1 Introduction

In order to perform High Altitude Long Endurance (HALE) missions and be effective, a solar-powered Unmanned Aerial Vehicle (UAV) has to show the fundamental capability to fly continuously, even at high latitudes angles or during Winter. This means that, for each day of mission, during daylight hours the UAV has to collect enough solar energy to feed the propulsion system and to charge the accumulators to be used for night flight. This requirement can be fulfilled only if aerodynamic efficiency of the aircraft is high, which means lightweight structures and high aspect ratio wings.

On the other side, since the long-endurance requirement, such a system has to be reliable, and the lightweight structure has to succeed in facing all the flight loads, including those due to gusts, and to be stiff enough to guarantee the aircraft controllability and manoeuvrability.

The combination of these two aspects can be critical, as the experience of the NASA's prototype Helios has shown. Helios was developed within the Environmental Research Aircraft and Sensor Technology (ERAST) program, with the goal of proving the feasibility of the "eternal flight". After several successful results, the Helios was involved in a fatal accident due to unexpected gusts that made its structure collapse during the second flight test.

The idea on which the present paper is based is the possibility of adopting a different airframe architecture to solve this critical issue, overcoming the limitation of the cantilever wing, which brings to extremely flexible structures that may have unexpected aeroelastic behaviour when flying off-design conditions, as it happened to Helios.

The proposed architecture is a biplane reinforced by several vertical wings that have both aerodynamic and solar collection tasks. This solution, called Solar Powered Biplane (SPB) and shown in Fig. 1, comes from several years of research on box-wing airplanes carried out at Department of Aerospace Engineering (DIA) of Pisa University and, in particular, from a preliminary study in which the potentialities of this solution have been investigated for the first time [11].

Fig. 1 SPB concept

Since the introduction of a new architecture brings new questions about possible reduction in aerodynamic efficiency, increase of the total weight, solar energy collection and flight mechanics behaviour, it is required to verify the aircraft capability of fulfilling the operating requirements with an assigned level of performance. Therefore, this paper aims at:

- proposing an innovative airframe concept that may reduce the risk related to high flexibility of structures;
- defining the SPB sizing process;
- proving the capability of this kind of aircraft of fulfilling the "eternal flight" requirements, defined, according to Defense Advanced Research Projects Agency (DARPA) Vulture Program [5], as follows:
  - latitude up to 45°;
  - 18 000 m as minimum loiter altitude;
  - operative in each year's day.

2 The Solar Powered Biplane Layout

In the present paper, the SPB configuration is introduced under some assumptions [4], according to which the general layout can be simplified as shown in Fig. 2. In such a case, an SPB can be described through the following set of parameters:

- horizontal wing area (S_H);
- wingspan (b);
- number of vertical wings (N_V);
- non-dimensional vertical distance between wings (G_v), defined as the distance, along Z axis, between front and rear wing sections belonging to symmetry plane,

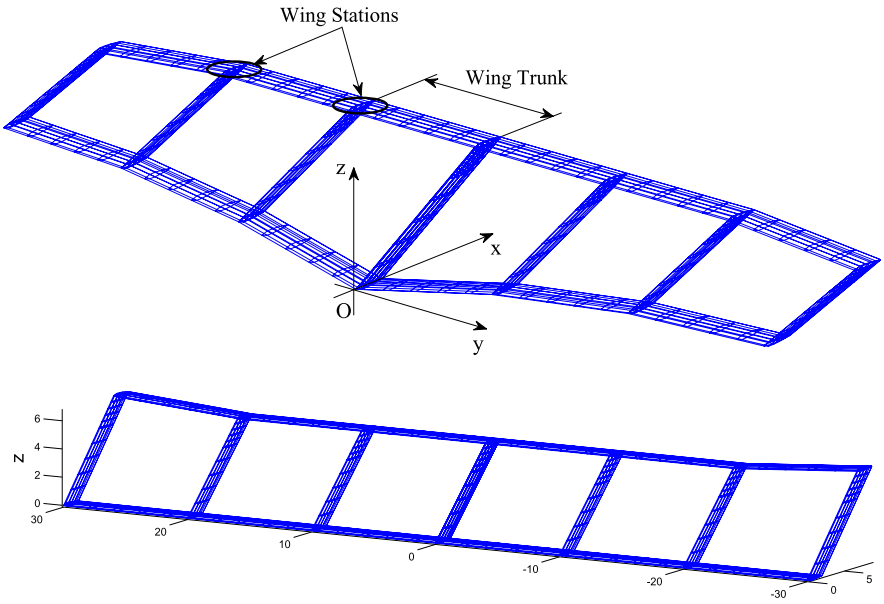

Fig. 2 General (*top*) and simplified (*bottom*) layout of the SPB configuration

divided by b:

$$G_v = \frac{\{Z_{\mathrm{LE2}} - Z_{\mathrm{LE1}}\}_{y=0}}{b}, \tag{1}$$

where LE1 and LE2 indicate the leading edges of wing sections;

- non-dimensional horizontal distance between wings (G_h), taken along X axis and defined as follows:

$$G_h = \frac{\{X_{\mathrm{LE2}} - X_{\mathrm{LE1}}\}_{y=0}}{b}; \tag{2}$$

- ratio between rear wing and front wing areas (S_R).

3 Mission Requirements

Two reference mission types have been selected as the most significant:

- a Telecommunication (TLC) mission, in which the payload is made of antennas;
- an Intelligence, Reconnaissance and Surveillance (IRS) mission, in which electro-optical sensors are mounted on board for image acquisition and remote sensing applications.

It is assumed that each mission has to be performed flying along a closed path that can be considered as elliptical. The dimensions of ellipse axes depend on the foot-

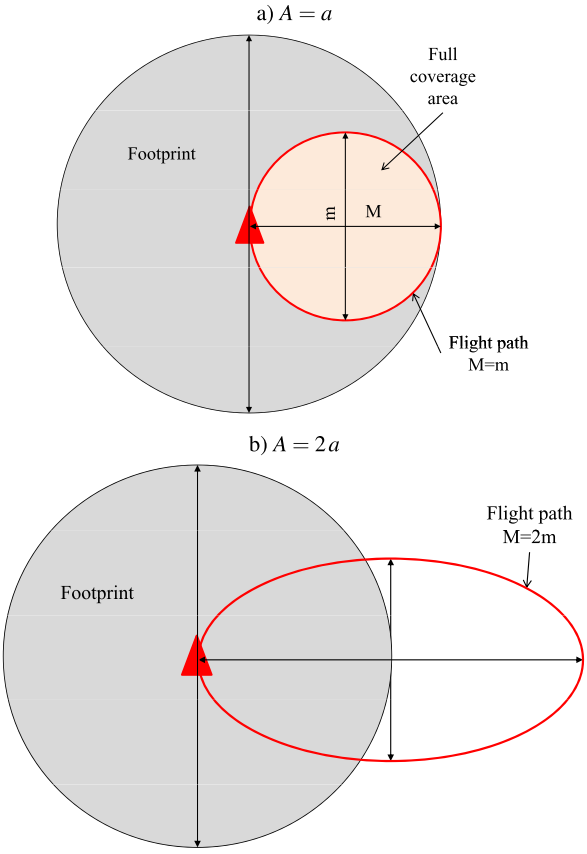

Fig. 3 Effect of flight path on full coverage area dimension

print of payload devices (sensors or antennas) and on the extension of the area that must be served.

Under the assumption

$$a = \frac{\phi_f}{2}, \tag{3}$$

where a is the minor axis length, and ϕ_f is the footprint diameter, the area which can be observed by sensors or antennas from every point of the flight path (*full coverage area*), has maximum extension when major axis (A) is equal to a, i.e. for a circular path (Fig. 3(a)). Increasing A, the covered area will be smaller (b) and disappear when $A = 2a$ (b).

Introducing the ratio between major and minor axes,

$$A_r = \frac{A}{a}, \tag{4}$$

the existence of a full coverage area gives a first constraint on the flight path:

$$A_r < 2. \tag{5}$$

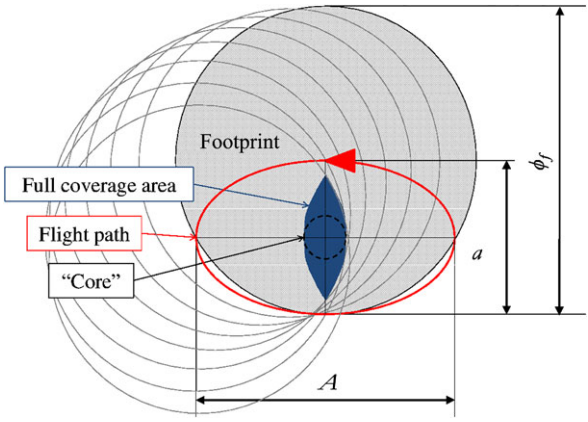

Fig. 4 Flight path, footprint, full coverage area and "core"

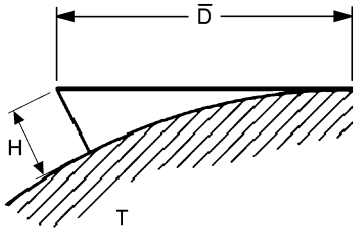

Fig. 5 Radio horizon concept

A conservative estimate of the full coverage area dimension is given by the diameter of the largest inscribed circle, ϕ_c. As shown in Fig. 4, such a circular area is called "core", and ϕ_c is calculated as follows:

$$\phi_c = \phi_f - A. \tag{6}$$

Given Eq. (3) and the definition of A_r, Eq. (6) becomes

$$\phi_c = \left(1 - \frac{A_r}{2}\right)\phi_f. \tag{7}$$

In the next sections, ϕ_c requirements are specialized for TLC and IRS design missions.

3.1 TLC Design Mission

In telecommunications, the operating range of an antenna is given by the *radio horizon*, which is the locus of points at which the direct waves transmitted are tangential to the surface of the Earth.

Hence, for a given antenna located at a height H from Earth, the distance from the radio horizon ($\bar{D}$), also called "line-of-sight", is given by the length of the line

shown in Fig. 5, multiplied by a factor (K), that takes the effect of atmospheric bending on waves into account. Assuming that the Earth is smooth out to the horizon, the communication range can be approximated through the following formula:

$$\bar{D} \simeq K \cdot \sqrt{2RH}, \tag{8}$$

where R is the Earth's radius, whose mean value is 6371 km. As can be found in the literature [1], K is usually taken equal to $\sqrt{4/3}$, which brings to the following formula:

$$\bar{D} \simeq 4124 \cdot \sqrt{H}, \tag{9}$$

with $\bar{D}$ and H in meters.

Approximating the footprint radius with the length $\bar{D}$, it follows that

$$\phi_f = 2 \cdot \bar{D} = 8248 \cdot \sqrt{H}. \tag{10}$$

Hence, substituting Eq. (10) into Eq. (7), the core diameter is given by the function

$$\phi_c = 4214 \cdot (2 - A_r) \cdot \sqrt{H}. \tag{11}$$

The TLC design mission is introduced as follows:

- the core diameter of the served area must be greater than 300 km;
- the flight altitude must be above 14 000 m;
- the mission must be performed also at Winter solstice for latitudes up to 45° North;

At the minimum altitude, ϕ_c is above 300 km for $A_r = 1.4$; hence, mission conditions can be written as follows:

- $A_r = 1.4$;
- $H \geq 14\,000$ m;
- latitude angle $= +45°$;
- Day $=$ 21 Dec (Winter Solstice).

3.2 IRS Design Mission

The IRS mission depends mainly on the electro-optical sensor, whose characteristics are given by the following parameters:

- the Angular Field of View ($AFOV$) angle that, depending on flight altitude (H), defines the footprint width of the sensor (also called *swath width*, Fig. 6):

$$\phi_f = 2H \cdot \tan \frac{AFOV}{2}; \tag{12}$$

by Eq. (7), ϕ_c becomes

$$\phi_c = H \cdot \tan \frac{AFOV}{2} \cdot (2 - A_r); \tag{13}$$

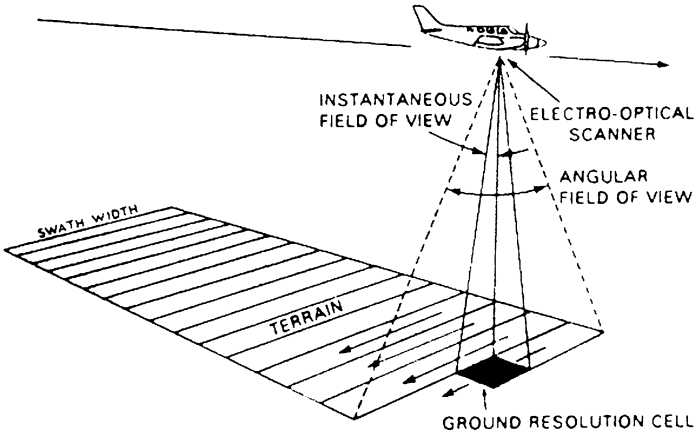

Fig. 6 Instantaneous Field Of View (*IFOV*) and Angular Field Of View (*AFOV*)

- the ground resolution (R_g), defined as the linear dimension of the smallest area on Earth's surface detectable by the sensor. In remote sensing, the ground resolution is commonly described through the Instantaneous Field of View (*IFOV*), which depends on the distance from target (H in this case) and on the number of pixels of the sensor (N_p). The ground resolution can be calculated dividing the swath width by the number of samples (N_p) as follows:

$$R_g = \frac{2H}{N_p} \cdot \tan \frac{AFOV}{2}. \tag{14}$$

When sensor characteristics *AFOV* and N_p are given, the core dimension requirement sets the minimum flight altitude, while the ground resolution one sets the maximum altitude. From (13) and (14) it follows:

$$\frac{\phi_c \cot \frac{AFOV}{2}}{2 - A_r} \leq H \leq \frac{R_g N_p \cot \frac{AFOV}{2}}{2}. \tag{15}$$

Then, the IRS design mission is introduced taking the following requirements into account:

- the surveilled area with core diameter of 2 km;
- the ground resolution of 10 m or less;
- operative also at winter solstice for latitudes up to 45° North.

The given sensor is a hyperspectral camera with the following specifications:

- $AFOV = 18.4°$;
- $N_p = 640$.

Using Eq. (15), altitude constraints are found:

$$\frac{12348}{2 - A_r} \leq H \leq 19757, \tag{16}$$

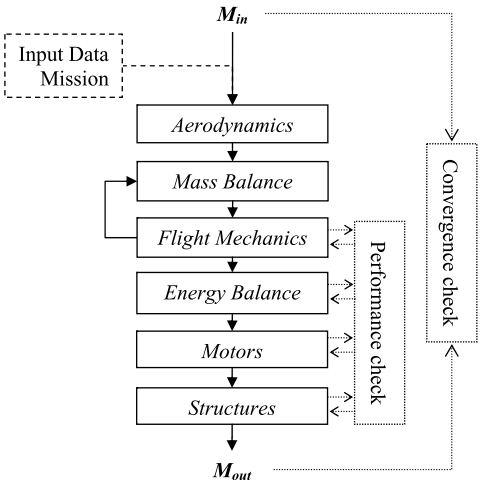

Fig. 7 Overview of the sizing process

where the values are in metres. In order to avoid the air traffic, $H_{\min} = 16000$ is chosen and, therefore, A_r is found from Eq. (16):

$$A_r = 1.22.$$

Therefore, mission conditions are:

- $A_r = 1.22$;
- $15831 \text{ m} \leq H \leq 19757 \text{ m}$;
- latitude angle $= +45°$;
- Day = 21 Dec (Winter Solstice).

3.3 Payload Requirements

Payload requirements are related to UAV capabilities to fly sensors/antennas with given weight and required power. Such requirements are defined on the basis of previous UAV projects as follows:

- $M_{\text{pay}} = 100$ kg;
- $P_{\text{pay}} = 1$ kW.

4 The Sizing Process

4.1 Overview

The sizing process aims at evaluating the actual aircraft mass (M_{out}) through the steps illustrated in Fig. 7, which are:

- the input mass (M_{in}) definition, where a guess value of the aircraft mass is calculated;
- the aerodynamic analysis, where the minimum required power conditions are calculated;
- the flight mechanics/mass balance cycle, where the equilibrium and stability requirements are met by means of a mass balance strategy;
- the energy balance, where the flight endurance and accumulators mass are calculated;
- the sizing of motors, where the motors mass is defined in order to fulfill the maximum power request;
- the sizing of structures, where the structural components are sized to operate under an assigned stress level.

As the flow chart shows, the process requires the definition of some input data, such as constants and settings for the several models implemented, and mission parameters as defined in Sect. 3.

In addition, Flight Mechanics, energy balance, motors and structures sections are linked to a "Performance check" block, in which other requirements related to expected performance are introduced:

- *Flight Mechanics*
  - trimmed flight;
  - longitudinal stability;
  - directional stability;
  - dihedral effect;
  - spiral stability.
- *Energy Balance*
  - minimum mission endurance (T) given by

$$T_{\min} \geq 24 - \Delta T_{\text{th}} \quad \text{(in hours)}, \tag{17}$$

    where the endurance variation threshold (ΔT_{th}) is set to 0.5 hours, that is, the 2% of the nominal 24 hours mission duration.
- *Structures*
  - maximum structural stress.

If such requirements are met, the sizing process leads to the evaluation of the actual aircraft mass, which is compared to the M_{in} value, in order to check the convergence of the whole process. The convergence requirement is fulfilled if the following inequality holds:

$$|M_{\text{out}} - M_{\text{in}}| \leq \Delta M_{\text{th}}, \tag{18}$$

where mass variation threshold (ΔM_{th}) is the accumulators mass that, for a given configuration and a given required power, if added or removed, gives a flight endurance variation equal to ΔT_{th}. Such definition can also be written as follows:

$$\Delta M_{\text{th}} = \frac{P_{\text{req}} \Delta T_{\text{th}}}{\varepsilon_g}, \tag{19}$$

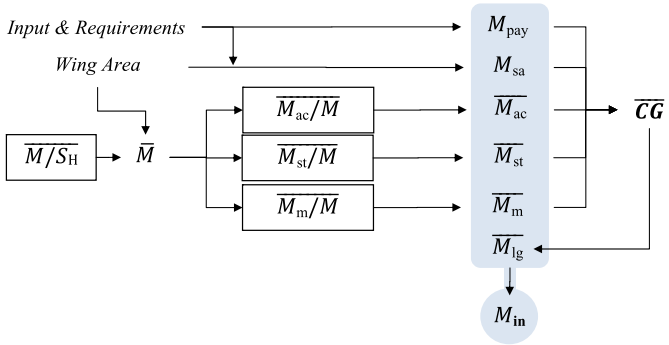

Fig. 8 Flow chart of the input mass evaluation

Table 1 Guess values for input mass evaluation

Guess values	
$\overline{M_{ac}/M}$	50%
$\overline{M_{st}/M}$	25%
$\overline{M_m/M}$	10%
$\overline{M/S_H}$	8–11 kg/m^2

where ε_g is the energy density of the accumulators.

4.2 Input Mass Evaluation

As Fig. 8 shows, the input mass is calculated as follows:

$$M_{in} = M_{pay} + M_{sa} + \overline{M_{ac}} + \overline{M_{st}} + \overline{M_m} + \overline{M_{lg}}, \tag{20}$$

where:

- M_{pay} is the payload mass, given as a requirement;
- M_{sa} is the mass of solar arrays, which can be calculated multiplying the surface density of solar panels by horizontal and vertical wing areas;
- $\overline{M_{ac}}$, $\overline{M_{st}}$ and $\overline{M_m}$ are the guess values of accumulators, structures and motors mass, respectively, which are calculated as fractions of the aircraft guess mass $\overline{M}$. This latter is calculated multiplying the horizontal wing area (S_H) by a guess wing loading value;
- $\overline{M_{lg}}$ is the guess landing gears mass, which depends on the estimated position of the aircraft centre of gravity (CG).

Table 1 shows the typical guess values used in this part of the sizing process.

4.3 Aerodynamics

The aerodynamic analysis aims at finding the minimum value of the required power for cruise flight (P_{req}) and the associated speed ($V_{P_{\min}}$), under the trim constraints. Therefore, the problem to be solved is the following:

$$\begin{cases} \min P_{\text{req}}(V_{\text{cruise}}), \\ C_L = \frac{M_{\text{in}} g}{\frac{1}{2}\rho S_H V_{\text{cruise}}^2}, \\ m|_{CG}(V_{\text{cruise}}) = 0, \end{cases} \tag{21}$$

where V_{cruise} is the cruise speed, C_L is the lift coefficient, g is the acceleration of gravity, ρ is the air density, and m is the pitching moment.

P_{req} is calculated as follows:

$$P_{\text{req}} = \frac{1}{2}\rho S_H V_{\text{cruise}}^3 C_D, \tag{22}$$

where the drag coefficient (C_D) is obtained by summing the following contributions:

- induced drag ($C_{D_{\text{ind}}}$), evaluated by means of a Vortex-Lattice Method (VLM) code, which gives good results in absence of non-lifting bodies;
- airfoil drag ($C_{D_{\text{airf}}}$), including both pressure and friction drag, calculated applying the strip theory to airfoil polar curves;
- friction drag of landing gear fairings, calculated through the flat plate analogy as in [10].

Concerning airfoil drag, it has been observed that a subsonic flow at low Reynolds number (*Re*), as it is for HALE UAVs, pressure drag and friction drag have comparable values and approximated methods which take only friction into account (e.g. flat plate analogy) are not accurate [2]. For this reason, the aforementioned airfoil polar curves have been calculated for different *Re* by means of the code XFOIL and then implemented in the VLM.

Since the parabolic polar curve approximation does not fit the real polar curve trend (Fig. 9) and introduces errors of $\pm 10\%$ on $V_{P_{\min}}$ evaluation, the minimum required power is calculated using an optimization algorithm that finds the local minimum of the continuous single-variable function $P_{\text{req}}(V_{\text{cruise}})$ on a fixed speed interval, typically inside the range 25–40 m/s.

4.4 Flight Mechanics and Mass Balance

Once the minimum power conditions are found, the aircraft mass balance is found by means of an iterative procedure, in order to fulfill the Flight Mechanics requirements, which are:

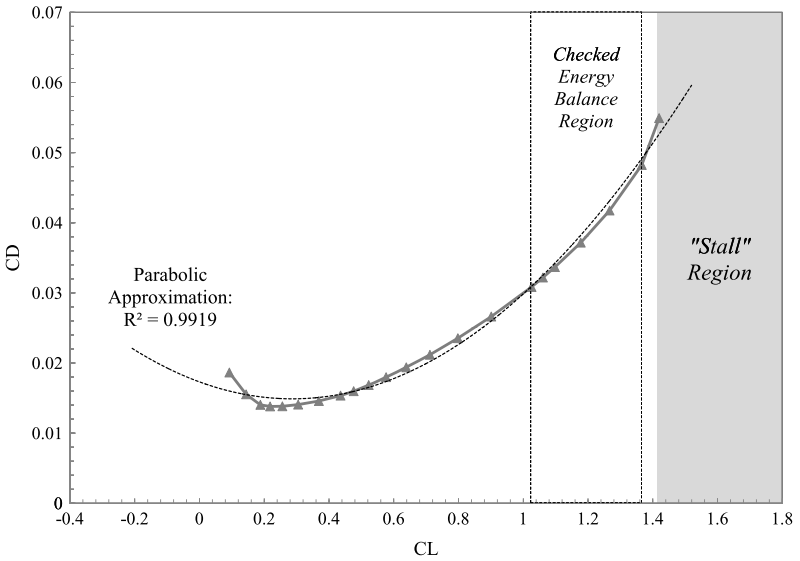

Fig. 9 Example of polar curve and parabolic approximation

- The trim requirement, defined like in Eq. (21), with the pitching moment equilibrium imposed as follows:

$$CP \equiv CG, \tag{23}$$

where CP is the centre of pressure.

- Longitudinal stability requirement, which is given applying upper and lower boundaries to the margin of longitudinal stability (MoS), defined as follows:

$$MoS = \frac{x_{NP} - x_{CP}}{mac}, \tag{24}$$

where x_{NP} and x_{CP} are the longitudinal coordinates of neutral point and centre of pressure, respectively, and mac is the mean aerodynamic chord.

- Directional stability requirement, which is defined by setting a minimum value for the vertical tail volume (V_V), defined as

$$V_V = \frac{S_V(x_{AC_V} - x_{CG})}{bS_H}, \tag{25}$$

where S_V is the vertical wing area, and AC_V is the aerodynamic centre of vertical surfaces.

- Dihedral effect requirement, fulfilled when the following inequality holds:

$$C_{l\beta} < 0, \tag{26}$$

where $C_{l\beta}$ is the change in rolling moment coefficient (C_l) due to a sideslip angle (β) variation.

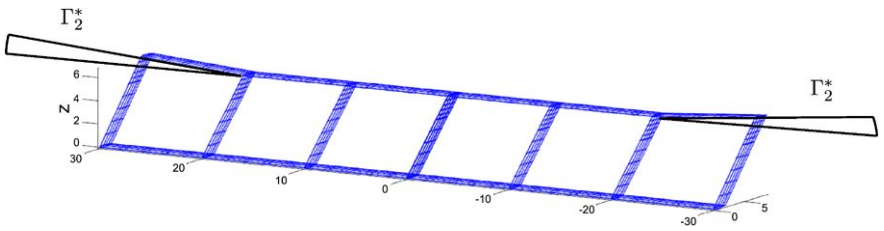

Fig. 10 Rear wing dihedral angles

- Spiral stability requirement, which is expressed as follows:

$$\frac{C_{l\beta}C_{nr}}{C_{lr}C_{n\beta}} > 1, \tag{27}$$

where C_{nr} is the derivative of the yawing moment coefficient (C_n) with respect to yaw rate (r), C_{lr} represents the rolling moment change due to yaw rate, and $C_{n\beta}$ gives the yawing moment variation due to sideslip angle.

Because of the trim constraint, Eq. (24) becomes

$$MoS = \frac{x_{NP} - x_{CG}}{mac}. \tag{28}$$

Therefore, the trim, longitudinal stability and directional stability requirements can be met by changing the distribution of batteries between the two horizontal wings in order to move the aircraft *CG*.

Dihedral effect and spiral stability requirements, instead, are fulfilled by modifying the dihedral angles of some rear wing trunks (Fig. 10), in order to change the $C_{l\beta}$ value.

4.4.1 Mass Balance Procedure

The mass balance procedure is based on the *CG* position evaluation, which is performed as follows:

$$\begin{aligned} CG = \frac{1}{M_{\text{in}}}(&M_{\text{pay}}CG_{\text{pay}} + M_{\text{sa}}CG_{\text{sa}} + \overline{M_{\text{ac}}}CG_{\text{ac}} \\ &+ \overline{M_{\text{st}}}CG_{\text{st}} + \overline{M_{\text{m}}}CG_{\text{m}} + \overline{M_{\text{lg}}}CG_{\text{lg}}), \end{aligned} \tag{29}$$

where subscripts have the same meaning as in Eq. (20). Then, the following assumptions are made:

- the payload mass can be positioned in order to have a small influence on the *CG* location; hence,

$$CG_{\text{pay}} \equiv CG;$$

- the structural components and solar arrays can be assumed as homogeneously distributed on both wings; therefore,

$$CG_{\mathrm{st}} \equiv CG_{\mathrm{sa}}.$$

Given these assumptions, Eq. (29) becomes

$$CG = \frac{1}{M_{\mathrm{in}} - M_{\mathrm{pay}}}\Big[(\overline{M_{\mathrm{st}}} + M_{\mathrm{sa}})CG_w + \overline{M_{\mathrm{ac}}}CG_{\mathrm{ac}} + \overline{M_{\mathrm{m}}}CG_{\mathrm{m}} + \overline{M_{\mathrm{lg}}}CG_{\mathrm{lg}}\Big], \tag{30}$$

where CG_w indicates the centre of gravity of horizontal and vertical wings, which coincides with CG_{st} and CG_{sa}.

The first step of the mass balance procedure consists in assuming that the centres of gravity of accumulators and horizontal wings (CG_{wH}) coincide, which means that the accumulators are considered as homogeneously distributed on horizontal wings. Therefore, the starting condition can be described as follows:

$$\begin{cases} M_{\mathrm{ac}_1} + M_{\mathrm{ac}_2} = \overline{M_{\mathrm{ac}}}, \\ \frac{M_{\mathrm{ac}_2}}{M_{\mathrm{ac}_1}} = S_R, \end{cases} \tag{31}$$

where subscripts 1 and 2 indicate front and rear wings, respectively, and S_R is the ratio between rear wing and front wing areas. Hence, batteries repartition on the two wings is given by

$$\begin{cases} M_{\mathrm{ac}_1} = \frac{1}{S_R+1}\overline{M_{\mathrm{ac}}}, \\ M_{\mathrm{ac}_2} = \frac{S_R}{S_R+1}\overline{M_{\mathrm{ac}}}. \end{cases} \tag{32}$$

The balancing process aims at finding the amount of batteries M^*_{ac} that has to be moved from the rear wing to the front one, in order to meet the Flight Mechanics requirement.

Introducing the Balancing Mass Fraction (B) as

$$B = \frac{M^*_{\mathrm{ac}}}{M_{\mathrm{ac}_2}}, \tag{33}$$

the modified battery repartition becomes

$$\begin{cases} M'_{\mathrm{ac}_1} = (1 + B \cdot S_R)\frac{1}{S_R+1}\overline{M_{\mathrm{ac}}}, \\ M'_{\mathrm{ac}_2} = (1 - B)\frac{S_R}{S_R+1}\overline{M_{\mathrm{ac}}}. \end{cases} \tag{34}$$

B is used to control the balancing procedure convergence: when $B > 1$, a divergence occurs, and Flight Mechanics requirements cannot be fulfilled. It has been observed that feasible solutions have $B < 0.5$.

Given the definition of B, the mass balance procedure is described here below:

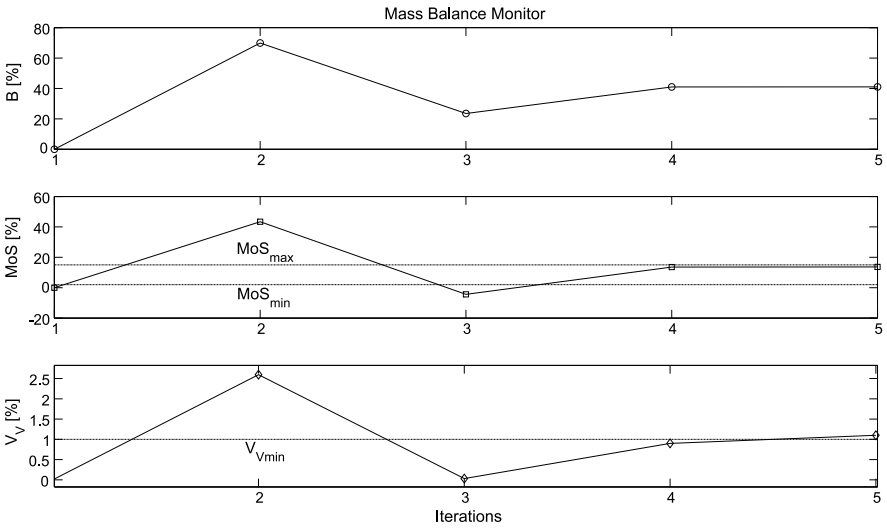

Fig. 11 Mass balance process

1. the results from Aerodynamics section provide initial flight mechanics characteristics, such as the neutral point (*NP*) and the aerodynamic centre of vertical surfaces (AC_V);
2. the *CG* longitudinal position is imposed as follows:

$$x_{CG} = \min\left(x_{NP} - MoS_{\min} \cdot mac, x_{AC_V} - V_{V_{\min}} \cdot \frac{S_H}{S_V} \cdot b\right); \tag{35}$$

3. the associated value of B is calculated;
4. if $B < 1$, the procedure continues, and trim conditions on lift and pitch moment are imposed;
5. the aerodynamic and flight mechanic characteristics are calculated by means of the VLM code, in which the trim requirement in Eq. (23) is met by modifying the angles of incidence of front and rear wings;
6. new values of *NP* and AC_V are calculated.

The procedure is reiterated from point 2 and stops if both requirements on *MoS* and V_V are fulfilled or if $B > 1$. In the first case, Flight Mechanics check is passed, otherwise the sizing process is stopped. Figure 11 shows an example of the balancing process iterations.

4.5 Energy Balance Evaluation

According to the scheme in Fig. 12, the main variables involved in energy balance evaluation are the following:

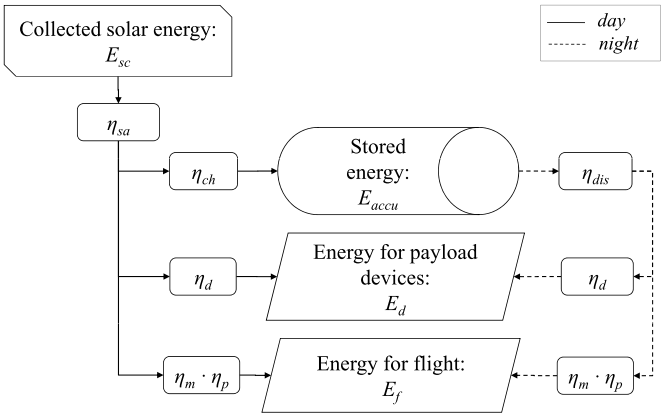

Fig. 12 Flow chart of the daily energy balance

- η_{sa}: solar array efficiency calculated taking Albedo effect into account;
- η_{m}: brushless motors efficiency;
- η_{p}: propeller efficiency;
- η_{d}: efficiency of payload devices (electro-optical sensors or antennas);
- η_{ch}: accumulators charge efficiency;
- η_{dis}: accumulators discharge efficiency;
- E_{sc}: collected solar energy;
- E_{f}: required energy for flight;
- E_{d}: energy required to feed payload devices;
- E_{ac}: energy stored in the accumulation system.

Energy balance can be "checked" when the energy flowing through accumulators during one day, ΔE_{ac}, is 0, "unchecked" if $\Delta E_{\mathrm{ac}} < 0$ and "over-checked" if $\Delta E_{\mathrm{ac}} > 0$.

If the energy balance is checked or over-checked, the aircraft is able to use solar energy to feed motors and devices during daylight hours and to charge batteries with an amount of energy that is sufficient to fly with all systems working during the night. In the second case, the exceeding energy can be used to feed optional devices, to climb and fly at a higher altitude or for speed variations.

Hence, the starting equation for energy balance evaluation is the following:

$$\Delta E_{\mathrm{ac}} = 0, \tag{36}$$

which can be written as the balance between the energy stored during daylight E_{ac}^{D} and the energy released during night E_{ac}^{N}:

$$E_{\mathrm{ac}}^{D} - E_{\mathrm{ac}}^{N} = 0. \tag{37}$$

The time intervals indicated by superscripts D and N depend on the collected solar power (P_{sc}), the required power for flight (P_{f}) and the required power for devices (P_{d}). They are defined as follows:

- D is the time interval in which solar panels suffice in providing power to motors and payload devices:

$$P_{sc}\eta_{sa} \geq \frac{P_f}{\eta_m \eta_p} + \frac{P_d}{\eta_d}; \tag{38}$$

- N is the time interval in which energy provided by solar panels is not sufficient to feed motors and payload devices and accumulators' contribution is required:

$$P_{sc}\eta_{sa} < \frac{P_f}{\eta_m \eta_p} + \frac{P_d}{\eta_d}. \tag{39}$$

The energy stored during daylight is obtained as follows:

$$E_{ac}^D = \eta_{ch}\left(\eta_{sa}E_{sc} - \frac{E_f^D}{\eta_m \eta_p} - \frac{E_d^D}{\eta_d}\right), \tag{40}$$

while the energy spent during night time is given by

$$E_{ac}^N = \frac{1}{\eta_{dis}}\left(\frac{E_f^N}{\eta_m \eta_p} + \frac{E_d^N}{\eta_d}\right). \tag{41}$$

Substituting Eq. (40) and Eq. (41) into Eq. (37), the energy balance equation is obtained:

$$\eta_{sa}E_{sc} = \left[\frac{E_f^D}{\eta_m \eta_p} + \frac{E_d^D}{\eta_d} + \frac{1}{\eta_{ac}}\left(\frac{E_f^N}{\eta_m \eta_p} + \frac{E_d^N}{\eta_d}\right)\right], \tag{42}$$

where η_{ac} is the accumulator charge/discharge efficiency, given by

$$\eta_{ac} = \eta_{ch} \cdot \eta_{dis}. \tag{43}$$

It is assumed that charge and discharge efficiencies are equal, and therefore,

$$\eta_{ch} = \eta_{dis} = \sqrt{\eta_{ac}}. \tag{44}$$

If the energy balance is checked or over-checked, the accumulators mass is calculated dividing the energy spent for night time flight by the Energy Density (ε_g) of accumulation system:

$$M_{ac} = \frac{E_{ac}^N}{\varepsilon_g}. \tag{45}$$

4.5.1 Incoming Solar Energy Model

The total incoming radiation (I_{tot}) is calculated through the following formula:

$$I_{tot} = I \cdot (\tau_b + \tau_d)^{AM}, \tag{46}$$

where

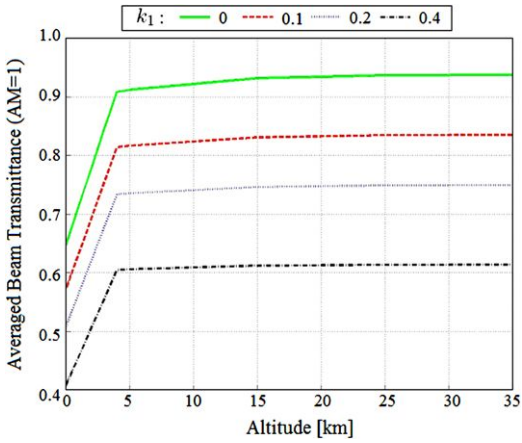

Fig. 13 Averaged beam radiation coefficient [11]

- I is the incoming solar power collected by a panel with unitary area, which depends on the angle of incidence of sunbeams respect to the normal direction to panel surface and is calculated as in [6];
- τ_b is the beam radiation coefficient, given by

$$\tau_b = \tau_{\text{scatt}}(\lambda_w, H, k_1, k_2) \cdot \tau_{\text{abs}}(\lambda_w, H, k_1), \tag{47}$$

where τ_{scatt} is the scattering coefficient due to particles (air, dust and water vapor), τ_{abs} is the absorption coefficient due to ozone and water vapour, λ_w is the radiation wavelength, H is the altitude, k_1 is the turbidity coefficient (0 = clear conditions, 0.4 = very turbid conditions), and k_2 is related to aerosols size.

According to previous works [11, 12], air scattering is evaluated with the Reyleigh model, water and dust scattering by means of the Ångström model and the absorption coefficient, assumed constant for altitudes between 3000 and 20 000 m, as a function of the atmospheric turbidity. Because of water vapour presence, λ_w effect is important only at low altitudes, where the aircraft flies for short periods. Therefore, it is possible to approximate τ_b with the λ_w averaged value, which depends on altitude and turbidity coefficient as Fig. 13 shows;

- τ_d is the diffused radiation coefficient, which is much smaller than the direct one and can be neglected [6];
- AM is the Air Mass, which represents the ratio between the actual distance covered by sunbeams to reach the panel and the minimum possible distance. It is related to the zenith angle (θ_z) through the following expression:

$$AM = \frac{1}{\cos\theta_z}. \tag{48}$$

4.5.2 Collected Solar Energy Model

The model used to calculate energy collected by solar panels take the following aspects into account:

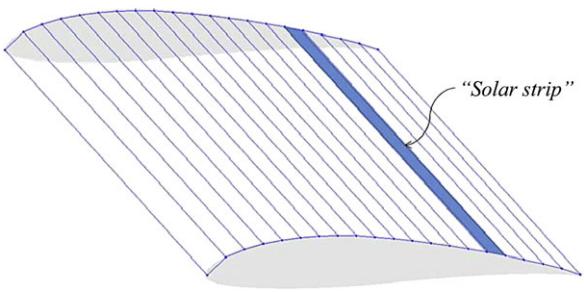

Fig. 14 Strip of solar panels on a wing surface

- solar cells on horizontal wings are placed on the upper surface and preserve the airfoil shape;
- solar cells on vertical wings are placed on both sides and preserve the airfoil shape;
- panels are defined as "strips", whose chordwise dimension is given by cell length and spanwise length is the wing trunk span (Fig. 14);
- angle of attack, angle of trajectory, angle of climbing and angles of incidence (one for each horizontal wings) contribute in panel elevation angles;
- at each time step in which the mission is discretized, the aircraft orientation is calculated in order to find the azimuth angle of panels.

For a given time (t), the total solar power collected by panels on aircraft is calculated as follows:

$$P_{\mathrm{sc}}(t) = \sum_{w} \left[\sum_{i} I_i(t) \cdot S_i \right]_w (\tau_b + \tau_d)^{AM(t)}, \tag{49}$$

where subscript w indicates a generic wing (horizontal or vertical), and subscript i indicates a generic solar panel strip having area S_i. For each strip, the term I_i is calculated taking the panel orientation (elevation and azimuth angles) and the mission condition (latitude, declination and hour angles) into account.

Since panel angles change as the aircraft moves along the flight path, the mission is divided in time steps, and for each of them, P_{sc} is evaluated. For each of these intervals, P_{sc} value is used to verify Eq. (38) or Eq. (39), and, if the first one holds, it is integrated to calculate the energy balance term E_{sc} (see Eq. (42)).

Details on power collection for a typical winter mission are shown in Fig. 15, where the chord station is 0% at the leading edge and 100% at the trailing edge.

4.6 Structures Sizing

The model for structures sizing is based on previous works [3, 9], whose achievements have been the determination of the SPB flight envelope, the definition of a design solution for the main components and the evaluation of the admissible stress level by means of Finite Element Methods (FEMs).

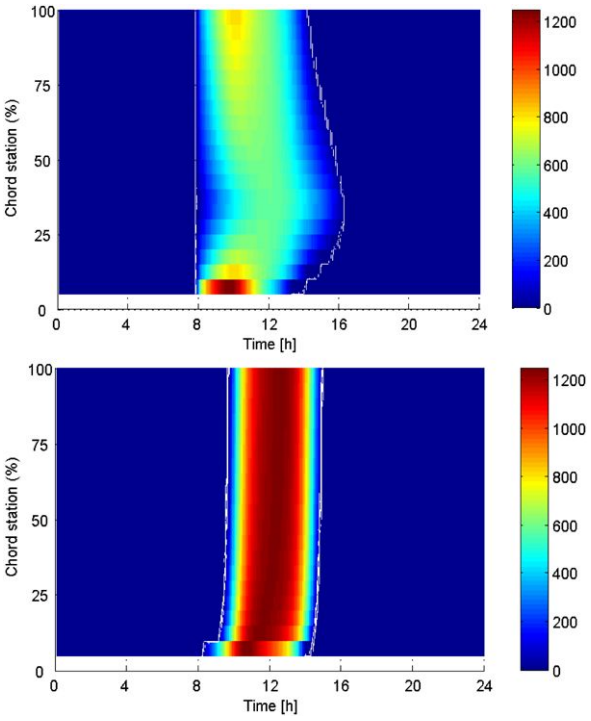

Fig. 15 Solar power per area unit collected by horizontal (*top*) and vertical (*bottom*) wings

4.6.1 The Flight Envelope

The flight envelope has been found according to MIL-F-8785C, MIL-STD-1797A and FAR regulations, adopting the $1 - \cos$ discrete model for gust loads. A reference SPB configuration, designed for Winter missions, has been considered, and it has been found that, because of the low wing load of such a kind of aircraft, the maximum load factors (n_z) are those due to gusts (Fig. 16).

As Fig. 17 shows, the n_z limit values are obtained for altitude around 10 000 m, at which the aircraft flies only for short periods, during climb and descent. Therefore, the related n_z values ($+6.5$ and -4.5) have been indicated as ultimate and then used for structural sizing.

4.6.2 The Design Solution

Concerning the design solution, structure components of each wing trunk, horizontal or vertical, have the same design scheme, which is shown in Fig. 18 and described hereafter:

- each wing section has a double spar, which provides a high bending stiffness;
- in order to improve the torsional stiffness, spars have a closed cross-section;

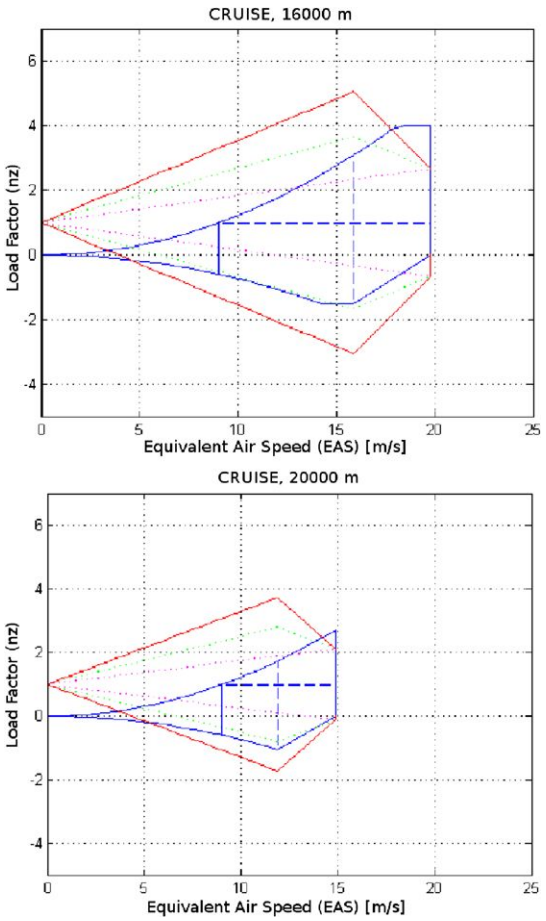

Fig. 16 Flight envelope at 16 000 m (*top*) and 20 000 m (*bottom*) [3]

- ribs consist of trusses placed at constant distance along the wingspan;
- spars and ribs are made of laminates of Carbon-Epoxy plies of thickness above 1 mm.

Spar sections are shaped in order to fit exactly inside wings, in order to provide a physical connection to solar panels with no need of other components. As shown in Fig. 19, the sizing parameters for leading edge (LE) and trailing edge (TE) spars are the width (w_{LE}, w_{TE}) and the average wall thickness (t).

4.6.3 FEM Analyses

By means of a commercial FEM code, static and buckling analyses have been carried out taking maximum (positive and negative) load factors conditions and impact at landing into account. For static analyses, spars and ribs have been modelled

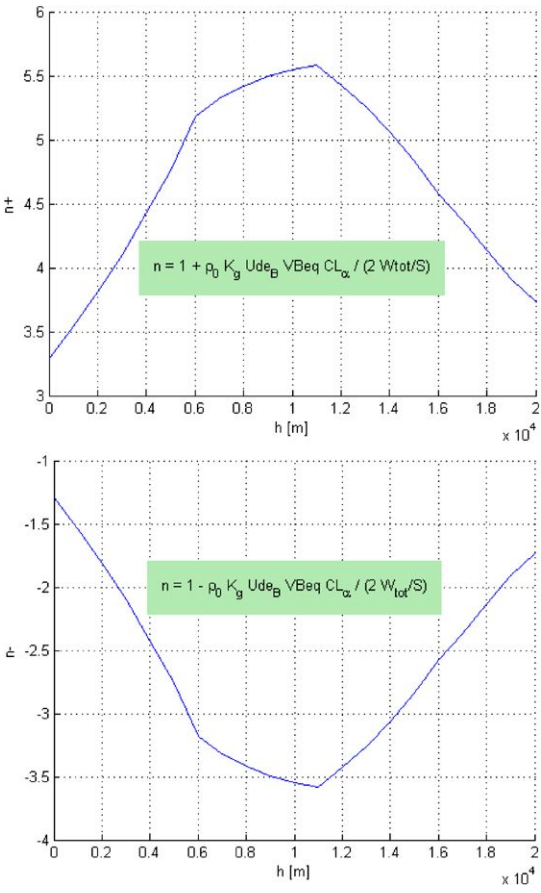

Fig. 17 Maximum positive (*top*) and negative (*bottom*) load factors at various altitudes [3]

by means of beam elements, while shell elements have been used to model spars' walls.

The structural components have been sized on the basis of FEM results, and the following achievements have been reached:

- at every load condition, stresses are below the *first-ply-failure* values of the composite material;
- at every load condition, the twist due to wing deformation does not provoke stall in any section;
- buckling phenomena take place on the internal and lower walls of the spars, where the integrity of cells is not affected (Fig. 20). The "allowed buckling" cases are indicated in Table 2, in which it can be observed that load factors intervals are compatible to the maximum and minimum values calculated from flight envelope.

As a further result, a distribution scheme for battery packs has been defined under the constraint of avoiding the impact of front wing on the ground during landing.

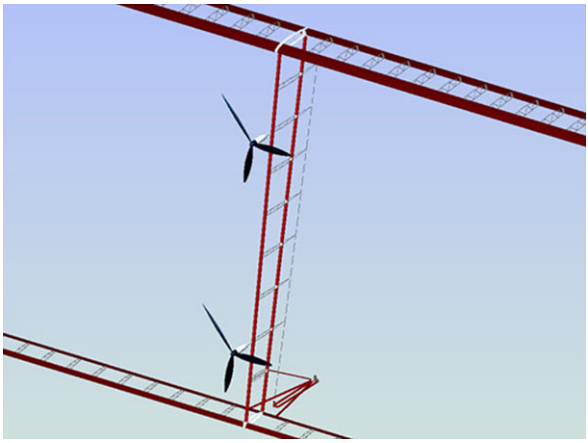

Fig. 18 Overview of the SPB main structures [9]

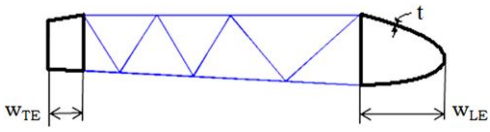

Fig. 19 Sizing parameters for spars

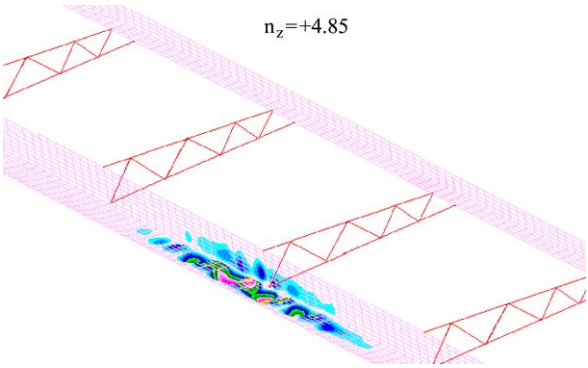

Fig. 20 "Allowed buckling" on a LE beam at positive load factor [9]

Table 2 Load factors intervals for "allowed buckling" on front and rear wing structures

Front wing	
Positive load factors	$+4.6 < n_z < +6.5$
Negative load factors	$-4.5 < n_z < -2.3$
Rear wing	
Positive load factors	$+6.6 < n_z <$ n.c.
Negative load factors	$-4.4 < n_z < -2.2$

4.6.4 Model for Structures Sizing

The structural model has been built on the basis of the assumption, derived from FEM results, that the sizing condition is given by the buckling absence requirement at the maximum positive load factor ($n_z = +6.5$). In addition, it has been observed that rear wing structures experience the highest stress levels, and hence a simplified model can be derived, isolating the rear wings and introducing the internal forces calculated through by FEM simulations. By means of this model, the bending moment distribution and the maximum tensile stress are then calculated.

According to the previous assumption and FEM results, a structural configuration able to fulfill the given requirements is characterized by Von Mises stress levels below 300 MPa at the maximum load factor condition. This characterization has been used to define a sizing criterion for the design of beams: the structure is efficient if the maximum Von Mises stress ($\sigma_{\max}$) is close to the "operating stress" (σ_{oper}) of 300 MPa, as expressed in the following relation:

$$\frac{|\sigma_{\max} - \sigma_{\text{oper}}|}{\sigma_{\text{oper}}} \leq 5\%. \tag{50}$$

The inequality in Eq. (50) represents the performance requirement for structures sizing, which is achieved, when possible, through the following procedure:

1. the initialization consists of setting the sizing parameters w_{LE}, w_{TE} and t to their minimum value;
2. while t is kept constant, $\sigma_{\max}$ is calculated for all the allowed combinations of w_{LE} and w_{TE};
3. if one or more (w_{LE}, w_{TE}) combinations meet the performance requirement, the solution is the one with the lowest structural mass, otherwise t is increased, and the procedure is repeated from previous step;
4. if a combination (t, w_{LE}, w_{TE}) does not exist, the structural sizing cannot be performed, and the SPB configuration is discarded.

4.7 Motors Sizing

The model for brushless motors sizing is taken from [11], in which the following statistical relation is used:

$$M_{\text{m}} = 0.0045 \cdot P, \tag{51}$$

where motor mass (M_{m}) is in kg, and the nominal power (P) is in W.

Observing that the power required for flight is obtained multiplying nominal power by motor efficiency (η_{m}) and propeller efficiency (η_{p}), Eq. (51) becomes

$$M_{\text{m}} = 0.0045 \cdot \frac{P_{\max}}{\eta_{\text{m}}\eta_{\text{p}}}. \tag{52}$$

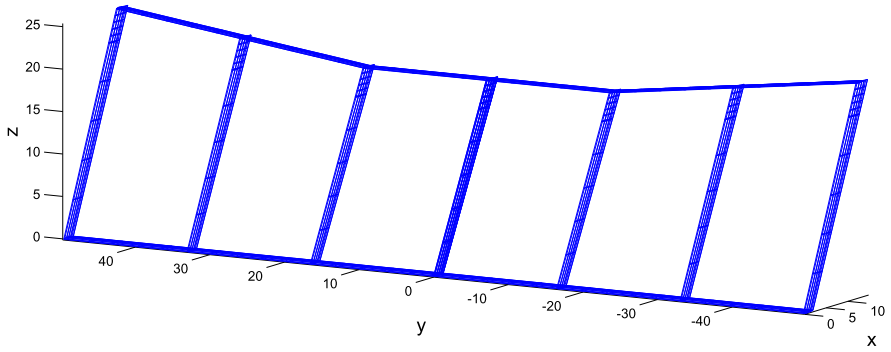

Fig. 21 SPB configuration for Winter TLC missions at 18 000 m

Therefore, the mass of the entire propulsion system can be defined by means of the maximum power request ($P_{\max}$) that the aircraft experiences during the mission. Such a value is found when the aircraft, flying at the maximum required altitude, climbs with a given angle of climb (γ). In such case, the required power has the following expression:

$$P_{\max} = P(H_{\max}) + \sqrt{\frac{(Mg)^3}{\rho(H_{\max}) S_H C_L}} \sin\gamma, \tag{53}$$

where C_L is referred to level flight at $H_{\max}$.

5 Results

In [4] the sizing process here presented has been implemented in an optimization problem, aiming at finding minimum mass SPB configurations, under different mission requirements.

In this paper, one of the most significant result is shown: it is an SPB designed for TLC missions at latitude of 45° and cruise altitude above 18 000 m. It has been found that such a configuration can operate continuously in each year's day and, therefore, is able to meet the aforementioned DARPA requirements.

A scheme of this solution is given in Fig. 21, and its main characteristics are listed in Table 3. It is worth noticing that the predicted Aerodynamic Efficiency is 38, which is comparable to other HALE UAVs (Fig. 22).

As a further result, Fig. 23 shows two *Operating Domains* used to evaluate the flexibility of such aircraft in performing TLC and IRS missions.

The Operating Domain is a design tool, introduced in [4], which consists of a chart, where, for each altitude, the region of the Day-Φ plane in which the given configuration can fulfill the energy balance requirement is represented. Such a region, assumed to be symmetric to acsLat = 0° and Summer Solstice axes, is bounded from above by a parabolic arc, whose vertex belongs to the Winter Solstice axis.

Table 3 Data of the SPB for Winter TLC missions at $H_{\text{cruise}} = 18\,000$ m and $\Phi = 45°$

DESIGN PARAMETERS	
S_H	392.4 m^2
b	99.1 m
G_v	0.214
S_R	0.8
G_h	0.12
N_V	7
CHARACTERISTICS	
M	3525 kg
M/S_H	9 kg/m^2
V_{cruise}	33.5 m/s
P_{req}	30509 W
P_{req}/S_H	78 W/m^2
ΔT	-0.3 h
E_A	38
MoS	19.9%
V_V	1.02%
P_{pay}	1000 W
M_{pay}	100 kg
ϕ_c	340 km

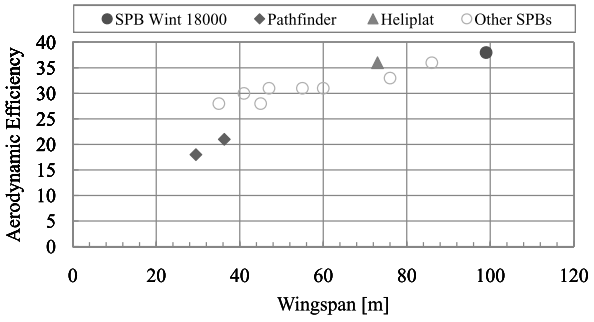

Fig. 22 Comparison between aerodynamic efficiencies

The vertex ordinate is the maximum Φ for which the aircraft is operative, i.e. it can fly continuously, at the given loiter altitude. Since the solar energy model is not valid for latitudes above 70°, in any case the chart is limited by the $\Phi = 70°$ line.

The Operating Domain analysis shows that such aircraft can perform both TLC and IRS missions: altitudes above 20 000 m can be reached at latitudes up to 16° (TLC) and 4° (IRS), while, at the minimum altitude of 16 000 m, the highest operating latitudes are 50° (TLC) and 38° (IRS).

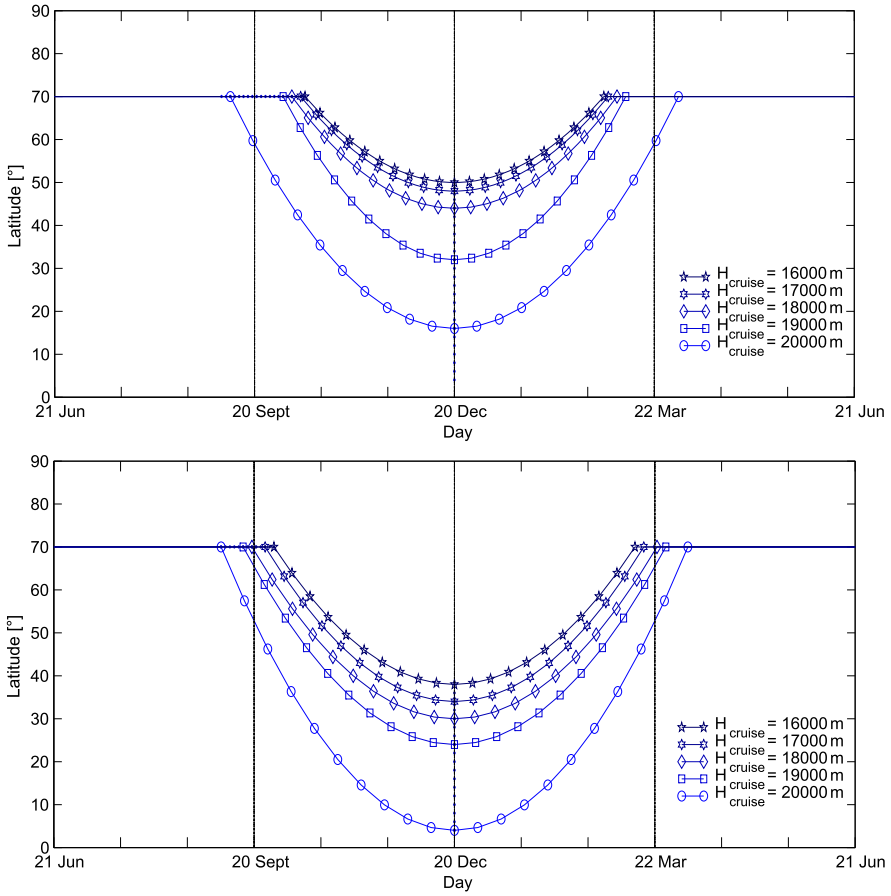

Fig. 23 Operating domain of the 18 000 m, winter SPB for TLC (*top*) and IRS (*bottom*) missions

6 Structural Design Review and Aeroelastic Analysis

The SPB configuration described in Sect. 5 has been the object of aeroelastic analyses inside the M.Sc. Thesis work carried out at DIA [8]. Such analyses have been performed by means of the software MSC Nastran, taking the structure resulting form the aforementioned sizing process as a starting point.

Beside the aeroelastic studies, one of the outcomes of this work has been a design review of wing structures, in which the D-shaped front beam of each wing has been replaced with a multi-box beam obtained by adding an internal vertical wall inside the previous section. This type of structure, Fig. 24, has been verified for static and buckling loads and has been chosen in order to improve the technological feasibility of the solution.

Concerning the static analysis, it has been observed that the in-plane stiffness of vertical wings requires an improvement, since the loading condition associated

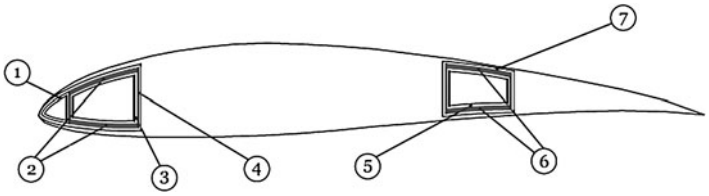

Fig. 24 The modified wing section structures [8]

Fig. 25 Stiffness improvement due to internal braces presence (*right*) on vertical wings [8]

to ground manoeuvres, in which the lift force is absent, causes significant deformations. Therefore, the wing design has been modified, increasing the distance between ribs and adding internal braces, which can reduce the rear wing displacement (Fig. 25).

Once static and buckling requirements have been fulfilled, the aeroelasticity of the SPB has been analysed, focusing on both steady and dynamic phenomena.

6.1 Steady Aeroelasticity

From the steady standpoint, it has been observed that the difference in deformations between rigid trim and flexible trim cases depends on the horizontal wings local equilibrium between lift and weight. In particular, when the weight distribution does not equilibrate the lift distribution, as it happens at wing tips, where lift decreases, aeroelastic effects on lift can be great (Fig. 26).

Although it has been found that such effects do not cause divergence, it is better to have them under control, hence a possible solution is to change the accumulators distribution along wingspan in order to achieve the local equilibrium. Figure 27 shows the distribution of batteries which minimizes this effect, and, as said before, it is worth noticing that its characteristic is an unloaded area close to wing tip.

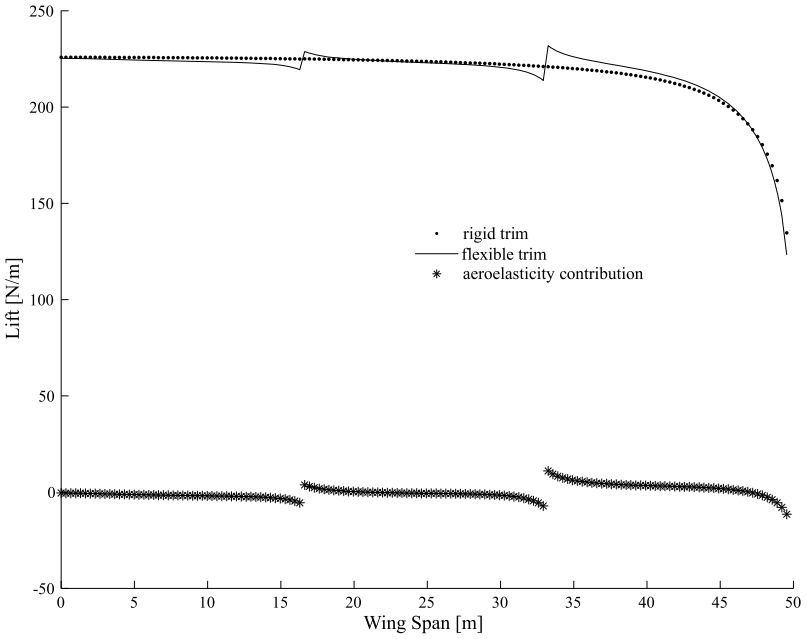

Fig. 26 Initial lift distributions along wingspan for rigid and flexible trim cases on front wing [8]

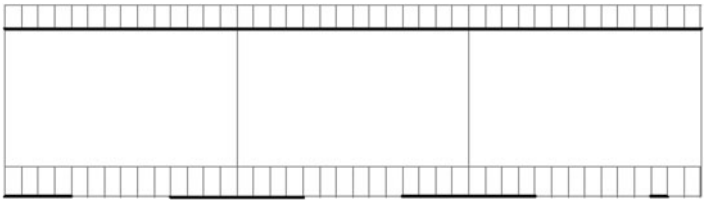

Fig. 27 Final distribution of batteries along wingspan [8]

As a result, in cruise condition the weight distribution given by such accumulator layout gives a maximum displacement of 0.65 m (0.6% of wingspan) against 5.24 m (5.2% of wingspan) obtained considering batteries also on wing tips. As a consequence, this layout minimizes also the steady aeroelasticity effects; Fig. 28, in fact, shows the small difference between rigid and flexible trim cases.

6.2 Dynamic Aeroelasticity

The dynamic aeroelasticity study has been focused on flutter and, as a first case, the SPB configuration modified with internal braces on vertical wings and the afore-

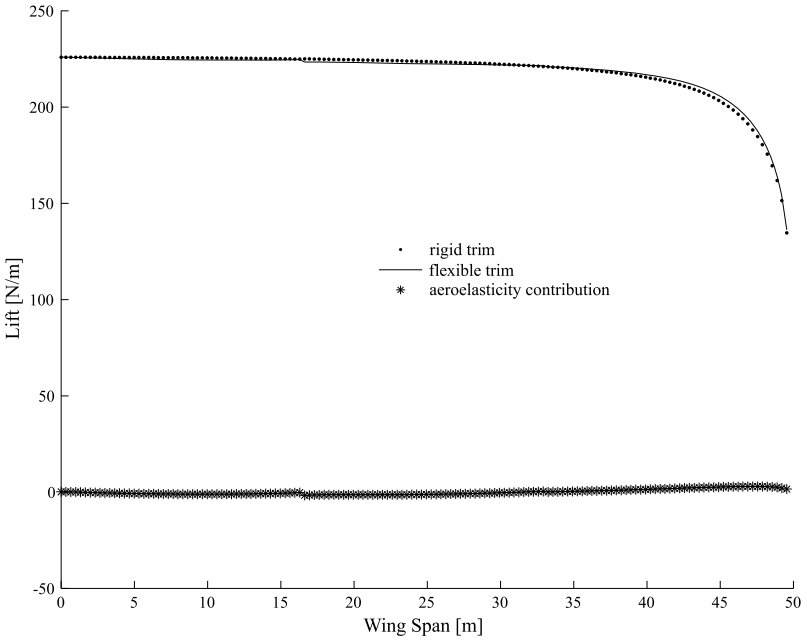

Fig. 28 Final lift distributions along wingspan for rigid and flexible trim cases on front wing [8]

Table 4 Structural modes of the initial configuration

Mode	Frequency [Hz]	Deformation
1	0.06	Bending out of the horizontal plane (mainly)
2	0.08	Bending inside the horizontal plane (mainly)
3	0.11	Torsion around wingspan direction (mainly)
4	0.30	Bending out of the horizontal plane (mainly)
5	0.38	Bending and torsion
6	0.47	Bending and torsion

mentioned batteries distribution, has been analysed by means of the $p - k$ method applied to the cruise condition, for speed between 10 m/s and 80 m/s.

The first six structural modes, for which details are given in Table 4, have been recognized as significant, and the associated flutter analysis has shown that the 2nd mode, which causes a bending almost inside the horizontal plane, is not damped ($g > 0$, Fig. 29).

The cause of such a behaviour has been found in the poor in-plane stiffness of the considered double-spar structure. As already done for vertical wings, the solution found is the addition of internal braces and the reduction of ribs, for both front and rear wings (Fig. 30).

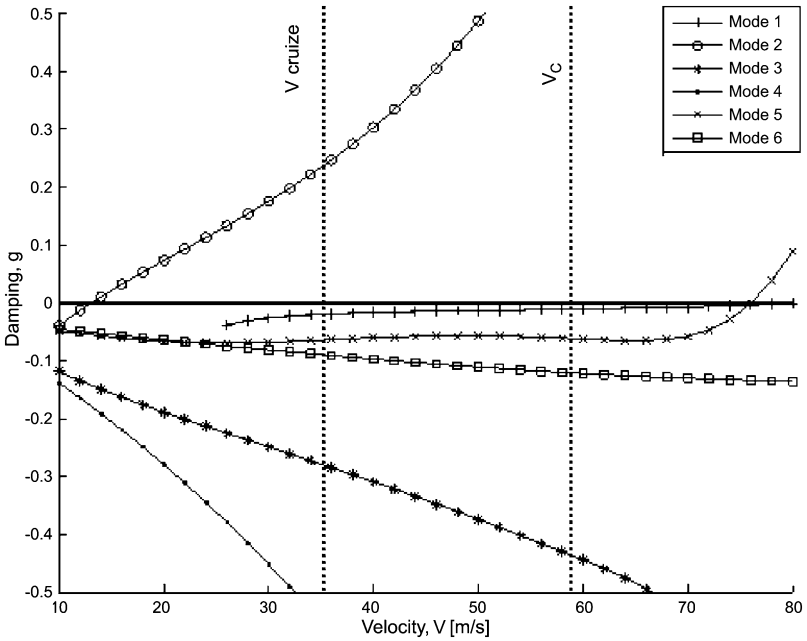

Fig. 29 Flutter diagram of the initial configuration ($H_{\text{cruise}} = 18\,000$ m) [8]

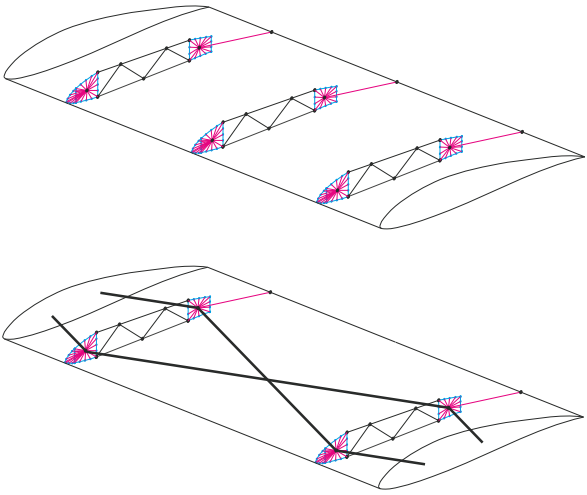

Fig. 30 Horizontal wing structures with internal braces [8]

Such a solution changes the structural modes of the SPB, making the natural frequencies of the system higher and removing any dynamic instability, as Table 5 and Fig. 31 show.

Finally, the previous analyses have been performed also at sea level conditions, for trim speed between 10 and 20 m/s, showing the absence of dynamic instability.

Table 5 Structural modes of the final configuration

Mode	Frequency [Hz]	Deformation
1	0.07	Bending out of the horizontal plane (mainly)
2	0.30	Torsion around wingspan direction (mainly)
3	0.31	Bending out of the horizontal plane (mainly)
4	0.40	Bending and torsion
5	0.72	Bending of vertical wings
6	0.76	Bending out of the horizontal plane (mainly)

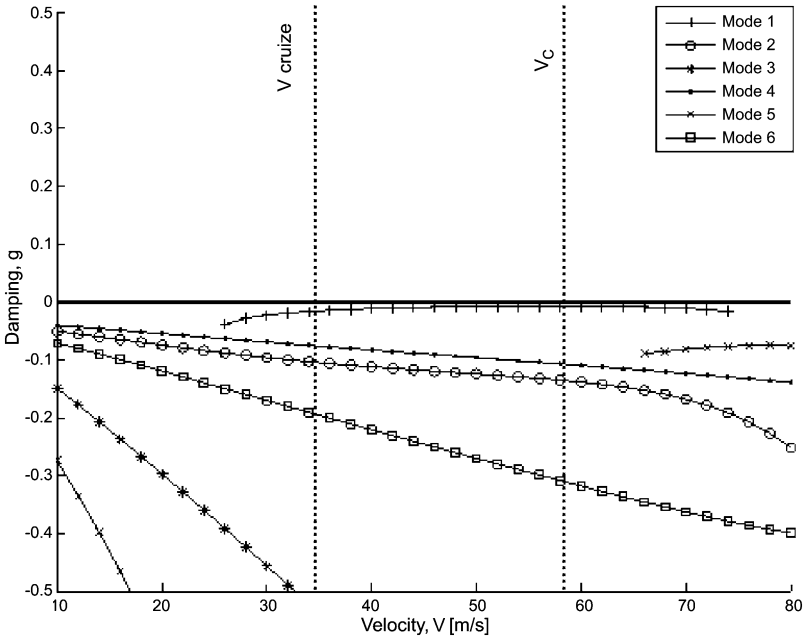

Fig. 31 Flutter diagram of the final configuration ($H_{\text{cruise}} = 18\,000$ m) [8]

7 Conclusions

The present paper has shown some of the outcomes of a research concerning the design of solar powered unmanned biplanes (SPB) for High Altitude Long Endurance (HALE) missions, whose architecture has been chosen in order to increase the structural stiffness without reducing the aerodynamic efficiency.

Inspired by several years of studies on box-wing airplanes at the Department of Aerospace Engineering (DIA) of Pisa, the main tasks of the present research have been the definition of a design methodology and the design of an SPB configuration able to fulfill the HALE flight requirements defined by DARPA within the *Vulture II*

program: to fly continuously in each year's day, at latitudes up to 45° and altitudes above 18 000 m.

The SPB layout has been presented, and, by means of some assumptions, a small set of geometric variables has been defined for the SPB description.

Two kinds of mission have been object of study: a first one for telecommunication (TLC), in which the aircraft has antennas as payload and operates on big areas (100–1000 km), and a second one for remote sensing purposes (IRS), in which the payload consists of electro-optical sensors and the operating area is much smaller ($<$10 km).

The design procedure, called "sizing process", has been described, presenting each model implemented in it. These are: the aerodynamic model, whose main task is to define the minimum required power conditions; the flight mechanic model, which is coupled with a Mass Balance model and aims to meet the stability and trim requirements; the energy balance section, in which the fulfillment of the endurance requirement is verified and the energy accumulation system is sized; the structural model, whose result is the structural components sizing, under a maximum stress constraint; and, finally, the propulsion system sizing, which defines the dimension of motors on the basis of the maximum power request.

For TLC missions, an SPB able to meet DARPA requirements has been found, and its characteristics have been shown, underlining that the predicted aerodynamic efficiency is comparable to those ones of flying wing and wing-tail configurations. A flexibility analysis has been carried out by means of a tool called Operating Domain, which has been applied in order to investigate the aircraft capabilities of performing both TLC and IRS missions under different altitude–latitude–day conditions. It has been found that it is possible to operate continuously at altitudes above 20 000 m for latitudes up to 16° in the case of TLC missions and 4° for IRS missions. On the other hand, given the minimum altitude of 16 000 m, the operating latitudes can reach 50° (TLC) and 38° (IRS).

In conclusion, the SPB configuration has been an object of a structural design review and an aeroelastic analysis, which have brought to some modifications: for horizontal wings, multi-box spars have been introduced to fulfill static and buckling loads requirements, internal braces have been added to avoid flutter phenomena, internal braces have been adopted also on vertical wings in order to minimize ground deformations, and, finally, the accumulators distribution along wingspan has been modified to reduce deformations and steady aeroelasticity effects on horizontal wings.

Acknowledgements My thanks go to all the people who worked with me on this topic at Department of Aerospace Engineering and, in particular, to the former students Paolo Rossi, Maurizio Borghi, Pasquale Cantisani, Luca Montanelli, Andrea Isoppo and Matteo Moisè. I also want to thank Prof. Aldo Frediani and Prof. Giuseppe Buttazzo for giving me the opportunity of presenting this work at the "Variational Analysis and Aerospace Engineering II" Workshop.

Appendix

This section contains information about the characteristics of main components taken into account for the design of SPBs (Table 6).

Table 6 Components data

Solar Cells	
Bi-facial Monocrystalline Silicon	
Efficiency (front)	20%
Efficiency (back)	17%
Density	0.32 kg/m^2
Solar Array	
Evaporated Back-Contacts [7, 13]	
Fill Factor	81%
Efficiency (@ 10% Albedo)	18%
Efficiency (@ 40% Albedo)	22%
Density	0.46 kg/m^2
Accumulators	
Li-S Rechargeable Batteries	
Energy Density (ε_g)	350 Wh/kg
Charge/Discharge Efficiency	99.7%
Life Cycles	100
Motors	
Brushless Direct Current Motors	
Efficiency	95%
Propellers	
Type	3-blade
Diameter	2 m
Efficiency	80%

References

1. Andress, K., Cebik, L.B., Severns, R., Lewallen, R., Witt, F.: The ARRL Antenna Book, 19th edn. (2000)
2. Borghi, M.: Progetto aerodinamico di un velivolo high altitude long endurance (HALE) ad energia solare. Master's thesis, University of Pisa, Department of Aerospace Engineering (2008) (Italian)
3. Cantisani, P.: Studi preliminari al progetto strutturale di un velivolo UAV biplano ad energia solare per missioni HALE (high altitude long endurance). Master's thesis, University of Pisa, Department of Aerospace Engineering (2008) (Italian)
4. Cipolla, V.: Design of solar powered high altitude long endurance unmanned biplanes. PhD thesis, University of Pisa, Ph.D. Course in Aerospace Engineering (2010)
5. DARPA: Vulture II, broad agency announcement. Technical Report DARPA-BAA-10-09, Defense Advanced Research Projects Agency (DARPA) (November 2009)
6. Duffie, J.A., Beckman, W.A.: Solar Engineering of Thermal Processes. Wiley, New York (1991)
7. Hubner, A., Aberle, A.G., Hezel, R.: Cost-effective bifacial silicon solar cells with 19% front and 18% rear efficiency. In: 14th European Photovoltaic Solar Energy Conference (1992)
8. Isoppo, A., Moisè, M.: Analisi aeroelastica mediante software MSC Nastran di un biplano UAV ad energia solare per missioni di tipo hale. Master's thesis, University of Pisa, Department of Aerospace Engineering (2011) (Italian)

9. Montanelli, L.: Analisi FEM di velivoli HALE-UAV ad energia solare e modelli di predizione del peso strutturale. Master's thesis, University of Pisa, Department of Aerospace Engineering (2010) (Italian)
10. Raymer, D.P.: Aircraft Design: A Conceptual Approach, 4th edn. AIAA Education Series. AIAA, Reston (2006)
11. Rizzo, E., Frediani, A.: A model for solar powered aircraft preliminary design. Aeronaut. J. **112**(1128), 57–78 (2008)
12. Rossi, P.: Studio di fattibilità di un sistema di conversione dell'energia solare per un velivolo a propulsione elettrica. Master's thesis, University of Pisa, Dipartimento di Ingegneria dell'Informazione (2007) (Italian)
13. Untila, G., Kost, T., Chebotareva, A., Zaks, M., Sitnikov, A., Solodukha, O.: A new type of high-efficiency bifacial silicon solar cell with external busbars and a current-collecting wire grid. Semiconductors **39**(11), 1346–1351 (2005)

The PrandtlPlane Configuration: Overview on Possible Applications to Civil Aviation

Aldo Frediani, Vittorio Cipolla, and Emanuele Rizzo

1 Introduction

From the advent of powered flight at the age of commercial aviation in the 1950s, the aeroplane conception changed completely. Comparing the first airliner in the 1950s to the present ones, however, the external shape of aircraft does not seem to have evolved a lot, as pointed out in [1]; the basic layout fuselage–wing–tail is still the dominant design. Changes happened however, as the costs were reduced by a factor of 3 through improvements in aerodynamics, structures and materials, control systems, propulsion technology and, according to [30], also to smoother skin surfaces, scale effects and winglets.

Recently, a great interest is devoted to new concepts of aircraft (or "innovative" in the rest of the paper), characterized by a layout different from the one still in use today (or "conventional"). The interest towards new designs is in the scope of the "Vision 2020" report [2]; here, the future of aviation is discussed, as well as the challenges laying ahead of its development. Future aviation will possibly need to respond to restrictive imperatives in terms of costs, environments, safety and security; at the advent of commercial aviation, the aim was to fly faster and higher than ever, while now the focus is on flying quieter and greener. A new document, named "Vision 2050" has been recently emitted; some new requirements are introduced (the entire aircraft should be fully recyclable, flying 24 hours a day, etc.), but we maintain the attention on the Vision 2020 document in this paper.

A. Frediani (✉) · V. Cipolla
Department of Aerospace Engineering, University of Pisa, Via G. Caruso 8, 56122 Pisa, Italy
e-mail: a.frediani@ing.unipi.it

V. Cipolla
e-mail: vittorio.cipolla@for.unipi.it

E. Rizzo
SkyBox Engineering S.r.l., Via San Biagio 49, 56124 Pisa, Italy
e-mail: e.rizzo@skyboxeng.com

G. Buttazzo, A. Frediani (eds.), *Variational Analysis and Aerospace Engineering: Mathematical Challenges for Aerospace Design*, Springer Optimization and Its Applications 66,
DOI 10.1007/978-1-4614-2435-2_8,

The main areas for development are: Quality and Affordability, Safety, Environmental concerns, Efficiency of Air Transport System, Security.

The challenge of quality and affordability is to provide high quality standards to customers, meanwhile having competitive economy and performance characteristics (e.g. broader choice for journey, higher punctuality, reduced time spent in the airports, reduced cabin noise, improved comfort) with a 30% or more cut in Direct Operating Costs.

Safety will remain the highest concern of aircraft industry, although air traffic is expected to grow significantly.

Requirements on environment will become more restrictive: a 50% cut in CO_2 emissions per passenger kilometre and 80% cut in NO_x emissions are required at the horizon 2020. Another objective is to eliminate noise nuisance outside the airport boundaries by day and night and to obtain a 50% reduction on perceived external noise by a proper design of aircraft.

The challenges for the air transport system efficiency are very ambitious: a threefold augmentation of passengers freight and air traffic, the time spent in airports reduced to less than 15 min for short-haul flights and to less than 30 min for long-haul flights, 99% of the flights able to depart within 15 min of their scheduled departure time in all weather conditions.

The security challenge have been greatly influenced by the 9/11 terrorist attacks; the navigation and ATM system must be protected from hostile actions, and the design should prevent the access to the cockpit during flight.

The operating costs of aircraft can be reduced with increasing size or capacity. So far, aircraft manufacturers have increased aircraft size by improving the scale of the smaller ones; this scaling-up process has been possible until hosting 700–800 passengers with the same aerodynamic configuration, but, as remarked in [13], the advantages of increasing aircraft size further has come to an end with the advent of the A380 aircraft, being already an issue the integration with current airport facilities. In fact, further extending the conventional concept to much larger size must satisfy external constraints as compatibility with existing airports (maximum dimensions 80×80 m) and meet noise and evacuation regulations.

The future commercial success will strongly depend on the improvement of aerodynamic performance. Improving drag would reduce operating costs through increased fuel efficiency, pollutant and noise emissions reduction. During cruise, friction drag of large aircraft accounts for 45–50% of the total drag and induced drag for 40–45%. Possible ways of reducing friction drag (e.g. boundary layer suction, turbulent flow control, etc.) are studied, and it appears that any friction reduction could be applicable to aircraft configurations, even the innovative ones. On the contrary, induced drag depends on the lift distribution over wing span, and the aircraft configuration is fundamental in this respect; besides, the fraction of induced drag becomes more important during take-off (typically, around 80–90% according to [19]), and this is particularly relevant considering that the one engine failure at climbing condition represents one of the most demanding constraints. For example, a 1% reduction on vortex drag would improve the low speed climb performance to allow an increase by 1% of take-off weight [18]. Apart from improving the lift distribution

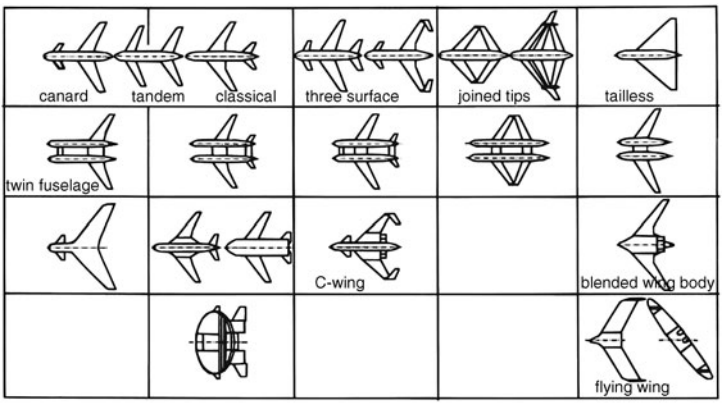

Fig. 1 Configuration matrix

along span, induced drag can be reduced by increasing span; this would however increase structural weight, and, for very large airplanes of the class of an A-380, the airport compatibility criteria can be soon overruled.

Finally, vortex separation increases with aircraft size and becomes a major problem for airport at which large airliners are operating.

On conventional aircraft, advanced CFD computation, wind tunnel tests, flight tests and a long service experience have produced such a refined aerodynamic design that further reductions of induced drag are not easy to be achieved.

Due to limitations of conventional designs, new concepts have been conceived for future aviation to meet the severe indications by the Vision 2020 report. A well-known matrix of new concepts is depicted in Fig. 1.

Horizontally, the matrix presents various combinations of one, two or three lifting surfaces; vertically, different strategies to allocate the payload inside one or two fuselages or partly or completely inside the wing are depicted.

All these new aircraft configurations are associated with high development risks and huge costs; thus, they have to be correctly assessed and carefully studied to convince manufacturers, airline companies and passengers that these concepts are feasible, viable and safe.

Aircraft manufacturers seem to be more interested to the Blended Wing Body configuration. Universities are also studying the BWB project; in the period 2002–2005, a European consortium studied different BWB configurations under the name VELA (Very Efficient Large Aircraft).

Lockheed–Martin and Stanford University (United States) are also studying the possibility of a Box-Wing aircraft and C-Wing aircraft. Pisa University (Italy) is currently developing a Box-Wing aircraft, named PrandtlPlane. The concepts briefly discussed in the following represent a significant departure from conventional configurations; they are: the Oblique Flying Wing, the Blended Wing Body, the C-Wing and the PrandtlPlane, the main subject of this paper.

2 Innovative Designs

2.1 Oblique Flying Wing

Oblique wing and Oblique Flying Wings (OFW) design are both based on a concept developed in the late 1950s from NASA (see [15] for example). The basic idea of the Oblique Flying Wing is to have an efficient wing at both subsonic and supersonic Mach numbers. The oblique flying wing was found to be a minimum drag solution in supersonic flow, dominated by wave drag; at low speeds, though, drag is dominated by induced drag, inversely proportional to the aspect ratio. The most efficient configuration is thus a high-aspect-ratio elliptically loaded wing, which allows variation in sweep angle depending on flight conditions and speed. A significant advantage of oblique wings in supersonic flight is discussed in [3] (lift distributed over about twice the wing length compared to a conventional one); moreover, the problem of the bending of isobars at the center part of the wing is avoided. The oblique wing is naturally area ruled, meaning better supersonic performances and lower drag. In addition, an OFW configuration was found to have a rapid decrease in cost per passenger-seat-mile with size increase [17].

However, some important challenges are still present in the development of the OFW. The complexity of the aerodynamic phenomena and their nonlinear and strongly coupled nature induce difficulties in flight dynamics characteristics: significant variations in rolling moment with angle of attack are observed. Longitudinal stability and control remain an issue, especially because of the short moment arms. Changes in control effectiveness with angle of sweep are observed at moderate and high lift coefficients. Changing sweep angle means that several parts like engines and vertical fin would have to move with respect to the body, which leads to complex mechanical systems and weight increase. The dimensions of the viable solutions exceed easily the 80×80 m horizontal square. The wheel track needed for stability during taxi and take-off would also greatly exceed taxiway width, and this would require to taxi at a sweep angle; take-off would be impossible in this position.

The most complex problem to solve remains the accommodation of passenger, payload and fuel in the fuselage; integrating passengers into the wing creates a fundamental conflict between the packaging capability, which is improved if aspect ratio is lower, and the aerodynamic efficiency. Passenger comfort is also an issue: a cabin is windowless, and load factors on passengers far from the centreline would be unacceptable. The necessary angle of attack of the OFW during flight would also tilt the seats in an unnatural position.

These showstoppers were judged unacceptable, and the OFW concept was dropped as a viable commercial aircraft in the 1980s. The new perspectives brought by the UAVs (Unmanned Air Vehicle) could benefit from the advantages of the OFW configuration, but this is not a subject of this paper.

Fig. 2 Design of a Blended Wing Body by Liebeck

2.2 Blended Wing Body

The Blended Wing Body (BWB) concept was initiated at McDonnell–Douglas in 1988 in order to create a new and more efficient configuration for a high-subsonic transport aircraft. The initial approach was to improve the aerodynamics of conventional aircraft by increasing the wetted aspect ratio. An early BWB design is shown in Fig. 2, and passenger accommodation is shown in Fig. 3.

The passenger cabin is double-decked and provided with windows on both decks; egress is effectuated via the main cabin doors in the leading edge and through doors in the rear spar. Passengers are located in the centerbody, the cargo compartments are outboard of the passenger bays and the fuel is into the wing, outboard of the cargo. In this layout, 450 passengers could be hosted in the cabin.

The possible advantages of the BWB configuration are listed below.

Aerodynamics Reduction of wetted area, structurally efficient use of wing span, optimum span loading, inherently area ruled (ameliorating thus the performances at transonic speeds), increase of the cruise speed in the transonic range.

Structures Quasi-elliptical distribution of lift, weight and lift applied at almost the same points of application (reducing thus bending moments), peak bending moment and shear about one-half of that of a conventional configuration [21, 22], simple hinged control surfaces and no spoilers.

Noise and Emissions Potential advantages for the BWB configuration could be a significant reduction in weight, less engine power required and a reduction in fuel burn per seat mile. The centrebody shields forward radiated noise emitted by the fan and engine exhaust, and noise is not reflected downward by the wing. An engine failure cannot impact the pressure vessel, other engines, fuel tanks or systems; fuel is separated from the passenger by large cargo bays, and the trailing edge controls are redundant.

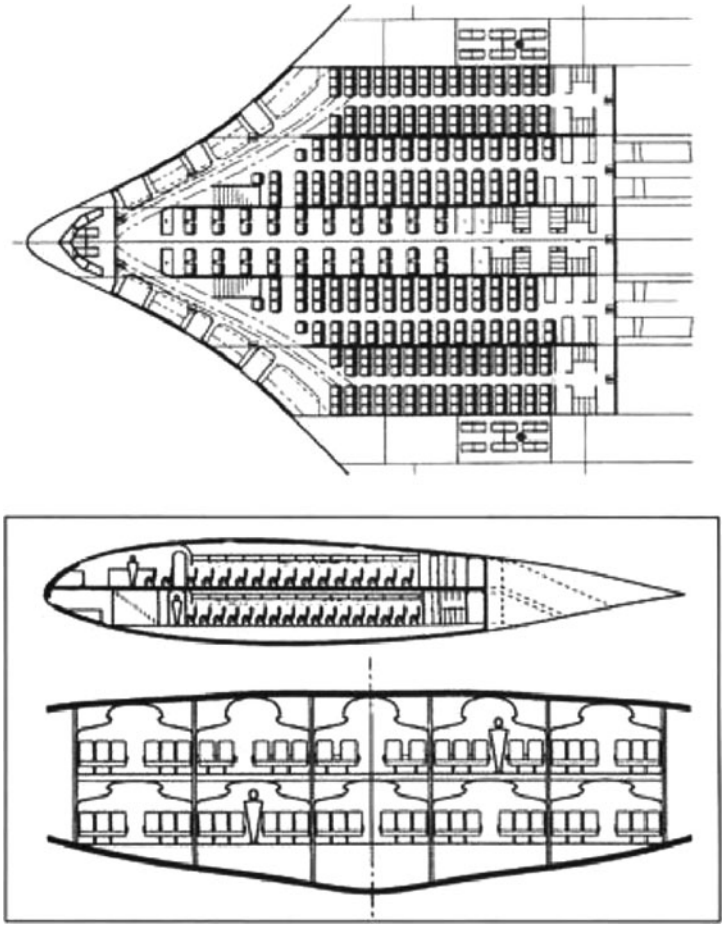

Fig. 3 Blended Wing Body passenger accommodation

The promising performances of the BWB configuration are supposed to represent a significant step forward in aeroplane design, but, to become operational, several aspects still need to be assessed. The natural tendency of a flying wing is to have an unstable behaviour. The instability of flight of a civil aircraft is not accepted for safety reasons, and, in such a case, the power needed to actuate the controls would be prohibitive due to the large deflections and the rate of movements of the controls.

Angle of attack and angle of yaw require hard limits in the flight control laws. Maximum deck angle requirement remains an issue, especially in approach. Airport compatibility is also an issue; indeed, for a high-capacity aircraft equivalent to a B747-8, the wing span attains 85 m. Several solutions for engine integration were proposed: pod and pylon concept (with engines on top of the body), S-bend with diverted or mid-bifurcated inlet with Boundary Layer Ingestion (BLI). It is however not clear which candidate is the most advantageous in terms of weight,

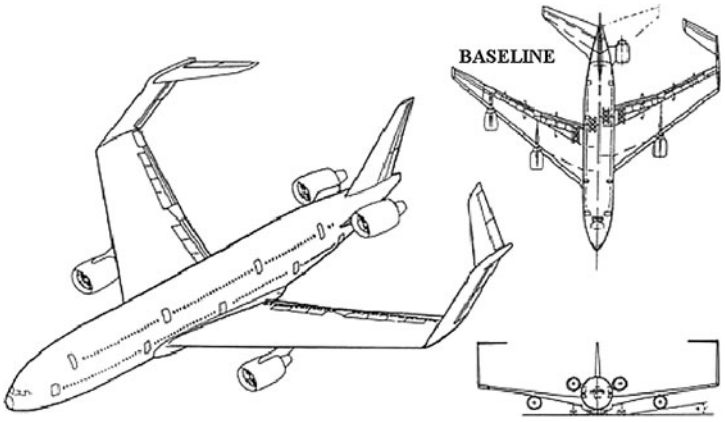

Fig. 4 General layout of a C-wing design

performances, noise and emissions; the whole design could depend on the concept selected. If a BLI engine were to be selected, a proper design of the thick airfoil would be necessary to provide attached flow at the inlet at all angles of attack. The thick airfoil needed for the passenger compartment is unusual for high subsonic or transonic speeds; obtaining an attached flow over the main part of the cabin section appears to be very challenging. Further difficulties could come from the doors positioned at the leading edge; this location is critical as it is subject to high pressure, and important drag penalties can be implied by small surface imperfection and door joints. Passenger accommodation remains the biggest challenge for the BWB. First of all, most passengers do not have access to any window, affecting the passenger acceptance, especially for long-haul flights. Another major concern [7] is the distance from the centre line: passengers will experience unacceptable vertical speed and acceleration. Emergency egress is also a challenge. The main issue found for this scheme is that the most central seats are far away from any exit and, thus, the certification process could fail.

2.3 C-Wing

The C-wing concept was proposed in the 1990s as a solution to the problem of accommodating more than 600 passenger in an aeroplane that does not exceed the 80-m wing span limit [1, 20, 23, 24]. A C-wing is a wing with vertical winglets at the tip and horizontal "winglet-let" at the tip of the winglets. Applied to a commercial aircraft, the design resembles to the one presented in Fig. 4, which features a canard design as well.

Studies on this configuration show the high value of the Oswald factor for the C-wing configuration ($e = 1.45$), meaning lower induced drag; thus, it was concluded that the C-wing configuration achieves almost the same span efficiency as

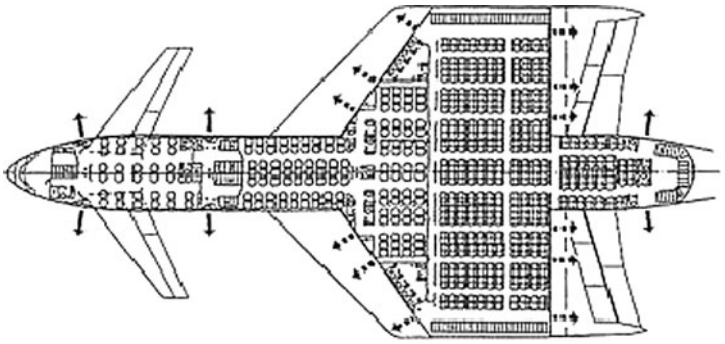

Fig. 5 C-Wing passenger accommodation

the Box-Wing configuration without needing an additional area to close the box. Besides, with a sweep angle of about 35°, the horizontal winglets are about at the same longitudinal position of a horizontal stabilizer of a T-tail design to produce a downward lift component just as the horizontal stabilizer of a conventional aircraft. Another advantage of the C-wing lays in the possibility offered for passenger accommodation. Studies proved that a sufficiently thick profile could be designed for the inner wing section that could meet performance requirements meanwhile being capable of containing passengers inside.

The configuration could allow to place 36 abreast seats in the widest section of a single deck, as depicted in Fig. 5. In addition, the C-wing configuration could possibly reduce the intensity of the wake sheet, shrinking separation between two aircrafts during take-off and landing.

This configuration offers several potential advantages over a conventional one, as: reduced vortex drag at a fixed span; possible wake vortex reduction; improved aero-structural performances; aerodynamic load and payload weight distributed along the span, acceptable balance between all-wing design risks and advantages (egress, presence of windows); growth potential by fuselage stretching; structure; single-deck layout (facilitating loading and emergency egress).

The following areas have been identified as challenges to be overcome:

- The aerodynamics of the thick inboard section is unusual for high subsonic or transonic speeds and has to be thoroughly investigated taking passenger accommodation constraints into account. The large wetted area of the vertical wing is a drawback for the aerodynamic efficiency.
- The effects of the wing shape on structural dynamic characteristics could produce a significant increase of the aircraft empty weight.
- The flutter characteristics could be dramatic.
- Stability and control characteristics are to be determined. In particular, the pitching moment behaviour could justify the use of a canard configuration.
- The structural concept for the flat pressure vessel needed for passenger accommodation in the central section has to be investigated.

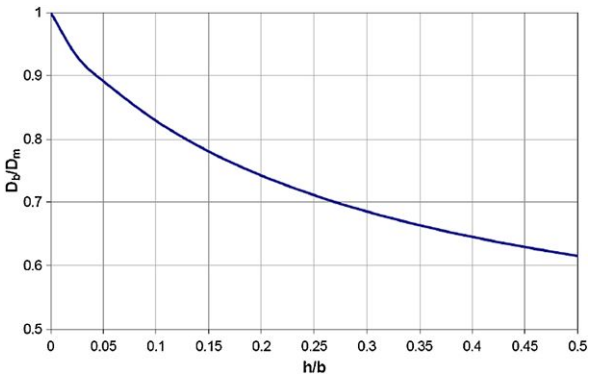

Fig. 6 Induced drag of "Best Wing System" (D_b) and monoplane (D_m)

– The detail of the emergency egress is still uncertain, mainly in the central section where the most central seats are far away from any exit.

In summary, we can remark that the challenges raised by the C-Wing are quite similar to the issues encountered by the BWB. The two concepts could indeed benefit from the advances of each other, and the airport compatibility issues of the BWB could be resolved, in principle, by applying a C-Wing design.

All the configurations examined so far are limited to the single category of a very large aircraft, which represents just a part of the future global market. In the rest of this paper, we examine the PrandtlPlane configuration to show that all aircrafts, from very small to very large ones, can be designed with this configuration.

2.4 PrandtlPlane

The PrandtlPlane concept follows an intuition of Prandtl. In 1924, Prandtl [26] showed that a particular layout exists, called "Best Wing System", that minimizes the induced drag for given span and total lift; an exact solution of Prandtl's problem can be found in [11].

This system is made of a box in the front view, where the two horizontal wings are carrying the same lift, and the lift distribution is the superposition of an elliptical part and a constant one; the induced velocity is constant, and its value depends on the total lift. Along the vertical wings, the lift distribution is symmetric and butterfly shaped, and the induced velocity is identically zero. In this configuration, an important parameter is the gap-to-span ratio, denoted h/b; as this ratio increases, the efficiency of the wing system increases correspondingly. In the interval $0.1 < h/b < 0.25$, this configuration achieves up to 30% reduction in induced drag with respect to a monoplane configuration (Fig. 6)

The application of Prandtl's configuration to a commercial aircraft stems mainly from the fact that, due to the Munk theorems, the induced drag is independent of the sweep angle of all wings, and thus this concept can be applied to any range of flight speed. During the period 2000–2002, five Italian Universities cooperated

in the frame work of a national project to develop a PrandtlPlane aircraft capable of carrying 600 passengers [8]. The main outcome was the resolution of the conflict between the aerodynamic efficiency and the static stability of flight, found in a previous preliminary study; this conflict is summarized as follows. The centre of gravity of the aircraft trimmed with equal lifts on both wings is in the middle of them; the aircraft is stable when the neutral point is backward to the centre of gravity, and, thus, a high aerodynamic efficiency of the rear wing is needed. The solution is a continuous upper wing over the rear fuselage and connected to the same with a double fin; the double fin solution is also fundamental to solve the flutter problem, and, consequently, a new section of the fuselage was conceived through enlarging it horizontally. The possible benefits of such a configuration are summarized below in terms of aerodynamics, flight mechanics, structure and operational.

Aerodynamics In addition to minimizing the induced drag, the lift on both wings points upward, allowing for improved efficiency, simple high lift devices, low approach and landing speeds, high control capacity.

Flight Mechanics and Control A PrandtlPlane aircraft is stable in flight with a proper margin of stability, and, at the same time, the two wings have the same lift. The shape of the PrandtlPlane presents unconventional controls. In particular, the pitch control could be obtained by means of two elevators located on both front and rear wing roots, moved in phase opposition; thus, a pure couple without variation in total lift is produced and safety for pitch manoeuvres is improved, especially close to the ground. Alternative control strategies are also possible, but they are not faced in this paper. The strength of the pitch command is high, even with small forces, due to the long distance between front and rear elevators. Stall is correctly induced in the front wing first, because the effective angle of attack of the rear one is decreased by the downwash effect. Locating the fuel in the two wing boxes achieves small centre of gravity variations, opening the opportunity to optimize one single flight condition. Concerning lateral control, a typical medium–large sized PrandtlPlane aircraft presents a twin fin; together with the two vertical tip wings, the system allows one to adopt different trim and control strategies for lateral motion, and, in particular, the ailerons can be typically positioned at both wing tip segments to gain efficiency (e.g. [31, 32]).

Aircraft Layout and Structures The fuselage is structurally equivalent to a beam, doubly supported by the attachments of the two wings; proper longitudinal positions of the wings could reduce significantly the maximum bending moment and, thus, structural weight of fuselage. In order to put the two fins far each other to check the aeroelastic constraints, the fuselage is enlarged horizontally; sections are designed to carry flight loads and pressurization. Contrary to conventional aircraft, the lifting system is over-constrained to fuselage, and it can be easily designed as "Damage Tolerant".

Fig. 7 Artistic view of a PrandtlPlane transport aircraft

Operational The most constraining limit to further improvements of aircraft capacity is the 80 × 80 m maximum dimensions. The PrandtlPlane configuration allows one to nearly double the capacity of the present aircraft, meanwhile remaining the overall dimensions into these limits without significant drag penalties. The front wing could cross the fuselage under the cargo bay, and, as a result, the cargo compartment is continuous along the fuselage, enhancing significantly the cargo capacity; if the wing crosses the fuselage under the passenger deck, the wetted fuselage surface is reduced, while the cargo capacity accords anyway to the standards. Moreover, the time to embark and disembark can be reduced by multiple cargo doors and by the possibility of loading and unloading at the same time. Certain areas need however further studies. From a flight dynamics perspective, the unconventional controls of the configuration induce a more complex dynamic behaviour. Due to the high moment of inertia along the pitch axis, the short period mode is stable and strongly damped, and the phugoid mode is believed to be stable, though with a lower damping. The asymmetric modes are however more problematic, and the double fin-rudder could pose questions on the dynamic behaviour. CFD studies would be needed to determine the dynamic derivatives, as empirical methods will not give accurate results. Also, as noted in [16], the high-lift device design still needs further studies. The design of high-lift devices will have important consequences on take-off drag with a possibility of reducing it, which in turn influences engine sizing. The aeroelastic phenomena remain a challenge. The static phenomena can be governed by structural parameters of the wings; in particular, the high stability against divergence of the positive-swept front wing allows the unstable negative-swept rear wing to be stabilized. In general, flutter is a critical aspect of the structural design of large PrandtlPlane aircraft, where the double fin solution is mandatory.

Applied to a transport aircraft, the PrandtlPlane concept could look like the one presented in Fig. 7.

From an operational viewpoint, the efficiency of the operations of embarking and disembarking cargo is improved through multiple doors and a continuous cargo bay.

Fig. 8 PrandtlPlane configuration adopted by Bauhaus Luftfahrt

Engine Integration Engine placement is not problematic; several options are possible, with different engines and propellers, as shown in [32] in the case of propfan propulsion, in [25] for turboprop and in [14], in the case of a solution adopted by Bauhaus Luftfahrt (Fig. 8).

In the rest of this paper, possible applications of the PrandtlPlane concept to develop aircraft of different categories are presented. All the aircrafts proposed are conceived by using the same basic design rules, in particular as far as aerodynamics and flight mechanics is concerned. Possible applications of different engines to freighter and passenger aircraft categories are also shown. The solutions proposed below are only preliminary; some of these solutions are analysed into more detail in other chapters of this book.

The PrandtlPlane aircraft was conceived in order to fulfill all the requirements which define a sustainable growth in the civil aviation of the future, as for example, high aerodynamic efficiency, intrinsic stability of flight, level 1 flight qualities, quick and easy ground operations, family of aircrafts ranging from small to very large ones, many possible engine integrations.

3 Civil Transport 250-Seat Category

The example shown in this section is the application of the PrandtlPlane concept to a 200–300 seat civil transport aircraft. A sketch of a typical configuration of the aircraft is shown in Fig. 9. There are two decks in the fuselage, one for passengers and the lower one for goods and luggage. The cockpit is positioned at the cargo deck level to meet the visibility requirements and, for security reasons, is fully separated from the passengers; behind the cockpit a room can be present for the pilot rest.

A typical solution consists into two cabin aisles with 10 passengers abreast in the economic class and 8 passengers in the business class; many solutions are possible for passenger accommodation, galleys and services as shown, for example, in Fig. 10, in the case of 258 passengers in two classes ($210 + 48$).

A family of aircrafts can be obtained with the adoption of same wings as shown in Fig. 11 [29].

Fig. 9 View of a 250-seat PrandtlPlane aircraft

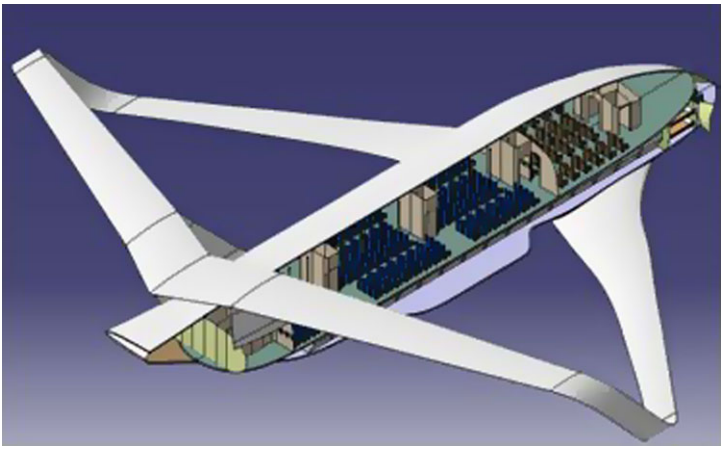

Fig. 10 Sketch of a solution with two classes

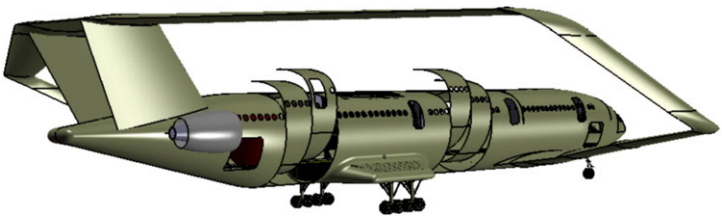

Fig. 11 Example of a 200–300 passenger family by the adjoin of fuselage barrels behind and afterwards the centre of gravity; the sweep angle of the vertical wings is changed accordingly

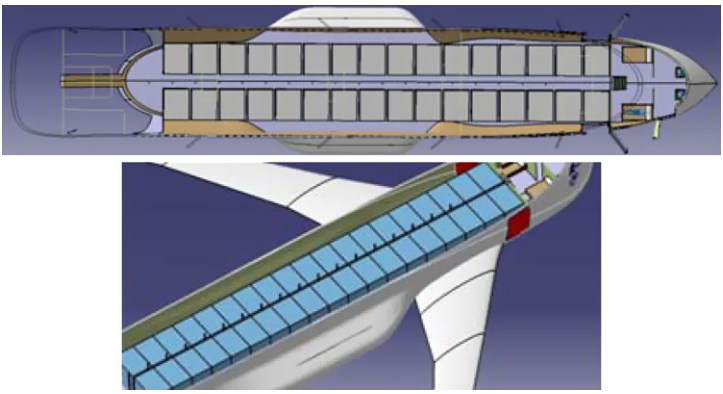

Fig. 12 The cargo deck with 32 LD3 (*top*) and 38 LD1 containers (*bottom*)

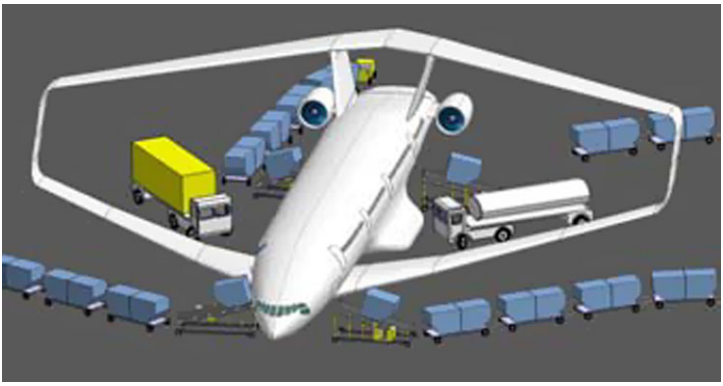

Fig. 13 Artistic view of a simulation of ground operations

A typical cargo compartment of a 250-seat aircraft contains 32 LD3 or 38 LD1 containers (Fig. 12), about the double of an equivalent conventional aircraft. In both cases, the containers are loaded through the two front doors and unloaded by the rear doors (or vice versa) to halve the time spent for ground operations.

Figure 13 shows a simulation of the ground operations and, in particular, the cargo loading and unloading, using both front and rear doors at the same time.

Other fuselage design are possible and, sometimes, more efficient. For example, Fig. 14 shows a fuselage section with a smaller eight. The front wing crossing of the cargo deck reduces from 38 to 24 the LD3 containers (the standards are satisfied), but the new cargo bay is continuous once more, and the loading operations are the same as before. The great advantage of the new solution is a higher efficiency of the aircraft due to the reduction of weight and wetted surface. The Load Index (LI) and the Comfort Index (CI) are 0.92 m^2 and 1.52 m^2, respectively.

The shape of the fuselage is designed in order to optimize the volume in the cargo compartment and also to obtain a better positioning of the passenger seats.

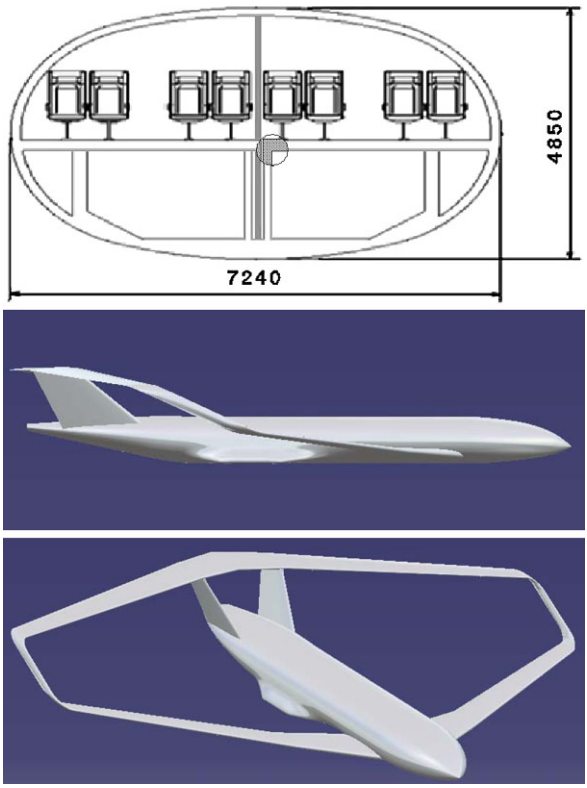

Fig. 14 Reduced height section

Figure 15 shows the external perimeter of the fuselage cross section of the aircraft in Fig. 9; the curve is joined together with the continuous first derivative; Fig. 15 shows a sketch of the fuselage structural solution. The internal width of the passenger compartment is 6500 mm, with a maximum height of 2300 mm; the cargo deck is 4200×1700 mm.

The overall dimensions of the aircraft are: 47-m wing span and 46-m length. As shown in Fig. 15, a vertical strut connects the top and bottom fuselages (except at the exit and emergency doors).

One keel beam is on bottom of the fuselage, and a second one is possible at the top to prevent the compression instability of the central fuselage during flight. The pressurized fuselage is the external contour; the air ducts and other installations occupy the two top fuselage spaces and the lateral spaces in the cargo deck. The passenger and cargo deck beams have a central vertical support, which is independent from the pressurization truss; this solution reduces the empty weight significantly.

The main undercarriage is designed according to the aircraft scale; in the present example, it is made of four groups with 4 wheels, for a total of 16 wheels, 30-inch diameter.

The structural solutions have been developped on the basis of Finite Element Method analysis, considering the loads in flight (gusts and manoeuvres) and pressurization into account.

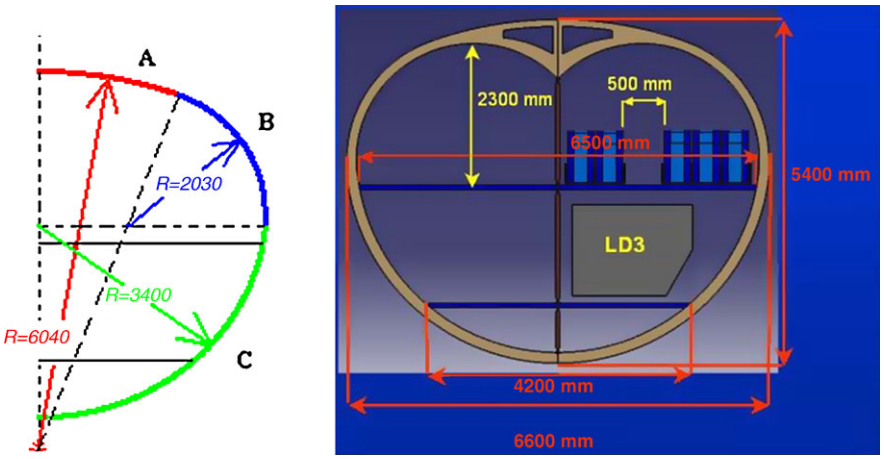

Fig. 15 Reference cross section (*left*) and structural solution (*right*) of the fuselage

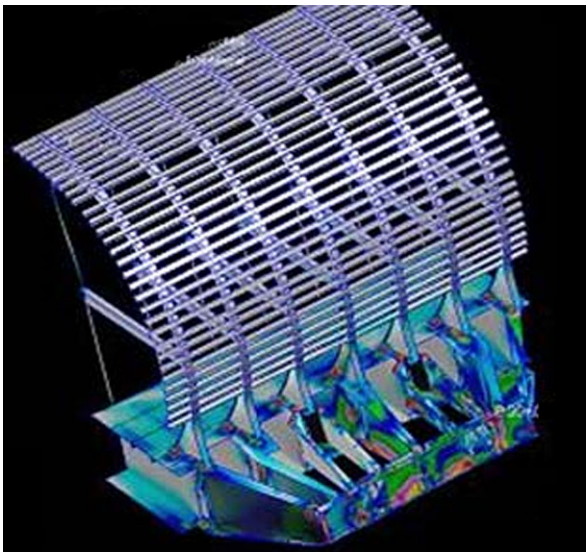

Fig. 16 Finite Element model of the central fuselage

Figure 16 shows a typical FEM result of the central fuselage which includes the sponsons of the main undercarriage (external skin is omitted for the sake of clarity).

These preliminary analyses aim at evaluating the fuselage structural weight, with the following conclusions: (i) the presence of the central bar (Figs. 15 and 16) reduces significantly the weight of the frame and passenger deck, (ii) the solution is very efficient as far as pressurization is concerned, (iii) a fuel tank is obtained just in the Centre of Gravity position (with this supplementary tank, the position of the C.G. during the mission is maintained unaltered), (iv) the presence of the lateral

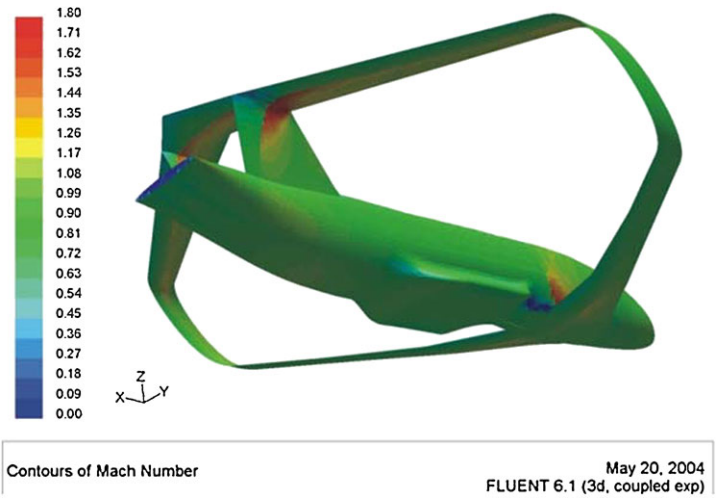

Fig. 17 Typical CFD result

sponsons for hosting the main undercarriage does not influence significantly the aerodynamics of the aircraft, as shown in Fig. 17.

One of the main characteristics of the PrandtlPlane concept is to obtain a Best Wing System condition in take-off and landing too and to reduce the approach speed, compared to conventional or innovative aircraft. This result is obtained by positioning high-lift devices along the two wings. Once again, the Centre of Gravity must be positioned between the two wings, because we can improve lift on both wings by the same amount. Hence, the condition of Best Wing System during cruise flight is valid also at low speed with high-lift devices extended. The system of flaps and slats is simple (plain flap and single Fowler) and the same is valid for controls. Figure 18 [31] shows a typical solution adopted; in particular, the pitch control is made by two elevators, one in the front wing and the second on the rear wing. They are activated in phase opposition in such a way as to generate a pure pitch control moment, but other strategies are possible by mixing canard and pure pitch moment controls. This solution could reduce noise and noxious emissions in take-off and landing according to the above-mentioned principle of sustainable growth. Ailerons are positioned on both wing tips.

The structural and aeroelastic problems of the lifting systems have been studied in the past, and some results are also reported in this book [9, 10, 12]; these studies indicate a high structural efficiency of the present solution.

4 Unmanned Aerial Vehicles

The PrandtlPlane configuration can be applied also to Unmanned Aerial Vehicles (UAVs). Besides the enhancement of the range, thanks to the lower induced drag,

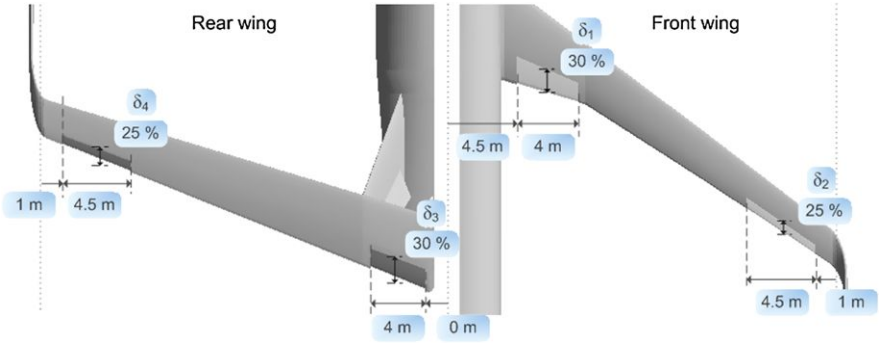

Fig. 18 PrandtlPlane high-lift devices layout

Fig. 19 Application to UAV

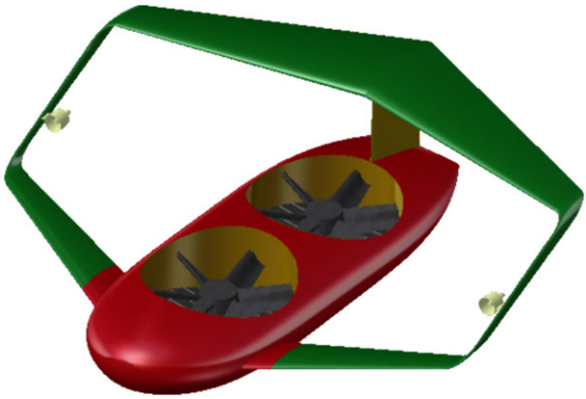

other advantages are related to the flight mechanics. As shown before, unconventional pitch controls lead to an increase of the manoeuvre capability, and a very high aerodynamic damping is favourable to the installation of sensors and observation devices.

One example of the application of the wing-box concept to a UAV is depicted in Fig. 19 [27]. This model has been conceived for a Vertical Take-Off and Landing application. The front and rear wings are equipped with elevators for pitch control and with moveable surfaces on trailing edge with the purpose of minimizing the wetted area during the vertical flight. The vertical take-off and landing is guaranteed by two counter-rotating electric motor fans located inside the fuselage; these fans permit also the hovering. At the nose of the fuselage the batteries are located. The horizontal thrust is produced by two electric motor ducted fans inserted on the vertical wings (bulkheads). If needed, these motors can be also tiltable. All the rotating parts are inside the structure or protected by the wings, giving a high level of safety for the operator at ground.

A PrandtlPlane wing arrangement allows one to integrate the vertical take-off propulsion system easily. Indeed, for the equilibrium during the vertical flight or while hovering, the vertical thrust system must be located on the centre of mass, or,

Fig. 20 Examples of ultralight PrandtlPlane

alternatively, more than one rotor shall be used. The same is worth for the lifting system, which, due to trim, shall be located near the centre of mass of the configuration. In a conventional configuration, this leads to a complex integration of propulsion system and aerodynamic solutions. On the contrary, in the case of the PrandtlPlane, the vertical thrust system (e.g. ducted fans or one helicopter-like rotor) can be installed between the two wings; moreover, the wings are not subjected to additional downward flow coming from the vertical thrust, and, therefore, drag during the vertical flight is reduced.

5 Ultralight Aircraft

For ultralight aircraft, such as those belonging to LSA and ULM categories, the induced drag reduction provided by the "best wing system" turns into a minor benefit in terms of operating cost, due to the small wing load and the reduced influence of fuel on the overall operating costs. Nevertheless, the application of the PrandtlPlane configuration, shown in Fig. 20, is interesting since it introduces new concepts that may increase the flight safety.

In the accidents of these aircraft, human errors represent about 2/3 of all cases (Italy, 2009); the occurrence of stall represents a significant part of these accidents (about 30%), and become fatal for the fire provoked by the contact of fuel with hot components, like the engine. The PrandtlPlane ultralight aircraft has been developped to reduce the probability of human errors and the risk of fire ignition inside the cabin. Regarding the stall occurrence, the advantages are due to an anti-stall behaviour and the control in pitch. As shown in Fig. 21 [6], wind tunnel tests have demonstrated that the PrandtlPlane lifting system reaches the stall condition at an angle of attack $(\alpha - \alpha_0)$ around 15°, and, after that point, the lifting force decreases smoothly inside a wide range of incidence. In addition, stall involves the front wing first, therefore a nose-down moment is generated by the rear wing, and the aircraft tends to oppose to a further angle of attack increase.

As far as pitch control devices is concerned, it has already said that the PrandtlPlane control is a pure couple, contrary to conventional one, where pitch control is a couple associated to a negative force. A sketch of a typical ultralight

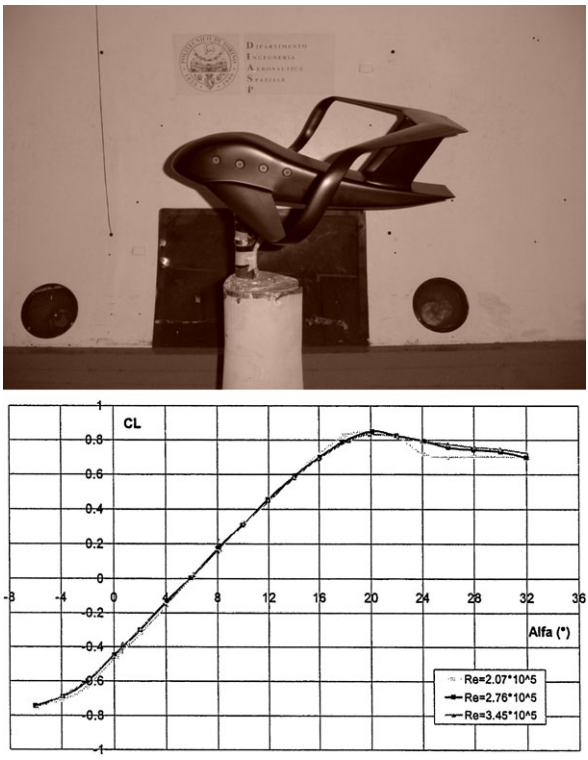

Fig. 21 Wind tunnel tests on a PrandtlPlane scaled model

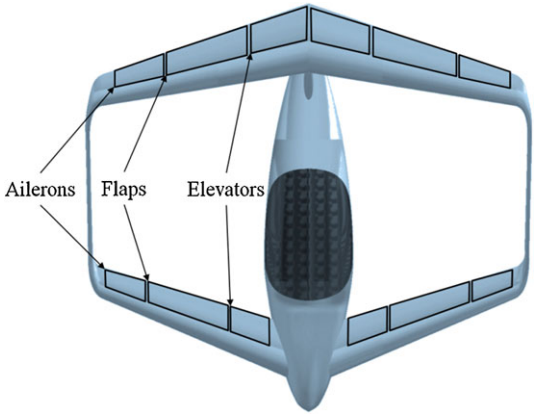

Fig. 22 Example of PrandtlPlane control surfaces positioning

PrandtlPlane is shown in Fig. 22. Both front and rear wings are provided with elevators, flaps and ailerons.

Another important safety aspect is the prevention from fire ignition inside pilots' cabin. In a conventional aircraft, the distance between the cabin, the fuel tank and the engine is small, and, in case of accident, pilots can be exposed to fire. In a

Fig. 23 Scaled R/C models

PrandtlPlane, since lift force is transmitted to fuselage through two points, it is easier to balance the aeroplane with the pilots far from fuel and engine.

The PrandtlPlane configuration can provide other advantages, such as high visibility and flight comfort. The visibility is high because the engine is behind the cabin; the high damping of the short period mode is obvious; it produces a smooth response to gust and turbulence and a flight comfort enhancement.

In last years, the Department of Aerospace Engineering of Pisa has carried out several research projects concerning the design of these aircraft, the development of design tools and the construction of scaled R/C models (Fig. 23).

As a result of this experience, a full scale prototype has been constructed, with the characteristics (Fig. 24):

- 2 seats in tandem layout
- Engine: Rotax 912 ULS, 100 hp
- Propeller: 3-blades, pusher, $\Phi = 1.6$ m
- Maximum Take-Off Weight: 500 kg
- Wingspan: 8 m
- Wing area: 14.2 m^2
- Cruise speed (approx.): 250 km/h
- Landing Speed (approx.): 65 km/h

6 Example of Application to an Executive Aircraft

Executive aircraft can be designed and modified according to the PrandtlPlane configuration. As an example, we consider the Piaggio P180 aircraft (Fig. 25, [28]), and we suppose, as an exercise, to improve the performances while maintaining the same layout and elegance.

The P180 reaches the maximum Mach number of 0.7 at an altitude of 9450 m and can have up to 9 passengers + 2 crew members, the stall speed is 97 kn, and the

Fig. 24 Full scale prototype of an ultralight PrandtlPlane

Fig. 25 The Piaggio P180

landing speed is 126 kn. The exercise consists in improving the number of passengers of 4 units, reducing the landing speed to 119 kn and flying at 0.85 Mach cruise speed.

Figure 26 shows a sketch of a possible new aircraft design; right side shows the original configuration, and the left side shows the modified aircraft using the PrandtlPlane configuration.

The number of passengers is increased by removing the cantilever wing from its present position, to gain the internal volume while the overall centre of gravity

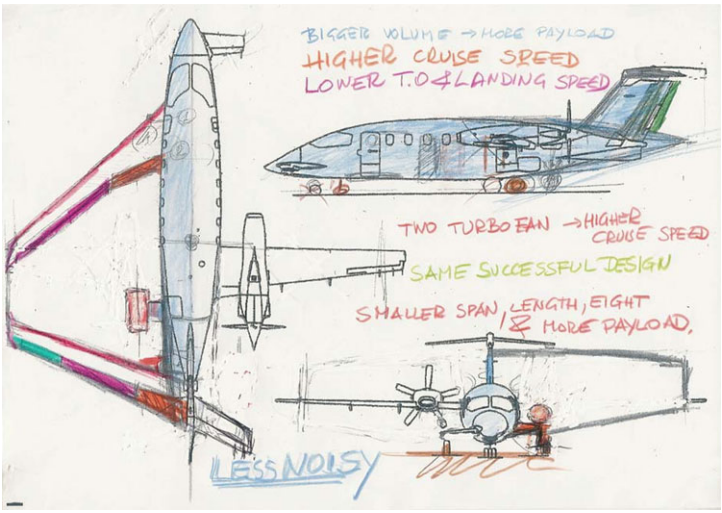

Fig. 26 PrandtlPlane version of the Piaggio P180

is moved backward. Thus, the present lifting system, made of canard, cantilever wing and T tail is substituted by the PrandtlPlane wing system, with the following effects: a reduction of the induced drag for the fixed span, possibility to enhance the maximum take-off weight and to reduce the maximum lift coefficient by an improvement of the lifting surface, new high-lift devices on both wings to reduce further the landing speed, a new aerodynamic control system to improve the safety during pitch manoeuvres. The new configuration can integrate different engines; the present turboprop engines could be maintained or substituted by two turbofan positioned on rear fuselage to get a cruise speed of 0.85 Mach. The modified aircraft has the same span, smaller overall length and total height, and the same elegant layout.

7 Liquid Hydrogen Propulsion

The main problems of conventional fuel (Kerosene) are pollution and availability in the next decades; the problem of new fuels is under discussion for medium long terms. The new fuels for future aviation could guarantee a reduction of emissions and allow the civil aviation to grow up. One possible fuel of the future is Liquid Hydrogen.

Figure 27 shows a comparison between the properties of Kerosene and Liquid Hydrogen; the liquid hydrogen has the following advantages on Kerosene: no production of CO_2 and CO, 80% reduction of NO_x, 2.8 times energy for unit mass. On the other side, the drawbacks are: a cryogenic temperature needed, the present costs of Hydrogen (3–5 times higher) and the volumes of tanks (4 times higher than

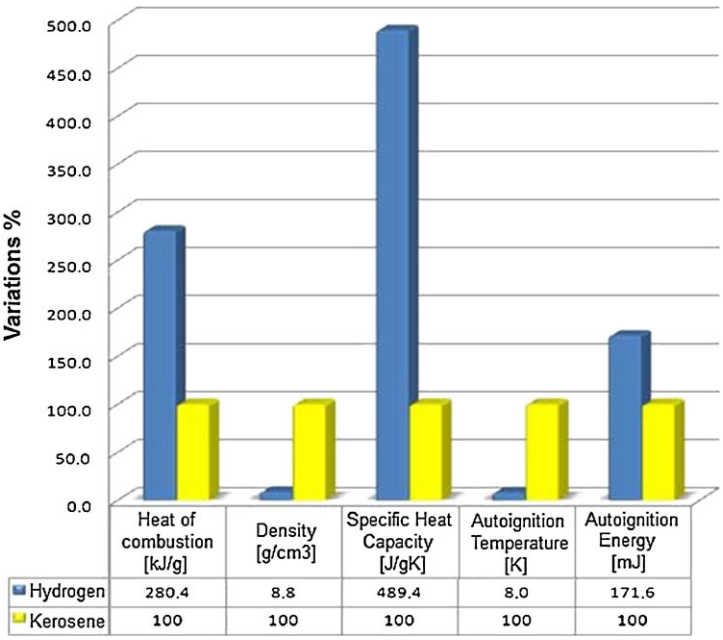

Fig. 27 Comparison between Kerosene and Liquid Hydrogen characteristics

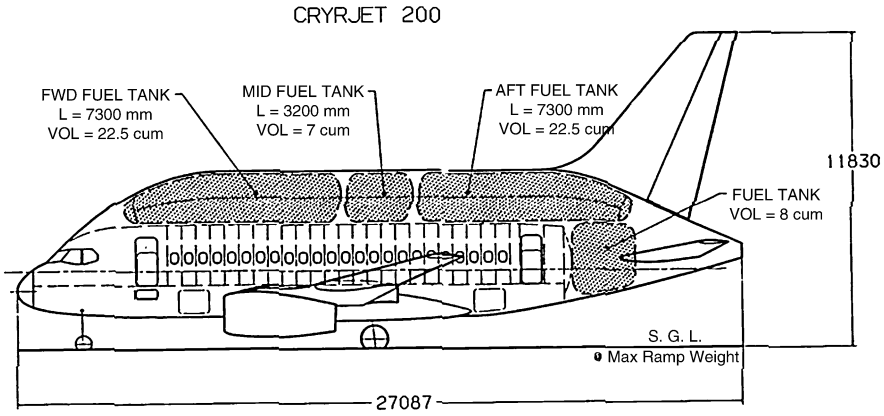

Fig. 28 Present idea on Hydrogen tanks positioning

Kerosene). The configurations proposed so far for using Hydrogen are similar to that in Fig. 28, made by conventional aircraft containing large tanks on top of fuselage.

The PrandtlPlane configuration provides new solutions avoiding the positioning of the Hydrogen tanks inside the fuselage. In fact, the main Hydrogen tanks could be located at the tips of front wing, taking advantage of the particular behaviour of the lifting system and, meanwhile, relieving flutter problems [10]. A more exten-

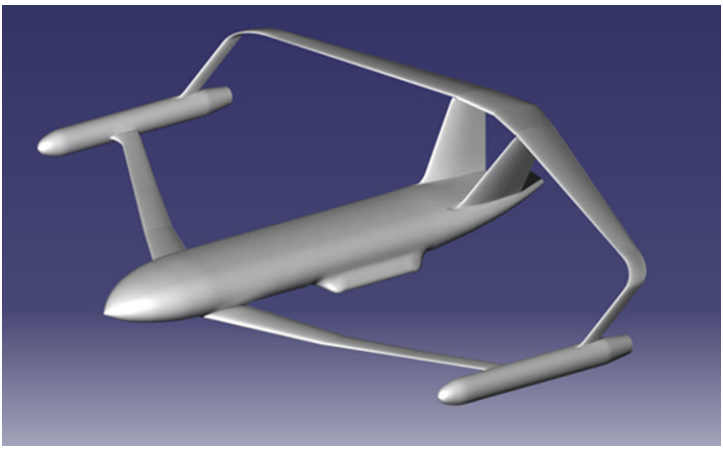

Fig. 29 Cryogenic 250 passenger PrandtlPlane solution

sive description of the PrandtlPlane solution is reported in [4], tuned for a 250-seat category aircraft as an example of application. In this case, the cruise speed is limited to 0.75 Mach, the cruise eight is 29.000 feet in order to minimize pollution and contrails, the range is 2.500 nm.

A sketch of the final configuration is depicted in Fig. 29. In this solution, a tank is also present in the rear portion of fuselage; reducing the range to 1.800 nm, which is the most common utilization in continental air transport, this last tank is no longer needed.

Although the sketch is qualitative and more research activities are needed, the solution shown in Fig. 29 suggests the way to solve the problem of the fire safety, taking Hydrogen very far from the passengers. The position of the tanks matches the requirement for alleviating flutter onset of the PrandtlPlane lifting system, discussed in [10].

8 Application to Freighters

In the next years, the airfreight may become a strategic sector for the air industry because of the very high growth expected (about +6% per year).

Air transport could potentially be a solution to improve the international commerce if the transportation costs will be cut at a level that the product of an emerging economy could be profitably transported by air. Thus, the rising of airfreight has to be supported by proper activities in economy, technology and logistics. This effort should result into the definition of a new concept of properly conceived freighter, and the aircraft design should be integrated by a new logistic arrangement in order to cut the current operating costs.

Given this picture, the PrandtlPlane configuration allows multiple benefits, starting from aerodynamic improvements. Other possible advantages are the following:

Table 1 Requirements of the very large freighter

Operating requirements	
Gross Payload	250 [tons]
Uld	20 ft intermodal container
Range	3000 [NM]
Mcr	0.6
H_{cruise}	20000 ft

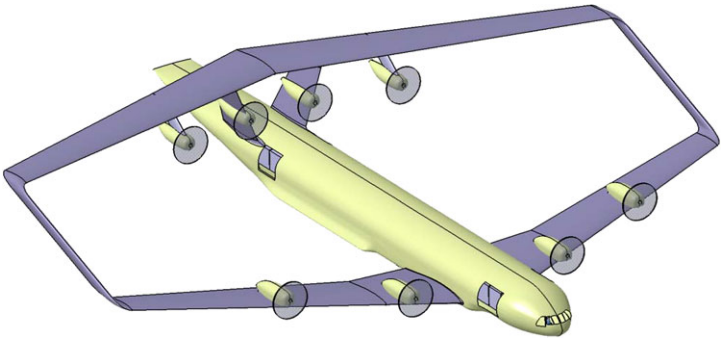

Fig. 30 General layout of a very large PrandtlPlane freighter

the load capacity can be easily increased (250 tons) while maintaining the allowable maximum dimensions; the longitudinal stability and manoeuvrability is significantly enhanced; the fuselage can be designed for intermodal container transportation; loading and unloading of containers are rapid and safe; the cargo deck is close to the ground; the fuselage structure is lighter than the conventional monoplane, etc.; a complete analysis of the application of PrandtlPlane concept to airfreight transport is to be found in this book [25].

A conceptual solution of a possible PrandtlPlane freighter is presented here to transport 24 intermodal containers; they are set transversally in the fuselage; the most important features are reported in Table 1, and a general layout of the aircraft is depicted in Fig. 30 [25].

In order to cut the operating costs, a new propulsion system is needed; in fact, the specific fuel consumption of current turbofans is not compatible with goods transportation, and there is no need to fly in the transonic range. From this perspective, the open rotor architecture represents an interesting solution: its specific fuel consumption is reduced more than 50% compared with existing turbofans, while the available power is about 14000 ehp per engine. From a first performance estimation, eight engines are required; the PrandtlPlane ensures a high engine integration, and many different solutions can be considered for the engine positioning. The main drawbacks of the present open rotors are high noise and vibrations due to the contra-rotating propellers, especially when flying at a cruise height of about 6.000 m. The possibility of an easy engine integration will be a key point in this respect.

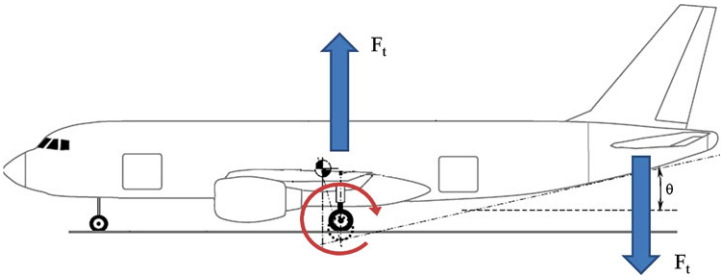

Fig. 31 Take-off rotation in a conventional aircraft

As previously said in Sects. 2.4 and 5, the pitch control of a PrandtlPlane is performed using two contra-rotating elevators, placed on the two wings. When applied to a freighter aircraft, this feature can turn into an advantage in terms of more payload. In fact, in a conventional (wing-tail) aircraft, the take-off rotation is given by a moment generated by the down-force produced by the horizontal tail and the induced reaction acting on the main landing gear. The rotation is performed around the landing gear and, being this at a significant distance from the fuselage aft, an upsweep angle is required, with the consequence that a fraction of the internal volume of fuselage is lost (Fig. 31).

In PrandtlPlane, instead, the particular pitch control allows one to generate the rotation moment aerodynamically. In fact, while the rear wing provides a down-force, the front wing gives an up-force, and a pitch-up moment is obtained; again, the take-off rotation takes place around the landing gear, but in this case its distance from the fuselage aft can be reduced, as well as the volume affected by the upsweep angle.

As a result, for given fuselage length and section, more internal volume becomes available; this property could be of great interest in the case of a freighter.

9 An Ultra-Large PrandtlPlane Application

As already said many times, the very large aircraft category is limited by the overall dimensions; the largest aircraft, Airbus A380, fills completely the 80 × 80 m horizontal square; the conventional configuration does not allow any larger solution. The contrary occurs for the PrandtlPlane configuration due to the reasons exposed in the following.

We consider a 1500-seat civil aircraft as reference, and, although preliminarily, we try to show how the disadvantages of a conventional aircraft can be overcame by the PrandtlPlane solution. In the conventional configuration, the wing root thickness is not compatible with overall dimensions of the fuselage; the opposite happens for the PrandtlPlane, where the total wing surface is divided into two wings, and the thickness of the front wing is nearly halved. The wing surface of a conventional very large aircraft, with the limitation to 80-m span, will result into a reduced aspect

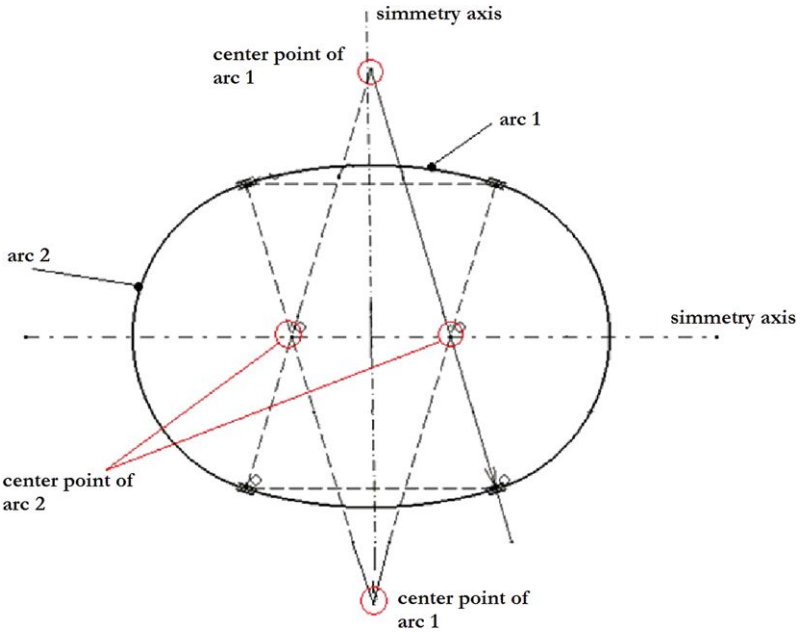

Fig. 32 Fuselage design procedure

ratio; in a PrandtlPlane this limitation is not present, and, moreover, we can reduce the induced drag by incrementing the vertical gap.

The fuselage section could be doubly symmetric and made by just two circular sectors; the design procedure is defined in Fig. 32. The first derivative is continuous everywhere, and the curvature is discontinuous only into four points of the external perimeter. The fuselage surface is obtained by using ASD (Aircraft Shape Design) code [5], and the final layout of the fuselage is depicted in Fig. 33. Preliminary structural analysis indicates that the fuselage empty weight per passenger can be reduced up to 80% compared to the 250 passengers class, due to the large-scale effect.

The fuselage section is divided into three decks, two for passengers and the bottom one for cargo. Upper and lower passenger decks contain 16 seats abreast with three isles each, with a total of 32 passengers per section. A reference solution for passenger accommodations and a sketch of possible services layout are shown in Fig. 34. The proposed configuration consists of 1498 passengers in one economy class, 43 flight assistants and 2 or 3 pilots; any passenger deck contains 19 toilets (1/40 passengers) and 10 class A emergency exits.

The cargo vain contains 3 LD3 containers abreast per section for a total of 51 containers, corresponding to 0.065 m^3 per passenger. As shown in Fig. 35, the fuselage webs are connected by three decks horizontally and two trusses vertically; the trusses, connecting top and bottom fuselage, are designed against pressurization to save much weight under internal pressure. The two passenger decks are also connected each other vertically, and they both to the bottom fuselage, by means of

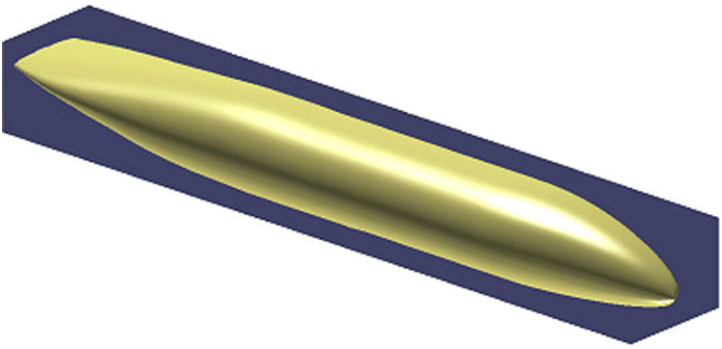

Fig. 33 Fuselage layout

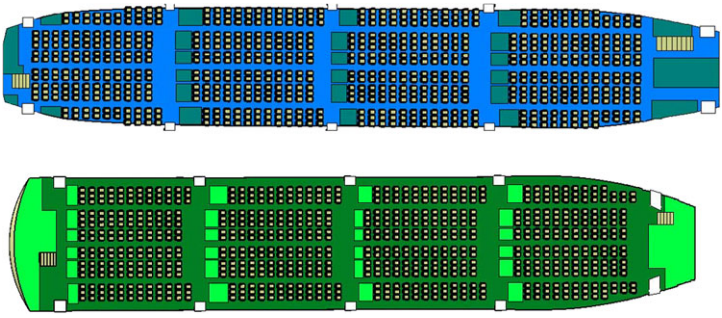

Fig. 34 Passenger accommodation

supports in order to reduce the empty weight of the two decks. In this way, the fuselage is divided into two lateral compartments and an internal one. In the areas in front of the exits, some vertical trusses are missing, and some structural problems could arise; they are solved by means of a proper structural design of the upper keel beams.

Figure 36 shows a sketch of the aircraft without the engines (different engine integrations are possible).

10 Conclusions

The interest towards non-conventional aircraft has increased in the last decade. In this paper, after a brief digression on Oblique Flying Wing, Blended Wing Body and C-Wing, possible applications of the PrandtlPlane configuration have been indicated. The thesis of this paper is that the PrandtlPlane configuration can be applied to any kind of transport aircraft, and some examples have been given, ranging from very small to very large, both civil and freighter, transport aircraft. Very large aircraft able to transport nearly the double passengers of the largest conventional aircraft fly-

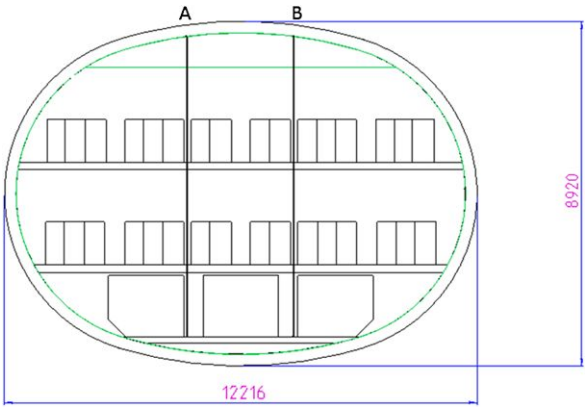

Fig. 35 A section of a very large aircraft

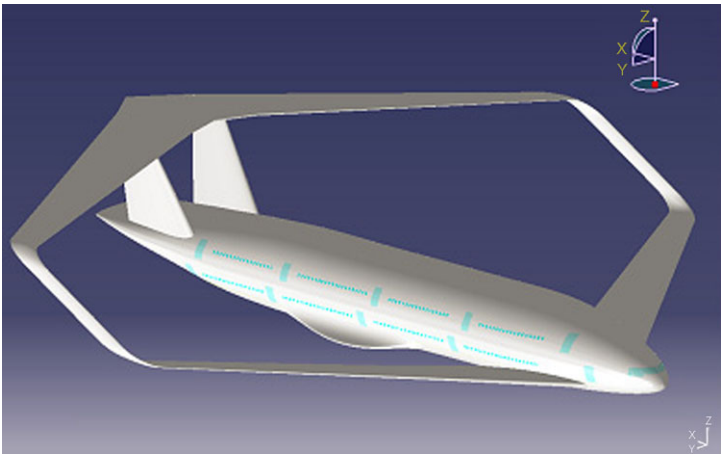

Fig. 36 General layout of the 1500-seat civil transport PrandtlPlane

ing today are made possible by the PrandtlPlane concept. The main characteristics are outlined.

References

1. Future technology and aircraft types. Stanford University Website (based on "Reinventing the Airplane: New Concepts for Flight in the 21st Century" presentation by Ilan Kroo)
2. Vision 2020: Strategic Research Agenda, vol. 1, October 2002
3. Oblique flying wings: An introduction and white paper, June 2005. Desktop Aeronautics Website
4. Beccasio, N., Tesconi, M., Frediani, A.: Liquid hydrogen propelled PrandtlPlane configuration: a preliminary study. In: Buttazzo, G., Frediani, A. (eds.) Variational Analysis and Aerospace Engineering II: Mathematical Challenges for Aerospace Design. Springer, Berlin (2012)

5. Cavallaro, R., Frediani, A.: A code for shape generation and aerodynamic design of aircraft. In: Buttazzo, G., Frediani, A. (eds.) Variational Analysis and Aerospace Engineering II: Mathematical Challenges for Aerospace Design. Springer, Berlin (2012)
6. Chiocchia, G., Iuso, G., Carrera, E., Frediani, A.: A wind tunnel model of a ULM configuration of PrandtlPlane: Design, manufacturing and aerodynamic testing. In: Proceedings of the XVII AIDAA Congress (2003)
7. Daly, K.: Will airsickness kill the blended wing-body (BWB) silent aircraft? Nov. 2006. Flight Global Website
8. Frediani, A., Balis Crema, L., Chioccia, G., Ghiringhelli, G.L., Morino, L.: Development of an innovative configuration for transport aircraft; a project of five Italian universities. In: Proceedings of the XVII AIDAA Congress, pp. 2089–2104 (2003)
9. Frediani, A., Dal Canto, D., Ghiringhelli, G.L., Terraneo, M.: The lifting system of a PrandtlPlane, Part 1: design and analysis of a light alloy structural solution. In: Buttazzo, G., Frediani, A. (eds.) Variational Analysis and Aerospace Engineering II: Mathematical Challenges for Aerospace Design. Springer, Berlin (2012)
10. Frediani, A., Divoux, N.: The lifting system of a PrandtlPlane, Part 2: preliminary study in flutter characteristics. In: Buttazzo, G., Frediani, A. (eds.) Variational Analysis and Aerospace Engineering II: Mathematical Challenges for Aerospace Design. Springer, Berlin (2012)
11. Frediani, A., Montanari, G.: Best wing system: an exact solution of the Prandtl's problem. In: Buttazzo, G., Frediani, A. (eds.) Variational Analysis and Aerospace Engineering, pp. 181–211. Springer, Berlin (2009)
12. Frediani, A., Quattrone, F., Contini, F.: The lifting system of a PrandtlPlane, Part 3: structures made in composites. In: Buttazzo, G., Frediani, A. (eds.) Variational Analysis and Aerospace Engineering II: Mathematical Challenges for Aerospace Design. Springer, Berlin (2012)
13. Frediani, A., Rizzo, E., Bottoni, C., Scanu, J., Iezzi, G.: The PrandtlPlane aircraft configuration. In: Aeronautics Days, Jun 2006
14. Frediani, A., Scanu, J., Bottoni, C., Rizzo, E., Cipolla, V., Iezzi, G.: Contractor report for Bauhaus Luftfahrt. Technical report, University of Pisa, Department of Aerospace Engineering, February (2008)
15. Hirschberg, M.J., Hart, D.M., Beutner, T.J.: A summary of a half-century of oblique wing research. In: 45th AIAA Aerospace Sciences Meeting (2007)
16. Iezzi, G.: PrandtlPlane high lift system preliminary aerodynamic design. Master's thesis, University of Pisa, Department of Aerospace Engineering (2006)
17. Jones, R.T.: Aerodynamic design for supersonic speeds. In: Proceedings of the 1st International Congress in the Aeronautical Sciences (ICAS), Advances in Aeronautical Sciences, vol. 1 (1959)
18. Kroo, I.M.: A general approach to multiple lifting surface design an analysis. In: AIAA, p. 2507, Oct 1984
19. Kroo, I.M.: Nonplanar wing concepts for increased aircraft efficiency. In: Torenbeek, E., Deconinck, H. (eds.) Innovative Configurations and Advanced Concepts for Future Civil Aircraft. Lecture Series of Von Karman Institute of Fluid Dynamics, Jun 2005
20. Kroo, I.M., McMasters, J.H., Smith, S.C.: Highly nonplanar lifting system. Technical report, NASA, Sept 1995
21. Liebeck, R.: Design of the blended wing body subsonic transport. J. Aircr. **41**, 10–25 (2004)
22. Liebeck, R.H., Page, M.A., Rawdon, B.K.: Blended-wing-body subsonic commercial transport. In: 36th AIAA Aerospace Sciences Meeting and Exhibit, January 1998
23. McMasters, J.H., Kroo, I.M.: Advanced configuration for very large transport airplanes. Invited AIAA paper, pp. 439 (1998)
24. McMasters, J.H., Paisley, D.J., Hubert, R.J., Kroo, I.M., Bofah, K.K., Sullivan, J.P., Drela, M.: Advanced configuration for very large subsonic transport airplanes. Technical report, NASA, Oct. (1996). Contractor Report 198351
25. Oliviero, F., Frediani, A.: Conceptual design of an innovative large PrandtlPlane freighter. In: Buttazzo, G., Frediani, A. (eds.) Variational Analysis and Aerospace Engineering II: Mathematical Challenges for Aerospace Design. Springer, Berlin (2012)

26. Prandtl, L.: Induced drag of multiplanes. Technical report, NACA (1924). Transl. of Technische Berichte Vol. 3, N. 7, pp. 309–315
27. Rizzo, E., Frediani, A.: Dimensionamento aerodinamico preliminare di un velivolo uav vtol elettrico in configurazione prandtlplane. Technical report, University of Pisa, Department of Aerospace Engineering, January (2008). Contract report for UTRI Srl (in Italian)
28. Sacco, G., Lanari, C.: The three lifting surface configuration concept and lessons learned from the Piaggio P180. In: Torenbeek, E., Deconinck, H. (eds.) Innovative Configurations and Advanced Concepts for Future Civil Aircraft. Lecture Series of Von Karman Institute of Fluid Dynamics, June 2005
29. Scanu, J., Bottoni, C., Cipolla, V., Frediani, A., Iezzi, G., Rizzo, E.: Research on fuselage design, lifting system at cruise conditions and low aerodynamic design of a PrandtlPlane aircraft. Technical report, University of Pisa, Department of Aerospace Engineering, February (2008). Contractor report for Airbus Deutschland
30. Torenbeek, E.: Nonplanar wing concepts for increased aircraft efficiency. In: Torenbeek, E., Deconinck, H. (eds.) Innovative Configurations and Advanced Concepts for Future Civil Aircraft. Lecture Series of Von Karman Institute of Fluid Dynamics (2005)
31. Van Ginneken, D.A.J., Voskuijl, M., Van Tooren, M., Frediani, A.: Automated control surface design and sizing for the PrandtlPlane. In: Journal on 51st AIAA Structures, Structural Dynamics and Materials Conference (2010)
32. Voskuijl, M., De Klerk, J., Van Ginneken, D.A.J.: Flight mechanics modeling of the Prandtl plane for conceptual and preliminary design. In: Buttazzo, G., Frediani, A. (eds.) Variational Analysis and Aerospace Engineering II: Mathematical Challenges for Aerospace Design. Springer, Berlin (2012)

The Lifting System of a PrandtlPlane, Part 1: Design and Analysis of a Light Alloy Structural Solution

Dario Dal Canto, Aldo Frediani, Gian Luca Ghiringhelli, and Mauro Terraneo

1 Introduction

In theory, a PrandtlPlane configuration can achieve up to a 30% reduction in induced drag with respect to an optimum monoplane configuration [6] with the same span and total lift; we assume that the lifting system has the same area of a conventional equivalent aircraft (cantilever wing plus elevator) to avoid any friction drag penalty. Therefore, for equal span and profiles, the local thickness and the chord are nearly the half (some more to take the area of elevator into account) of that pertaining to a conventional wing; thus, the structural design of the lifting system is a big challenge. In this paper, we aim at carrying out a preliminary structural design of the wings and to evaluate the overall empty weight. A weight estimation is not possible using empirical methods, no experience is available on such structures, and, also, aeroelasticity could have a strong influence on the preliminary design. The lifting system is made of an aluminium alloy, and the optimization of the structures is conducted using an approach, set up at Polytechnic of Milano, under the constraints of maximum allowable stress, stability of equilibrium in compression, aileron effectiveness, static aeroelasticity and flutter. Any step of the optimization can produce

D. Dal Canto (✉) · A. Frediani
Department of Aerospace Engineering, University of Pisa, Via G. Caruso, 56122 Pisa, Italy
e-mail: dariodalcanto@alice.it

A. Frediani
e-mail: a.frediani@dia.unipi.it

G.L. Ghiringhelli · M. Terraneo
Department of Aerospace Engineering, Polytechnic of Milano, Via La Masa, 20156 Milano, Italy

G.L. Ghiringhelli
e-mail: gianluca.ghiringhelli@polimi.it

M. Terraneo
e-mail: terraneo@aero.polimi.it

G. Buttazzo, A. Frediani (eds.), *Variational Analysis and Aerospace Engineering: Mathematical Challenges for Aerospace Design*, Springer Optimization and Its Applications 66,
DOI 10.1007/978-1-4614-2435-2_9,

Fig. 1 Artistic view of a 250-seat PrandtlPlane transport aircraft

a weight increment, the level of which indicates the sensitivity to the relevant constraint. Some aspects of the design against flutter suggested to investigate with more detail the flutter problem and also to make the wings in composites. A flutter analysis is reported [8], and a solution made in composites is presented in [9]; both papers can be found in this book.

The wing sections of both horizontal and vertical wings and the two fins are two-spar box; in a first model, the box is modelled in a simplified way and described by means of three parameters per section for a total of 162 degrees of freedom. The parameters are the skin thickness (the same for panels in tension and compression), the spar web thickness (the same in the front and rear spars) and the total area of the stringers (the same in tension and compression). The model proved to be unsatisfactory mainly because the out-of-plane bending moment is significant; a new asymmetric box section has then been designed with five parameters per sections for a total of 270 degrees of freedom. In the first hypothesis the structural weight estimation is 17.8% of the maximum takeoff weight, and, in the second one, the new structural weight results in 15.8% of MTOW. This result is not so different from the weight of wings, elevator and fin of an equivalent conventional aircraft with the same span and total lift.

2 The PrandtlPlane of Reference

We consider a 250-seat PrandtlPlane aircraft as reference for the evaluation of the efficiency of the structural solution. A sketch of the aircraft is depicted in Fig. 1.

The benefits of this configuration are: a more efficient aerodynamics, an innovative pitch control, a high efficiency of the operations of embarking and disembarking of passengers and cargo, easy engine integration, etc; more details can be found in [7]. The present aircraft configuration was developped to demonstrate the feasibility of the concept and to evaluate the empty weight without using statistical weight

Table 1 Characteristics of reference

Feature	Value
Range	6000 [nm]
Maximum take-off weight	230 000 [kg]
Take-off airport altitude	0 [m]
Cruise altitude	10 500 [m]
Cruise mach	0.85
W/S cruise	634.3 [kg/m^2]
Span	55 [m]
S_{ref}	394.52 [m^2]

estimations and starting from a preliminary maximum take off weight assumption. The useful characteristics of the aircraft are listed in Table 1.

The main characteristics of the aircraft are reported in [7]; in the present analysis we examine the wing system only. The aircraft shown in Fig. 1 is the result of an aerodynamic optimization with the constraint of the static stability of flight. The front wing presents a kink at zero angle of dihedral; at the end of the kink, the dihedral angle passes from zero to third degree. This solution could introduce local stress concentration; the present analysis aims also at verifying whether this aerodynamic solution could be maintained or, on the contrary, needs to be modified.

A reliable evaluation of the empty weight is mandatory in any design approach of aircraft. In the case of conventional aircraft, empirical and statistical methods of weight predictions are usually adopted (e.g. [12, 13]); the reliability of these methods derives from more than 50 years experience on design and utilization. In the case of a PrandtlPlane, these statistical methods are no longer valid, and no previous experience is available so far; the only way to predict the structural weight is to design the lifting system.

The design method adopted in this paper has been carried out at the Department of Aerospace Engineering of Polytechnic of Milan. This method is an optimization tool initially conceived for cantilever wings, and it was applied successfully to predict the empty weight of wings [3]. This tool was then modified to include also a PrandtlPlane wing system. The optimization procedure is applied to the wing box only, while the weight of the leading and trailing edge systems is evaluated with a statistical method developped in [13]; these systems are equivalent to dead loads positioned along the span. The objective function is thus the weight of the lifting system box beam, and the optimization is carried out at different stages: results concerning the first stage are reported in this document.

In the first stage the wings are simulated as beams, a mono-dimensional model subjected to external aerodynamic and inertial forces; the shape of the wing box is a rectangular section supposed to be continuous along the span so as to use a gradient-based module for the optimization (SOL200 of Nastran [1]), which was used at the beginning, while recently OPTIMUS (LMS) has been preferred as optimization driver, coupled with Nastran for static, dynamic and aeroelastic analyses.

The positions of ribs are given, and the distance between them is kept constant both in horizontal and vertical wings and, also, in the fins. In the present preliminary design, this assumption allows a great numerical simplification of the problem while the weight estimation was supposed to be acceptable; the final results suggest that some weight saving could be obtained by removing this hypothesis.

The optimization procedure takes different constraints into account; stability of the compressed structures, aileron aeroelastic stability, aeroelastic effects on the loads applied, and flutter. Because the optimization against flutter could depend on the simplified procedure used, the structure obtained has been then selected as a basis for specific further analyses reported in this book [8].

The results of the optimization process on the doubly symmetric wing box indicate that the empty weight of the lifting system, including the two fins, is 17.8% of maximum take-off weight; the optimization was conducted supposing that the total fuel embarked into the box is 79.790 kg. This structural solution is not the optimum one due to the hypothesis of double symmetry of the wing box. A new wing box has been studied with the introduction of two more parameters, namely the areas of two spar flanges; in this case, the empty weight becomes 15.8% of MTOW, similar to the actual most efficient conventional aircraft. After the second stage of design, a 3D Finite Element analysis could allow us to check the reliability of the procedure used or to study local details of the wing structure; this analysis is reported in a chapter of this book [9].

3 First-Stage Optimization Procedure

The first-stage optimization is mainly used into the preliminary design stage to determine the best stiffness distributions along the beam axes. The layout of the process, with the interactions between the different computer codes, is shown in Fig. 2:

"Interface to aircraft design" is the set of information on wing geometrical properties, aerodynamic characteristics, load conditions, constraints and constitutive characteristics of materials. The aerodynamic module is a Boundary Element Method code to determine the pressure distribution on the wings and, also, to locate the aerodynamic and inertial forces along the wing axes, together with the associated moments; these data are transferred to the Structural Optimization module. The inputs of the Structural Optimization module are the aerodynamic forces applied and the structural data; the outputs are masses and inertial properties along the wing spans, local forces and moments applied and the stiffness distribution that minimize the overall weight resulting from Nastran SOL200 optimizer.

3.1 Structural Model

The process starts with the translation of the basic aircraft design into data for both structural and aerodynamic models; the initial data include non-structural mass

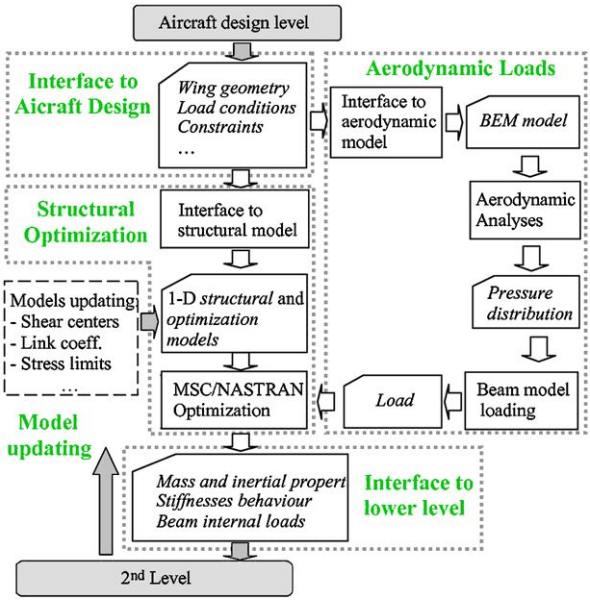

Fig. 2 Stage-1 optimization procedure

(leading and trailing edge) and the fuel mass. The total fuel mass embarked is 79.790 kg, inside both front and rear wings, in accordance to the local volume available into the wing box. The leading and trailing edge masses are estimated by means of empirical formulae to take also the masses of the hydraulic, pneumatic and electric devices into account; the estimation of the total mass of these devices is 8.638 kg; these masses are assumed to be proportional to the chord lengths and positioned along the wings as point masses by means RB2 elements. According to [14], the single plants influence total weight as follows: 29% leading edge mobile systems, 17% leading edge fixed systems, 21% fixed trailing edge systems, 22% mobile trailing edge systems, 9% ailerons and spoilers, and 2% others. Figure 3 shows the one-dimensional model of the lifting system, including the masses on the leading and trailing edge, the masses of fuel and the positions of them. The lifting system has been divided into 54 beam elements, and the nodes are numbered starting from the centreline of the front wing; elements 1–23 identify the front wing including the connection wing–winglet, elements 24–29 identify the vertical wing, elements 30–48 the aft wing, and elements 49–54 the fin of the half wing. Rigid elements RBE2 are used to connect the beam section to punctual masses, i.e. leading and trailing edge masses put on their centre of gravity; in addition, the structural mass of the ribs is applied at each end of the beam elements, whereas fuel mass is divided into a set of concentrated masses, positioned along the span and linked to the nodes. The local reference system is defined according to Fig. 4; the x-axis in node i is directed to node $i + 1$, starting from node 1 of the front wing and following the sequence of nodes given before; the y axis is directed from the local leading edge towards the trailing edge, and z-axis is defined according to the right-hand rule. The model shown in Fig. 3 is generated automatically.

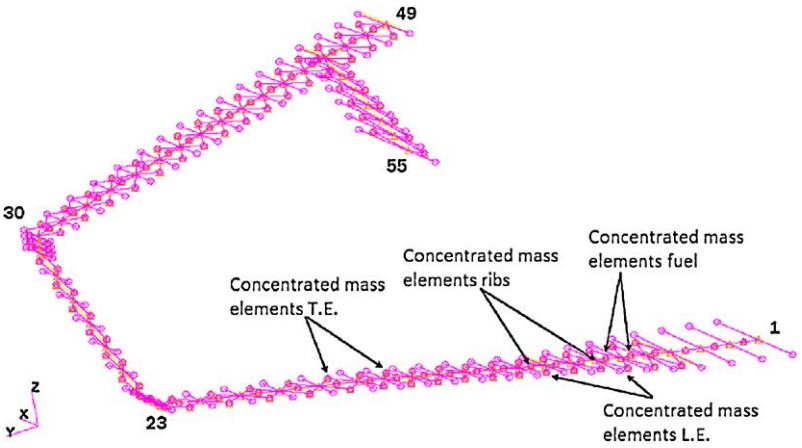

Fig. 3 One-dimensional structural model of the PrP250, isometric view

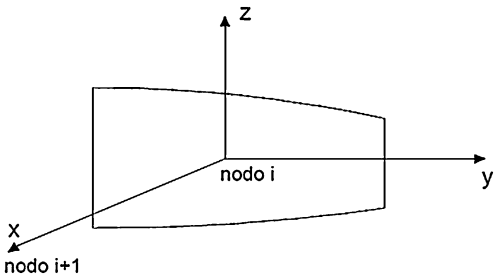

Fig. 4 Definition of the local reference system

The aerodynamic loads are assessed by means of ALIS code [2], developed at Polytechnic of Milano in the case of linear stationary and non-stationary aerodynamics. ALIS is a zero-order BEM code, based on a direct integration of the Green integral equation for stationary and non-stationary aerodynamics corrected with the compressibility effects; the wake is fixed. A code, ALISEO, generates the surface mesh, starting from the wing profiles. The aerodynamic analysis is performed by means of code ALISSTA, which generates the pressure distribution on the wings; finally, a loading interpolation procedure generates the aerodynamic forces and moments at the aerodynamic nodes. The interaction between aerodynamic loads and structural flexibility is accounted for by looping ALIS and NASTRAN, by means of geometry modifications due to structural deflection; there is no need for a full convergence, being 98% and more the effects obtained by two iterations and being load used to modify the structure.

The lifting system is made of Aluminum alloy 2024, with the following properties: density = 2800 kg/m^3, Young's modulus = 70 GPa, Poisson's ratio = 0.33, shear modulus = 27 GPa.

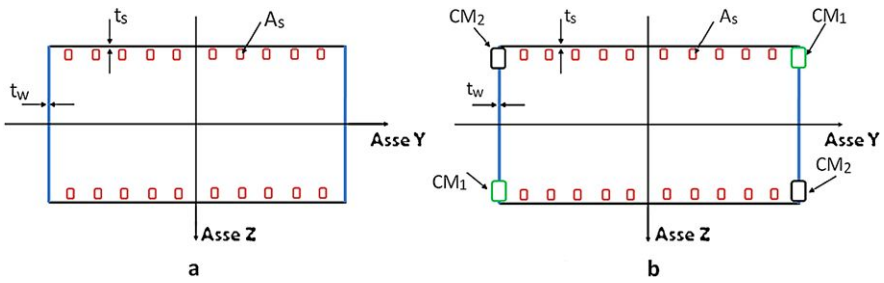

Fig. 5 Parameter wing section

4 Second-Stage Optimization Procedure

Once the one-dimensional beam system has been optimized, the second stage of the design procedure is activated in order to define the sections of the wing box (generated automatically along the span). As said before, this optimization is conducted by means of a neural network, starting from some preliminary assumptions summarized as follows:

- position of front spar and rear spar: 18% and 68% of the local chord, respectively;
- rib spacing: 0.75 m for all the wings, normal to the local beam axis;
- rectangular shaped wing box (eight and width are the average values of the actual sections);
- two different models of the wing box, shown in Fig. 5, cases (a) and (b).

The parameters used in Fig. 5(a) to describe the sections have been limited to the following:

- t_s: skin thickness (the same for upper and lower skins).
- t_w: spar web thickness (the same for front and rear spars).
- A_s: total area of the stringer sections (the same for upper and lower panels).

The solutions in Fig. 5(a) and (b), will be discussed separately in this paper; in the case of the solution in Fig. 5(b), the following parameters have been added:

- CM1, CM2: areas of the flanges in the positions northeast–southwest and northwest–southeast, respectively.

Other approximations are added to the previous ones, namely:

1. The relationships between the design parameters and the geometric properties are approximated as follows (Dvprel of Nastran is used):

$$\begin{cases} J_z = (t_w h + CM1 + CM2 + (A_s * N))\frac{c^2}{2} + t_s \frac{c^3}{6}, \\ J_y = t_w \frac{h^3}{6} + (t_s h + CM1 + CM2 + (A_s * N))\frac{h^2}{2}, \\ J_t = \frac{2\Omega^2 t_w t_s}{c t_w + h t_s}, \end{cases} \tag{1}$$

where c, h and Ω are width, eight and area of the section, respectively;

2. The initial position of the shear centre is supposed to coincide with the centre of gravity; during the optimization, the error is corrected;
3. The beam axis coincides with the centre of the section, independently of the efficiency of the panels in tension and compression;
4. The stiffener sections are the same in the upper and lower panels.

4.1 Objective Function and Constrains

The objective function is the volume of the structure to be minimized. The constraints considered are: (i) maximum allowable stress, (ii) instability of stiffened panels under compression, (iii) aileron's effectiveness, (iv) aeroelastic effects on load distribution and (v) flutter speed. A brief description of the single constraints is exposed in the following.

4.1.1 Stress

Von Mises allowable stress is assumed as 233 MPa at $n_z = 2.5$ limit load factor; this value is lower than yield stress of the Aluminum alloy ($\sigma_y = 290$ MPa) in order to account for phenomena like local stress concentrations, fatigue strength, stability of compressed structures, etc. The allowable stress corresponds to $\sigma = 93$ MPa at cruise speed and Maximum Take Off Weight.

4.1.2 Static Stability Under Compression Loads

The critical stress is evaluated in any compressed panel and is compared with the actual stress; the optimizer guarantees that the critical stress is not lower than the allowable one (233 MPa). The critical stress of stringers is given by the Euler formula

$$\sigma_{S\mathrm{cr}} = \frac{\pi^2 E I_s}{l^2 A_s}, \tag{2}$$

where I_z is relevant to the stringer together with the collaborating skin; l is the distance between the ribs ($l = 0.75$ m, constant); A_z is the area of stringer plus the collaborating skin. All the stringers are identical with a Z section and a constant ratio between flange width (d) and height (h) independently of the position along the span; we assume that $d/h = 0.3$. The critical stress of a panel under compression stress is

$$\sigma_{P\mathrm{cr}} = \frac{\pi^2 E k_c}{12(1-\nu^2)}\left(\frac{t}{b}\right)^2, \tag{3}$$

where t is the equivalent thickness of the panel, ν is the Poisson modulus, b is the stringer distance, and K_c is a non-dimensional coefficient related to t/b [4].

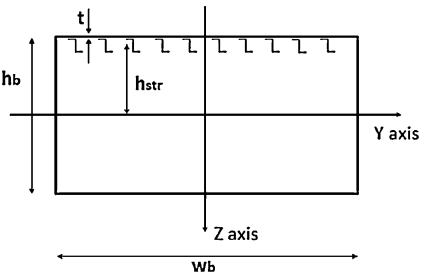

Fig. 6 Parameters of the wing sections

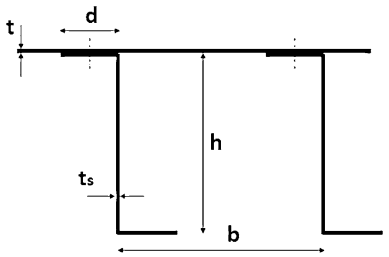

Fig. 7 Stringer section

As said before, we assume a Z section of the stringers and a constant thickness of the skin (Figs. 6 and 7); besides, the initial area of the stringers is nil because the efficiency is maximum when all material is into the skin. Thus, we introduce the stringers to enhance the critical stresses of the panels, and we reduce the skin thickness step by step, while controlling that the inertial properties from stage 1 are satisfied at any cycle. This design process is described in the following procedure.

(i) The number of stiffeners, N_r, is initially assumed as a percentage of the box width, w_b.
(ii) The critical Euler and local stresses are prescribed; they are smaller of the yielding stress of material and higher of the allowable stress, 233 MPa. The ratio between the stringer thickness and the skin thickness in prescribed in the range 0.6–1.6 for technological reasons.
(iii) The skin thickness is reduced by steps of 0.01 mm, and, at any iteration, we impose that the reduction of inertia of the skin (Iskin) is accomplished by an improvement of the inertia due to the stringers (Istr); in this process the weight, obviously, cannot decrease.
(iv) Given Istr, we solve a fourth-degree polynomial equation which gives the height (h) of the stringer and, consequently, the flange width (d), the thickness (t), the stringers area (A_s) and the centre of gravity of the stringers are determined.
(v) The Euler and local critical stresses of the section made by the stringer plus the collaborating skin area are calculated and compared with the critical stresses stated before. If the actual stresses are higher than the critical stresses, a new reduction of the skin thickness is performed and a cycle repeated. The crippling stress is also assessed together with a check to verify that this stress is higher than the yielding one.

(vi) The previous procedure is repeated with a new number of stringers.
(vii) The final solution minimizes the total area of the section.

4.1.3 Aileron Effectiveness

Aileron effectiveness is a requirement able to constrain the stiffness of a wing. The incremental load due to the aileron deflection induces a change in airfoil attitude and a modification of lifting forces; a positive sweep angle reduces the aileron efficiency due to the well-known bending effect; the opposite happens for a negative sweep angle. It is to be noted that PrandtlPlane wings allow one to position the ailerons on the rear negative swept wing or to split it between the front and rear wings. The best solution from the point of view of the control efficiency is to split the aileron on both the wings [10, 15, 16]. In the present analysis, however, only one aileron is put on the rear wing for simplicity sake and, also, because the aileron efficiency is very high and no weight increment is produced. Roll effectiveness is evaluated as

$$\eta = \frac{M_{\text{Roll}}}{M_{\text{RollRigid}}}, \tag{4}$$

where M_{Roll} is the actual rolling moment, and $M_{\text{RollRigid}}$ is the rigid body rolling moment; the condition $\eta = 0$ corresponds to the aileron reversal. The two terms are obtained as outputs of the application of a unit step of aileron, using the strip theory to assess the aeroelastic effect.

4.1.4 Static Aeroelasticity

Static aeroelasticity is introduced as follows: initial aerodynamic loads are calculated in the hypothesis of rigid wing and the weight is minimized; the deflections of the optimized structure are calculated under aerodynamic loads by modifying the aerodynamic mesh accordingly; a new calculation is conducted on the deformed aerodynamic mesh, and the optimization is restarted accounting for the new loads; the process ends when the deflection stays within a certain tolerance between two steps.

4.1.5 Flutter Speed

It must be demonstrated that the aeroplane must be free from flutter in the flight envelope enlarged by 15%. At the cruise altitude of 10 500 m, the calculation is based on cruise Mach number, $M_C = 0.85$; at sea level, the diving speed, V_D, is directly correlated to V_C, $V_D = 1.25 V_C$. In order to maintain the CPU time affordable, the flutter analysis is executed at fixed altitudes (0 m and 10 500 m) and fixed Mach number (0.8) up to the maximum velocity, $V_{\max}$, during the optimization process; of course, this produces some errors to be discussed later on.

Table 2 Influence of the constraints on wing weights

	Case A	Case B	Case C	Case D	Case E
Wingbox, fuselage	1345	1414	1414	978	996
Wingbox, front wing	5313	5837	5837	3845	4065
Wingbox, rear wing	5776	6405	6405	8914	8914
Wingbox, bulk	500	617	617	638	684
Wingbox, fin	1000	1167	1167	1471	1471
Wingbox, complete	27868	30880	30880	31692	32260
Wing, complete	36506	39518	39518	40330	40898

5 Optimization Model with a Three-Parameter Wing Box Section

The optimization process was applied in the case of a wing box defined by the three parameters (web thickness, skin thickness and stringer area) for a total of 162 variables with 54 beam elements. The optimization is conducted in the presence of the wing plants (8.638 kg including all the ribs for a total of 716 kg), and the weight of the fuel inside (79.790 kg). The constraints are applied successively so that their influence on the structural design can be easily evaluated; the cases considered are the following.

Case A: Constraint on maximum stress (233 MPa at the limit load factors $n = 2.5$).
Case B: Same as Case A with an additional constraint on the stability of stiffened panels.
Case C: Same as Case B with the additional constraint of aileron's effectiveness. The minimum aileron's effectiveness has been stated as 52%.
Case D: Same as Case C taking static aeroelasticity effects on loads distribution into account.
Case E: Same as Case D with the additional constraint on flutter speed.

Table 2 shows the evolution of the objective function (weights) following to the constraints application.

Table 3 shows the percentage of weight increments due to the single constraints. It is interesting to remark that the design against instability under compression loads produces the highest weight penalty; the penalty is remarkable on the vertical wings, subjected to a high compression stress deriving from the lift difference of the front and rear wings (about 54% on the front wing and 46% on the rear one); in the case of the fins, the high weight penalty is due to an anomalous sweep angle. The present sweep angle is too high, and the fin shape has to be modified by increasing root chord and reducing the sweep angle accordingly, as shown also in [16].

The estimated total weight of the wing box, fins included, is 32.260 kg, and, considering the control systems, it becomes 40.898 kg, 17.8% of MTOW. In a modern two-engine transonic aircraft (e.g. A300) the weight of the lifting system is about 16.5% of MTOW; the fuel weight is not included, though it has been considered in

Table 3 Percentage variation of structural weights

	Δ_{A-B}	Δ_{B-C}	Δ_{C-D}	Δ_{D-E}
Wingbox, fuselage	+5.1%	0%	−30.8%	+1.8%
Wingbox, front wing	+9.9%	0%	−34.1%	+5.7%
Wingbox, rear wing	+9.8%	0%	+39.1%	0%
Wingbox, bulk	+23.4%	0%	+3.4%	+7.2%
Wingbox, fin	+16.7%	0%	+26%	0%
Wingbox, complete	+10.8%	0%	+2.6%	0%
Wing, complete	+8.2%	0%	+2.0%	+1.4%

the structural model. Thus, the first solution found is unfavourable compared with the empty weight of an efficient conventional aircraft.

The constraint on aileron's effectiveness does not require any additional weight; the particular geometry of the lifting system, with the ailerons mounted on the negative swept wings, offers high aileron efficiency. As said before, the final configuration of ailerons will be different, with double ailerons at the tips of both wings; the efficiency of this system will not vary significantly. Static aeroelastic effect on load redistribution is favourable for the front wing, where lift is reduced due to out-of-plane bending and torsion coupling that generates lower angles of attack and is unfavourable for the aft wing where the opposite occurs. Taking these previous effects into account, the overall result is a 2% increase in total weight. The movement of the centre of gravity of the whole wing during the optimization is taken into account. The introduction of the Flutter constraint produces a weight increment on the front wing (including the trunk inside the fuselage) and also in the vertical wings; owing to the stiffness improvement introduced before, the rear wing already satisfies the flutter constraint. Some comments on flutter are needed; first, the flutter analysis is approximate; second, there is a total lack of data and experience about the flutter phenomenon of a PrandtlPlane wing. For these reasons, a detailed study on flutter has been reported into a proper paper, published in this book [8]. According to the results shown before, the flutter constraint produces 1.4% increment of total weight. The final weight repartition is the following:

- Back wing 55%
- Front wing 32%
- Winglets 4%
- Fins 9%

Now, some characteristics of the sections are illustrated. Figure 8 shows the skin thickness of the aft wing and the variations due to the constraints application. Node 1 is at the central section of the aircraft, node 4 is at the outer fuselage, node 9 is the end of the kink, and node 23 is the wing tip. The curve corresponding to step A is the highest one, and the maximum is located at node 9, the end of the kink. Passing from A to B (B and C are equal), the thickness diminishes of about 7 mm; more significant reductions occur for step D (static aeroelasticity), and no other variation is introduced for step E (flutter). The thickness is reduced when passing

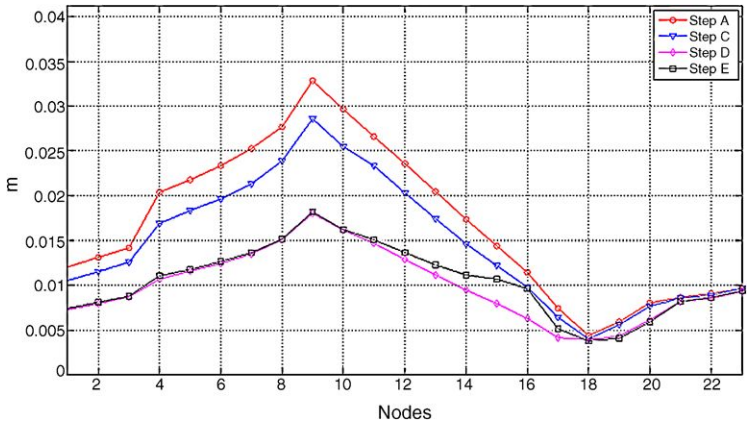

Fig. 8 Skin thickness of the aft wing along the span

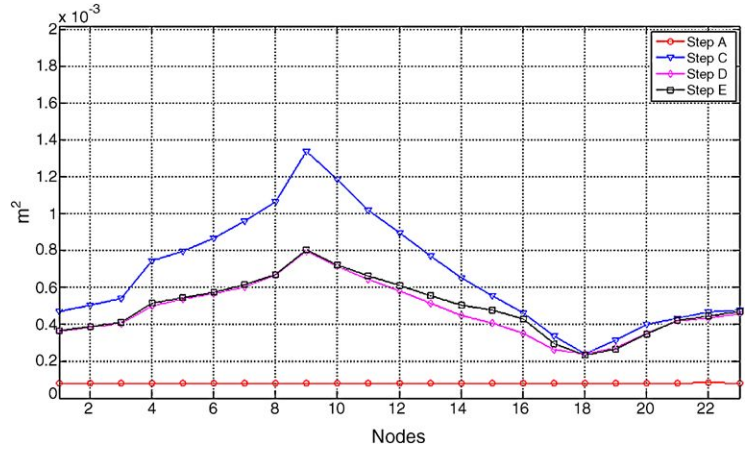

Fig. 9 Stringer section along the aft wing

from step A to B due to the introduction of stiffeners; in total, the presence of the stiffeners produces an improvement of material volume given the lower efficiency of them, compared to the pure skin. The end of the kink appears to be a critical point; the results of the structural analysis confirm this conclusion, as shown in the next figures. All the curves converge in node 18 (at about 78%, of the span), where bending moment M_y becomes zero. Flutter produces only a slight modification of thickness; on the contrary, static aeroelastic effects on load distribution reduce the thickness significantly (from 33 mm to 18 mm).

The area of the stringers in the aft wing is deployed in Fig. 9; the variation along the span is similar to the skin thickness; the static aeroelasticity reduces the stringer sections, and the aeroelastic constraint does not modify the weight of the stringers

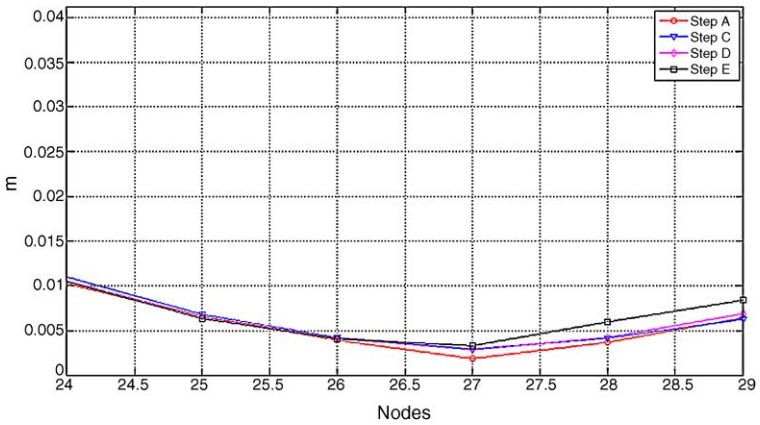

Fig. 10 Skin thickness variation on the vertical wings

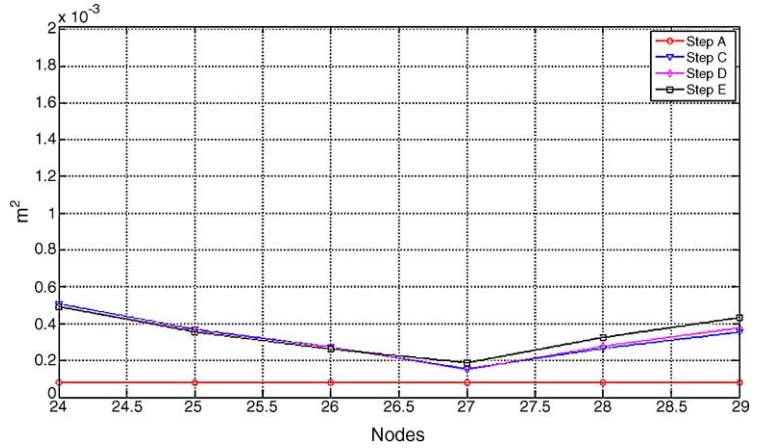

Fig. 11 Stringers section area on the vertical wings

with the exception of node 16. Once again the end of the kink, node 9, is the most critical section of the aft wing.

Along the vertical wing, the skin thickness experiments small variations; the same happens for the area of the stringers (Figs. 10 and 11).

The evolution of the skin thickness along the aft wing box is presented in Fig. 12, where node 30 is the wing tip, node 46 corresponds to the position of the fin, and node 48 to the symmetry plane. Between node 38 and wing tip, the thickness improves, and the contrary happens (with a more evidence) from the root to node 38. The skin thickness is always maximum at the fin support (node 46). Contrary to the aft wing, the static aeroelasticity constraint produces a weight increment; the flutter constraint is more influent in the tip segment (between node 37 and the tip). The thickness is very high (very close to 40 mm) around the fin support even though the

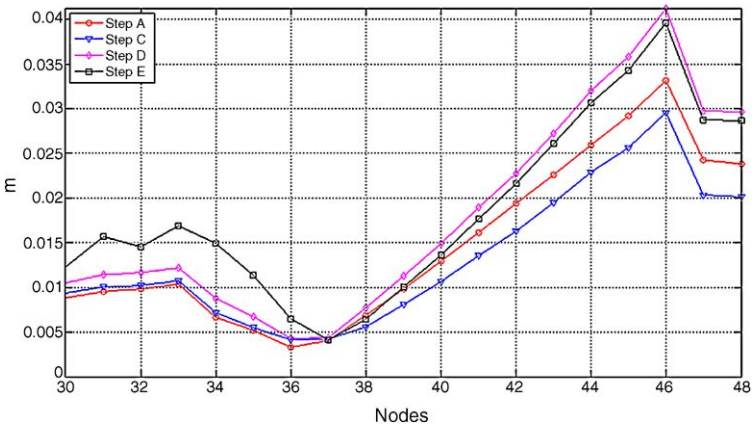

Fig. 12 Skin thickness of the aft wing

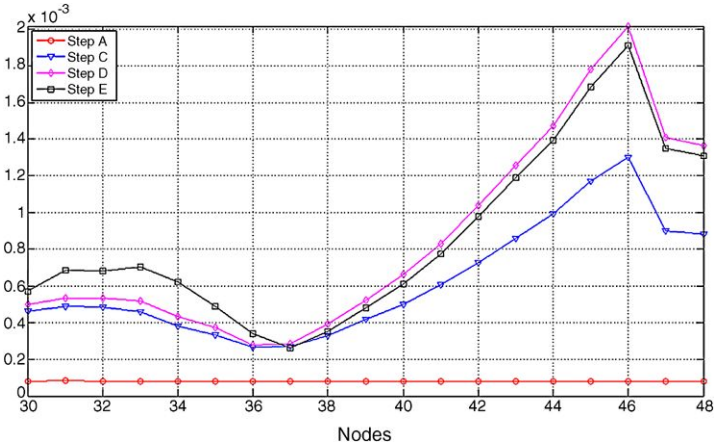

Fig. 13 Area of the stringer section of the aft wing

peak of thickness is local and can be reduced in a local design; serious technological problem could arise, but, fortunately, the skin thickness in that region will be strongly reduced when adopting an asymmetrical box section (see the next section). A similar behaviour happens for the stringer section in Fig. 13, which, in turn, is the same of the M_y bending moment [5].

The skin thickness of the fin varies according to Fig. 14. The differences are more significant close to the aft wing (node 49), where the final thickness is near to 32 mm; the thickness variations are very small in correspondence with the rear wing tip (node 54), where the thickness is about 7 mm. The area of the stringer sections varies in accordance to the variation of the thickness, as deployed in Fig. 15.

The final thickness of the spar webs is, in general, high: in the front wing (Fig. 16) it varies between 6 mm at node 16 to 20 mm at node 9, and, the rear wing (Fig. 17),

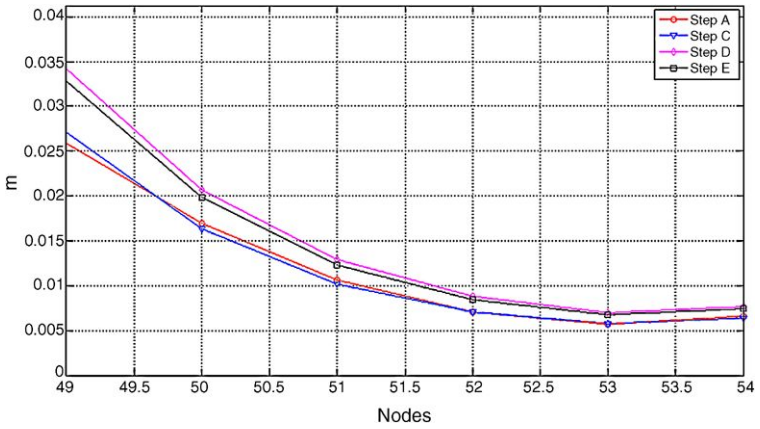

Fig. 14 Skin thickness of the fin box

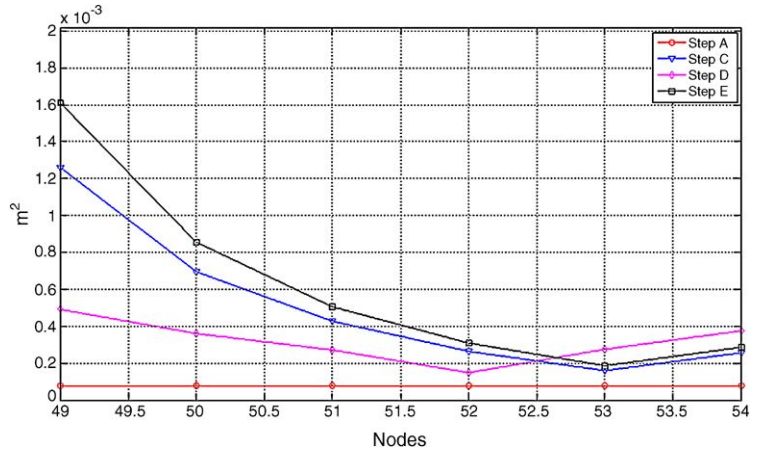

Fig. 15 Area of stringers in the fin box

between 5 mm at node 38 to 44 mm at node 45. The end of the kink in node 9 continues to be critical.

The primary difference between a PrandtlPlane wing and a cantilever wing is shown by the out of plane bending moment diagram. On a cantilever wing the bending moment is nil at the tip, while in the case of a PrandtlPlane is nil before (about 3/4 of span); thus, the maximum bending moment at the wing root is lower than that of a traditional aircraft under the same total loads. The bending moment distribution on the rear wing is clearly influenced by the presence of the fin, and, in order to reduce empty weight, the design features a maximum distance between the two fins.

The rear wing, even though the volume of the structural material is higher, has a smaller out of plane, in plane and torsional inertias with respect to the front one,

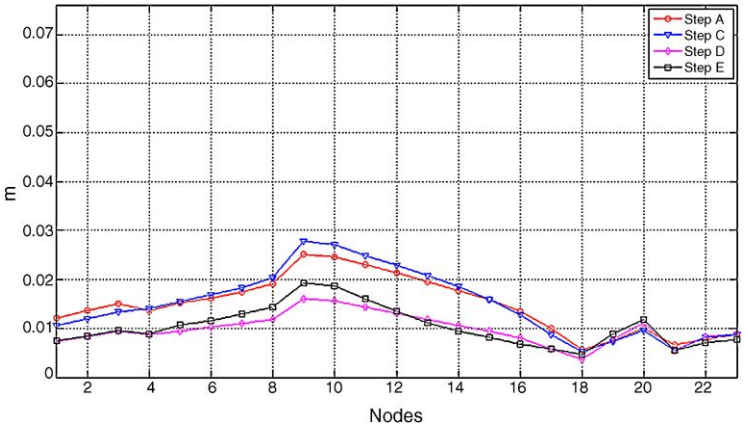

Fig. 16 Spar web thickness of the front wing

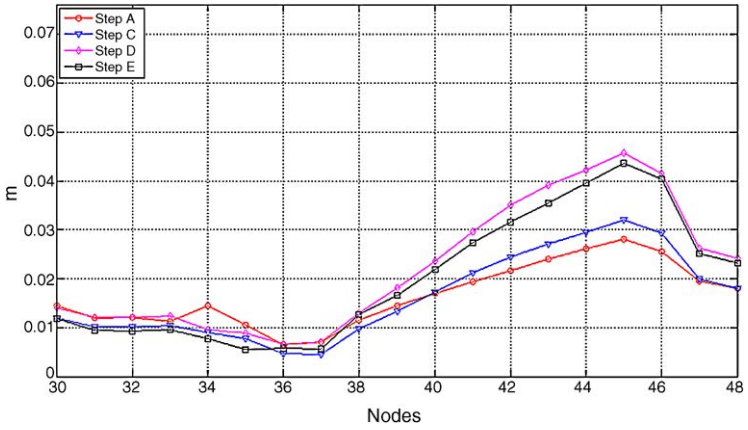

Fig. 17 Spar web thickness of the rear wing

due to the smaller thickness of the airfoils; more details on the final inertial characteristics can be found in [5].

Following the optimization process, a comprehensive flutter study was conducted in order to give more insight into the flutter mechanism and to understand the limits of the simplification adopted. For the PrandtlPlane lifting system, the problem of flutter prediction is particularly important owing to the lack of data and flight experience. A comprehensive flutter analysis is reported in a chapter of this book [8].

6 Optimization Model with a Five-Parameter Wing Box Section

The box beams of the lifting system experience in-plane and out-of-plane bending moments along the span. In plane is referred to the moment vector in the plane of the

Table 4 Total weight variation history of the asymmetric section

	Case A	Case B	Case C	Case D	Case E
Wingbox, fuselage	1228	1304	1304	933	933
Wingbox, front wing	4425	4701	4701	3362	3362
Wingbox, rear wing	5039	5502	5502	7277	7298
Wingbox, bulk	662	814	814	842	842
Wingbox, fin	984	1152	1152	1477	1477
Wingbox, complete	24676	26946	26944	27782	27824
Wing, complete	33314	35584	35584	36420	36462

wings and produces compression or tension in the skins, typical of a cantilever wing; out of plane is the component orthogonal to the first one, similar to the bending moments due to wing drag. The stiffness to react against the out-of-plane bending moment is given by the front and rear webs. In a PrandtlPlane, the out-of-plane component is relatively high; thus, two corners of the rectangular box (the farthest from the resultant neutral axis of the section) are the most stressed, and more axial stringers have to be positioned there to gain the maximum efficiency. A symmetric box wing section is clearly unfit to minimize the empty weight; an unsymmetrical section is needed, and there are many ways to do so. We examine the one, in which the external section shape is rectangular again, but two new variables are introduced: the areas of the spar flanges. With reference to Fig. 5b, flanges 1 are positioned in the NorthEast and SouthWest corners, and flanges 2 are in the NorthWest and SouthEast positions.

Consequently, the number of the variables improves from 162 to 270 with a very relevant increase in computational time. The equations to evaluate the beam cross section (A), principal inertia moments (I_1 and I_2), static inertia moment (I_{12}) and the torsional stiffness coefficient (J) are changed correspondingly. After having improved the number of parameters, the optimization process proceeds in the same way as before. Starting from the base solution (step A), where the von Mises stress is limited to 233 MPa, the sequence of constraints is the same. Table 4 summarizes the influence of the constraints on the weight of the single parts in the asymmetric wing box; Table 5 shows the incremental percentage variations.

Total weight (fuel excluded) has been reduced to 36.462 kg corresponding to a structural wing box of 27.824 kg; compared with the weight of the symmetric box (32.260 kg), we obtain a reduction of 4.436 kg, i.e. a reduction of 13.75% of the initial one; the total weight is now 15.8% of the MTOW, very close to that of a conventional aircraft. From Tables 2 and 4 it results that the main advantage of the asymmetric box concerns the condition of maximum allowable stress; flutter constraint is also less critical than before. Some remarks could be interesting. The introduction of the constraint on the static stability under compression (case B), produces a weight penalty of 9.2% on the rear wing and 6.2% on the front one; this result is also influenced by the dihedral angles (negative on the rear wing and positive on the front one). The weight increment of the vertical wings is caused by the

Table 5 Relative variation history of the asymmetric section

	Δ_{A-B}	Δ_{B-C}	Δ_{C-D}	Δ_{D-E}
Wingbox, fuselage	+6.2%	0%	−28.5%	0%
Wingbox, front wing	+6.2%	0%	−28.5%	0%
Wingbox, rear wing	+9.2%	0%	+32.3%	0.3%
Wingbox, bulk	+23%	0%	+3.4%	0%
Wingbox, fin	+17%	0%	+28.3%	0%
Wingbox, complete	+9.2%	0%	+3.1%	0.1%
Wing, complete	+6.8%	0%	+2.4%	+0.1%

compression loads, which depend on the higher lift acting on the lower wing (53% on the front wing and 47% on the rear one). The effect of the static aeroelasticity constraint is twofold: a reinforcement of the rear wing to recover stability against divergence and a reduction of material on the front wing; on the whole, it results in a modest weight increment (about 3.1%). A small weight increment is due to Step E (flutter) only on the rear wing. In total, the final weight distribution is the following: Rear wing 52% , front wing 31%, two fins 11%, winglets 6%. Now, we can compare the local characteristics of the sections, described by three and five parameters.

7 Comparison of Symmetric and Asymmetric Wing Box

The skin thickness of the optimum front wing asymmetric box is smaller of the symmetric one; the maximum reduction is from 19 mm to 11 mm and occurs at the end of the kink (node 9 in Fig. 18); a thickness improvement occurs (from about 9 to 14 mm) in the transition with the vertical winglet (nodes 20–23). The thickness peak around the end of the kink is due to a stress peak produced by the geometric discontinuity, and it could be reduced by local modifications, to be introduced in a detailed design step. In the symmetric case, the reduction of the skin thickness is localized in the range between nodes 18 and 19; in the asymmetric case the presence of the flanges produces a skin thickness reduction in a larger segment (between nodes 14 to 20).

In the lower segment of the winglet (starting from node 24), the opposite happens, with a thickness improvement of about 6 mm. As shown in Fig. 19, the thickness is small in the middle of the winglet, where the aerodynamic loads are small as well.

The comparison between skin thicknesses of symmetric and asymmetric sections of the rear wing is depicted in Fig. 20. The skin thickness reduction in the asymmetric section occurs along the whole span. The comparison of the skin thickness of the fins is depicted in Fig. 21; the thickness variations are more evident in the connection between fin and rear wings, where the difference is not totally realistic; no significant variation occurs elsewhere.

In the following figures the comparisons between the web thicknesses are presented. The effect of the asymmetric solution is very important in the case of the

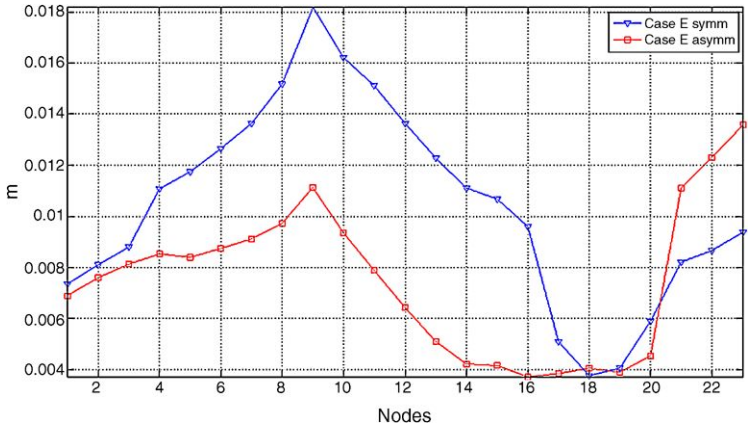

Fig. 18 Comparison between skin thicknesses of symmetric and asymmetric box of front wing

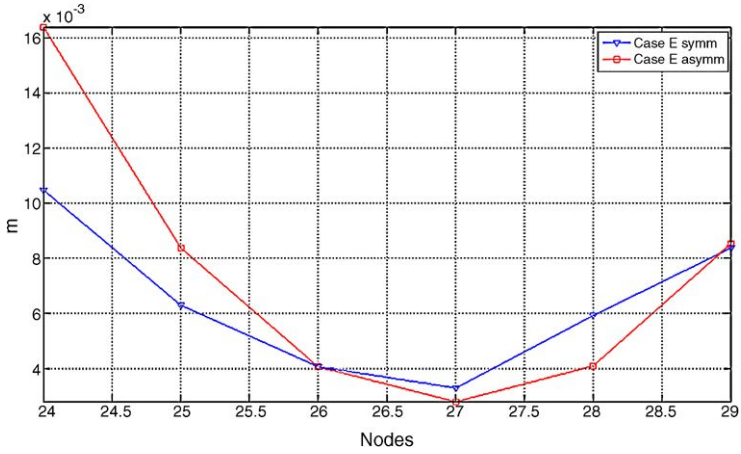

Fig. 19 Comparison between skin thicknesses of symmetric and asymmetric box of winglet

front wing where a reduction from 19 mm to 12 mm happens in the kink region; the thickness is reduced everywhere in the span (Fig. 22). Figures 23, 24 and 25 show a trend which is common to the other parameters, that is, a weight relief along all the span and a cut of the local peaks of thickness; this last aspect is an important benefit of the asymmetric section as far as technology is concerned. The same conclusions can be carried out as far as the area of the stringers are concerned; these results can be found in [5].

Due to the introduction of the cross lumped masses at the vertices, the principal axes of inertia rotate from the horizontal direction; this rotation is a consequence of the section design and, thus, is taken into account during the optimization process. More details on this modifications are to be found in [5] and show that, even though the rotation is smaller than 10 degrees, the weight reduction is relevant, as proved

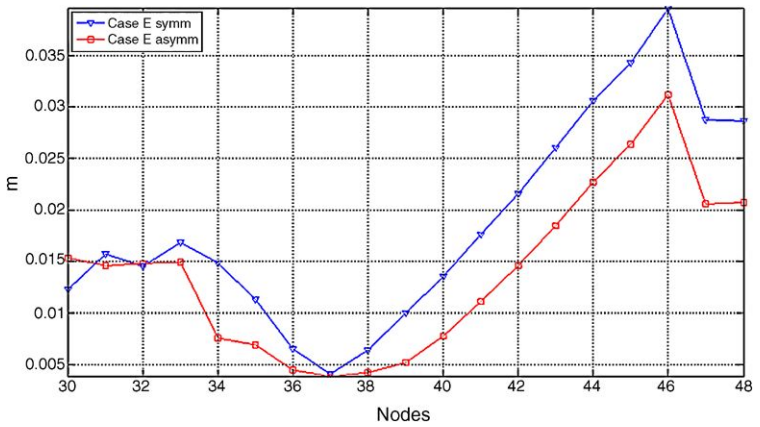

Fig. 20 Skin thickness comparison on the rear wing

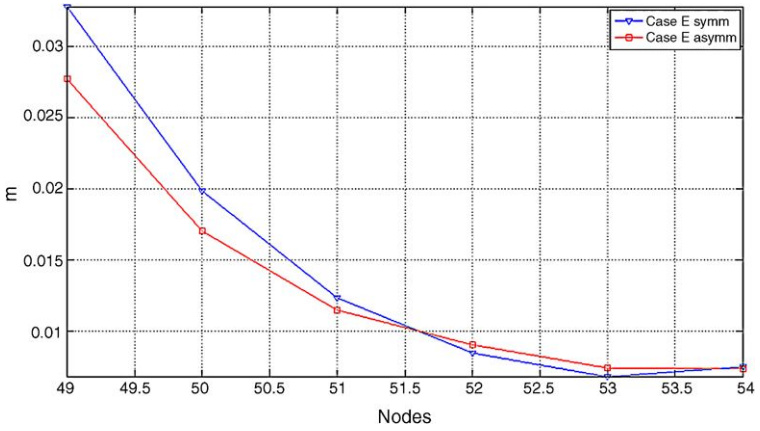

Fig. 21 Skin thickness comparison on the fin

by the significant. decrease of the total weight. The material to react to torsion is reduced thanks to the introduction of the asymmetry. In the case of the front wing, the reduction is large between the root and half span, and the same occurs for the rear wing [5].

Lastly, a comparison between the structural weight of the PrandtlPlane wing (fuel excluded) and three conventional airplanes have been chosen for comparison. The wing mass of A330-300, B767-300 and B777-300 are not explicitly available, and, thus, some analytical/statistical procedures have been conducted; also the tail weight has been estimated. The comparison is reported in Table 6.

In the limit of the approximations adopted in the present conceptual design, the PrandtlPlane configuration results comparable, in terms of wing structural efficiency, to standard solutions once the same material, an Aluminium alloy, is used.

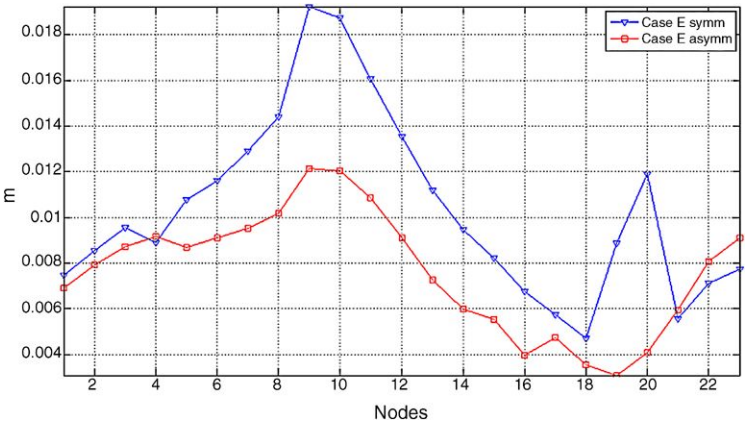

Fig. 22 Spar web thickness comparison in the front wing

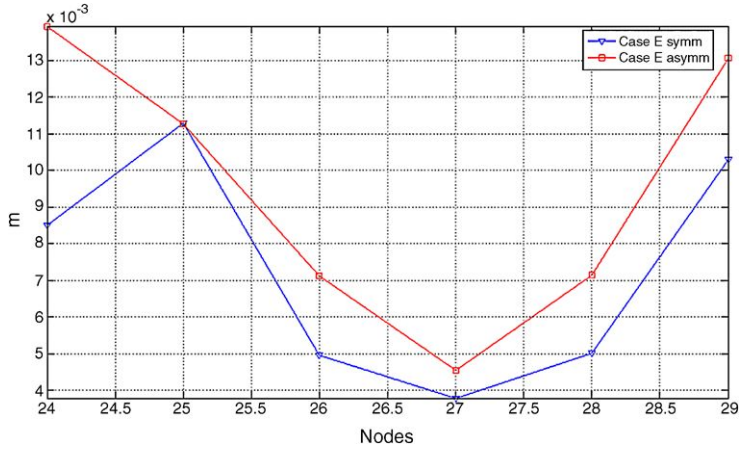

Fig. 23 Spar web thickness comparison in the vertical wing

Table 6 Comparison of the wing weights of different transport aircraft

	A330-300	B767-300	B777-300	PrP250
W_{to} [kg]	230000	158758	299370	230000
$W_{\text{wing+tail}}$ [kg]	37067	22701	52438	36462
$\frac{W_{\text{wing+tail}}}{W_{\text{to}}}$ [%]	16.1	14.3	17.5	15.8

8 Conclusions

A structural design of a PrandtlPlane wing system is carried out in order to evaluate the efficiency to be compared with conventional aircraft wings. The aerodynamic design of the wing system includes a kink and, at the end of it, a variation of the di-

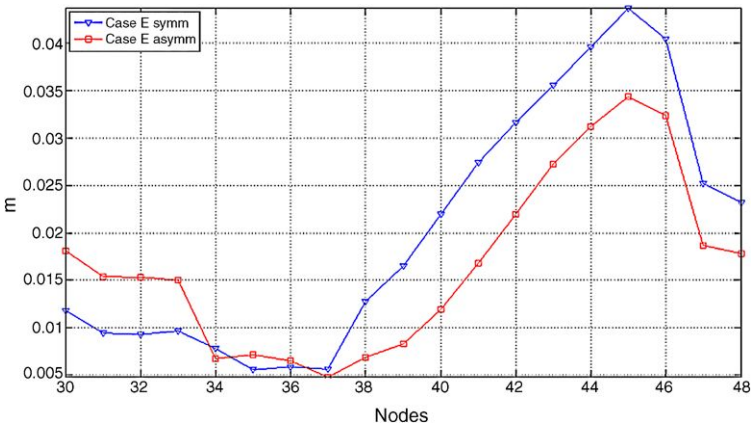

Fig. 24 Spar web thickness comparison in the rear wing

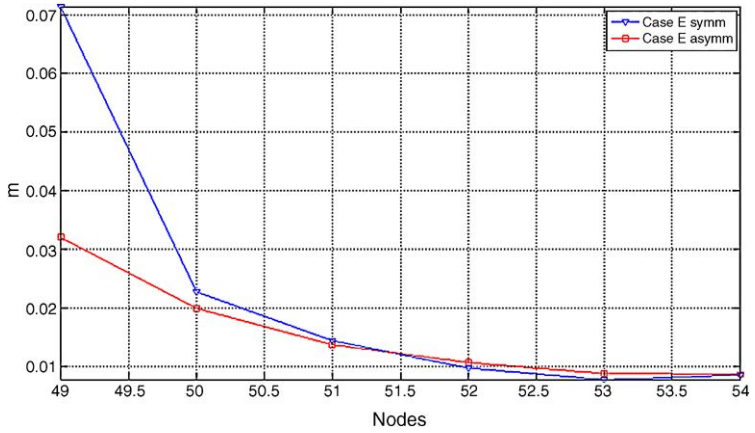

Fig. 25 Spar web thickness comparison on the fin

hedral angle. The structural design has been developed by means of an optimization procedure set up at Milan Polytechnic, with the following constraints: maximum stress of 233 MPa at the limit load factor $n = 2.5$, stability of compressed panels, aileron efficiency, static aeroelastic effects on load distribution and flutter.

The results obtained indicate to modify the doubly symmetric wing box shape introducing an asymmetric section.

This modification proved to be successful and the total $W_{\text{wing}}/MTOW$ passed from 17.5% to 15.8%, similar to well-optimized conventional transport aircraft. Skin and spar webs are thick, and the consequent technological aspects have to be faced with great attention. In particular, the skin thickness, web thickness and area of the stringer section present a peak in correspondence of the end of the kink. The analysis performed in this paper indicates that the double dihedral angle of the front

wing must to be modified into a single constant dihedral angle all over the span. Thus, the weight estimation performed so far could be ameliorated.

References

1. MSC Nastran User's Manual. MSC Software Corporation
2. Bindolino, G.: Determinazione delle forze aerodinamiche per la soluzione di problemi aeroelastici di configurazioni complesse in campo subsonico. Master's thesis, Politecnico di Milano (1984)
3. Bindolino, G., Ghiringhelli, G., Ricci, S., Terraneo, M.: Multilevel structural optimization for preliminary wing-box weight estimation. J. Aircr. **47**, 475–489 (2010)
4. Bruhn, E.F.: Analysis and Design of Flight Vehicles Structures. Jacobs Publishing, Phoenix (1973)
5. Dal Canto, D.: Progetto preliminare del cassone alare di un velivolo di tipo Prandtl-Plane mediante l'applicazione di un ottimizzatore multilivello. Master's thesis, Università di Pisa (2009)
6. Frediani, A.: The Prandtl Wing. In: Lecture series on Innovative Configuration and Advanced Concepts for Future Civil Aircraft (2005)
7. Frediani, A., Cipolla, V., Rizzo, E.: The PrandtlPlane configuration: overview on possible applications to civil aviation. In: Buttazzo, G., Frediani, A. (eds.) Variational Analysis and Aerospace Engineering II: Mathematical Challenges for Aerospace Design. Springer, Berlin (2012)
8. Frediani, A., Divoux, N.: The lifting system of a PrandtlPlane, Part 2: Preliminary study on flutter characteristics. In: Buttazzo, G., Frediani, A. (eds.) Variational Analysis and Aerospace Engineering II: Mathematical Challenges for Aerospace Design. Springer, Berlin (2012)
9. Frediani, A., Quattrone, F., Contini, F.: The Lifting System of a PrandtlPlane; Part 3: Structures Made in Composites. In: Buttazzo, G., Frediani, A. (eds.) Variational Analysis and Aerospace Engineering II: Mathematical Challenges for Aerospace Design. Springer, Berlin (2012)
10. Van Ginneken, D.A.J.: Automatic control surface design & sizing for the PrandtlPlane. Master's thesis, Delft University of Technology (2009)
11. Piasentin, F.: Progetto preliminare del cassone alare di un velivolo in fase di avanprogetto mediante ottimizzatore multilivello. Master's thesis, Politecnico di Milano (2003)
12. Roskam, J.: Airplane Design: Preliminary Sizing of Airplanes. DAR Corporation (1997)
13. Torenbeek, E.: Synthesis of Subsonic Airplane Design. Delft University Press, Delft (1972)
14. Torenbeek, E.: Development and application of a comprehensive, design-senstive weight prediction method for wing structures of transport category aircraft. Technical report, Delft University of Technology (1992)
15. Van Ginneken, D.A.J., Voskuijl, M., Van Tooren, A., Frediani, A.: Automatic control surface design & sizing for the prandtlplane. In: AIAA Conference in Orlando (USA) (2010)
16. Voskuijl, M., De Klerk, J., Van Ginneken, D.A.J.: Flight mechanics modeling of the Prandtl plane for conceptual and preliminary design. In: Buttazzo, G., Frediani, A. (eds.) Variational Analysis and Aerospace Engineering II: Mathematical Challenges for Aerospace Design. Springer, Berlin (2012)

The Lifting System of a PrandtlPlane, Part 2: Preliminary Study on Flutter Characteristics

N. Divoux and A. Frediani

1 Introduction

Aeroelasticity is the field in aerospace engineering that considers phenomena of *interaction* between aerodynamic flow and elastic structures. At the event of aviation, aeroelasticity was not entirely understood, and its influence not recognized. Aeroelastic issues became important when aircraft increased their size and became lighter, while flying faster and higher. Unexpected large deflections and self-sustained oscillations with dramatic rate of growth that could both lead to structural failure started to appear. Once these phenomenons were recognized after World War I, simplified static and dynamic analyses were carried out. During World War II, significant improvements in aeroelastic analysis were made by taking the effect of compressibility and unsteady aerodynamics into account. In the 1960s, digital computers contributed to new prediction methods, and the first methods for three-dimensional incompressible unsteady flow appeared. In the 1970s it became possible to predict the dynamics of real aircraft configuration. These analysis took place during the verification stage of the design. The growing power and availability of today's computing methods tend to consider aeroelasticity earlier in the design cycle, and modern transport aircrafts are now optimized taking aeroelasticity into account. The problem of aeroelasticity is thus shifting from preventing instability at the stage of design verification to designing a configuration in which aerodynamics, structure and active control are optimally combined for maximum performance and efficiency.

N. Divoux (✉)
Delft University of Technology, Delft, The Netherlands
e-mail: nicolas.divoux@gmail.com

A. Frediani
Department of Aerospace Engineering, University of Pisa, Via G. Caruso 8, 56122 Pisa, Italy
e-mail: a.frediani@dia.unipi.it

G. Buttazzo, A. Frediani (eds.), *Variational Analysis and Aerospace Engineering: Mathematical Challenges for Aerospace Design*, Springer Optimization and Its Applications 66,
DOI 10.1007/978-1-4614-2435-2_10,

Flutter, in particular, is a self-sustained excitation of the structure by the airflow around it arising at certain conditions of airspeed, dynamic pressure, centre of gravity position and configuration. It must be demonstrated that all different configurations of the aircraft are free from flutter. Thus, all aerodynamic and structural variations have to be assessed. Aerodynamic variations are particularly critical in combat aircraft, in which external store configurations significantly affect both aerodynamic and mass properties, but different loading conditions are present in civil aviation as well, according to the fuel on board and flight altitude. Combining all possible variations leads to a significant amount of cases, and computation costs and time increase significantly. It is thus of common practice to reduce these cases to a subset that can be treated in a realistic amount of time. They are called critical configurations and are most susceptible to cause problems. These configurations are based mainly on previous experience and empirical methods. There is then the risk that the most critical configuration is not detected and not analysed; this risk is present also in the actual case of a non-conventional lifting system.

In the previous structural analysis of the lifting system of a 250-seat PrandtlPlane ("PrP250"), the wing design was performed through an optimization procedure under the constraints of allowable static stress, structural stability under compression loads, static aeroelasticity and flutter too. Thus, the constraint of static aeroelasticity has been already accomplished; the introduction of the flutter constraint produced a weight increment, but the final flutter speed was close to the critical one, and, also, some approximations were present in the computation procedure; finally, no past experience is available on the PrandtlPlane wings. Thus, the design against flutter has been performed once more with the aim of investigating the influence of the main parameters and possibly finding the weight penalty associated to modify the structural configuration.

For an unconventional concept as the PrP250, the problem of flutter prediction is particularly delicate. For traditional aircraft, flutter analysis is in general based on previous experiences; for the case of the PrP250, the total absence of previous analysis requires theoretical studies. The structurally closed lifting system of the PrandtlPlane offers though new opportunities to solve possible flutter problems. On conventional aircraft, if flutter is detected in the increased flight envelope, the solution is to increase the stiffness (and weight) of the structure. This is not easy in our system because it is six-degree-of-freedom overconstrained to the fuselage, as shown in Figs. 1 and 2, and any local stiffness modification influences the behaviour of the whole lifting system. No previous study on this subject is available till now. A preliminary study of the flutter characteristics of the lifting system is presented in this paper.

From an airworthiness point of view, aeroelastic effects and particularly flutter are of primary importance. The JAR-25, relative to transport aircraft, states that:

(a) The aeroplane must be designed to be free from flutter and divergence (unstable structural distortion due to aerodynamic loading) for all combinations of altitude and speed encompassed by the V_D/M_D versus altitude envelope enlarged at all points by an increase of 15% in equivalent air speed at both constant Mach

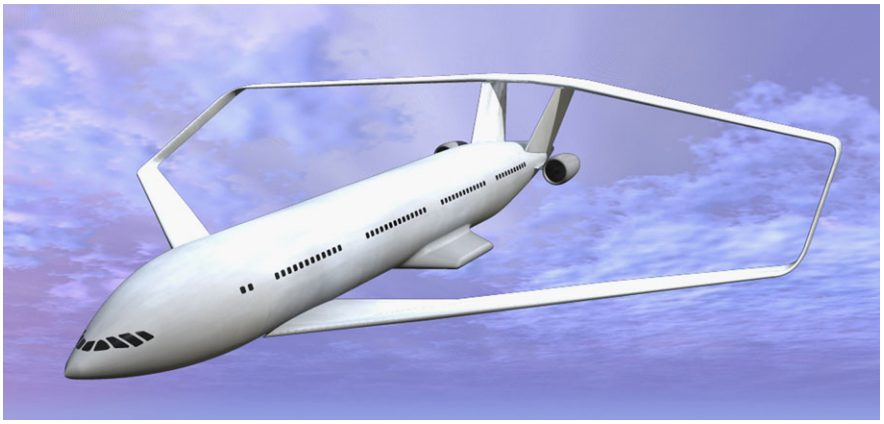

Fig. 1 Artistic view of a PrandtlPlane transport aircraft

Fig. 2 Concept of a PrandtlPlane aircraft presented at the Berlin air show ILA 2008 by Bauhaus Luftfahrt

number and constant altitude, except that the envelope may be limited to a maximum Mach number of 1.0 when M_D is less than 1.0 at all design altitudes [...].

(b) When $M_D < 1$, a proper margin of damping exists at all speeds up to M_D, and there is no large and rapid reduction in damping as M_D is approached.

(c) The aeroplane must be free of flutter or divergence that would preclude safe flight, at any speed up to V_D after:

(c1) Failure of any single element of the structure supporting any engine, independently mounted propeller shaft, large auxiliary power unit or large externally mounted aerodynamic body.

(c2) Absence of propeller aerodynamic forces resulting from the feathering of any single propeller, and, for aeroplane with four or more engines, the feathering of the critical combination of two propellers.

(c3) Any single propeller rotating at the highest likely overspeed.

(c4) Failure of critical component identified in 25.571 (e.g. wing, empennage, control surfaces, fuselage, engine mounted landing gear).
(c5) Any single failure in any flutter damping system.

The wing system shown in Fig. 1 is the result of a previous analysis regarding Flight Mechanics and Control and, also, an optimization of the propulsion system; this analysis has indicated that the best propulsion system consists of two turbofans positioned in the rear fuselage; the wings are then free of concentrated loads and aerodynamically clean; consequently, all the constraints (c1–c5) are satisfied.

The certification process is strongly influenced by flutter verification, and compliance with the requirements must be shown by analysis, wind-tunnel tests and flight tests. Practically, analytical results are often verified by wind-tunnel flutter models and ground vibration tests. The final verification is done by flight tests to prove the compliance of the aircraft to the requirements.

The development of flight flutter test technique becomes then essential to accurately determine the flutter characteristics of the actual aircraft. Although essential, these tests are very delicate to perform because of their dangerousness and the possible loss of vehicle. Even today, these tests are considered hazardous. Indeed, the speed needed for accurate predictions must be close to the actual flutter speed. Then, the trends in damping used to determine stability at a higher speed are not always accurate. Finally, aeroelastic stability may change from a stable to an unstable condition abruptly for a small increase in airspeed so that sudden flutter arises. In the case of the innovative PrandtlPlane, the difficulties are even more incremented. The advent of computers improved greatly the prediction speed. Frequency and damping were determined by parameter identification and their trends established as functions of airspeed. Extrapolation was used to determine the flutter speed. The drawback of this technique is that it requires many test points (e.g. 177 for a Gulfstream III aircraft [6]) to clear the flight envelope of the aircraft. A damping trend is then computed as a function of airspeed and extrapolated to determine the stability of the next point. In any case, a preliminary flutter analysis is fundamental in the development of the aircraft.

Flutter analyses are conducted using the flutter resolution method of the MSC NASTRAN® program. It was found that the structure optimized for all constraints does not meet exactly the requirement on flutter speed due uncertainty of the structural damping and to a simplistic flutter analysis in the optimization process; as said before, the structure optimized for all constraints but the one on flutter was thus selected as a basis for further analyses. Two different methods are then used to meet the flutter requirement: first, the skin thickness is increased on both wings. A parametric study allowed us to find out that the most efficient way to meet the flutter speed requirement was to increase the front wing's skin thickness. A 3.58% increase in structural weight is necessary to meet the flutter speed requirement. Finally, fuel mass was added at the tip of the wings; again different parameters (weight, position, distribution front/aft wing) were varied, and it was found that adding fuel mass at the front wing's tip allowed the structural design to clear flutter speed.

2 Flutter Analysis with MSC NASTRAN®

The default method to solve the flutter equation in MSC NASTRAN® is the p–k method. In order to implement a flutter analysis into MSC NASTRAN®, we start from the equation of flutter [2]:

$$\left[M_{hh}p^2 + \left(B_{hh} - \frac{1}{4}\rho\bar{c}V\,Q^I_{hh}/k\right)p + \left(k_{hh} - \frac{1}{2}\rho V^2 Q^R_{hh}\right)\right]\{u_h\} = 0, \quad (1)$$

where

M_{hh}: Modal mass matrix
B_{hh}: Modal damping matrix
K_{hh}: Modal stiffness matrix
Q^I_{hh}: Modal aerodynamic damping matrix, a function of M and k
Q^R_{hh}: Modal aerodynamic stiffness matrix, a function of M and k
p: Eigenvalue
g: Artificial structural damping
γ: Transient rate of decay coefficient. The structural damping coefficient is $g = 2\gamma$
$\bar{c}$: Reference chord length.

The eigenvalue p is

$$p = \omega(\gamma \pm i). \quad (2)$$

As written in Eq. (1), all the matrices are real. Q^R_{hh} and Q^I_{hh} are, respectively, the real and imaginary parts of the aerodynamic force matrix Q_{hh}. The reduced frequency and circular frequency are related by

$$k = \frac{\omega\bar{c}}{2V} \quad \text{or} \quad (3)$$

$$k = \frac{\bar{c}}{2V}\,\mathrm{Im}(p). \quad (4)$$

The solution of the p–k method is found by writing Eq. (1) in state space form,

$$[A - pI]\{\bar{u}_h\} = 0, \quad (5)$$

where $[A]$ is the real matrix

$$[A] = \begin{bmatrix} 0 & I \\ -M^{-1}_{hh}[K_{hh} - \frac{1}{2}\rho V^2 Q^R_{hh}] & -M^{-1}_{hh}[\frac{1}{4}\rho\bar{c}V\,Q^I_{hh}/k] \end{bmatrix}, \quad (6)$$

and $\{\bar{u}_h\}$ now contains both modal displacement and velocities. Now, the oscillatory solutions of Eq. (1) require an iterative solution satisfying both Eqs. (1) and (4). Once the k values are found, as well as the converged values for p, γ is computed as follows:

- For real root,

$$\gamma = \frac{p\bar{c}}{V \ln 2}; \tag{7}$$

- For complex root,

$$\gamma = \frac{\mathrm{Re}(p)}{\mathrm{Im}(p)}. \tag{8}$$

Then, the virtual structural damping g is computed from $g = 2\gamma$. The flutter is assumed in the point where $g = 0$, and flutter occurs for $g > 0$, i.e. for a complex root with a positive real part.

One advantage of the p–k method is that the matrices treated are real, making the computations easier. The aerodynamic forces matrix is decomposed into real and imaginary parts; the imaginary matrix is interpreted as a damping, and the real part is related to a stiffness. The convergence to the solution is rapid, and the results are produced directly for given values of the velocity. The following treats how the analysis is set up for application to the case of the PrP250. The structural model has already been presented in [4].

2.1 Aerodynamic Model

An aerodynamic model is used to solve the following matrix equations that in turn will give the aerodynamic forces and moments.

The aerodynamic method used by MSC NASTRAN® in subsonic regime is called the Doublet-Lattice method (DLM) and was first presented by Albano and Rodden [1]. This method, based on linearized aerodynamic potential theory, is commonly used for the calculation of unsteady air loads on an aircraft. The downwash factors in the DLM are calculated as the sum of an exact steady component and an approximated unsteady component. All lifting surfaces are assumed to lie nearly parallel to the flow and are divided into flat finite panels, as shown in Fig. 3. As the lifting surfaces are divided into finite panels, the DLM suffers from a discretization error and is sensitive to chordwise panelling. Thus a minimum number of chordwise boxes per wavelength has to be specified to limit this error, as well as a maximum box aspect ratio to limit the integration error. These issues are addressed in Ref. [11]. In MSC NASTRAN®, a minimum of 12.5 boxes per wavelength is advised, as well as a maximum box aspect ratio of 3. In Figs. 4(a) and 4(b), the boxes per wavelength are depicted for two different velocities. The number of boxes per wavelength is calculated as follows:

$$\frac{\text{box}}{\text{wavelength}} = \frac{\pi c}{k\Delta x} = \frac{V}{f\Delta x}. \tag{9}$$

The minimum number of box, the worst case, encountered during the flutter analysis is for $V_{\min}$ and $f_{\max}$. The maximum frequency chosen is of 8.25 Hz, corresponding to the frequency of the 10th mode. From Fig. 4(a) it is clear that the

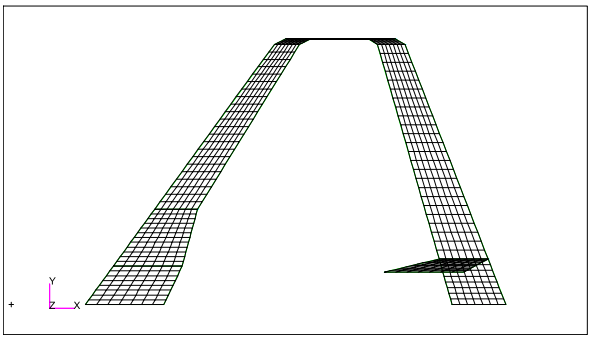

(a) Top view

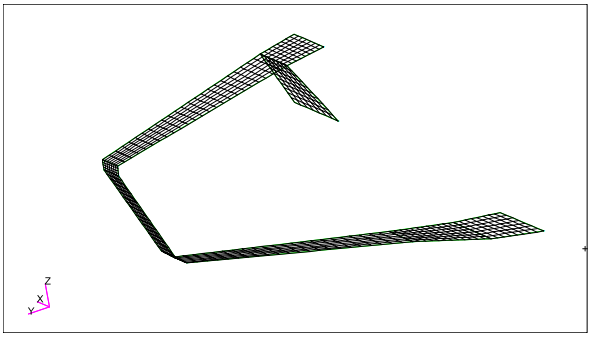

(b) Isometric view

Fig. 3 Aerodynamic model of the PrP250

aerodynamic model does not respect the minimum criteria at $V = 58$ m/s, but for a small increase in speed ($V = 128$ m/s), this criteria is met (see Fig. 4(b)). It is however not of primary importance to meet this criteria at low velocities and high frequencies, as the region of interest is the one in the vicinity of the flutter point which lies further in the velocity plot (see Sect. 3). Also, the 10th mode is unlikely to cause instability, and thus the considered frequency may be too high. Moreover, as discussed previously, the flutter model far from the flutter point does not give an exact solution; the results at low velocities are thus to be taken as trends, and an approximate model is sufficient for that. Finally, modifying the aerodynamic mesh to meet the criteria at the lowest velocity of the analysis (6 m/s for the analysis at cruise altitude) would increase significantly the size of the mesh and induce an unacceptable increase in required computer memory and computing time.

As already said, a maximum aspect ratio is set for the aerodynamic mesh in order to limit integration errors. The following figure (Fig. 5) shows the aspect ratio of the adopted aerodynamic model. The criteria of a maximum aspect ratio is met for the whole mesh. Meeting these criteria was also a reason why the previous criteria is not met for low velocities. To meet the first criteria, the chordwise elements had to be diminished. In order to meet the aspect ratio criteria, the spanwise elements would have to be diminished accordingly, increasing even further the size of the mesh.

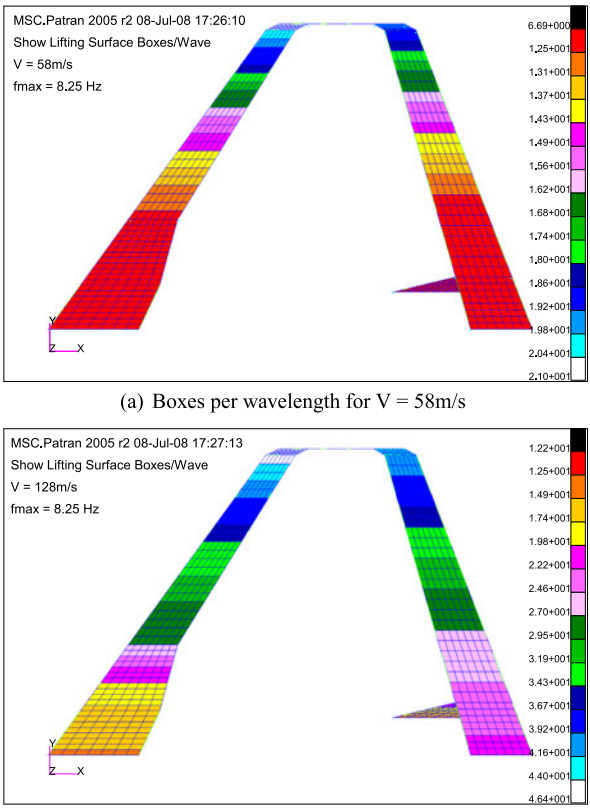

(a) Boxes per wavelength for V = 58m/s

(b) Boxes per wavelength for V = 128m/s

Fig. 4 Number of box per wavelength of the aerodynamic mesh

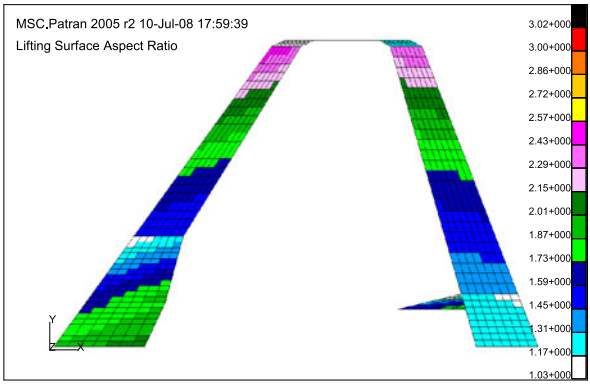

Fig. 5 Boxes aspect ratio of the aerodynamic mesh

2.2 Aero-structure Coupling

Now that the structural and aerodynamic models needed for flutter analysis are provided, a special tool is needed to connect them and make them interact. The structural deformations need to be transferred to the aerodynamic mesh so that it can deform, and the forces on the aerodynamic mesh need to act on the structure. In MSC NASTRAN®, the two grids are connected by interpolation. This way, a number of grid points of the structural grid are selected by the user to be connected to the aerodynamic surfaces. The interpolation method is called splinning, and the group of selected points a spline. In the splinning theory of MSC NASTRAN®, the structural points are chosen as independent degrees of freedom; the aerodynamic degrees of freedom are dependent. For the structural model of the PrP250, the chosen structural points are the points on the leading edge and trailing edge; this choice allows a limited number of structural points to describe correctly deflections and twisting, which is an asymmetrical deflection of two points at the same span position. The dependent aerodynamic points are the middle points of the aerodynamic mesh. A matrix relates the dependent degrees of freedom to the independent ones. The components of the structural grid point deflection $\{u_g\}$ and the deflection of the aerodynamic grid points $\{u_k\}$ are related through the interpolation matrix $[G_{kg}]$ as [2]:

$$\{u_k\} = [G_{kg}]\{u_g\}. \tag{10}$$

The derivation of the $[G_{kg}]$ matrix is the main objective of the theory of splines. The basic idea stems from the requirement that the two force systems must be "structurally equivalent" rather than statically equivalent. Structural equivalence means that the two systems deflect the structure equally. A statically equivalent system however does not yield to equal deflections. As in aeroelasticity, the deflection are of more interest than the resultant loads, and the first equivalence has been opted in MSC NASTRAN®. More detail on these theories can be found in [2].

2.3 Analysis Setup

As already said, in order for the p–k method to be efficient, a fairly accurate initial guess for k is needed. The reduced frequency is

$$k = \frac{\pi f \bar{c}}{V}, \tag{11}$$

where $\bar{c}$ is the reference chord, and V the velocity. Then, the minimum value $k_{\min}$ is computed by substituting the maximum velocity $V_{\max}$ and the value of the dimensional frequency $f_{\min}$ of the first structural eigenmode of interest (generally the first mode). Inversely, the maximum value $k_{\max}$ is computed with the minimum velocity and the frequency of the last mode of interest (in our case the 5th mode). It is advised that for analysis, the number of reduced frequencies should be 6–10; increasing this

number further would actually decrease the accuracy of the results. Next, a set of velocities is selected, as well as a density and a Mach number at which the analysis should be performed. It is interesting to note that the information given is redundant, as when two values between Mach number, velocity and density (i.e. altitude), are selected, the third one is fixed. That means also that as the analysis is performed at constant Mach number and density, but varying the velocity, the points at which the velocity is inconsistent with the two other parameters contain an error.

3 Flutter Results

In this section, the results obtained for different configurations at sea level and cruise altitude are presented. First, a modal analysis is conducted in order to find the eigenmodes of the structure, used to determine the initial guesses for the reduced frequencies. The mode shapes will be discussed as well, as they differ from the shapes traditionally found in conventional aircraft. Next, flutter analysis is conducted at two different altitudes; the damping and frequency of the modes of interest are plotted against the velocity. In the following, the first five modes are plotted, as the other modes are unlikely to appear on the actual aircraft and are not contributing to aeroelastic instability.

As already discussed, each analysis in MSC NASTRAN® is conducted at constant Mach number and density, but with varying velocity, inducing thus an error. The solution adopted here is to run several analyses at different Mach numbers and constant density, and take only into account the velocity which is consistent with respect to the two other parameters. However, as the Mach number becomes supersonic, the aerodynamic model and the mesh have to be changed. In the present case, only a few velocities in the analysis are supersonic. Then, in order to simplify the analysis, the Mach number is kept subsonic, so the model does not need to be changed, and the velocities are allowed to go supersonic. In other words, if one would compute the Mach number from the velocity and density, it would be supersonic, but the analysis in itself is conducted at a subsonic Mach number. This means that at supersonic velocities, the analysis contains an error. This was however judged acceptable, because at these points, flutter had already occurred. In the following, the flutter velocity is found using a MATLAB® routine.

3.1 Flight Envelope

It must be demonstrated that the aeroplane is free from flutter in the flight envelope enlarged by 15%. It is then of primary importance for flutter analysis to determine precisely the design speeds at the different altitudes. The following figure (Fig. 6) shows the Equivalent Air Speed (EAS) against flight altitude for a jet aircraft. At high altitude, the limiting factor is the Mach number, thus the curve of constant

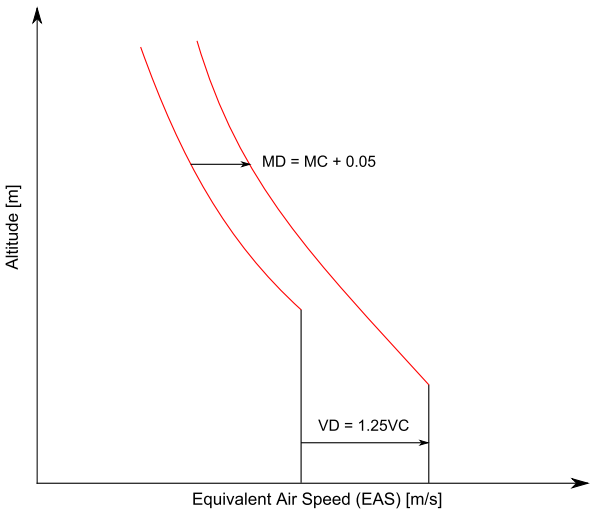

Fig. 6 EAS versus altitude for a jet aircraft

Mach number is depicted. Indeed, for a constant Mach number and increasing altitude, the EAS decreases. At lower altitude though, the cruising velocity V_C is used as a limitation.

To determine the flutter velocities, the cruising velocities must be found first through two different calculations, one at cruise altitude and the other at sea level. The methodology is taken from [10]. The FAR regulations state that the calculation for flutter speed have to be based on EAS; the following calculations take this into account. These calculations are used to determine $V_{\max}$, that is the velocity under which no flutter should occur.

1. At the cruise altitude of 10500 m, the calculation is based on Mach number, as it is the limiting number. The cruise Mach number being $M_C = 0.85$, the design dive Mach number at cruise altitude is computed as

$$\begin{aligned} M_D &= M_C + 0.05 \\ &= 0.90. \end{aligned}$$

   Meaning a diving speed of $V_D = 267.55$ m/s, True Air Speed (TAS). The TAS is related to the EAS by $\text{TAS} = \text{EAS}\sqrt{\rho_0/\rho}$. Taking the EAS, one obtains $V_D = 150.52$ m/s. Enlarging the flight envelope by 15%, one obtains $\boxed{V_{\max} = 173.1 \text{ m/s}}$.
2. At sea level, the diving velocity is directly computed from the cruise velocity. The issue is then to find the value of the cruising speed at sea level. This speed is conveniently calculated at the point of intersection of the curve and the straight line as shown in Fig. 6. According to Ref. [10], this point is generally situated at altitudes comprised between 20,000 and 25,000 ft for jet aircraft. Taking the most constraining case at 20,000 ft, one obtain for a cruise Mach number of $M_C = 0.85$, a cruising velocity of $V_C = 268.63$ m/s, TAS. Taking the EAS following

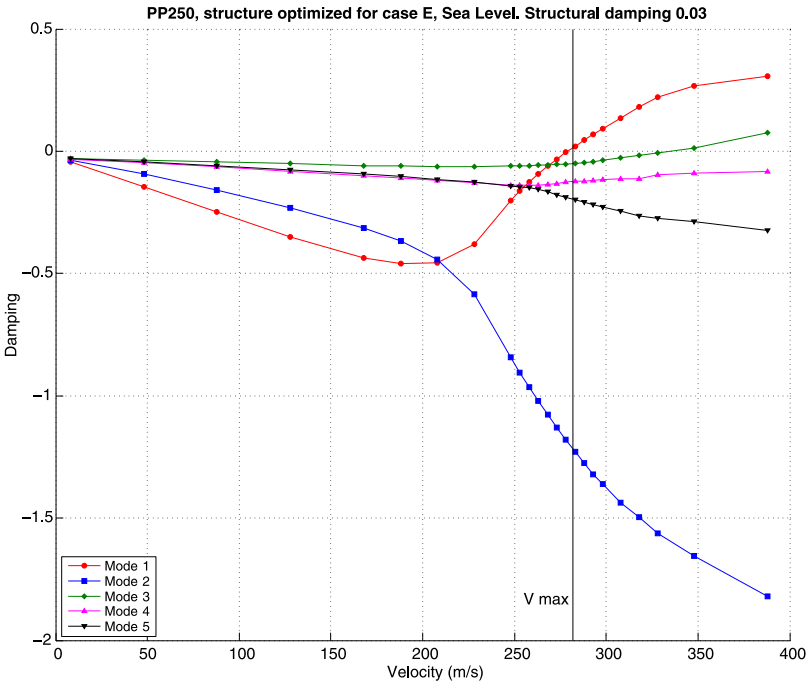

Fig. 7 Damping against velocity plot at cruise altitude

the same relation as previously, one obtains $V_C = 196.08$ m/s. The diving speed is then computed as

$$\begin{aligned} V_D &= 1.25 V_C \\ &= 245.10 \text{ m/s}. \end{aligned}$$

Again enlarging the flight envelope by 15%, one obtains $\boxed{V_{\max} = 281.87 \text{ m/s}}$.

The flutter analysis must then show that no flutter occurs before the speeds determined above.

3.2 Optimized Structure

A first flutter analysis was made on the structure optimized for all constraints as described in [4]. The damping against velocity graph is presented in Fig. 7. Here, we can clearly see that this design does not meet perfectly the requirements for the flutter velocity, although this structure was optimized for flutter. Indeed, flutter arises at 279 m/s, 3 m/s below the maximum velocity previously computed. This discrepancy is explained by the fact previously discussed that the flutter analysis in

Table 1 Principal modes of the PrP250

Mode	Frequency (Hz)	Comment
1	0.741	In-phase quarter wavelength bending of the two wings, No in-plane deformation
2	1.453	Out-of-phase quarter wavelength bending of the two wings, Out-of-phase in-plane deformation
3	2.072	In-phase half wavelength bending of the two wings, In-phase in-plane deformation
4	2.824	In-phase half wavelength bending of the two wings, In-phase in-plane deformation
5	3.065	Out-of-phase half wavelength bending of the two wings, Out-of-phase in-plane deformation

the optimization process is conducted at constant Mach number and altitude, but with varying velocity; an error is thus introduced in the calculation of one of the three parameters.

If it was assumed that $g = 0.05$, no discrepancies would be present, but the subject of flutter is so important, and moreover for the PrandtlPlane configuration, that a proper analysis has to be conducted. Then, it was decided to work on the structure optimized for all constraints but the one on flutter, as the flutter analysis and the method to increase the stiffness in the optimization process was believed to be too basic.

3.3 Pre-optimized Structure

The structure used in the following flutter analysis was optimized following the process described in [4], with all constraints active except the one on flutter. The solution adopted here is to take the pre-optimized structure, make a first flutter analysis and determine the flutter speed, and in case of a non-compliance with the requirements, find solutions to increase the flutter speed, as explained in the following.

Normal Modes Eigenmode shape and frequencies are obtained with MSC NASTRAN® using the "SOL 103" analysis, a normal mode analysis. Results are presented in Table 1. Figures 8(a) to 8(e) also show the different mode shape. The first mode, with a fairly low frequency of 0.741 Hz, is principally a quarter wavelength bending mode, where the front and aft wings are moving in phase; the node for the front wing is situated at the junction with the fuselage, whereas the node of the aft wing is situated at the connection with the fin. This causes the vertical surface connecting the two wings to vertically oscillate parallel to itself around its equilibrium position. The second mode is less simple: the bending of the two wings is also of a quarter wavelength, but the two wings move in opposition of phase.

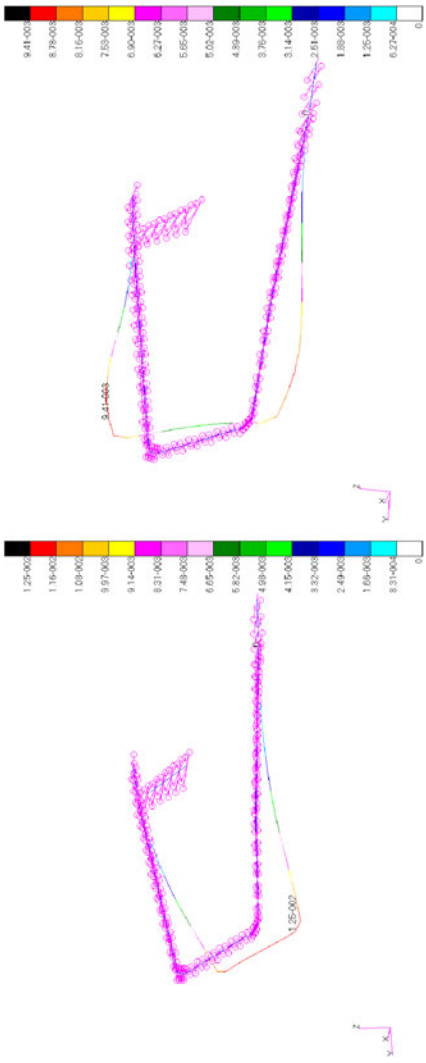

(a) Mode shape for mode 1

(b) Mode shape for mode 2

Fig. 8 Mode shapes for the PrP250

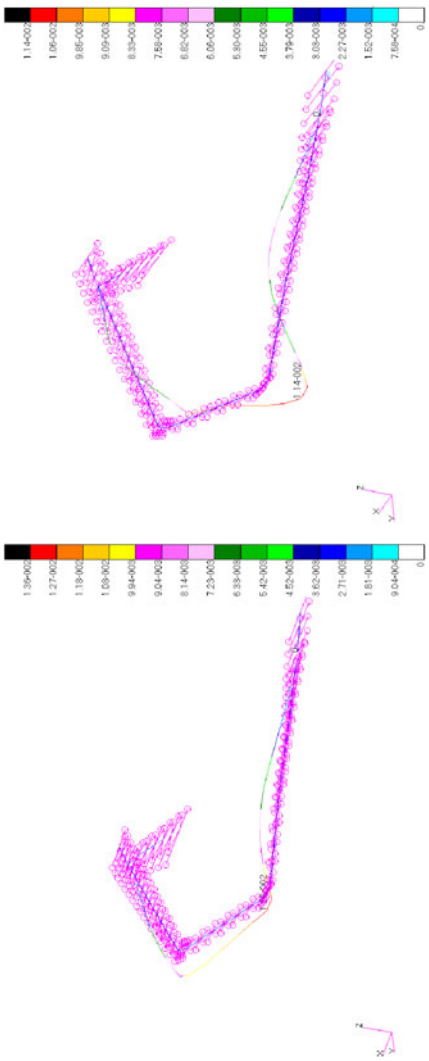

(c) Mode shape for mode 3

(d) Mode shape for mode 4

Fig. 8 (Continued)

Fig. 8 (Continued)

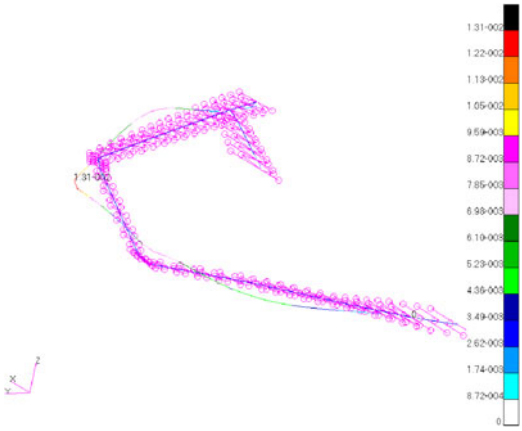

(e) Mode shape for mode 5

This causes the vertical wing to rotate about a point situated at around a third of its span, closer to the front wing. The vertical wing is thus working in compression, without significant deformation. As a consequence, a non-negligible amount of in-plane deformation is introduced on both wings; when the front wing moves forward, the aft wing moves backward and vice versa. The third mode exhibits a half-wavelength bending deformation; the nodes are, in addition to the two already cited, situated at the wing-tips. The vertical wing is moving parallel to itself, following a quasi-horizontal axis. Here also, the in-plane deformations are significant, but the two wings are moving in phase. Similarly to the situation encountered in the first mode, in the fourth mode the vertical wing is vertically translating parallel to itself. The bending shape of the wings however exhibits a half wavelength. In-plane deformation is also non-negligible; the observed behaviour is similar to the one of the third mode, where the two wings move in phase. Finally, the fifth mode exhibits a behaviour analogous to the second mode. The vertical wing rotates around a point, and the in-plane movements of the wings are out-of-phase. The bending shape exhibits slightly more than a half wavelength, the nodes being at around 6 m from the wing tips on each wing.

We can remark that for all these modes, neither the fin nor the vertical wing are deforming. This is principally due to the fact that they are both working in compression, for which the deformation energies are much higher than the one involved in bending modes. During the optimization process, the constraint in buckling increased significantly the weight (and thus its stiffness) of the vertical wing. Also, their relatively small span compared to the span of the wings requests more energy to bend them. For higher modes, it can be seen that the vertical wing and fin are indeed working in bending, but these modes occur at much higher frequencies and are not physically relevant.

Flutter Analysis Flutter analysis was conducted at both sea level and cruise altitude. As we can see in Fig. 9, no flutter is encountered at cruise altitude. All modes

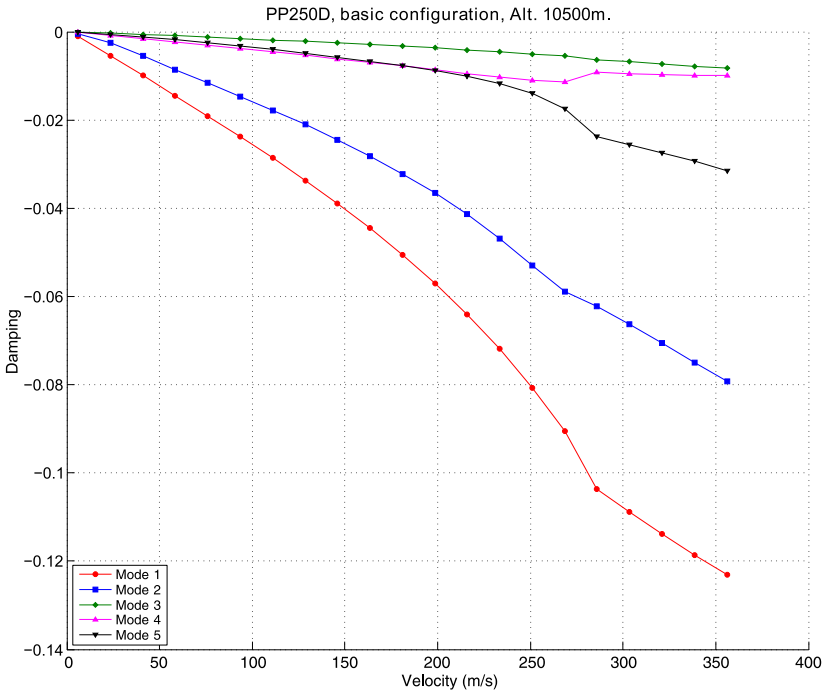

Fig. 9 Damping against velocity plot at cruise altitude

have a negative damping. Analysis at sea level however exhibits flutter, as shown in Fig. 10. Indeed, in Fig. 10(a), we can see that the damping for both modes 1 and 3 becomes positive at a certain velocity. The first mode encounters flutter at a velocity of circa 276 m/s, corresponding to a Mach number of 0.81, in the vicinity of the cruise Mach number. The third mode however becomes unstable at around 330 m/s. The flutter of mode 3 is progressive, as its damping is small (in an absolute sense) for all velocities. Flutter of the first mode is much more sudden and can be more dangerous as the difference in speed from a stable condition to an unstable one is relatively small. The critical mode for this configuration seems thus to be the first mode, as its flutter velocity is the smallest. Recalling the previous considerations on flight envelope in Sect. 3.1, the structure does not comply to the flutter speed requirement. The first mode becomes unstable some 7 m/s before $V_{\max}$.

On conventional aircraft, flutter appears to be a combination of a bending and a torsion mode (generally modes 1 and 2); both dampings become positive around the same frequency. In the case of the PrandtlPlane, however, no coupling between two modes is observed. Although the damping of the third mode is relatively low, flutter for this mode appears much later. Recalling the description of the modes made previously, it seems that bending movement is primarily excited. Also observed on conventional aircraft, the frequencies of the bending and torsion modes tend to merge in a single frequency. As it can be seen in Fig. 10(b), it is also the case here;

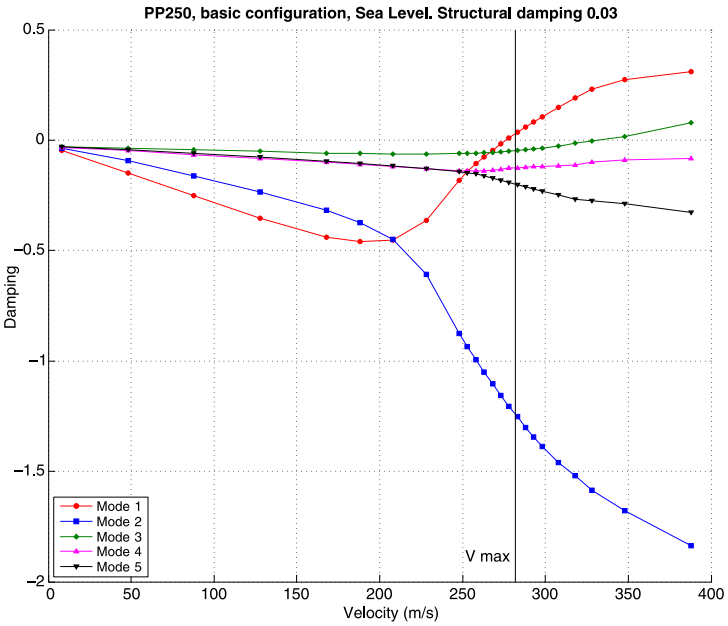

(a) Damping against velocity

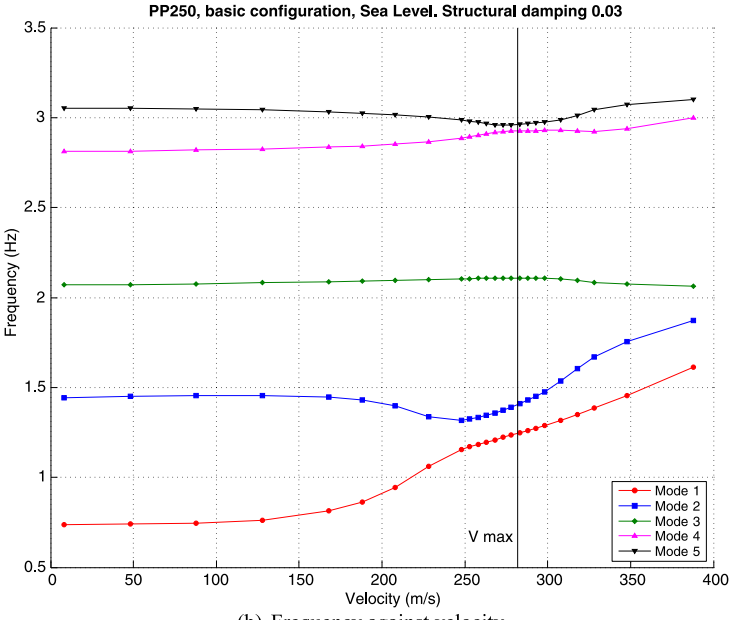

(b) Frequency against velocity

Fig. 10 Flutter analysis at sea level for the clean configuration

Table 2 Skin thickness modifications[1]

	Skin thickness increase	Box weight (kg)	Total weight (kg)
Basic configuration		30754.22	39392.62
Mod. 1	+10% front wing	31079.24 (+1.06%)	39717.64 (+0.83%)
Mod. 2	+10% aft wing	31323.44 (+1.85%)	39961.84 (+1.44%)
Mod. 3	+10% front and aft wings	31866.1 (+3.62%)	40504.5 (+2.82%)
Mod. 4	+20% front wing	31621.9 (+2.82%)	40260.3 (+2.20%)
Mod. 5	+20% front wing +10% aft wing	32408.76 (+5.38%)	41047.16 (+4.20%)
Mod. 6	+30% front wing	32164.56 (+4.59%)	40802.96 (+3.58%)

the frequencies of modes 1 and 3 get closer at the flutter point and still approach after but in a much lower extend than on conventional wings.

4 Modified Version, Increased Skin Thickness

As seen in the previous section, the basic configuration does not meet the requirement on flutter speed. A different structural solution is then needed to meet this requirement. From the previous analysis it seems that the first mode is the critical one. The first mode being principally a bending mode, the idea was to increase the bending stiffness by increasing the skin thickness. Moreover, the two wings being involved in the bending movement, the skin thickness is increased on the front wing and/or the aft wing. The area of the stiffeners was not modified, as the cross-section model was believed to be too basic to clearly separate both effects. Table 2 presents the modification added to the structure and their effects on the total box and wing weights (that includes non-structural weight like leading edge and trailing edge weight). The increases in weight with respect to the basic configuration are also presented (percentages into parenthesis). Flutter analysis for these modifications is presented in the following. Only the results at sea level are presented, as

[1]The percentages in parenthesis represent the change in the respective weight with respect to the Basic configuration.

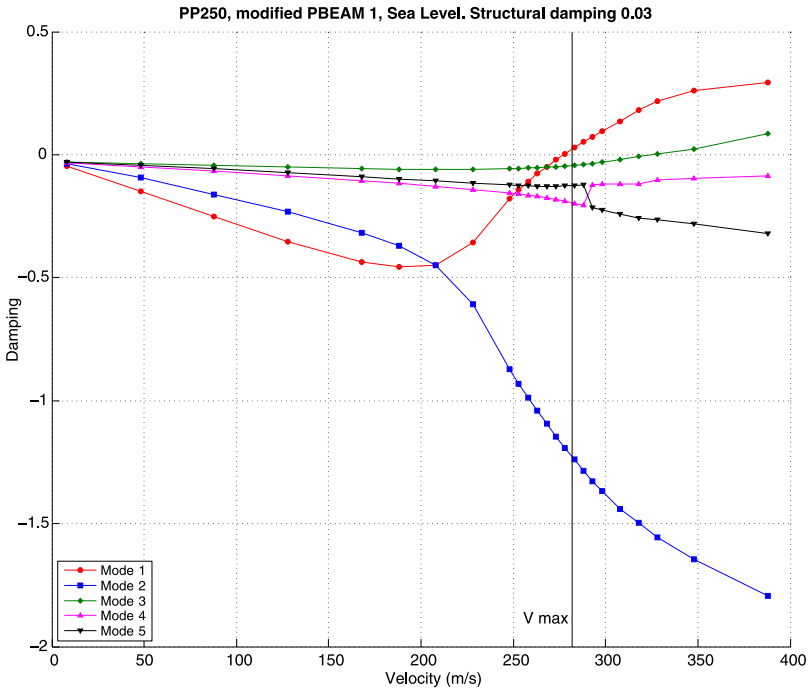

Fig. 11 Flutter analysis at sea level for Mod. 1

the results at cruise altitude present the same characteristics, with no occurrence of flutter.

Modification 1. The first modification added to the structure consists in increasing the skin thickness of the front wing by 10%, inducing an increase in total weight of 0.83% to attain 39717 kg, representing roughly 17.2% of the maximum take-off weight. The effect of the increase in skin thickness is to raise the flutter velocity by 1 m/s, taking it to 277 m/s (see Fig. 11). The structure still does not meet the requirements, but the flutter velocity has been taken to 5 m/s below the required velocity.

Modification 2. Increasing the skin thickness of the aft wing seems to be more penalizing for the structure in terms of weight, adding 1.44% on the total weight. Flutter for the first mode appears at a velocity of 276.5 m/s, as shown in Fig. 12, even before the occurrence of flutter in the first modification.

Modification 3. Increasing by 10% the skin thickness on both wings induces an increase in total weight of 2.82%. It has a positive effect on flutter velocity, as it is raised to 279.5 m/s (see Fig. 13). It appears thus that increasing the skin thickness on both wings is an efficient solution to raise the flutter velocity.

Modification 4. It was however noticed that increasing the skin thickness for the front wing only seemed to be more efficient; in this case, indeed, a 20% increase for the front wing only induces a 2.2% increase in total weight, less than the preceding

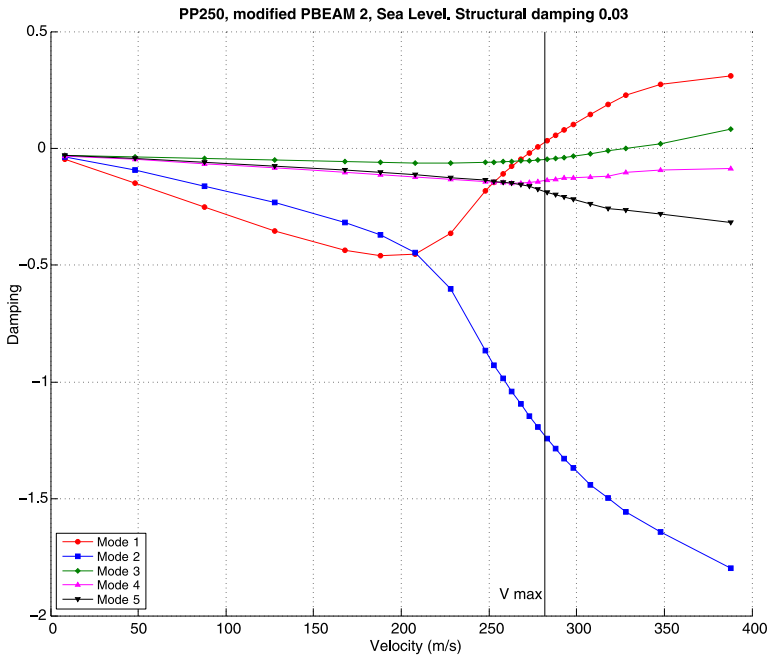

Fig. 12 Flutter analysis at sea level for Mod. 2

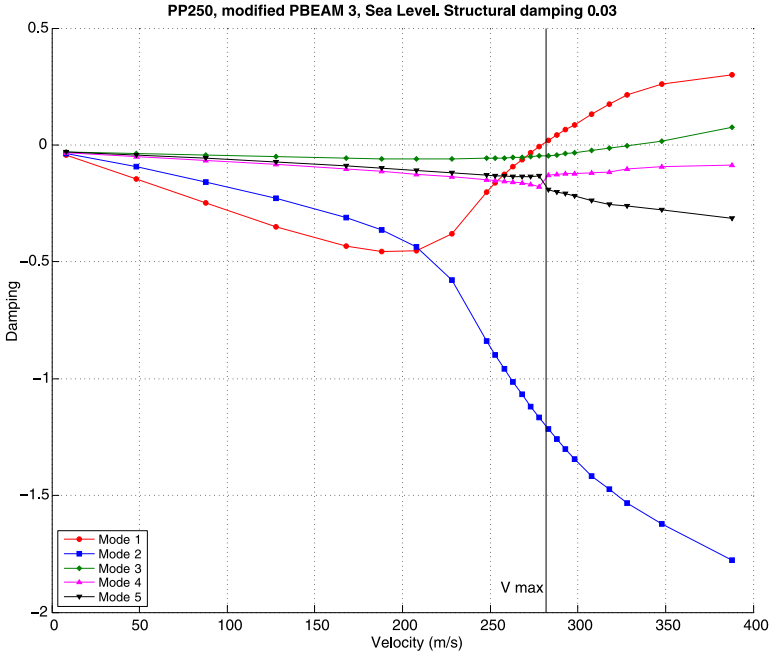

Fig. 13 Flutter analysis at sea level for Mod. 3

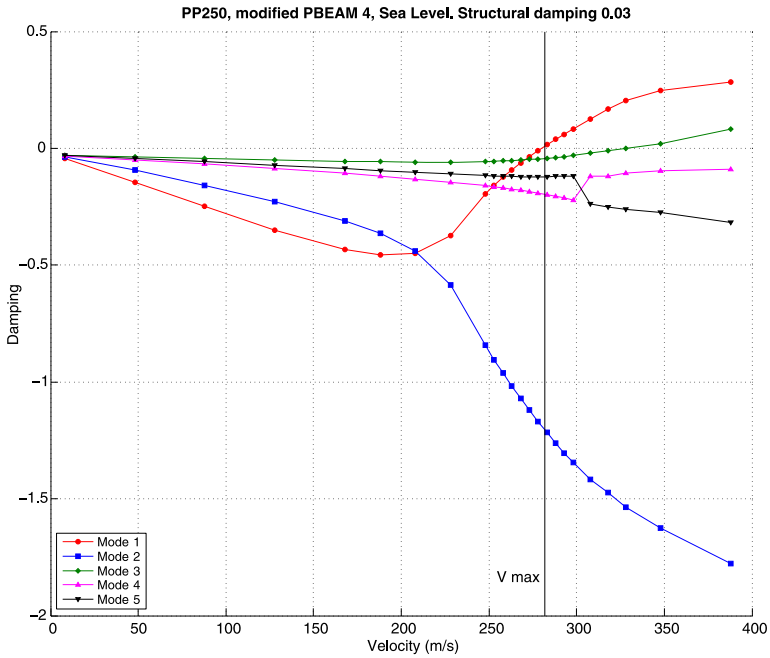

Fig. 14 Flutter analysis at sea level for Mod. 4

solution, while the flutter velocity is raised to 280 m/s (see Fig. 14). The maximum velocity is however not attained.

Modification 5. The idea was then to keep the previous solution, adding 10% skin thickness to the aft wing. This modification induces a 4.2% increase in total weight, while raising the flutter velocity to 282 m/s, slightly higher than the maximum velocity, as shown in Fig. 15. This solution meets then the requirement on flutter velocity.

Modification 6. Increasing the skin thickness by 30% on the front wing only is less penalizing for the structure than the previous solution; a 3.58% increase in total weight is experienced, raising the flutter velocity to 282.5 m/s (see Fig. 16), even higher than the previous solution.

5 Modified Version, Addition of Tip Tanks

Motivation. After first analysis on the basic configuration, the idea was to add fuel mass at the tips of the wing in order to see if it was possible to have a certain control on flutter characteristics. In first approximation, it was assumed that the optimum structural solution would not change due to the addition of the tip tank. Different configuration were studied, in order to understand which parameters could influence flutter characteristics and how. To get an overview of this influence, three parameters were varied: the fuel mass in the tanks, their chordwise position and the

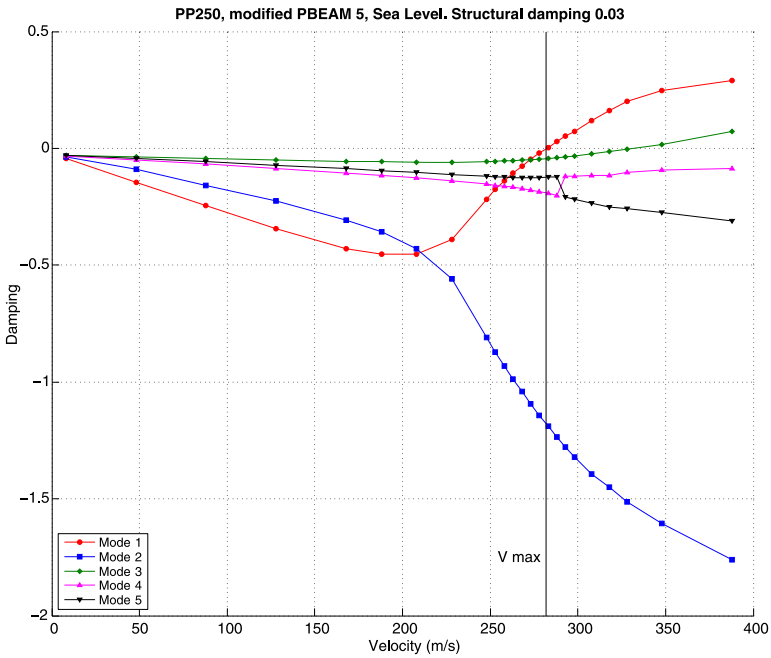

Fig. 15 Flutter analysis at sea level for Mod. 5

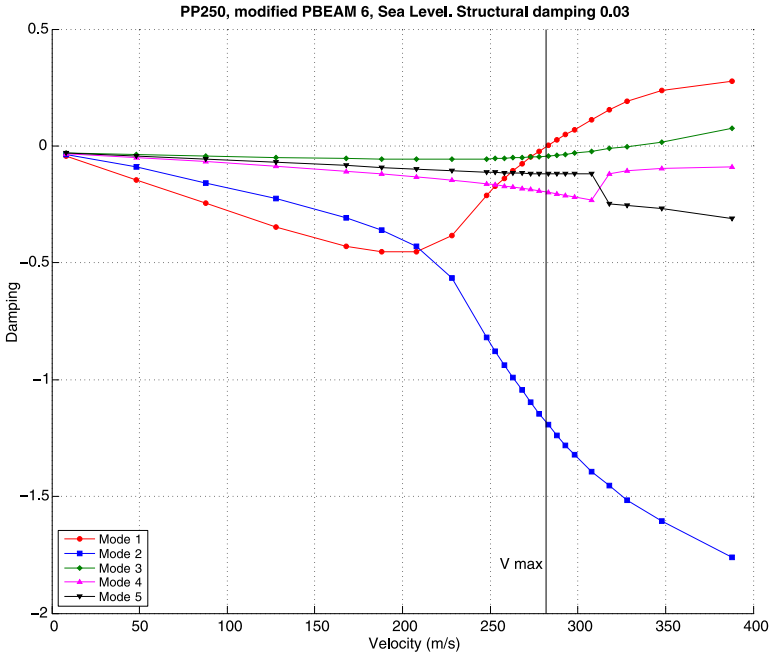

Fig. 16 Flutter analysis at sea level for Mod. 6

repartition of mass between front and aft wing. The geometry of the tip-tank is a simple cylinder with an ogival-shaped nose and aft body. The aerodynamic influence of the tip-tanks was not taken into account, as their contribution to the overall coefficients is not significant. However, a careful design is needed to prevent an adverse superposition of velocities at the junction between the wing and the vertical surface. Though further studies would be needed, the fuel contained could serve as a fraction or the totality of the reserve fuel (5% extra of the fuel needed for the mission and loiter, i.e. around 4050 kg [3]); the benefits (if any) of the addition of tip-tanks could then apply for the entire duration of the flight.

Model. The structural model of the PrP250 was modified in order to reflect the addition of tip-tanks. The aerodynamic model, however, was unchanged as the contribution of the tip-tanks to the aerodynamics of the aircraft is not significant. The structural contribution of the tip-tanks was modelled as three CONM2 elements, each of them positioned at the mass centre of a third of tip-tank and carrying a third of the total weight. The different configurations analysed are described below.

- Configuration 0: 1500 kg at the tip of the front wing, centre of gravity at mid-chord
- Configuration 1: 1000 kg at the tip of the front wing, centre of gravity at mid-chord
- Configuration 2: 500 kg at the tip of the front wing, centre of gravity at mid-chord
- Configuration 3: 1500 kg at the tip of the front wing, centre of gravity at 1 m in front of the mid-chord
- Configuration 4: 750 kg at the tip of the front wing, 750 kg at the tip of the aft wing, centers of gravity at mid-chords
- Configuration 5: 1500 kg at the tip of the aft wing, centre of gravity at mid-chord

Prior to the flutter analysis, a modal analysis was effectuated. It is interesting to note that the mode shapes are not significantly influenced by the addition of tip-tanks.

Flutter. Next, the flutter analysis is effectuated. From the results obtained for the eigenmodes, a new set of reduced frequency is computed and used in the analysis. In order to compare the different configurations, this is the only parameter to vary, all the others are kept constant, e.g. velocity set, Mach numbers and altitude (density). The reference configuration is the clean configuration; comparison will be made on the basis of its flutter characteristics.

Configuration 0. This first configuration features a tip tank of 1500 kg at the tip of the front wing and was actually the first configuration to be thought (therefore the term “configuration 0”). It principally influences the first mode, although a small change (in the negative sense) is perceived for the third mode, decreasing the velocity from 328 m/s to 318 m/s (see Fig. 17). The first mode is however favourably influenced, the damping becoming positive at 285.5 m/s. The structure complies then to the requirements in terms of flutter velocity.

Configuration 1. In this configuration, the tank was lightened to 1000 kg. Again, the biggest influence is seen on the first mode, now becoming unstable at a velocity of 282 m/s (see Fig. 18), slightly more than the $V_{\max}$ calculated previously. This configuration meets the requirement as well.

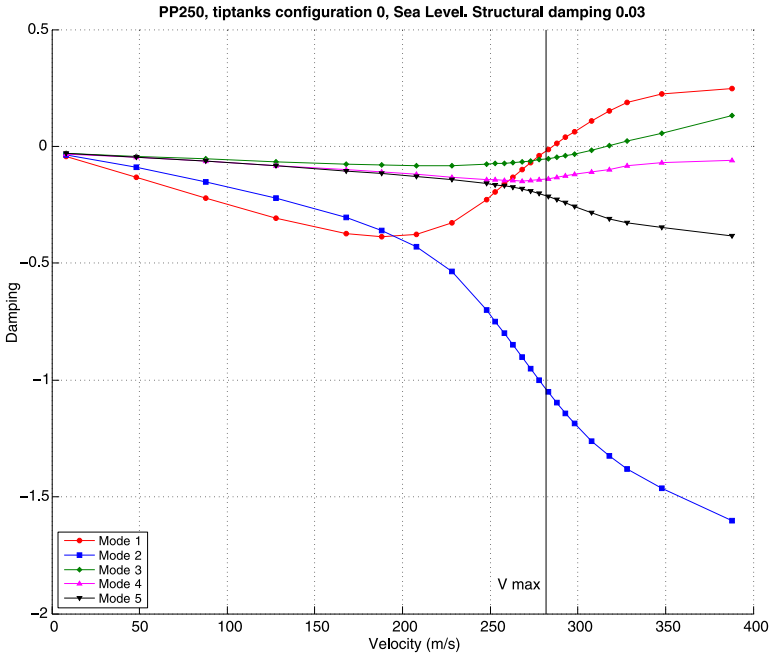

Fig. 17 Flutter analysis at sea level for configuration 0

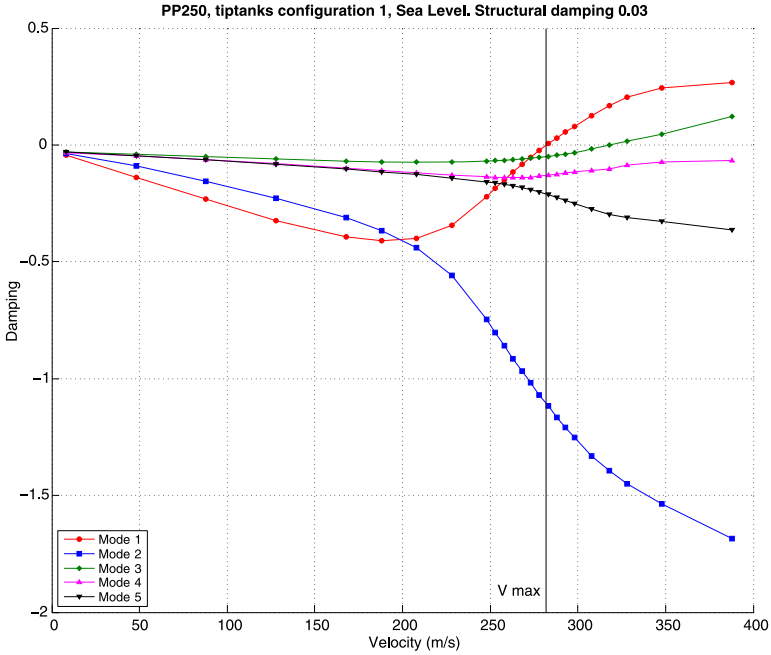

Fig. 18 Flutter analysis at sea level for configuration 1

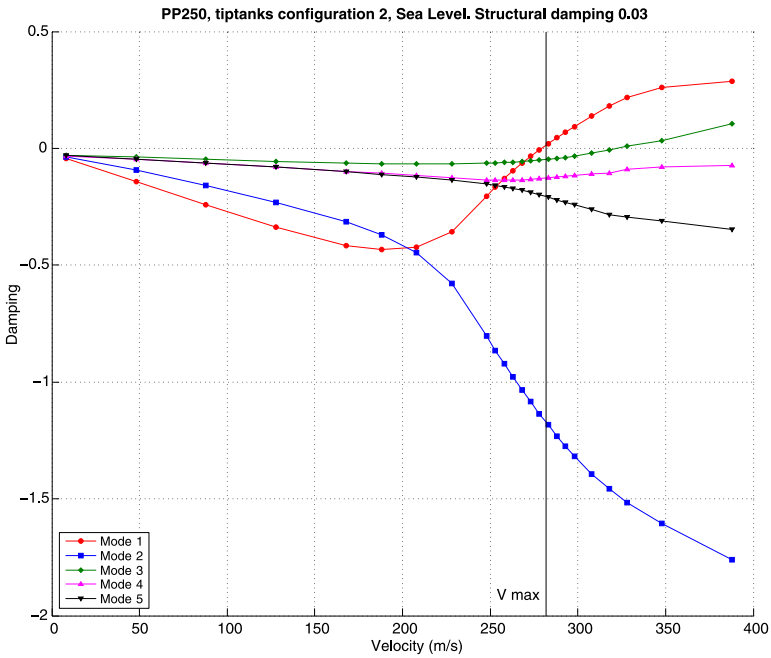

Fig. 19 Flutter analysis at sea level for configuration 2

Configuration 2. As shown in Fig. 19, with a weight of 500 kg at the tip of the front wing, the structure does not meet the requirement on flutter speed. Indeed, the first mode becomes unstable at 279 m/s, below the maximum velocity, but higher than the clean configuration.

Configuration 3. As instability also involves a torsional component, a configuration in which the tip tank would counteract the torsional movement was imagined. This way, the tank has been moved 1 m in front of the mid-chord. The results however do not seem to improve compared to configuration 0, where the same weight was used. Indeed, the flutter velocity was found to be 282 m/s, as shown in Fig. 20. This configuration meets flutter requirement.

Configuration 4. Putting a tip tank on the aft wing affects particularly the first and third modes; the flutter velocity has now decreased to 272 m/s, 5 m/s below the clean configuration (see Fig. 21). The effect is thus clearly unfavourable for flutter characteristics; from a flight dynamics point of view, it is also not preferable as the centre of gravity is moved aft and up.

Configuration 5. This configuration, with a 1500-kg tank at the tip of the aft wing, clearly shows the unfavourable effect of adding mass at the rear wing (see Fig. 22). Indeed, the flutter appears now at a velocity of 258 m/s, decreasing it by almost 20 m/s with respect to the clean configuration.

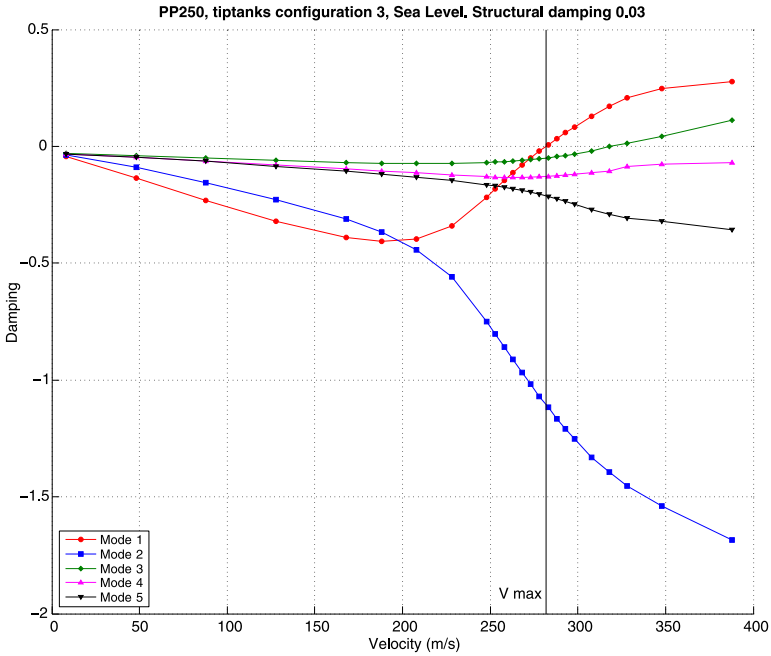

Fig. 20 Flutter analysis at sea level for configuration 3

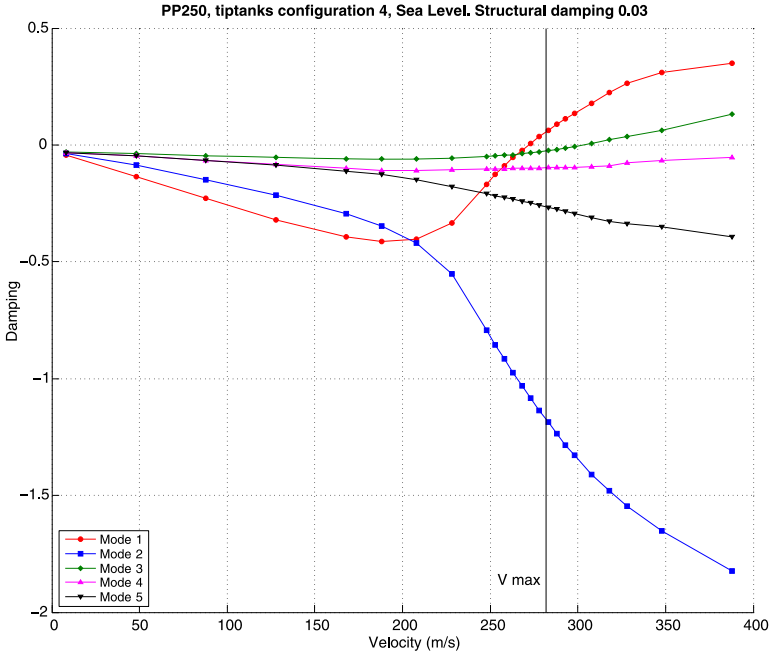

Fig. 21 Flutter analysis at sea level for configuration 4

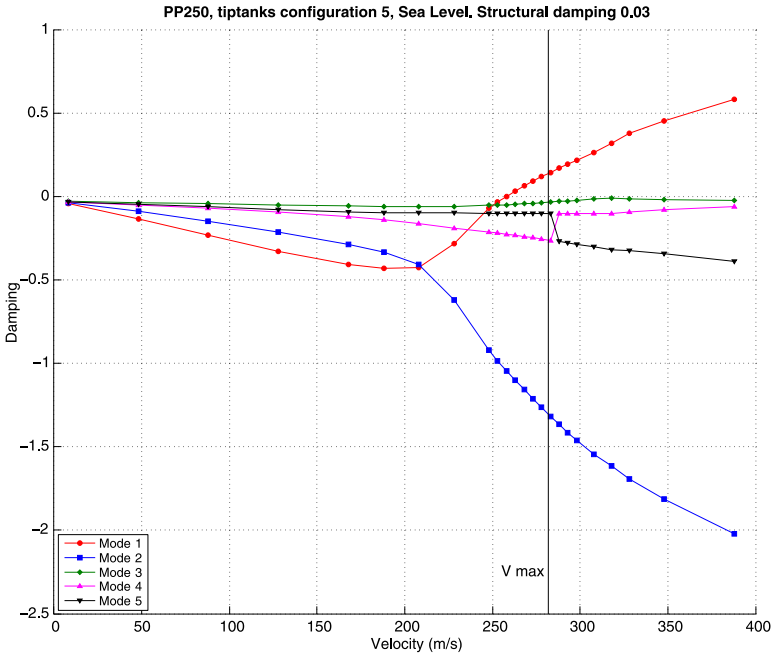

Fig. 22 Flutter analysis at sea level for configuration 5

6 Conclusions and Recommendations for Further Studies

An optimization tool, conceived at Politecnico di Milano, was used to make the preliminary design of the wing box. It was however believed that the flutter analysis carried in the optimization process was not accurate enough, due to a discrepancy in the determination of the Mach number.

Indeed, once flutter analysis was carried on the structure optimized for all constraints including the one on flutter, it was seen that the structure was not exactly complying to the requirements regarding flutter speed. It was then decided to base the analysis on the structure non-optimized for flutter speed; this structure did not meet the requirement on flutter but was taken as a basis for further investigations. Two different strategies were adopted to raise the flutter speed. First, the skin thickness was increased on the front and/or aft wing. From these analyses two different solutions met the flutter requirement; adding 20% skin thickness on the front wing and 10% on the aft wing, as well as 30% on the front wing only allows the flutter to occur after the maximum velocity. Out of these two solutions, the most advantageous one is the latter, as the weight associated with the increase in skin thickness is lower than with the other solution. Increasing the skin thickness on the front wing seemed to be the most efficient and least penalizing solution for the structure. Then, solutions with addition of a fuel tank at the tip of the wings were studied. These solutions allow one to meet flutter requirement without additional structural weight. Different parameters of the tanks were varied: their weight, position and distribution

Table 3 Flutter velocities for different configurations

Configuration	Remark	Flutter velocity V_f (m/s)
	Maximum velocity	**281.87**
Optimized for case G		279
Optimized for case D	Base configuration	276
Mod. skin thickness 1	+10% front wing	277
Mod. skin thickness 2	+10% aft wing	276.5
Mod. skin thickness 3	+10% front and aft wing	279.5
Mod. skin thickness 4	+20% front wing	280
Mod. skin thickness 5	+20% front wing, +10% aft wing	**282**
Mod. skin thickness 6	+30% front wing	**282.5**
Tiptanks 0	1500 kg front wing	**285.5**
Tiptanks 1	1000 kg front wing	**282**
Tiptanks 2	500 kg front wing	279
Tiptanks 3	1500 kg moved 1 m forward front wing	**282**
Tiptanks 4	750 kg front wing and aft wing	272
Tiptanks 5	1500 kg aft wing	258

on the wings (front/aft). This way, three configurations met the flutter requirement: configurations with 1000 kg, 1500 kg at the tip of the front wing, and 1500 kg at the tip of the front wing, moved 1 m in front of the mid-chord. In order to improve flutter performances, it seems favourable to place a mass at the tip of the front wing only; it is however very disadvantageous to place the tank on the aft wing, as the flutter velocity experiences a important decrease with respect to the other configurations. Operational considerations could be used to determine the desirable weight of the tip-tanks, providing that they are heavier than 1000 kg. To summarize, Table 3 presents the flutter velocities found for each configuration.

Here some remarks should be done on the method used by MSC NASTRAN® to solve the flutter equation. A DLM aerodynamic code is used in the program, which models the aerodynamic surfaces in finite panels, neglecting thus their thickness. This way, the effects of the compressibility of the air are not included in the DLM. These effects are however of importance in the transonic regime ($M \geq 0.8$); the flutter points in the previous analyses being in this region, the results obtained do not take compressibility effects into account. It boils down to the fact that flutter in transonic regimes is still an open question, also in industrial environment; the definitive characteristics are known only at the last stage of flight test, where the actual aircraft is being flown. The analyses made in the frame of this research are thus to be taken as trends and indications on the behaviour of this innovative structure.

The problem of flutter, and in a more general sense aeroelasticity, of a PrandtlPlane aircraft is an unexplored domain, plenty of issues, and still needs to be investigated. First, the structures with the tip-tanks of 1000 and/or of 1500 kg have to be optimized through the method described previously. Indeed, the additional

mass of the tanks influences the mass distribution and thus the structural solution meeting the different constraints. Then, the second level optimization should be run for the structures meeting the requirement on flutter speed (see Table 3) to get more insight into the behaviour of the structure. If necessary, a loop can be executed between the first- and second-level optimization. Also, a conventional aircraft's wing should be designed for the same mission in order to assess the actual advantages of the PrandtlPlane configuration. Finally, body freedom flutter could be of importance for the PrandtlPlane configuration. This phenomenon, often mentioned in the literature (see for example Refs. [7] and [8]), is a coupling between a rigid body mode (pitch, roll) and the low-frequency structural modes. In the case of the PrP250, the first bending mode has a frequency of 0.741 Hz, which is fairly low and could thus interact with rigid modes. On the other side, it is well known that the pitch damping of a civil transport PrandtlPlane is very high compared to a conventional aircraft and this behaviour could prevent the flutter associated to the body pitch motion; anyway, the problem is still open.

Appendix

The generalized stiffness and generalized mass being introduced, generalized coordinates can be used in the problem of flutter prediction:

$$[M]\{\ddot{q}\} + [D]\{\dot{q}\} + [K]\{q\} = Q_A, \tag{12}$$

where:

$[M]$: Generalized mass matrix
$[D]$: Structural damping matrix
$[K]$: Generalized stiffness matrix
$\{q\}$: Vector of generalized coordinates
Q_A: Generalized aerodynamic forces

In Eq. (12), Q_A is determined by an appropriate aerodynamic model.

In general, the flutter equation is solved by assuming a harmonic solution of the form $\{q\} = \{\hat{q}\}e^{pt}$ and finding roots of the characteristic equation for p. It can still be done to solve Eq. (12), provided that the aerodynamic forces Q_A can be explicitly expressed as algebraic functions of $\{q\}$. It can be done for simple aerodynamic models, but not when only pure harmonic results are available or when the data is available only in tabular form from experiments.

An intuitive approach to solve this would be to add a harmonic forcing term $F(t)$ to the system and evaluate its response as a function of flight conditions (e.g. the dynamic pressure q of the flight speed U) and the frequency ω of the forcing function. This is actually the method used for flight tests, but it is quite inefficient from a numerical standpoint as it requires harmonic time domain simulation for each point in the U–ω plane.

A number of more efficient methods have been developed and will be described in the following. These methods are less time-consuming than the forcing approach and generate directly approximate flutter diagrams. The two presented methods, the k method [9] and p–k method [5], are both assuming that aerodynamic data is pure harmonic. As we know that at the flutter points, the response is indeed pure harmonic, the solution at these points will be exact.

For the sake of ease and generality, we will manipulate non-dimensional equations. Thus, we will employ a non-dimensional expression for p,

$$p = \frac{b}{U}(\sigma + i\omega) = \delta + ik, \tag{13}$$

where b is the half-chord, and k is called the *reduced frequency* and is a parameter of primary importance in the determination of the aerodynamic forces; it is computed as

$$k = \frac{\omega b}{U}. \tag{14}$$

The solutions will be assumed to be of the form $\{q\} = \{\hat{q}\}e^{p\frac{Ut}{b}}$. The equations of motion (12) are then written as

$$\left[\frac{U^2}{b^2}[M]p^2 + \frac{U}{b}[D]p + [K]\right]\{\hat{q}\} = \frac{1}{2}\rho U^2\big[A(p)\big]\{\hat{q}\}. \tag{15}$$

Here, $A(p)$ is the aerodynamic matrix and is a function of the Mach number and Reynolds number. It is important to note here that if the aerodynamic forces can be expressed as a sufficient simple function of p, Eq. (15) defines a polynomial in p with real coefficients. In this case, this expression is equivalent to the equations of motion developped in the two-degree-of-freedom model.

The p–k method is based on the assumption that it is possible to approximate the aerodynamics of sinusoidal motions with slowly increasing or decreasing amplitudes using purely harmonic aerodynamic data, i.e. that

$$\big[A(p)\big] = \big[A(\delta + ik, M, Re, \ldots)\big] \approx \big[A(ik, M, Re, \ldots)\big]$$

for sufficiently small δ. With this assumed form of aerodynamic terms, the equation of motion is written as

$$\left[\frac{U^2}{b^2}[M]p^2 + \frac{U}{b}[D]p + [K]\right]\{\hat{q}\} = \frac{1}{2}\rho U^2\big[A(ik)\big]\{\hat{q}\}, \tag{16}$$

which we can write

$$\big[F(p,k)\big]\{\hat{q}\} = 0. \tag{17}$$

Once $[A(ik)]$ has been computed from a first estimation of k, one can solve Eq. (16) for $p_1 = \delta_1 + ik_1$, compute $[A(ik_1)]$, and again solve equation (16) for $p_2 = \delta_2 + ik_2$, etc., until the imaginary part k_i of the solution p_i equals the k_{i-1}

value of the aerodynamics. Hence, this method is called method p–k. An iterative solution method is normally used, the most common one being the "determinant iteration" [5]. For this method to work properly, the initial guesses for p must be reasonably good and are thus determined from the previously analysed flight condition. The assumption on the form of the aerodynamic data proved to be accurate in Ref. [5], as the p–k method is compared with an exact method for damping (the p method), giving a good agreement between the two.

To obtain flutter diagrams, the basic procedure is as follows. First, the mode that will be tracked is chosen as well as a starting value for U, near $U = 0$. The Mach and Reynolds numbers are computed from this U. A first guess, p_1, can be made using the natural frequency of the chosen mode. Another guess p_1' is made by adding a small damping to p_1. Then the following steps are performed:

1. Compute or interpolate for $[A(k_1, M, \ldots)]$ and $[A(k_1', M, \ldots)]$.
2. Compute the determinants $F_1 = |[F(p_1, k_1)]|$ and $F_1' = |[F(p_1', k_1')]|$.
3. Update p using $p_3 = \frac{p_2 F_1 - p_1 F_2}{F_1 - F_2}$.
4. Set $p_1' = p_2$ and $p_1 = p_1'$, and repeat from step 1 until converged.
5. Choose the next flight condition $(\rho, U, M, Re, \ldots)$.
6. Choose two new values for p based on extrapolation from previous flight conditions.
7. Return to step 1 and repeat to find the new p at the next flight condition.

This procedure is repeated for each desired mode. Once a converged solution $p_c = \delta_c + ik_c$ has been found, the frequency and damping are computed as

$$f = \frac{U k_c}{2\pi b} \quad \text{and} \quad \gamma = \frac{\delta_c}{k_c} = \frac{g}{2} \tag{18}$$

and used to draw the frequency-damping-velocity diagrams, or flutter diagrams.

The p–k method has two distinct advantages. First, the plots obtained are interpreted much easier. Indeed, the non-physical behaviours that can arise with the k method are not present. Then, no further iteration is required to incorporate Mach or Reynolds number effects, as the density computed already contains this information.

References

1. Albano, E., Rodden, W.P.: A doublet lattice method for calculating lift distributions on oscillating surfaces in subsonic flows. AIAA J. **7**, 279–285 (1968)
2. Anonymous: MSC Nastran User's Manual. MSC Software Corporation, Santa Ana, California. MSC Software Corporation
3. Bottoni, C., Scanu, J.: Preliminary design of a 250 passenger PrandtlPlane aircraft. Master's thesis, Università di Pisa, Facolta di Ingegneria (2004)
4. Frediani, A., Dal Canto, D., Ghiringhelli, G.L., Terraneo, M.: The lifting system of a PrandtlPlane; Part 1: Design and analysis of a light alloy structural solution. In: Buttazzo, G., Frediani, A. (eds.) Variational Analysis and Aerospace Engineering II: Mathematical Challenges for Aerospace Design. Springer, Berlin (2012)

5. Hassig, H.J.: An approximate true damping solution of the flutter equation by determinant iteration. J. Aircr. **8**(11), 885–889 (1971)
6. Kehoe, M.W.: A historical overview of flight flutter testing. NASA Technical Memorandum 4720, NASA, Oct. (1995)
7. Livne, E., Weisshaar, T.A.: Aeroelasticity of nonconventional airplane configurations—past and future. J. Aircr. **40**(6), 1047–1065 (2003)
8. Love, M.H., Scott Zink, P., Wieselmann, P.A.: Body freedom flutter of high aspect ratio flying-wings. In: 46th AIAA/ASME/ASCE/AHS/ASC Structures, Structural Dynamics & Materials Conference, Austin, Texas, April 2005
9. Theodorsen, T.: General theory of aerodynamic instability and the mechanism of flutter. NACA Report No. 496, NACA (1935)
10. Torenbeek, E.: Synthesis of Subsonic Airplane Design. Delft University Press, Delft (1976)
11. Van Zyl, L.H.: Convergence of the subsonic doublet lattice method. J. Aircr. **35**(6), 977–979 (1998)

The Lifting System of a PrandtlPlane, Part 3: Structures Made in Composites

Aldo Frediani, Flavio Quattrone, and Francesco Contini

1 Introduction

The structures of a 250-seat PrandtlPlane wing system has been designed and, even though at a preliminary stage, optimized as reported in [10]. The optimization process used in [10] starts with an initial solution based on a beam model, in which the section characteristics are defined in such a way that the maximum von Mises stress is lower than the allowable one (233 MPa at $n = 2.5$ load factor); this has been named as level 1. Afterwards, a standard cross-section is assumed, and the parameters defining the section geometry are defined in order to satisfy a sequence of constraints, namely: the design against instability under compression loads, static aeroelasticity, including aeroelastic effects on load distribution and aileron efficiency, and flutter.

The wings are made in an Aluminium Alloy typical of aeronautical applications, in order to compare the results obtained with those of equivalent conventional metallic aircraft. In this optimization process the wing box was first assumed as doubly symmetric; this solution was then modified into a non-symmetric section, introducing two new unknowns per section, namely the areas of the spar flanges; the weight saving appears to be very significant.

In conclusion, this analysis showed that the empty weight of the selected PrandtlPlane wing system is nearly the same as a traditional one of an equivalent

A. Frediani (✉)
Dipartimento di Ingegneria Aerospaziale, Università di Pisa, Via G.Caruso 8, 56122 Pisa, Italy
e-mail: a.frediani@dia.unipi.it

F. Quattrone
Departement Physique et Mecanique des Materiaux, ENSMA – Teleport 21, avenue Clement Ader, BP 40109F86961, Futuroscope Chasseneuil Cedex, France
e-mail: flavio.quattrone@ensma.fr

F. Contini
Carbench International S.p.A., Via Dorsale 22, 54100 Massa, Italy
e-mail: francesco.ct@gmail.com

G. Buttazzo, A. Frediani (eds.), *Variational Analysis and Aerospace Engineering: Mathematical Challenges for Aerospace Design*, Springer Optimization and Its Applications 66,
DOI 10.1007/978-1-4614-2435-2_11,

aircraft. The results of the research activity described so far were considered encouraging to try to improve further the solution.

A further step towards the improvement of the structural efficiency has been performed in this paper. The non-symmetric wing box resulting from the optimization process with the constraint of stability under compressive loads was analysed with the Finite Element method in order to check the efficiency of the optimization procedure and, also, to provide a reference configuration for further solutions. The F.E. analysis shows that the optimization procedure adopted cannot give an absolute optimum; as a matter of fact, indeed, the local von Mises stress is higher than the allowable one, but, almost everywhere, there exists a part of the same section where the stress level is lower than the allowable one. We could then conclude that the local stress level after optimization is not correct locally but the average level of von Mises stress is acceptable and a reasonable preliminary weight estimation is provided.

As shown in [18], the propulsion system of the aircraft is provided by two turbofans, positioned into the rear fuselage; thus, the lifting system is free of concentrated loads due to the engines, and a solution in composites becomes more attractive. The main structures manufactured in composites are becoming usual in modern civil transport aircraft; wings, in particular, are free of possible strokes and impacts during ground operations and are a candidate to be such a structural solution.

Thus, a design of the lifting system main structures has been performed using Carbon Fibres composites. In particular, a special sequence of layers has been adopted which produces an isotropic material. This staking sequence of layers has been adopted for the whole system, similar to the brick of a building, and the solution was verified with a new F.E. analysis. This design process is a trade off, being the lifting system over constrained to the fuselage; the final result is that the weight reduction could be very significant. Another characteristic of the solution is the high thickness of the skins as a consequence of the smaller chord lengths compared to cantilever wings; when the technological problems could be solved, the wing box could be manufactured without stringers: it could be a very remarkable saving in the manufacturing costs.

2 FEM Analysis of the Aluminium Alloy Structure

The 250-seat PrandtlPlane aircraft of reference is shown in Fig. 1, and the lifting system in Fig. 2; the main characteristics of the aircraft, including the general layout and architecture are to be found in [6]. The main dimensions of the lifting system are presented in Table 1.

The structural design and optimization process of the lifting system, including the fins, are described in [9]. For the reader's convenience and, also, to realize the limits of the results obtained, we summarize here the main steps and the relevant outputs.

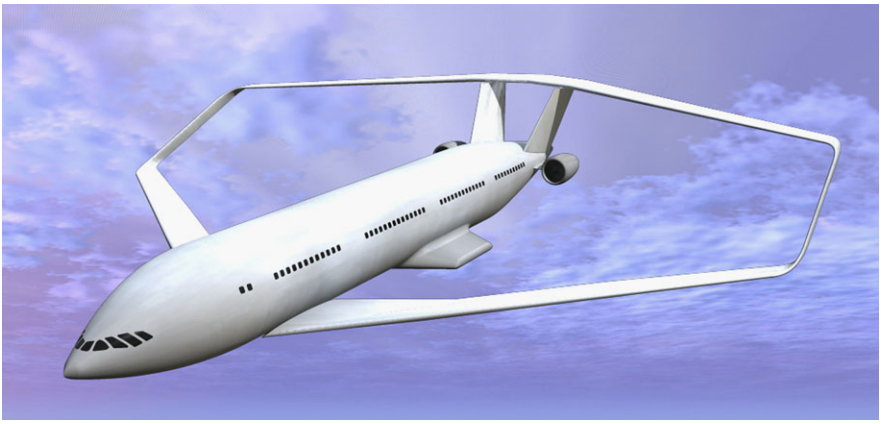

Fig. 1 The 250-seat PrandtlPlane, aircraft of reference

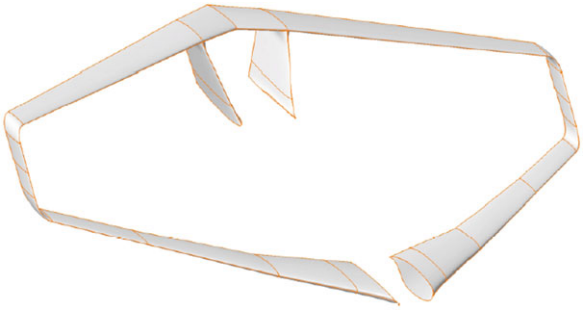

Fig. 2 250-seat PrandtlPlane wing system

Table 1 Wings main dimensions

Wing surface	394.52 m^2
Front wing surface	205.5 m^2
Back wing surface	189 m^2
Wing span	55 m
Angle of sweep front wing	+36°
Angle of sweep back wing	−16.5°
Angle of sweep side bulkheads	38.5°
Wing chord at front center-line	7.4 m
Wing chord at back center-line	5.04 m
Wing chord at front tip	2.32 m
Wing chord at back tip	2.32 m
Fuselage width	7 m
Percentage airfoil thickness at front root	14%
Percentage airfoil thickness at back root	12%
Percentage airfoil thickness at front tip	10%
Percentage airfoil thickness at back tip	10%

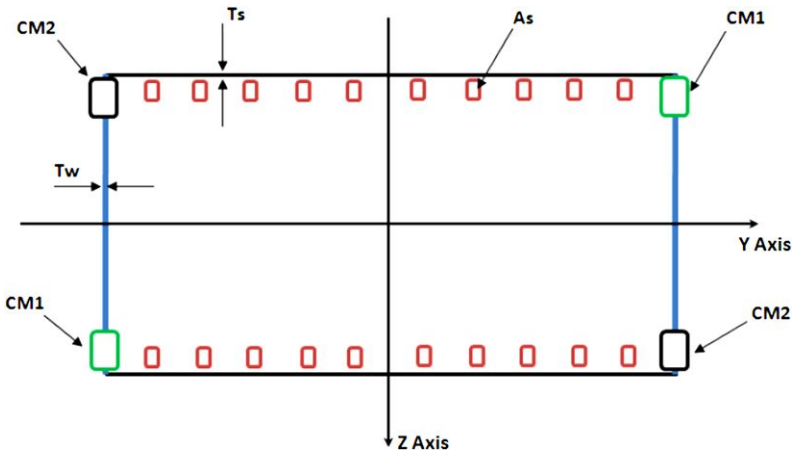

Fig. 3 Asymmetric wingbox layout with notation

In the first step, the wing section was assumed as a doubly symmetric box with the following parameters: web thickness, skin thickness, area of a fixed number of stringers; the structural design was the result of a multistep optimization including the constraints of: Aluminium alloy characteristics, aeroelastic effects on load distribution, design against instability under compression loads, aileron effectiveness and flutter. The assumption of the double symmetry of the wing section is not satisfactory for a PrandtlPlane lifting system, and, in a second analysis, new parameters were introduced, namely two areas of the spar flanges, equal in the cross positions, and a second optimization under the same constraints was performed with the final result of a significant weight saving.

In this paper, two next steps are performed. The first one is a Finite Element analysis of the structure resulting from the procedure before. The second one is the design of a new solution of the lifting system made in composites.

As said before, the Finite Element analysis is performed in order to verify the reliability of the optimization code; to do so, we verify the stress levels after the first steps of the process, where the only constraints of allowable stress and instability under compression are satisfied. The FEM analysis is then conducted on the structural solution with unsymmetrical wing box, the best structural result obtained, under the loads corresponding to the $n = 2.5$ load factor in symmetric flight.

The condition on instability is not active, because we assume a priori that any instability could ever occur, and, thus, only the area of the stringers and their centre of gravity (but not the shape of them) are the actual ones.

The model of the wing structure is divided into 54 sections, characterized by different properties assignment: for example, the number of the stringers (having a fixed pitch), the overall area of the sections, etc. The wing box layout is shown in Fig. 3; this layout remains the same for all the wings, both horizontal and vertical.

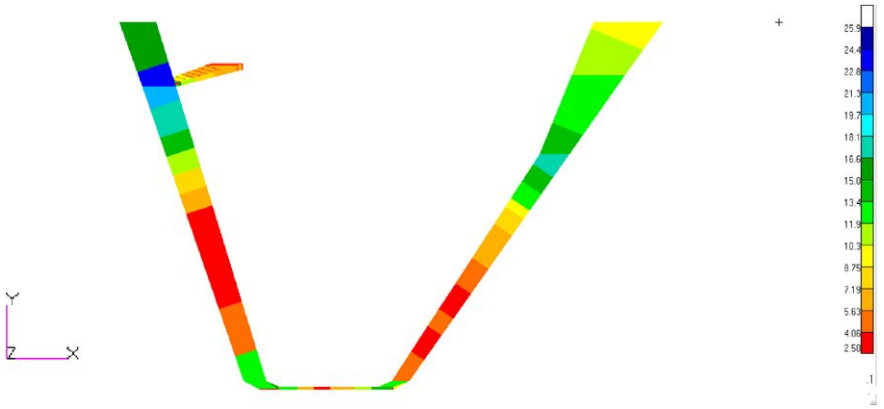

Fig. 4 Thickness distribution top view

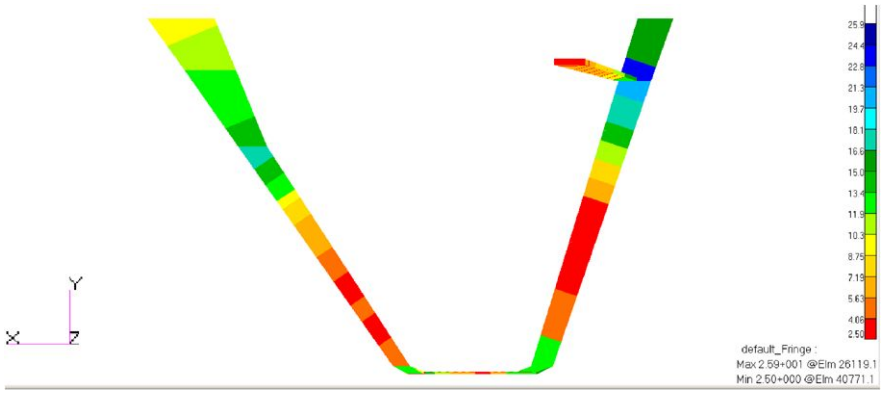

Fig. 5 Thickness distribution bottom view

The output data, section by section, are the following:

1. A_s = stringer area;
2. CM_1 = Area of the "South–West" and "North–East" spar flanges (see Fig. 3 for reference);
3. CM_2 = Area of the other spar flanges;
4. t_s = Skin thickness, the same for upper and lower wing panels;
5. t_w = Spar web thickness, the same for the two spars.

The other dimensions of the wing box (positions of the spar, webs, stringers, etc.) are deduced from the aerodynamic layout, considering that the front spar is at the 18% of the wing chord, and the rear spar is at the 68%.

In the beam model, the ribs are equivalent to masses positioned along the beam with a fixed pitch of 750 mm, perpendicular to the beam axis. The thickness distribution of the whole F.E. model, in mm, can be deduced from Figs. 4 and 5. In the

Table 2 Mechanical properties of 2024-T3 Aluminium alloy

$E = 70$ GPa
$\nu = 0.3$
$\rho = 2800 \frac{\text{kg}}{\text{m}^3}$

top view the thickness of the upper skin is maximum (25.9 mm) in correspondence of the fin, in a very local region of the rear wing; in the front wing the thickness is maximum (about 19 mm) around the end of the kink.

As for the stringer runouts, we assume that each stringer ends in coincidence with a rib [5]. In order to obtain a FEM model similar as more as possible to the beam model resulting from the previous optimization, the external loads are applied in coincidence with the 54 station points, and each station point is connected to the ribs with an RBE3 multi-point constraint (MPC); more details on this constraint are given in [2].

Any external load is made by a force and a moment, generated as outputs from the aerodynamic simulation; the inertial loads result from a gravity acceleration of 9.8 m/s^2. Structure constraints are the following:

- At the front wing root, all the degrees of freedom are blocked;
- At the rear wing centerline, a symmetry constraint is applied;
- The fin root is clamped to the fuselage, which in turn is assumed to be rigid.

Once the whole FEM model is defined, we need to assign the element properties. The shell elements are the QUAD4 thin shell elements with constant thickness. The beam elements are BAR2; the section area is that obtained from the optimization process, while the section shape is whatever because the constraint of the instability under compression loads is satisfied by the structural solution under examination; in this analysis the section is assumed as circulate around the C.G. According to the requirements, the material chosen is 2024-T3 Aluminium alloy, isotropic and homogeneous, with the properties listed in Table 2.

3 Results of the Finite Element Analysis of the Metallic Wing

The elements composing the upper and lower skins have equal thickness, and the same occurs for the two spar webs. The thickness of the single elements is the average value along the span segment, derived from the optimized solution in [10]. The first check of the F.E. model is the assessment of the resulting total weight of the system. The weight of the half lifting system resulting from the F.E. analysis and the weight of reference are, respectively,

- Finite Element model (structural weight): 13.007 kg,
- Optimization procedure (structural weight): 13472 kg.

Because the difference is about 3%, we consider the F.E. model as sufficiently accurate. Thus, we can determine the stress state under the same reference loads in

Fig. 6 Von Mises's stress for the asymmetrical wing box in the step B case—top isometric view

Fig. 7 Von Mises's stress for the asymmetrical wing box in the step B case—bottom isometric view

any point of the system and verify the stress state to be lower than the allowable equivalent stress. The FEM results show that the maximum stress condition is not fully satisfied everywhere. The following Figs. 6, 7, 8, 9 show the results of the simulation. The von Mises' stress, in MPa, and displacements, in mm, are displayed. Figures 6 and 7 show the von Mises stress in the whole system, and Figs. 8 and 9 show stress details in the front and rear wings.

The von Mises stress overcomes the maximum stress of 233 MPa somewhere, but with very high local peaks. Some part of the stress peaks are due to the local introduction of the external loads, and, thus, these peaks are not considered as totally reliable. An interesting remark is that, in the wing sections where some high stresses

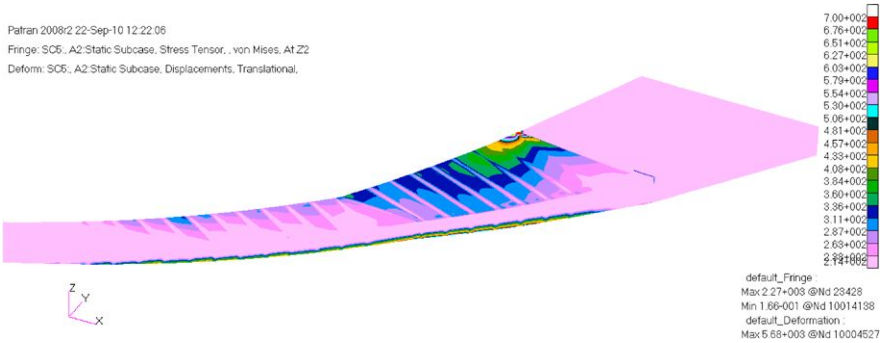

Fig. 8 Von Mises's stress for the asymmetrical wing box in the step B case—detail of the front wing

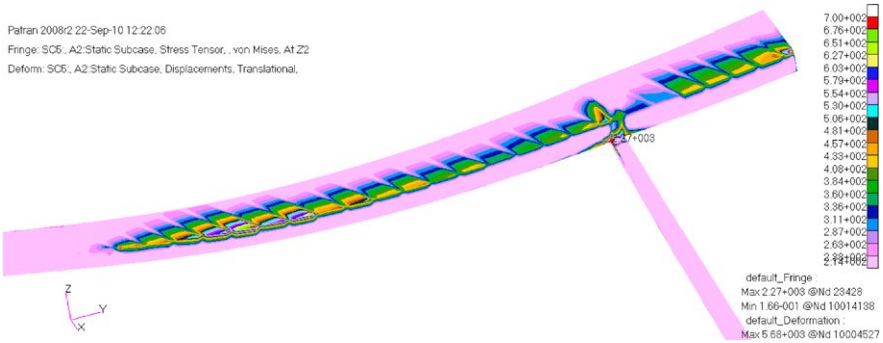

Fig. 9 Von Mises's stress for the asymmetrical wing box in the step B case—detail of the rear wing

are present, some part of the section is always under-stressed, to compensate the first ones.

In the present preliminary design, this averaged stress condition is supposed to be acceptable; in view of a more advanced design in which the thickness along some sections can be modified, a more refined analysis shows that in some sections the average stress along the span is too high, but these regions are so limited that the reinforcements are very local and with a so small weight penalty to be disregarded.

In these hypotheses, the deformation of the system is displayed in Fig. 10; the maximum displacement is about 5650 mm, equivalent to abut $1/10$ of the span under the loads corresponding to the limit condition and about 2 m, equivalent to $1/25$ of span, under the cruise load at maximum take-off weight. The hypothesis of F.E. linear analysis could be questionable under limit loads, but, at this stage of approximation, we retain it acceptable.

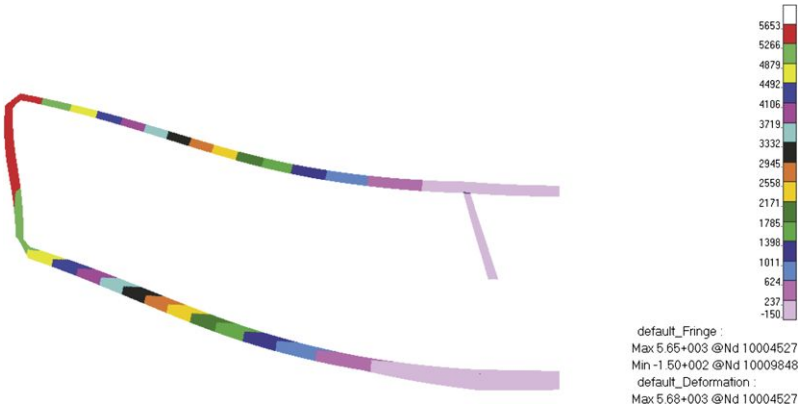

Fig. 10 Step B deformed structure solution

4 PrandtlPlane Wing Box Design Using Composites

As shown in [10], the skin thickness of the wing box is higher than the corresponding of conventional wings; this result is reasonable because of the reduced local stiffness of the wings. When a new structural design is performed using composites, the optimal layout of the very large thickness is very hard to be obtained without advanced optimization algorithms; this is a necessary activity for the fully exploitation of composites. The required thickness, as well, needs a great amount of layers, and, for this reason, the FEM model could be very hard to handle. Another problem connected with the large thickness is that the 3D stress state does not fit with the typical orthotropic behaviour of standard stacking sequences for composite applications. Finally, the 3D layout of the PrandtlPlane wings requires an appropriate manufacturing strategy. All these aspects are analysed in the following.

4.1 Manufacturing

Composite materials are ideal for structural applications where both high strength-to-weight and high stiffness-to-weight ratios are required; it is well known that, in aeronautics, these two requirements must be satisfied; in addition, a reduction of manufacturing costs could be obtained by reducing the operations and the number of sub-elements to be joined together. Therefore, composite materials can be truly cost-effective for the present applications. The half-wing structure is more than 27 meters wide, and, thus, the present manufacturing equipment allows one to produce the complete half-wing by assembling a small number of substructures.

The stress state behaviour along the span suggests where positioning the sections to be joined together. Figure 11 shows a possible solution of joints in the case of three main elements; the junction can be placed in the region where the bending moment is small, approximately from 3/4 of the wing span to the tip, depending on

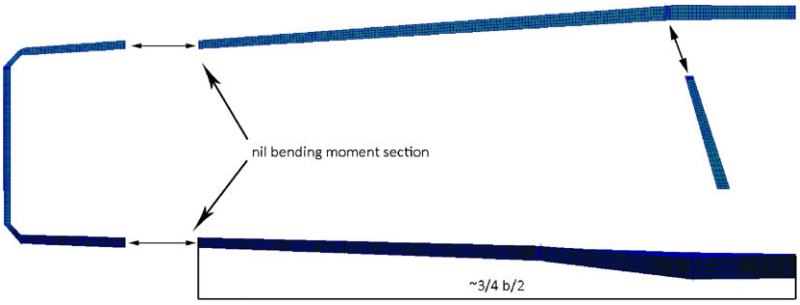

Fig. 11 Substructures to be assembled

the ailerons span; as said before, ailerons are positioned on both wing tips and can have different spans [18].

The composite solution is also appealing because, due to the very high skin thicknesses, the wing box could be designed without stringer inside, using skin thickness associated with a proper number of ribs to avoid instability phenomena under compression loads.

Finally, the particular configuration of the 250-seat PrandtlPlane characterized by the engines mounted in the back of the fuselage, and the undercarriage system, positioned far from the wing structure, eliminates the problem of concentrated loads on the wings; the wings are aerodynamically clean.

With a no-stringer wing box, a standard procedure could be applied, as, for example: the spars can be laminated first, then connected together with the ribs, and, finally, the upper and lower laminated skins are bonded to the structure in a vacuum bag. The connection between fins and upper wing needs to be carefully studied, because the solution affects the overall stress distribution.

4.2 Laminates

The theory of composites has produced many interesting results in the last years. Completely isotropic, both in stretching and in bending, and decoupled laminates are named "quasi-homogeneous laminates". Many exact non-symmetrical solutions exist, obtained by solving the constitutive equations iteratively [16]. Is interesting to notice that the quasi-homogeneous property is maintained with a stacking of quasi-homogeneous sequences, obtained overlaying these sequences. The following 24 layers stacking sequence is a quasi-homogeneous one, and it is here reported because the angles used are common in aeronautical applications; the sequence is the following [16]:

$$0\,1\,2\,3\,3\,2\,3/1\,3\,0\,2\,0\,1/0\,1\,3\,1\,2\,0/2\,3\,2\,3\,0\,1$$

Each sequence number is a tag, and it can be a whatsoever orientation, among these angles: 0°, 45°, 90°, −45°. In the current design, the quasi-homogeneous

Table 3 Torayca M55J cured laminae properties

Longitudinal tensile modulus	340 GPa
Longitudinal compression modulus	285 GPa
Transverse tensile modulus	6.4 GPa
In-plane shear modulus	3.9 GPa
ν Poisson's ratio	0.30
Longitudinal tensile strength	2.01 GPa
Longitudinal compression strength	880 MPa
Transverse tensile strength	34 MPa
Transverse compression strength	108 MPa
Shear strength	44 MPa
ILSS	69 MPa

Table 4 Constitutive properties

E_{11}	119 GPa
E_{22}	119 GPa
G_{12}	44.8 GPa
ν	0.32

stacking sequence is adopted with the consequence that the mechanical properties of the composites could be diminished, the layout configuration fits the internal stress distribution, and the typical problems of anisotropic materials (such as peculiar deformations under asymmetric thermal loads) are avoided. The sequence adopted is also interesting at the light of a possible comparison between the Aluminium alloy and the composite solutions. The fibre chosen is M55J Torayca, and the epoxy resin is #2500–250°F; the characteristics are listed in Table 3.

The laminae thickness is 0.125 mm, with a density of 1603 kg/m^3; using the sequence shown before the minimum thickness becomes 3 mm. The material so obtained is chosen for its very high elastic modulus, the very high strength in tension and compression, the low specific weight and, finally, because the thickness is not a drawback because of the high thickness required in the presented structural solution.

With the stacking sequence told above, the laminate has the properties shown in Table 4, calculated with the classic theory of laminates [16].

5 The Composite Wing Box: CAD and FEM Set-Up

The wing external shape is derived from the aerodynamic surface, considering a front spar at 18% and a rear one at 68% of the wing chord. The maximum rib pitch has been determined to avoid the buckling stress of the non-reinforced upper skin, and, in the present analysis, it is assumed as constant along the span; the analysis showed that, when the rib is 3-mm thick, the maximum rib pitch allowable along the span is 425 mm in the kink region.

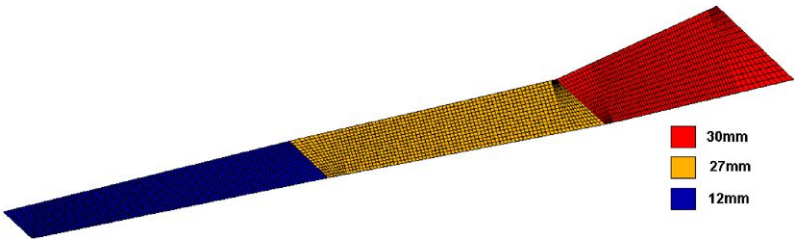

Fig. 12 Skin thickness—front wing upper panels

The rounds between the bulkheads and the wings have been re-designed to minimize local effects of stress concentration and simplify the F.E. computation; the same for the connections of fin and rear wing, which strongly influence the deformation and the stress distribution of the entire structure. These zones have been carefully analysed, to meet a reasonable FEM solution and to provide adequate stiffness without significant variations of the structural weight. The maximum dimension of the mesh elements is 100-mm wide, with more refined meshes where needed. The lack of stringers simplify the generation of the mesh grid.

The design process begins with the assessment of the inertial properties along the wing span of the optimized configuration made of Aluminium; then, we determine the new box in composites with the same distribution of inertial properties along the wingspan.

According to before, the thickness is a multiple of 3 mm (the minimum thickness for the quasi-homogeneous stacking sequence), and, besides, in order to simplify the fabrication procedure, the skin thickness is kept constant in any wing strip, normal to the longitudinal axis.

5.1 Upper and Lower Panels

The upper and lower skin panels are set up with the quasi-homogeneous laminate stacking sequence described before; this assumption, together with the hypothesis of constant thickness in any wing section, leads to a thickness distribution presented in the following.

Figures 12, 13, 14 and 15 show the thickness distribution designed for the upper and lower skin panels of the front and back wings. The thickness is maximum (30 mm) on the front wing upper panel in the region of the kink and is 24 mm in the lower panel of the same kink; at the root of the back wing, the thickness is lower (27 mm), both in the upper and lower panels; the thickness is 12 mm at the tip regions of all the wings. The total weight of the skin is about 6700 kg, corresponding to 67.5% (35.4% for the lower and 32.1% for the upper skins).

These thickness sequences could be revisited when dealing with manufacturing; in fact, the passage from 27, 21 and 24 mm to 12 mm (at tip regions) needs to be smoother, and some modest weight penalty may be paid.

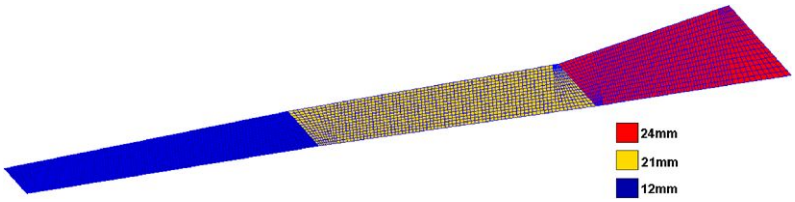

Fig. 13 Skin thickness—front wing lower panels

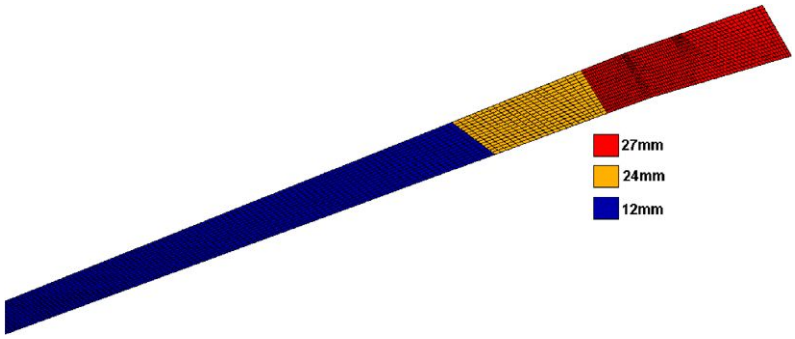

Fig. 14 Skin thickness—back wing upper panels

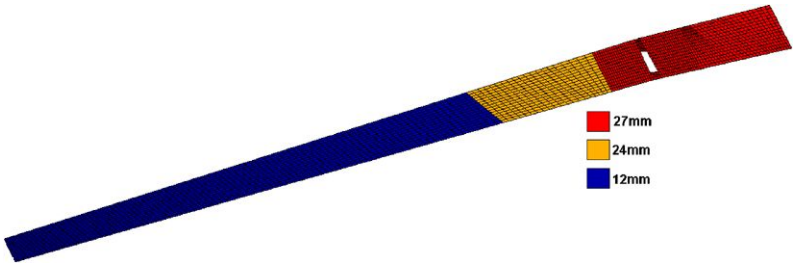

Fig. 15 Skin thickness—back wing lower panels

5.2 Spar Webs and Flanges

The spar webs and flanges are both modelled with shell elements, in order to obtain a double T-shaped section. They are set up with the quasi-homogeneous laminate stacking sequence pre-described. It is worth saying that a better solution could be obtained using $+45°/-45°$ stacking sequences for the webs, and unidirectional laminates for the flanges, but at this stage of the design, quasi-homogeneous laminates could be a simpler choice. The weight of the spars corresponds to 14.1% of the total (10% for the webs and 4.1% for the flanges).

Figures 16, 17, 18, 19 show the thicknesses obtained. The front spar flanges of the fore wing are 15-mm thick and the web thickness varies from 12 at the root to 9

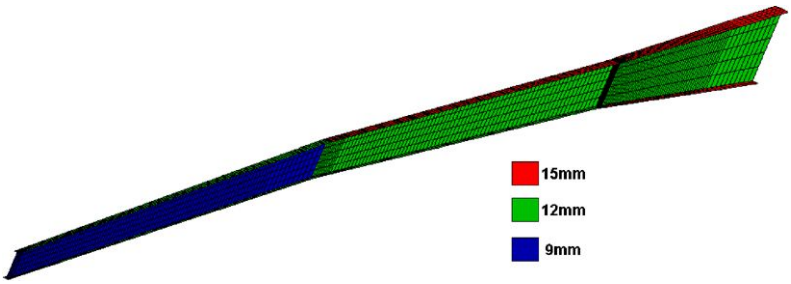

Fig. 16 Web and flanges thickness—front wing front spar

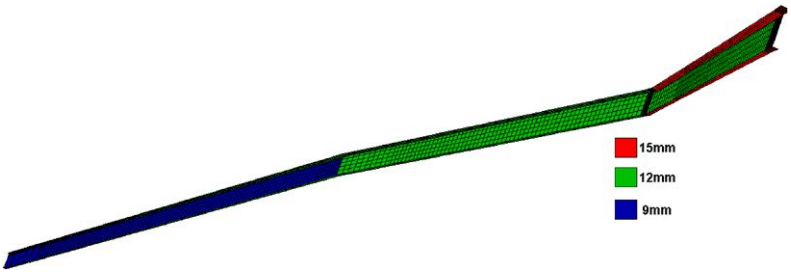

Fig. 17 Web and flange thicknesses—front wing back spar

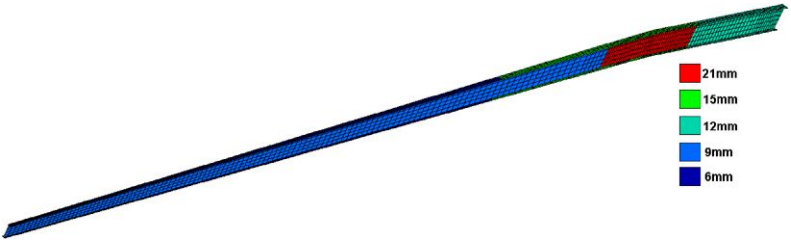

Fig. 18 Web and flange thicknesses—back wing front spar

at tip (Fig. 16); the same occurs for the rear spar of the same wing (Fig. 17). A larger thickness is needed in the back wing, and, once more, the critical region is the end of the kink (Figs. 18 and 19). According to the conclusions established in [10], the variation of dihedral angle needs to be eliminated.

5.3 Ribs

The ribs are made up with 3-mm constant thickness quasi-homogeneous carbon fibre laminate. The kink rib and the fin ribs have, instead, different thickness with more 3-mm basic laminates. A local design of these ribs has been carried out in

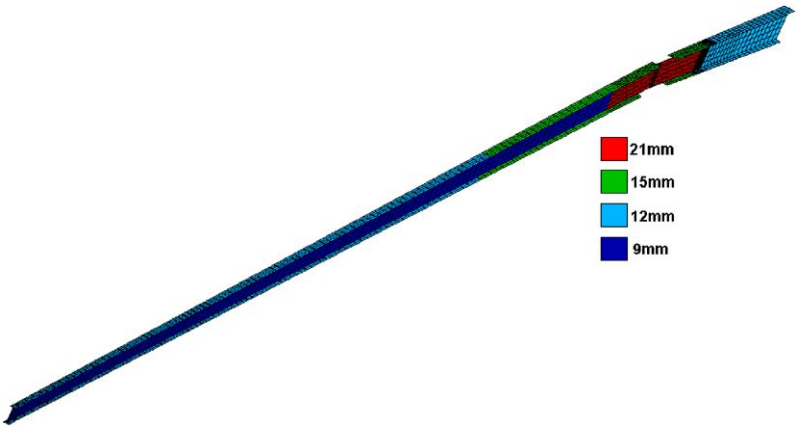

Fig. 19 Web and flange thicknesses—back wing back spar

order to evaluate the total weight; more accurate analysis will be necessary when dealing with the detail structural design. The total weight of the ribs is 380 kg, corresponding to 4.61%.

6 Structural Efficiency of Composite Solution

The Finite Element analysis has be conducted under flight symmetric loads corresponding to the limit load factor. The requirements concerning aeronautical structures made in composites impose the limit load to be multiplied by a safety factor of 1.5, so the total value of n_z is 3.75.

This safety factor is necessary to take manufacturing defects into account. The analysis is linear, and, thus, the results could be no longer valid in the nonlinear range when constitutive or geometric nonlinearities have a significant influence. The geometric nonlinearities are not very significant, because overall deformations are smaller than those relevant to Aluminium alloy structure. We assume as the total weight of the lifting system (including fins) the one in which the stress state of such lifting system verifies the failure index conditions of composites. The failure index used here is the maximum stress criterion [16], based on the comparison between the real stresses and the strengths for the considered material; since these parameters are known in the orthotropic direction, the comparison is made in those directions, and the failure is assumed to occur when one of the following conditions is not verified:

$$\begin{aligned} -X_c \leq \sigma_1 \leq X_t, \\ -Y_c \leq \sigma_2 \leq Y_t, \\ \sigma_6 \leq S, \end{aligned} \tag{1}$$

where σ_1 is the stress in the first orthotropic direction, σ_2 is the stress in the second orthotropic direction, and σ_6 is the shear stress. This criterion is included in the

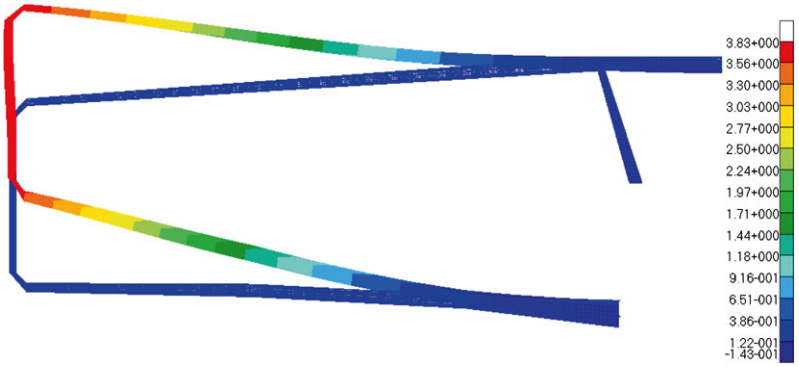

Fig. 20 Structural deformation

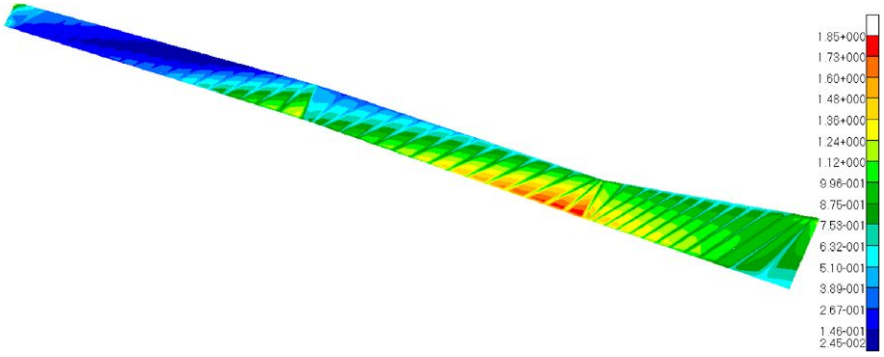

Fig. 21 Failure index—upper panels of the front wing

Nastran SOL100, in terms of failure index; when this index equals 1, the failure occurs in one ply, and this single failure is assumed to make the entire laminate fail as well. The first ply failure criterion is conservative, not taking the further residual static strength of the laminate into account.

In the next figures the results of the F.E. analysis are reported, with reference to the structural solution shown in the previous figures. Figure 20 shows the overall displacements under 3.75 limit load factor with the total displacement of 3.83 m. Comparing these results with those in Fig. 10 (metallic solution with 2.5 limit load factor) we have:

$$\frac{\text{Composite solution displacement}}{\text{Metallic solution displacement}} = \frac{3.83}{5.65} = 0.67.$$

This result, accompanied with a lighter solution, as shown later on, allows us to avoid any other investigation on static aeroelasticity and flutter to conclude that the solution in composites is more efficient from the structural viewpoint. Figures 21, 22, 23, 24 and 25 present the failure indexes of the main parts of the lifting system.

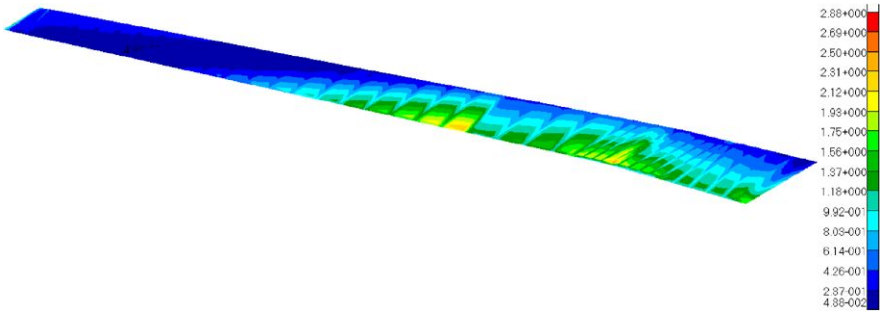

Fig. 22 Failure index—upper panels of the back wing

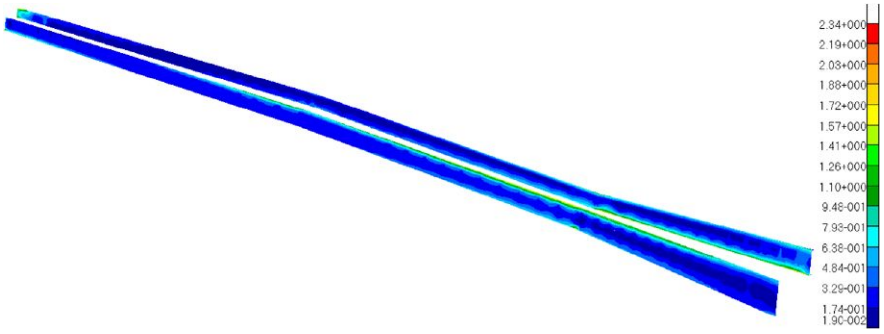

Fig. 23 Failure index—front wing spars

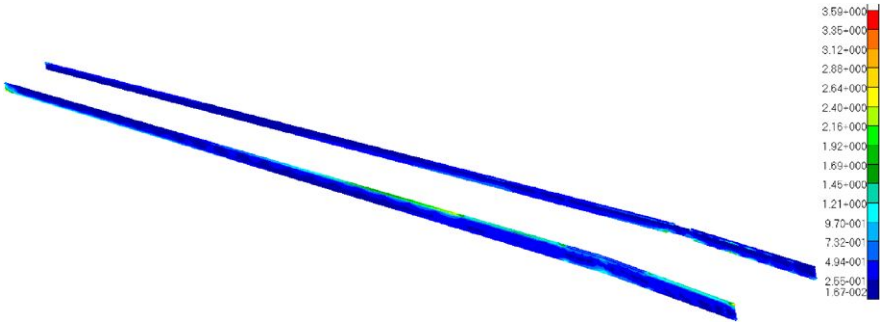

Fig. 24 Failure index—back wing spars

These figures need some comments. Figures 21 and 22 show that the failure index condition of upper skins of both wings is not verified in the local area of the kink; we accept this discrepancy because it is due to the dihedral jump, which will be eliminated. In the case of the spars, the index is correct apart from single spots. With these assumptions, the structural weight of the complete lifting system is given in Table 5, where the weight of the solution in Aluminium alloy is also reported.

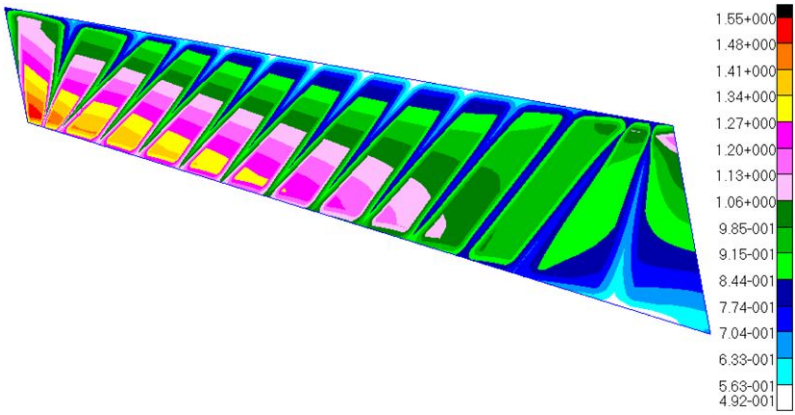

Fig. 25 Detail of the critical zone, next to the kink

Table 5 Wing-box weight of metal and composite solutions

Weight of metal structure	26014 kg
Weight of composite structure	16501 kg
Weight saving	9513 kg

It is evident that the weight saving of the wing system made in composite is remarkable. Although results may be affected by errors, the conclusion could be that the PrandtlPlane lifting system made in composites allows a weight reduction of about $1/3$ compared to the metallic solution, while the overall deformation is about $2/3$ (0.67) of the metallic one, at the limit load condition.

7 Conclusions

The wing structure of a 250-seat PrandtlPlane has been analysed in this paper.

The wing structure, being globally overconstraint to the fuselage, needs to be dealt with a non-conventional approach; furthermore, no historical data are available for the preliminary weight estimation. For this reason, the structure was preliminarily optimized with a multistep tool developed by the Politecnico of Milan, and a minimum weight solution complying with static and dynamic load conditions was assessed.

A FEM analysis has been conducted in the first part of the paper, highlighting some problems in the optimization process; in fact, the stress constraints were violated somewhere, but locally. In spite of these local stress peaks, the solution obtained could be assumed as a starting point of new developments.

In the second part of this paper a hypothesis of composite design for the structure under the same loads and constraints has been presented. A first preliminary sizing was performed, using the composite material as obtained from the classical theory of laminates to reproduce the same stiffness distribution of the previous solution.

To gain a significant technological advantage, a no-stringer wing box was designed, with the hypothesis of modifying the rib pitch to control the buckling phenomena. A model has been build up in order to check the stress constraints for each lamina, and the first ply failure criterion was adopted, using the failure index within the theory of maximum stress. Full compliance with constraints has been obtained, with the exception of small critical zones, even though very localized.

In the framework of many approximations and assumptions, some significant conclusions can be carried out, namely:

- the zone of the kink of the front wing is characterized by a change of dihedral angle with the effect, both in the Aluminium and in the composite structure, of localizing peaks in term of von Mises stress or failure index. This zone represents a very little portion of the whole structure and should be treated in detail. A new design with no change in dihedral angle should be provided;
- the composite solution examined is more rigid than the metallic solution, and the maximum displacements at limit load conditions are in the ratio of $2/3$;
- the composite solution is approximately 30% lighter than the metallic one, under the same loads and constraints.

References

1. 6th Framework Programme (2000–2006): Aeronautics and Space. http://www.eu.com
2. MSC Nastran User's Manual. MSC Software Corporation
3. The Seventh Framework Programme (FP7). http://www.eu.com
4. Torayca: http://www.torayca.com/techref/en/images/fcp02.html
5. Bitossi, M.: Sviluppo di metodi per la progettazione di strutture alari: validazione mediante analisi agli elementi finiti. Master's thesis, University of Pisa (2007)
6. Bottoni, C., Scanu, J.: Preliminary design of a 250 passenger PrandtlPlane aircraft. Master's thesis, University of Pisa (2004)
7. Bruhn, E.F.: Analysis and Design of Flight Vehicle Structures. Revised edn. Jacobs Publishing, Phoenix (1973)
8. Dal Canto, D.: Progetto preliminare del cassone alare di un velivolo di tipo Prandtl-Plane mediante l'applicazione di un ottimizzatore multilivello. Master's thesis, University of Pisa (2009) (In Italian)
9. Frediani, A., Cipolla, V., Rizzo, E.: The PrandtlPlane configuration: overview on possible applications to civil aviation. In: Buttazzo, G., Frediani, A. (eds.) Variational Analysis and Aerospace Engineering II: Mathematical Challenges for Aerospace Design. Springer, Berlin (2012)
10. Frediani, A., Dal Canto, D., Ghiringhelli, G.L., Terraneo, M.: The lifting system of a PrandtlPlane; part 1: design and analysis of a light alloy structural solution. In: Buttazzo, G., Frediani, A. (eds.) Variational Analysis and Aerospace Engineering II: Mathematical Challenges for Aerospace Design. Springer, Berlin (2012)
11. Montanelli, L.: Analisi FEM di velivoli HALE-UAV ad energia solare e modelli di predizione del peso strutturale. Master's thesis, University of Pisa (2009)
12. Niu, M.C.Y.: Composite Airframe Structures. Hong Kong Conmilit Press, Hong Kong (2005)
13. Piasentin, F.: Progetto preliminare del cassone alare di un velivolo in fase di avanprogetto mediante ottimizzazione multilivello. Master's thesis, Politecnico di Milano (2004)
14. Prandtl, L.: Induced Drag of Multiplanes (1924). NACA TN-182
15. Torenbeek, E.: Synthesis of Subsonic Airplane Design. Delft University Press, Delft (1972)

16. Vannucci, P.: Dispense del Corso di Dottorato in Materiali Compositi per Impieghi Strutturali. http://www.speculumatrum.it/dis/dottoratocorsi.html (in Italian)
17. Crivelli Visconti, I.: Materiali Compositi. Tecnologie, Progettazione e Applicazioni (2009). OEPL
18. Voskuijl, M., De Klerk, J., Van Ginneken, D.A.J.: Flight mechanics modeling of the Prandtl-Plane for conceptual and preliminary design. In: Buttazzo, G., Frediani, A. (eds.) Variational Analysis and Aerospace Engineering II: Mathematical Challenges for Aerospace Design. Springer, Berlin (2012)

Elastic Structures in Adhesion Interaction

Francesco Maddalena, Danilo Percivale, and Franco Tomarelli

1 Introduction

One goal of modern structural engineering relies in understanding and modeling the improvement of several characteristics of structural members, such as the load capacity, ductility, and durability. The request of upgrading inadequate or damaged structures stimulates the study of suitable tools to deal with nonconventional design issues such as debonding problems in fiber-reinforced elements. Indeed, the application of fiber-reinforced polymer (FRP) sheets as an externally bonded reinforcement is generally accepted as an efficient technique to reinforce concrete structures. Though numerical techniques based on classical elastic models are very often considered as a quantitative tool helping the design process, the lack of a qualitative understanding of the mechanical and/or analytical aspects of the phenomena hides the fundamental facts regulating these intriguing mechanical interactions.

It is generally accepted that the essential mechanical behavior of FRP-strengthened structural elements relies in the stress transfer between the fiber and the concrete beam through bonding interface (see, for instance, [4, 6, 11, 12, 23]). Therefore the overall mechanical behavior crucially depends on the interfacial bonding and its governing laws.

F. Maddalena (✉)
Dipartimento di Matematica Politecnico di Bari, via Re David 200, 70125 Bari, Italy
e-mail: f.maddalena@poliba.it

D. Percivale
Dipartimento di Ingegneria della Produzione Termoenergetica e Modelli Matematici, Università di Genova, Piazzale Kennedy, Fiera del Mare, Padiglione D, 16129 Genova, Italy
e-mail: percivale@diptem.unige.it

F. Tomarelli
Dipartimento di Matematica "Francesco Brioschi", Politecnico di Milano,
Piazza Leonardo da Vinci 32, 20133 Milano, Italy
e-mail: franco.tomarelli@polimi.it

G. Buttazzo, A. Frediani (eds.), *Variational Analysis and Aerospace Engineering: Mathematical Challenges for Aerospace Design*, Springer Optimization and Its Applications 66,
DOI 10.1007/978-1-4614-2435-2_12,

Here we pursue an energetic approach by exploiting a unifying perspective for the problems of adhesion and reinforcement of elastic thin structures ([8–10, 13–18]) and show that reinforcement reduces to adhesion when the stiffness of one of the structures involved becomes arbitrarily large (for adhesion problems, see also [2, 3, 5, 7, 20–22]).

In this paper, we study a variational model describing two one-dimensional material bodies (typically a reinforcement fiber and a concrete beam) that interact through an adhesive layer (typically a soft material) under prescribed displacement conditions. Both the reinforcing fiber and the matrix are described as elastic bodies, while different constitutive assumptions on the adhesive layer are investigated.

In Sect. 2 we assume that the adhesive layer reacts elastically to the slip of the reinforcing fiber with respect to the matrix, while in Sect. 3 the interfacial bond is modeled with a governing law exhibiting a softening branch for the slip exceeding a maximum value.

The analysis of the solutions suggests that the quadratic interaction described in of Sect. 2 is not able to capture the essence of adhesion, and this fact justifies the assumption of a softening law for the slip constitutive behavior.

In Sect. 3 we obtain a full characterization of equilibrium states when the matrix has elastic behavior, by studying two different constitutive assumptions, both discontinuous and smooth softening behaviors for the adhesive layer. Moreover we deal with the limit case of rigid matrix (concrete beams): the main results are presented in Theorem 41, Corollary 1, and Remark 3, which provide a length estimate of the elastically detached portion of the beam; such an estimate depends on the carrying capacity of the glue and the constitutive parameter of the fiber.

2 Adhesion of Elastic Structures

We consider a system composed of two elastic one-dimensional structures that are bonded through an adhesive layer. One structure is a fiber, the other one is a matrix, and both are parameterized by the variable x in the interval $[0, L]$. The fiber and the matrix are endowed respectively with the elastic energies E_{f}, E_{m}:

$$\begin{aligned} E_{\mathrm{f}}(v_{\mathrm{f}}) &= \frac{1}{2}\int_0^L k_{\mathrm{f}}|v_{\mathrm{f}}'|^2\,dx, \quad k_{\mathrm{f}} > 0; \\ E_{\mathrm{m}}(v_{\mathrm{m}}) &= \frac{1}{2}\int_0^L k_{\mathrm{m}}|v_{\mathrm{m}}'|^2\,dx, \quad k_{\mathrm{m}} > 0; \end{aligned} \tag{1}$$

where the functions $v_{\mathrm{f}}, v_{\mathrm{m}} : [0, 1] \to \mathbb{R}$ denote the axial displacements respectively in the fiber and in the matrix, while the strictly positive constants $k_{\mathrm{f}}, k_{\mathrm{m}}$ are the extensional stiffnesses (the Young modulus times the area of the transverse section).

The adhesion material layer which bonds together the two elastic structures is energetically represented by the functional

$$E_{\mathrm{ad}}(s) = \frac{1}{2}\int_0^L k_{\mathrm{ad}}|s|^2\,dx, \quad k_{\mathrm{ad}} > 0, \tag{2}$$

where k_{ad} is a constitutive parameter characterizing the adhesion material, and the slip function s is given by

$$s(x) = v_{\mathrm{f}}(x) - v_{\mathrm{m}}(x). \tag{3}$$

The slip s measures the difference of the elastic displacements occurring at the interface separating the two different materials. We introduce the notation $\mathbf{v} = (v_{\mathrm{f}}, v_{\mathrm{m}})$ and examine the total potential energy

$$E = E_{\mathrm{f}} + E_{\mathrm{m}} + E_{\mathrm{ad}}$$

of the following form:

$$E(\mathbf{v}) := E(v_{\mathrm{f}}, v_{\mathrm{m}}) = \frac{1}{2}\int_0^L \left(k_{\mathrm{f}}|v_{\mathrm{f}}'|^2 + k_{\mathrm{m}}|v_{\mathrm{m}}'|^2 + k_{\mathrm{ad}}|v_{\mathrm{f}} - v_{\mathrm{m}}|^2\right) dx. \tag{4}$$

We assume that the displacement $d > 0$ is given. Then the admissible configurations belong to the set

$$\mathscr{A} = \left\{\mathbf{v} = (v_{\mathrm{f}}, v_{\mathrm{m}}) \in H^1\big((0, L); \mathbb{R}^2\big),\ v_{\mathrm{f}}(L) = d,\ v_{\mathrm{m}}(0) = 0\right\}. \tag{5}$$

The equilibrium states of the system are the solutions the following variational problem:

$$\min\left\{E(\mathbf{v}) \mid \mathbf{v} \in \mathscr{A}\right\}. \tag{6}$$

The existence of solutions of (6) follows by a straight application of the direct methods of the calculus of variations. For this purpose, we observe that $E(\mathbf{v}) \geq \|v_{\mathrm{f}}'\|_{L^2}^2 + \|v_{\mathrm{m}}'\|_{L^2}^2$ for every $\mathbf{v} \in \mathscr{A}$, and hence the functional E enjoys the coercivity property due to the Poincaré inequality and the boundary conditions in $\mathscr{A}$. Moreover, the convexity of E with respect to $\mathbf{v}'$ ensures the weak lower semicontinuity in $H^1(0, L)$.

By employing a standard variation argument we get that any minimizer of (6) satisfies the following Euler–Lagrange equations:

$$\begin{cases} -k_{\mathrm{f}} v_{\mathrm{f}}''(x) = k_{\mathrm{ad}}(v_{\mathrm{m}} - v_{\mathrm{f}}) \quad \forall x \in (0, L), \\ -k_{\mathrm{m}} v_{\mathrm{m}}''(x) = k_{\mathrm{ad}}(v_{\mathrm{f}} - v_{\mathrm{m}}) \quad \forall x \in (0, L), \\ v_{\mathrm{f}}'(0) = 0, \quad v_{\mathrm{f}}(L) = d, \\ v_{\mathrm{m}}(0) = 0, \quad v_{\mathrm{m}}'(L) = 0. \end{cases} \tag{7}$$

The unique solution of (7) is explicitly given by

$$\begin{aligned} v_f(x) &= \mu(c_2 - c_1)x + k(c_2 + c_1) + c_1 e^{\mu x} + c_2 e^{-\mu x}, \\ v_m(x) &= \mu(c_2 - c_1)x + k(c_2 + c_1) - k\big(c_1 e^{\mu x} + c_2 e^{-\mu x}\big), \end{aligned} \tag{8}$$

where we have set

$$\mu = \sqrt{\frac{k_{\mathrm{ad}}}{k_{\mathrm{m}}} \frac{(k+1)}{k}}, \quad k = \frac{k_f}{k_m}, \tag{9}$$

and

$$\begin{aligned} c_1 &= d \frac{(k + e^{\mu L})}{1 + 4ke^{\mu L} + k^2 - \mu kL + e^{2\mu L}(1 + k^2 + \mu kL)}, \\ c_2 &= d \frac{e^{\mu L}(1 + ke^{\mu L})}{1 + 4ke^{\mu L} + k^2 - \mu kL + e^{2\mu L}(1 + k^2 + \mu kL)}. \end{aligned} \tag{10}$$

Then

$$v_f(x) - v_m(x) = (1 + k)\big(c_1 e^{\mu x} + c_2 e^{-\mu x}\big) > 0 \quad \forall x \in [0, L], \tag{11}$$

and hence v_{f} is strictly convex, and v_{m} is strictly concave; moreover, $v_{\mathrm{f}} - v_{\mathrm{m}}$ attains its minimum value

$$m = v_{\mathrm{f}}(\bar{x}) - v_{\mathrm{m}}(\bar{x}) = 2(1 + k)\sqrt{c_1 c_2}$$

at the point

$$\bar{x} = \frac{1}{2\mu} \ln \frac{c_2}{c_1} \in (0, L).$$

In the limit case where the supporting matrix becomes rigid, say $k_m \to \infty$, we have

$$\bar{x} \to 0, \qquad \mu \to \sqrt{\frac{k_{\mathrm{ad}}}{k_{\mathrm{f}}}}, \qquad m \to m_\infty := \frac{d}{\cosh(L\sqrt{k_{\mathrm{ad}}/k_{\mathrm{f}}})}.$$

Notice that, if k_{ad} is of the same order as k_{f}, then the value m_∞ is smaller than d, but, as $d \to 0$, it is of the same order as d. This last remark may suggest some inadequacy of the constitutive assumption (2). Nevertheless, in problems arising in structural engineering, typically the ratio $k_{\mathrm{ad}}/k_{\mathrm{f}}$ is very large, and so for any d, the value m_∞ goes to zero much faster than d. It follows that the quadratic interaction described in this section is able to capture the essence of adhesion only in the case $k_{\mathrm{ad}}/k_{\mathrm{f}}$ is very large. For this reason, in the next section we examine a different constitutive assumption given by (14) and (15) (or (47) and (48)). Figures 1 and 2 display the graphs of v_{f}, v_{m} and $s = v_{\mathrm{f}} - v_{\mathrm{m}}$, for relevant choices of the parameters: we emphasize the resulting small magnitude of the slip.

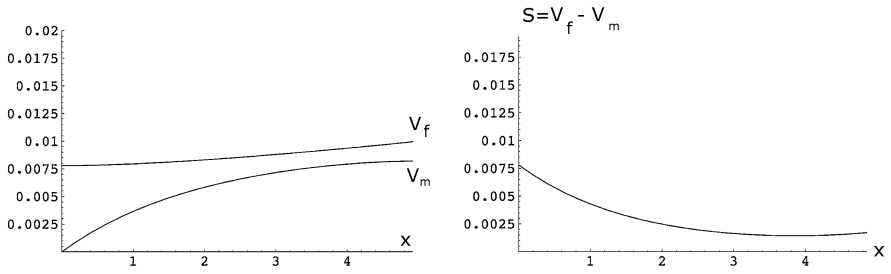

Fig. 1 $k_f = 210000$ MPa; $k_m = 30000$ MPa; $k_{ad} = 10000$ MPa; $L = 5$ m; $d = 0.01$ m [1]

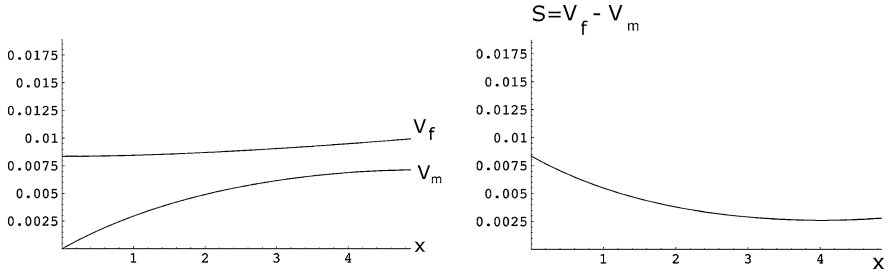

Fig. 2 CFRP plate: $k_f = 165000$ MPa; Concrete: $k_m = 25000$ MPa; Epoxy adhesive: $k_{ad} = 4500$ MPa; $L = 5$ m; $d = 0.01$ m [6]

Remark 1 Notice that, if $k_f = k_m$, then the unique minimizer $\mathbf{v} = (v_f, v_m)$ exhibits a graph which is symmetric with respect to the point $(L/2, d/2)$, that is,

$$\begin{cases} v_f(x) = \frac{d}{2} - v_m(\frac{L}{2} - x), \\ v_m(x) = \frac{d}{2} - v_f(\frac{L}{2} - x). \end{cases} \tag{12}$$

Relationship (12) is a consequence of the uniqueness and the following invariance property of the energy:

$$E\left(\frac{d}{2} - v_m\left(\frac{L}{2} - x\right), \frac{d}{2} - v_f\left(\frac{L}{2} - x\right)\right) = E(v_f, v_m), \quad \forall (v_f, v_m) \in \mathscr{A}.$$

3 Adhesion with Softening

In this section we examine two constitutive softening laws for the adhesion layer. The first one (discontinuous softening, Sects. 3.1, 3.2) presents a sudden transition of the stress which goes to zero discontinuously, while the second one (smooth softening, Sect. 3.3) exhibits a smooth decay of the stress after a certain value of the slip. For the first one, we also consider the limit case where the supporting matrix becomes rigid.

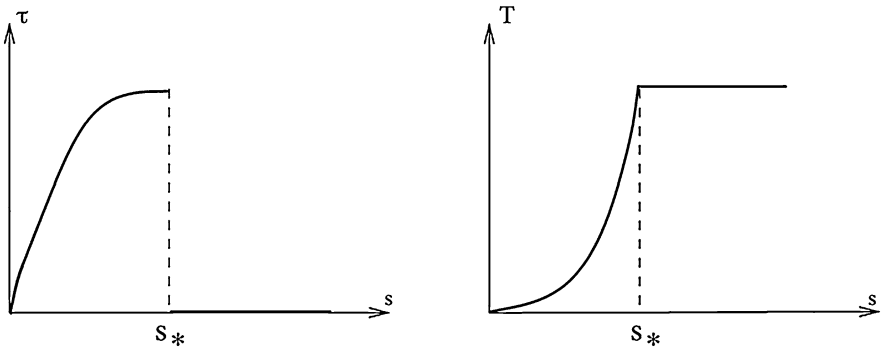

Fig. 3 Energy and constitutive law for discontinuous softening

3.1 Elastic Supporting Matrix with Discontinuous Softening Glue

In this section we assume that the interface law governing the constitutive behavior of the glue behaves elastically up to a given value of the slip, while beyond such a threshold the stress discontinuously drops to zero. More precisely, we assume

$$\big\{\tau : \mathbb{R}_+ \to \mathbb{R}_+ \text{ continuous and weakly increasing in } [0, S_*],$$

$$\tau(0) = 0,\ \ \tau(s) > 0\ \ \forall s \in (0, S_*],\ \ \tau(s) = 0\ \ \forall s > S_*\big\}. \tag{13}$$

The function τ represents the stress-slip constitutive relationship of the adhesive material, and for the adhesion energy, we assume the following density function defined for every $\sigma \geq 0$:

$$T(\sigma) = G \int_0^\sigma \tau(t)\, dt, \tag{14}$$

where $G > 0$ represents the stiffness of the glue. (A qualitative graph of an admissible constitutive law is displayed in Fig. 3.)

Notice that T is continuous and convex in $[0, S_*]$ since $\tau \in BV(0, S_*)$ and $T'' = \tau' \geq 0$ in $(0, S_*)$. We set

$$\widehat{E}_{\rm ad} = \int_0^L T\big(|s(x)|\big)\, dx, \tag{15}$$

where $s(x) = v_{\rm f}(x) - v_{\rm m}(x)$.

The total energy of the system takes the form

$$\widehat{E}(\mathbf{v}) := E_{\rm f}(\mathbf{v}) + E_{\rm m}(\mathbf{v}) + \widehat{E}_{\rm ad}(\mathbf{v}), \quad \mathbf{v} = (v_{\rm f}, v_{\rm m}), \tag{16}$$

where the elastic energies $E_{\rm f}$ and $E_{\rm m}$ are defined in (1), and $\widehat{E}_{\rm ad}$ is defined in (15).

Remark 2 Note that, if $d > S_*$, then $\mathbf{v}_0 = (d, 0) \in \mathscr{A}$ corresponds to the completely detached state of the two structures.

Motivated by the above remark, we analyze only the nontrivial case occurring when

$$0 < d < S_*. \tag{17}$$

Along this subsection we assume (1) and (14)–(17) and select the same admissible set of displacements $\mathscr{A}$ defined in (5). The effective role played by (17) and the consequences of its failure will be clarified at the end of this section.

The equilibrium states of the system are the solutions the following variational problem:

$$\min\{\widehat{E}(\mathbf{v}) \mid \mathbf{v} \in \mathscr{A}\}. \tag{18}$$

Let us note that $\mathbf{v}_0 = (d, 0) \in \mathscr{A}$, i.e., $\mathbf{v}_0$ is an admissible displacement, and, by taking into account (17), we have the following energy estimate:

$$\widehat{E}(\mathbf{v}) \le \widehat{E}(\mathbf{v}_0) \le LT(S_*) \quad \forall \mathbf{v} \in \operatorname*{argmin}_{\mathscr{A}} \widehat{E}. \tag{19}$$

Lemma 1 *Assume* (1), (5), (14)–(17), *and* $\mathbf{v} \in \operatorname{argmin}_{\mathscr{A}} \widehat{E}$.
Then $0 \le v_{\mathrm{f}} \le d$ *and* $0 \le v_{\mathrm{m}} \le d$.

Proof The thesis follows by observing that for every $(v_{\mathrm{f}}, v_{\mathrm{m}}) \in \mathscr{A}$, by setting $\tilde{v}_{\mathrm{f}} = \min(v_{\mathrm{f}}, d)$ and $\tilde{v}_{\mathrm{m}} = \min(v_{\mathrm{m}}, d)$ we have

$$({v_{\mathrm{f}}}^+, {v_{\mathrm{m}}}^+) \in \mathscr{A}, \qquad (\tilde{v}_{\mathrm{f}}, \tilde{v}_{\mathrm{m}}) \in \mathscr{A}, \tag{20}$$

$$T\big(|{v_{\mathrm{f}}}^+ - {v_{\mathrm{m}}}^+|\big) \le T\big(|v_{\mathrm{f}} - v_{\mathrm{m}}|\big), \tag{21}$$

and the inequality in (21) is strict if $|\{x \mid v_{\mathrm{f}}(x) < 0 \text{ or } v_{\mathrm{m}}(x) < 0\}| > 0$,

$$T\big(|\tilde{v}_{\mathrm{f}} - \tilde{v}_{\mathrm{m}}|\big) \le T\big(|v_{\mathrm{f}} - v_{\mathrm{m}}|\big), \tag{22}$$

and the inequality in (22) is strict if $|\{x \mid v_{\mathrm{f}}(x) > d \text{ or } v_{\mathrm{m}}(x) > d\}| > 0$. □

Theorem 1 *Assume* (1), (5), *and* (14)–(17). *Then problem* (18) *admits a unique solution* $\mathbf{v} \in C^2([0, L]; \mathbb{R}^2)$. *Moreover,* $\mathbf{v}$ *fulfills* $v_{\mathrm{f}}(x) \ge v_{\mathrm{m}}(x)$ $\forall x \in [0, L]$ *and the Euler–Lagrange equations*

$$\begin{cases} k_{\mathrm{f}} v_{\mathrm{f}}''(x) = G\tau(v_{\mathrm{f}} - v_{\mathrm{m}}), & x \in (0, L), \\ -k_{\mathrm{m}} v_{\mathrm{m}}''(x) = G\tau(v_{\mathrm{f}} - v_{\mathrm{m}}), & x \in (0, L), \\ v_{\mathrm{f}}'(0) = 0, \quad v_{\mathrm{f}}(L) = d, \\ v_{\mathrm{m}}(0) = 0, \quad v_{\mathrm{m}}'(L) = 0. \end{cases} \tag{23}$$

Moreover, the following Compliance Identity holds:

$$\widehat{E}(\mathbf{v}) = \int_0^L \left[\frac{G}{2}\tau\big(v_{\mathrm{f}}(x) - v_{\mathrm{m}}(x)\big)\big(v_{\mathrm{f}}(x) - v_{\mathrm{m}}(x)\big) + T\big(v_{\mathrm{f}}(x) - v_{\mathrm{m}}(x)\big)\right] dx + k_{\mathrm{f}} d\, v_{\mathrm{f}}'(L). \tag{24}$$

The previous theorem will be proved through a pair of lemmas.

Lemma 2 *Assume* (1), (5), *and* (14)–(17). *Then the variational problem* (18) *admits a solution, and if* $\mathbf{v} \in \operatorname{argmin}_{\mathscr{A}} \widehat{E}$, *then* $\mathbf{v} \in C^2([0,L];\mathbb{R}^2)$ *and satisfies the following Euler–Lagrange equations in* $(0,L)$:

$$\begin{cases} -k_{\mathrm{f}} v_{\mathrm{f}}''(x) = G\tau(|v_{\mathrm{f}} - v_{\mathrm{m}}|)\,\operatorname{sign}(v_{\mathrm{m}} - v_{\mathrm{f}}), \\ -k_{\mathrm{m}} v_{\mathrm{m}}''(x) = G\tau(|v_{\mathrm{f}} - v_{\mathrm{m}}|)\,\operatorname{sign}(v_{\mathrm{f}} - v_{\mathrm{m}}), \\ v_{\mathrm{f}}'(0) = 0, \quad v_{\mathrm{m}}'(L) = 0, \end{cases} \tag{25}$$

together with boundary conditions

$$v_{\mathrm{m}}(0) = 0, \qquad v_{\mathrm{f}}(L) = d. \tag{26}$$

Proof Notice that $\widehat{E}(\mathbf{v}) \geq \|v_{\mathrm{f}}'\|_{L^2}^2 + \|v_{\mathrm{m}}'\|_{L^2}^2$ for every $\mathbf{v} \in \mathscr{A}$, and hence the functional $\widehat{E}$ enjoys the coercivity property due to the Poincaré inequality and the boundary conditions in $\mathscr{A}$. Moreover, the convexity of $\widehat{E}$ with respect to $\mathbf{v}'$ ensures the weak lower semicontinuity in $H^1(0,L)$. Then existence of solutions for the minimization (18) follows by a straight application of the direct method of the calculus of variations.

The usual computation shows that the Euler–Lagrange equations (25) and the boundary conditions (26) are satisfied in $\mathscr{D}'(0,L)$, and by recalling Lemma 1 and assumptions on τ, we have that $\tau(|v_{\mathrm{f}} - v_{\mathrm{m}}|)\,\operatorname{sign}(v_{\mathrm{m}} - v_{\mathrm{f}})$ is continuous in $[0,L]$ and hence $\mathbf{v} \in C^2([0,L];\mathbb{R}^2)$. □

Lemma 3 *Assume* (1), (5), (14)–(17), *and* $\mathbf{v} \in \operatorname{argmin}_{\mathscr{A}} \widehat{E}$. *Then*

$$v_{\mathrm{m}}(x) \leq v_{\mathrm{f}}(x) \quad \forall x \in [0,L], \tag{27}$$

and the equality may occur only in a (*possibly empty*) *closed interval* $[a,b]$ *s.t.*

$$[a,b] \subsetneqq [0,L].$$

Proof Two alternatives may occur: either $v_m \geq v_f$ in the whole $[0,L]$, or there exists $\bar{x} \in [0,L]$ such that $v_m(\bar{x}) < v_f(\bar{x})$.

In the first case by Lemma 1 we get $v_f(0) = v_m(0) = 0$, $v_m(L) = v_f(L) = d$, and by the Euler–Lagrange equations we have that v_m is convex and v_f is concave, and hence $v_m - v_f$ is convex, and therefore $v_m \leq v_f$, that is, $v_f \equiv v_m$, which is in contradiction with the boundary conditions in (25).

We prove now that if there exists $\bar{x} \in [0,L]$ such that $v_m(\bar{x}) < v_f(\bar{x})$, then $v_m \leq v_f$ in the whole $[0,L]$.

We set $x_1 = \inf\{x \leq \bar{x} : \ v_m(x) < v_f(x) \text{ in } (x,\bar{x})\}$, $x_2 = \{x \geq \bar{x} : \ v_m(x) < v_f(x) \text{ in } (\bar{x},x)\}$, and we may consider the following cases:

(i) $0 < x_1 < x_2 < L$: then by the E–L equations we get $v_f - v_m$ convex in $[x_1,x_2]$ and $v_m(x_1) - v_f(x_1) = v_m(x_1) - v_f(x_1) = 0$, that is, $v_f \leq v_m$ in $[x_1,x_2]$, a contradiction.

(ii) $x_1 = 0 < x_2 < L$: then $v_f(x_2) = v_m(x_2) = 0$, and again either $v_m \geq v_f$ in the whole $[x_2, L]$, or there exists $x_3 \in (x_2, L]$ such that $v_m(x_3) < v_f(x_3)$. Therefore, either $v_f \equiv v_m$ in $[x_2, L]$, or $v_f \geq v_m$ in $[0, x_2] \cup [x_3, L]$ and $(v_f - v_m)(x_2) = 0 = (v_f - v_m)(x_3)$. By the minimality of (v_f, v_m), it is readily seen that $v_f = v_m$ in $[x_2, x_3]$, thus proving the statement in this case. Since the case $0 < x_1 < x_2 = L$ can be handled as the previous one, the proof of (27) is achieved. By the boundary conditions in (25), equality in (27) may occur only in a proper subset of $[0, L]$, a closed interval $[a, b] \subset [0, L]$ with $[a, b] \not\equiv [0, L]$.

Proof of Theorem 1 Let $\mathbf{v} \in \operatorname{argmin}_{\mathscr{A}} \widehat{E}$. By Lemma 2 we deduce that $\mathbf{v} \in C^2([0, L]; \mathbb{R}^2)$ and fulfills Euler–Lagrange equations (23). We are left to show the uniqueness that we will obtain by a technique similar to [19], Theorem 5. We set

$$\begin{aligned} &\psi(\mathbf{p}, \mathbf{q}) = k_{\mathrm{f}}(q_1)^2 + k_{\mathrm{m}}(q_2)^2 + T(p_1 - p_2), \\ &\forall \mathbf{p} = (p_1, p_2), \quad \mathbf{q} = (q_1, q_2). \end{aligned} \tag{28}$$

If there exist two solutions $\mathbf{v} = (v_{\mathrm{f}}, v_{\mathrm{m}})$ and $\mathbf{w} = (w_{\mathrm{f}}, w_{\mathrm{m}})$ with $\mathbf{v} \not\equiv \mathbf{w}$, then recalling (27) and

$$0 \leq s(x) = v_{\mathrm{f}}(x) - v_{\mathrm{m}}(x) \leq d \leq S_* \quad \forall x \in [0, L],$$

from the convexity of T in $[0, S_*]$ we get

$$\psi\big(t\mathbf{v} + (1-t)\mathbf{w}, t\mathbf{v}' + (1-t)\mathbf{w}'\big) - t\psi(\mathbf{v}, \mathbf{v}') - (1-t)\psi(\mathbf{w}, \mathbf{w}') \leq 0; \tag{29}$$

hence the minimality of $\mathbf{v}$ and $\mathbf{w}$ implies

$$\begin{aligned} &\int_0^L \psi\big(t\mathbf{v} + (1-t)\mathbf{w}, t\mathbf{v}' + (1-t)\mathbf{w}'\big)\, dx \\ &\quad = t\int_0^L \psi(\mathbf{v}, \mathbf{v}')\, dx + (1-t)\int_0^L \psi(\mathbf{w}, \mathbf{w}')\, dx, \end{aligned} \tag{30}$$

and by (29) we have

$$\begin{aligned} &\psi\big(t\mathbf{v} + (1-t)\mathbf{w}, t\mathbf{v}' + (1-t)\mathbf{w}'\big) - t\psi(\mathbf{v}, \mathbf{v}') - (1-t)\psi(\mathbf{w}, \mathbf{w}') = 0 \\ &\quad \forall x \in [0, L], \ \forall t \in [0, 1]. \end{aligned} \tag{31}$$

By differentiating the previous equality with respect to t we get

$$\begin{aligned} &\psi_p\big(t\mathbf{v} + (1-t)\mathbf{w}, t\mathbf{v}' + (1-t)\mathbf{w}'\big) \cdot (\mathbf{v} - \mathbf{w}) \\ &\quad + \psi_q\big(t\mathbf{v} + (1-t)\mathbf{w}, t\mathbf{v}' + (1-t)\mathbf{w}'\big) \cdot (\mathbf{v}' - \mathbf{w}') \\ &\quad = \psi(\mathbf{v}, \mathbf{v}') - \psi(\mathbf{w}, \mathbf{w}') \quad \forall x \in [0, L], \ \forall t \in [0, 1]. \end{aligned} \tag{32}$$

Hence by evaluating (32) at $t = 1$ and $t = 0$ we have

$$\begin{aligned} &\psi_p(\mathbf{v}, \mathbf{v}') \cdot (\mathbf{v} - \mathbf{w}) + \psi_q(\mathbf{v}, \mathbf{v}') \cdot (\mathbf{v}' - \mathbf{w}') \\ &\quad = \psi_p(\mathbf{w}, \mathbf{w}') \cdot (\mathbf{v} - \mathbf{w}) + \psi_q(\mathbf{w}, \mathbf{w}') \cdot (\mathbf{v}' - \mathbf{w}'). \end{aligned} \tag{33}$$

Then, taking into account (27), (28), and (33) and the fact that τ is nondecreasing, we get

$$2k_{\mathrm{f}}(v_{\mathrm{f}}' - w_{\mathrm{f}}')^2 + 2k_{\mathrm{m}}(v_{\mathrm{m}}' - w_{\mathrm{m}}')^2 = (v_{\mathrm{f}} - v_{\mathrm{m}} - w_{\mathrm{f}} + w_{\mathrm{m}})\big\{\tau(w_{\mathrm{f}} - w_{\mathrm{m}}) - \tau(v_{\mathrm{f}} - v_{\mathrm{m}})\big\} \le 0, \tag{34}$$

that is, $v_{\mathrm{f}}' - w_{\mathrm{f}}' = v_{\mathrm{m}}' - w_{\mathrm{m}}' = 0$. Hence $\mathbf{v} = \mathbf{w}$ in the whole $[0, L]$.

Eventually, integrating by parts the elastic energies in (1) and taking into account (23) and (25), we get the Compliance Identity (24). □

A slight modification of the proof of the previous theorem permits to show also the following:

Theorem 2 *Assume* (1), (5), *and* (14)–(17). *If the odd extension of* τ *is analytic in a neighborhood of the origin*, *then*, *in addition to the statement of Theorem* 1, *we have*

$$v_{\mathrm{m}}(x) < v_{\mathrm{f}}(x) \quad \forall x \in [0, L]. \tag{35}$$

Proof Since here all the assumptions of Theorem 1 hold, we have only to prove (35).

If there exists $\bar{x}$ such that $v_{\mathrm{f}}(\bar{x}) = v_{\mathrm{m}}(\bar{x})$, then by $\mathbf{v} \in C^2([0, L]; \mathbb{R}^2)$ and Lemma 2 we get $v_{\mathrm{f}}'(\bar{x}) = v_{\mathrm{m}}'(\bar{x})$, and by using the Euler–Lagrange equations we deduce that $v_{\mathrm{f}}^{(j)}(\bar{x}) = v_{\mathrm{m}}^{(j)}(\bar{x})$ for every $j \ge 0$ and hence $v_{\mathrm{f}}(x) \equiv v_{\mathrm{m}}(x)$ in $[0, L]$ by the identity principle of analytic functions, so that

$$v_{\mathrm{f}} \equiv v_{\mathrm{m}} \equiv \frac{d}{L}x,$$

in contrast with the Neumann boundary conditions $v_{\mathrm{f}}'(0) = 0$, $v_{\mathrm{m}}'(L) = 0$. □

3.2 Rigid Supporting Matrix with Discontinuous Softening Glue

In this subsection we face the case of a rigid matrix, as is the case of concrete beams.

When assuming the structural assumptions of the previous subsection (say, (1), (5), and (14)–(17)), if k_{f} is fixed, $k_{\mathrm{m}} \to +\infty$, and $(v_{\mathrm{f}}, v_{\mathrm{m}})$ is the minimizer of $\widehat{E}$ on $\mathscr{A}$, then $v_{\mathrm{m}} \to 0$ in $H^1(0, L)$.

This claim is a straightforward consequence of estimate (19) since we have

$$0 \le \|v_{\mathrm{m}}'\|^2_{L^2(0,L)} \le \frac{1}{k_{\mathrm{m}}}\widehat{E}(\mathbf{v}) \le \frac{1}{k_{\mathrm{m}}}LT(S_*).$$

Then it is natural to describe the rigid supporting matrix by selecting as admissible only those axial displacements $\mathbf{v}$ that fulfill $v_{\mathrm{m}} \equiv 0$. Moreover, in this case we can assume without any restriction that the length of the matrix is greater than the length

L of the fiber. To simplify the notation, we set $v \equiv v_{\mathrm{f}}$, and so we reduce to study the energy

$$H(v) = \int_0^L \left(\frac{k_{\mathrm{f}}}{2} |v'|^2 + T\big(|v|\big) \right) dx. \tag{36}$$

Precisely, we deal with the problem

$$\min\big\{ H(v) \mid v \in H^1(0, L),\, v(L) = d \big\}. \tag{37}$$

Theorem 3 *Assume* (13), (14), (17), (36). *Then*:

(i) *Problem* (37) *admits a unique solution* $v \in C^2([0, L])$. *Moreover*, $0 \le v(x) \le d$ $\forall x \in [0, L]$.

(ii) *The solution* v *of* (37) *fulfills the Euler–Lagrange equation*

$$\begin{cases} k_{\mathrm{f}} v''(x) = G\, \tau(v(x)), & x \in (0, L), \\ v'(0) = 0, \quad v(L) = d. \end{cases} \tag{38}$$

(iii) *The solution* v *of* (37) *fulfills the Compliance Identity*

$$H(v) = \int_0^L \left[\frac{G}{2} \tau\big(v(x)\big) v(x) + T\big(v(x)\big) \right] dx + k_{\mathrm{f}}\, d v'(L). \tag{39}$$

(iv) *The solution* v *of* (37) *fulfills the following equation* (*first integral*):

$$T\big(v(x)\big) - \frac{k_{\mathrm{f}}}{2} \big(v'(x)\big)^2 \text{ is constant in } [0, L]. \tag{40}$$

(v) *If* v *is the solution of* (37), *then either* $v(x) > 0$ $\forall x \in [0, L]$, *or there exists* $\xi \in [0, L)$, *with* $\xi = \xi(d)$, *such that* $v(x) = 0$ $\forall x \in [0, \xi]$ *and* v *is strictly increasing in* $[\xi, L]$.

Proof Statements (i), (ii), (iii) and the fact that $v \not\equiv 0$ can be proved as in the proof of Theorem 1.

(iv) Since $H(v) = \int_0^L f(v, v')dx$, we get $\frac{d}{dx}[f - p f_p] = 0$ and hence (40).

(v) The fact that the null set of v, when nonempty, is connected and contains $x = 0$ is true since otherwise we could modify v by setting $v = 0$ in the interval $[0, \xi]$ and strictly reduce the energy, in contradiction to the minimality of v. Then, by (38), since $\tau(0) = 0$ and $\tau(s) > 0$ $\forall s \in (0, S_*)$, we get the statement. □

Theorem 4 *Assume* (13), (14), (17), (36) *and let* v *be the solution of* (37). *Set* $\xi = \inf\{x \in [0, L] \mid v(x) > 0\}$. *Then*

$$L - \xi = \sqrt{\frac{k_f}{2}} \int_{v(\xi)}^{d} \frac{dt}{\sqrt{T(t) - T(v(\xi))}}. \tag{41}$$

Proof Clearly $v'(\xi) = 0$, and since $v'(x) \geq 0$, by (40) we get

$$\sqrt{\frac{k_f}{2}}\, v'(x) = \sqrt{T\big(v(x)\big) - T\big(v(\xi)\big)} \quad \forall x \in [\xi, L],$$

$$L - x = \sqrt{\frac{k_f}{2}} \int_{v(x)}^{d} \frac{dt}{\sqrt{T(t) - T(v(\xi))}} \quad \forall x \in (\xi, L],$$

and now the statement easily follows by letting $x \to \xi$. □

A straightforward consequence of (41) is the following statement, which, in the spirit of [1], where an estimate analogous to (41) is deduced through heuristic arguments, establishes a sharp estimate on the length of the fiber according to the carrying capacity of the glue and the constitutive parameters of the reinforcing fiber.

Corollary 1 *Assume* (13), (14), (17), (36) *and let* v *be the solution of* (37). *Set*

$$\overline{L} := \sqrt{\frac{k_{\mathrm{f}}}{2}} \int_0^d \frac{dt}{\sqrt{T(t)}}. \tag{42}$$

Then:

(i) *If* $\overline{L} < L$, *then* $0 < \xi = L - \overline{L}$.
(ii) *If* $\overline{L} = L$, *then* $\xi = 0$ *and* $v(0) = 0$.
(iii) *If* $\overline{L} > L$, *then* $\xi = 0$ *and* $v(0) > 0$.

Proof By $T(0) = 0$ and the convexity of T, we get

$$T(y - z) + T(z) \leq T(y) \quad \forall y \in [z, d],\ 0 < z < d,$$

$$\int_z^d \frac{dy}{\sqrt{T(y) - T(z)}} \leq \int_z^d \frac{dy}{\sqrt{T(y - z)}} = \int_0^{d-z} \frac{d\eta}{\sqrt{T(\eta)}} < \int_0^d \frac{d\eta}{\sqrt{T(\eta)}}, \tag{43}$$

and therefore, if $\overline{L} = L$, then by (41) and (43) we get $\xi = 0$ and $v(0) = 0$, and (ii) is proved. If $\overline{L} < L$, then either $\xi = 0$, $v(0) > 0$, or $0 < \xi = L - \overline{L}$, but if $\xi = 0$ and $v(0) > 0$, then by using (43) with $z = v(0)$ we get $L < \overline{L}$, a contradiction. Eventually (iii) is an obvious consequence of (41). □

Remark 3 Assume (13), (14), (17), (36), and (42).

- If $L \leq \overline{L}$, then $\xi[d] = 0$.
  Then the mathematical solution v describes a state in which the whole fiber is elastically detached from the matrix: $v(x) > 0$ for every x when $L < \overline{L}$, $v(x) = 0$ iff $x = 0$ when $L = \overline{L}$. This suggests the possibility of structural breakdown. This case includes the case $\overline{L} = +\infty$, which corresponds to the nonintegrability at 0 of $T^{-\frac{1}{2}}$.

- If $L > \overline{L}$, then $\xi[d] = L - \overline{L} > 0$.
  Then the mathematical solution v describes a state in which the fiber is only partially elastically detached from the matrix. This suggests that the structure is able to sustain the traction without breakdown. This case may happen only if $T^{-\frac{1}{2}} \in L^1(0, S_*)$, hence it is not compatible with any linear or superlinear stress-slip law for the adhesive material.

An interesting outcome of Corollary 1 is the suggestion to study suitable adhesive property of the glue, say qualitative behavior of τ, in order to make $\overline{L}$ as small as possible.

Now we prove that when τ is concave near the origin, then the displacement in 0 is negligible with respect to d. This result is in good agreement with the experimental observations (in contrast with the one obtained in Sect. 2 in the case of quadratic adhesion law), and hence it provides reasons in favor of the choice of constitutive assumptions (13) and (14).

To make explicit the dependence of the solution v on the Dirichlet datum d, we label the unique v solution of (37) by $v[d] = v[d](x)$ and set $\xi[d] = \inf\{x \in [0, L] \mid v[d](x) > 0\}$ for every $d \in (0, S_*)$.

Theorem 5 *Assume* (13), (14), (17), (36), *and*

$$\lim_{s \to 0^+} s^{-1}\tau(s) = +\infty. \tag{44}$$

Then either $v[d](0) \equiv 0$ *in a neighborhood of* $d = 0$, *or* $d^{-1}v[d](0) \to 0$ *as* $d \to 0$.

Proof If $d_n \to 0$ and $v[d_n](0) > 0$, then $\xi[d_n] = 0$, and formula (41) holds; moreover, since $v[d_n](L) = d_n > 0$, $\xi = 0$, and $v[d_n](\xi) = v[d_n](0) > 0$, we have

$$L = \sqrt{\frac{k_{\mathrm{f}}}{2G}} \int_{v[d_n](0)}^{d_n} \frac{dt}{\sqrt{\int_{v[d_n](0)}^{t} \tau(s)\, ds}}. \tag{45}$$

Recalling that τ is increasing and $v[d_n](0) < d_n$, we get

$$\frac{2G}{k_{\mathrm{f}}} L^2 \left(\int_{v[d_n](0)}^{d_n} \frac{dt}{\sqrt{(d_n - v[d_n](0))\tau(v[d_n](0))}} \right)^2 \leq \frac{d_n - v[d_n](0)}{\tau(v[d_n](0))},$$

$$2G\tau\big(v[d_n](0)\big)L^2 \leq k_f d_n,$$

which, together with (44), yields the thesis. □

3.3 Elastic Supporting Matrix with Smooth Softening Glue

In this section we assume that the stress-slip law governing the constitutive behavior of the glue is continuous with compact support.

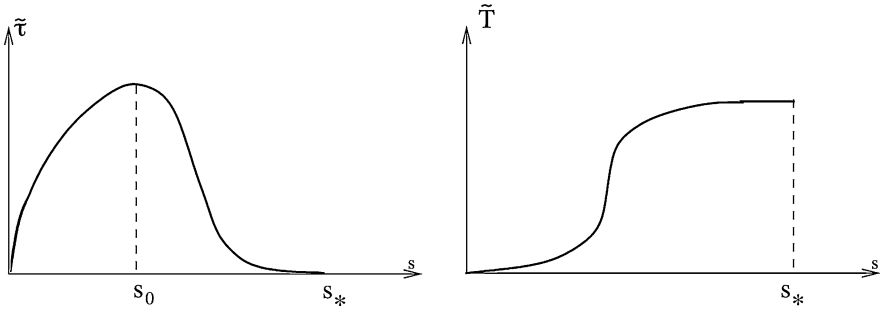

Fig. 4 Energy and constitutive law for smooth softening

The scheme includes the case of unimodal law which behaves elastically up to a given value of the slip and exhibits a softening range beyond such a value. Nevertheless, we do not make any assumption about the monotonicity region of $\tilde{\tau}$. More precisely, let

$$\begin{aligned}&\big\{\tilde{\tau} : \mathbb{R}_+ \to \mathbb{R}_+ \text{ continuous}, S_* > 0,\\ &\tilde{\tau}(0) = 0,\ \tilde{\tau}(s) > 0 \text{ in } [0, S_*],\ \tilde{\tau}(s) = 0\ \forall s \geq S_*\big\}.\end{aligned} \tag{46}$$

$\tilde{\tau}$ represents the stress-slip constitutive relationship of the adhesive material (a qualitative graph is displayed in Fig. 4); hence the adhesion energy is now defined as follows:

$$\widetilde{T}(\sigma) = G \int_0^{\sigma} \tilde{\tau}(t)\, dt, \tag{47}$$

$$\widetilde{E}_{\text{ad}} = \int_0^L \widetilde{T}\big(|s(x)|\big)\, dx. \tag{48}$$

The total energy of the system takes the form

$$\widetilde{E}(\mathbf{v}) := E_{\text{f}}(\mathbf{v}) + E_{\text{m}}(\mathbf{v}) + \widetilde{E}_{\text{ad}}(\mathbf{v}), \quad \mathbf{v} = (v_{\text{f}}, v_{\text{m}}), \tag{49}$$

where v_{f} and v_{m} are the axial displacements of the fiber and the matrix, the elastic energies E_{f} and E_{m} are defined in (1), and $\widetilde{E}_{\text{ad}}$ is defined in (48). Referring to (5) and (49), we face the minimization problem

$$\min\big\{\widetilde{E}(\mathbf{v}) \mid \mathbf{v} \in \mathscr{A}\big\}. \tag{50}$$

Theorem 6 *Assume* (1), (5), (17),(46), (47), (48), *and* (49). *Then problem* (50) *admits a solution* $\mathbf{v} \in C^2([0, L]; \mathbb{R}^2)$, *which satisfies the Euler–Lagrange equations*

$$\begin{cases} k_{\text{f}}\, v_{\text{f}}''(x) = G\, \tilde{\tau}(v_{\text{f}} - v_{\text{m}}), & x \in (0, L),\\ -k_{\text{m}}\, v_{\text{m}}''(x) = G\, \tilde{\tau}(v_{\text{f}} - v_{\text{m}}), & x \in (0, L),\\ v_{\text{f}}'(0) = 0, \quad v_{\text{f}}(L) = d,\\ v_{\text{m}}(0) = 0, \quad v_{\text{m}}'(L) = 0. \end{cases} \tag{51}$$

Moreover, the following Compliance Identity holds:

$$\widetilde{E}(\mathbf{v}) = \int_0^L \left[\frac{G}{2} \tilde{\tau}\big(s(x)\big) s(x) + \widetilde{T}\big(s(x)\big) \right] dx + k_{\mathrm{f}}\, dv_{\mathrm{f}}'(L). \tag{52}$$

If, in addition to the previous assumptions, the odd extension of $\tilde{\tau}$ is analytic in a neighborhood of the origin, then the minimizer $\mathbf{v}$ *fulfills*

$$v_{\mathrm{m}}(x) < v_{\mathrm{f}}(x) \quad \forall x \in [0, L]. \tag{53}$$

Proof Lemmas 2 and 3 can be proved in the same way when $\tilde{\tau}$ is substituted to τ. Then the proofs of the existence, (51), and (52) follow as in Theorem 1. The final part of the proof of Theorem 1 was based on the convexity of T in $[0, S_*]$, hence it cannot be adapted to $\widetilde{T}$, and therefore we cannot deduce the uniqueness of the minimizer in general. Nevertheless, inequality (53) can be proved exactly as in the proof of Theorem 2. □

Remark 4 We set $\tilde{\tau}(S_0) = \max_{s\in[0,S_*]} \tilde{\tau}(s)$, hence $\dot{\tilde{\tau}}(s) \geq 0$ if $0 \leq s \leq S_0$ and $\dot{\tilde{\tau}}(s) \leq 0$ if $S_0 \leq s \leq S_*$. Let $\mathbf{v} \in \operatorname{argmin} \widetilde{E}$. For any $\varphi \in C_0^1([0, L]; \mathscr{R}^2)$, we compute the second variation of $\widetilde{E}$, given by (16), at $\mathbf{v}$ in the direction of φ, say

$$\delta^2 \widetilde{E}(\mathbf{v}, \varphi) = 2 \int_0^L \big((k_{\mathrm{f}} + k_{\mathrm{m}}) |\varphi'|^2 + G \dot{\tilde{\tau}} |\varphi|^2 \big)\, dx. \tag{54}$$

By virtue of (54) we conjecture that instability phenomena may occur since for large values of the slip, i.e., $s > S_0$, $\tau'(s) < 0$, and $\delta^2 \widetilde{E}(\mathbf{v})$ could be negative for some φ.

References

1. Biolzi, L., Ghittoni, C.: Personal communication
2. Burridge, R., Keller, J.B.: Peeling, slipping and cracking—some one-dimensional free-boundary problems in mechanics. SIAM Rev. **20**(1), 31–61 (1978)
3. Bilteryst, F., Marigo, J.-J.: An energy based analysis of the pull-out problem. Eur. J. Mech. A/Solids 55–69 (2003)
4. Corr, D., Accardi, M., Graham-Brady, L., Shah, S.: Digital image correlation analysis of interfacial debonding properties and fracture behavior in concrete. Eng. Fract. Mech. **74**, 109–121 (2007)
5. Frémond, M.: Contact with adhesion. In: Topics in Nonsmooth Mechanics. Birkhäuser, Basel (1988). Chapter IV
6. Gunes, O., Buyukozturk, O., Karaca, E.: A fracture-based model for FRP debonding in strengthened beams. Eng. Fract. Mech. **76**, 1897–1909 (2009)
7. Han, W., Kuttler, K.L., Shillor, M., Sofonea, M.: Elastic beam in adhesive contact. Int. J. Solids Struct. **39**, 1145–1164 (2002)
8. Maddalena, F., Percivale, D.: Variational models for peeling problems. Interfaces Free Bound. **10**, 503–516 (2008)
9. Maddalena, F., Percivale, D., Puglisi, G., Truskinowsky, L.: Mechanics of reversible unzipping. Contin. Mech. Thermodyn. **21**, 251268 (2009)

10. Maddalena, F., Percivale, D., Tomarelli, F.: Adhesive flexible material structures. Discrete Contin. Dyn. Syst. B **17**(2), 553–574 (2012)
11. Mazzotti, C., Savoia, M., Ferracuti, B.: An experimental study on delamination of FRP plates bonded to concrete. Constr. Build. Mater. **22**, 1409–1421 (2008)
12. Panigrahi, S.K., Pradhan, B.: Delamination damage analyses of adhesively bonded lap shear joints in laminated FRP composites. Int. J. Fract. **148**, 373–385 (2007)
13. Percivale, D., Tomarelli, F.: Scaled Korn–Poincaré inequality in BD and a model of elastic–plastic cantilever. Asymptot. Anal. **23**, 291–311 (2000)
14. Percivale, D., Tomarelli, F.: From special bounded deformation to special bounded Hessian: the elastic-plastic beam. Math. Mod. Methods Appl. Sci. **15** (2005)
15. Percivale, D., Tomarelli, F.: Smooth and creased equilibria for elastic–plastic plates and beams. In: Variational Problems in Material Science (Trieste 2004). Progr. Nonlinear Differential Equations Appl., vol. 68, pp. 127–136. Birkhäuser, Basel (2006)
16. Percivale, D., Tomarelli, F.: A variational principle for plastic hinges in a beam. Math. Models Methods Appl. Sci. **19**(12), 2263–2297 (2009)
17. Percivale, D., Tomarelli, F.: Regular minimizers for some free discontinuity problems. Quaderno Digitale N. 52 (2009), Dip. Mat. Politecnico di Milano. Available at http://www1.mate.polimi.it/biblioteca/qddview.php?id=1374&L=i
18. Percivale, D., Tomarelli, F.: A variational principle for plastic hinges in a beam. Math. Models Methods Appl. Sci. **19**(12), 2263–2297 (2009), **19**(7), 1009–1058
19. Percivale, D., Zolezzi, T.: Wellposed Convex Integral Functionals. Numer. Funct. Anal. Optim. **18**(1–2), 201–212 (1997)
20. Shillor, M., Sofonea, M., Telega, J.J.: Models and Analysis of Quasistatic Contact. Lecture Notes in Physics, vol. 655. Springer, Berlin (2004)
21. Sofonea, M., Han, W., Shillor, M.: In: Analysis and Approximations of Contact Problems with Adhesion or Damage. Pure and Applied Mathematics, vol. 276. Chapman & Hall/CRC, Boca Raton (2006)
22. Täljsten, B.: The importance of bonding—A historic overview and future possibilities. In: Chen, J.F., Teng, J.G. (eds.) Proc. of the Intern. Symposium on Bond Behavior of FRP in Struct. (BBFS 2005) (2005). Intern. Inst. for FRP in Construction
23. Wei, Y., Hutchinson, J.W.: Interface strength, work of adhesion and plasticity in the peel test. Int. J. Fract. **93**, 315–333 (1998)

Conceptual Design of a Very Large PrandtlPlane Freighter

Fabrizio Oliviero and Aldo Frediani

1 Introduction

The airfreight represents a marginal sector of the air industry, due to the high operating costs, compared to the other means of transport. This situation is based on the assumption that a large-scale air freight is currently not optimized because it is not profitable.

An efficient airfreight transport could improve the international commerce, and it could be fundamental to sustain the economies of the developing countries, especially those currently far from the main communication routes.

This paper shows how the air freight could become an efficient transport system with a cut of the operating costs and how to improve both aircraft technology and worldwide logistic system.

The study results in the conceptual layout of a new freighter, properly conceived for the transportation of intermodal containers; its operational requirements are selected in order to fit with the long-term developments of markets.

The proposed aircraft is a PrandtlPlane box wing concept, and the propulsion system makes use of open rotor engines. The technological improvements in both the wing and propulsion systems could reduce significantly the fuel consumption compared with the ones of the current freighters.

Further improvements in transport efficiency are possible thanks to the creation of an adequate net of freight airports, in order to optimize the goods flows and to increase the aircraft load factor.

F. Oliviero (✉) · A. Frediani
Department of Aerospace Engineering, University of Pisa, Via G. Caruso, 56122 Pisa, Italy
e-mail: fabrizio.oliviero@for.unipi.it

A. Frediani
e-mail: a.frediani@dia.unipi.it

G. Buttazzo, A. Frediani (eds.), *Variational Analysis and Aerospace Engineering: Mathematical Challenges for Aerospace Design*, Springer Optimization and Its Applications 66,
DOI 10.1007/978-1-4614-2435-2_13,

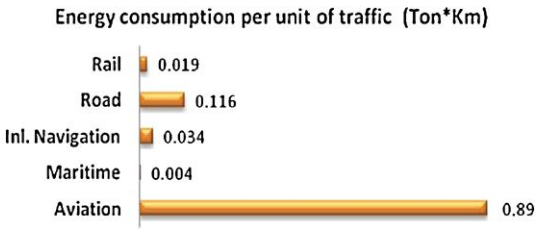

Fig. 1 Energy consumption (kg of equivalent oil) per unit of traffic

2 Current Aspect of Airfreight

Today, the importance of the airfreight is negligible when compared to the other means of transport in terms of quantity of carried goods; only 0.2–0.5% of the total moved tons are carried by air. Nevertheless, the scenario changes radically when considering the money exchanges: in this case the airfreight represents about 30% of the total economic flows connected to the goods transportation. This situation is totally unfavourable for the market economies that are able to produce only low-cost goods. A point-to-point transportation by air could change these economies and, maybe, improve also the life standard of the populations of many countries of Africa, South America and Asia.

The difference between quantity of carried goods and economical flows depends mostly on the very high costs of the fuel consumed: in fact, in the case of air transport, the consumed energy per *TonxKm* of transported goods can become even two orders of magnitude higher than the other means of transport [1] as displayed in Fig. 1.

Hence, only few categories of freight that can support an elevated value-added are carried by air; according to some economical studies (e.g. [2]), air transport becomes not convenient under a total value of about 15 US$/kilogram.

Even though the air transport appears totally unfavourable in terms of specific energy consumption, the comparison shown in Fig. 1 is misleading. Several factors tend to reduce significantly the differences with the other means of transport when the global shipping costs are considered:

Reliability The air transport is not affected by geographical obstacles, and a point-to-point connection could be done easily along the minimum distance; in the case of all the other means of transport, a direct connection is often not possible, the effective journey is many times larger, and intermediate transfers to other carrier are often necessary. In addition, both the origin and destination points can be located far from the sea ports, so that changes in the mode of transport are needed when maritime and ground transportation is involved; this aspect determines a rise in the warehousing, storage and load–unload operations.

Service Speed and Efficiency The air freight ensures the best on time service together with the lowest block time; typical long-haul routes can be covered in 14–18 hours, including also the load–unload operations, while the correspondent service by ships is performed in about 12–15 days. The air transports becomes the only possible choice in case of perishable transport or emergency scenarios. In the case

Table 1 Accident costs in EU, year 2001

Mode	Eur (billion)
Road	162
Air	0.5
Rail	2.74
Maritime	1.78

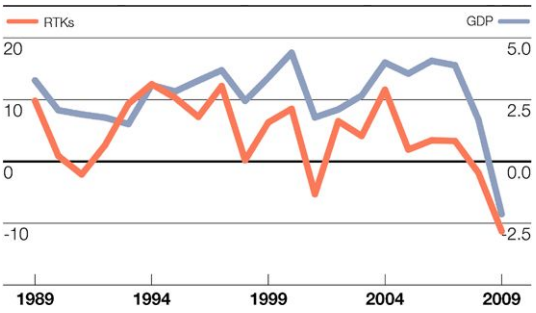

Fig. 2 Global growth of the Gross Domestic Product GDP and air freight volumes

of road and rail transportation, the costs related to jams and congestions are becoming significant especially in areas like Europe and America; the efficiency of the air ensures negligible jams costs, increasing the competitiveness further on.

Safety and service quality Aircraft is the safest mean of transport with the lowest costs related to accidents; for example, Table 1 reports the year 2001 accident costs over Europe for different modes of transport [3].

Infrastructure Airports have the smallest land requirements in terms of construction costs and environmental impact. Moreover, the construction costs can be also amortized by the productivity of the airports itself.

In the case of air transport the global growth rate in the last two decades has been nearly double of the global Gross Domestic Product, GDP, growth rate [2] as shown in Fig. 2.

The distribution of the traffic among the different geographical areas is uneven: for example, in 2009 [4] air freight growth in Asia was $+10\%$, while a strong contraction occurred in America (-10%) and in Europe (-12%) due to the economical crisis.

At present, only about 50% of the air freight is carried by cargo aircraft with about 2000 units. Most cargo aircraft, about 90% of total, comes from the conversion of old passenger aircraft. Although acquisition costs are very low, many disadvantages can be denoted.

- Aircraft have old technology and short operative life, so that maintenance and flight costs are high.
- Their operational requirements are properly conceived for passenger transportation with a low efficiency for freight transport, especially in terms of cruise speed, payload (capacity and typology) and range.

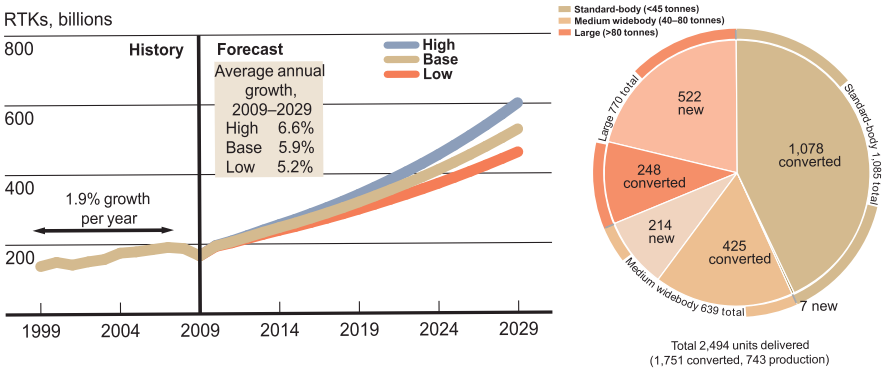

Fig. 3 20 year forecast: global growth margin and fleet composition

- Large wide-body freighters (payload $>$ 80 tons), used mainly for point-to-point commerce, represent only 25% of the current global fleet, and their load factor hardly exceeds 65%; the operational costs per unit of freight transported are increased consequently.
- The usual Unit Load Devices (ULD) have been designed to optimize the cargo volume of passenger aircraft, not used for ground or rail transportation.

The long-term forecast model proposed by Boeing [2] and displayed in Fig. 3 predicts that traffic will more than triple between 2009 and 2029 reaching about 600 billion Revenue Tonne Kilometer (RTK) while the fleet will be doubled, shifting towards the use of large wide bodies, that will derive directly from the production of new aircraft, in order to reduce flight costs.

3 New Generation Freighter

The economical aspect is the primary driver for the design of an innovative freighter; the operating requirements have to be properly conceived for an "optimum" goods transportation. No compromise for a future passenger conversion could be accepted.

3.1 Payload

An increase in aircraft capacity is desirable in order to reduce costs per unit of freight carried. At the same time, the aircraft dimension cannot exceed the maximum allowed ones by the airport operations, a 80×80 [m] square.

Although the dimensions limit the aircraft capacity in the case of monoplane configuration, a payload increase until 250 tons is possible through the adoption of a non-conventional lifting system.

Fig. 4 M2-AGA container

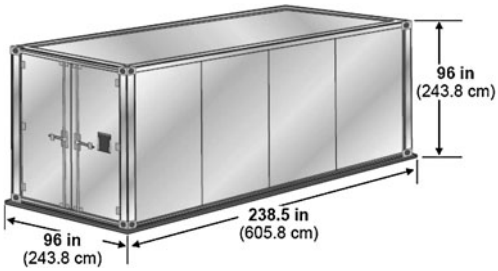

Table 2 AGA intermodal container

Feature	Value
Designation (IATA)	M-2 (AGA)
Maximum gross weight [kg]	11 340
Tare weight [kg]	1000
Available volume [m^3]	33.7

In the case of freighter design, the determination of an adequate average goods density is necessary to optimize the fuselage dimensions. In the present aircraft design we assume a density of about 220 kg/m^3 despite the currently used value of 160 kg/m^3, representative only of the density of passenger luggage.

3.2 Intermodality

The integration within a more efficient intermodal system plays a critical role in the airfreight future development. The possibility to carry intermodal containers that can be quickly moved out of the airport area by rail or truck helps to consistently reduce ground costs avoiding the break of the unit load in the airport area. The aluminium ISO containers allow a reduction of the elevated tare of the current marine and rail ones (about 3 tons); Fig. 4 shows the "AGA-M2" IATA 20-ft intermodal container, and its features are reported in Table 2.

The aircraft proposed in this paper can transport 24 ISO containers 20-ft length.

3.3 Range

A design range of 3000 [nm] is assumed as the optimum, contrary to the current trend of wide bodies aircraft, able to cover long routes (5000–6000 n.m.) without intermediate landings. In the present case, typical routes could be: Boston–Dublin (2889 nm), Sapporo–Anchorage (2993 nm), Brasilia–Dakar (2952 nm), Mombasa–New Delhi (2920 nm), Shanghai–Mumbai (2715 nm), Frankfurt–Dubai (3000 nm).

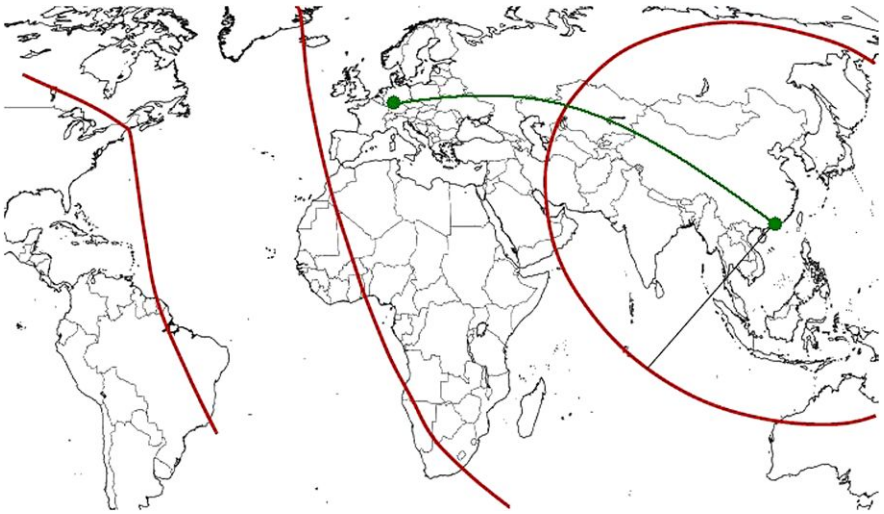

Fig. 5 Typical long-haul route (HGK–FRA) covered with one intermediate landing

The range reduction allows us multiple benefits: first, the requested fuel per ton·km is reduced; at the same time, the air transport can become efficient also for the continental commerce that is destinated to become more and more important in the next years as also remarked in [2] and [5].

Long-haul missions can be covered through intermediate landings that do not reduce the competitiveness of air transport because the block speed reduction is unsignificant in the case of goods transport. Taking also the flight performance (described later on this paper) into account, the projected block time of a typical long haul route displayed in Fig. 5 (Hong Kong–Frankfurt, about 5100 nm), with one intermediate landing, is increased only by 40% (15,5 hours) with respect to the current block time (11-hour direct flight).

The intermediate landings become also strategic for an optimization of the logistic system: in fact, a network of freight airports is necessary to distribute the payload coming from one origin for multiple destinations, increasing the aircraft load factor and reducing the flight costs per unit of freight further more.

3.4 Flight Performance and System Propulsion

The specific fuel consumption of existing turbofans is not compatible with any cost reduction. In order to cut the fuel consumption, the new freighters will be propulsed by means of open rotor engines. Open rotor cannot easily be integrated into aircraft, and, in particular, conventional aircraft cannot integrate a large number of engines; thus, the integration of the propulsion system into the aircraft represents one of the most important challenges in the aircraft design; in this sense, the PrandtlPlane configuration allows a greater flexibility in engine location, and several configurations

Table 3 Operating requirements

Feature	Notation	Value
Gross payload [kg]	W_{pay}	250 000
ULD type	–	24 ISO container
Range [nm]	R	3000
Cruise speed	M	0.6–0.7
Cruise altitude [ft]	h	20 000
Engine	–	Open rotor
Max. length [m]	L_{fus}	80
Max. wingspan [m]	b	80

are possible with a high number of engines. Flight performance must fit with the chosen engines; so the data of existing open rotor [6] are selected as the following reference point: $M = 0.60$–65 and $h = 18\,000$–$21\,000$ ft.

The altitude allows one to avoid possible congestions of the airways currently used by the passenger transonic aircraft; moreover, the loss of speed due to the cruise Mach reduction is partly balanced by the increase of the sound speed; the True Airspeed is calculated as follows for the two cases:

$$\begin{cases} TAS_{M=0.65,\ h=20000} \cong 205\ [\text{m/s}] \\ \\ TAS_{M=0.85,\ h=33000} \cong 254\ [\text{m/s}] \end{cases} \tag{1}$$

The operating requirements of the aircraft are reported in Table 3:

4 Freighter Conceptual Design

4.1 The PrandtlPlane

The conceptual layout reported in the present paper and in [7] refers to the PrandtlPlane configuration based on the Prandtl's concept of the Best Wing system [8]. As is well known, this box wing is composed by a front wing and a rear one, connected each other by two lateral bulks; the front wing has a positive sweep angle, the contrary on the rear one; the box wing efficiency depends on the non-dimensional gap between the vertical distance and wingspan h/b, and for values in [0.15–0.20] ratio, the induced drag is reduced by 20–30% with respect to the correspondent optimum monoplane [9]. The PrandtlPlane presents two vertical fins disposed in order to avoid flutter as illustrated in [10], and also it determines other interesting advantages when applied to a Very Large Aircraft:

- The static stability of flight is obtained by a proper design of the wings; in general, the rear wing chords are larger than the front one. The static stability of flight is

also affected by the sweep angles, and, in particular, it is enhanced by reducing that of the rear wing.
- The pitch control is obtained by means of elevators in both the front and rear wings that operate in phase opposition so that the control can be a pure moment in pitch. Thus, the pitch control can be neutral with respect the lift variations, and it becomes safer especially close to the runway. The elevators are positioned at the wings roots.
- The high-lift devices are located along the entire wingspan of both the wings; thus, an increase of the low speed performance, lower noise and oxide emissions in take off, climb, approach and landing, are expected.
- The ailerons can be divided into two parts positioned at the tips of both wings to enhance the roll control with a reduced aileron total surface as shown in [11].
- The yaw stability and control are obtained by means of a double fin which connect the rear wing to the fuselage. The efficiency of the fins is high due to the reflection effect of the rear wing. The distance between the fins is the maximum possible in order to prevent flutter.
- The maximum thickness of the single wing is nearly the half of that of a correspondent monoplane; the front wing can cross the fuselage without any interference with the cargo deck.

4.2 Definition of the Fuselage

The fuselage is enlarged horizontally in order to position the containers, to locate the main under carriage with a proper distance and to have the vertical fins as far as possible. Moreover, the front wing crosses the fuselage in the lower part, without interferences with the cargo deck.

The fuselage is not pressurized, and from a structural point of view, it is equivalent to a beam doubly supported in correspondence with the front and rear wing connections.

The fuselage section is in accordance to the ISO container transportation: no windows are required, pressurization is limited to cockpit area, and doors allow easy and quick load/unload operations.

In order to facilitate loading and unloading, the container are disposed in a single deck, set transversally to the aircraft longitudinal axis, as shown in Fig. 6. The corresponding fuselage transversal section is created in order to minimize the wetted surface, to avoid any interferences between payload and structures and to ensure the adequate bending stiffness.

Figure 6 shows the cross sections of cargo aircraft: B747-F (A), AN-225 (B), the "ecolifter" project [5] (C), and the fuselage of the PrandtlPlane Freighter (D).

Section A is typical of a passenger aircraft, where the cargo container is adapted to the fuselage shape, and not the contrary; section B is a conventional very large aircraft not properly designed for an intermodal transport but for carrying a large variety of goods, from packages to tanks, fuselage sections, etc. Section of solution C

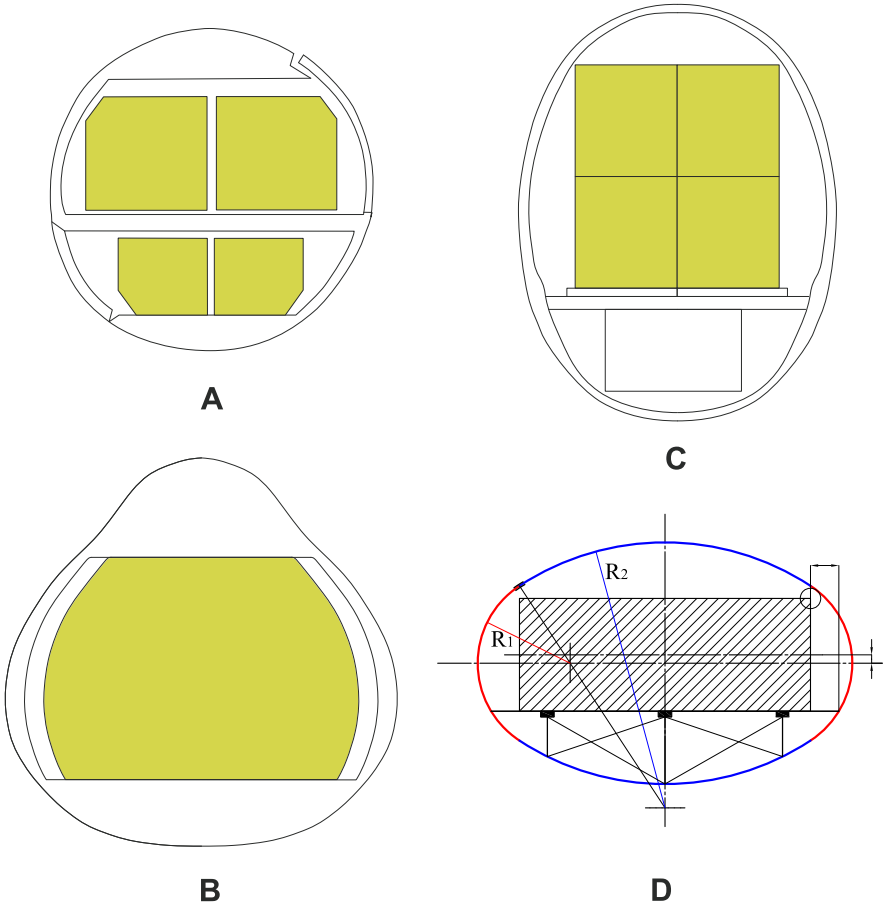

Fig. 6 Definition of the transversal shape

is designed for ISO container transportation, but the loading/unloading operation seems to be complicated apart from structural design problems and high inertial loads during flight manoeuvres.

The present PrandtlPlane section (D) is doubly symmetric, and, in this figure, it is obtained by two circular portions joined with the continuity of the first derivative. The containers, set in a single level, are positioned transversally, and thus the weight load is applied in proximity of points (1) and (2) of Fig. 7, very close to the web; the lateral gap between the container and the fuselage shape allows the passage of the crew during the ground operations. As shown in Fig. 7, the front wing of the aircraft crosses the fuselage under the cargo deck (the red line refers to the fuselage shape in correspondence of the wing cross, while the reference section is reported in blue line).

The main undercarriage is located in lateral sponsons, designed in order to obtain an adequate stability for ground manoeuvres. The volume under the cargo deck is

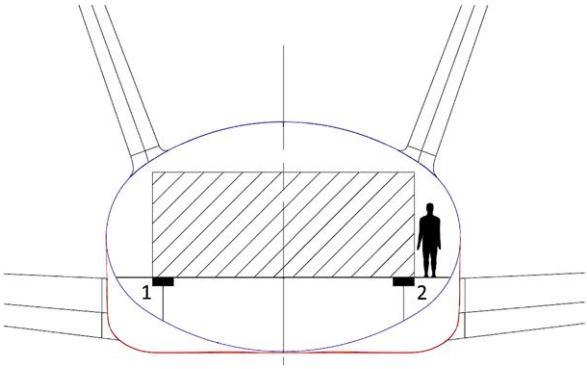

Fig. 7 Section of the fuselage in correspondence of the front wing

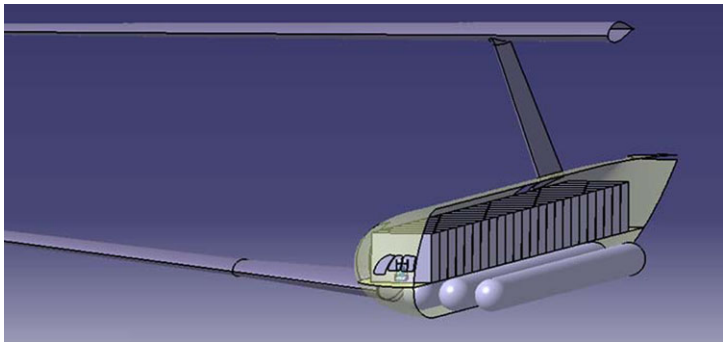

Fig. 8 Definition of the transversal shape

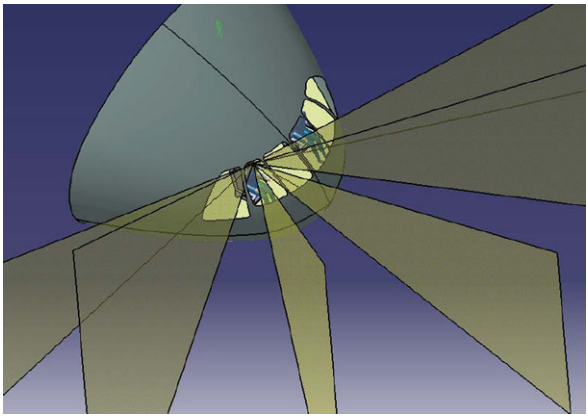

Fig. 9 View envelope

continuous along the fuselage length; this volume could be utilized to add more payload or to introduce tanks for Liquid Hydrogen engines, as displayed in Fig. 8.

The cockpit is located in the front part of the fuselage obtaining adequate living space and ensuring a correct view envelope (Fig. 9).

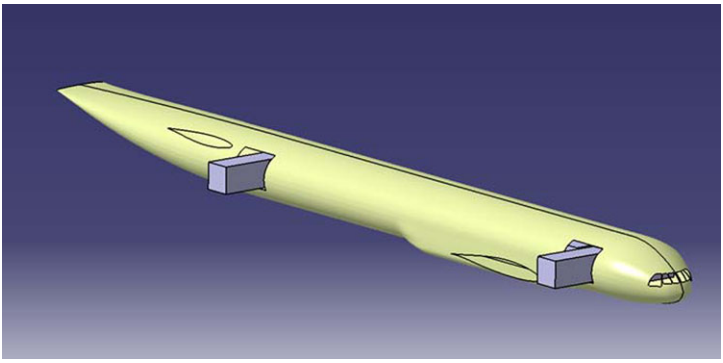

Fig. 10 Side doors

The loading/unloading operations are simply conducted through two side doors in front and back fuselage (Fig. 10); during the loading procedure, the container is introduced from the two side doors and then simply translated along the aircraft longitudinal axis by means of a proper system of rollers (the contrary happens during the unloading operations). The structural reinforcements required in the area of the side doors and also the hydraulic system for the opening are very simple and lighter than the ones required in the case of front and rear ramps, as shown, for example, in Fig. 12. In the case of rear ramp, the upsweep angle of the tail cone can become very high, and thus the aerodynamics can become often deteriorated. In the present case, the tail cone can be designed to optimize the aerodynamics, reducing the friction drag and avoiding the flow separation.

Moreover, as remarked in [12], for a given overall fuselage length, the PrandtlPlane freighter ensures an increase of the useful length to locate the payload, displayed in Fig. 11 with the red line, because the tail cone volume can be reduced maintaining the adequate margin of stability.

A solution shown in Fig. 12 is also possible, but it is not the optimum when production and maintenance costs have to be minimized. Nevertheless the configuration shown in Fig. 12 could become the optimal one when increasing the design payload and positioning the containers longitudinally.

4.3 Weight and Performance Estimation

Weight and flight performance has been estimated by the use of preliminary simple models: the operative weight fraction W_{eo}/W_{to} is determined by the statistical model developed by Jane [13], using proper values for the coefficients A and B in the case of very large aircraft:

$$\frac{W_{eo}}{W_{to}} = A \cdot W_{to}^{B} \quad \text{with } A = 2.385 \text{ and } B = -0.1246. \tag{2}$$

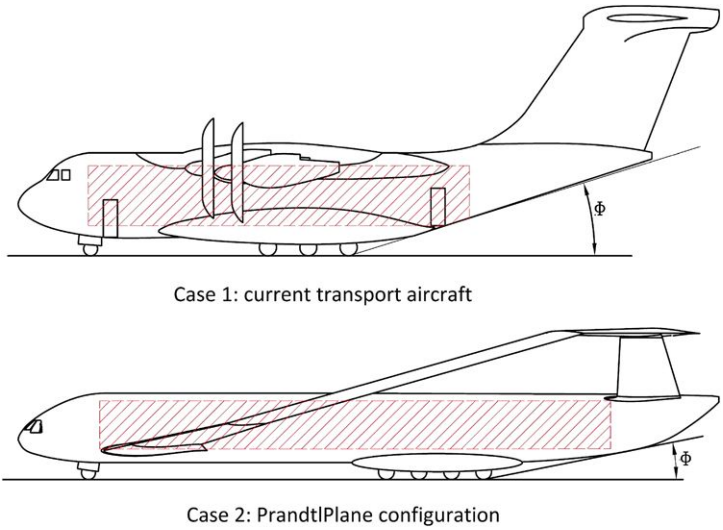

Fig. 11 Comparison of the useful length for different wing configurations

Fig. 12 Frontal door possible configuration

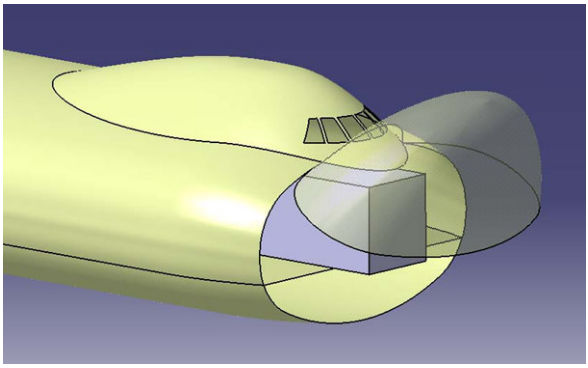

The Breguet formula is used to estimate the fuel consumption during cruise and loiter segments, in the case of propelled aircraft; for the cruise, we have

$$\frac{W_{\text{fin}}}{W_{\text{in}}} = e^{-\frac{R \cdot SFC_{\text{cr}}}{\eta_{\text{prop}} \cdot E_{\text{cr}}}}, \tag{3}$$

and, in the case of loiter, we have

$$\frac{W_{\text{fin}}}{W_{\text{in}}} = e^{-\frac{v_{\text{loi}} \cdot Loi \cdot SFC_{\text{loi}}}{\eta_{\text{prop}} \cdot E_{\text{loi}}}}, \tag{4}$$

where:

- $\frac{W_{\text{fin}}}{W_{\text{in}}}$ is the ratio between the weight at the end of the flight segment and the initial one;

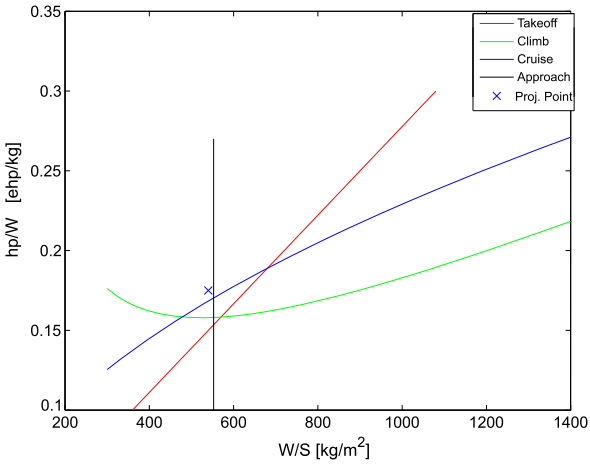

Fig. 13 Project Point determination

- R is the design range;
- LOI is the time of loiter segment;
- SFC_{cr} and SFC_{loi} indicate the specific fuel consumption of the engine during the cruise and loiter, respectively;
- v_{loi} is the aircraft speed during loiter;
- E is the flight efficiency;
- η_{prop} is the propeller efficiency.

Since both (2) and (3)–(4) depend on the MTOW, they have been inserted within an iterating process to determine the weights.

The preliminary sizing is completed by the estimation of the wing surface and the requested power in such the way that all the flight segments can be accomplished. Then the "Project point", defined as the couple of the wing loading W/S and the power-to-weight ratio, hp/W, can be graphically determined considering simple relations of flight mechanics for the following conditions: take-off, climb, cruise, approach and landing. The results are graphically shown in Fig. 13.

The results reported in Table 4 show that the empty operative weight represents about 40% of the MTOW smaller than ones of an existing aircraft. This reduction is due to different aspects: first, the larger the aircraft, the lower the empty weight fraction (note that the coefficient B in (2) is negative); moreover, the fuselage structure of a PrandtlPlane results lighter than that of a monoplane one by about 7.5–8%.

The fuel weight fraction is highly reduced as well because of both the very low specific fuel consumption of the propfans and the improved aerodynamic efficiency of the box-wing system. The requested power resulting by the calculation procedure, can be satisfied by eight existing propfan engines "Ivchenko Progress D-27" [6]: in the layout reported in Fig. 14, one possible configuration consists in locating four engines in the upper surface of the front wing, two engines on the vertical fins and the last ones on the rear wing. The wing planforms are preliminary designed in order to obtain the optimal lift distribution according to the PrandtlPlane aerodynamics, and the airfoils are chosen for the required flight subsonic cruise speed. All these

Table 4 Weights and performance results

Feature	Notation	Value
Maximum take-off weight [kg]	W_{to}	624 800
Gross payload [kg]	W_{pay}	250 000
Empty operative weight [kg]	W_{eo}	250 400
Fuel weight [kg]	W_{fuel}	124 460
Wing loading [kg/m^2]	W/S	540
Power to weight ratio [ehp/kg]	hp/W	0.175
Requested power [ehp]	hp	109 000

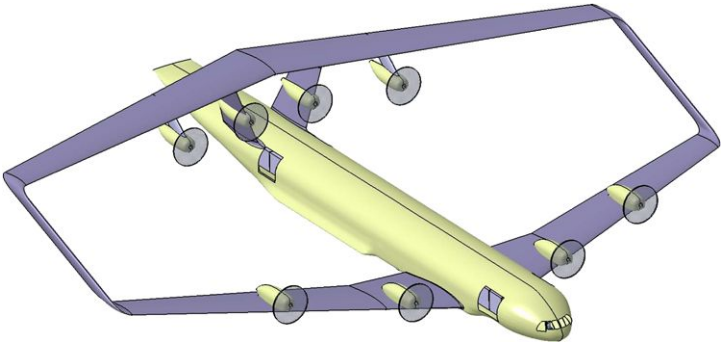

Fig. 14 Conceptual layout

aspects contribute to limit the MTOW to 625 tons that is the value comparable with the existing large aircrafts although the Payload is increased by about 30%.

4.4 Fuselage Structure

During flight, the PrandtlPlane fuselage is equivalent to a beam doubly supported in correspondence of the rear and front wings. A preliminary structural model of the fuselage is carried out in order to evaluate the weight saving due to the lack of pressurization and first of all, the effects of the position of the wing crossing. In fact, the position of the wing is the main parameter affecting the fuselage design, taking in mind that the payload per unit of length is one order of magnitude higher than in the case of passenger aircraft.

The fuselage section is designed against fatigue on the parts under tensile stresses and against instability of equilibrium in the case of the compressed parts. A first F.E. analysis allows us to estimate the dimensions of main structural elements and to assess the effect of the wing positions; the stringers and frames are modelled as mono-dimension beams, and the skin is modeled with two-dimension shell elements; the material is Aluminium alloy 2024-T3. Figures 15 and 16 present the

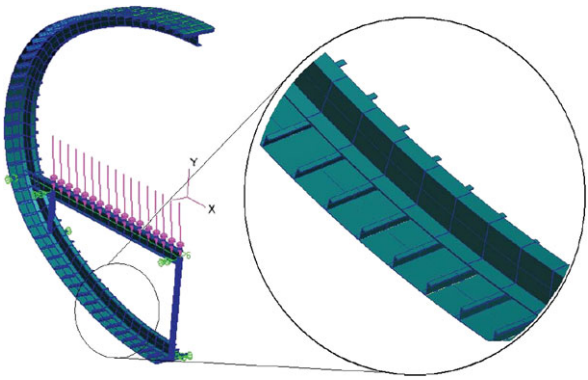

Fig. 15 Model of the reference bay

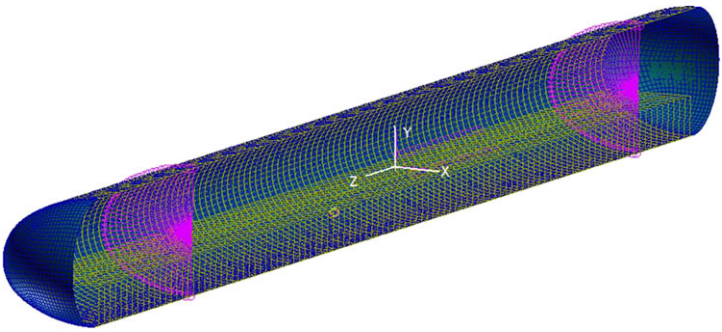

Fig. 16 3D model of the fuselage main section

structural arrangement adopted for the preliminary fuselage bay and the 3D F.E. model used.

Figure 17 shows the Von Mises maximum stress due to the wing position along the upper fuselage. The upper fuselage is in compression contrary to the monoplane configuration (reported in green line as a reference). When the distance between the wings is reduced, the loads on the fuselage behind the front wing and the ones after the rear one reduce the maximum negative bending moment as in the case of a doubly supported beam. The optimum distance can be easily obtained, and with this solution, the preliminary results indicate a possible weight saving of about 7.5–10% between the reference case and the correspondent monoplane configuration.

5 Conclusions

The reduction of air transport costs is possible through the introduction of a new-generation very large freighter flying at about 6000-m altitude, at a cruise speed of Mach 0.6–0.7 and able to operate from existing airfields.

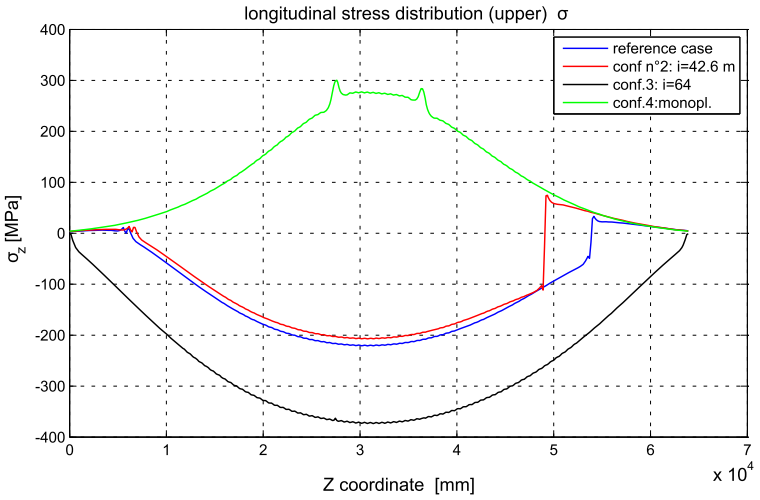

Fig. 17 Stress distribution on the upper fuselage

A possible layout for a large freighter has been presented at a conceptual level, remarking all the possible advantages/disadvantages with respect to the conventional aircraft and the aspects that have to be analysed in further studies.

The improved aerodynamic efficiency of the PrandtlPlane configuration allows us to obtain a total drag reduction of about 15–20% during cruise, and the Specific Fuel Consumption of existing open rotor engines is nearly halved if compared to current turbofan performance. Considering the fuel weight reported in Table 4, the reduction of fuel costs is about 20% in terms of \$/(tons·km) when compared with the current ones.

The primary challenge is represented by the design of new open rotor engines able to satisfy the power requirement in order to reduce the number of mounted engines. Nevertheless, the present research programs seems to be oriented into improving both the speed ($M = 0.85$) and altitude ($h > 30\,000$ ft) performance during the cruise and not to improve the engine power, in order to extend the fuel saving benefits to the passenger transonic aircraft. The main drawback in improving the produced power is represented by the weight increase and overheating of the mechanical transmissions from turbine to fans. The preliminary estimation proves that it is possible to accomplish the flight conditions with eight existing open rotor engines.

The technological effort towards a PrandtlPlane and open rotor configuration must be integrated within a global optimization of the air freight logistic system in order to reduce costs further on. The possibility to insert air into an intermodal system involves a re-definition of the ground facilities that will be able to move quickly the container from/towards the airport area. The creation of a net of low-cost freight airports, simply constructed, can increase the global efficiency of the air freight.

The airports must be located in such a way that transportation costs are minimized: "optimum location models" can be used to determine the airport positions when some transportation "rules" are preliminary defined; for example, for the hub-and-spoke system or point-to-point connection between the airports, the minimum airport distance must not exceed 3000 nm, etc.

When the long routes are investigated, the net of new freight airport can result efficient especially in the developing countries of the African continent which represent the natural bridge between the America and Europe/Asia, improving the economies and the way of life of the emerging countries.

References

1. Authors Various: The future of transport. Technical report, European Commission, Focus Group Report, 2009
2. Authors Various: World air cargo forecast. Technical report, Boeing, Airline Market Analysis, 2010
3. Authors Various: Transport accident and incident investigation in the European Union. Technical report, European Transport Safety Council, 2001
4. Authors Various: Cargo e-Chartbook Q4 2009. Technical report, IATA, 2009
5. Schmitt, D., Roeder, J.: The Ecolifter: a new concept for a dedicated advanced cargo transport. In: 21st ICAS Congress, Melbourne (1998)
6. Ivchenko-Progress. D-27 aircraft propfan engine: performance
7. Oliviero, F.: Conceptual design of a large PrandtlPlane freighter. Master's thesis, University of Pisa (2010)
8. Prandtl, L.: Induced drag of multiplanes. Technical report, NACA, 1924
9. Frediani, A., Montanari, G.: Best wing system: an exact solution of the Prandtl's problem. In: Buttazzo, G., Frediani, A. (eds.) Variational Analysis and Aerospace Engineering, pp. 183–211. Springer, Berlin (2010)
10. Divoux, N., Frediani, A.: The lifting system of a PrandtlPlane, Part 2: Preliminary study on flutter characteristics. In: Buttazzo, G., Frediani, A. (eds.) Variational Analysis and Aerospace Engineering II: Mathematical Challenges for Aerospace Design. Springer, Berlin (2012)
11. Voskuijl, M., De Klerk, J., Van Ginneken, D.A.J.: Flight mechanics modeling of the PrandtlPlane for conceptual and preliminary design. In: Buttazzo, G., Frediani, A. (eds.) Variational Analysis and Aerospace Engineering II: Mathematical Challenges for Aerospace Design. Springer, Berlin (2012)
12. Frediani, A., Cipolla, V., Rizzo, E.: The PrandtlPlane configuration: overview on possible applications to civil aviation. In: Buttazzo, G., Frediani, A. (eds.) Variational Analysis and Aerospace Engineering II: Mathematical Challenges for Aerospace Design. Springer, Berlin (2012)
13. Jane's: Jane's all the World's Aircraft. Martin & Co, New York (1999)

Mesh Adaptivity and Optimal Shape Design for Aerospace

Frédéric Alauzet, Bijan Mohammadi, and Olivier Pironneau

1 Introduction

Optimal shape design is the next step once the numerical simulation is mastered and computationally reasonably cheap. It is so important for airplane design that it is practiced everywhere now (see [13–16, 18, 19] and their bibliographies). For cars, aerodynamic optimization is important at high speed, but internal engine optimization is even more so. Boats are harder to optimize (see [6]), and even a fraction of percent improvement implies substantial savings. There are in fact so many applications that we cite only just a few like airplane and boat propellers [9], car ventilators [18], windmill design, and so many more.

Environment friendly airplane design has brought new optimization criteria such as noise reduction. In earlier papers [3, 18, 20] we pointed out that the calculus of variation is not valid in the presence of shocks, at least in the continuous problems. Thanks to Ulbrich and Giles [12, 23, 24], the problem is solved for one-dimensional conservation laws. For the Euler equation, an extended numerical study was performed and will be reported in [2], but we will give here some of the findings.

F. Alauzet (✉)
INRIA, Le Chesnay, France
e-mail: Frederic.Alauzet@inria.fr

B. Mohammadi
CERFACS, Toulouse, France
e-mail: Bijan.Mohammadi@cerfacs.fr

O. Pironneau
Laboratoire J-L. Lions, University of Paris VI, Paris, France
e-mail: Olivier.Pironneau@upmc.fr

G. Buttazzo, A. Frediani (eds.), *Variational Analysis and Aerospace Engineering: Mathematical Challenges for Aerospace Design*, Springer Optimization and Its Applications 66,
DOI 10.1007/978-1-4614-2435-2_14,

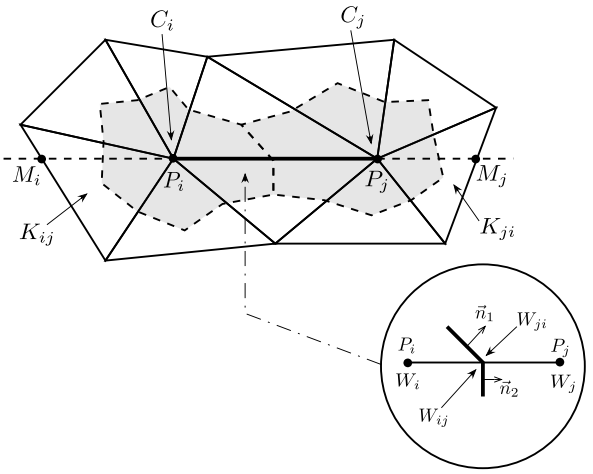

Fig. 1 Two finite volume cells C_i and C_j, and the upwind triangles K_{ij} and K_{ji} associated with edge $P_i P_j$. The common boundary ∂C_{ij} with the representation of the solution extrapolated for the MUSCL correction is shown

2 Compressible Euler Solver

The two-dimensional compressible Euler equations are

$$\partial_t W + \nabla \cdot F(W) = 0, \quad W(0) = 0, \tag{1}$$

where $W = (\rho, \rho u, \rho v, \rho E)^T$ is the vector of conservative variables, and the tensor F represents the convective flux: $F(W) = F_1(W)\, e_x + F_2(W)\, e_y$ with

$$F_1(W) = \begin{pmatrix} \rho u \\ \rho u^2 + p \\ \rho uv \\ (\rho E + p)u \end{pmatrix} \quad \text{and} \quad F_2(W) = \begin{pmatrix} \rho v \\ \rho uv \\ \rho v^2 + p \\ (\rho E + p)v \end{pmatrix}.$$

We assume that W is given at time $t = 0$, and we add boundary conditions which we will discuss later at length and which we denote loosely by $W \in W_{ad}$. As usual, ρ is the density, u, v the velocity, p the pressure, and E the energy at position x and time t in the fluid.

In this study, (1) is discretized by a vertex-centered finite volume (FVM) scheme applied to simplicial unstructured meshes; it uses a particular edge-based formulation with upwind elements [1, 7]. The formulation consists in associating with each vertex P_i of the mesh a finite volume cell, C_i, built by joining each vertex to the middle point of its opposite edge. The common boundary between two neighboring cells C_i and C_j is denoted $\partial C_{ij} = \partial C_i \cap \partial C_j$ (see Fig. 1).

The FVM assumes W piecewise constant on the cells and integrates (1) on each cell C_i:

$$|C_i| \frac{dW_i}{dt} + \int_{\partial C_i} F(W_i) \cdot \mathbf{n}_i \, d\gamma = |C_i| \frac{dW_i}{dt} + \sum_{P_j \in \mathscr{V}(P_i)} F|_{ij} \cdot \int_{\partial C_{ij}} \mathbf{n}_i \, d\gamma = 0, \tag{2}$$

where $\mathbf{n}_i$ is the outer normal to cell C_i, $\mathscr{V}(P_i)$ is the set of all neighboring vertices of P_i, and $F|_{ij}$ represents the constant value of $F(W)$ at interface ∂C_{ij} from the P_i-side. A numerical flux function, denoted Φ_{ij} and compatible with $F|_{ij}$, is introduced:

$$\Phi_{ij} := \Phi_{ij}(W_i, W_j, \mathbf{n}_{ij}) = F|_{ij} \cdot \int_{\partial C_{ij}} \mathbf{n}_i \, d\gamma, \tag{3}$$

where $\mathbf{n}_{ij} = \int_{\partial C_{ij}} \mathbf{n}_i \, d\gamma$. Several upwind numerical flux functions are available, but here the Roe approximate Riemann solver described in [21] is used.

Roe's Approximate Riemann Solver It is based on the Jacobian $F'(W)$:

$$\Phi^{\mathrm{Roe}}(W_i, W_j, \mathbf{n}_{ij}) = \frac{F(W_i) + F(W_j)}{2} \cdot \mathbf{n}_{ij} + \left|\tilde{A}(W_i, W_j)\right| \frac{W_i - W_j}{2}, \tag{4}$$

where $\tilde{A} = F'(\tilde{W})$ is evaluated for the Roe average variables $\tilde{W} := (\tilde{\rho}, \tilde{\rho u}, \tilde{\rho v}, \tilde{\rho E})$ as explained in [21]. For a diagonalizable matrix $A = P \Lambda P^{-1}$, $|A|$ stands for $|A| = P|\Lambda|P^{-1}$. The eigenvalues of $F'(W)$ are real and equal to u, $u + c$ and $u - c$.

The previous formulation gives at best only a first-order scheme; higher-order extensions are possible with a MUSCL addition (see [2]). Such MUSCL schemes are not monotone, and therefore a slope limiter is needed such as the Superbee limiter [5].

Boundary Conditions *Slip boundary conditions* are imposed for the walls because the flow is inviscid: $\mathbf{U}.\mathbf{n} = 0$. This boundary condition is imposed weakly by setting

$$\Phi^{\mathrm{Slip}}(W_i) = (0, p_i \, \mathbf{n}_i, 0)^t. \tag{5}$$

For free-stream external flow conditions at inflow boundaries Γ_∞ which approximate infinity, a free-stream uniform flow W_∞ is known. There, the Roe flux is replaced by the Steger–Warming flux [22]:

$$\Phi^{\infty}(W_i) = A^+(W_i, \mathbf{n}_i) W_i + A^-(W_i, \mathbf{n}_i) W_\infty, \tag{6}$$

where $A^\pm = \frac{1}{2}(|A| \pm A)$ and $A = F'(W)$.

At free-stream outflow boundaries no condition is imposed, so nothing is done to the finite volume scheme.

To discretize in time, an implicit Euler scheme (implicitEuler) is used, the linearized version of which is

$$\left(\frac{|C_i|}{\delta t_i^n} I_d + \Psi_i^{2'}\left(W^n\right)\right)\left(W_i^{n+1} - W_i^n\right) = -\Psi_i^2\left(W^n\right). \tag{7}$$

3 Implied FVM for the Discrete Adjoint

As the second-order flux is too difficult to differentiate by hand, the second-order Jacobian matrix is approximated by the first-order one leading to

$$\left(\frac{|C_i|}{\delta t_i^n} I_d + \Psi_i^{1'}(W^n)\right)(W_i^{n+1} - W_i^n) = -\Psi_i^2(W^n).$$

Thus the variation of the state variables δW is given by

$$\mathscr{A}^n \, \delta W^{n+1} = -\Psi^2(W^n).$$

Consequently, for a given functional $J(W)$, the adjoint state W^* is defined by

$$\mathscr{A}^{n*} W^* = J'(W), \tag{8}$$

where $\mathscr{A}^{n*}$ is the transposed of matrix $\mathscr{A}^n$. Note however that it suffices to take $\mathscr{A}^{n*} = (\Psi_i^{1'}(W^n))^T$ because at convergence the solution does not depend on time and $\Psi^2(W^n)$ tends to 0.

4 Goal Oriented Self Adapting Meshes

4.1 Multiscale Anisotropic Mesh Adaptation

Recall the *Delaunay–Voronoi criteria*: *The fourth point of the quadrilateral made by two adjacent triangles should be outside the circle defined by the three other points.* If not, the diagonal of the quadrilateral should be swapped.

On convex domains, applying the criteria within a loop on the edges of a triangulation increases the minimum angle in the triangulation. Thus, the loop converges, and the triangulation ends up "looking good" though there is no solid definition for this.

The generalization of this criteria can be done by replacing the Euclidian circles by M-circles where M is symmetric positive definite:

$$\mathscr{M} - \text{circle} := \left\{x : \|x - x_c\|_{\mathscr{M}} := (x - x_c)^T M (x - x_c) = r\right\}. \tag{9}$$

Let $h_i(a)$ be the edge length in the ith direction at point a, and let

$$\mathscr{M}(a) = R(a) \begin{pmatrix} \frac{1}{h_1^2(a)} & & \\ & \frac{1}{h_2^2(a)} & \\ & & \frac{1}{h_3^2(a)} \end{pmatrix} R(a)^T. \tag{10}$$

If $H(u) = R_u^{-1} \Lambda_u R_u$ is the Hessian of u, and $\Pi_{\mathscr{M}}$ is the M-orthogonal projection, then the following problem has a solution [17]:

$$\min_{\mathscr{M}} \|u - \pi_{\mathscr{M}} u\|_{L^p} \;\Rightarrow\; \mathscr{M}_{L^p} = \left(\frac{N}{\int_\Omega \det|H(u)|^{\frac{p}{2p+3}}}\right)^{\frac{2}{3}} \left(\det|H(u)|\right)^{-\frac{1}{2p+3}} R|\Lambda_u|^t R, \tag{11}$$

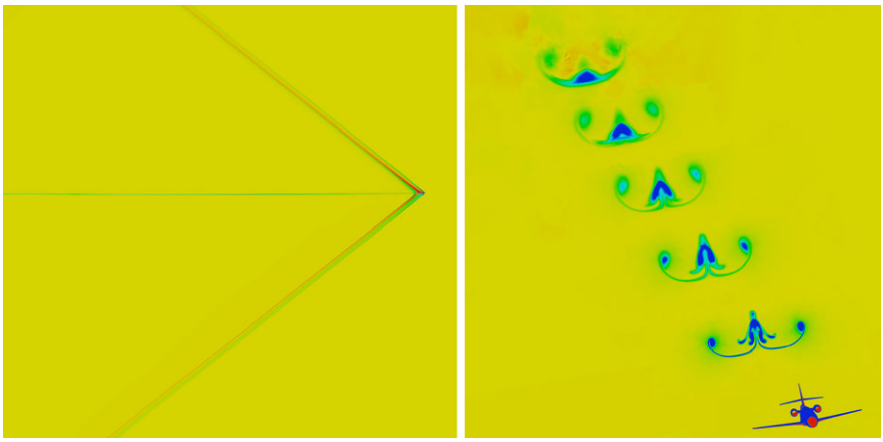

Fig. 2 With appropriate mesh adaptation, it is possible to propagate accurately shock wave in the whole domain (*left*) or to track down the main vortices behind an airplane quite far downstream (*right*)

where N is the mesh size. Therefore in a sense to distribute the L^p error evenly, one should choose h_i proportional to Λ_i in the direction of the eigenvectors of the Hessian of u. Applications of this criteria are shown in Figs. 2 and 3.

4.2 Goal-Oriented Mesh

For optimal control and optimal shape design, one would like to find the best mesh to compute a criteria, for instance,

$$j(a) = \frac{1}{2}\int_C |BW_h - b|^2 : \big(F(W_h), \hat{w}_h\big) = 0 \quad \forall \hat{w}_h \in W_h, \tag{12}$$

where a is a parameter in the boundary conditions, B is a rectangular matrix, and b is a vector or scalar.

There is a solution to this problem (see [4]), and an empirical proof goes as follows: first linearize the continuous state equation $F(W) = 0$:

$$F(W_h) = F(W) + F'(W)(W_h - W) \;\Rightarrow F(W_h) + F(W)'(W - W_h) = 0. \tag{13}$$

Then introduce an adjoint state W^* solution of $F(W)'^T W^* = B^T(BW_h - b)$, so that

$$j(W_h) - j(W) \approx \big(BW_h - b, B(W - W_h)\big) = -\big(W^*, F(W_h)\big). \tag{14}$$

Therefore, to reduce the error, one should adapt the mesh so as to compute $(W^*, F(W_h))$ with the best possible precision. An illustration of this procedure is shown in Fig. 3.

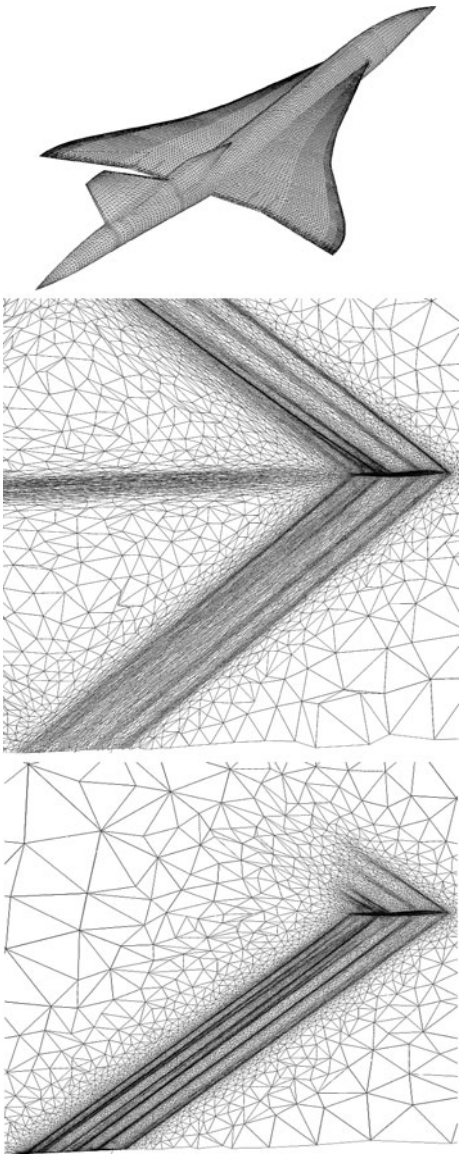

Fig. 3 *Top*, supersonic business jet geometry. Comparison between multiscale (*middle*) and goal-oriented (*bottom*) anisotropic mesh adaptation. Multiscale adaptation is based on a control of the interpolation error in L^2 norm of the local Mach number. Goal-oriented adaptation focuses on the observation of the pressure on the ground

5 Mesh Adaptation and Approximate Gradient

Consider

$$\min_{z\in Z} J(z) \quad \text{approximated by} \quad \min_{z\in Z_h} J_h(z).$$

Let us solve it using the method of Steepest descent with Goldstein's rule for the step size:

Algorithm 1
while $\|\operatorname{grad}_z J_h(z^m)\| > \epsilon$ **do**
{
$z^{m+1} = z^m - \rho \operatorname{grad}_z J_h(z^m)$ where ρ is any number satisfying

$$-\beta\rho\|w\|^2 < J_h\big(z^m - \rho w\big) - J_h\big(z^m\big) < -\alpha\rho\|w\|^2$$

with $w = \operatorname{grad}_z J_h(z^m)$. Set $m := m + 1$;
}

Now consider the same algorithm with parameter refinement.

Algorithm 2 (Steepest descent with refinement)
while $h > h_{\min}$ **do**
{
while $\|\operatorname{grad}_z J_h(z^m)\| > \epsilon h^\gamma$ do
{
$z^{m+1} = z^m - \rho \operatorname{grad}_z J_h(z^m)$ where ρ such that

$$-\beta\rho\|w\|^2 < J_h\big(z^m - \rho w\big) - J_h\big(z^m\big) < -\alpha\rho\|w\|^2$$

with $w = \operatorname{grad}_z J_h(z^m)$. Set $m := m + 1$;
}
$h := h/2$;
}

The convergence is obvious because it is either Steepest Descent or $\operatorname{grad} J_h \to 0$ because $h \to h/2$. There is a great gain in speed because we can begin the algorithm with a very coarse mesh!

Now let N be an iteration parameter, and let $J_{h,N} \approx J_h$ and $\operatorname{grad}_z J_{h,N} \approx \operatorname{grad}_z J_h$ in the sense that

$$\begin{aligned} &\lim_{N\to\infty} J_{h,N}(z) = J_h(z) \quad \text{and} \\ &\lim_{N\to\infty} \operatorname{grad}_{zN} J_{h,N}(z) = \operatorname{grad}_z J_h(z). \end{aligned} \tag{15}$$

Let γ, K, and $N(h)$ be given with $N(h) \to \infty$ as $h \to 0$. The final algorithm is the Steepest descent with Goldstein's rule mesh refinement and approximate gradients. It is particularly suited to Euler's equation in which h is the mesh size and N is the number of iterations (or the time step) for the implicit Euler solver and/or the precision with which the adjoint is computed:

Algorithm 3 (E. Polak et al., see [18])
while $h > h_{\min}$
{
while $|\mathrm{grad}_{z_N} J^m| > \epsilon h^\gamma$
{
try to find a step size ρ with $w = \mathrm{grad}_{z_N} J(z^m)$

$$-\beta\rho\|w\|^2 < J\left(z^m - \rho w\right) - J\left(z^m\right) < -\alpha\rho\|w\|^2$$

if success then
$\left\{z^{m+1} = z^m - \rho\mathrm{grad}_{z_N} J^m; \quad m := m+1;\right\}$
else $N := N + K;$
}
$h := h/2; \quad N := N(h);$
}

In the case of strictly convex J the convergence can be established from the observation that Goldstein's rule gives a bound on the step size:

$$-\beta\rho\,\mathrm{grad}_z J \cdot h < J(z+\rho h) - J(z) = \rho\,\mathrm{grad}_z J \cdot h + \frac{\rho^2}{2} J'' hh$$

$$\Rightarrow \quad \rho > 2(\beta-1)\frac{\mathrm{grad}_z J \cdot h}{J''(\xi)hh} \quad \text{so}$$

$$J^{m+1} - J^m < -2\frac{\alpha(1-\beta)}{\|J''\|}\left|\mathrm{grad}_z(J)\right|^2. \tag{16}$$

Thus at each grid level the number of gradient iterations is bounded by $O(h^{-2\gamma})$. Therefore the algorithm does not jam, and so it must converge.

6 Calculus of Variations with Euler Equations

Calculus of variation is not valid across shocks. For instance, if the density ρ and the velocity u are discontinuous, but with ρu continuous, it is meaningless to write

$$\delta(\rho u) = u\delta\rho + \rho\delta u \tag{17}$$

because $\delta\rho$ and δu have Dirac singularities at the shock and u, ρ are discontinuous there.

Although (17) is not allowed, yet one has

$$\delta(\rho u) = (\delta\rho)\bar{u} + \bar{\rho}\delta u, \tag{18}$$

where $\bar{\rho}$ (and $\bar{u}$) stands for the mean value of ρ at all points:

$$\bar{\rho}(x) = \frac{1}{2}\left(\rho(x^+) + \rho(x^-)\right).$$

Let $[u]$ denote the jump across the shock; then on the right-hand side of (18), the weight of the Dirac mass is

$$\begin{aligned}
&-[\rho]x_s'\delta a\bar{u} - [u]x_s'\delta a\bar{\rho} \\
&\quad = -x_s'\frac{\delta a}{2}\big((\rho^+ - \rho^-)(u^+ + u^-) + (u^+ - u^-)(\rho^+ + \rho^-)\big) \\
&\quad = -x_s'\delta a[\rho u] = 0. \qquad (19)
\end{aligned}$$

Even if $[\rho u] \neq 0$, the weights on the Dirac masses are the same on both sides, so (18) is true pointwise and singularity wise at the shock.

More complex functions need to be decomposed into elementary products; for instance, $\rho^{-1}u^2$ being $(\rho^{-1})v$ with $v = uu$, the mean value can be computed as such. For nonrational functions, the overline operator on derivatives is the Volpert ratio

$$\delta F(u) = \overline{F(u)'}\delta u \quad \text{with } \overline{F(u)'} = \int_0^1 F_u'\big(su^+ + (1-s)u^-\big)\,\mathrm{d}s. \qquad (20)$$

7 Optimal Wing Profile with Least Sonic Boom

7.1 Optimization with the Euler Equations

Consider the cost function

$$J = \frac{1}{2}\int_S |BW - b|^2 : W \text{ solution of Euler equations,}$$

where S is a part of the boundary of $\partial\Omega$. The adjoint equation for the minimization of J with respect to boundary parameters is

$$\frac{\partial W^*}{\partial t} + \overline{F'(W)}\nabla W^* = 0, \quad W^*(T) = 0. \qquad (21)$$

Let us multiply this equation by δW and integrate it in time and space:

$$\begin{aligned}
0 &= \int_{\Omega\times(0,T)} \delta W \cdot \left(\frac{\partial W^*}{\partial t} + \overline{F'(W)}\nabla W^*\right) \\
&= -\int_{\Omega\times(0,T)} W^* \cdot \left(\frac{\partial \delta W}{\partial t} + \nabla\cdot\big(\overline{F'(W)}\delta W\big)\right) \\
&\quad + \int_\Omega W^*\delta W|_0^T + \int_{\partial\Omega\times(0,T)} W^*\cdot\big(n\cdot\overline{F'(W)}\delta W\big) \qquad (22) \\
&\Rightarrow \quad \int_{\partial\Omega\times(0,T)} W^*\cdot\big(n\cdot\overline{F'(W)}\delta W\big) = 0. \qquad (23)
\end{aligned}$$

This gives δJ if the boundary conditions are on $\partial\Omega - S$, so that $W^*\cdot(n\cdot(\overline{F'(W)})\delta W) = 0$, and

$$W^*\cdot\big(n\cdot\overline{F'(W)}\big) = (B\overline{W} - b)B^T \quad \text{on } S. \qquad (24)$$

Then we obtain

$$\delta J = -\int_{\partial\Omega\setminus S\times(0,T)} W^* \cdot \big(n \cdot \overline{F'(W)}\delta W\big).$$

7.2 Supersonic Wing Profile Optimization

An airfoil Σ at rest is a semi-infinite domain Ω.

Air comes in from the left boundary L at $M > 1$ and exits by right boundary R. S is the ground.

$$\min_{\Sigma}\left\{J = \frac{1}{2}\int_S (p - p_0)^2 \;\Rightarrow\; \delta J = \int_S (p - p_0)\delta p\right\}. \tag{25}$$

Then, since J has no part on R,

$$W^* \cdot F'(W).\mathbf{n} = 0 \quad \text{on } R.$$

As $F'(W).\mathbf{n}$ is a nonsingular matrix when the flow is supersonic, this equation implies that all four components of W^* are zero on R:

$$W^* = 0 \quad \text{on } R. \tag{26}$$

The flow is supersonic on L, so all components of the linearized flow δW are equal to zero. All the characteristics are coming in, so for the adjoint state, the characteristics are coming out, and hence,

$$W^* \text{ needs no boundary conditions on } L. \tag{27}$$

The shock is assumed to reflect perfectly, so the vertical component of the velocity is zero: $W_3 = 0$. There is only one incoming characteristic. Assume that $\delta W_3 = 0$ is the boundary condition for the linearized Euler system. Giles and Pierce have showed that W_3^* should be given. Let us justify this choice. On S, the normal is $(0, 1)^T$, and the velocity is $(u, 0)^T$, so

$$\begin{aligned} &W^* \cdot \big(n \cdot F'(W)\big)\delta W \\ &\quad = \begin{pmatrix} 0 & 0 & \dfrac{(\gamma-1)}{2}u^2\delta W_1 - (\gamma-1)u\delta W_2 + (\gamma-1)\delta W_4 & 0 \end{pmatrix} W^* \\ &\quad = (\gamma-1)\left(\frac{u^2}{2}\delta W_1 - u\delta W_2 + \delta W_4\right)W_3^*. \end{aligned} \tag{28}$$

On the other hand,

$$\begin{aligned} p = (\gamma-1)\rho e - \frac{\gamma-1}{2}\frac{(\rho u)^2 + (\rho v)^2}{\rho} &= (\gamma-1)\left(W_4 - \frac{W_2^2 + W_3^2}{2W_1}\right) \\ \Rightarrow \quad \delta p &= (\gamma-1)\left(\frac{W_2^2}{2W_1^2}\delta W_1 - \frac{W_2}{W_1}\delta W_2 + \delta W_4\right) \\ &= (\gamma-1)\left(\frac{u^2}{2}\delta W_1 - u\delta W_2 + \delta W_4\right). \end{aligned}$$

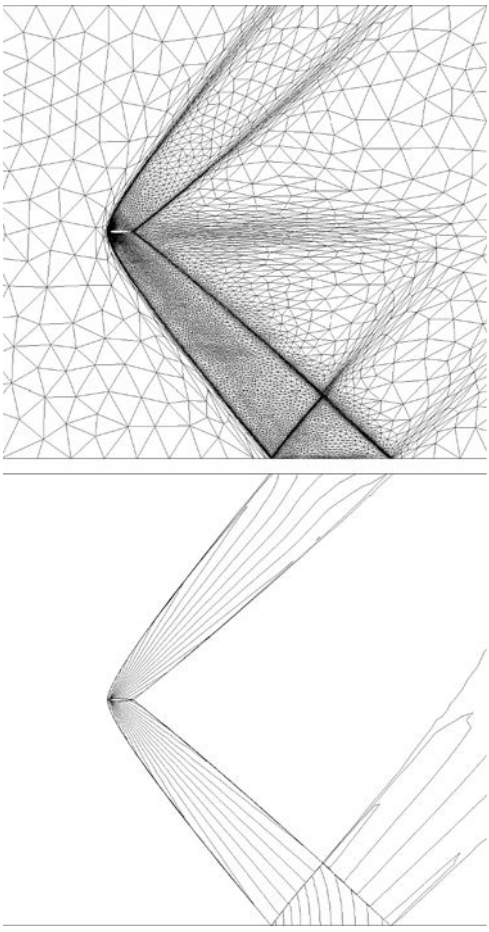

Fig. 4 NACA airfoil: goal-oriented adapted mesh (*top*) and associated level lines of the density (*bottom*)

By choosing $W_3^*|_S = \overline{p - p_0}$ we have $W^* \cdot (n \cdot F'(W))\delta W = W(p - p_0)\delta p$, and so

$$\delta J = -\int_{\partial\Omega\setminus S} W^* \cdot \big(n \cdot \overline{F'(W)}\delta W\big). \tag{29}$$

Boundary Conditions on the Adjoint at airfoil Σ The flow is subsonic and tangent to Σ so $u \cdot n = 0$. As for S, one boundary condition is required for δW. Let $\delta W \cdot n$ be given. An elementary calculus gives

$$\begin{aligned} W^* \cdot \big(F'(W) \cdot n\big)\delta W = (\gamma - 1)W^* \cdot n\left(\frac{1}{2}\big(u^2 + v^2\big)\delta W_1 - u\delta W_2 - v\delta W_3 + \delta W_4\right) \\ + \big(W_1^* + uW_2^* + vW_3^*\big)\delta W \cdot n. \end{aligned} \tag{30}$$

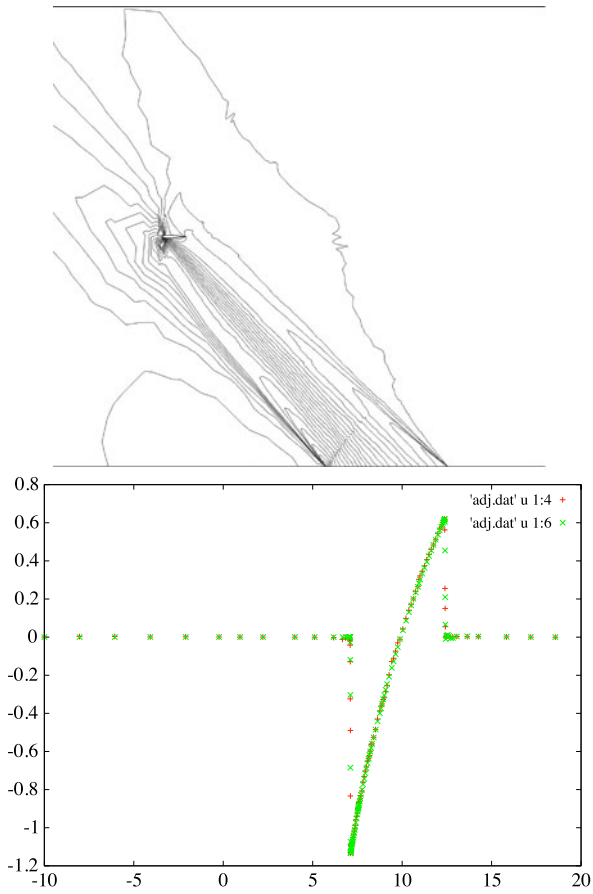

Fig. 5 NACA airfoil. *Top*, level lines of the density adjoint associated with the goal-oriented adapted mesh of Fig. 4. *Bottom*, comparison between W_3^*, the component of the adjoint in duality with ρv and $p - p_0$ on S. Although the adjoint's equation is generated by automatic differentiation for discrete case, it agrees with continuous limit

This expression involves only $\delta W \cdot n$ when

$$W^* \cdot n = 0 \quad \text{on } \Sigma. \tag{31}$$

Thus the following holds (already in [10, 11]).

Proposition 1 *Let W^* be defined by*

$$\begin{aligned} &\partial_T W^* + \overline{F'(W)}^T \nabla W^* = 0, \quad W(T) = 0, \\ &W^* \cdot n = 0 \quad \textit{on } \Sigma, \\ &W^*|_R = 0, \qquad W_3^*|_S = \overline{p - p_0}. \end{aligned} \tag{32}$$

Then, asymptotically in time,

$$\delta J = -\int_\Sigma \left(W_1^* + \mathbf{U} \cdot \mathbf{W}_{2,3}^*\right) \delta \mathbf{W}_{2,3} \cdot \mathbf{n}. \tag{33}$$

This is essential to set up descent algorithms for optimal shape design to minimize J.

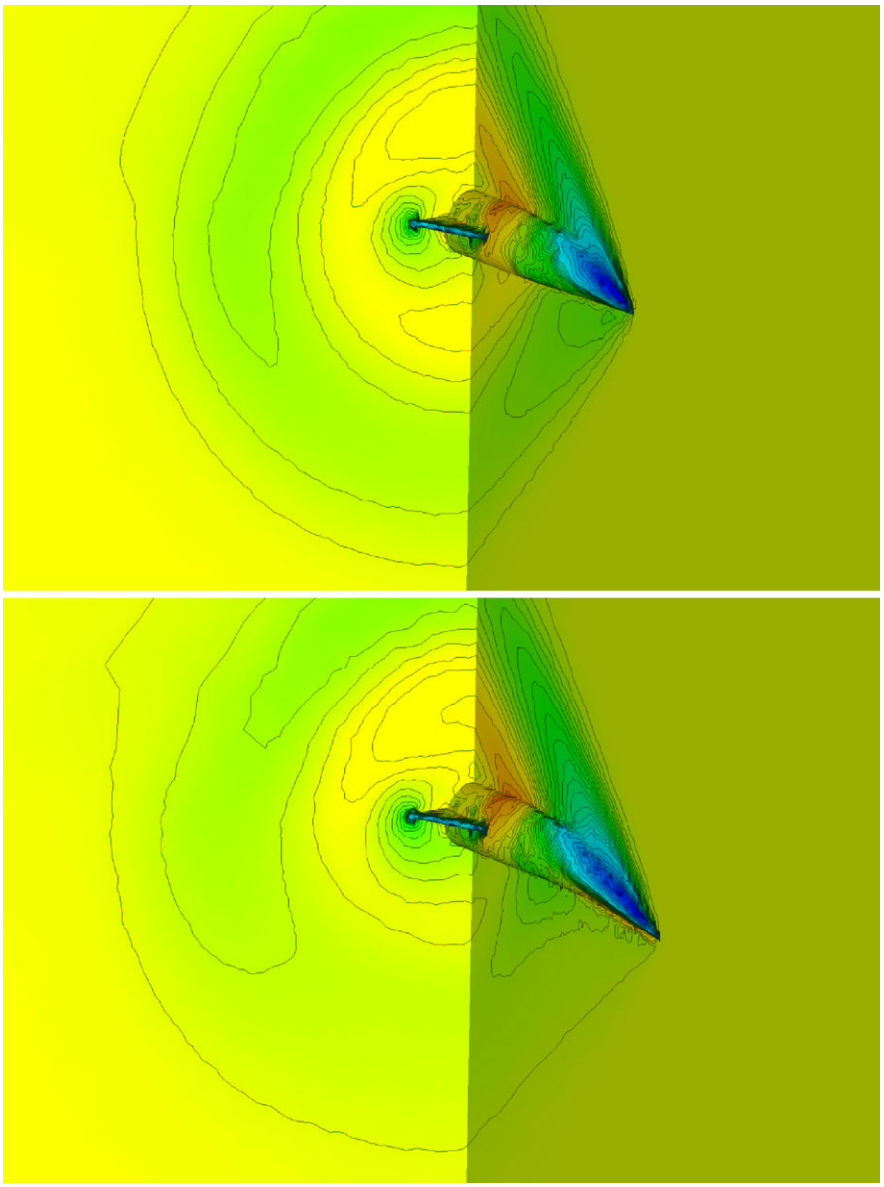

Fig. 6 Optimization of a supersonic business jet: the shape before optimization (*top*) and after (*below*)

Remark It may be more readable to rewrite the result as

$$\delta J = -\int_{\Sigma} \left(\rho^* + \mathbf{U} \cdot (\rho \mathbf{U})^*\right) \delta(\rho \mathbf{U}) \cdot \mathbf{n}.$$

7.3 A Gradient Method for Shape Optimization

Consider the wing profile deformation $\Sigma_\alpha = \{x + \alpha(x)n(x) : x \in \Sigma\}$; then

$$\delta V \cdot n|_\Sigma = -\alpha\left(\frac{\partial V_n}{\partial n} - \kappa V_t\right), \tag{34}$$

where t is the tangent vector associated with n, and κ is the curvature (inverse of the radius of curvature). Therefore, by choosing

$$\alpha = -\lambda\left(\rho^* + \mathbf{U}\cdot(\rho\mathbf{U})^*\right)\left(\frac{\partial(\rho U_n)}{\partial n} - \kappa\rho U_t\right) \tag{35}$$

for a small enough constant scalar λ, J will decrease because

$$\delta J = -\lambda\int_\Sigma \left(\rho^* + \mathbf{U}\cdot(\rho\mathbf{U})^*\right)^2\left(\frac{\partial(\rho U_n)}{\partial n} - \kappa\rho U_t\right)^2 + o(\lambda). \tag{36}$$

7.4 Numerical Tests: Mesh Compatibility

A NACA0012 wing profile at Mach 1.6 is computed together with its adjoint. The mesh and the density are shown in Fig. 4. The adjoint density is shown in Fig. 5 together with a comparison of the trace of $(\rho u)^*$ on the ground, calculated by the code where the adjoint is the discrete adjoint (with boundary conditions imposed in weak form by the FVM), and the analytical value. Agreement is excellent.

7.5 Optimization of a 3D Business Jet

Already some years ago [18], combining all these techniques, the authors improved the design of business jets so as to minimized the sonic boom at the ground (see Fig. 6). But the model used Thomas' approximations to transport the sound waves away from the aircraft up to the ground some 10 km below. Since then, the technique has been used in an industrial code [8].

References

1. Alauzet, F., Loseille, A.: High order sonic boom modeling by adaptive methods. Journal of Computational Physics **229**, 561–593 (2010)
2. Alauzet, F., Pironneau, O.: Continuous and discrete adjoints to the Euler equations for fluids. J. Numer. Methods Fluid. Mech. (2012, accepted)
3. Bardos, C., Pironneau, O.: Sensitivities for Euler flows. C. R. Acad. Sci., Paris, Ser I **335**, 839–845 (2002)
4. Becker, R., Rannacher, R.: An optimal control approach to error control and mesh adaptation. In: Iserles, A. (ed.) Acta Numerica 2001. Cambridge University Press, Cambridge (2001)

5. Cournède, P.-H., Koobus, B., Dervieux, A.: Positivity statements for a Mixed-Element-Volume scheme on fixed and moving grids. European Journal of Computational Mechanics **15**(7–8), 767–798 (2006)
6. Cowles, G.W., Martinelli, L.: Control theory based shape design for the incompressible Navier–Stokes equations. Int. Journal Computational Fluid Dynamics **17**(6), 1415–1432 (2003)
7. Debiez, C., Dervieux, A.: Mixed-element-volume MUSCL methods with weak viscosity for steady and unsteady flow calculations. Comput. & Fluids **29**, 89–118 (2000)
8. Dinh, Q., Rogé, G., Sevinand, C., Stoufflet, B.: Shape optimization in computational fluid dynamics. European Journal of Finite Elements **5**, 569–594 (1996)
9. Dreyer, J., Martinelli, L.: Design optimization of propeller blades. In: Caughey, D., Hafez, M. (eds.) Frontiers of Computational Fluid Dynamics 2004. World Scientific, Singapore (2005)
10. Giles, M.B.: Discrete adjoint approximations with shocks. In: Hou, T., Tadmor, E. (eds.) Hyperbolic Problems: Theory, Numerics, Applications. Springer, Berlin (2003)
11. Giles, M., Pierce, N.: Adjoint equations in CFD. AIAA 97-1850. See also: on the properties of solutions of the adjoint Euler equations. In: Baines, M. (ed.) Numerical Methods for Fluid Dynamics VI. ICFD, June 1998
12. Giles, M.B., Ulbrich, S.: Convergence of linearised and adjoint approximations for discontinuous solutions of conservation laws. Part 1: Linearised approximations and linearised output functionals. Technical Report, Mathematical Institute, University of Oxford (2009)
13. Gunzburger, M.D.: Perspectives in Flow Control and Optimization. SIAM, Philadelphia (2002)
14. Jameson, A.: Optimum aerodynamic design using control theory. In: Hafez, M., Oshima, K. (eds.) Computational Fluid Dynamics Review 1995, pp. 495–528. Wiley, New York (1995)
15. Kim, S., Alonso, J.J., Jameson, A.: Design optimization of high-lift configurations using a viscous continuous adjoint method, AIAA-2002-0844. In: 40th AIAA Aerospace Sciences Meeting, Reno, NV, January 2002
16. Lions, J.L.: Optimal Control of Distributed Systems. Dunod (1968)
17. Loseille, A., Alauzet, F., Dervieux, A.: Fully anisotropic goal-oriented mesh adaptation for 3D steady Euler equations. Journal of Computational Physics **229**, 2866–2897 (2010)
18. Mohammadi, B., Pironneau, O.: Applied Optimal Shape Design, 2nd edn. Oxford University Press, Oxford (2009)
19. Pironneau, O.: Optimal Shape Design for Elliptic Systems. Springer, Berlin (1983)
20. Pironneau, O.: Schock Optimization for Airfoil Design Problems. In: Buttazo, G. (ed.) Proc. Erice Conf. (2007)
21. Roe, P.: Approximate Riemann solvers, parameter vectors, and difference schemes. J. Comp. Phys. **43**, 357–372 (1981)
22. Steger, J.L., Warming, R.F.: Flux vector splitting of the inviscid gas dynamic equations with application to finite-difference methods. J. Comput. Phys. **40**, 263–293 (1981)
23. Ulbrich, S.: A sensitivity and adjoint calculus for discontinuous solutions of hyperbolic conservation laws with source terms. SIAM Journal of Control and Optimization **41**(3), 740–797 (2002)
24. Ulbrich, S.: Adjoint-based derivative computations for the optimal control of discontinuous solutions of hyperbolic conservation laws. Systems & Control Letters **48**(3–4), 313–328 (2003)

Numerical Simulation of Sailing Boats: Dynamics, FSI, and Shape Optimization

Matteo Lombardi, Nicola Parolini, Alfio Quarteroni, and Gianluigi Rozza

1 Introduction, Motivation, and Problem Setting

The analysis of the dynamics of a boat advancing into the sea and the corresponding numerical simulations is an interesting and challenging problem [16]. From an engineering point of view it is useful to evaluate the dynamic behaviour of a hull in as many configurations as possible. This can be a helpful tool for boat design, where it could be used to improve the hull performance. This task can be accomplished in two (complementary) ways: experimentally in a towing tank or numerically by Computational Fluid Dynamics (CFD) simulations. Not surprisingly, experimental measurements are usually very expensive since they require the construction of as many scale-models as the number of configurations to be analysed and also technical equipments and facilities are particularly onerous. Furthermore it is possible to reproduce only a limited range of configurations due to practical limitations with the experimental set-up. For these reasons, numerical computations are becoming more and more relevant in this field, and much effort is being devoted in the industrial and academic research to make them as accurate as possible. When a numerical simulation approach is used, it is easy to switch from a model to another one, and the spectrum of configurations that it is possible to analyse is

M. Lombardi (✉) · A. Quarteroni · G. Rozza
MATHICSE, CMCS Chair of Modelling and Scientific Computing, EPFL, Lausanne, Switzerland
e-mail: matteo.lombardi@epfl.ch

A. Quarteroni
e-mail: alfio.quarteroni@epfl.ch

G. Rozza
e-mail: gianluigi.rozza@epfl.ch

N. Parolini · A. Quarteroni
MOX, Politecnico di Milano, Milano, Italy

N. Parolini
e-mail: nicola.parolini@polimi.it

G. Buttazzo, A. Frediani (eds.), *Variational Analysis and Aerospace Engineering: Mathematical Challenges for Aerospace Design*, Springer Optimization and Its Applications 66,
DOI 10.1007/978-1-4614-2435-2_15,

a priori unlimited. On the other hand, the physical problem is very complex, and the most advanced mathematical models have to be used to simulate the problem correctly.

The computation of the flow around ships is a subject studied since long time, at first through the analysis of simplified models and more recently with use of increasingly complex and accurate numerical models. The earliest important theoretical results concerning ship hydrodynamics date back to the end of the nineteenth century. Froude, Kriloff and Reynolds were the fathers of the first theories about ship motion. Froude investigated the role of the wave component of the resistance defining the important dependence on a parameter, nowadays called the Froude number. In 1898, a thin ship theory was proposed in [53] to describe the wave generated by an advancing ship and an analytical estimation of the wave resistance (based on the Mitchell integral) was derived. More complex models date back to the 1960s with the solution of potential flow equations, thanks to important efforts in the aerodynamic fields (see, e.g., the pioneering work by Hess and Smith [32]). Those models were later extended to the solution of ship hydrodynamic problems [18, 19] and added mass models. Although based on simple irrotational and inviscid flow models, potential flow panel codes are still commonly used in the ship hydrodynamics community [75] thanks to their low computational cost and because in several situations they manage to reproduce the main features of the flow quite accurately. With the continuous growth of computation power and improvement of the numerical models for the solution of partial differential equations, more and more complex ship hydrodynamics problems can be simulated accounting for viscous (and turbulent) flows and moving domain (for boat dynamics). Indeed, in the last two decades, numerical methods based on the solution of complex PDEs, the Navier–Stokes (and Euler) equations, have been successfully applied to naval engineering problem (see, e.g., [1, 22, 33, 36, 65]) and are, nowadays, standard numerical tools adopted in the design process for ship performance evaluation.

The Navier–Stokes equations can be written as

$$\frac{\partial}{\partial t}(\rho \mathbf{u}) + \nabla \cdot (\rho \mathbf{u} \otimes \mathbf{u}) = \nabla \cdot T(\mathbf{u}, p) + \mathbf{G} \quad \text{in } \Omega \times (0, T), \tag{1}$$

$$\frac{\partial \rho}{\partial t} + \nabla \cdot (\rho \mathbf{u}) = 0 \quad \text{in } \Omega \times (0, T), \tag{2}$$

where $\mathbf{u}$ is the velocity field, p is the pressure, $T(\mathbf{u}, p) = \mu(\nabla \mathbf{u} + \nabla \mathbf{u}^T) - pI$ is the stress tensor, ρ the density, μ the viscosity coefficient, and $\mathbf{G}$ the gravity term. In the case of incompressible fluids, the second equation reduces to $\nabla \cdot \mathbf{u} = 0$. Finally, Ω is the computational domain occupied by the fluid, while (O, T) is time interval in which the problem will be studied. The Reynolds number $Re = \frac{\rho U L}{\mu} = \frac{UL}{\nu}$ is a dimensionless indicator of the ratio of inertial forces to viscous forces and thus quantifies the relative importance of these two types of forces for given flow conditions. Another fundamental dimensionless number is the Froude number $Fr = \frac{U}{\sqrt{gL}}$, which involves the ratio between the gravity force and the inertial forces.

Typically, the Reynolds numbers that characterize ship hydrodynamics problems are large (order of magnitude 10^7–10^9); the flow is indeed fully turbulent around a large portion, to a first approximation all of it, of the boat, and suitable turbulence models have to be used to correctly estimate the forces acting on it. A Direct Numerical Simulation (DNS) of such flows is unaffordable with the computational power available today. Although the Large Eddy Simulation (LES) [79] and the Detached Eddy Simulation (DES) [84] are gaining interest also in the ship hydrodynamics community [2, 90], the Reynolds Averaged Navier–Stokes equations (RANS) still represent the most common approach to solve this kind of problems. In the RANS approach, velocity and pressure are decomposed in two components, an average one and a fluctuation part, and the Navier–Stokes equations are solved only with respect to the averaged variables, while the effect of the fluctuation part is modelled via some extra turbulence models [9, 24, 88].

If we split the flow variables into an averaged part and a fluctuation part

$$\mathbf{u} = \bar{\mathbf{u}} + \mathbf{u}', \qquad p = \bar{p} + p', \tag{3}$$

where $\bar{\mathbf{u}} = \frac{1}{\Delta t}\int_t^{t+\Delta t} \mathbf{u}\, dt$ with the value of Δt higher than the turbulent time scale but smaller than the one chosen for the actual numerical discretization of the equations, and we substitute into Eqs. (1)–(2) (under the assumption of incompressibility), the RANS equations are obtained as:

$$\frac{\partial}{\partial t}(\bar{\rho}\bar{\mathbf{u}}) + \nabla \cdot (\bar{\rho}\bar{\mathbf{u}} \otimes \bar{\mathbf{u}}) = \nabla \cdot T(\bar{\mathbf{u}}, \bar{p}) + \nabla \cdot \mathbf{R} \quad \text{in } \Omega \times (0, T), \tag{4}$$

$$\frac{\partial \bar{\rho}}{\partial t} + \bar{\mathbf{u}} \cdot \nabla \bar{\rho} = 0 \quad \text{in } \Omega \times (0, T), \tag{5}$$

$$\nabla \cdot \bar{\mathbf{u}} = 0 \quad \text{in } \Omega \times (0, T), \tag{6}$$

where $\mathbf{R}$ is the so-called Reynolds stress tensor $R_{ij} = \rho\overline{u_i' u_j'}$ which is derived from the nonlinear convective term. From a physical point of view, this term corresponds to the extra mixing due to the turbulent eddies not represented by the averaged variables. Many different turbulent models exist in literature, and they can be grouped into the following three classes:

- algebraic models,
- models based on differential equations (one- or two-equation models),
- models based on the Reynolds stress tensor transport equation.

In this work, we have considered the SST (Shear Stress Transport) [51] model, which is a combination of the *K-epsilon* [54] and *K-omega* [50] models. This model has been validated extensively in the literature [88] and successfully applied to naval hydrodynamics problems [65, 91].

Two main classes of methods for the solution of free surface flows are present in the specialized literature: front tracking methods and front capturing methods. In the formers, only one phase is simulated, the water, and the boundary of the domain follows the free-surface evolution. In this case, the computational domain

Ω in Eqs. (1) and (2) does depend on time. The main drawback is that complex free-surface behaviour, like spray or overturning waves, cannot evidently be simulated, and the mesh quality can rapidly deteriorate. By front tracking methods, on the contrary, both air and water are simulated, and the computational domain and mesh are kept fixed. An extra variable is introduced to specify for every cell of the domain whether it belongs to the air or water. The most common methods that belong to this class are the Volume of Fluid (VOF) method [5, 34] and the Level Set (LS) method [60, 61]. The volume of fluid method is based on a *homogeneous* approach, where a unique velocity and pressure field is defined for both fluids. A new variable c, called the *volume fraction* of the water, is defined on the whole domain and such that $c = 0$ if the element corresponds to an air zone, $c = 1$ if the element corresponds to a water zone and an intermediate value if both fluids are present in the element. Furthermore, c must be bounded between 0 and 1. With this approach, it is thus possible to solve a unique fluid-dynamic problem for both fluids and Navier–Stokes equations (1)–(2), under the assumption of incompressibility, become:

$$\frac{\partial}{\partial t}(\rho \mathbf{u}) + \nabla \cdot (\rho \mathbf{u} \otimes \mathbf{u}) = \nabla \cdot T(\mathbf{u}, p) + \mathbf{G} \quad \text{in } \Omega \times (0, T), \tag{7}$$

$$\nabla \cdot \mathbf{u} = 0 \quad \text{in } \Omega \times (0, T), \tag{8}$$

where N_{el} is the number of different fluids, i.e. two in this case, and ρ and μ are defined as

$$\rho = c\rho_{\text{water}} + (1 - c)\rho_{\text{air}}, \qquad \mu = c\mu_{\text{water}} + (1 - c)\mu_{\text{air}}, \tag{9}$$

where μ is present in the tensor T. For the evolution of the interface between air and water, a further transport equation for the *volume fraction* variable has to be solved:

$$\frac{\partial c}{\partial t} + \nabla \cdot (c\mathbf{u}) = 0. \tag{10}$$

In order to keep the interface sharp, ad hoc numerical terms can be introduced into those equations. In this work, the Volume of Fluid (VOF) model is adopted and solved using the Multidimensional Universal Limiter with Explicit Solution (MULES) algorithm, in which a compression term is added to the standard VOF formulation in order to keep the interface sharp (see [78] for details).

In the case of mesh motion, for example when simulating the boat dynamic or when solving the Fluid-Structure interaction problem, the Arbitrary Lagrangian Eulerian (ALE) formulation has to be implemented [17, 28, 29, 35]. This correction takes care of the fact that the mesh is moving and thus corrects the convective term with the actual mesh motion velocity.

Equations (4) thus become

$$\frac{\partial}{\partial t}\left(\bar{\rho}\bar{\mathbf{u}}\right) + \nabla \cdot \left(\bar{\rho}(\bar{\mathbf{u}} - \mathbf{w}) \otimes \bar{\mathbf{u}}\right) = \nabla \cdot T(\bar{\mathbf{u}}, \bar{p}) + \nabla \cdot \mathbf{R} \quad \text{in } \Omega(t) \times (0, T), \tag{11}$$

where $\mathbf{w}$ is the mesh velocity. The same correction has to be applied to the turbulence and volume fraction equations.

An important feature of this research project is the use of open-source codes. All over the world, the scientific community is investing a great effort in the development and validation of free software like *FreeFem* [68], *DealII* [45], *LifeV* [25], *OpenFOAM* [59]. The latter is growingly very rapidly and is being extensively used and developped by many academic and industrial research centres. It features many of the key-points needed for our kind of applications, more notably a Navier–Stokes solver, turbulence models, VOF models, and parallel scalability. Furthermore its modular organization allows one to easily transfer specific development to other applications/solvers, yielding a larger impact of the research carried out by single research groups on the global scientific community. For these reasons, the authors have chosen to use OpenFOAM as the base library to solve the flow problem.

OpenFOAM (Open Field Operation and Manipulation) is a C++ object-oriented programming toolbox capable of solving several continuum mechanics problems, among which the solution of partial differential equations like the Navier–Stokes equations [38]. It works on structured and unstructured meshes, and the space discretization is done by means of finite volume method. The time marching scheme is based on a pseudo PISO algorithm, where the pressure and velocity are solved in a segregated way and, for every time step, sub-iterations are needed to reach convergence [24].

An accurate solution of the flow problem is the starting point for the solution of more complex physical behaviour such as the rigid-body boat dynamics [4, 16] or the fluid-structure interaction between sails and wind [20, 73, 87, 89]. Another valuable development direction of numerical tools for hydrodynamic design is represented by the integration of the flow solver in a shape optimization process. In the naval engineering community, shape optimization techniques are receiving an increasing interest, both when considering gradient-based optimization schemes [48, 85] and derivative-free algorithms [8, 18].

In this paper, we present a numerical model that has been developped for the simulation of free-surface boat dynamics problems and the Fluid-Structure interaction algorithm devised for the prediction of the flying shape of downwind sails. We also introduce a shape optimization technique for hydrodynamic drag reduction based on gradient methods (with and without the solution of the adjoint problem), which makes use of the FFD method for the shape parameterization and mesh motion. Finally, a set of simulations obtained with the different methods proposed are presented and discussed.

2 Hull Dynamics

In order to simulate the dynamics of the hull, it is necessary to estimate the loads exerted by the fluids (air and water) on the structure and the dynamic response of the structure to these loads. Our attention has been focused, in particular, on the resolution of the equations of motion of the boat and the coupling algorithm for the fluid-structure interaction.

The motion of a boat, once neglecting the deformation of the hull (provided that they are small) is governed by the equations of motion of a rigid body: those can be split in a translation motion of a point, which for simplicity is usually chosen the barycentre (equivalent in this case to the centre of mass, i.e. the mean location of all the mass in the system) and the rotation of the body around it.

The equation for the variation of the linear momentum referred to the barycentre is

$$m\ddot{\mathbf{X}}_G = \mathbf{R}, \tag{12}$$

where m is the mass of the boat. $\mathbf{R}$ is the total force acting on the boat obtained via

$$\mathbf{R} = \mathbf{F}_{\text{Flow}} + m\mathbf{g} + \mathbf{F}_{\text{ext}}, \tag{13}$$

where F_{flow} is the hydrodynamic force, $m\mathbf{g}$ the gravity force, and $\mathbf{F}_{\text{ext}}$ corresponds to the resultant of the external forces. The hydrodynamic force $\mathbf{F}_{\text{Flow}}$ can be evaluated integrating the viscous and pressure stresses acting on the wetted surface of the boat:

$$\mathbf{F}_{\text{Flow}} = \sum_{j=1}^{n} (-p_j \mathbf{n}_j + \boldsymbol{\tau}_j) S_j, \tag{14}$$

where the sum is taken over all faces of the volume that defines the surface of the boat, and S_j are the corresponding areas.

In order to solve the equation for the variation of angular momentum, first of all it is necessary to define two reference systems: one referred to the fixed domain, which we will call the *principal reference system*, and one that rotates with boat, the *secondary reference system*. It can be shown that the union of the unit vectors $\mathbf{i}, \mathbf{j}, \mathbf{k}$ of the secondary reference system expressed in the principal system generates the rotation matrix form one system to the other.

The equation of variation of angular momentum, referred to the principal reference system, can be finally expressed as

$$\bar{\bar{T}}\,\bar{\bar{I}}_G\,\bar{\bar{T}}^{-1}\dot{\omega} + \boldsymbol{\omega} \times \bar{\bar{T}}\,\bar{\bar{I}}_G\,\bar{\bar{T}}^{-1}\boldsymbol{\omega} = \mathbf{M}_G, \tag{15}$$

where ω is the angular velocity, $\bar{\bar{I}}_G$ is the matrix of the *moments of inertia*,

$$\bar{\bar{I}}_G = \begin{bmatrix} I_{XX} & I_{XY} & I_{XZ} \\ I_{YX} & I_{YY} & I_{YZ} \\ I_{ZX} & I_{ZY} & I_{ZZ} \end{bmatrix},$$

and $\mathbf{M}_G$ is the total moment around the rotation centre acting on the boat expressed in the principal reference system. The total moment can be expressed as

$$\mathbf{M}_G = \mathbf{M}_{\text{Flow}} + \mathbf{M}_{\text{ext}}, \tag{16}$$

where $\mathbf{M}_{\text{ext}} = (\mathbf{X}_{\text{ext}} - \mathbf{X}_G) \times \mathbf{F}_{\text{ext}}$ is the moment due to the external forces, and $\mathbf{M}_{\text{Flow}}$ is the moment due to the hydrodynamic forces, which, analogously to

Eq. (14) for the hydrodynamic forces, corresponds to

$$\mathbf{M}_{\text{Flow}} = \sum_{j=1}^{n} (\mathbf{X}_j - \mathbf{X}_G) \times (-p_j \mathbf{n}_j + \boldsymbol{\tau}_j) S_j. \tag{17}$$

These equations form a system of six second-order ordinary differential equations, three for the translation motion and three for the rotation. The translation equations are not coupled and can be resolved separately. The rotation ones, except when the rotation is around one single axis, are coupled nonlinear equations and have to be resolved as a coupled system. The rotation is handled via Euler angles, and the dynamic problem is solved via Adams–Bashforth/Crank–Nicholson schemes, see [46] for a detailed analysis.

As mentioned in the previous sections, the RANS model has been adopted to simulate the fluid-dynamic behaviour of the flow around the boat, and particular care has been paid to model the boundary layer around the hull. The free-surface dynamics has been tracked using a VOF model. The coupling between the fluid solver and the hull dynamics solver has been done explicitly: for every time step, the fluid solver advances using the hull position at the previous time step, then the fluid forces at time t_{n+1} are evaluated, and the new boat position is obtained. Finally the fluid mesh is adjusted, and the next time step can be computed. For this kind of applications, such a simple and explicit coupling algorithm is usually stable since the transient fluid solver requires a quite restrictive time step constraint while the hull dynamic time-scale is usually much higher. A more general and detailed analysis of Fluid-Structure Interaction coupling algorithm is presented in the following sections. For more details on the hull dynamics model, we refer to [4, 16, 64].

3 Wind/Sail Fluid-Structure Interaction

The problem of modelling and simulating the interaction between fluids and solids arises in many different applied fields. Examples are the interaction of the blood flow within arterial walls, the flow around the sails of a sailing boat, the deformation of the wing of an aeroplane or a Formula-1 car. Although extensively studied in literature, due to its complexity, this problem is still a subject of intensive investigation. A complete review of the existing literature goes far beyond the scope of this work, however we refer for example to [12, 13, 58, 71] and the references therein. Here we would simply like to mention the different approaches that can be chosen and the reasons behind those choices. The first classification depends on whether one is interested only in the equilibrium solution or to the whole transient behaviour. In case of wind/sail fluid structure interaction, both situations are of interest.

Secondly, one should consider which level of accuracy is needed for the simulation of the fluid and solid parts and if any simplified model could be meaningful. For example, in upwind sailing configuration, it is usually not indispensable to solve the full Navier–Stokes equations around the sails; indeed, simpler models, like the one

based on potential flow, are accurate enough to obtain realistic flow fields. The same argument can be applied to the structural part, where assumptions like linear elasticity model or small deformation can lead to simplified, and much faster, numerical methods.

In this work, a full RANSE solver has been used since, in the configurations to be analysed, flow separations may occur and viscous stresses may be important, phenomena which cannot be simulated accurately with potential flow solver. As structural solvers, different options may be considered. For cases where a linear elasticity model is adequate, classical simple structural solver, like the one already implemented in OpenFOAM, can be used. For the sails simulations, a specific solver for membranes/shells specifically tuned for sails must to be used. More details are given in the following subsection.

Another important aspect to be taken into consideration is the amplitude of the deformation and the added-mass [10] effect; this determines the FSI coupling strategy to be used in order to obtain stable simulations. In this respect, we refer to *partitioned strategies* when we solve iteratively the fluid and structure sub-problems (and never assemble the full matrix). This allows the possibility of coupling two existing codes, one solving the fluid equations and the other the structure problem. We refer instead to *monolithic* schemes when we solve the nonlinear coupled problems all at once. In this case, a global linear system is assembled and solved for all the unknowns of the problem: fluid and structural variables as well as all the geometrical information (like the interface position). The complete fluid–solid system has to be solved as a whole, and memory issue may arise due to the size of the global matrix. Other possible models that are in between these two approaches exist: for instance, one can formally write the monolithic problem and then use a block preconditioner to solve it. In this way one recovers partitioned procedures [12].

In case of small deformation and/or high density ratio between air and fluid, a simple coupling strategy can be used, e.g. the so-called *weakly coupled partitioned approach* where the two solvers can be run in a *segregated* way. For example, at first the fluid solver is run, then the interface conditions (the stresses) are passed from the fluid mesh to the solid mesh, and then the solid solver is run; the solid interface conditions (the interface positions and its rate of deformations) are then passed back to the fluid solvers, and the fluid mesh and boundary conditions are updated accordingly; a new time step can then be computed. Unfortunately, when the added mass effect gets more important, it has been proven (see e.g. [10]) that this kind of schemes becomes unconditionally unstable and it is necessary to sub-iterate, with relaxation, for every time step. The *strongly coupled partitioned approach* consists in introducing sub-iterations at every time step between the two solvers. Usually the interface conditions are imposed via a relaxation procedure, for example with the *Aitken* relaxation method, see [13]. A potential drawback of this approach is that the number of sub-iterations may become large, of the orders of a few tens depending on the case, and thus the computational cost may rise very quickly. In our case, since the fluid and structural solvers are in general two different codes and the FSI problem is stiff, the strongly coupled partitioned approach has been adopted.

In Fig. 1 a schematic flow chart of the strongly coupled partitioned FSI algorithm adopted in this work is shown. For every time step, sub-iteration cycles have to be

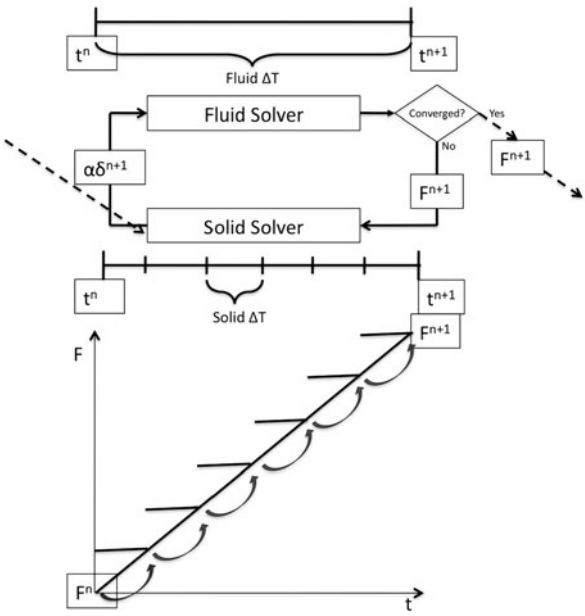

Fig. 1 Schematic flow-chart of the Fluid-Structure interaction coupling algorithm

computed. At first, the structural solver is run using as boundary condition the fluid solver stresses from the previous time step. The new position of the sail is passed to the fluid, and an iteration of the fluid solver is computed. The updated fluid stresses are then transferred back to the solid, and the structural solver is run again. Once again, the new deformed sail position is passed to the fluid, and the new flow solution is computed. If the difference between the solid deformation and fluid stresses at the previous and current sub-iterations is below a given tolerance, the FSI is considered converged, and a new time step is computed, otherwise, a new sub-iteration cycle is carried out. In order to accelerate the convergence and ensure the stability, the deformation passed from the solid to the fluid is relaxed with the one obtained at the previous sub-iteration cycle via Aitken relaxation technique. Furthermore, since the structural solver is explicit, a smaller time step has to be used for the solid solver than for the fluid solver. For every sub-iteration, the solid solver performs many iterations, until it covers the whole fluid solver time interval; the boundary condition imposed at every sub-step is obtained via linear interpolation of the fluid stresses at times t^n and t^{n+1}.

3.1 The Sails Structural Solver

In this section, we present the shell model used for the simulation of the sail deformation. Consider a shell body of constant thickness h immersed in a fixed reference frame $\{\mathbf{i}_i\}$, $i = 1, 2, 3$. Within the context of the inextensible director shell theory,

the geometry of the shell in the reference configuration is described by the mapping

$$\mathbf{X} = \boldsymbol{\Phi}(\bar{\boldsymbol{\xi}}) = \bar{\boldsymbol{\Phi}}\left(\xi^1, \xi^2\right) + \xi^3 \mathbf{L}\left(\xi^1, \xi^2\right), \qquad -\frac{h}{2} \leq \xi^3 \leq \frac{h}{2}, \tag{18}$$

where $\mathbf{X}$ is the position vector of a material point in the shell body identified by the convective system of coordinates $\bar{\boldsymbol{\xi}} = (\xi^1, \xi^2, \xi^3)$; $\bar{\boldsymbol{X}} = \bar{\boldsymbol{\Phi}}(\xi^1, \xi^2)$ is the position vector of points belonging to the shell middle surface $\mathcal{M}(\xi^3 = 0)$ with boundary $\partial\mathcal{M}$, and the unit vector $\mathbf{L}(\xi^1, \xi^2)$ denotes the director field. In the present formulation, $\mathbf{L}$ is assumed to be normal to the middle surface in the original configuration, but, according to the Mindlin–Reissner assumption, it is not forced to remain normal during the deformation.

A shell deformed configuration at time $t \in [0, T]$ is defined by the mapping $\mathbf{x} = \chi_t(\mathbf{X})$ where χ_t represents the motion. The displacement $\mathbf{s}$ at a generic point $\mathbf{X}$ follows from the kinematic description as

$$\mathbf{s}(\bar{\boldsymbol{\xi}}) = \mathbf{x}(\bar{\boldsymbol{\xi}}) - \mathbf{X}(\bar{\boldsymbol{\xi}}). \tag{19}$$

For a generic solid medium with density ρ and subjected to the body forces $\mathbf{B}$, the equation of motion (momentum conservation) in the reference configuration, can be written as

$$\rho_0 \frac{\partial^2 \mathbf{s}}{\partial t^2} = \nabla_R \cdot \mathbf{S} + \mathbf{B}, \tag{20}$$

where $\nabla_R \cdot$ is the divergence operator in the reference configuration, and $\mathbf{S} = J\boldsymbol{\sigma}\mathbf{F}^{-T}$ is the first Piola–Kirchhoff stress tensor, $\boldsymbol{\sigma}$ is the Cauchy stress tensor, $\mathbf{F}$ is the deformation gradient, and J is the determinant of $\mathbf{F}$.

From the numerical point of view, the structural problem is solved by the Galerkin Finite Element method [72]. More specifically, the MITC4 elements [19] have been used for the space discretization. These shell elements are three-dimensional solids, but the typical constraints of the shell kinematics are forced. To avoid shear locking, a mixed interpolation of the tensorial component has been adopted [11].

The assumption of large displacements and small strains are considered, and a linear elastic constitutive model with an isotropic material is implemented.

After space discretization, the semi-discrete equations of motion governing the structural dynamic response of a system can be written as

$$\mathbf{M}\ddot{\mathbf{s}} + \mathbf{C}\dot{\mathbf{s}} + \mathbf{F}(\mathbf{s}) = \mathbf{P}, \tag{21}$$

where $\mathbf{M}$ is the mass matrix, $\mathbf{C}$ the damping matrix, $\mathbf{F}$ the vector of internal force, and $\mathbf{P}$ is the vector representing the external loads. $\ddot{\mathbf{s}}$, $\dot{\mathbf{s}}$ and $\mathbf{s}$ are respectively the acceleration, velocity and displacement vectors, collecting all the nodal degrees of freedom employed to describe the solid kinematics.

The central difference explicit method [6] has been chosen for the time integration of Eq. (21). A variable time increment version of the algorithm is used,

in which, inside the single time marching step, the velocity is approximated at the midpoints of the time interval with the following formula:

$$\dot{\mathbf{s}}^{n+1/2} = \frac{\mathbf{s}^{n+1} - \mathbf{s}^{n}}{\Delta t^{n+1/2}}, \tag{22}$$

while the acceleration can be written as

$$\ddot{\mathbf{s}}^{n} = \frac{\dot{\mathbf{s}}^{n+1/2} - \dot{\mathbf{s}}^{n-1/2}}{\Delta t^{n}}, \tag{23}$$

where $\Delta t^{n+1/2} = t^{n+1} - t^{n}$ and $\Delta t^{n} = t^{n+1/2} - t^{n-1/2}$. Finally, the acceleration can be directly expressed in terms of the displacements:

$$\ddot{\mathbf{s}}^{n} = \frac{\Delta t^{n-1/2}(\mathbf{s}^{n+1} - \mathbf{s}^{n}) - \Delta t^{n+1/2}(\mathbf{s}^{n} - \mathbf{s}^{n-1})}{\Delta t^{n+1/2}\Delta t^{n}\Delta t^{n-1/2}}. \tag{24}$$

Using approximations (22)–(24) and the equation of motion (21), the nodal velocity can be updated as

$$\dot{\mathbf{s}}^{n+1/2} = \dot{\mathbf{s}}^{n-1/2} + \Delta t^{n}\mathbf{M}^{-1}\left(\mathbf{F}^{n} - \mathbf{P}^{n} - \mathbf{C}\dot{\mathbf{s}}^{n-1/2}\right). \tag{25}$$

At every time step the displacements $\mathbf{s}$, the external forces $\mathbf{P}^{n}$ (or $\mathbf{P}^{n+1}$, depending on the coupling) and the viscous forces are known; the internal nodal forces $\mathbf{F}^{n}$ can be determined by the constitutive law and the strain-displacement relation. So the right-hand side of (25) is known, the velocity can be obtained, and the displacement can be subsequently computed using (22).

If the mass matrix $\mathbf{M}$ is diagonal (e.g. due to a mass-lumping reduction), the update of the nodal velocities and nodal displacements can be obtained without solving any linear system. This choice has significant computational advantages: problem (21) is transformed into an uncoupled system of algebraic equations in which each solution component may be computed independently, with no need for assembly or factorization of any global matrix.

The central difference method is not unconditionally stable, so that the time interval Δt needs to be small to satisfy the CFL (Courant–Friedrichs–Levy) condition.

At the moment, a simple homogeneous constitutive law for the sail material property is being used, but more complex models are under implementations. A modern sailing boat sail is in fact a complex masterpiece of modern technology, with the use of carbon fibres inside two PET (polyethylene terephthalate) films cooked in a vacuum oven to get very light but also very resistant sails. The disposition and orientation of the fibres is done in a way that the material properties of the sails vary greatly from zone to zone so that the sail shape under load is the closest to the optimum shape (chosen at the sail design stage).

4 Shape Optimization

For the design of a sailing boat, an efficient numerical scheme ought to be combined with a shape optimization strategy through the minimization of suitable cost functionals [37, 56]. A general abstract formulation of shape optimization problems can be set up as follows: given a set of admissible shapes $\mathcal{O}_{\text{ad}}$, find the optimal shape $\hat{\Omega} \in \mathcal{O}_{\text{ad}}$ such that

$$\hat{\Omega} = \underset{\Omega \in \mathcal{O}_{\text{ad}}}{\arg\min}\, J\big(\Omega, y(\Omega)\big), \quad \text{with } \mathcal{R}\big(y(\Omega)\big) = 0, \tag{26}$$

where $J(\cdot, \cdot)$ is the cost functional to be minimized, $y(\Omega)$ are the state variables, and $\mathcal{R}$ represents the state equations (i.e. the Navier–Stokes equations in the current context).

Many possible ways to achieve this target exist, each bringing its own advantages and disadvantages, and therefore some clear choices have to be made. In Fig. 2, a schematic diagram of the different methodology for shape optimization cited in this section is drawn. In particular, the two approaches adopted in this work have been highlighted with solid and dashed–dot arrows. The results obtained are reported in Sect. 6.

4.1 Optimum Research Algorithm

The next step is the choice of the optimization algorithm. Given a certain cost functional and parameter space, many different ways to reach the optimum can be pursued [37, 56], e.g. the gradient-like methods, genetic algorithms (GA) and neural networks. Gradient-like methods [57] require the gradients of the cost functional and constraints (dependent variables) with respect to the shape design (independent) variables. These gradients, commonly referred to as *sensitivity* derivatives, provide a mechanism for changing the design variables in order to improve the objective function without violating the given constraints. Sensitivity derivatives may be approximated by finite differencing; however, besides being computationally expensive, unless carefully monitored, this approach can produce inaccurate gradient approximations. In this case, the number of control points must be small. The preferable approach [72] is to derive the analytical expression of the sensitivity field; however this requires the solution of the *adjoint* field. The latter can be obtained writing the adjoint equations either at continuous level and using the same approach as for the discretization of the direct fluid problem, or at discrete level, thus via a proper manipulation of the already assembled discrete elements. Another possible technique to obtain the adjoint field is through automatic differentiation [55] algorithms.

In this case, the control points are precisely all the surface mesh points (possibly many). In fact, the advantage of this technique is that the cost of the optimization does not depend linearly on the number of control points, the drawback being that for every optimization step, also the adjoint problem has to be solved.

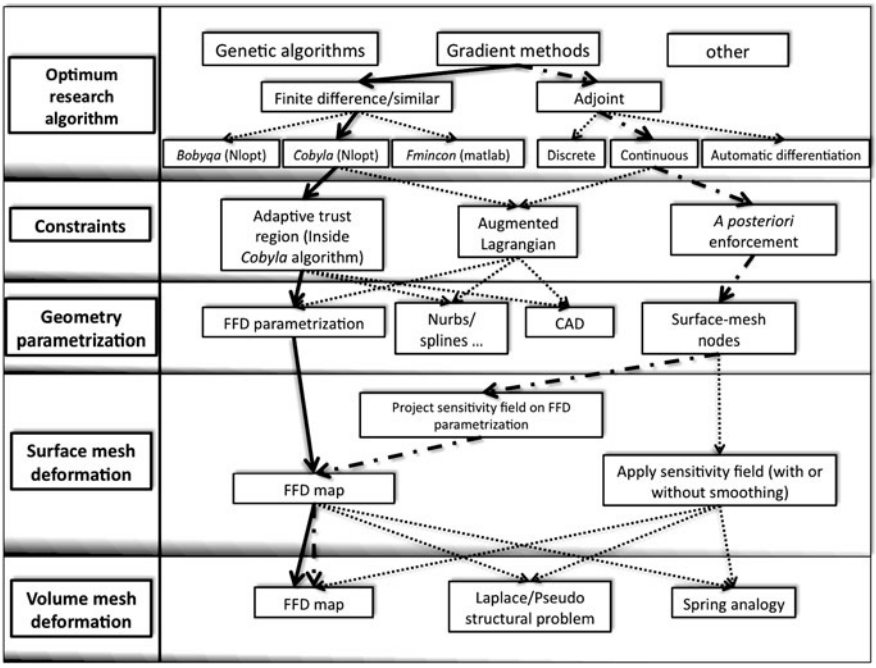

Fig. 2 Diagram showing a range of possible approaches to perform shape optimization, subdivided into the five main steps to be performed. The *solid* and *dashed-dot* arrows represent the two approaches developped in this article, while the *thin-dotted* ones are other possible methodologies taken in consideration by the authors but not used in this work

Once the direct and adjoint fields have been computed, the sensitivity field, i.e. the gradient of the cost functional for every surface mesh point, can be obtained. After a proper choice of the sensitivity-descent step size, the surface mesh points position can be updated, and a new optimization step can be computed.

The adjoint approach should thus be very fast to converge to the optimal solution since for every iteration, the best descent direction is chosen. A weakness of this approach is that there is no control over the shape that the geometry may assume, since every node is moved independently. If applied "directly", this approach may not maintain the smoothness and regularity of the geometry or other features that one may want to preserve, e.g. symmetry. Usually some smoothing iterations of the gradient field are performed and, only after this regularizing steps, the geometry is deformed. In the following, a combination of adjoint-gradient method with surface parameterization technique to improve mesh quality and surface smoothness is proposed.

Another weakness of gradient-like methods is that they may converge to a local optimum and not to the global one. Genetic algorithms (GAs) [30, 31], on the other hand, have proven their strength in avoiding local extrema and numerical noise in aerodynamic optimization. In problems with constraints, however, they may require a very high number of parameter evaluations to converge. In our case, the cost of

GAs methods is still not affordable, and thus we are oriented to the use of a deterministic approach, and we will focus at first only on gradient-like methods.

In this work, two approaches for shape optimization have been chosen. The first one consists in using optimization algorithms that do not require the direct evaluation of the gradient of the cost functional. Thanks to the open-source library *Nlopt* [39], many different derivative-free methods are available. For our test cases, we have used the *Cobyla* (Constrained Optimization By Linear Approximations) and *Bobyqa* (Bound Optimization By Quadratic Approximation) methods. The *Cobyla* algorithm constructs successive linear approximations of the objective function and constraints via a simplex of $n + 1$ points (in n dimensions) and optimizes these approximations in a trust region at each step [69]. The *Bobyqa* algorithm instead performs gradient-free optimization using an iteratively constructed quadratic approximation of the objective function [70]. As stated before, the drawback of using gradient-free methods is that the cost of the optimization is linearly dependent on the number of control points and, due to the high cost of every cost function evaluation (i.e. the cost of the solution of a full Navier–Stokes simulation), only a small number of control points can be used. It is thus infeasible to use as control points the location of all nodes of the surface mesh to be optimized, which may be in the order of tens of thousands, while an FFD parameterization fulfills very well this requirement.

The second approach that has been explored is based on the solution of the adjoint Navier–Stokes equations for the direct evaluation of the gradient of the cost functional. In this work the continuous adjoint formulation of the Navier–Stokes have been adopted. Here a short description on this approach is reported; for a more detailed analysis, we refer to [62, 63].

With the introduction of a Lagrange multiplier $\boldsymbol{\lambda}$, problem (26) can be rewritten as an unconstrained minimization problem for the Lagrangian functional L given by

$$L = J + \int_{\Omega} \boldsymbol{\lambda} \mathcal{R} \, d\Omega. \tag{27}$$

In the specific case of drag minimization around an object under a steady laminar Newtonian flow, the state equations governing the problem are the Navier–Stokes equations (1) (without the time derivative term) and the cost functional can be expressed as

$$J = -\int_{\Gamma_{\text{Body}}} \big(T(\mathbf{u}, p)\mathbf{n}\big) \cdot \hat{\mathbf{u}}_f \, d\Gamma = \int_{\Gamma_{\text{Body}}} \big(p \cdot \mathbf{n} - 2\nu\sigma(\mathbf{u})\mathbf{n}\big) \cdot \hat{\mathbf{u}}_f \, d\Gamma, \tag{28}$$

where Γ_{body} is the boundary associated to the shape to be optimized, $\sigma(u) = \frac{1}{2}(\nabla\mathbf{u} + \nabla\mathbf{u}^T)$ is the *strain rate tensor*, and $\hat{\mathbf{u}}_f$ is the unit-vector in the main flow direction. The Lagrange multiplier is given as $\boldsymbol{\lambda} = (\mathbf{v}, q)$, where $\mathbf{v}$ and q are the so-called adjoint velocity and pressure, respectively.

If we define as design variables β the deformation of every boundary point in the normal direction, the Lagrange problem (27) can be expressed as $L =$

$L(\mathbf{u}, p, \mathbf{v}, q, \beta)$, and its total variation becomes

$$\delta L = \delta_{\mathbf{u}} L + \delta_p L + \delta_{\mathbf{v}} L + \delta_q L + \delta_\beta L. \tag{29}$$

The first-order optimality condition for the Lagrange functional entails that the first four terms on the right-hand side of Eq. (29) are equal to zero. The third and fourth terms correspond to the Navier–Stokes equations and are indeed equal to zero since fields $(\mathbf{u}, p)$ satisfy those equations. The first and second terms are equal to zero if the so-called *adjoint Navier–Stokes* equations are satisfied by adjoint variables $(\mathbf{v}, q)$. If we decompose the cost functional into contributions from the boundary J_Γ and from the interior of the domain J_Ω, after integration by parts, the adjoint Navier–Stokes equation are defined as:

$$\left(\nabla \mathbf{v}^T\right)\mathbf{u} - (\mathbf{u}\cdot\nabla)\mathbf{v} = -\nabla q + \nabla\cdot\left(2\nu\sigma(\mathbf{v})\right) - \frac{\delta J_\Omega}{\delta \mathbf{u}} \quad \text{in } \Omega \tag{30}$$

$$\nabla\cdot\mathbf{v} = -\frac{\delta J_\Omega}{\delta p} \quad \text{in } \Omega, \tag{31}$$

with the boundary conditions

$$\begin{cases} \mathbf{v} = -\left(\frac{\delta J_{\Gamma_{\text{Body}}}}{\delta p}\cdot\mathbf{n}\right) = -\hat{\mathbf{u}}_f & \text{on } \Gamma_{\text{Body}}, \\ \mathbf{v} = 0 & \text{on } \Gamma_{\text{in}} \cup \Gamma_w, \\ T(\mathbf{v}, q)\cdot\mathbf{n} + (\mathbf{u}\cdot\mathbf{n})\mathbf{v} = 0 & \text{on } \Gamma_{\text{out}}. \end{cases} \tag{32}$$

They have been derived under the assumption that in the primal problem, Dirichlet boundary conditions on the velocity have been imposed on the inlet and external wall ($\Gamma_{\text{in}} \bigcup \Gamma_w$) as well as a free-stress condition on the outlet (Γ_{out}).

Furthermore, since in our case the cost functional does not depend on volume values but only on boundary integrals, problem (30)–(31) reduces to

$$\left(\nabla \mathbf{v}^T\right)\mathbf{u} - (\mathbf{u}\cdot\nabla)\mathbf{v} = -\nabla q + \nabla\cdot(\nu\nabla\mathbf{v}) \quad \text{in } \Omega, \tag{33}$$

$$\nabla\cdot\mathbf{v} = 0 \quad \text{in } \Omega. \tag{34}$$

The adjoint problem (33)–(34) has a structure similar to that of the primal Navier–Stokes equations, and the solution of its numerical counterpart has been implemented and solved with the OpenFOAM library. Albeit linear, problem (33)–(34) is computationally not much cheaper than the primal Navier–Stokes equations, being often a stiffer problem, and thus the final cost is strongly affected by the actual algorithm implemented in the solver.

Equation (29) thus reduces to

$$\delta L = \delta_\beta J + \int_\Omega (\mathbf{v}, q)\delta_\beta \mathcal{R}\, d\Omega. \tag{35}$$

Since there is no explicit dependence of the cost functional on the deformation, the term $\delta_\beta J$ is equal to zero.

Finally, it is possible to show (see [83] for details) that the volume integral in (35) can be expressed as a boundary integral defined on the portion of the boundary to be optimized,

$$\delta L = \int_{\Gamma_{\text{Body}}} \mathbf{g} \cdot \mathbf{n} \, d\Gamma, \tag{36}$$

reducing its computation cost to a simple post-processing step. It can be demonstrated [62] that, after some simplification, the sensitivity field $\mathbf{g}$ can be approximated as

$$\mathbf{g} = \mathbf{A}\big(2\nu\sigma(\mathbf{u}) : \sigma(\mathbf{v})\big)\mathbf{n}, \tag{37}$$

where A represents the area of every face.

4.2 Parameters Constraints

Another issue to be addressed is how to treat the control parameter constraints. Usually the object to be deformed cannot deform freely but is subject to some geometrical constraints, like keeping the constant or imposing a minimum size of certain parts of the shape to be optimized. One of the most common methods to enforce a constraint is to add a penalization term inside the cost function whose magnitude is adjusted dynamically until the constraint is satisfied. In this respect, a very popular method is the augmented Lagrangian method [74].

Another more empirical technique consists instead in recovering the constraint a posteriori, i.e. after the shape deformation due to the sensitivity field, via a second mesh motion. For example, in the case of a volume constraint, after each sensitivity-based deformation, the shape can be inflated/deflated homogeneously, i.e. the same amount in the normal direction of every face, until the required volume is obtained.

Finally, some optimum research algorithms, like *Cobyla*, satisfy the constraints modifying the trust region dynamically at each step based on the information available at the previous iterations. Notice that during the initial stages the constraints may not be respected, but as soon as more data are available and the magnitude of deformation becomes smaller, the constraints requirements are fulfilled. In this work the a posteriori recovery technique [69] and the adjustable trust region technique have been used.

4.3 Geometry Parameterization

At this point, decision on how to model the geometry (and how to control the morphing process) has to be taken. Usually, industrial geometries are drawn using specific *CAD* programs, e.g. *Rhino* [14], *AutoCad* and *Maya* [26], *SolidWork* [82], etc. Those geometries are then exported in a suitable format and imported into the mesh generator, where a space discretization of the domain is produced.

One can therefore, at every iteration of the shape optimization algorithm, modify the geometry directly inside the CAD program, and then re-export it to the mesh generator. By so doing, one has to link the shape optimization method with the CAD program, create a new geometry assembly (a process which may not be easy to automatize on complex geometries) and finally generate a new mesh. In the case of unstructured meshes this last part, although very expensive, may be relatively easily automatized, while in the case of structured meshes, like the one typically used by the authors for the hydrodynamic solver component, the automation is usually not feasible. For those reasons, we have decided not to follow this approach.

Another possible way to proceed is to deform directly the computational mesh. By this approach one can decide whether to modify just the nodes that define the mesh-surface of the geometry that one wants to optimize or to deform the whole mesh. In the first case, a suitable numerical algorithm has to be used in order to modify the volume mesh according to the imposed surface-mesh displacement. In the mesh motion framework, many alternatives exist. The most common one is to solve a Laplace problem on the whole domain using as boundary conditions the surface displacements. Another popular mesh-motion technique is the so-called spring analogy model [21]. Many variants and sophisticated numerical modification of those schemes can be implemented in order to help preserving the mesh quality. The important advantage of this choice is that the mesh must not be recreated but simply modified. The disadvantage is that nothing assures that the quality of the mesh is maintained, and, in case of large deformations, the mesh can even become invalid. In this case either special untangling schemes are adopted, see for example [15], or the mesh has to be fully regenerated. Furthermore, the solution of the internal mesh node displacement may have a not negligible computational cost.

For the actual shape parameterization, different techniques can be used, like *B-splines* [7], *NURBS* [67], or similar. By changing the value of the shape parameters, representing for example the position of the control points of the spline, the shape is modified. An "interpolator" to reduce the continuous shape displacement to the discrete level, i.e. to the mesh, is needed.

Another possible technique is that based on the so-called Free-Form Deformation (FFD). Originally introduced in the late 1970s [80], FFD has been first used in computer graphics; only in recent years it has been employed in optimal design problems [3].

Recently, this technique has been coupled with Reduced Basis methods [44, 47, 77] and used also for simple FSI problems [42, 43]. A free-form deformation operates on a bivariate Bezier control area, built around (and regardless of) the shape we want to optimize, manipulating a lattice of control points. In this way, design parameters are directly connected neither to geometrical properties nor to the shape boundary, see Fig. 3. This is at the same time a great advantage and disadvantage of this technique: on the positive side, it does not bound the optimization process to a restricted subset related to geometrical quantities; on the other hand, it is very difficult to control some geometrical quantities, like, e.g. the length of an edge or the angle of attack of a foil, in a "classical" way.

A brief description follows in the simple case of a 2D computational domain. Given a fixed rectangular 2D domain D such that $\Omega \subset D$, we assume the exis-

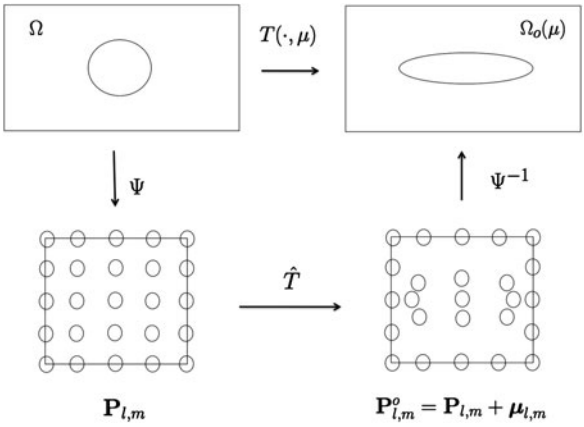

Fig. 3 Schematic illustration of the Free-From Deformation (FFD) technique. Through a series of maps and transformation, the geometry is deformed following the movement of the control points

tence of a differentiable and invertible map $\Psi : (x_1, x_2) \to (s, t)$ such that $\Psi(D) = (0, 1)^2$; by this *freezing* procedure, FFD can be defined in a simpler way in the coordinates (s, t) of the spline parameter space $(0, 1)^2$. We thus select a lattice of $(L + 1) \times (M + 1)$ unperturbed control points $\mathbf{P}_{l,m} = [l/L, m/M]^T$, $l = 0, \ldots, L$, $m = 0, \ldots, M$, and modify the object by moving control points to a new position. The corresponding perturbed control points $\mathbf{P}^o_{l,m}(\boldsymbol{\mu}_{l,m}) = \mathbf{P}_{l,m} + \boldsymbol{\mu}_{l,m}$ are thus specified by a set of $(L + 1)(M + 1)$ parameter vectors $\boldsymbol{\mu}_{l,m} \in \mathbb{R}^2$, giving in all $2(L+1)(M+1)$ possible degrees of freedom. In general, among the control points $\mathbf{P}_{l,m}$, we indicate the effectively free scalar-valued parameters, chosen as design variables, $\mu_1, \ldots, \mu_P$—each corresponding to the displacement of a control point in the s or t direction—and define the parametric map $\tilde{T}(\cdot, \boldsymbol{\mu}) : D \to \mathbb{R}^2$ by which the uploaded geometry is computed as follows:

$$\tilde{T}(\mathbf{x}; \boldsymbol{\mu}) = \Psi^{-1}\left(\sum_{l=0}^{L}\sum_{m=0}^{M} b^{L,M}_{l,m}\big(\Psi(\mathbf{x})\big)\mathbf{P}^o_{l,m}(\boldsymbol{\mu}_{l,m})\right), \tag{38}$$

where $b^{L,M}_{l,m}(s, t) = b^L_l(s)b^M_m(t)$ are tensor products of one-dimensional *Bernstein basis polynomials* $b^L_l(s) = \binom{L}{l}s^l(1-s)^{L-l}$ and $b^M_m(t) = \binom{M}{m}t^m(1-t)^{M-m}$ defined on the unit square $(s, t) \in [0, 1] \times [0, 1]$. Finally, we have $\Omega_o(\boldsymbol{\mu}) = T(\Omega; \boldsymbol{\mu})$ by using the restriction $T = \tilde{T}|_\Omega$.

4.4 Surface and Volume Mesh Deformation

Once the new value of the shape parameters is obtained, the surface mesh describing the shape has to be deformed. If the shape has been parameterized via FFD, the new position of the surface mesh nodes is obtained applying the FFD map to every node. If, instead, the adjoint approach has been used and the sensitivity field is known for every surface mesh node, two approaches can be adopted: either move the mesh

points directly, or "project" them to some other shape parameterization. In the first case, usually some smoothing of the sensitivity field has to be done, otherwise the nodes near the edges and corners tend to be over-deformed, the mesh anisotropy may create small oscillations, and in general the smoothness of the deformed shape is not guaranteed. Another possibility is to use once again the FFD parameterization, projecting the sensitivity field on the FFD control parameters. This time we are not limited to a small lattice and can indeed choose a very fine one, in order to reduce the loss of information due to the projection below an acceptable threshold. This projection can be accomplished for example by a least-square interpolation of the surface mesh points and the FFD control points:

$$\hat{\boldsymbol{\mu}} = \underset{\boldsymbol{\mu}\in\boldsymbol{\mu}_{\text{ad}}}{\arg\min} \sum_{i\in\text{Surf nodes}} \left(\mathbf{x}_i - \tilde{T}\left(\Psi(\mathbf{x}_i);\boldsymbol{\mu}\right)\right)^2, \tag{39}$$

where $\tilde{T}(\Psi(\mathbf{x}_i);\boldsymbol{\mu})$ is the FFD map as defined in Sect. 4, Eq. (38), and $\boldsymbol{\mu}_{\text{ad}}$ is the domain of admissible $\boldsymbol{\mu}$ such that the FFD control points $\mathbf{P}^o_{l,m}$ stay inside the domain $[0,1]\times[0,1]$. Furthermore, stricter constrains on the deformation $\boldsymbol{\mu}$ are usually imposed in order to avoid excessive mesh deformation. Without the interval constraints, the least square minimization reduces to the solution of a linear problem, with size the number of FFD control points, of the form

$$F^T F\hat{\boldsymbol{\mu}} = F^T\mathbf{x}, \tag{40}$$

where F is the FFD map matrix, and $\mathbf{x}$ is the vector containing the displacement of the surface mesh points. The solution of the same problem but with interval constraints is a typical problem of linear programming, and its solution requires that of an optimization sub-problem by itself. In order to save computation time, we have chosen to use a numerical trick to maintain the magnitude of the control points small: we impose some extra line to problem (40) thus requiring m to be close to zero (this turns out to add an identity matrix at the bottom of F and a vector of 0 at the bottom of x). Although not equivalent to the constrained minimization problem, this technique allows us to obtain all the control points displacements with a single solution of the now modified problem (40). We believe that this inaccuracy introduced is justified by the fact that the error committed is anyway smaller than the one introduced by the other numerical steps of the optimization procedure.

Once the new shape has been evaluated, the volume mesh can be deformed either by solving a modified Laplace problem or directly using the FFD map. We believe, and our numerical results are in agreement with our conjecture, that using the FFD map is the best solution in this case. The mesh motion technique is in fact mesh-independent and thus is not affected by the typical problem generated by Laplace-like methods with small and skewed elements and in general produces meshes with higher quality.

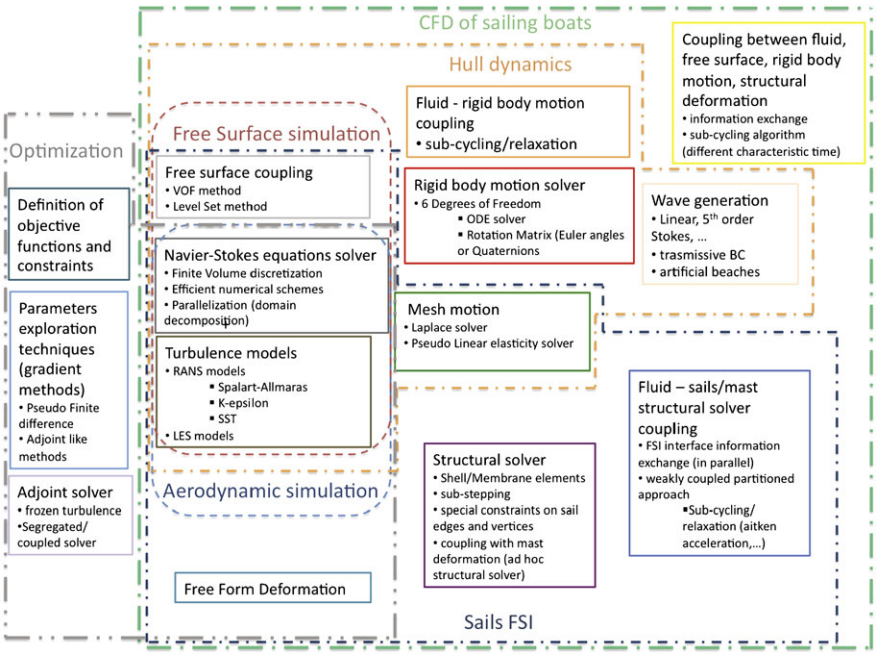

Fig. 4 Overview of the different methodologies and tools considered in this work

5 Numerical Results

In this section an overview of the numerical results obtained is presented. The results concern free-surface flows and hull dynamics, shape optimization and fluid-structure interaction problems. In Fig. 4 a flow diagram of the entire simulation and optimization processes for a sailing boat is drawn. Obviously, some parts are shared by more than one part, like the Navier–Stokes solver which is used for simulating both the water field and air field or the mesh motion technique found in both the boat dynamics and the optimization steps. For every sub-section, a diagram of the numerical/methodological tools needed by that section is outlined.

5.1 Hull Dynamics

As described in the previous sections, the numerical tools needed for the simulation of the hull dynamics are (Fig. 5): a Navier–Stokes solver with free-surface capabilities, suitable turbulence models, a dynamic model for the rigid body of the hull and a mesh motion solver. Furthermore, if one is interested in the simulations of waves, a mathematical model for the imposition of the correct boundary condition in order to generate and maintain the wave on the whole domain is needed [23, 41, 49].

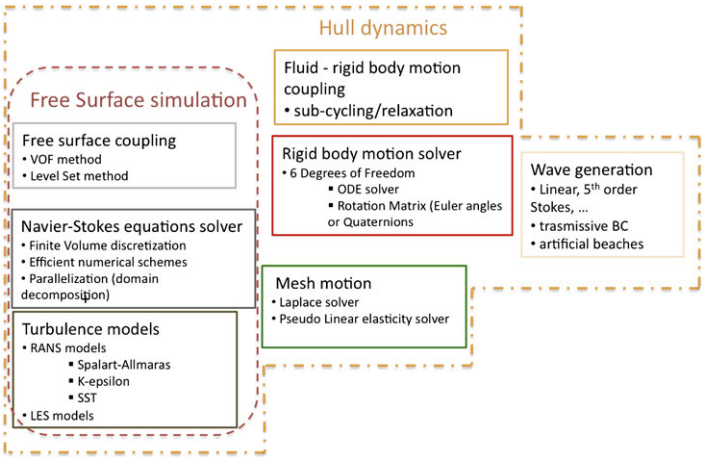

Fig. 5 Overview of the different methodologies and tools considered for the simulation of the hull dynamics

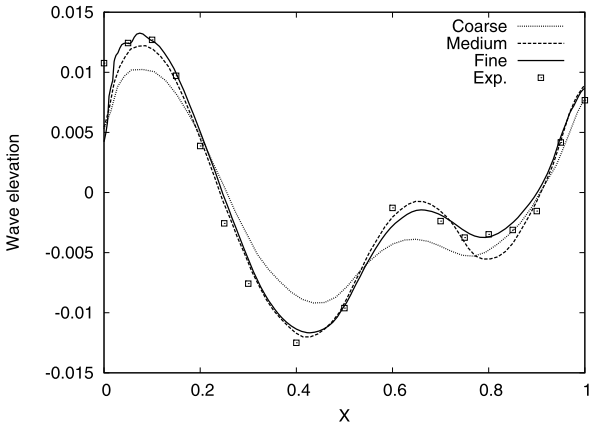

Fig. 6 Wave profiles along the Series 60 hull for different grid resolutions

The free-surface solver and its interaction with the rigid-body hull dynamic module have been tested on a classical benchmark problem, namely the Series 60 hull with a block coefficient $C_B = 0.6$ (see [86]). We have considered a flow at a Reynolds number $Re = 4 \times 10^6$ and a Froude number $Fr = 0.316$. First, the steady solution at a fixed attitude has been computed on three different grid resolutions with a number of cells of around 70 000, 200 000 and 650 000, respectively, and a time step $dt = 0.001$ s. The wave profiles on the hull obtained with the different grid resolutions are presented in Fig. 6 and compared with the experimental measurements. These results, together with the drag coefficients reported in Table 1, show a good convergence to the experimental data.

Starting from the steady solution obtained with the medium resolution grid, we have activated the hull dynamics module and left the hull free to sink and pitch.

Table 1 Pressure, viscous and total drags coefficient for different grid resolutions

Grid	C_p	C_v	C_t
Coarse	0.00274	0.00344	0.00619
Medium	0.00179	0.00372	0.00552
Fine	0.00163	0.00388	0.00551
Experiment			0.00542

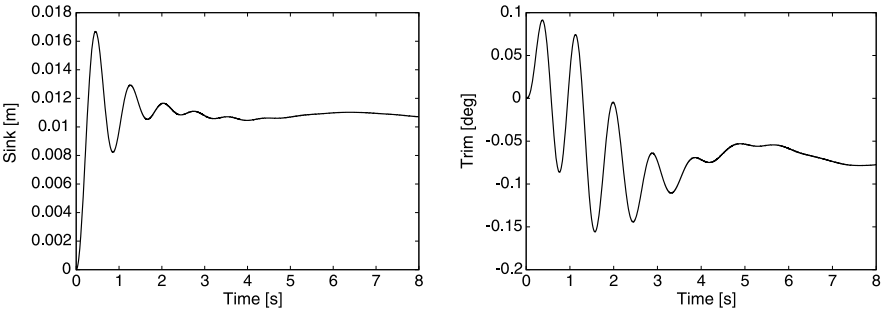

Fig. 7 Sink (*left*) and trim (*right*) evolutions of the Series 60 hull towards hydrodynamic equilibrium

The time evolution of the two degrees of freedom towards the hull running attitude (hydrodynamic equilibrium) are presented in Fig. 7.

Finally, we tested the behaviour of the model simulating the dynamics of the hull in waves. This was achieved imposing at the inflow an incoming wave modelled using the fifth-order Stokes wave expansion, see [66] for more details. The wave model sets a time-dependent wave elevation and the correspondent orbital velocity at the inflow boundary of the domain. We have considered a wave amplitude $\lambda = 0.01L$ where L is the boat length, about 3.5 m for the problem at hand, and a wave frequency correspondent to an incoming wave length of $0.2L$. In Fig. 8 the free-surface elevation is represented: the incoming wave and its typical pattern modification in the boat wake can be clearly observed.

A comparison between the time evolution of drag and pitching moment for the two-dynamics case (with and without the incoming wave) is reported in Fig. 9.

Free-surface simulation of this type has been extensively adopted during the past few years in the framework of a collaboration of our research group with the Alinghi Team for the design of the boats which participated to the last three America's Cup campaigns preparation [16, 64, 65].

In particular, more recently, the focus has been on the simulation of the free-surface flows around the Alinghi multi-hull catamaran designed for 33rd America's Cup. A large-scale simulation analysis was performed to predict the drag and lift on the hulls in many sailing conditions and attitudes. All those data were then integrated in a Velocity Predictor Program (VPP) that estimates the performance of a sailing yacht for given boat design and sailing conditions.

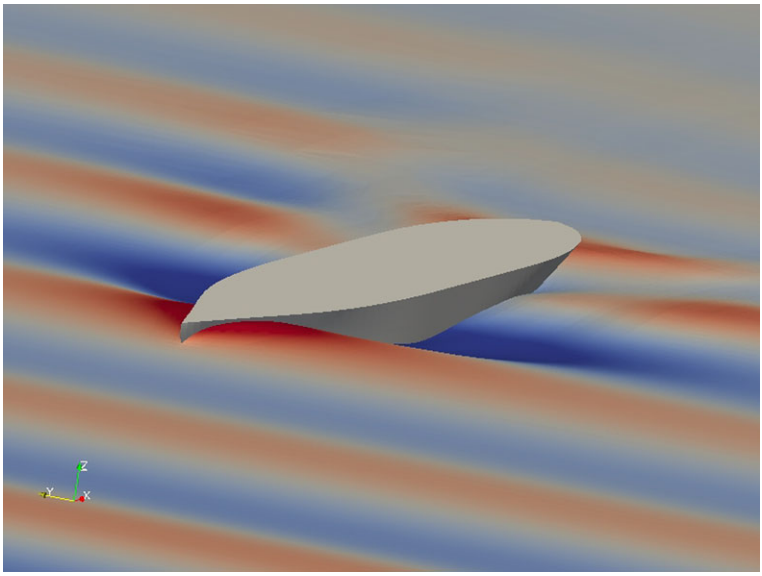

Fig. 8 Series 60 dynamic simulation with waves: free-surface elevation

For this analysis, different simulation software were used, including the OpenFOAM free-surface solver described above, the Ansys CFX free-surface solver [27] and a linear free-surface potential solver, with the viscous component predicted via ITTC formulas, developped by the Alinghi Design team. In Fig. 10, the drag prediction obtained with the different codes are compared with the experimental results. As can be seen, OpenFOAM data trend is in line with the other numerical solvers, predicting drag values slightly higher than CFX. The potential flow solver under-predicts the drag values, which is acceptable since the viscous contribution is obtained through empirical formulas and flow solver is based on a more simplified model. The drag values obtained via experimental test in a towing tank are quite close to the numerical values obtained (less than 5% of error on average), with higher values for small trim angles and lower values for high trim angles.

5.2 High Performance CFD: Parallel Scalability

An investigation on the parallel scalability of the code has also been carried out, and some important features that allowed us to fully benefit of the parallel computational power have been highlighted. We compared the parallel performance of the free-surface solver implemented in OpenFOAM on a clusters available at the École Polytechnique Fédérale de Lausanne. The technical specifications of the cluster are: 56 bi-processor nodes of Intel Xeon Nehalem quads-cores at 2.66 GHz with 24 GB of RAM and connected via InfiniBand.

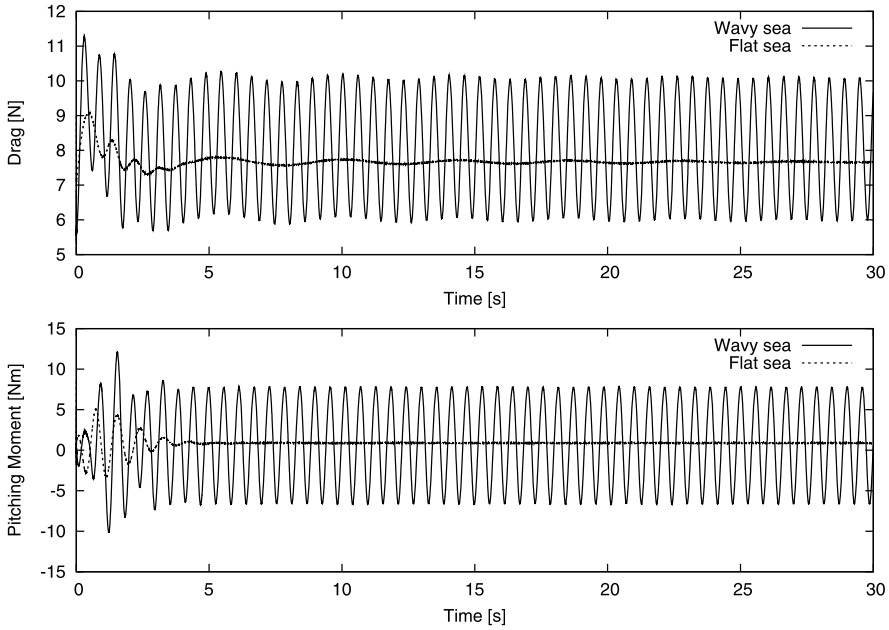

Fig. 9 Drag (*top*) and pitching moment (*bottom*) for the dynamic Series 60 simulations in wavy and flat sea

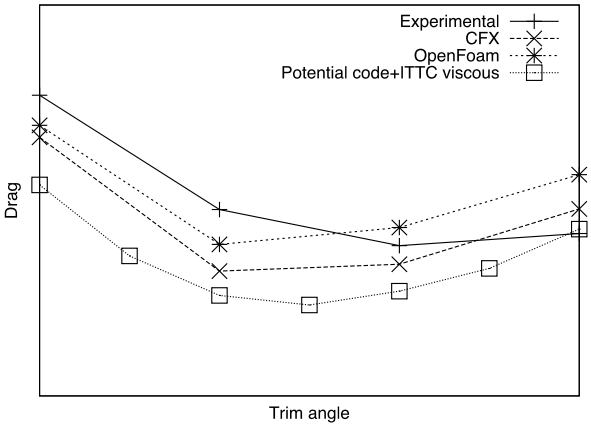

Fig. 10 Drag prediction results on the Alinghi AC33 catamaran hull obtained with different numerical tools and compared with the experimental results. No axis values are reported due to confidentiality agreement with the Alinghi team

A transient free-surface Navier–Stokes simulation for the Series 60 hull with a large grid (about 4 millions cells) has been considered as a test case.

A brief scalability analyses has the been performed on the Nehalem cluster and results are reported in Table 2.

As reported in the table, OpenFOAM, for a fixed number of partitions, is significantly slower when using all cores of a node rather than twice the number of nodes but using only half of the cores available per node. This is due to the fact that when

Table 2 OpenFOAM scalability test on the Nehalem cluster

Nodes*core	# partitions	Wall clock time
4*4	16	647
2*8	16	664
4*8	32	350
8*4	32	296
8*8	64	177

using all 8 cores, a bit of memory communication bottleneck arises. When keeping the number of cores per node fixed and increasing just the number of nodes, the scalability factor is instead very high (at least for the number of partition tested), namely 95–98%.

OpenFOAM has been installed also on the EPFL cluster BlueGene-P [30], whose major strength is not the speed of every single node, only 800 MHz, but rather the possibility to use a very large number of cores, up to 16 000 in this case, and the highly optimized memory communications. In order to be able to use this cluster efficiently, the solver must scale well up to a high number of partitions. Special attention has thus to be taken in compiling the code properly to benefit from the special architecture.

Two different grid decomposition methods have been considered in this case: the former, referred to as *Xdir* decomposition, simply subdivides the grid into slices (each containing approximately the same number of grid cells) in a given direction (in this case the stream-wise direction X); the latter is based on the *Metis* [40] library, which decomposes the grid trying to minimize the number of faces on the partition interfaces.

The results obtained with the partitioner " Xdir" shows a deterioration of the scalability property of the solver when increasing the number of partitions beyond 64, see Fig. 11. This is due to the fact that with this partitioner, as the number of domains increases, the number of faces on the partition interface increases linearly. Since the amount of data passed from core to core is proportional to this value, it is easy to reach the memory communication bottleneck. With the Metis partitioner, much better scalability is achieved: 87.5%, up to 512 partitions. When using a even higher number of partition, i.e. 1024, no gain is observed compared to the run with 512 partitions. This is due to the fact that, the test case having 4 million cells, when using 1024 partitions, every partition has about only 4 thousand cells. This number is too small for the solver to be efficient requiring a too short computational time for every node when compared to the communication lag time. If a bigger test case were to be chosen, the solver would be able to scale efficiently up to a higher number of partitions. For BlueGene-P as well, the fact of using just one, two or all four cores of every node has some effects on the scalability, although not as much as on classical clusters.

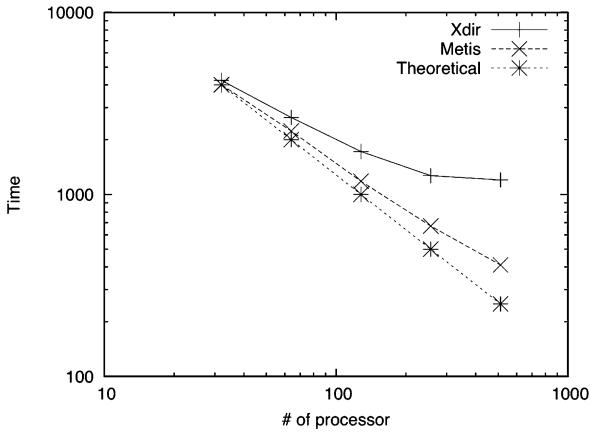

Fig. 11 Scalability trend of the solver OpenFOAM on the BlueGene/P cluster for two different partitioning method

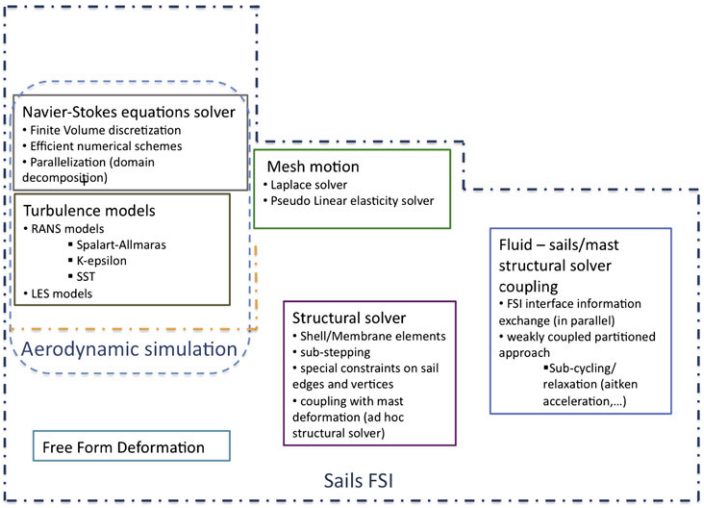

Fig. 12 Overview of the different methodologies and tools considered for the simulation of the Fluid-Structure interaction of the sail

5.3 Fluid-Structure Interaction

In Fig. 12, the main tools for the simulation of the Fluid-structure interaction of a sail are reported. The Navier–Stokes solver and the turbulence model are the same ones used in the previous section, while the mesh motion is in general more critical due to the higher deformation, and thus special care has to be taken to preserve the quality of the mesh. The structural solver for the simulation of the sail deformation under the aerodynamics loads and the coupling algorithm have been introduced in Sect. 3.

The fluid structure interaction between wind and sails has been analysed. An external structural solver capable to simulate the membranes/shells structural defor-

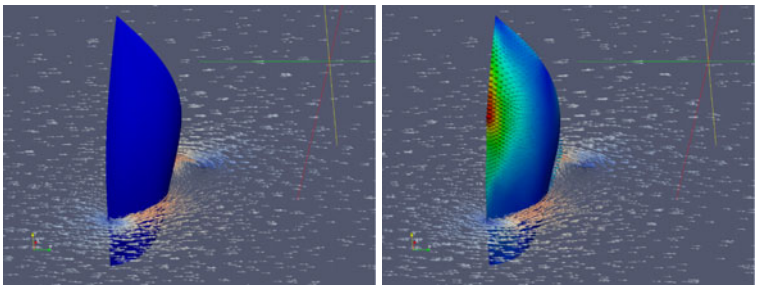

(a) Time= 2s. No structural deformation.

(b) Time= 2.5s.

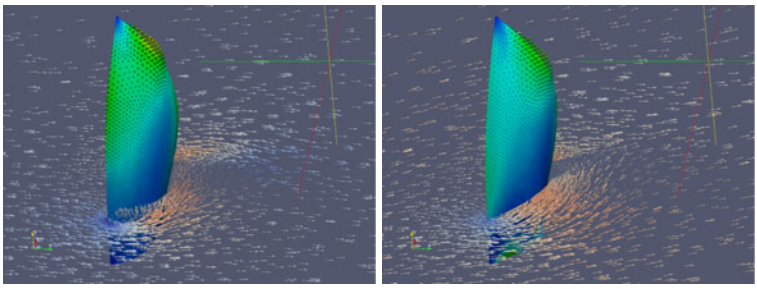

(c) Time= 4s.

(d) Time= 6s.

Fig. 13 Gennaker FSI: velocity vectors on a slice at $Y = 15$ m and displacement vectors and displacement magnitude on the sail surface

mations has been used. The coupling algorithm between the two solvers is described in Sect. 3.1, with the extra complexity of the communication and data interpolation from the two independent solvers. In this case the fluid solver has been considered as the master program responsible for the interpolation of the stresses from the fluid mesh to the structural solver and the interpolation of the sail displacement to the fluid mesh, as well as starting and pausing the structural solver when needed. The meshes used for the flow solver, generated with the commercial code ICEM [52], are made of hexahedra, tetrahedra and pyramids and are not geometrically conforming with the one of the shell solver. As an initial condition, the steady converged solution of the flow field obtained while keeping the sail fixed has been used. First, a single sail, a gennaker, immersed in a steady atmospheric flow has been simulated; in Fig. 13 the flow field and the sail deformation are presented at different time-steps.

Many different configurations are currently under investigation, and the results are so far very encouraging. For example, a variation of the structural property of the sail has been investigated: setting the width of the sail to a higher value produces a final shape that is rounder near the bottom and flatter near the top, see Fig. 14, and in general less deformed. This is due to the fact that now the sail is heavier and more rigid: the weight of the sail plays now a more important role. Furthermore, from a numerical point of view, this configuration is easier to compute from an FSI point

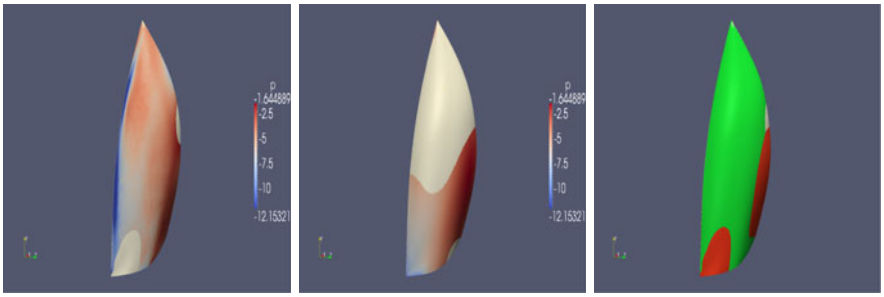

(a) Base run final shape (pressure) vs initial position (white)

(b) Higher width run final shape (pressure) vs initial position (white)

(c) Base run (green) vs Higher width run (red) vs initial position (white)

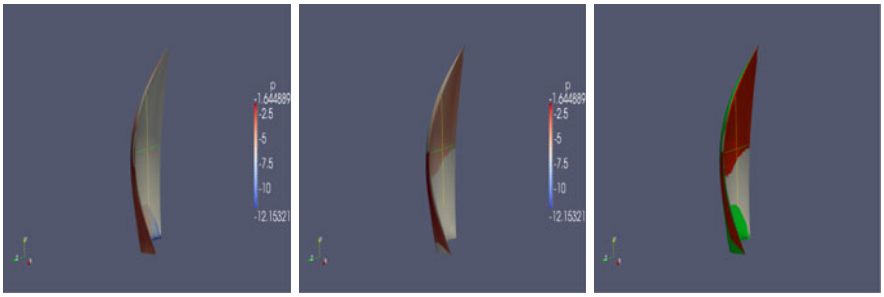

(d) Base run final shape (pressure) vs initial position (white)

(e) Higher width run final shape (pressure) vs initial position (white)

(f) Base run (green) vs Higher width run (red) vs initial position (white)

Fig. 14 Comparison of the final shape (i.e. at convergence) of the sail for different structural properties and versus the initial shape. View from the front and from the side

of view, since the inertia of the sail is higher: in good agreement with this concept, the number of FSI sub-iterations for every time step drop from about 50 to 20 (for a relative convergence criteria of 0.05%).

In these simulations the three vertices of the sails are kept fixed, but the possibility to insert more realistic constraints is possible. More complex configurations, such as multiple sails (main sail plus gennaker), mast deformation and full sailing boat dynamics are currently under investigation and will be reported in a future paper.

In terms of efficiency, the resolution of a full transient FSI problem is much more demanding than the sole aerodynamic simulations. To give a general idea of the FSI overhead, hereafter we provide some data of the computation time for one of the simulations described above run on 32 i7 2.66 GHz processors. The cost for one time step of the aerodynamic simulation is about 8 seconds. The cost of a single FSI sub-iteration step comprehends the aerodynamic solver, about 8 seconds, the mesh motion, about 2–5 seconds (depending on the mesh motion technique) plus the structural solver. The latter, being an explicit solver in our case, usually requires a much smaller time step than the fluid one and thus requires several sub-iterations.

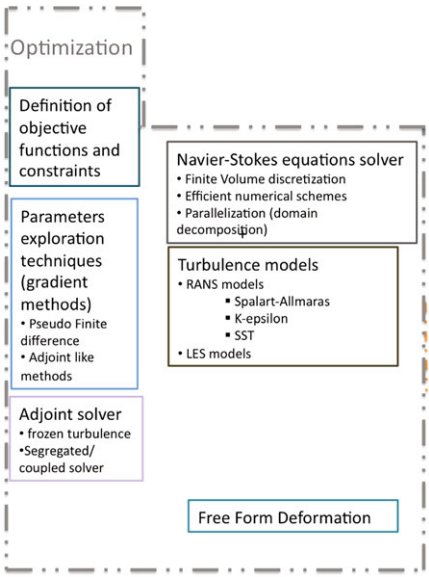

Fig. 15 Overview of the different methodologies and tools considered for the shape optimization problem

The constraint on the structural solver time step depends heavily on the structural property of the sail: a very stiff material induces very fast modes on the structures, and thus a very small time step constraint is required to be stable. In our case, the structural solver required about 2–5 seconds for FSI sub-iteration. Finally, for every time-step, there are about 20–50 FSI sub-iterations, mainly depending on the time step chosen, convergence criteria and structural property of the sail, and thus the total time for an FSI time step is about 30–100 times longer than the one of a simple aerodynamic simulation.

6 Shape Optimization Test Cases

For the shape optimization, besides the solver needed for the solution of the Navier–Stokes equations, a solver for their adjoint counter-part may be required, as well as a proper geometric parameterization technique (Fig. 15). Once the objectives function and constraint are defined, a module that takes care of the parameters exploration and that adjusts the mesh accordingly has to be implemented.

The Free-Form Deformation method has been chosen for the geometry deformation. An analysis of the FFD method aimed at shape optimization algorithm on ship-related geometries, like the bulb and the rudder of a sailing boat, has been done at first with the use of the code COMSOL [81] for the solution of the Navier–Stokes problem and used the Matlab Optimization toolbox for the exploration of the parameters set. This work showed a good potential of this approach, although it also outlined the necessity to use much more efficient numerical tools to obtain reasonable computation time even for simple test problems.

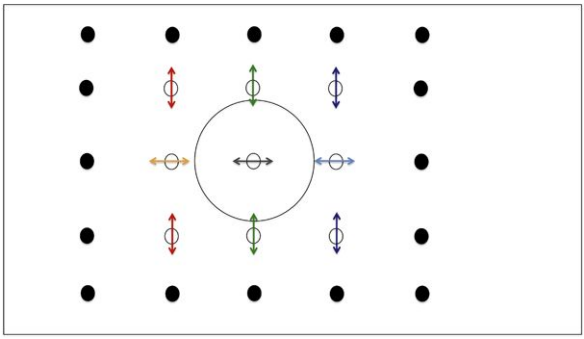

Fig. 16 FFD lattice over the 2D domain for the shape optimization of a cylinder. Although the lattice is composed of $5 \times 5 = 25$ control points, only six FFD points have actually been chosen as control points. The full black points are kept fixed, while the empty one can move in the arrows directions. Control points with the same colours mean that the two movements have the same value but opposite sign (symmetrical displacement)

In fact, although Matlab is a very powerful program with many built-in functions, it is fairly slow compared to an efficient C/C++/Fortran code. Furthermore, since our final goal is to have an automatized program for shape-optimization, the code have been rewritten in C++ in order to allow us a better integration with OpenFOAM.

An FFD class has been implemented directly into OpenFOAM so that a call can be made inside the code, using the flexibility of the C++ class structure, to update the position of the mesh points with the FFD module. This allows us to use both approaches of mesh motion based on the FFD: one can either decide to move all points, both surface and internal nodes, or just to move the surface meshes and then use the other options, i.e. Laplacian solvers, already implemented in OpenFOAM for the movement of the internal nodes. Special care has also to be taken so that the code works in a parallel environment as well.

The test case that we have chosen is a 2D cylinder immersed in a flow in laminar regime, $Re = 40$, with the drag as cost functional to minimize under the constraint of fixed volume. The shape has been parameterized via an FFD lattice made of 5×5 control points set around the cylinder inside the domain. Out of the total 50 degrees of freedom (25×2, because all control points can move in both longitudinal and vertical directions) we have chosen to keep fixed the external points, so that the points on the FFD lattice border are not deformed and thus the FFD map can be used also for the volume mesh deformation. Thanks to the symmetry with respect to the horizontal axis of the problem and geometry, the same symmetry condition can be imposed on the control points movement in the vertical direction. We have thus chosen to select only six control points, three in the longitudinal direction and three in the vertical direction (which counts as double thanks to the symmetry), as represented in Fig. 16.

Besides the volume constraint, a bound-constrain of $[-0.4; 0.4]$ has been imposed to the value of the control points. The optimization problem has been solved via the *Cobyla* algorithm, and the results are reported in Figs. 17–18. In the first

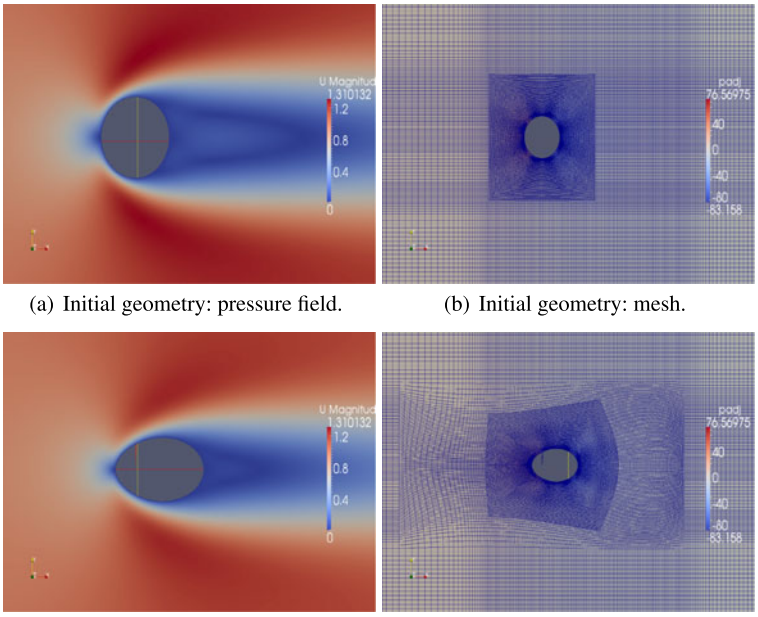

(a) Initial geometry: pressure field. (b) Initial geometry: mesh.

(c) Optimized geometry: pressure field. (d) Optimized geometry: mesh.

Fig. 17 Shape Optimization of a 2D cylinder in laminar regime. Comparison between the initial geometry and optimized ones

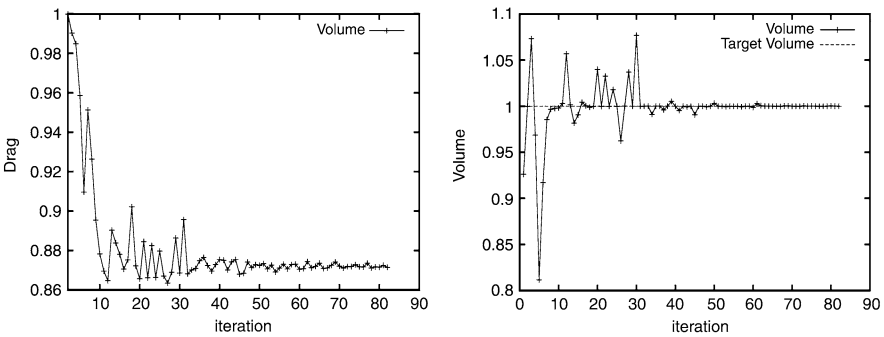

(a) Drag. (b) Volume.

Fig. 18 Shape Optimization of a 2D cylinder in laminar regime. Cost functional: drag minimization. Constraint: fixed volume. Method: *Cobyla*. The data in the plot have been non-dimensionalized with the initial (i.e. not deformed) values

figure, the qualitative comparison between initial and final shape and corresponding meshes is reported. As can be seen, the magnitude of the deformation is quite big, although only six control points have been used, and the mesh deformation is very smooth. Quantitatively, the new shape has reduced the drag by 11–12% in about 80

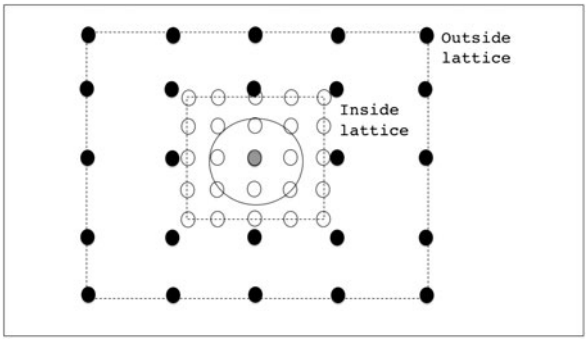

Fig. 19 2D section of the two-level FFD lattice over the 3D domain for the shape optimization of a sphere. External lattice: *black dots*. Internal lattice: *white dots*

iterations, but more than half of them have been spent in very small adjustment to satisfy with high accuracy, i.e. 10^{-4}, the volume constrained. With a less restrictive constraint, about 40 iterations would suffice.

The exploration of the parameters space at first does not necessarily produce a better geometry, neither fulfills the volume constraints. As more information is available and the control parameters influence is better defined, the descent to the (local) optimum is achieved, and the calibration of the penalty terms for the volume constraint imposed so that the volume condition is satisfied.

We then consider a similar test case, where we look for the drag minimizing shape in 3D, $Re = 40$, starting from an initial spherical shape and considering the volume fixed. In this case the adjoint-based gradient method has been used, and the volume constraint has been recovered at every iteration via a posteriori mesh motion. The sensitivity field has been projected to a double FFD lattice around the sphere (see Fig. 19): an external one able to capture the macro-deformation and have them "absorbed" by a wide region of the domain, and an inner one to capture more details. In this case as well, the outer control points of the lattices are kept frozen, so that the FFD mapping can be used for both surface and volume mesh deformation.

The methodology has proven to be robust and efficient, see Figs. 20–21. The magnitude of the deformation is very important, and, although no symmetry condition is imposed this time, the optimal shape is symmetric with respect to the span-wise and vertical directions (as expected). The sensitivity field and the volume constraints tend to deform the shape in opposite ways; indeed, the sensitivity field tends to make the shape smaller, while the volume constraints recovery re-inflates it. Thus the optimization stopping criteria is reached when the sensitivity field is uniform in the normal direction all over the shape. At the beginning, the sensitivity field mainly tends to squeeze vertically the sphere and the volume constraints, acting uniformly, and makes the resulting deformation equal to a vertical/span-wise contraction and longitudinal expansion. At convergence, being the shape already elongated, the sensitivity field requires a uniform contraction in all directions which is counter-balanced by the volume constraint.

The optimized shape is about 30% more efficient than the initial one while maintaining the same volume. The optimum search, thanks to the gradient evaluation, is monotonic and stops after about 80 iterations, although after 40 iterations a value

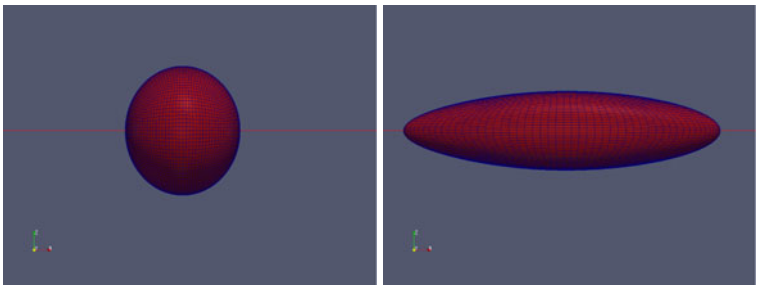

(a) Initial shape. (b) Final shape.

Fig. 20 Shape optimization of a 3D sphere in laminar regime

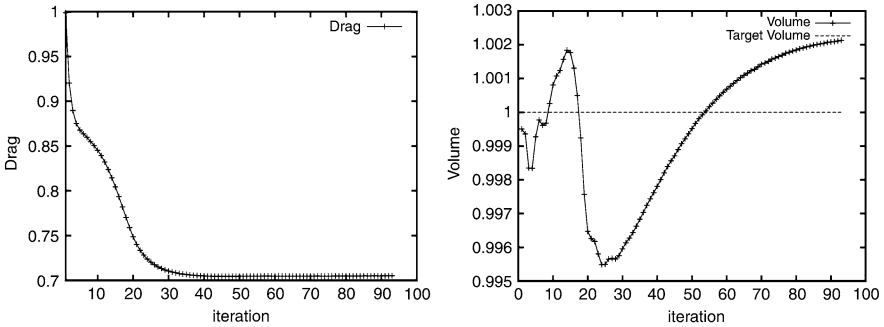

(a) Drag. (b) Volume.

Fig. 21 Shape optimization of a 3D sphere in laminar regime. Cost functional: drag minimization. Constraint: fixed volume. Method: gradient-like. The data in the plot have been non-dimensionalized with the initial (i.e. not deformed) values

very close to the optimum is already reached. In this case the descent step size has been kept fixed and relatively small: with a higher value or, even better, a dynamic step size, the convergence could be even faster. The error on the volume constrains is always very small and never higher than 0.7%.

7 Perspectives

In this section we report some perspectives in the numerical models and simulation of sailing boat dynamics and its shape optimization.

Further methodological and code development has to be carried out in order to achieve the targets highlighted in the previous sections. Although a substantial work has already been accomplished, further developments are needed in order to be able to simulate more accurately the full dynamics of a sailing boat. After the successful shape optimization test cases, more realistic geometries and conditions have to be analysed. Below a more detailed description of the future development plan is reported.

7.1 Fluid-Structure Interaction

An accurate and stable coupling technique has to be proposed for more complex and fast-varying dynamics, and an analysis on the interpolation of the data from non-conformal meshes has to be conducted. At the moment the structural and fluid solvers are computed in serial, i.e. one after the other, while a better synchronized strategy, relying on running media at the same time and exchanging information only at given times, may be investigated. Other mesh motion techniques can also be explored; in particular it would be interesting to couple the FFD techniques developped for the shape optimization analyses for this kind of problems. The capability of the FFD technique to keep the mesh valid also for large deformations could in fact be very useful in the case of large motion, like the one of a gennaker under a gust. A coupled local FFD/Laplacian may indeed perform very well.

From a programming point of view, the FSI codes available need further development in order to be able to handle realistic flow conditions and geometries. The structural solver also needs to be methodologically developped to take into account the complex constitutive law of modern sails and account for more realistic constraints. Furthermore the mast deformation has to be taken into account as well as real sailing boat sail configurations, i.e. gennaker-main sail-mast.

7.2 Full Sailing Boat Dynamics

Once both the sail FSI and the free surface simulations have been validated, the simulation of the full dynamic of the sailing boat can be finally computed.

To accomplish it, a proper way to couple the FSI solution of the sails with the 6-dof motion of the hull has to be set up, taking into account all the physical constraints, like where are the sails forces applied on the hull, and numerical issue, for example, the fact that the boat cannot freely move into the domain, but it has to be kept more or less at the centre. One way to achieve this point would be to fix the longitudinal position of the boat and insert an acceleration term inside the Navier–Stokes equations like if we were in a non-constant-reference system, or we could just keep the average speed fixed and let the boat floats (if it does not drift away; otherwise the mesh may easily become invalid).

7.3 Optimization

The performance of shape optimization tools for turbulent flows is of interest and subject of many studies nowadays. Although recently the full adjoint formulation of the Navier–Stokes equations with turbulent models has been proposed [92, 93], the most common approach in literature is to *freeze* the turbulent viscosity obtained by the direct solver and use it in the laminar Navier–Stokes adjoint equations. Special care has to be taken when the direct turbulent model uses wall functions, since this

is not seen "naturally" by the laminar adjoint equations and may lead to un-physical results.

Complex geometries may prove critical in terms of smooth deformation and validity of the deformed mesh and thus may require special care in the motion algorithm and smoothing techniques. The possibility to use combined local-FFD have to be developped to further enhance the effectiveness of the methodology. Also the coupling of the proposed approach with Reduced Basis/Reduced models [76] techniques is a subject of current interest. Due to the very heavy computational load entailed by every direct and adjoint computation, the possibility to use reduced models may greatly benefit the effectiveness of the proposed methodology and could allow one to tackle even more complex problems. Instead of computing a full RANS simulation for every geometry, an approximated solution could indeed be extrapolated thanks to RB techniques, thus reducing drastically the computational cost.

8 Conclusions

This work represents an overview of state-of-the art numerical models for the simulation and shape optimization of sailing boats combined with the experience about methodological development and numerical simulations accomplished by the authors.

A preview of the complexity of the task of a full simulation of a sailing boat has been highlighted, and the main tools to achieve everyday more complex and accurate simulations have been described. Successively, some of the results obtained so far by the authors with open-source codes have been presented. Promising results in the simulation of free-surface flows and hull dynamics have been achieved, and soon more complex configurations will be tackled.

The set-up for the simulation of the Fluid-Structure interaction of a sail under steady wind conditions has been established, and the results obtained are very promising. The full transient FSI simulation of a gennaker has been successfully computed for different sail structural properties, and the shape deformation obtained seems qualitatively very reasonable.

The basic tool for automatic shape optimization has been presented, and the combination of classical optimization methods with modern shape parameterization techniques, the FFD parameterization, have been proposed. The FFD control points have been used both as optimization control parameters and/or as shape parameterization space on which the sensitivity field is to be projected. This last approach is innovative and has proven its effectiveness in some initial test cases. More challenging and realistic configurations are foreseen for this topic as well.

Finally, the work presented here has direct applications in many real-life cases, not only for sports competitions, but also for helping sails/boat manufacturers and naval and ocean engineering groups in general. Furthermore, the flexibility of the fluid code used and the numerical tools under development may be relatively easily modified to be applied to many other fields, like the shape optimization of the

geometry of cardiac bypass and stents or the shape and structural composition of aeroplane wings under aerodynamic loads.

The most significant contribution of the methodology is the combination of several techniques to provide a platform for the simulation of complex systems from a geometrical and multi-physics point of view.

Acknowledgements The authors would like to thank the EPFL University and the Alinghi Design Team for providing the financial support and the technical expertise necessary to accomplish this work.

We are also grateful to Prof. A. Frangi, Dr. M. Cremonesi and Dr. A. Giampieri from the Structural Engineering Department (DIS) of Politecnico di Milano for sharing their structural code and the collaboration undergone for the sail simulations.

The financial support for CADMOS and the Blue Gene/P system is provided by the Canton of Geneva, Canton of Vaud, Hans Wilsdorf Foundation, Louis-Jeantet Foundation, University of Geneva, University of Lausanne, and École Polytechnique Fédérale de Lausanne.

This work has been partially supported by Regione Lombardia and CILEA Consortium through a LISA Initiative (Laboratory for Interdisciplinary Advanced Simulation) 2010 grant assigned to the second author.

References

1. Alessandrini, B., Delhommeau, G.: A fully coupled Navier–Stokes solver for calculation of turbulent incompressible free surface flow past a ship hull. Int. J. Numer. Methods Fluids **2**, 125–142 (1999)
2. Alin, N., Bensow, R.E., Fureby, C., Huuva, T., Svennberg, U.: Current capabilities of DES and LES for submarines at straight course. J. Ship Res. **54**, 184–196 (2010)
3. Andreoli, M., Janka, A., Désidéri, J.A.: Free-form-deformation parameterization for multilevel 3D shape optimization in aerodynamics. INRIA, Rapp. de rech. No. 5019 (2003)
4. Azcueta, R.: Computation of Turbulent Free-Surface Flows around Ships and Floating Bodies. PhD thesis, Technical University of Hamburg, Hamburg (2001)
5. Azcueta, R.: Computation of turbulent free-surface flows around ships and floating bodies. In: Ship Technology Research, vol. 49 (2002)
6. Belytschko, T., Liu, W.K., Moran, B.: Nonlinear Finite Elements for Continua and Structures. Wiley, New York (2000)
7. Braibant, V., Fleury, C.: Shape optimal design using b-splines. Comput. Methods Appl. Mech. Eng. **44**(3), 246–267 (1984)
8. Campana, E.F., Peri, D., Tahara, Y., Stern, F.: Shape optimization in ship hydrodynamics using computational fluid dynamics. Comput. Methods Appl. Mech. Eng. **196**, 634–651 (2006)
9. Canuto, C., Hussaini, M.Y., Quarteroni, A., Zang, T.A.: Spectral Methods: Evolution to Complex Geometries and Applications to Fluid Dynamics. Scientific Computation. Springer, Berlin (2007)
10. Causin, P., Gerbeau, J.F., Nobile, F.: Added-mass effect in the design of partitioned algorithms for fluid-structure problems. Comput. Methods Appl. Mech. Eng. **194**, 4506–4527 (2005)
11. Chapelle, D., Bathe, K.J.: The Finite Element Analysis of Shells—Fundamentals. Springer, Berlin (2003)
12. Crosetto, P., Reymond, P., Deparis, S., Kontaxakis, D., Stergiopulos, N., Quarteroni, A.: Fluid structure interaction simulations of physiological blood flow in the aorta. Technical report, MATHICSE, EPFL (2010)
13. Deparis, S.: Numerical analysis of axisymmetric flows and methods for fluid-structure interaction arising in blood flow simulation. PhD thesis, EPFL (2004)
14. Rhino: 3D design software for CAD, CAE, and CAM designers

15. Detomi, D.: Mesh modifications for finite element methods in complex three-dimensional domains. PhD thesis, Politecnico di Milano (2004)
16. Detomi, D., Parolini, N., Quarteroni, A.: Numerical models and simulations in sailing yacht design. In: Peters, M. (ed.) Computational Fluid Dynamics for Sport Simulation, pp. 1–31. Springer, Berlin (2009)
17. Donea, J., Giuliania, S., Halleuxa, J.P.: An arbitrary Lagrangian–Eulerian finite element method for transient dynamic fluid-structure interactions. Comput. Methods Appl. Mech. Eng. **33**, 689–723 (1982)
18. Duvigneau, R., Visonneau, M.: Hybrid genetic algorithms and neural networks for fast CFD-based design. In: 9th AIAA/ISSMO Symposium on Multidisciplinary Analysis and Optimization (2002)
19. Dvorkin, E.N., Pantuso, D., Repetto, E.A.: A formulation of the MITC4 shell element for finite strain elasto-plastic analysis. Comput. Methods Appl. Mech. Eng. **125**, 17–40 (1995)
20. Burns Fallow, J.: America's Cup sail design. J. Wind Eng. Ind. Aerodyn. **63**, 183–192 (1996)
21. Farhat, C., Degand, C., Koobus, B., Lesoinne, M.: Torsional springs for two-dimensional dynamic unstructured fluid meshes. Comput. Methods Appl. Mech. Eng. **163**, 231–245 (1998)
22. Farmer, J.R., Martinelli, L., Jameson, A.: A fast multigrid method for solving incompressible hydrodynamic problems with free surfaces. AIAA J. **32**(6), 1175–1182 (1993)
23. Fenton, J.D.: A fifth-order Stokes theory for steadywaves. J. Waterw. Port Coast. Ocean Eng. **111**, 216–234 (1985)
24. Ferziger, J.H., Peric, M.: Computational Methods for Fluid Dynamics, 2nd edn. Springer, Berlin (1999)
25. LifeV: finite element library
26. AutoCad: 3D Design & Engineering Software for Architecture
27. ANSYS CFX CFD Software for Fluid Flow Modeling
28. Formaggia, L., Nobile, F.: Stability analysis of second-order time accurate schemes for ALE–FEM. Comput. Methods Appl. Mech. Eng. **193**, 4097–4116 (2004)
29. Formaggia, L., Quarteroni, A., Veneziani, A.: Cardiovascular Mathematics: Modeling and Simulation of the Circulatory System. MS&A. Springer, Berlin (2009)
30. Gara, A., Blumrich, M.A., Chen, D., Chiu, G.L.T., Coteus, P., Giampapa, M.E., Haring, R.A., Heidelberger, P., Hoenicke, D., Kopcsay, G.V., Liebsch, T.A., Ohmacht, M., Steinmacher-Burow, B.D., Takken, T., Vranas, P.: Overview of the BlueGene/L system architecture. IBM J. Res. Develop. (2010). doi:10.1147/rd.492.0195
31. Goldberg, D.E.: Genetic Algorithms in Search, Optimization and Machine Learning. Addison-Wesley, Reading (1989)
32. Hess, J.L., Smith, A.M.O.: Calculation of potential flow about arbitrary bodies. Prog. Aerosp. Sci. **8**, 1–138 (1967)
33. Hino, T.: Computation of viscous flows with free surface around an advancing ship. In: Proc. of the 2nd Osaka International Colloquium on Viscous Fluid Dynamics in Ship and Ocean Technology (Osaka) (1992)
34. Hirt, C.W., Nichols, B.D.: Volume of fluid (VOF) method for the dynamics of free boundaries. J. Comput. Phys. **39**, 201–225 (1981)
35. Hughes, T.J.R., Liu, W.K., Zimmermann, T.K.: Lagrangian–Eulerian finite element formulation for incompressible viscous flows. Comput. Methods Appl. Mech. Eng. **29**(3), 329–349 (1981)
36. Idelsohn, S.R., Onate, E., Sacco, C.: Finite element solution of free-surface ship-wave problems. Int. J. Numer. Methods Eng. **45**, 503–528 (1999)
37. Jameson, A., Martinelli, L.: Aerodynamic shape optimization techniques based on control theory. In: Computational Mathematics Driven by Industrial Problems, pp. 151–221. Springer, Berlin (2000)
38. Jasak, H.: Error analysis and estimation for the finite volume method with applications to fluid flows. PhD thesis, Imperial College (London) (1995)
39. Johnson, S.G.: The nlopt nonlinear-optimization package
40. Karypis, G., Kumar, V.: A fast and high quality multilevel scheme for partitioning irregular graphs. SIAM J. Sci. Comput. **20**, 359–392 (1998)

41. Kim, M.H., Celebi, M.S., Kim, D.J.: Fully nonlinear interactions of waves with a three-dimensional body in uniform currents. Appl. Ocean Res. **20**, 309–321 (1998)
42. Lassila, T., Quarteroni, A., Rozza, G.: A reduced basis model with parametric coupling for fluid-structure interactions problems. SIAM J. Sci. Comput. (2012) accepted
43. Lassila, T., Rozza, G.: Reduced formulation of a steady-fluid structure interaction problem with parametric coupling. In: Makinen, R.A.E., Valpe, K., Neittaanmaki, P., Tuovinen, T. (eds.) Proc. of the 10th Finnish Mechanical days, December 2009
44. Lassila, T., Rozza, G.: Parametric free-form shape design with PDE models and reduced basis method. Comput. Methods Appl. Mech. Eng. **199**, 435–465 (2010)
45. Deal II: A Finite Element Differential Equations Analysis Library
46. Lombardi, M.: Simulazione numerica della dinamica di uno scafo. Master's thesis, Politecnico di Milano (2006)
47. Manzoni, A., Quarteroni, A., Rozza, G.: Shape optimization for viscous flows by reduced basis methods and free-form deformation. Submitted (2010)
48. Martinelli, L., Jameson, A.: An adjoint method for design optimization of ship hulls. In: Proc. of the 9th International Conference on Numerical Ship Hydrodynamics, Ann Arbor, Michigan, 2007
49. Le Méhauté, B.: An Introduction to Hydrodynamics and Water Waves. Springer, Berlin (1976)
50. Menter, F.R.: Improved two-equation k-omega turbulence models for aerodynamic flows. NASA STI/Recon Technical Report N (1992)
51. Menter, F.R., Kuntz, M., Langtry, R.: Ten years of industrial experience with the SST turbulence model. Heat Mass Transf. **4**, 625–632 (2003)
52. ANSYS ICEM CFD meshing software
53. Michell, J.H.: The wave resistance of a ship. Philos. Mag. **45**, 106–123 (1898)
54. Mohammadi, B., Pironneau, O.: Analysis of the K-Epsilon Turbulence Model. Wiley, New York (1993)
55. Mohammadi, B., Pironneau, O.: Mesh adaption and automatic differentiation in a CAD-free framework for optimal shape design. Int. J. Numer. Methods Fluids **30**, 127–136 (1999)
56. Mohammadi, B., Pironneau, O.: Applied Shape Optimization for Fluids. Oxford University Press, Oxford (2009)
57. Newman, J.C., Taylor, A.C., Newman, P.A., Hou, W.: Overview of sensitivity analysis and shape optimization for complex aerodynamic configurations. J. Aircr. **36**(1), 87–96 (1999)
58. Nobile, F.: Numerical approximation of fluid-structure interaction problems with application to haemodynamics. PhD thesis, EPFL (2001)
59. OpenFOAM: Open Field Operation and Manipulation
60. Osher, S., Fedkiw, R.: The Level Set Method and Dynamic Implicit Surfaces. Springer, Berlin (2002)
61. Osher, S., Sethian, J.A.: Fronts propagating with curvature-dependent speed: Algorithm based on Hamilton–Jacobi formulations. J. Comput. Phys. **79**, 12–49 (1988)
62. Othmer, C.: A continuous adjoint formulation for the computation of topological and surface sensitivities of ducted flows. In: International Journal for Numerical Methods in Fluids, pp. 861–877 (2008)
63. Othmer, C., de Villiers, E., Weller, H.: Implementation of a continuous adjoint for topology optimization of ducted flows. In: 18th AIAA Computational Fluid Dynamics Conference, Miami, Florida (2007)
64. Parolini, N.: Computational fluid dynamics for naval engineering problems. PhD thesis, EPFL (2004)
65. Parolini, N., Quarteroni, A.: Mathematical models and numerical simulations for the America's cup. Comput. Methods Appl. Mech. Eng. **194**, 1001–1026 (2005)
66. Piazza, S.: Simulazioni numeriche della dinamica di uno scafo in mare ondoso. Master's thesis, Politecnico di Milano (2007)
67. Piegl, L., Tiller, W.: The NURBS Book. Springer, Berlin (1997)
68. Pironneau, O., Hecht, F., Le Hyaric, A., Morice, J.: FreeFem++: Free finite element method
69. Powell, M.J.D.: A Direct Search Optimization Method that Models the Objective and Constraint Functions by Linear Interpolation (1994)

70. Powell, M.J.D.: The BOBYQA algorithm for bound constrained optimization without derivatives. Technical report, Department of Applied Mathematics and Theoretical Physics, Cambridge (2009)
71. Quaini, A., Quarteroni, A.: A semi-implicit approach for fluid-structure interaction based on an algebraic fractional step method. Math. Models Methods Appl. Sci. **17**(6), 957–983 (2007)
72. Quarteroni, A.: Numerical Models for Differential Problems. MS&A. Springer, Berlin (2009)
73. Renzsch, H., Müller, O., Graf, K.: Flexsail—a fluid structure interaction program for the investigation of spinnakers. In: 21st International HISWA Symposium, Amsterdam (2010)
74. Rodrigues, J.F., Renaud, J.E., Watsen, L.T.: Convergence of trust region augmented Lagrangian methods using variable fidelity approximation data. Struct. Multidiscip. Optim. **15**, 141–156 (1998)
75. Rosen, B.S., Laiosa, J.P., Davis, W.H., Stavetski, D.: Splash free-surface code methodology for hydrodynamic design and analysis of IACC yachts. In: Proc. of 11th Chesapeake Sailing Yacht Symposium, Annapolis (1993)
76. Rozza, G., Huynh, D.B.P., Patera, A.T.: Reduced basis approximation and a posteriori error estimation for affinely parameterized elliptic coercive partial differential equations. Arch. Comput. Methods Eng. **15**, 229–275 (2008)
77. Rozza, G., Lassila, T., Manzoni, A.: Reduced basis approximation for shape optimization in thermal flows with a parameterized polynomial geometric map. In: Hesthaven, J., Ronquist, E. (eds.) Selected papers from the ICOSAHOM 09 Conference, NTU Trondheim, Norway, 22–26 June 2009. Lecture Notes in Computational Science and Engineering, vol. 76. Springer, Berlin (2010)
78. Rusche, H.: Computational fluid dynamics of dispersed two-phase flows at high phase fractions. PhD thesis, Imperial College (London) (2002)
79. Sagaut, P.: Large Eddy Simulation for Incompressible Flows. Springer, Berlin (2009)
80. Sederberg, T.W., Parry, S.R.: Free-form deformation of solid geometric models. Comput. Graph. **20**(4), 151–160 (1986)
81. The COMSOL Multiphysics simulation software
82. SolidWorks: 3D CAD Design Software
83. Soto, O., Loehner, R.: On the computation of flow sensitivities from boundary integrals (2004)
84. Spalart, P.R.: Detached-eddy simulation. Annu. Rev. Fluid Mech. **41**, 181–202 (2009)
85. Tahara, Y., Stern, F., Himeno, Y.: Computational fluid dynamics-based optimization of a surface combatant. J. Ship Res. **48**, 273–287 (2004)
86. Toda, Y., Stern, F., Longo, J.: Mean-flow measurement in the boundary layer and wake and wave field of a series 60 cb = 0.6 ship model. Part 1: Froude numbers 0.16 and 0.36. J. Ship Res. **36**(4), 360–377 (1992)
87. Trimarchi, D., Turnock, S.R., Taunton, D.J., Chapelle, D.: The use of shell elements to capture sail wrinkles, and their influence on aerodynamic loads. In: The Second International Conference on Innovation in High Performance Sailing Yachts, Lorient, France (2010)
88. Wilcox, D.: Turbulence Modeling for CFD. DCW Industries, La Canada (1998)
89. Wright, A.M., Claughton, A.R., Paton, J., Lewis, R.: Off-wind sail performance prediction and optimisation. Technical report, The Royal Institution of Naval Architects (2010)
90. Yang, J., Michael, T., Bhushan, S., Hanaoka, A., Wang, Z., Stern, F.: Motion prediction using wall-resolved and wall-modeled approaches on a Cartesian grid. In: Proc. of the 28th Symposium on Naval Hydrodynamics, USA, Pasadena (2010)
91. Zwart, P.J., Godin, P.G., Penrose, J., Rhee, S.H.: Simulation of unsteady free-surface flow around a ship hull using a fully coupled multi-phase flow method. J. Mar. Sci. Technol. **13**, 346–355 (2008)
92. Zymaris, A.S., Papadimitriou, D.I., Giannakoglou, K.C., Othmer, C.: Continuous adjoint approach to the Spalart–Allmaras turbulence model for incompressible flows. Comput. Fluids **38**, 1528–1538 (2009)
93. Zymaris, A.S., Papadimitriou, D.I., Giannakoglou, K.C., Othmer, C.: Adjoint wall functions: A new concept for use in aerodynamic shape optimization. J. Comput. Phys. **229**(13), 5228–5245 (2010)

On the Way to ACARE 2020 and Beyond

Dieter Schmitt

1 Air Transport System

The air transport system is today a global business and has several stakeholders who have to work closely together to provide an efficient transportation system. Figure 1 is highlighting the main actors and their interrelationship.

Air Transport system is traditionally an essential activity of national interest for each state/government, and this is especially true for air transport because this happens mainly internationally. Transport recognizes a privilege compared to other domains of the economy:

- Economic Reasons:
  - Export-oriented industries need proper means of transport for goods.
  - Production areas need fast, cheap and reliable ways of transport.
- National Reasons:
  - Demonstration of power/sovereignty, one of the reasons to have a national air force to demonstrate Air supremacy.
  - National Air fleet Reserve for transport needs during war.
  - Prestige national "flag carrier" (Air France, Iberia, Air India, Alitalia, British Airways, etc.).

Due to the internationality of air transport on one side and the air supremacy of the national states on the other side, a lot of contact points and common interests exist between state/government and air transport! A strong link between economic growth and air transport can be seen by the surprising correlation between Domestic Growth Product GDP and the transportation performance, expressed in Revenue passenger Miles (RPM).

As shown in Fig. 2, there is a strong similarity in percentage growth per year for GDP and RPM (revenue passenger miles), which means in simple terms sold air

D. Schmitt (✉)
Aeronautical Consultant, Coventry Str. 33, 65934, Frankfurt am Main, Germany
e-mail: dieter.schmitt@sfr.fr

G. Buttazzo, A. Frediani (eds.), *Variational Analysis and Aerospace Engineering: Mathematical Challenges for Aerospace Design*, Springer Optimization and Its Applications 66,
DOI 10.1007/978-1-4614-2435-2_16,

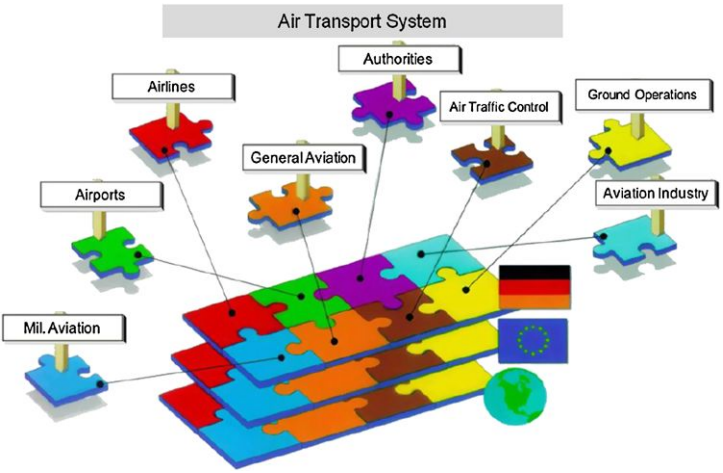

Fig. 1 Air transport system

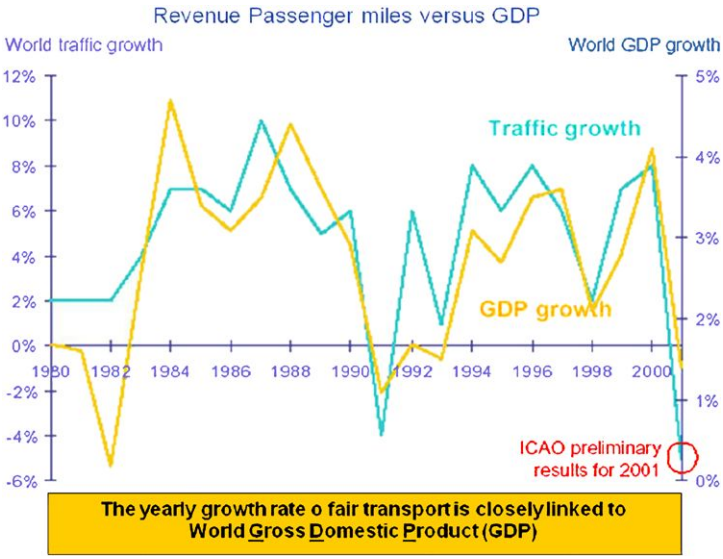

Fig. 2 Revenue Passenger miles versus GDP

tickets per year. All world crises like 11th of September or the beginning of Iraq war can be seen directly in the GDP curve, but are also directly reflected by the sold air tickets. The RPM is, however, by a factor of 2–3 higher. This means that the air travel request is a very sensitive indicator for world economy and its growth potential.

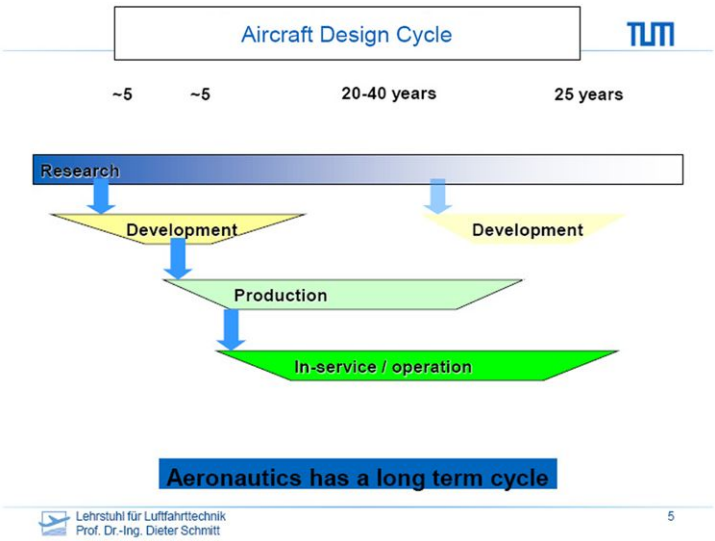

Fig. 3 Typical life cycle of a civil aircraft programme

The aeronautical industry is a very specific business [3, 5, 6, 12]. The product is very complex, the number of production units is fairly small, at least compared to other sectors like automotive industry, and the investment for new products is very high. Therefore a lot of risk is involved when a company is deciding to invest in a new aircraft programme. Figure 3 is showing the development cycle of an aircraft programme.

It takes 10 years to define the product corresponding to the market requirements, then it takes another five years to develop the aircraft, certify it and deliver it to the market. If the design was market adequate, there will be a chance to produce the aircraft for 20 to 40 years (B747, B737, A320, etc.) with sometimes some improved versions, and the final aircraft will still have an operative life of roughly 25 years.

Taking such a cycle, it becomes obvious, that all financial institutions will be hesitating to invest in such critical long-term programmes. On the other hand, the civil aeronautical industry is seen by many countries as a strategic industry, closely linked to the military aircraft market and with a lot of synergies between both.

2 ACARE Vision 2020

In the year 2000, a Group of Personalities (GoP) has started in Europe to think about a long-term strategy for the European aeronautical industry.

Background was that the USA had launched some years before a Supersonic Research Programme, with a financial volume of more than 2 billion US$.

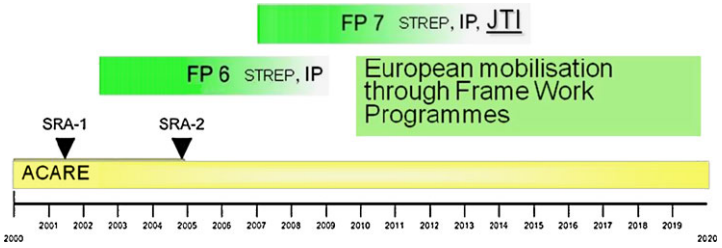

Fig. 4 ACARE and the development of aeronautical research in Europe

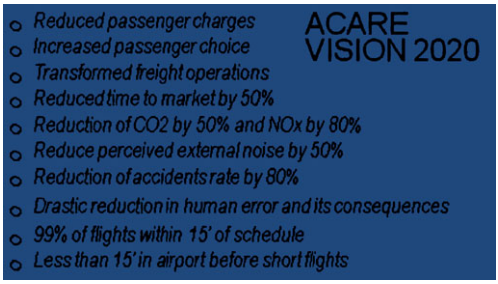

Fig. 5 ACARE Vision 2020 and the goals

It was obvious that this supersonic research programme would not only develop technologies for a possible future SST aircraft (Concorde successor) but also deliver a lot of technologies for the subsonic civil aircraft design.

This GoP defined a Vision 2020 for the European aeronautical industry. But more important was the creation of an Advisory Group with all useful and mandatory partners involved. This Advisory Group was named ACARE (Advisory Group for Aeronautical Research in Europe) and included all necessary stakeholders for this domain, the operators, the industry, the political decision makers and the research institutions (see Fig. 6).

The ACARE Vision 2020 identified the major challenges for the future and defined very ambitious goals. The goals covered all domains, the aircraft development the operation and the society. 50% of reduction in CO_2 was the obvious goal, and major progress has been achieved over the last 10 years (Fig. 5).

However, this could only be done by national and European research programmes that were established to identify the necessary technologies to reach the targets. Two Strategic Research Agendas (SRA1 and SRA 2) have been identified (see Fig. 4), and the following European Research Framework programmes (FP6 and FP7) were using the technology guidelines from SRA1 and SRA2 for the internal evaluation of the projects.

In SRA1 one of the five major challenges was "Environment" and in SRA2 High-level target Concepts have been defined [9], and the "Ultra Green Air transport system" was one of the leading concepts.

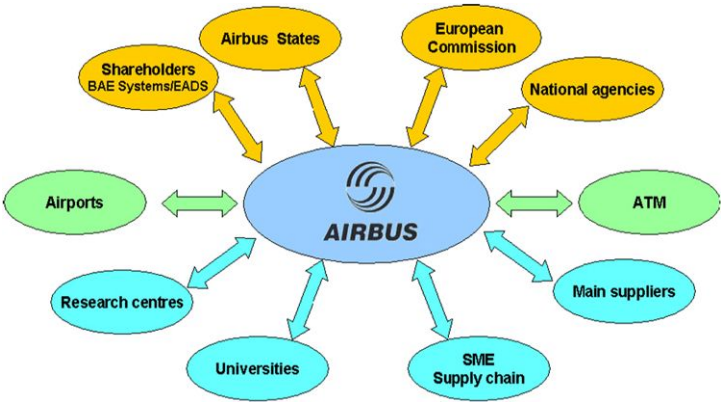

Fig. 6 ACARE Stakeholders—European Technology Platform

3 Aircraft Design Drivers

In the past the aircraft design drivers have been aimed:

Further: increase in range
Larger: increase in size
Faster: increase in speed

The design driver "range" has come to a natural stop.

The increase in range has been a major objective in the 1980s and 1990s, to follow the intention from the airlines to fly all major routes, even the very long ones (Singapore–New York, London–Sydney) as non-stop routes [8].

Both aircraft manufacturers, Boeing and Airbus, have demonstrated that their latest long-range aircraft (B777 and A340-500) can fly nearly half around the world, if needed, however with some payload restriction. A greater range capability is not really needed, as it will also have some impact on the fuel used to fly the mission (see Chap.: *Optimal Location of Support Points in the Kirchhoff Plate*).

The design driver "size" has also considerably increased with the development of the Airbus A380, which can transport up to 850 passengers in a high-density version. The further market survey will show whether the travelling public is accepting or even preferring a large aircraft compared to a smaller long-range aircraft. A larger aircraft will only be accepted by the airlines if it can be shown that it is more fuel efficient than the smaller ones. Some specialists are already postulating that with an aircraft even larger than the A380, no further improvement in fuel efficiency with same technology standard will be achievable (economy of scale) [6]. There is the possibility of using and developping a larger aircraft, but only when other factors, such as airport congestion, public acceptance, economy of scale, etc., will give a clear advantage even to larger planes.

The design driver "speed" is no longer a design driver. For a long-range aircraft, the typical cruise speed in terms of Mach number is 0.85. Flying faster would mean a higher fuel consumption, and flying at lower speed (as A330 and A340) is giving

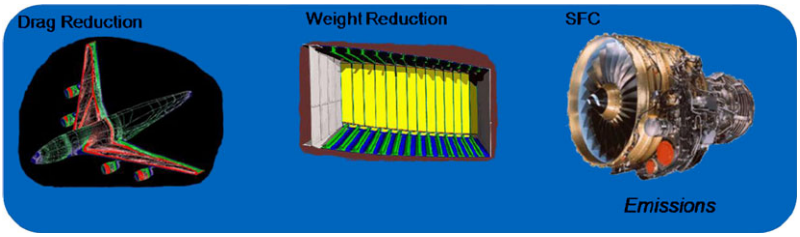

Fig. 7 Classical design drivers for an aircraft

a disadvantage in the operation as these aircrafts will not always get the optimum flight altitudes from ATC, where a faster aircraft will get the better cruise altitude. So a certain standard has been achieved [3, 5, 6, 12]:

Long-range cruise: Ma = 0.85
Short-range cruise: Ma = 0.78

There have been some attempts in the 1990s to develop a new Supersonic civil transport aircraft, but the studies have shown that there are still two major obstacles:

- noise issue in cruise (shock waves will be heard on ground);
- emission problems (CO_2 will be emitted in the stratosphere, and the impact on Greenhouse gas, radiation, etc. is not predictable).

Therefore, the classical design drivers are no longer valid. The obvious new aircraft design drivers are:

Greener
Cheaper

All greening efforts are also linked with further fuel reduction. In this respect ecological and economical improvement efforts are going in the same direction.

As can be seen in Fig. 7, the main efforts and technologies for further fuel efficiency are the further improvement in aerodynamics (L/D improvement), the improvements in light weight structure, i.e. reducing the Manufacturing Weight Empty (MWE) relative to the Max Takeoff Weight (MTOW), and improvements in the propulsion efficiency of the engines.

Figure 8 identifies some additional technological areas, where new technologies are leading to further improvements, but these areas are targeting to mainly reduce cost, passenger acceptance or are secondary features in the design cycle.

Safety is not a design driver by itself. All new aircrafts have to meet the certification requirements, and it is mandatory to constantly improve the safety standards and keep a reasonable compromise between efficiency and safety.

A safe and reliable operation is a major criterion for all airlines when buying a new aircraft.

In order to achieve the ACARE Vision in 2020, the 50% fuel efficiency improvements have to be broken down in three major parts as shown in Fig. 9. An aircraft and engine will have to contribute with 20%, and the Air Traffic Management has

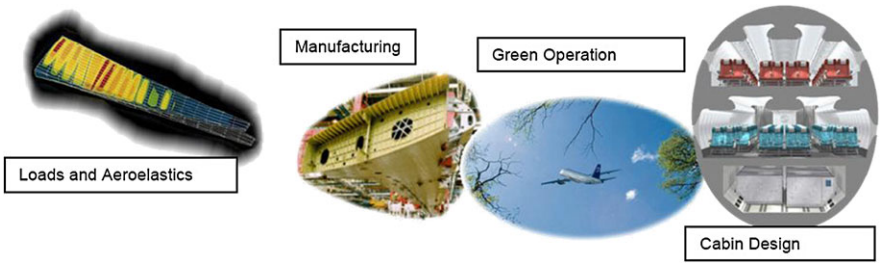

Fig. 8 Additional research supporting green aircraft manufacturing

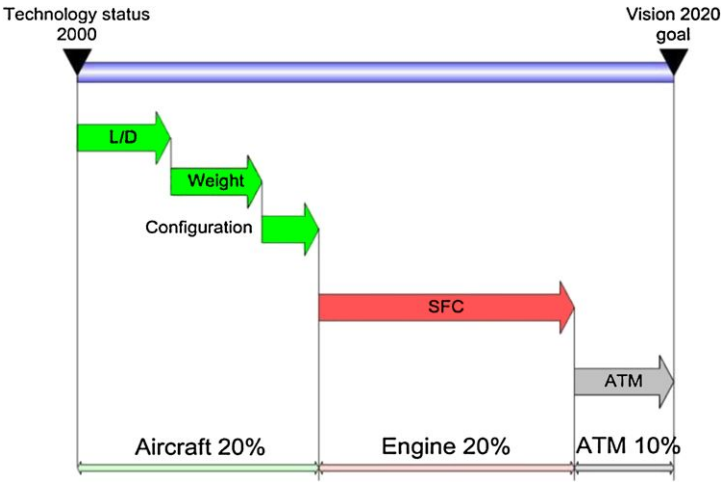

Fig. 9 Breakdown of ACARE target

to provide the final 10%. This target of 50% is ambitious and may not be reached, but about 30% improvement will be available in 2020 compared to 2000 technology standard. The verification is difficult, as there is no a new design in 2020 and a corresponding design in 2000 that can be directly compared. But the A320 NEO, to be delivered in 2016, is showing already a +15% fuel improvement, without major improvements on the aircraft and ATM side. So the target is visible, and a constant technology effort is mandatory.

4 Environmental Challenges

The environmental challenge is very important for the air transport sector. The recent discussion about the constantly increasing CO_2 emissions and the impact on the climate change is and will further push the transport sector to strengthen all efforts to reduce the emissions.

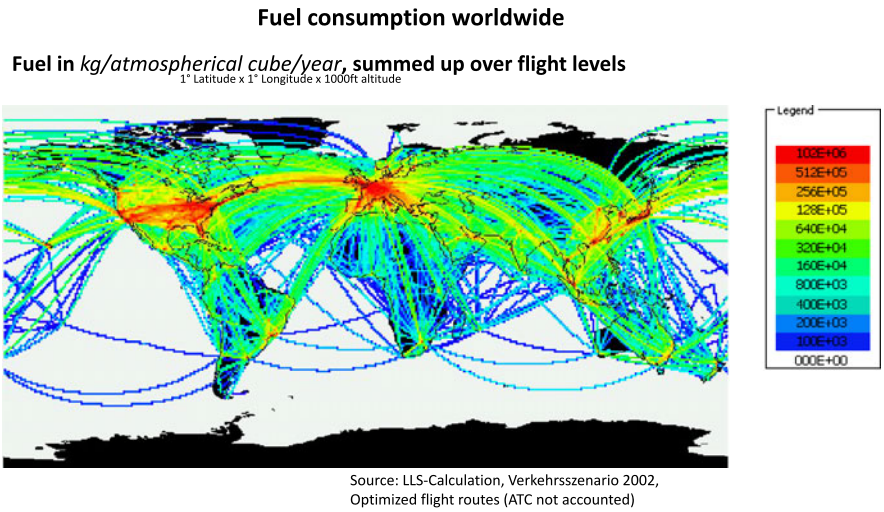

Fig. 10 Fuel in kg/atmospherical cube/year, summed up over flight levels

The proposed Emission Trading System (ETS) and the decision of the European parliament and the EC to introduce the air transport sector in Europe into the ETS System from 2012 onwards is a clear signal from the political side. So there is the political push to improve the efficiency of the aircraft and also the efficiency of the operational elements of the air transport system. ACARE is just redefining their objectives and have issued a new Vision called Flight Path 2050 [1].

Figure 10 is providing a visual impression of all the fuel used in air transport in the year 2002. The situation today is similar, and with the further increase in air transport demand and new aircraft entering the market, the situation will be further increasing, despite the efforts of new aircraft with better fuel efficiency. Figure 10 is also showing a very uneven distribution of emissions with a very strong impact on the northern hemisphere compared to the southern hemisphere.

Figure 11 is a picture from the IPCC report [7] highlighting the Radiative Forcing from the air transport sector. The emissions with highest impact are CO_2, NO_x and Contrails.

While the impact of CO_2 is fairly well understood, there is a clear route for improving the CO_2 emission by either further reducing the fuel consumption or by using alternative fuels with a lower carbon footprint. There is no specific effect for the air transport system and specifically the aircraft flying at high altitudes. All CO_2 is accumulating anyhow over some time in the stratosphere and stays there for some 100 years, the dominating emission gas with high and real climate impact [7].

NO_x is more difficult than a green house gas. NO_x is partly increasing the temperature and partly cooling the atmosphere, depending on the different interactions with other radicals like Methan and Ozone in the higher atmosphere. Here the different atmospheric research teams are not giving the same explanations. The impact of NO_x is varying with altitude, and there is yet no clear indication and common

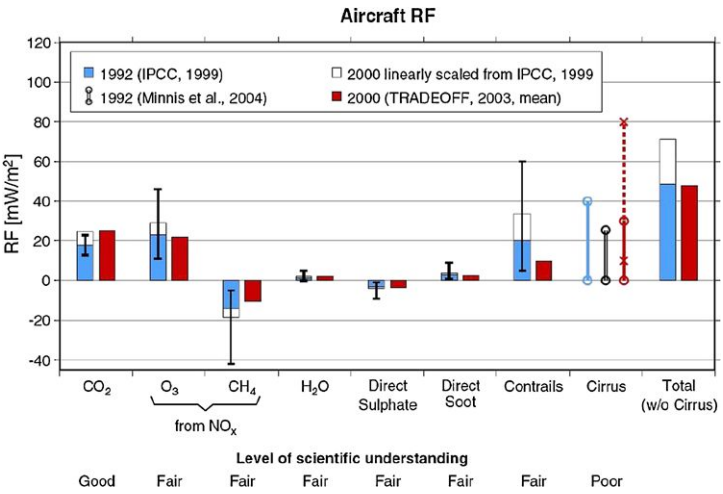

Fig. 11 Climate relevant emissions—radiative forcing (RF) (IPCC report [7])

sense, whether this would mean to fly higher or lower, if this would help to reduce the relevant emission impact.

Contrails are also not fully evaluated in their relation to the Radiative Forcing. But there seems to be a common understanding that there is an impact on the total temperature increase, but not yet agreed how much and how important this might be.

First conclusion about the impact of air transport on climate:

- CO_2 is the main impact component.
- There is not yet any clear indication about the optimal altitude.
- Contrails and the additional water vapour may give an additional negative impact.

The first means to reduce the fuel consumption could be the design of aircraft with less range. In [2] a simulation has been done for the layout of a long-range aircraft. At similar technology standard, an aircraft which is designed for a long-range mission of 6500 nm will have a Specific Air range (SAR) of about 0.083 nm/kg fuel. SAR is an important indicator, showing how far in nautical miles an aircraft can fly with a given fuel quantity (1 kg fuel). This SAR is improving if the same aircraft (designed for $R = 6500$ nm) will only be operated at a distance of 4000 nm to 0.089, which is nearly 8% better in fuel efficiency. If now the aircraft is designed for a lower range (i.e. $R = 4000$ nm) than the specific air range will be improved to SAR = 0.107, which is nearly a 20% improvement of fuel efficiency (see Fig. 12).

So a first indicator is already given: Design the new transport aircraft for lower range and operate the long-range missions with an interim stop. This however will not yet be very clear and popular with the operators. They want to have a lot of flexibility for their fleet and operate the same aircraft at different stage lengths. But as shown in [2], there is quite a huge potential for efficiency improvement by just

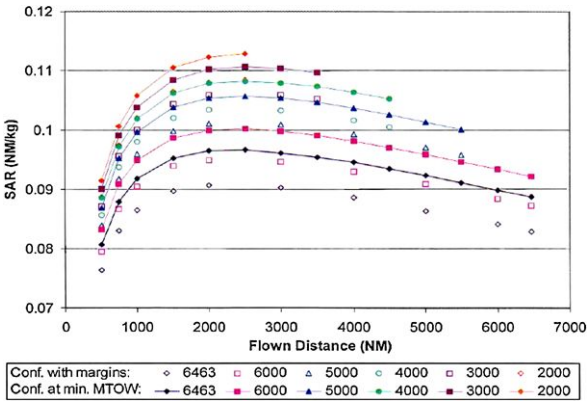

Fig. 12 Improvement in Specific Air Range (SAR) with reduced design range

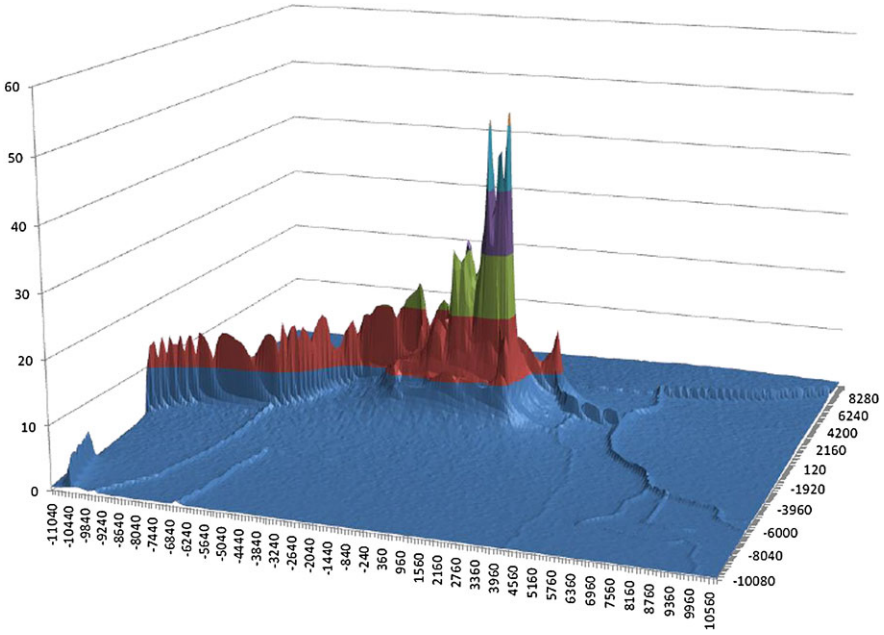

Fig. 13 Emissions from the airport Munich and the local distribution [2]

reducing the design range for a new aircraft and operate them with an interim stop on long-haul routes.

But it also has been stated in several papers (see [11]) that modern aircraft like B737 and A320 are consuming not more primary energy per passenger and km compared to other transport systems like High-Speed trains, Megalev or Transrapid or private cars. A380 for example consumes on a long-range flight less than 2.9 l of kerosene per passenger and 100 km!

Another aspect of environmental impact of the aircraft operation is the local impact at an airport. In [4] a simulation of all vehicles around an airport and their emission has been conducted. Besides the aircraft and their emissions, which are now calculated in the LTO cycle, a realistic study, with the modelling of all vehicles, circulating in the airport areas with the buses, the small baggage handling vehicles, the GPU vehicles, aircraft service vehicles, de-icing features, etc., has been done. The result is insofar interesting, as the emissions from the aircraft are quite important but not as dominant as expected. The emissions from the cars and car parks are also very important, and as shown in a summary chart in Fig. 13, the emissions around and within the airport area are quite high. But as it can be seen from Fig. 13, also the emissions from the motorways leading to the airport are significant and can be seen clearly. On the other hand, the impact of aircraft operation at the airport on the surrounding communities is not very significant even outside of the airport areas; there is only a very small impact from the emissions of the airport activities. More dominant are then also the motorways and their related emissions. This has also been confirmed by measurements around the airport. But the importance of [6] is that now the airport has a qualified model and can simulate how to further improve the emissions around the airport by:

- changing the fuel of the buses and use Hydrogen,
- reducing the GPU vehicles and install fixed power stations at each gate,
- relocating parking areas and collect the passengers with hydrogen buses,
- etc.

The item noise has not to be forgotten, but it is not the subject of this paper.

5 Fuel Reduction Potential

The main goal in all aeronautical research programmes is still the reduction of fuel consumption for a given mission. As has been explained in Chap. *Crack Extension Energy Rate and Energetic Approaches in Elastic–Plastic Fracture Mechanics* and Fig. 8, the main efforts for achieving these goals are in the domains of aerodynamics, structures, engines and new aircraft configurations. The following items are high on the research agenda.

5.1 Aerodynamic

Decreasing drag is the main objective in the aerodynamic field. The main potential is still to be identified in the following fours areas:

- Blended Winglets, Spiroids, other wingtip devices (see Fig. 14);
- Improved profiles, Riblets, reduction of turbulent skin friction drag;
- Hybrid laminar flow (HLFC);
- Adaptive wings, morphing structures.

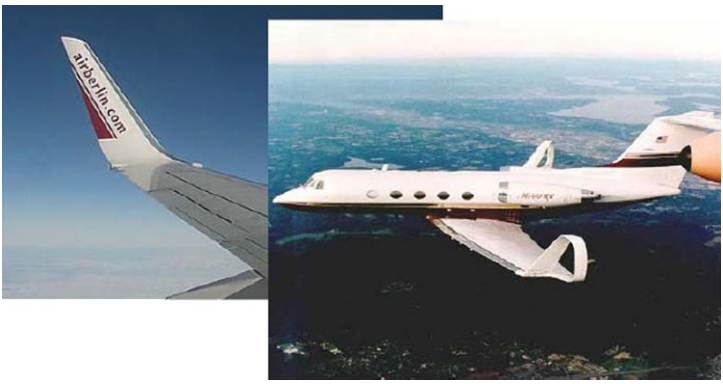

Fig. 14 Winglets and other wingtip devices

5.2 Structures

Decreasing mass for a given mission is the main objective for all structural related research. The new aircraft designs from Airbus and Boeing are pushing in this direction, to use CFRP for the main wing and fuselage structure. However there are more problems than anticipated, mainly with the manufacturing of large barrels and panels out of CFRP, the precision needed and the quality and reliability of the manufacturing process. Partly new problems are to be solved like lightning strike, electromagnetic interference and impact acceptability. So the two main domains are:

- Materials: GLARE, CFRP, new aluminium alloys, metal matrix structures, etc.
- Design and manufacturing processes.

5.3 Configurations

Decreasing mass and drag and proper integration of the engine are the domains for all alternative aircraft concepts under investigation. The main areas are:

- Flying wing, Blended Wing Body Concepts (BWB);
- Three-Surface Aircraft (TSA);
- Joined Wing and Box-Wing concepts;
- Low-noise concepts (shielding of engine noise).

Several examples are shown in Fig. 15.

6 CREATE Proposals

All research areas described before are very much technology oriented and are on the agendas of all the industrial research portfolios. There are however also a lot of

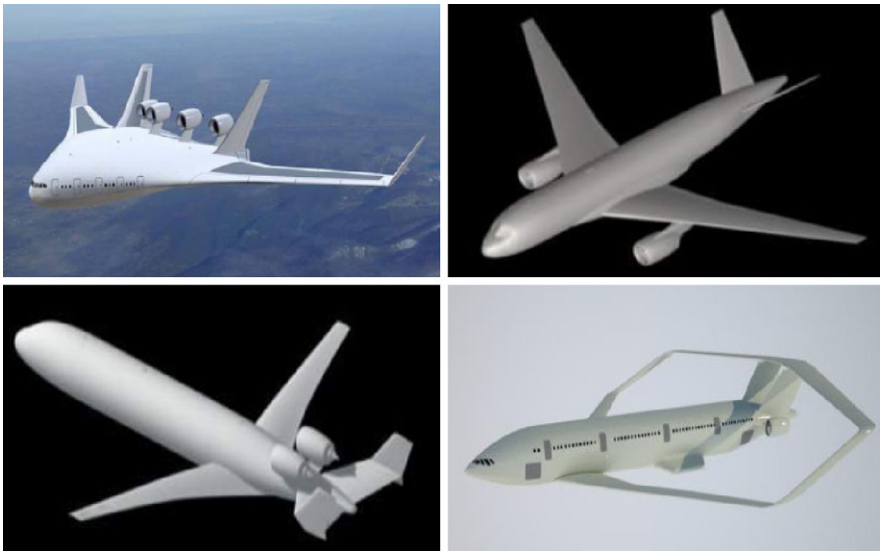

Fig. 15 New aircraft concepts with potential for future fuel improvements

"crazy" ideas in the air where it is not always obvious whether there is any value or benefit in it or whether it is really nonsense and should be no longer considered. For the evaluation of all these ideas, a certain budget and a specific process are needed.

In December 2006, the "Out Of the Box" report from ACARE, sponsored by the European Commission (EC), has been published [13], where a lot of those long-term ideas for future air transport options have been identified and published. A follow-on study has been launched in 2008 from the EC under the name "CREATE" [10].

This project investigated several concepts how to prepare a process for these long-term research projects and finally proposed a process for the incubation of "innovative ideas" with the important elements:

- Generation and Developing of unconventional ideas;
- Support possibilities for individuals, assessing the value of these ideas;
- Evaluation of the project proposals following specific criteria and launch conditions;
- Project start and project accompanying measures;
- Documentation of results for further incubation/risk reduction steps.

Figures 16 and 17 show some of those ideas, which have been identified for further exploration in a future CREATE process.

This CREATE process would be mainly targeted for research institutions (Universities and Research Centers) with small budgets but allowing the incubation of innovative ideas.

The Project CREATE [10] is finished, and the main process elements have been discussed with relevant personalities from industry, Research Centers and Funding

Fig. 16 Flying Car Concept

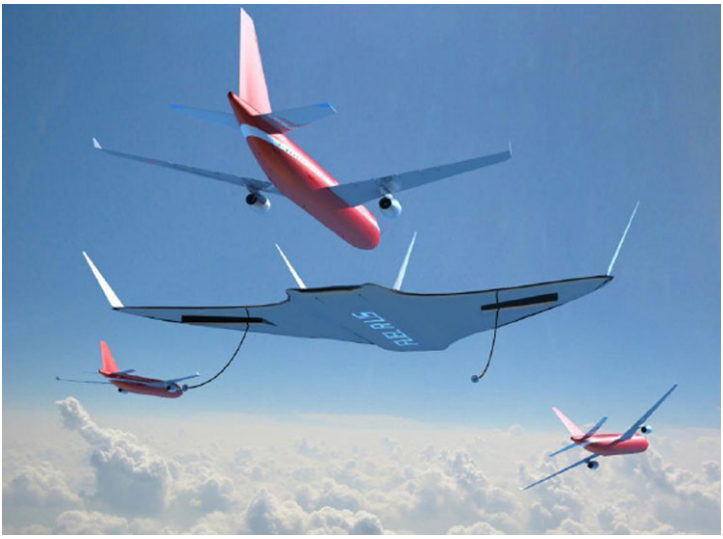

Fig. 17 Civil Transport Aircraft refuelling in the air

authorities. Main feedback from different stakeholders is also that they confirm the pressing need for such an incubation process.

There are some different opinions about the boundary conditions for the incubation process. The following conclusions are supported:

- Fund more smaller projects rather than fewer and bigger incubation projects;
- Public funding is mandatory to achieve the long-term focus of incubation;
- Excellence of the technical and scientific approach should be the main evaluation criteria;
- Some trials for incubation should already be integrated in the running FP7 programme.

These long-term research studies are now an element in the next Calls of the EC FP7 programme. These instruments are vital for the technical education of students and PhD students, to allow them to familiarize with technological upfront research work, improve skills in project management and get in close international contact with their research studies.

7 Conclusion

The following conclusions can be drawn:

- Air transport is still a very important element in the transport sector.
- Air transport is still growing over the next 20 years with quite high rates.
- The design drivers for aircraft will slightly change. The dominant factor in research will be the further reduction of fuel consumption, but environmental aspects are becoming more importance.
- The classical research domains like aerodynamics, structures and engines are already at a very high level, but further improvements are mandatory. Especially the integrated research items will need further attention.
- More results from the "Atmospheric climate research" are needed to give guidance of a future green air transport.
- Aeronautical research has to continue in all technology levels, but the low TRL research needs specific attention in the future to prepare ideas for future changes in the air transport sector.

References

1. ACARE FlightPath 2050 (2011)
2. Egelhofer, R.: Aircraft design driven by climate change. Dissertation TU Munich, Lehrstuhl für Luftfahrttechnik (2008)
3. Fielding, J.P.: Introduction to Aircraft Design. Cambridge University Press, Cambridge (1999)
4. Gaffal, R.: Modell zur nachhaltigen Schadstoffreduktion an Flughäfen. Dissertation TU Munich, Lehrstuhl für Luftfahrttechnik (2010)
5. Jenkinson, L.R., Rhodes, D., Simpkin, P.: Civil Jet Aircraft Design. AIAA Education Series. AIAA, Washington (1999)
6. McMasters, J.H., Kroo, I.M.: Advanced configurations for very large transport airplanes. Aircr. Des. **1**, 217–242 (1998)

7. Penner, J.E.: Aviation and the Global Atmosphere: A Special Report of IPCC Working Groups I and III in Collab. with the Scientific Assessment Panel to the Montreal Protocol on Substances that Deplete the Ozone Layer. Cambridge University Press, Cambridge (1999)
8. Schmitt, D.: Bigger, faster, greener, cheaper? Developing the AIRBUS response to the Vision 2020 demands. In: 24th ICAS Congress, Yokohama (Japan) (2004)
9. Schmitt, D.: Aircraft related agenda. In: European Commission Aerodays (2005)
10. Schmitt, D., Muller, R., de Graaff, A., Truman, T.: CREATE—a European initiative for incubation of upstream research projects. In: International Council of the Aeronautical Sciences Conference, Madrid (2011)
11. Schmitt, D., Niedzballa, H.A.: Comparison of the specific energy demand of aeroplanes and other vehicle systems. Aircr. Des. **4**, 163–178 (2001)
12. Steiner, J.E.: How decisions are made: major considerations for aircraft programs. In: Wright Brothers Lectureship in Aeronautics. AIAA, Washington (1982)
13. Truman, T., de Graaff, A.: Out of the box project (2006). www.acare4europe.org

Design Problems of Anisotropic Structures: Some Recent Results

Paolo Vannucci, Boris Desmorat, and Angela Vincenti

1 Introduction

Stiff and robust lightweight structures are of paramount importance in aeronautics, and a common way to obtain them is to use laminated composite materials. The drawback, for the engineer, is the fact that the design process is much more complicate than in the case of classical materials, like alloys. In fact, not only the properties concerning stiffness, strength and so on must be controlled and/or designed, but in addition, the *general elastic properties* must be taken into account in the design process. These properties concern namely the elastic symmetries and the elastic and multi-physics (e.g. thermo-elastic) couplings. The usual approach used by designers consists in a drastic simplification of the problem: some simple rules are used in order to automatically obtain some desired properties. The most well known of these rules is the use of symmetric stacking sequences, in order to get the uncoupling between the in-plane and the bending behaviour. The use of such rules has some drawbacks on the final design; for instance, the symmetric stacking sequence strategy has the immediate consequence of doubling the weight, which is a serious problem with aeronautical structures. In addition, some general properties, like

P. Vannucci (✉)
Institut Jean Le Rond d'Alembert, Université Versailles Saint Quentin, UMR7190, Université Paris 6 – CNRS, 4, Place Jussieu, Case 162, 75252 Paris, France
e-mail: paolo.vannucci@uvsq.fr

B. Desmorat
Institut Jean Le Rond d'Alembert, Université Paris Sud, UMR7190, Université Paris 6 – CNRS, 4, Place Jussieu, Case 162, 75252 Paris, France
e-mail: boris.desmorat@upmc.fr

A. Vincenti
Institut Jean Le Rond d'Alembert, UMR7190, Université Paris 6 – CNRS, 4, Place Jussieu, Case 162, 75252 Paris, France
e-mail: angela.vincenti@upmc.fr

G. Buttazzo, A. Frediani (eds.), *Variational Analysis and Aerospace Engineering: Mathematical Challenges for Aerospace Design*, Springer Optimization and Its Applications 66,
DOI 10.1007/978-1-4614-2435-2_17,

for instance bending orthotropy, cannot be, generally speaking, obtained using such simple rules.

An alternative approach is a proper and modern use of optimization strategies: the design problem is entirely formulated as an optimization problem, the requirements concerning the elastic symmetries being part of the problem, as an objective or a constraint, according with the problem at hand. Under a mathematical point of view, this leads to the formulation of a global optimization problem in the double sense that the feasible domain is not reduced by simplifying rules and that the global minimum of the objective function has to be found. Such problems are generally non-convex, the objective function is highly nonlinear. Nevertheless, modern strategies of computation can effectively approach and solve such problems.

In this presentation, we show a general procedure to tackle the problem of designing anisotropic laminates corresponding to given criteria and optimizing a given objective function. The method is based, on one side, on the use of tensor invariants for the description of the anisotropic properties and, on the other side, on a free-material approach for the determination, first, of the optimal fields of anisotropic properties and, then, using numerical metaheuristics, of a suitable stacking sequence. Some general results concerning the method are introduced, along with a brief discussion of the influence of anisotropy on the optimal design of laminates. Finally, for showing the effectiveness of the approach, we present different problems that are mainly concerned with some potential applications in aeronautics.

2 Basic Equations and the Polar Method

All the equations of the Classical Laminated Plates Theory (CLPT) can be written with the polar formalism, and this can be advantageous in several cases, namely in design problems. The polar method is a mathematical tool introduced as early as 1979 by Verchery, [26]. Basically, this is just a method for representing the Cartesian components of a plane tensor **T** by a minimal set of independent invariants.

The basic relations, giving the Cartesian components in a frame rotated counterclockwise through an angle θ from the x_1 direction, are:

$$\begin{cases} T_{xxxx}(\theta) = T_0 + 2T_1 + R_0 \cos 4(\Phi_0 - \theta) + 4R_1 \cos 2(\Phi_1 - \theta), \\ T_{xxxy}(\theta) = R_0 \sin 4(\Phi_0 - \theta) + 2R_1 \sin 2(\Phi_1 - \theta), \\ T_{xxyy}(\theta) = -T_0 + 2T_1 - R_0 \cos 4(\Phi_0 - \theta), \\ T_{xyxy}(\theta) = T_0 - R_0 \cos 4(\Phi_0 - \theta), \\ T_{xyyy}(\theta) = -R_0 \sin 4(\Phi_0 - \theta) + 2R_1 \sin 2(\Phi_1 - \theta), \\ T_{yyyy}(\theta) = T_0 + 2T_1 + R_0 \cos 4(\Phi_0 - \theta) - 4R_1 \cos 2(\Phi_1 - \theta). \end{cases} \tag{1}$$

In Eqs. (1), the quantities T_0, T_1, R_0, R_1 are invariant moduli that, together with the difference $\Phi_0 - \Phi_1$, constitute a minimal set of independent tensor invariants

for tensor **T**. For the sake of shortness, in the following the Cartesian components of a tensor in the original frame $\theta = 0$ will be denoted by numerical indexes (e.g. $T_{xxyy}(\theta = 0) = T_{1122}$, and so on). Equations (1) show that the polar representation allows for splitting the Cartesian components in their isotropic, T_0 and T_1, and anisotropic, R_0, R_1, $\Phi_0 - \Phi_1$, parts. The choice of one of the two polar angles fixes the frame (usually $\Phi_1 = 0$).

An important property of the polar method is the fact that the invariants so found are linked to the elastic symmetries of the tensor **T**: the necessary and sufficient condition for ordinary orthotropy is

$$\Phi_0 - \Phi_1 = k\frac{\pi}{4}, \quad k \in \{0, 1\}. \tag{2}$$

Hence, ordinary orthotropy is actually of two types, determined by the two possible values of the parameter k; we will see in the next section how k affects the optimal solution of a design problem, i.e. how the two ordinary types of orthotropy have different behaviours with respect to optimal solutions.

Besides the two ordinary orthotropies above, two types of special orthotropy are also possible, both determined by the vanishing of the invariants R_0 or R_1; the last one is the classical case of square symmetry, the 2D equivalent of cubic syngony, while the first one is called R_0-orthotropy, and it must be considered separately for stiffness and compliance, see [18].

The same Eqs. (1) can of course be adapted to represent the Cartesian components of the tensors describing the elastic behaviour of a laminate in the framework of the CLPT:

$$\begin{Bmatrix} \mathbf{N} \\ \mathbf{M} \end{Bmatrix} = \begin{bmatrix} \mathbf{A} & \mathbf{B} \\ \mathbf{B} & \mathbf{D} \end{bmatrix} \begin{Bmatrix} \varepsilon \\ \kappa \end{Bmatrix}, \tag{3}$$

relating the internal action tensors **N** (extension forces) and **M** (bending moments) to in-plane and curvature tensors ε and κ, respectively.

The Cartesian components of tensors **A**, **B** and **D**, describing respectively the extension, coupling and bending elastic response of the laminate, can be given as functions of their polar components in the same way of Eqs. (1). Let us denote by the superimposed symbols $-$, $\hat{}$ and $\sim$ the polar components of, respectively, the normalized tensors

$$\mathbf{A}^* = \frac{\mathbf{A}}{h}, \qquad \mathbf{B}^* = 2\frac{\mathbf{B}}{h^2}, \qquad \mathbf{D}^* = 12\frac{\mathbf{D}}{h^3}, \tag{4}$$

h being the total thickness of the laminate. Then, using the composition laws given by the CLPT, for equal layer laminates, we obtain, after some standard manipulations, the polar components of $\mathbf{A}^*$, $\mathbf{B}^*$ and $\mathbf{D}^*$ as functions of the orientation angles δ_j, of the stacking sequence and of the polar components of the basic layer, T_0,

T_1, R_0, R_1, Φ_0 and Φ_1:

$$\begin{cases} \overline{T}_0^* = T_0, \\ \overline{T}_1^* = T_1, \\ \overline{R}_0^* e^{4i\overline{\Phi}_0} = \frac{1}{n} R_0 e^{4i\Phi_0} \sum_{j=1}^{n} e^{4i\delta_j}, \\ \overline{R}_1^* e^{2i\overline{\Phi}_1} = \frac{1}{n} R_1 e^{2i\Phi_1} \sum_{j=1}^{n} e^{2i\delta_j}; \end{cases} \tag{5}$$

$$\begin{cases} \widehat{T}_0^* = 0, \\ \widehat{T}_1^* = 0, \\ \widehat{R}_0^* e^{4i\widehat{\Phi}_0} = \frac{1}{n^2} R_0 e^{4i\Phi_0} \sum_{j=1}^{n} b_j e^{4i\delta_j}, \\ \widehat{R}_1^* e^{2i\widehat{\Phi}_1} = \frac{1}{n^2} R_1 e^{2i\Phi_1} \sum_{j=1}^{n} b_j e^{2i\delta_j}; \end{cases} \tag{6}$$

$$\begin{cases} \widetilde{T}_0^* = T_0, \\ \widetilde{T}_1^* = T_1, \\ \widetilde{R}_0^* e^{4i\widetilde{\Phi}_0} = \frac{1}{n^3} R_0 e^{4i\Phi_0} \sum_{j=1}^{n} d_j e^{4i\delta_j}, \\ \widetilde{R}_1^* e^{2i\widetilde{\Phi}_1} = \frac{1}{n^3} R_1 e^{2i\Phi_1} \sum_{j=1}^{n} d_j e^{2i\delta_j}; \end{cases} \tag{7}$$

in the above equations (5) to (7), n is the number of layers, while the coefficients b_j and d_j are given by

$$\begin{aligned} b_j &= 2j - n - 1, \\ d_j &= 12j(j - n - 1) + 4 + 3n(n + 2). \end{aligned} \tag{8}$$

3 Influence of Anisotropy on Optimal Solutions

A subject that has been largely unconsidered by literature is the influence that anisotropy has on the solution of a given optimum problem. The question is not simple, because one should consider at first what parameter describing anisotropy is of some importance in examining the dependence of a solution on anisotropy of the material. The advantage of the polar formalism is that it is based on material invariants, so these ones can be used as intrinsic quantities characterizing the material in order to consider their influence on an optimal solution. This point constitutes by itself an intrinsic advantage with respect to the use of frame-dependent quantities. More specifically, we will see in the following that interesting dimensionless invariant parameters are introduced using the polar invariants. The considerations presented hereafter concern two problems; the first one, rather elementary but very helpful in understanding the influence of anisotropy on optimal solutions, concern an in-plane problem, while the second regards the flexural optimal design of a laminate. In both cases, we are concerned with the influence that the *anisotropy of the material*, not of the final behaviour of the laminate, has on the optimal solution.

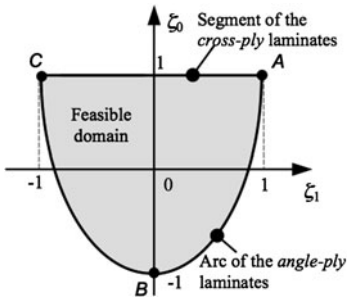

Fig. 1 Feasible domain in the lamination plane

The first case that we consider here is a simple problem: design the laminate having the greatest shear modulus G^m_{xy} in extension. By assumption, the laminate is composed of identical orthotropic plies whose polar parameters are T_0, T_1, $(-1)^k R_0$ and R_1. Formalizing the problem by the polar method, it is simple to show that the problem becomes

$$\max_{\delta_j} G^m_{xy} = \max_{\delta_j} \left[T_0 - (-1)^k R_0 \zeta_0 \right], \tag{9}$$

where ζ_0 and ζ_1, this last not appearing in (9), are the classical *lamination parameters* (see for instance [9]):

$$\begin{cases} \zeta_0 = \frac{1}{n} \sum_{j=1}^{n} \cos 4\delta_j , \\ \zeta_1 = \frac{1}{n} \sum_{j=1}^{n} \cos 2\delta_j . \end{cases} \tag{10}$$

Lamination parameters take into account for the *geometry* of the stack; they satisfy the following bounds:

$$-1 \le \zeta_1 \le 1, \qquad 2\zeta_1^2 - 1 \le \zeta_0 \le 1; \tag{11}$$

they define a feasible domain in the *lamination plane*: the sector of parabola shown in Fig. 1. Each point of this domain is a *lamination point* that defines the in-plane elastic properties of the laminate, but not its stacking sequence. In Fig. 1, there are also shown the line of the *cross-ply* laminates (sequences of plies at 0° and 90°) and the arc of *angle-ply* laminates (sequences of plies at $\pm\delta$, in equal number).

The objective function (9) is linear and does not depend on ζ_1: it is a plane defined on the feasible domain (11), whose slope is along ζ_0 and depends essentially on the value of k. The optimal solution is hence on the boundary of the feasible domain, and it is easy to see that:

- if $k = 0$, the solution is the point $\zeta_0 = -1$ and $\zeta_1 = 0$, to which corresponds an angle-ply laminate with orientation angles $\delta = \pm 45°$;
- if $k = 1$, the solution is any point on the line $\zeta_0 = 1$, $-1 \le \zeta_1 \le 1$: any cross-ply combination, including unidirectional laminates with all the layers at 0° or 90°, is a solution.

In addition, it is immediate to recognize that what is an optimal solution for a value of k, is an antioptimal (i.e. the worst one) for the other possible value of k.

Hence, we can see by this simple example that the parameter k, determining the type of ordinary orthotropy, affects considerably the optimal solution of a problem: it works like a switch from an optimal to an antioptimal solution (we will find again this effect of k) and, in this case, it determines the uniqueness or not of the solution. However, in both cases of $k = 0$ or 1, the value of the optimal solution is $(G^m_{xy})_{\max} = T_0 + R_0$, while the antioptimal solution is $(G^m_{xy})_{\min} = T_0 - R_0$.

Let us now turn our attention to a rather unusual problem in laminate design: the flexural optimal design of a laminate. Normally, in fact, literature pays a lot of attention to extension design of laminates, and only a very small part of it is devoted to the optimal design with respect to flexural properties. This is due to the fact that the flexural design is much more complicate than the extensional one. The results presented hereafter have been presented, in more detail, in [17].

More specifically, we consider here the flexural behaviour of bending-extension uncoupled laminates composed of identical layers; the plate is rectangular, with sides' of length a and b, respectively, along the axes x and y. Along its boundary, the plate is simply supported, and its mass per unit area is μ. A constraint is imposed on the anisotropy of the laminate: tensor $\mathbf{D}^*$ has to be orthotropic, and the axes of orthotropy to be aligned with the axes of the plate. These assumptions, along with that of uncoupling, are needed for having exact solutions for flexural problems and are, anyway, those normally used by designers. We bound ourselves to remark here that it is possible to find uncoupled laminates with $\mathbf{D}^*$ orthotropic, see [13] for more details.

In the above assumptions, it can be shown that (cf. [17]):

- the compliance J of the plate, loaded by a sinusoidal load orthogonal to its mean surface, is given by

$$J = \frac{\gamma_{pq}}{p^4 h^3 (1+\chi^2)^2 \sqrt{R_0^2 + R_1^2}} \frac{1}{\varphi(\xi_0, \xi_1)}; \tag{12}$$

- the buckling load multiplier λ_{pq} for the mode pq when the plate is loaded by in-plane distributed forces N_x and N_y is given by

$$\lambda_{pq} = \frac{\pi^2 p^2 h^3}{12 a^2} \frac{(1+\chi^2)^2 \sqrt{R_0^2 + R_1^2}}{N_x + N_y \chi^2} \varphi(\xi_0, \xi_1); \tag{13}$$

- the frequency of transversal vibrations ω_{pq} for the mode pq is expressed by

$$\omega^2_{pq} = \frac{\pi^4 p^4 h^3}{1 \mu a^4} \left(1+\chi^2\right)^2 \sqrt{R_0^2 + R_1^2} \varphi(\xi_0, \xi_1). \tag{14}$$

In the above equations, h is the laminate's thickness, γ_{pq} is a coefficient depending on the geometry of the plate and on the loading, p and q are the number of half-waves in the directions x and y respectively, while the dimensionless parameter

χ is the ratio of the wavelengths in the two directions, i.e.

$$\chi = \frac{a}{b}\frac{q}{p}. \tag{15}$$

Finally, the function $\varphi(\xi_0, \xi_1)$ is

$$\varphi(\xi_0, \xi_1) = \tau + \frac{1}{\sqrt{1+\rho^2}}\big[(-1)^k \rho \xi_0 c_0(\chi) + 4\xi_1 c_1(\chi)\big], \tag{16}$$

and it is a dimensionless function of dimensionless parameters and variables:

$$\tau = \frac{T_0 + 2T_1}{\sqrt{R_0^2 + R_1^2}} \tag{17}$$

is the *isotropy-to-anisotropy ratio*;

$$\rho = \frac{R_0}{R_1} \tag{18}$$

is the *anisotropy ratio*;

$$\begin{cases} \xi_0 = \frac{1}{n^3}\sum_{j=1}^{n} d_j \cos 4\delta_j, \\ \xi_1 = \frac{1}{n^3}\sum_{j=1}^{n} d_j \cos 2\delta_j, \end{cases} \tag{19}$$

are the *bending lamination parameters*, see [9]; they obey to the same kind of limitations as in (11) and define a feasible domain identical to that sketched in Fig. 1;

$$c_0(\chi) = \frac{\chi^4 - 6\chi^2 + 1}{(1+\chi^2)^2} \quad \text{and} \quad c_1(\chi) = \frac{1-\chi^2}{1+\chi^2} \tag{20}$$

are two dimensionless functions of χ, hence accounting of the geometry of the problem.

From the above equations, it is apparent that in the three cases, regarding all the possible situations concerning the flexural response of the plate, this response is always a function of $\varphi(\xi_0, \xi_1)$; in this dimensionless function, the isotropic part is well separated from the anisotropic one.

The question here is the dependence of the optimal solutions on the values of τ and ρ. It can be shown that all the optimal solutions can be of only two types, cross-ply or angle-ply laminates. Let us first consider cross-ply solutions, for which $\xi_0 = 1$ and $-1 \le \xi_1 \le 1$. The conditions to be satisfied for (16) to be a maximum are:

$$\begin{aligned} &(-1)^k c_0(\chi) > 0 \Leftrightarrow \begin{cases} k = 0 \text{ and } \chi \in [0, \sqrt{2}-1] \text{ or } \chi > \sqrt{2}+1, \\ k = 1 \text{ and } \sqrt{2}-1 < \chi < \sqrt{2}+1, \end{cases} \\ &\frac{c_1(\chi)}{\sqrt{1+\rho^2}} = 0 \Leftrightarrow \chi = 1 \quad \text{or } \rho = \infty. \end{aligned} \tag{21}$$

The corresponding highest values of the function, hereafter denoted by φ_{cp}, are

$$\begin{aligned} \varphi_{cp} &= \tau - \frac{(-1)^k \rho}{\sqrt{1+\rho^2}} \quad \text{for } \chi = 1, \\ \varphi_{cp} &= \tau + (-1)^k c_0(\chi) \quad \text{for } \rho = \infty. \end{aligned} \tag{22}$$

The maximum value of φ_{cp} is

$$\begin{aligned} \varphi_{cp}^{\max} &= \left[\tau - \frac{(-1)^k \rho}{\sqrt{1+\rho^2}}\right]_{k=1,\rho=\infty} = \left[\tau + (-1)^k c_0(\chi)\right]_{k=0,\chi=\{0,\infty\}} \\ &= \left[\tau + (-1)^k c_0(\chi)\right]_{k=1,\chi=1} = \tau + 1. \end{aligned} \tag{23}$$

Some remarks can be done; first of all, cross-ply solutions exist only in the presence of a generalized square symmetry: of the material, i.e. $\rho = 0$ (hence, a basic ply reinforced by a balanced fabric) or of the geometry and mode, i.e. $\chi = 1$ (e.g. a square plate with $p = q$). Then, we see easily that changing the type of ordinary orthotropy, i.e. changing k from 0 to 1, corresponds once again to transforming an optimal into an antioptimal solution. Finally, as the lamination parameter ξ_1 disappears from the above equations, this means that any laminate composed by a combination of layers at 0° and at 90° is an optimal solution: the uniqueness of the solution is not present for the optimal (or antioptimal) case whenever cross-ply laminates are sought for.

Let us now consider angle-ply solutions; in such a case, the two lamination parameters are linked by the relation (cf. Eq. (11))

$$\xi_0 = 2\xi_1^2 - 1, \tag{24}$$

and the objective function becomes

$$\varphi(\xi_1) = \tau + \frac{1}{\sqrt{1+\rho^2}}\left[(-1)^k \rho c_0(\chi)\left(2\xi_1^2 - 1\right) + 4c_1(\chi)\xi_1\right], \tag{25}$$

whose maxima and minima can be only

$$\begin{aligned} \varphi_{11} &= \varphi(\xi_1 = 1) = \tau + \frac{1}{\sqrt{1+\rho^2}}\left[(-1)^k \rho c_0(\chi) + 4c_1(\chi)\right], \\ \varphi_{22} &= \varphi(\xi_1 = -1) = \tau + \frac{1}{\sqrt{1+\rho^2}}\left[(-1)^k \rho c_0(\chi) - 4c_1(\chi)\right], \\ \varphi_{\delta\delta} &= \varphi\left(\xi_1 = \xi_1^{st}\right) = \tau - \frac{(-1)^k}{\sqrt{1+\rho^2}} \frac{\rho^2 c_0^2(\chi) + 2c_1^2(\chi)}{\rho c_0(\chi)}, \end{aligned} \tag{26}$$

with

$$\left.\frac{\partial \varphi}{\partial \xi_1}\right|_{\xi_1^{st}} = 0 \Rightarrow \xi_1^{st} = -\frac{(-1)^k}{\rho} \frac{c_1(\chi)}{c_0(\chi)}. \tag{27}$$

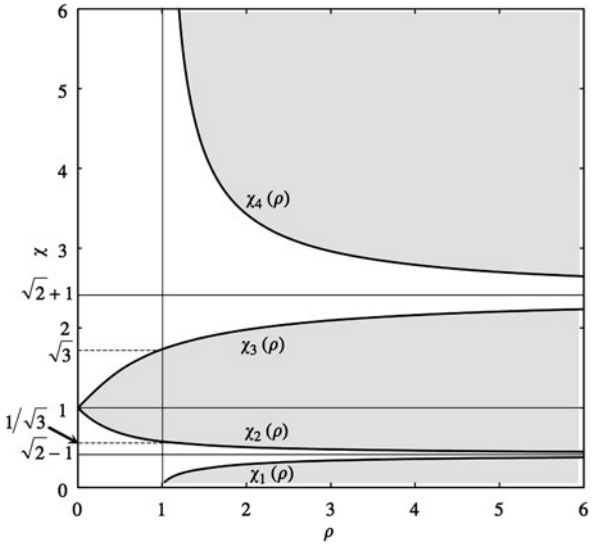

Fig. 2 Domain of the plane (ρ, χ) where solution $\varphi_{\delta\delta}$ exists (*shaded*)

Actually, only $\varphi_{\delta\delta}$ is an angle-ply solution, because the orientation angle corresponding to $\xi_1 = 1$ is $\delta = 0°$, while to $\xi_1 = -1$ corresponds $\delta = 90°$, so these two cases determine laminates with all the layers aligned along the x or y directions, respectively. The orientation angle giving solution $\varphi_{\delta\delta}$ is

$$\delta = \frac{1}{2} \arccos \xi_1^{st}. \tag{28}$$

Angle-ply solutions do not always exist because of the bounds $\xi \in [-1, 1]$, imposed to each lamination parameter, hence to ξ_1^{st} too. These bounds are satisfied for

$$\begin{aligned} &\rho > 1 \quad \text{and} \quad 0 < \chi \leq \chi_1(\rho), \\ &\rho \geq 0 \quad \text{and} \quad \chi_2(\rho) < \chi \leq \chi_3(\rho), \\ &\rho > 1 \quad \text{and} \quad \chi \geq \chi_4(\rho), \end{aligned} \tag{29}$$

where the functions $\chi_i(\rho)$, $i = 1, \ldots, 4$, are the solutions of the equations $\xi_1^{st} = \pm 1$ with $k = 0$ or 1:

$$\begin{aligned} \chi_1(\rho) &= \sqrt{\frac{3\rho - \sqrt{8\rho^2 + 1}}{\rho + 1}}, \qquad \chi_2(\rho) = \sqrt{\frac{3\rho - \sqrt{8\rho^2 + 1}}{\rho - 1}}, \\ \chi_3(\rho) &= \sqrt{\frac{3\rho + \sqrt{8\rho^2 + 1}}{\rho + 1}}, \qquad \chi_4(\rho) = \sqrt{\frac{3\rho + \sqrt{8\rho^2 + 1}}{\rho - 1}}. \end{aligned} \tag{30}$$

Conditions (29) determine, in the plane (ρ, χ), the region where angle-ply solutions exist; in Fig. 2, this region is shaded; inside it, the optimal solution is an

angle-ply laminate, outside it, the optimal solution is a unidirectional laminate, either at 0° or at 90°.

Computing the second derivative of the function in Eq. (25) gives

$$\frac{\partial^2 \varphi}{\partial \xi_1^2} = 4(-1)^k \frac{\rho}{\sqrt{1+\rho^2}} c_0(\chi);$$

therefore, once more, optimal solutions become antioptimal whenever k changes from 0 to 1. Namely, by Eq. (20), it can be easily seen that:

- if $(\rho > 1, 0 < \chi \leq \chi_1(\rho))$ or $(\rho > 1, \chi \geq \chi_4(\rho))$, then $\varphi_{\delta\delta} = \varphi_{\max}$ for $k = 1$ and $\varphi_{\delta\delta} = \varphi_{\min}$ for $k = 0$;
- if $(\rho \geq 0, \chi_2(\rho) < \chi \leq \chi_3(\rho))$, then $\varphi_{\delta\delta} = \varphi_{\max}$ for $k = 0$ and $\varphi_{\delta\delta} = \varphi_{\min}$ for $k = 1$.

We can see hence that anisotropy affects optimal solutions also in this case: the parameter k, determining the type of ordinary orthotropy, changes each optimal solution into an antioptimal one and vice versa, whilst parameter ρ, along with the geometric parameter χ, determines the region where the optimal solution is of the angle-ply type, i.e. the region where optimisation is meaningful. Actually, unidirectional laminates are limit solutions, and in such cases an optimization procedure, i.e. the computation of angle δ by Eq. (28), becomes unnecessary. Nevertheless, the value of these three solutions φ_{11}, φ_{22} and $\varphi_{\delta\delta}$ can be compared. It is not difficult to find the following result:

$$\begin{aligned} &\varphi_{11} > \varphi_{22} \Leftrightarrow \chi > 1, \\ &\varphi_{\delta\delta} > \begin{cases} \varphi_{11} \\ \varphi_{22} \end{cases} \Leftrightarrow \begin{cases} \sqrt{2} - 1 < \chi < \sqrt{2} + 1 & \text{if } k = 0, \\ 0 < \chi \sqrt{2} - 1 \text{ or } \chi > \sqrt{2} + 1 & \text{if } k = 1. \end{cases} \end{aligned} \tag{31}$$

These results are summarized in Fig. 3, which completely shows, along with Eqs. (26), (27) and (28), the influence of the two anisotropic dimensionless parameters k and ρ on the optimal and antioptimal solutions; in Fig. 2, the layer orientations of the different solutions are indicated by simple schemes.

More details can be found in [17]; finally, these cases show that anisotropy of the material actually has a great influence on the solution of an optimization problem; it can affect the uniqueness of the solution, it can switch an optimum into an antioptimum, it determines the size and shape of the feasible domain, and it affects, of course, the value of the minimum or maximum.

4 Design Problems of Laminates

Design problems concerning structural laminates can be of various types; in the most elementary cases, only some basic properties are of concern, e.g. extension orthotropy and bending-extension uncoupling. In some other cases, some minimal properties are asked for in addition, and in more involved cases, precise quantities

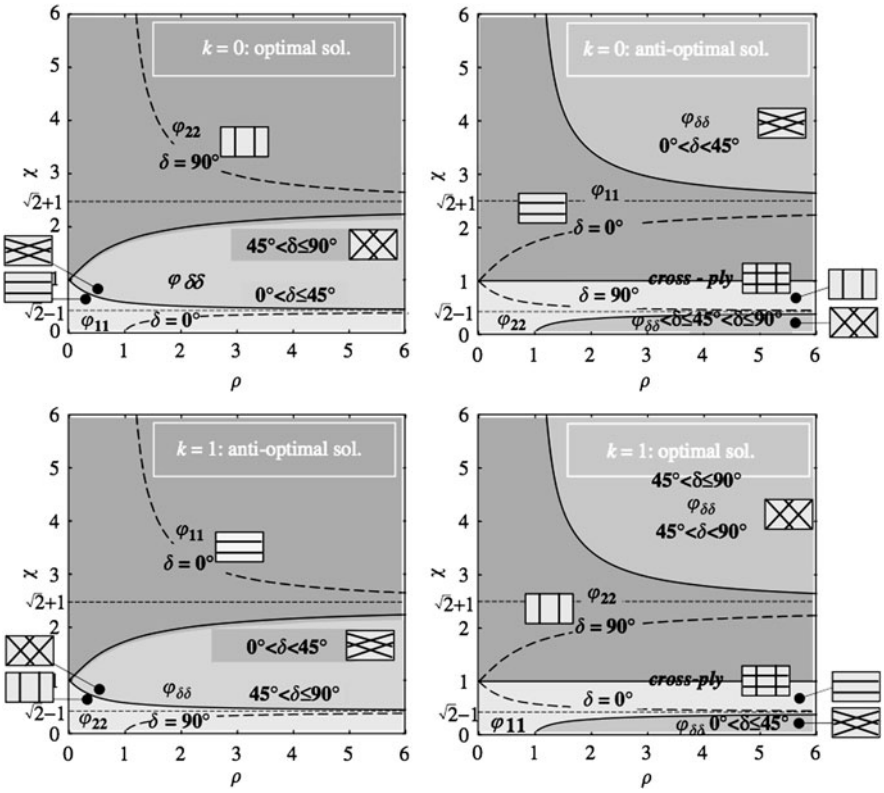

Fig. 3 Map of the optimal and antioptimal solutions

are to be maximized or minimized, like for instance compliance or vibration frequencies or strength. As already said in the introduction, usually designers use some simple sufficient conditions to ensure automatically the basic elastic properties, e.g. they use symmetric stacking sequences to automatically ensure bending-extension uncoupling. Under a mathematical point of view, this corresponds always to a severe shrinking of the feasible domain, dramatically lowering the number of possible optimal solutions. Vannucci and Verchery [22, 23], for instance, have shown that the number of uncoupled symmetric laminates is far less than the number of uncoupled and unsymmetrical laminates: limiting the search of an optimal uncoupled laminate to symmetrical stacking sequences corresponds, hence, to depriving the problem of the most part of possible candidates to be solution, and it is very likely that the true best solution is among the unsymmetrical sequences. Such a simple example shows why another approach to the design of laminates should be used, in which the design problem has to be formulated as an optimization problem including, besides the objective to be optimized, the basic elastic properties desired for the laminate, for instance in the form of constraints imposed to the problem. This approach is possible, and we illustrate it in the following of this section, classifying the design

problems of the laminates in three different classes, depending on the mathematical structure of the problem itself. Before, we give a rapid account of a special class of laminates, the quasi-homogeneous laminates, that can be profitably used in several cases of laminate optimal design problems.

4.1 Quasi-homogeneous Laminates

Thanks to the polar formalism, the concept of quasi-homogeneous laminates has been introduced in 1988 by Kandil and Verchery [11]; then, in 1992, Wu and Avery [30] have also used this concept, as well as Grédiac [4], who gave some approximated numerical solutions. Vannucci et al. [20, 22, 23] have shown the existence of a particular set of quasi-homogeneous laminates that they called *quasi-trivial solutions*, having the particularity of being not only exact solutions, but also the fact that in such cases quasi-homogeneity does not depend on the orientation of the layers, only on the stacking sequence.

Quasi-homogeneous laminates are defined as the laminates having the double property of being uncoupled and with the same behaviour in bending and in extension; if one introduces the homogeneity tensor $\mathbf{C}$,

$$\mathbf{C} = \mathbf{A}^* - \mathbf{D}^*, \tag{32}$$

then a laminate is quasi-homogeneous if and only if

$$\mathbf{B} = \mathbf{C} = \mathbf{O}. \tag{33}$$

Recalling Eqs. (5) and (7), the polar components of $\mathbf{C}$ are

$$\begin{cases} \check{T}_0 = 0; \\ \check{T}_1 = 0; \\ \check{R}_0 e^{4i\check{\Phi}_0} = \frac{1}{n^3} R_0 e^{4i\Phi_0} \sum_{j=1}^{n} c_j e^{4i\delta_j}; \\ \check{R}_1 e^{2i\check{\Phi}_1} = \frac{1}{n^3} R_1 e^{2i\Phi_1} \sum_{j=1}^{n} c_j e^{2i\delta_j}; \end{cases} \tag{34}$$

in Eq. (34) the coefficients c_j are given by

$$c_j = n^2 - d_j = 4n^2 + 6n + 4 - 12j(j - n - 1). \tag{35}$$

The interest of quasi-trivial quasi-homogeneous (QT–QH) laminates is due to the fact that they can be profitably used in optimization problems. In fact, they automatically ensure uncoupling and the same behaviour in extension and bending. So, several problems of laminates optimization can be drastically simplified if one decides to look for solutions within the set of QT–QH sequences because, on one side, uncoupling is automatically obtained and, on the other side, optimization can be done directly upon the extension properties, which is simpler than on the bending ones, and the same results will apply to the bending behaviour.

The QT–QH sequences have been used in the past for finding special laminates; for instance, Vannucci and Verchery [24] have shown the existence of five exact fully isotropic laminates with a minimum of 18 layers that are five quasi-trivial sequences, while Valot and Vannucci [13] have used the same type of sequences to give an exact solution for fully orthotropic laminates (the design of bending orthotropic laminates is a cumbersome problem that has been almost always neglected by designers because of its difficulty). Gong et al. [3] have used special QT–QH sequences with 16 plies to experimentally study the propagation of a crack in a laminate. More recently, some works of York, [31] and [32], show the interest of quasi-homogeneous laminates for special applications.

4.2 Design Problems of the First Class

A problem of the first class concerns only the design of basic elastic properties, like for instance bending-extension uncoupling, orthotropy, isotropy and so on. All problems of this kind can be formulated as follows:

$$\min_{P_j} I(P_j) = H_{rs} P_r P_s, \quad r, s = 1, \ldots, 18. \tag{36}$$

In the above equation, H_{rs} are the components of a 18×18 symmetric matrix, whose entries determine the objective of the problem to be solved, see [14]. The terms P_r are the eighteen polar parameters of the laminate, representing the tensors $\mathbf{A}^*$, $\mathbf{B}^*$ and $\mathbf{D}^*$; eventually, they are used in a dimensionless form, after diving them by a suitable modulus (e.g. the Euclidean norm of the stiffness tensor of the basic layer).

The form (36) is positive semi-definite; its absolute minima are zero valued, and they are the solution of the problem; hence, the problems of class 1 are reduced to the search for the minima (zeros) of the form (36); by its nature (cf. Eqs. (5), (6) and (7)), problem (36) is non-convex, and several minima can exist (usually, the number of solutions is infinite). So, a suitable numerical strategy is needed to effectively search for the minima. Some very effective methods are metaheuristics; we have successfully used Genetic Algorithms (GA) and Particle Swarm Optimization (PSO); both are very indicated for this class of problems, see [16, 27].

The problems of the first class formulated as in (36) concern exclusively elastic properties; nevertheless, by a similar approach, also other properties, like the thermal, hygral or piezoelectric ones, can be handled in the same manner.

Example 1 As a numerical example of the first-class problems, let us consider the following case: a 12-plies laminate, made of T300/5208 carbon-epoxy unidirectional layers, whose properties are summarized in Table 1 [12, 25].

For what concerns its elastic properties, it has to be isotropic in extension, $k = 0$ orthotropic in bending and uncoupled ($\mathbf{B}^* = \mathbf{O}$). In addition, its thermoelastic response has to be isotropic in membrane (i.e. the thermal expansion coefficients, for

Table 1 Properties of T300/5208 carbon-epoxy pre-preg layers (moduli in GPa)

E_1	E_2	G_{12}	ν_{12}	T_0	T_1	R_0	R_1	Φ_0	Φ_1
181	10.3	7.17	0.28	26.88	24.74	19.71	21.43	0°	0°

α_1 (°C^{-1})	α_2 (°C^{-1})	Thickness (mm)
2×10^{-8}	2.25×10^{-5}	0.125

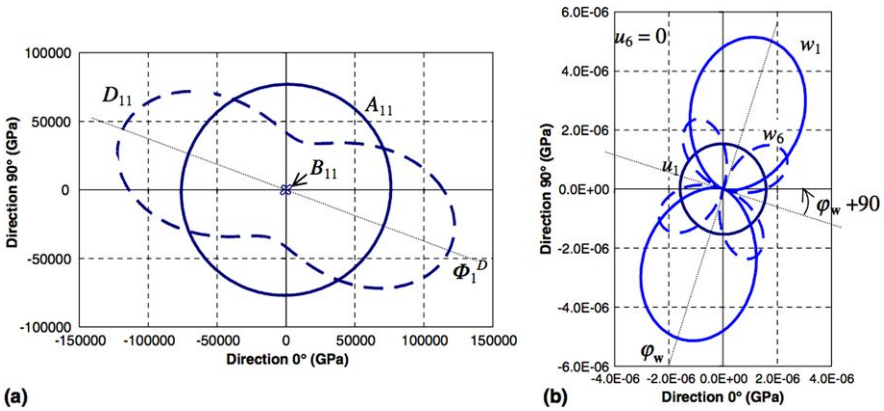

Fig. 4 Directional diagrams of some Cartesian components for the case test of Example 1: (**a**) elastic moduli; (**b**) thermal coefficients

a change of temperature uniform through the thickness, have to be the same in each direction), while under a linear temperature variation across the thickness of the laminate, this has to bend in a cylindrical way (i.e. the tensor of the coefficients of thermal curvature has to be orthotropic). This is a very cumbersome problem that has been solved using the GA BIANCA, [25], specially conceived for laminate optimization problems. The best solution found is (angles in degrees)

$$[0/-29.9/44.3/-61.8/89.3/61.8/31.5/-89.1/33.4/-71.7/-11.6/-28.1].$$

Figure 4 shows the directional diagrams of some of the Cartesian components of the elastic tensors and of the tensors of thermal coefficients. It is apparent that the extension behaviour is isotropic, the bending one orthotropic, both for the elastic and the thermal behaviour, and that the smallness of component B_{11} compared to A_{11} and D_{11} testifies, practically, of a null coupling.

4.3 Design Problems of the Second Class

The second class of problems concerns problems for which the objective function is still like in class 1, but in addition some constraints have to be satisfied. Generally

speaking, class 2 problems can be formulated as follows:

$$\min_{P_j} I(P_j) = H_{rs} P_r P_s, \quad j, r, s = 1, \ldots, 18, \\ \text{with } g_i(P_j) \leq 0, \ i = 1, \ldots, n_g, \tag{37}$$

with n_g the number of inequality constraints imposed to the problem. Hence, in this class we find classical minimal requirement problems, typical of engineering, but with the peculiarity that the objective is still a requirement concerning the basic elastic properties, just like in class 1.

Example 2 This is the case of a rectangular laminated plate with 12 plies, designed to be uncoupled and orthotropic in bending, with axes of orthotropy at 0° and 90°; the plate is simply supported, with side lengths along the axes x and y respectively equal to a and b. The minimal requirement imposed here is that the frequency of the first mode of the bending vibrations must be greater than a minimum specified value ω_0. So, the objective function is still $I(P_j)$, with $H_{rr} = 1$ for $r = 9, 10, 17, 18$, while the other components H_{rs} are null. The constraint is $\omega_{11} - \omega_0 \leq 0$ with ω_{11} given by (14).

The results of the numerical tests for this example refer to the case of a T300/5208 carbon-epoxy plate with sides $a = 1$ m, $b = 0.5$ m, designed to have $\omega_{11} \geq \omega_0 = 150\ \text{s}^{-1}$; the mass of the plate per unit of area is $\mu = 2.4\ \text{kg/m}^2$. To find a solution, we have used the PSO code ALE-PSO, [16]. The best result obtained is (angles in degrees)

[66.15/66.53/44.83/36.44/48.52/5.68/77.57/89.94/84.48/38.45/57.48/46.03].

For this sequence, the objective function is very close to zero (7.20×10^{-35}), while for the frequency, we get $\omega_{11} = 162.72\ \text{s}^{-1}$. We show in Fig. 5 the directional variation of two moduli, for bending and extension; the diagram shows clearly that the laminate is orthotropic in bending, with the axes of orthotropy aligned with the sides of the plate (axes x and y), while the extension behaviour is not orthotropic, as a consequence of the fact that no requirement has been imposed on this behaviour.

4.4 Design Problems of the Third Class

Problems of class 3 are classical optimization problems: an objective has to be minimized, with some constraints to be satisfied. But, in this particular case of laminates design, also some selected basic elastic properties have to be guaranteed. So, now the requirements concerning the elastic properties of the laminate play no more the role of the objective, but they become an equality constraints. This is possible because the form $I(P_j)$ determines the type of the elastic property and its value in correspondence of a solution is known: it is zero.

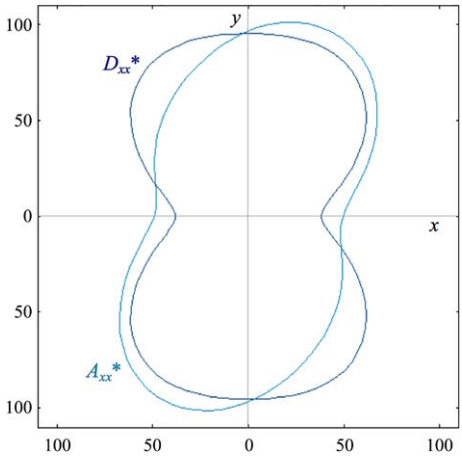

Fig. 5 Directional diagrams of some elastic Cartesian components for the case test of Example 2

So, generally speaking, a problem of the third class is formulated as follows:

$$\begin{aligned} &\min_{P_j} f(P_j) \\ &\quad \text{with } I(P_j) = H_{rs} P_r P_s = 0 \quad \text{and} \\ &\quad g_i(P_j) \leq 0,\ i = 1, \ldots, n_g. \end{aligned} \tag{38}$$

Of course, Eq. (38) can be easily generalized, considering for instance additional design variables and equality constraints. The true difference between this class of problems and the two others is in the fact that now the form $I(P_j)$ is no more the objective but rather an equality constraint. Really, by its algebraic nature, this is a hard constraint, and a formalization like (38) will be useful only if the numerical strategy used for the search of the solutions will be able to deal very effectively with hard equality constraints. We have implemented in the GA BIANCA a new strategy for handling constraints that we called ADP (*Automatic Dynamic Penalization*) that has revealed to be very effective in handling not only inequality constraints, but also equality constraints once these have been transformed, by a classical procedure, into two equivalent inequality constraints [27]. Actually, for the problem in (38), this can be done easily because the form $I(P_j)$ is positive semi-definite; hence, once chosen a small positive residual ε, problem (38) can be transformed into another equivalent one, depending only on inequality constraints:

$$\begin{aligned} &\min_{P_j} f(P_j) \\ &\quad \text{with } I(P_j) = H_{rs} P_r P_s \leq \varepsilon \quad \text{and} \\ &\quad g_i(P_j) \leq 0,\ i = 1, \ldots, n_g. \end{aligned} \tag{39}$$

The real advantage of the formulation in Eq. (38), or equivalently in (39), is that it is completely general: the design of the basic elastic properties of the laminate

being part of the problem itself, no restrictions are artificially imposed on the solutions, due to some simplifying assumptions. The problems of the optimal design of laminates is in this way completely formulated without restrictions, and the problem is now to dispose of a suitable, effective numerical tool for the search of the solutions; GAs like the code BIANCA have proven to be able to solve very effectively this kind of problems.

Example 3 As a numerical example, let us consider the following one: maximize the buckling load multiplier λ_{cr} for a simply supported rectangular laminate, acted on in-plane compressive distributed loads N_x and N_y along the boundary. The plate has to be $k = 1$ orthotropic in bending, with the axes of orthotropy aligned with the plate's sides, and bending-extension uncoupled. In such hypotheses, the buckling multiplier can be calculated using Eq. (13). We have added some supplementary requirements: the plate has to be $k = 1$ orthotropic also in extension, with the same axes of orthotropy as in bending; two constraints, minimal requirements, are imposed on the value of the Young's modulus E^m in extension, along the orthotropy directions, and in addition we admit discrete orientation angles that can take values each 1° only. Finally, this problem can be formulated as

$$\begin{aligned} &\max_{\delta_j}\left(\min_{p,q}\lambda_{cr}\right) \\ &\text{with } I(P_j) = H_{rs}P_rP_s \le \varepsilon, \\ &E_x^m \ge E_x^0, \\ &E_y^m \ge E_y^0. \end{aligned} \tag{40}$$

We have considered, as numerical application, the following values: $a/b = 1.5$, $N_x = N_y = 1$ N/mm, $\varepsilon = 10^{-4}$, $E_x^0 = 60$ GPa, $E_y^0 = 30$ GPa; the laminate is composed of 16 identical T300/5208 carbon-epoxy layers. The best solution found by the GA BIANCA, running with the ADP strategy, is (angles in degrees)

$$[-24/39/-47/37/32/-47/-6/-47/55/59/18/-38/-38/19/-40/42].$$

For this solution, we obtain $E_x^m = 60.61$ GPa, $E_y^m = 31.16$ GPa and $I(P_j) = 8.8 \times 10^{-5}$. We show in Fig. 6 the directional diagrams of some elastic moduli of the laminate solution. Once again, the coupling component is so small compared to the extension and bending ones that uncoupling can be considered as obtained. We remark the respect of the conditions of orthotropy in extension and in bending, along with the values of the two constraints on the value of the Young's modulus in extension.

4.5 General Remarks

Some general remarks can be done about the strategy shown above. First of all, it is completely general, so it lets, in principle, to attain all the solutions, in particular

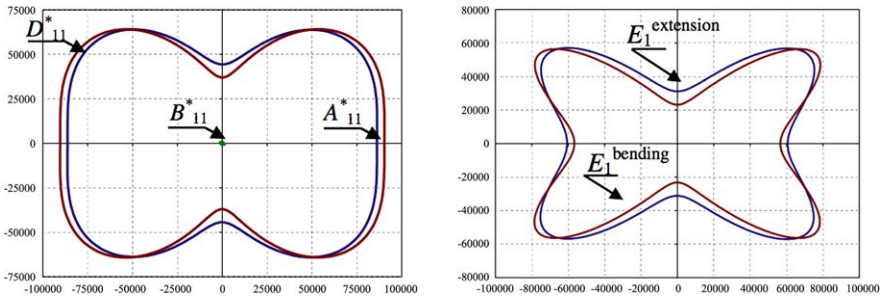

Fig. 6 Directional diagrams of some elastic Cartesian components and moduli for the case test of Example 3

true global optimal solutions. No restrictions, like for instance the symmetry of the stack, are imposed to the procedure. Generality means also that all the problems concerning the design of laminates can be formulated as problems of class 1, 2 or 3.

The approach is based on the use of the polar formalism, which has some advantages, mainly in the formalization of the elastic symmetries and also in the separation of the anisotropic from the isotropic part, this last being redundant (it cannot be modified) in all the cases of laminates composed by identical layers, which is by far the most common case.

The success of the approach depends on the use of a suitable numerical strategy for the search of the solutions; we have verified on several examples that PSO and especially GAs are particularly suited for these problems. Namely, we have proposed a strategy for handling constraints that reveals to be very effective and able to tackle also the problems of class 3 type, having hard equality constraints. The problems presented as examples are rather cumbersome and difficult, and we have not been able to find in the literature something comparable to them. Nevertheless, with this approach that we called *polar-genetic*, we are able to solve them.

5 Optimal Design Problems of Piezoelectric Laminates

The above approach can be used also in the case of multiphysics couplings, like for instance those deriving from the thermal or hygral behaviour or from the use of bonded piezoelectric patches, used as actuators and/or sensors. Some thermal and hygral problems have been considered by Vannucci and Vincenti [25]; all these problems are reduced to problems of class 1 type, like the one in Example 1, and for the sake of shortness, they will not be presented here; the reader is addressed to the cited paper for more details.

The design of laminates acted upon by piezoelectric patches can be very interesting in several applications. Also in this field, the use of the polar formalism can be very helpful. By this method, the invariants of the piezoelectric tensor in the bidimensional case [15] have been found. The number of different potential problems concerning smart piezoelectric laminates is very great, so it becomes necessary to be

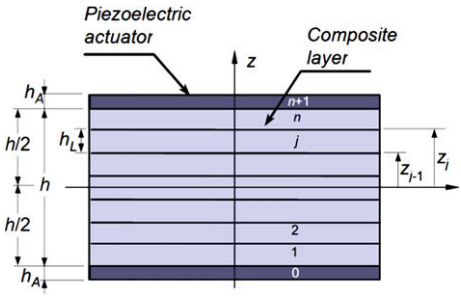

Fig. 7 General sketch of an SPL (Standard Piezoelectric Laminate)

specific. Some researches have been conducted by Vannucci and co-workers on what could be called a Standard Piezoelectric Laminate (SPL), see [19, 21] and [29]. This is a laminate composed of identical anisotropic layers; on its top and bottom surfaces two identical piezoelectric patches are perfectly bonded. These patches have an in-plane isotropic behaviour, under both the piezoelectric and elastic points of view (i.e. they are classical piezoelectric actuators, like for instance PZT patches). The patches are chosen and cannot be modified; this assumptions has a consequence: the whole piezoelectric part disappears from the optimal design process that will concern only the laminate. The general sketch of an SPL is shown in Fig. 7.

In [21], the problem of finding SPL with a direction of null piezoelectric expansion coefficient is addressed as an optimum problem in the framework of the polar formalism and analytically solved for the extension case. In [29], several problems concerning the case of the bending piezoelectric response are formulated; nevertheless, it is not possible to obtain an analytical solution for bending problems, so they are formulated just like a problem of class 1 and solved by the use of the GA BIANCA.

A different problem is dealt with in [19], and a novel approach is proposed. It is the case of an SPL designed to be uncoupled, orthotropic in bending and to have a bending piezoelectric response which is cylindrical. In other words, under the isotropic action of standard PZT actuators, the laminate will bend cylindrically; in addition, this piezoelectric bending has to be maximized when a difference of electric potential of equal amount but opposite sign is applied to the two actuators. This study was motivated by possible aerospace applications. Generally speaking, this is a class 3 problem; in fact, in the framework of the CLPT, by some simple passages the problem can be formalized as follows, see [19]:

$$\begin{aligned} &\max_{\delta_j} f = d_{12}^* + d_{22}^*, \\ &\quad \text{with } g_1 = d_{12}^* + d_{11}^* = 0, \\ &\quad g_2 \rightarrow \mathbf{B} = \mathbf{O}, \\ &\quad g_3 \rightarrow \mathbf{D} \text{ orthotropic}. \end{aligned} \tag{41}$$

In the above equation, d^*_{ij} are the Cartesian components of the tensor

$$\mathbf{d}^* = \mathbf{D}^{*-1} = \frac{h^3}{12}\mathbf{D}^{-1}, \tag{42}$$

which is the normalized compliance bending tensor in absence of coupling. The constraint g_1 imposes the cylindrical bending around axis x (i.e. null curvature of this axis), while the objective function prescribes the maximization of the bending of axis y.

The problem in (41) can be tackled numerically by the same procedure described in Sect. 4.4. Nevertheless, here another approach can be more effective. In fact, using the polar formalism and the lamination parameters, problem (41) can be transformed into two linked problems; the first one can be solved analytically and is very simple; the second one becomes a problem of class 1 type, so much easier to be solved numerically than a problem of class 3, like (41), because it is unconstrained. Addressing the reader to [19] for the details of the procedure, the result is the following one:

- Problem 1:

$$\begin{aligned} &\max_{\xi_0} f(\xi_0), \quad \text{where } f(\xi_0) = \frac{1}{4(2T_1 - T_0 - (-1)^k R_0 \xi_0)}, \\ &\text{with } g(\xi_0, \xi_1) = T_0 + (-1)^k R_0 \xi_0 - 2R_1 \xi_1 = 0, \\ &-1 \le \xi_1 \le 1, \\ &2\xi_1^2 - 1 \le \xi_0 \le 1. \end{aligned} \tag{43}$$

- Problem 2:

$$\min_{\delta_j} F(\delta_j) = \left(\xi_0 - \xi_0^s\right)^2 + \left(\xi_1 - \xi_1^s\right)^2 + \xi_2^2 + \xi_3^2 + \eta_0^2 + \eta_1^2 + \eta_2^2 + \eta_3^2. \tag{44}$$

In the above equations, T_0, T_1, $(-1)^k R_0$ and R_1 are the polar parameters of the basic layer (without loss of generality, we have chosen a frame fixing $\Phi_1 = 0$ for the basic layer), and ξ_2 and ξ_3 are the two remaining bending lamination parameters,

$$\begin{cases} \xi_2 = \frac{1}{n^3} \sum_{j=1}^n d_j \sin 4\delta_j, \\ \xi_3 = \frac{1}{n^3} \sum_{j=1}^n d_j \sin 2\delta_j, \end{cases} \tag{45}$$

and

$$\begin{cases} \eta_0 = \frac{1}{n^2} \sum_{j=1}^n b_j \cos 4\delta_j, \\ \eta_1 = \frac{1}{n^2} \sum_{j=1}^n b_j \cos 2\delta_j, \end{cases} \quad \begin{cases} \eta_2 = \frac{1}{n^2} \sum_{j=1}^n b_j \sin 4\delta_j, \\ \eta_3 = \frac{1}{n^2} \sum_{j=1}^n b_j \sin 2\delta_j \end{cases} \tag{46}$$

are the coupling lamination parameters, with the coefficients b_j given by (8). Finally, ξ_0^s and ξ_1^s are the solutions of Problem 1; these ones must be inserted into Problem 2 to find a stacking sequence satisfying all the requirements. Problem 2 is a classical problem of class 1, and, being unconstrained, it is particularly easy to be solved numerically. About Problem 1, its solution is elementary; in fact, the constraint $g(\xi_0, \xi_1)$ is a straight line, and on it the objective function increases with ξ_0 if $k = 0$, while it decreases if $k = 1$. Hence, once again k switches an optimal solution to an antioptimal one, and, more important here, the solution is on the boundary of the feasible domain, which is a sector of parabola just like the one sketched in Fig. 1, but with ξ_0 and ξ_1 along the axes. So, only two situations are possible:

- the straight line $g(\xi_0, \xi_1) = 0$ crosses the curved boundary only in the two points

$$A = \left(\xi_1^s = \frac{R_1 + \sqrt{R_1^2 - 2(-1)^k R_0[T_0 - (-1)^k R_0]}}{2(-1)^k R_0}, \quad \xi_0^s = 2\left(\xi_1^s\right)^2 - 1\right),$$
$$B = \left(\xi_1^s = \frac{R_1 - \sqrt{R_1^2 - 2(-1)^k R_0[T_0 - (-1)^k R_0]}}{2(-1)^k R_0}, \quad \xi_0^s = 2\left(\xi_1^s\right)^2 - 1\right); \tag{47}$$

- the straight line $g(\xi_0, \xi_1) = 0$ crosses once the boundary $\xi_0 = 1$ and once the curved boundary:

$$A' = \left(\xi_1^s = \frac{T_0 + (-1)^k R_0}{2R_1}, \quad \xi_0^s = 1\right),$$
$$B' = \left(\xi_1^s = \frac{R_1 - \sqrt{R_1^2 - 2(-1)^k R_0[T_0 - (-1)^k R_0]}}{2(-1)^k R_0}, \quad \xi_0^s = 2\left(\xi_1^s\right)^2 - 1\right); \tag{48}$$

It should be noticed that Problem 1 determines the lamination point and that it depends only on the mechanical characteristics of the basic layer (its polar parameters). Hence, all the laminates made by the same material have the same solution for Problem 1, i.e. the same lamination point and hence the same normalized tensors, i.e. the same elastic behaviour, regardless of the number of layers.

Example 4 As an example, let us consider the case of a laminate composed of T300/5208 carbon epoxy identical layers; in such a case, the solution is given by point A above (Eq. (47)) and is $\xi_1^s = 0.88$, $\xi_0^s = 0.55$, which brings to the following value of the optimum: $f_{\max} = 0.021$, Eq. (43). The lamination point solution of Problem 1, once inserted into Eq. (44), defines Problem 2 that can be solved numerically to find a laminate realizing the properties prescribed by the solution of Problem 1. In this case we have used the PSO code ALE-PSO for looking for a 16-layer laminate with the additional constraint to choose the possible orientation

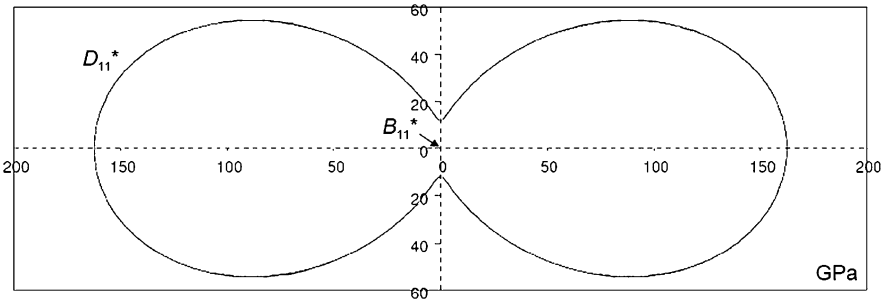

Fig. 8 Directional diagrams of D_{11}^* and B_{11}^* for the case of Example 5

angles among the multiples of 5° (discrete problem). The best solution found is (angles in degrees)

$$[-20/5/0/15/15/5/40/45/90/-10/20/-15/10/5/20/-15],$$

which gives directional diagrams of D_{11}^* and B_{11}^* shown in Fig. 8; these diagrams confirm that the laminate is orthotropic in bending, with orthotropy axes parallel to the coordinate axes, and that it is uncoupled.

6 Topological Optimization of the Anisotropy Fields

Structural optimization is the process of designing structures that give the best response to a given set of criteria. Topology optimization allows for the definition of the optimal distribution of material, within a given domain and under given loads, with respect to a given criterion (e.g. maximizing global stiffness).

Applied to composite materials such as laminates, Vincenti and Desmorat [7, 8, 10, 28] developped a methodology of topology optimization of the anisotropic fields that is twofold: it involves structural design—via topology optimization—and the definition of the local architecture of the material (i.e. fibre orientations and stacking sequence), which is likely to change from one point of the structure to another one, leading to pointwise variable stiffness laminates. The optimization methodology combined with the polar method can be applied to both in-plane loading and bending loading. The use of the polar parameters allows us to solve independently the problem of designing the lamination of the optimized structure.

6.1 Structural Optimization Problem

Two assumptions are made: in-plane only or bending only loading and bending-extension uncoupling.

Because of uncoupling between extension and bending, the compliance matrices $\mathbf{a}$ and $\mathbf{d}$ of the laminate for extension and bending are respectively $\mathbf{a} = \mathbf{A}^{-1}$ and $\mathbf{d} = \mathbf{D}^{-1}$, and the normalized compliance matrices $\mathbf{a}^*$ and $\mathbf{d}^*$ in membrane and bending respectively are such that

$$\mathbf{a} = \frac{1}{h}\mathbf{a}^*, \qquad \mathbf{d} = \frac{12}{h^3}\mathbf{d}^*. \tag{49}$$

The objective is to maximize the global stiffness of an elastic plate. This objective can be realized by minimizing the compliance G, which is twice the energy of deformation in linear elasticity:

$$G = \int_S \psi S_{ijkl}\sigma_{ij}\sigma_{kl}\, dS, \tag{50}$$

in which the stress $\sigma_{\alpha\beta}$ and the homogenized stiffness matrix $\mathbf{S}$ are defined as:

- in extension: $\sigma_{\alpha\beta} = N_{\alpha\beta}$ (membrane stresses), $\mathbf{S} = \mathbf{a}^*$ and $\psi = \frac{1}{h}$;
- in bending: $\sigma_{\alpha\beta} = M_{\alpha\beta}$ (bending moments), $\mathbf{S} = \mathbf{d}^*$ and $\psi = \frac{12}{h^3}$.

The optimization criterion is written in the same generic form in extension or in bending. To simplify the notation, we denote by t_0, t_1, r_0, r_1, φ_0 and φ_1 the polar parameters of $\mathbf{S}$ (i.e. of $\mathbf{a}^*$ or $\mathbf{d}^*$) and T_0, T_1, R_0, R_1, Φ_0 and Φ_1 those of S^{-1} (i.e. of $\mathbf{A}^*$ or $\mathbf{D}^*$).

In the case of a laminate with identical orthotropic layers, the elementary layer parameters T_0^{EL}, T_1^{EL}, R_0^{EL}, R_1^{EL}, K^{EL} are given. We will consider orthotropic elementary layers with $K^{\mathrm{EL}} = 0$, which corresponds for example to the most part of unidirectional carbon-epoxy layers (see [10] for a more general discussion).

Because the layers are identical, the polar isotropy parameters of the laminate are equal to those of the elementary layer: $T_0 = T_0^{\mathrm{EL}}$ and $T_1 = T_1^{\mathrm{EL}}$ for both $\mathbf{A}^*$ and $\mathbf{D}^*$. Considering orthotropic laminates, the orthotropy shape is represented by the polar parameter $K \in \{0, 1\}$. The optimization parameters are then the polar parameters (R_0, R_1, K) and the orientation Φ_1 of the orthotropic homogenized laminate.

Two types of optimization constraints are to be considered:

- *Thermodynamic admissibility*: The polar parameters R_0 and R_1 satisfy the conditions

$$\begin{cases} R_0 < T_0^{\mathrm{EL}}, \\ T_1^{\mathrm{EL}}[T_0^{\mathrm{EL}} + (-1)^K R_0] - 2R_1^2 > 0. \end{cases} \tag{51}$$

- *Feasibility constraints*: The polar parameters R_0 and R_1, of $\mathbf{A}^*$ or $\mathbf{D}^*$, are bounded by those of the elementary layer:

$$\begin{cases} R_0 \in [0, R_0^{\mathrm{EL}}], \\ R_1 \in [0, R_1^{\mathrm{EL}}]. \end{cases} \tag{52}$$

For displacements boundary conditions fixed to zero, the optimization problem takes the form of a double minimization with respect to the polar parameters

(R_0, R_1, K, Φ_1) and to statically admissible stress (S.A.) τ_{ij} (i.e. satisfying the equilibrium equations and the boundary conditions in terms of forces):

$$\min_{(R_0,R_1,K,\Phi_1)} G = \min_{(R_0,R_1,K,\Phi_1)} \min_{\tau\ S.A.} \left[\int_\Omega \psi S_{ijkl} \tau_{ij} \tau_{kl}\, dS \right]. \tag{53}$$

6.2 Structural Optimization Algorithm

The use of the algorithm presented in this section allows for performing the minimization of the compliance and for finding the associated distributed fields of polar parameters (R_0, R_1, K) and of orientation Φ_1 of a homogenized orthotropic behaviour. The problem of finding, from the distributed optimal field, an associated layup of a laminated plate will be considered in Sect. 6.3.

The structural optimization problem (53) is solved by the convergent optimization algorithm introduced by Allaire and Kohn [1] in which every iteration is composed of two parts:

- local minimizations with respect to optimization parameters with a fixed stress field (i.e. for every finite element),
- one global minimization with respect to the stress field with fixed optimization parameters (i.e. a finite element calculation).

The local minimization problem to be solved during the iteration of the optimization algorithm reads

$$\begin{aligned} &\min_{(R_0,R_1,K,\Phi_1)} G(R_0, R_1, K, \Phi_1), \\ &\text{such that} \quad \begin{cases} R_0 < T_0^{\mathrm{EL}}, \\ T_1^{\mathrm{EL}}[T_0^{\mathrm{EL}} + (-1)^K R_0] - 2R_1^2 > 0, \\ 0 \le R_0 \le R_0^{\mathrm{EL}}, \\ 0 \le R_1 \le R_1^{\mathrm{EL}}. \end{cases} \end{aligned} \tag{54}$$

This local optimization problem, which is more general than the optimisation problem with respect to the orientation only considered by Cheng and Pedersen [2], is solved analytically [7, 10].

The optimal orientation Φ_1^{opt} corresponds to the main direction of the maximum principal stress:

$$\Phi_1^{\mathrm{opt}} = \mathrm{direction}\big(\max\big(|\sigma_{\mathrm{I}}|, |\sigma_{\mathrm{II}}|\big)\big), \tag{55}$$

where σ_{I}, σ_{II} represent the principal stresses in membrane or in bending.

Locally, the stress state is described by the polar parameters $T = \frac{\sigma_{\mathrm{I}}+\sigma_{\mathrm{II}}}{2}$ and $R = \frac{\sigma_{\mathrm{I}}-\sigma_{\mathrm{II}}}{2}$ and characterized by the parameter $X = \frac{R}{|T|}$. The optimal values of R_0, R_1 and K are described by three types of solutions with increasing values of X:

- **Case 1** (Free Lamination Sequence): for $0 \leq X \leq \frac{R_1^{\mathrm{EL}}}{T_1^{\mathrm{EL}}}$,

$$K \in \{0, 1\}, \quad R_0^{\min} \leq R_0^{\mathrm{opt}} \leq R_0^{\max}, \qquad R_1^{\mathrm{opt}} = T_1^{\mathrm{EL}} X, \tag{56}$$

such that

$$\text{for } K = 0, \begin{cases} R_0^{\min} = \max\{2T_1^{\mathrm{EL}} X^2 - T_0^{\mathrm{EL}}; 0\}, \\ R_0^{\max} = R_0^{\mathrm{EL}}; \end{cases}$$

$$\text{for } K = 1, \begin{cases} R_0^{\min} = 0, \\ R_0^{\max} = \min\{T_0^{\mathrm{EL}} - 2T_1^{\mathrm{EL}} X^2; R_0^{\mathrm{EL}}\}. \end{cases}$$

- **Case 2** (Unidirectional Lamination Sequence): for $\frac{R_1^{\mathrm{EL}}}{T_1^{\mathrm{EL}}} \leq X \leq \frac{T_0^{\mathrm{EL}} + R_0^{\mathrm{EL}}}{2R_1^{\mathrm{EL}}}$,

$$K = 0, \qquad R_0^{\mathrm{opt}} = R_0^{\mathrm{EL}}, \qquad R_1^{\mathrm{opt}} = R_1^{\mathrm{EL}}. \tag{57}$$

- **Case 3** (Cross-ply Lamination Sequence): for $(T_0^{\mathrm{EL}} + R_0^{\mathrm{EL}})/2R_1^{\mathrm{EL}} \leq X$,

$$K = 0, \qquad R_0^{\mathrm{opt}} = R_0^{\mathrm{EL}}, \qquad R_1^{\mathrm{opt}} = \frac{T_0^{\mathrm{EL}} + R_0^{\mathrm{EL}}}{2X}. \tag{58}$$

6.3 Optimal Design of the Stacking Sequence

On the local scale (i.e. at every point within the structure), the search for a stacking sequence corresponding to the optimal values of the distributed polar parameters needs to be performed. It requires to formulate and solve a new local optimization problem with respect to optimization parameters relative to the laminate layup.

Let us consider a single element within the plate under in-plane or bending loads. For this element, topology optimization produced a couple of optimal polar components $(R_0^{\mathrm{opt}}; R_1^{\mathrm{opt}})$ for membrane or bending loading.

The optimal material is chosen as an orthotropic, uncoupled laminate made of n identical layers (i.e. with the same thickness and the same material). The latter condition ensures that polar components (T_0, T_1) of $\mathbf{A}^*$ or $\mathbf{D}^*$ are fixed and equal to those of the elementary layer.

Therefore, the optimization parameters of this new local optimization problem are the orientation angles δ_k, $k = 1, \ldots, n$, of the fibres within the kth layer, expressed in the element's orthotropy axes. The local optimization problem, in case of membrane or bending loading, can be formulated as:

$$\text{given } \left(R_0^{\mathrm{opt}}; R_1^{\mathrm{opt}}\right), \text{find}\{\delta_1, \ldots, \delta_n\} \text{ such that } \begin{cases} R_0 = R_0^{\mathrm{opt}}, \\ R_1 = R_1^{\mathrm{opt}}. \end{cases}$$

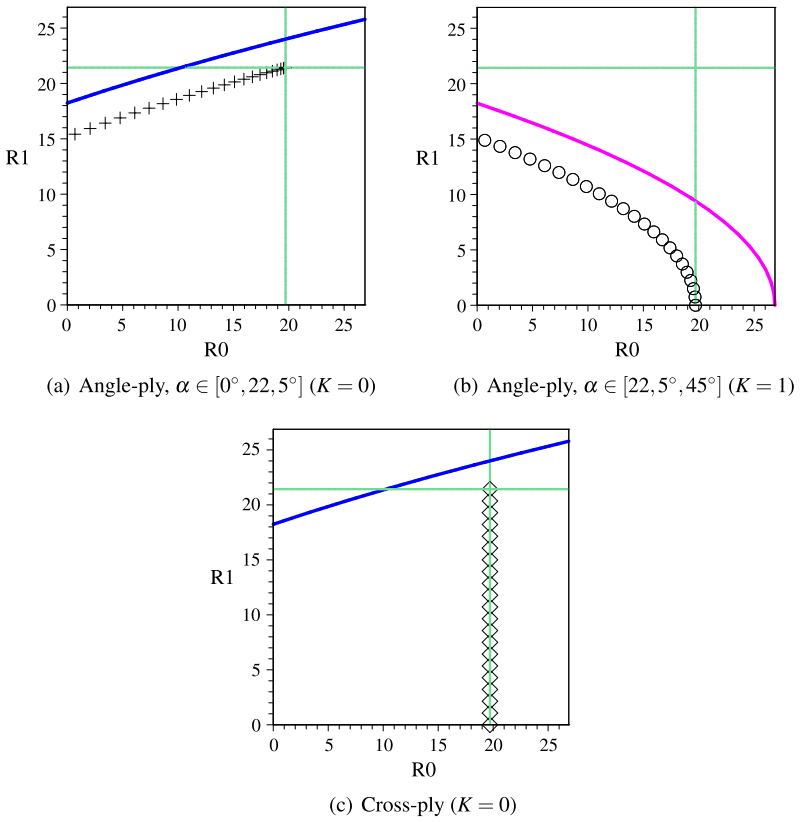

(a) Angle-ply, $\alpha \in [0°, 22,5°]$ $(K = 0)$

(b) Angle-ply, $\alpha \in [22,5°, 45°]$ $(K = 1)$

(c) Cross-ply $(K = 0)$

Fig. 9 Admissibility of angle-ply or cross-ply laminates with respect to polar parameters

An analytical resolution method for the problem is found through the use of closed-form relations linking lamination parameters to the elastic properties of the laminate. Two specific types of laminates for which this link is easily written and workable are considered, cross-ply laminates (orthogonal layers) and angle-ply laminates. For these laminates, the lamination sequence is described with only two orientations (even though the actual sequence remains undetermined): $\{0°, 90°\}$ for cross-ply laminates and $\{\alpha, -\alpha\}$ for angle-ply laminates, with $\alpha \in [0°, 45°]$. Considering specific stacking sequences assuring uncoupled behaviour, there is only one independent optimization parameter remaining: the relative thickness h (ratio of $0°$ layers thickness over total thickness) for cross-ply laminates and the orientation angle α for angle-ply laminates.

The optimization problem is solved by replacing the optimal moduli $(R_0^{\text{opt}}, R_1^{\text{opt}})$ in the closed-form relations relating the polar parameters to the relative thickness for cross-ply laminates or to the orientation angle for angle-ply laminates. Figure 9 shows, in the $(R_0$–$R_1)$ axis system, the laminate design space. Its bounds are the maximal values of the moduli (i.e. those of the elementary layer) on one hand and thermodynamic admissibility conditions on the other hand. They are represented

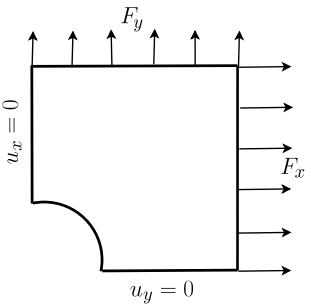

Fig. 10 Schematic representation of the centre-hole plate under membrane loading

respectively by the solid straight lines and the solid curve on each figure. The orthotropy shape K of the material influences the shape of the design space.

Within these different design spaces, the symbols represent the properties obtained for several values of the polar parameters, be it for angle-ply or cross-ply laminates. Figure 9(a) shows the characteristic points (crosses) of an angle-ply with $K = 0$ ($\alpha \in [0°, 22, 5°]$), Fig. 9(b) those (circle points) of an angle-ply with $K = 1$ ($\alpha \in [22, 5°, 45°]$), and finally Fig. 9(c) those (square points) of a cross-ply laminate.

It is proved that the cross-ply laminates are acceptable optimal solutions for every case (cases 1, 2 and 3), while angle-ply laminates are acceptable optimal solutions only for cases 1 and 2 (recalling that these results are valid in membrane only *and* in bending only cases). The fact that the cross-ply is an optimal layup in membrane loading was demonstrated by Hammer et al. [5, 6]. The extension of this result to bending, and the optimality of the angle-ply in cases 1 and 2 are new results.

6.4 Numerical Example: Centre-Hole Plate Under Membrane Loads

The structure and the boundary conditions (forces and displacements) considering the symmetries of the problem are shown in Fig. 10. The line load F_x is equal to twice the line load F_y. The elementary layer is made of carbon-epoxy T300/5208, whose polar components are given in Table 1.

The initial polar parameters are those of a unidirectional laminate ($R_0 = R_0^{\mathrm{EL}}$, $R_1 = R_1^{\mathrm{EL}}$) aligned with the x-axis ($\Phi_1 = 0$). During the local minimization steps, the optimal value of R_0^{opt} is chosen equal to R_0^{EL} in case 1. The optimal distributions of polar components are shown in Fig. 11. The case distribution is presented in Fig. 12. It is worth noting that only cases 1 and 2 occur. During the optimization process, the compliance decreases by 65%, while the maximal displacement decreases by 80%.

For cross-ply solutions, the local orientations of the layers are already determined and equal to $\{\Phi_1^{\mathrm{opt}}; \Phi_1^{\mathrm{opt}} + \frac{\pi}{2}\}$. The layup parameter is the relative thickness of plies

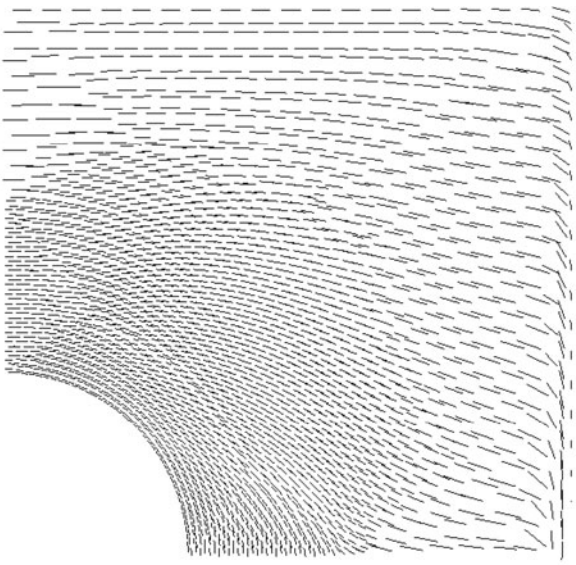

(a) Optimal orthotropy orientation Φ_1^{opt}

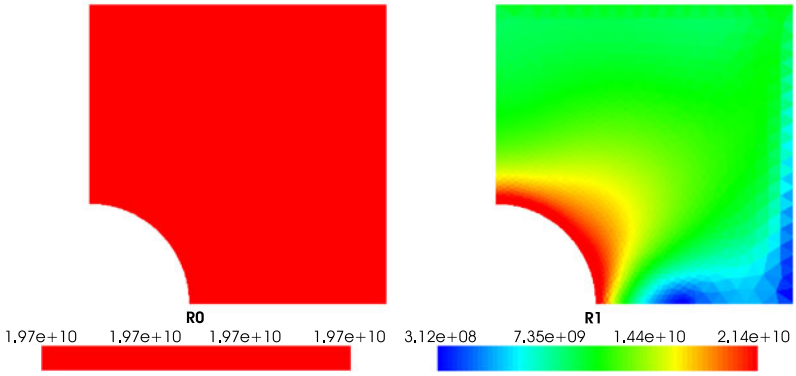

(b) Optimal polar parameter R_0^{opt} (c) Optimal polar parameter R_1^{opt}

Fig. 11 Optimal polar parameters

oriented at the angle Φ_1^{opt}, shown in Fig. 13. The variations of h coincide with those of R_1^{opt} because they are linearly related: $R_1 = R_1^{\text{EL}}(2h - 1)$.

For an angle-ply solution, we consider lamination sequences that lead to uncoupled behaviour. The principal orthotropy direction is Φ_1^{opt}. Figures 14(a) and 14(b) show the local fibre orientations of the layers corresponding to $\delta_1 = \Phi_1^{\text{opt}} + \alpha^{\text{opt}}$ and $\delta_2 = \Phi_1^{\text{opt}} - \alpha^{\text{opt}}$.

This example demonstrates that it is possible to design laminated cross-ply or angle-ply plates that are optimal solutions to the problem of the centre-hole plate

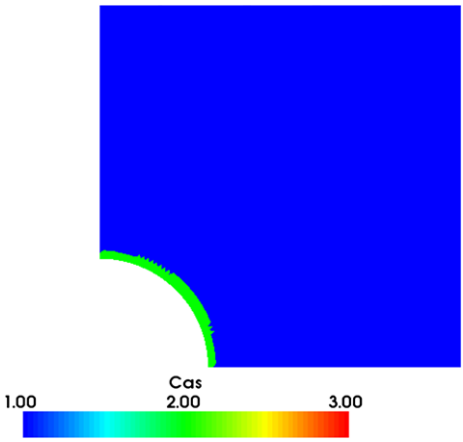

Fig. 12 Distribution of cases in the optimal state

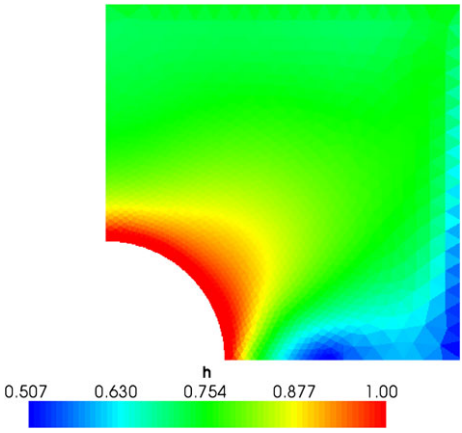

Fig. 13 Optimal relative thickness distribution for a cross-ply laminate

under in-plane loads. The use of the polar method has permitted to find the optimal angle-ply plate solution.

7 Final Remarks and Conclusion

We have shown some recent developments in the field of laminates design. They are mainly based on the use of the polar formalism that allows an effective representation of anisotropy in terms of tensor invariants. The approach proposed is completely general and has allowed us to deal with complicate problems, never considered before in the literature. The examples reported in the paper show that it is today possible to tackle effectively any problem of laminates design in a completely general way, without the use of simplifying and limiting assumptions. The polar formalism has proven to be effective also in a very new field, the design of the anisotropy fields, allowing for a local tailoring of laminates, which is today possible,

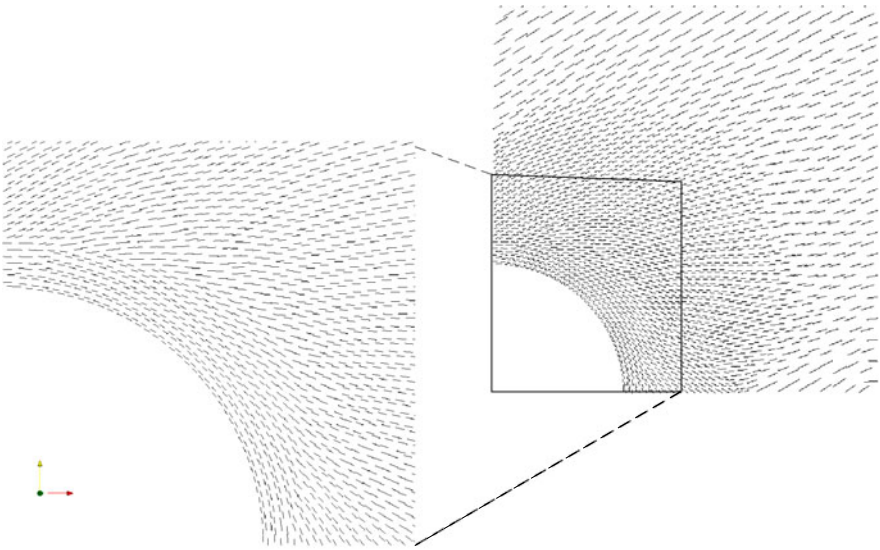

(a) δ_1-oriented layers ($\delta_1 = \Phi_1^{opt} + \alpha^{opt}$)

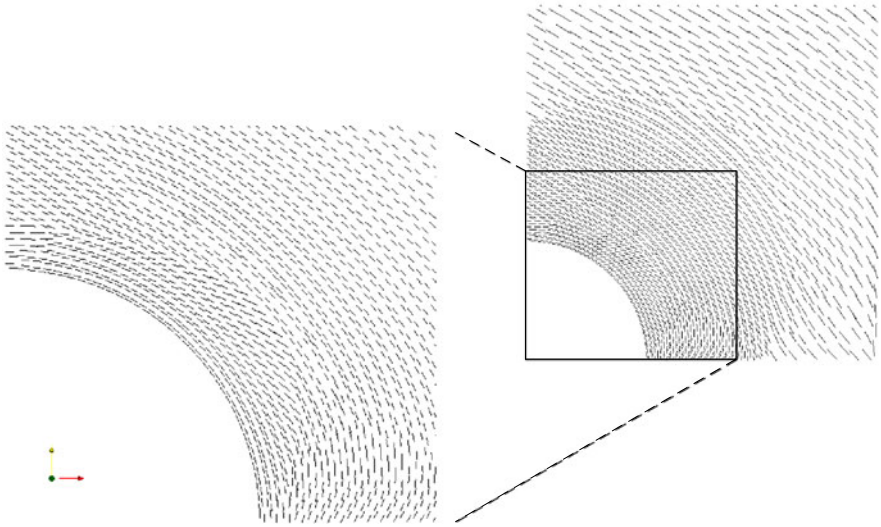

(b) δ_2-oriented layers ($\delta_2 = \Phi_1^{opt} - \alpha^{opt}$)

Fig. 14 Representation of local fibre orientations within δ_1/δ_2 plies for an angle-ply laminate

under a practical point of view, by the use of numerically controlled machineries. Multiphysics problems can be considered too, in a very effective way, and this is rather interesting for modern applications, like smart structures. The effectiveness of the approach is based, on one side, on the polar formalism and, on the other side, on a robust numerical strategy for the search of solutions. We have used two kinds of metaheuristics, specially conceived for the optimal design of laminates,

the GA BIANCA and the PSO code ALE-PSO. Both have proven to be very effective and robust for solving the different problems that we have formulated. Several other problems are still waiting to be solved, namely those concerning the design of laminated structures with respect to strength or to other resistance, in a generalized sense, criteria, or the optimal design of thermally stable laminated structures. Research is going on in these directions.

References

1. Allaire, G., Kohn, R.V.: Optimal design for minimum weight and compliance in plane stress using external micro structures. Eur. J. Mech. A, Solids **12**, 839–878 (1993)
2. Cheng, G., Pedersen, P.: On sufficiency conditions for optimal design based on extremum principles of mechanics. J. Mech. Phys. Solids **45**, 135–150 (1997)
3. Gong, X.J., Vannucci, P., Verchery, G.: Effect of adjacent layer fiber orientation on the resistance of laminates to delamination fracture. In: Proc. of ICCM13—International Conference on Composite Materials 13, Beijing (2001)
4. Grédiac, M.: A procedure for designing laminated plates with required stiffness properties. Application to thin quasi-isotropic quasi-homogeneous uncoupled laminates. J. Compos. Mater. **33**, 1939–1956 (1999)
5. Hammer, V.B., Bendsoe, M., Lipton, R., Pedersen, P.: Parameterization in laminate design for optimal compliance. Int. J. Solids Struct. **34**, 415–434 (1997)
6. Hammer, V.B.: Optimal laminate design subject to single membrane loads. Struct. Multidiscip. Optim. **17**, 65–73 (1999)
7. Jibawy, A., Julien, C., Desmorat, B., Vincenti, A., Léné, F.: Optimisation de plaques stratifiées en représentation polaire. In: Proceedings of the 9th Colloque National en Calcul des Structures, Giens, France, vol. 1, pp. 499–504 (2009)
8. Jibawy, A.: Optimisation structurale de coques minces composites stratifiées. PhD Thesis, Université Pierre et Marie Curie (2010)
9. Jones, R.M.: Mechanics of Composite Materials. McGraw-Hill, New York (1975)
10. Julien, C.: Conception optimale de l'anisotropie dans les structures stratifées à rigidité variable par la méthode polaire-génétique. PhD Thesis, Université Pierre et Marie Curie (2010)
11. Kandil, N., Verchery, G.: New methods of design for stacking sequences of laminates. In: Proc. of CADCOMP88–Computer Aided Design in Composite Materials 88. Southampton, UK (1988)
12. Tsai, S.W., Hahn, T.: Introduction to Composite Materials. Technomic, Lancaster (1980)
13. Valot, E., Vannucci, P.: Some exact solutions for fully orthotropic laminates. Compos. Struct. **69**, 157–166 (2005)
14. Vannucci, P.: Designing the elastic properties of laminates as an optimisation problem: A unified approach based on polar tensor invariants. Int. J. Struct. Multidiscip. Optim. **31**, 378–387 (2006)
15. Vannucci, P.: The polar analysis of a third order piezoelectricity-like plane tensor. Int. J. Solids Struct. **44**, 7803–7815 (2007)
16. Vannucci, P.: ALE-PSO: an adaptive swarm algorithm to solve design problems of laminates. Algorithms **2**, 710–734 (2009)
17. Vannucci, P.: Influence of invariant material parameters on the flexural optimal design of thin anisotropic laminates. Int. J. Mech. Sci. **51**, 192–203 (2009)
18. Vannucci, P.: On special orthotropy of paper. J. Elast. **99**, 75–83 (2010)
19. Vannucci, P.: A new general approach for optimising the performances of smart laminates. Mech Adv. Math. Struct. **15**, 558–568 (2012)
20. Vannucci, P., Gong, X.J., Verchery, G.: Determination des stratifies quasi-homogènes par l'approche polaire. In: Proc. of JNC11—11 èmes Journées Nationales sur les Composites, Arcachon, France (1998)

21. Vannucci, P., Pouget, J.: Laminates with given piezoelectric expansion coefficients. Mech. Adv. Mat. Struct. **13**, 419–427 (2006)
22. Vannucci, P., Verchery, G.: A special class of uncoupled and quasi-homogeneous laminates. Compos. Sci. Technol. **61**, 1465–1473 (2001)
23. Vannucci, P., Verchery, G.: Stiffness design of laminates using the polar method. Int. J. Solids Struct. **38**, 9281–9294 (2001)
24. Vannucci, P., Verchery, G.: A new method for generating fully isotropic laminates. Compos. Struct. **58**, 75–82 (2002)
25. Vannucci, P., Vincenti, A.: The design of laminates with given thermal/hygral expansion coefficients: A general approach based upon the polar-genetic method. Compos. Struct. **79**, 454–466 (2007)
26. Verchery, G.: Les invariants des tenseurs d'ordre 4 du type de l'élasticité. In: Proc. of Colloque Euromech 115, Editions du CNRS, Villard-de-Lans, France (1979)
27. Vincenti, A., Ahmadian, M.R., Vannucci, P.: BIANCA: A genetic algorithm to solve hard combinatorial optimisation problems in engineering. J. Glob. Optim. **48**, 399–421 (2010)
28. Vincenti, A., Desmorat, B.: Optimal orthotropy for minimum elastic energy by the polar method. J. Elast. **102**, 55–78 (2011)
29. Vincenti, A., Vannucci, P.: Optimal design of smart composite laminates by the polar method and the genetic algorithm BIANCA. In: Proc. of 3rd European Conference on Computational Mechanics—Solids, Structures and Coupled Problems in Engineering, Lisbon (2006)
30. Wu, K.M., Avery, B.L.: Fully isotropic laminates and quasi-homogeneous laminates. J. Compos. Mater. **26**, 210–2117 (1992)
31. York, C.B.: Characterization of nonsymmetric forms of fully orthotropic laminates. J. Aircr. **46**, 1114–1125 (2009)
32. York, C.B.: Unified approach to the characterization of coupled composite laminates: Benchmark configurations and special cases. J. Aerosp. Eng. **23**, 219–242 (2010)

The Warlike Interest in Impact Theories

Piero Villaggio

1 The Neolithic Revolution and the Advent of Fortresses

According to climatologists (Burroughs [1, p. 24]), the latest ice age (Wurmian) ended 25 000 years ago, and the present interglacial age started with the prospect of lasting 50 000 years at least. In the beginning, the global warming was continually adjusting by huge shifts, but, thereafter, the turbulent climate became stable so that, about 15 000 years ago, the temperature rose to values comparable with those of our modern times.

This stabilizations of the climate to higher temperatures and the consequent melting of large iced zones determined an unpredictable enlargement of habitable regions and the birth of agriculture and animal-husbandry. Humans, from being hunters and gatherers, became farmers. As Diamond describes in one of his books [2, p. 180–191], this conversion not only permitted the accumulation and conservation of food, but caused a radical change in the way of life. People had more time to communicate with each other, transmit technical knowledge and poetry. The average life span doubled.

Unfortunately, the progress was inhomogeneous. The geographic map of the distribution of population about 10 000 years ago in the Mediterranean basin shows the contemporary presence of areas inhabited by stable farmers and others controlled by nomadic hunters (Fig. 1). However, the coexistence was not peaceful because nomads, especially in case of necessity, found it easier to get food by making sudden incursions into the lands of their neighbours, and these reacted with punitive expeditions.

This alternation of raids and reprisals did not last too long because sedentary populations protected their territories by surrounding them with fences and, possibly, with walls. The most celebrated examples of town walls are those of Jericho (8000 B.C., 8 m high), Hattusas (1600 B.C., 25 m high), Niniveh (1200 B.C., 25 m

P. Villaggio (✉)
Department of Structures, University of Pisa, Via Diotisalvi 2, 56126 Pisa, Italy
e-mail: g.merlo@ing.unipi.it

G. Buttazzo, A. Frediani (eds.), *Variational Analysis and Aerospace Engineering: Mathematical Challenges for Aerospace Design*, Springer Optimization and Its Applications 66,
DOI 10.1007/978-1-4614-2435-2_18,

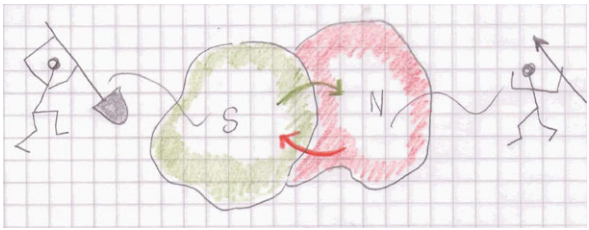

Fig. 1 Contiguous stable and nomadic populations

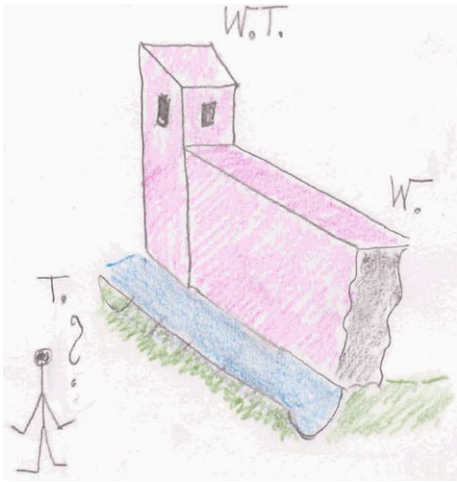

Fig. 2 The classic shape of a wall

high) and Babylon (600 B.C., 35 m high). Babylon's walls, made of burnt bricks, represent the greatest monumental fortified work for antiquity until the time of the Romans (see Oravas, [7, p. 62]). The typical defensive structure was made of three elements: the wall, the watch tower and the trench filled with water (Fig. 2). In his book on the history of war strategies, Keegan [5, p. 144] writes that a city surrounded by a belt of walls endowed with these three elements was impregnable. The only hope of conquering the city was the starving of the inhabitants and treachery (eventually with a wooden horse!).

This technique of self-defence lasted for about 12 000 years until the discovery of gun powder in Europe. Gun powder, a highly inflammable mixture of Carbon–Sulphur–Saltpeter, was already known in China since the beginning of the 11th century A.D., but the three substances were ground too finely so that they burned slowly because of inadequate airspace between its constituent particles. The explosive property of the gun powder was discovered by chance in the second decade of the 14th century A.D. by a team of alchemists monks in Freibourg who kindled the "corned powder" that is an aggregate of grains if the same mixture (Oravas, [7, p. 400]). However, notwithstanding the efforts of four generations of artisans, the military success and widespread of gun powder for launching projectiles from a ri-

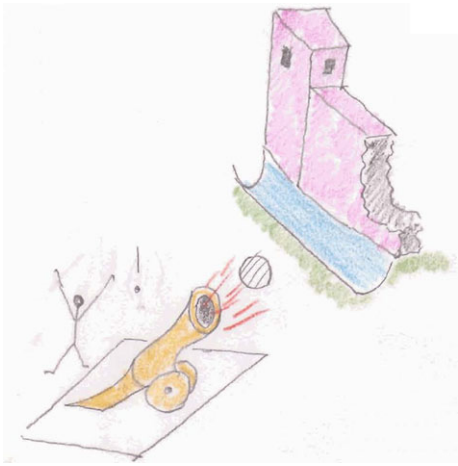

Fig. 3 End of the traditional fortresses

fle or a cannon started only in the first half of the 15th century, when metallurgists found that pure cast iron was too brittle for supporting the forces generated by an abrupt blow of the explosive charge, but the newly introduced alloys, in particular bronze (a combination of iron–copper–tin), permitted the construction of guns sufficiently tough for firing balls of stone and iron at a distance of 1000 m without affecting the efficiency of the gun barrels. The first historical use of gun powder was in the siege of Byzantium in A.D. 1453 by the Ottoman Turks. The besiegers owned only one giant cannon that, set up at the main gate of the city, succeeded in breaking the massive walls which had withstood countless attacks over many centuries (Oravas, [7, p. 290]). But after 40 years, exactly in A.D. 1494, when the French King Charles VIII invaded the Kingdom of Naples, the artillery demonstrated its enormous destructive efficiency. The French used thirty cannons, easily transportable and capable of shooting iron balls without long pauses between two subsequent detonations. The era of the great fortifications, huge walls and long sieges was at an end (Fig. 3).

But the crisis did not last a long time because military engineers soon found a remedy against the effect of artillery. In the course of five decades the architecture of fortifications was radically changed. Protagonists of the new technique were men like Francesco di Giorgio Martini and Giuliano da San Gallo. Also Michelangelo and Leonardo were hired as military architects, but with less success. The new fortresses were much lower (less than 10 m high), their walls were protected on the outside by a deep layer of soft material and on the inside by a clay embankment able to absorb the shocks (Fig. 4). The plan was a pentagonal star with a tower at each of the five vertices, from which riflemen could fire against the opposing artillerists. This shape of fortress was, almost identically, maintained during the subsequent four centuries until the beginning of the Second World War, when defensive works were made of reinforced concrete.

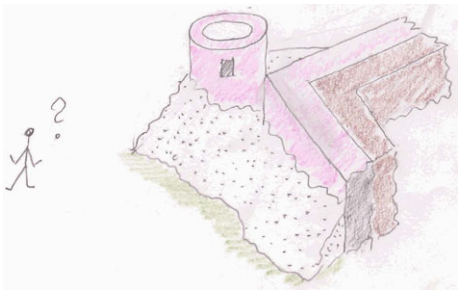

Fig. 4 The new fortresses

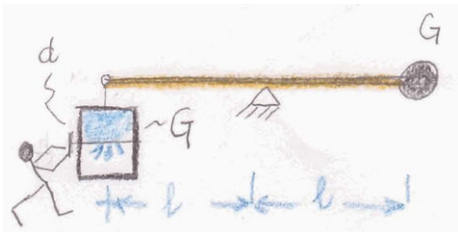

Fig. 5 Galilei's ideal experiment for measuring the impact force

2 The First Scientific Theories on Impact

The 17th century is considered the period of birth of the modern science, and it is not surprising that the great scholars of the century committed themselves with the militarily important problems of the collision between solid bodies. The fundamental question was that of predicting the velocities of rebound of two centrally colliding rigid spheres. The problem was tackled successively by Galilei, Descartes, Huygens, Newton and others. The surprising common feature of these theories is that all are wrong or, at least, defective, since the proponents considered only particular features of the phenomenon mixing inaccurate experiments with primitive mathematics. For example, the most debated quarrel was that about the mechanical quantities conserved during the impact: momentum or kinetic energy? The "Western" scholars (Marcus Marci, Descartes, Wren and Newton) affirmed that momentum is conserved; "Continental" scholars (Huygens, Johann Bernoulli, Leibniz) defended the principle of conservation of energy. The dispute was, however, futile because both these quantities must be conserved as first integrals of the differential equations of motion.

Galilei (1564–1642) is credited as the initiator of the impact theory, discussed on the Sixth Day of his Discorsi (1638), but the accounts of historians (of science) on his achievement are discordant. The great historian Dijksterhuis [3, p. 358] writes that Galilei tried to weigh the forces during impact, but this attempt was bound to fail, since momentum and energy have different physical dimensions. On the other hand, Dijksterhuis praises Galilei for having realized that impact force, if any, must be infinite. Another historian of mechanics, Szabó [9, p. 427–428], examines Galilei's conceptual experiment. A balance carries a weight G at one extremity and a small reservoir at the other (Fig. 5). The reservoir is divided into two chambers:

one above, filled by water, and one below, empty. The weight of water is G, so that the system is in equilibrium at rest. The two chambers are separated by a removable diaphragm d. If the diaphragm is instantaneously removed, the water falls down, hits the bottom of the reservoir, the left arm of the balance sinks, and the additional weight that must be added to the right arm in order to restore the equilibrium measures the impact force. Galilei's argument is wrong, and Szabó explains why.

The subsequent two important contributions to the impact theory are due to two contemporaneous scientists, Marcus Marci (from Kronland) (1595–1667) and Descartes (1596–1650). Marcus Marci proposed the first correct quantitative laws on the elastic collision between spheres. But the work of Marcus Marci was ignored for two centuries and rediscovered and appreciated by E. Mach (see Szabó [9, p. 430]). In contrast, Descartes's work was instead popular since its publication, he enunciated seven qualitative propositions concerning the impact, but all are wrong! (see Dijksterhuis [3, p. 410–412]).

The two last contributors of the 17th century to the impact theory were Huygens (1629–1695) and Newton (1642–1727). Both of them considered the central collision and rebound of two rigid spheres, and both proposed mathematical equations (not qualitative criteria) for describing and predicting the phenomenon. Huygens applied the principle of conservation of kinetic energy; Newton introduced the notion of "coefficient of restitution" in order to account for the loss of impulse between the initial and final instants of the collision. Both theories represented a decisive step towards a precise formulation and systematic treatment of impact problems. Both theories, however, are questionable. Huygens's method is incomplete, because in the case of multiple impacts between several particles, the principle of conservation of momentum is also necessary. On the other hand, Newton's definition of coefficient of restitution has given rise to some unphysical paradoxes (see Stronge [8, p. 47]).

3 The Concept of Impact as a Continuous Phenomenon

At the end of the 17th century the debate about the true physical quantities conserved during the impact was still open. In a celebrated memoir published in 1686, Leibniz (1646–1716) attacked the Cartesian concept of "force" exerted by a colliding body as represented by the product mv, where m is the mass, and v the velocity, and replaced it by the concept of "living force" mv^2. The question was fundamental since it put into discussion the intimate concept of force. Is it a continuous action exerted on a body or a sudden entity impressing instantaneous variations to the motion of a body? The Italian historian G. Maltese [6, p. 73] writes that even Newton was led to accept two forms of the Second Law of motion, $F = Ma$ and $F = \Delta(mv)$.

Historians agree that the dilemma was resolved by Euler (1707–1783) in favour of the law $F = ma$, by abandoning the model of the perfectly rigid body and considering its unavoidable deformability as a small spring interposed between the body and the other body with which it collides (Fig. 6). But Euler's priority is not universally accepted. Stronge [8, p. 262] points out that the artifice of concentrating the

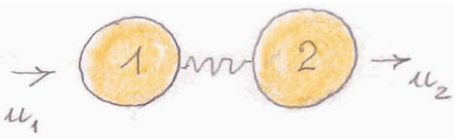

Fig. 6 u_1, u_2 are the velocities just before the first contact

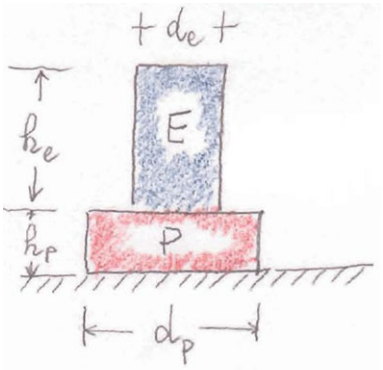

Fig. 7 E and P represent the elastic and the plastic regions

deformability of a body in an elastic or inelastic small element concentrated at the point of collision was originally introduced by Maclaurin and not by Euler.

The precise, mathematical, evaluation of the mutual compliance of two spherical or ellipsoidal bodies, pushed each against the other, is the result of a celebrated solution by Hertz (1857–1894), in the case of perfect linear elasticity [4]. If the material is perfectly plastic, a rigorous and elegant solution, like that of Hertz, is not available, because the plastic region is localized around the point of first contact and its shape and extent is one of the unknowns of the problem. In recent decades a great effort has been made to suggest simple, but satisfactory, approximate solutions to the problem of the elastic–plastic impact (see Stronge [8, p. 119–126]).

In the particular case of the plastic impingement of a cylindrical bullet against rigid armour, G.I. Taylor (1886–1975) proposed an ingenious model for determining the boundary between the elastic and plastic regions after the partial splashing of the bullet (Fig. 7). Taylor's model [10] is able to predict the height h_p of the plasticized region, its transversal dilatation d_p, the impulse against the rigid surface, and the time of arrest of the bullet after the first contact. Taylor's model has proven itself valid for describing other impact phenomena, like the crash between two cars or the spreading of an avalanche when it reaches the bottom of a valley.

4 Structural Impact

The studies on impact surveyed so far consider the collision between compact bodies for which the contact region is relatively small and the times of propagation of deformations are almost instantaneous. The situation is, however, very different

when a compact body hits a flexible structure or a system containing flexible elements. In this case the contact period may be long, the maximum contact force is reduced, and a significant amount of energy is converted into structural vibrations.

Saint-Venant (1797–1886) found an explicit solution for the wave propagation in an elastic uniform bar struck at one end by a rigid mass and clamped at the opposite end. Saint-Venant (1867) succeeded in integrating d'Alembert's equation with non-standard boundary conditions and singular initial data. His results is astonishingly skilful, but limited to one-dimensional problems.

The difficulty of treating cases of impact in more than one dimension was recognized one century before Saint-Venant, and history registers several attempts for finding approximate procedures of solution to structural impact problems. The first result in the field is due to Daniel Bernoulli (1700–1783), who determined the maximum inflection of an initially straight beam due to a central percussion. Bernoulli's solution is variational and, according to Szabó [9, p. 467], anticipated by more than one century the classical Rayleigh–Ritz method.

In the middle of the 19th century, during the diffusion of railways, engineers introduced an approximate method for evaluating the forces induced in iron bridges by the rapid transit of trains. They simply reduced complex structures to systems with one or few degrees of freedom, determined the maximum elongations, and calculated the related internal forces. The most representative user of this method was the English engineer H. Cox (1821–1895). These techniques may appear too primitive in an era in which numerical calculations can provide a detailed estimate of the stress state at every point of a structure during the whole period of compression and rebound (if any). Nevertheless, the approximate procedures, owing their elegance and their sound mathematical foundation to the calculus of variations, are still popular.

5 New Extensions

Impact theory is a branch if classical mechanics. Its retarded development rests on the fact that the equations governing impulsive actions are singular. But its importance is growing because many phenomena, traditionally modelled in terms of smooth mathematics, involve discontinuous quantities. In some fields of science and technology these properties of the solutions were known for a long time, like in seismology or in moulding metals. But there are other emerging fields, like finance, social revolutions, epidemiology, in which impact theory will find promising applications.

References

1. Borrough, W.J.: Climate Change in Prehistory. The End of the Reign of Chaos. Cambridge University Press, Cambridge (2005)

2. Diamond, J.: The Third Chimpanzee. Harper, New York (2006)
3. Dijksterhuis, E.J.: The Mechanization of the Word Picture. Princeton University Press, Princeton (1986)
4. Hertz, H.: Über die Berührung fester elasticher Körper. J. Reine Angew. Math. **92**, 156–171 (1882)
5. Keegan, J.: La Grande Storia della Guerra. Mondadori, Milano (1994). Trans. of "A History of Warfare" by D. Panzieri
6. Maltese, G.: La Storia di "$F = ma$". La Seconda Legge del Moto Nel Xvii Secolo. Olschki, Firenze (1992)
7. Oravas, G.: Lectures on the History of Technology and Engineering. Olms, Hildesheim (2004)
8. Stronge, W.J.: Impact Mechanics. Cambridge University Press, Cambridge (2000)
9. Szabó, I.: Geschichte der Mechanischen Prinzipien. Birkhäuser, Basel (1979)
10. Taylor, G.I.: The testing of materials at high rates of loading. J. Inst. Civ. Eng. **26**, 486–518 (1946)

Flight Mechanics Modeling of the PrandtlPlane for Conceptual and Preliminary Design

Mark Voskuijl, Jan de Klerk, and Daan van Ginneken

Nomenclature

A	System matrix –
B	Input matrix –
B	Aerodynamic effectiveness matrix –
C	Output matrix –
D	Direct matrix –
D_{nac}	Nacelle diameter m
h	Altitude m
L_{nac}	Nacelle length m
$\mathbf{m_d}$	Desired moments vector Nm
M	Mach number –
n	Load factor –
p	Body axis roll rate rad/s
q	Body axis pitch rate rad/s
r	Body axis yaw rate rad/s
T	Thrust N
T_4	Burner outlet temperature K
u	Longitudinal velocity in body axis m/s
$\mathbf{u}$	Vector of input variables –
v	Lateral velocity in body axis m/s
w	Vertical velocity in body axis m/s
W_{TO}	Take-off weight N
$\mathbf{x}$	State vector –
$\mathbf{y}$	Output vector –

M. Voskuijl (✉) · J. de Klerk · D. van Ginneken
Faculty of Aerospace Engineering, Delft University of Technology, Kluyverweg 1, 2629HS Delft, The Netherlands
e-mail: m.voskuijl@tudelft.nl

G. Buttazzo, A. Frediani (eds.), *Variational Analysis and Aerospace Engineering: Mathematical Challenges for Aerospace Design*, Springer Optimization and Its Applications 66,
DOI 10.1007/978-1-4614-2435-2_19,

Greek symbols

α	Angle of attack rad
β	Sideslip angle rad
$\boldsymbol{\delta}$	Vector of control surface deflections rad
δ_i	ith control surface deflection rad
δ_{throttle}	Throttle position –
ϕ	Roll attitude rad
θ	Pitch attitude rad
ω_d	Dutch roll natural frequency rad/s
ω_{ph}	Phugoid natural frequency rad/s
ψ	Yaw attitude rad/s
ζ_d	Dutch roll damping ratio –
ζ_{ph}	Phugoid damping ratio –
ζ_{sp}	Short period damping ratio –

Abbreviations

BPR	Bypass Ratio
DLC	Direct Lift Control
FMT	Flight Mechanics Toolbox
MIMO	Multi-Input Multi-Output
OPR	Overall Pressure Ratio
P	Proportional control
PI	Proportional plus Integral control
RC	Rate Command
TC	Turn Coordination

1 Introduction

With respect to aircraft performance, the need for a significant reduction in CO_2 emissions, reduction of the perceived noise level, improved safety and larger capacity has been expressed by the European Union [6]. A large number of publications can be found in the literature, addressing these challenges with novel aircraft designs and/or new propulsion systems. The main focus however is on the Blended Wing Body aircraft configuration [28] and open-rotor propulsion systems [8]. Several technical problems are still present for the Blended Wing Body: pressurized fuselage design, the inherent stability in the longitudinal and lateral directional axes, passenger comfort, high-lift system design, aerodynamics (center body profile with large thickness over chord ratio) and airport compatibility [28]. One aircraft configuration that has received less attention is the box-wing configuration, designated as the PrandtlPlane. Ludwig Prandtl predicted already in the 1920s that this is the ideal configuration with respect to induced drag [37]. This prediction was verified nearly 80 years later by Frediani et al. [15]. Various other research studies support the findings of Prandtl [11, 24, 27]. A consortium of Italian Universities therefore investigated the box-wing configuration recently, which resulted in a new aircraft design [16]. This design was called the PrandtlPlane in honor of the work of

Prandtl. Currently there are still many technical issues which must be investigated thoroughly to demonstrate the feasibility of this configuration. Examples are the elastic behavior of the closed-wing system [27] and the fuselage design, which is loaded in a manner different from the conventional aircraft configuration. This research study is focused on two aspects of the PrandtlPlane design: (1) the propulsion system and (2) the flight control system, where the flight control system design includes the sizing and placement of the primary control surfaces, the allocation of the controls following a control input, and the design of an automatic flight control law.

The design of the propulsion system, in terms of the selection of the propulsion system type, the number of engines and their location, is still an open issue. Only limited information can be found in the literature about the propulsion system design for box-wing configurations. Iemma et al. [23] performed a multidisciplinary design optimization of a large PrandtlPlane with four turbofan convention turbofan engines. The location of these engines is unfortunately not mentioned, nor is the rationale for the choice of four conventional engines elaborated upon. Lange et al. [27] investigated a box-wing configuration which had four jet-fan engines on the front wing. The inboard engines were located at 50% span and the outboard engines near the tips. Relocation of these engines to the aft section of the fuselage was also considered in this study to improve the flutter characteristics. This relocation only resulted in a small improvement with respect to flutter and created difficulties with respect to obtaining a smooth area distribution for minimum wave drag. Hence the relocation was abandoned. The limited information in the open literature supports the fact that a propulsion system design study should be performed. There are various opportunities for the propulsion system design of the aircraft considered in this study. For example, open-rotor systems can be placed underneath the rear wing without having ground clearance issues. These opportunities and possible technical issues should be identified.

Flight control of the PrandtlPlane is quite different than the control of a conventional aircraft. If one places control surfaces on the front and rear wings, then a pure moment can be created by differential deflection of these controls. This is a clear advantage over conventional aircraft configurations which show nonminimum phase behavior; an upward deflection of the elevator first results in a slight downward motion before the aircraft rotates and starts to climb. In this respect, the PrandtlPlane could have superior handling qualities over a conventional configuration. Furthermore, a combined deflection of the front and rear wing control surfaces allows the use of direct lift control. Direct lift control has proven to improve handling qualities in the landing and approach phase [10, 41]. However, the disadvantage of implementing such a system on a conventional configuration is that flaps or spoilers must be utilized for this purpose. The PrandtlPlane does not have this disadvantage. Furthermore, the inherent stability can differ substantially due to the novel wing system and the inertia of the aircraft.

One cannot rely on traditional handbook methods for the design of an unconventional configuration such as the PrandtlPlane because there are simply no reference aircraft. The design methodology should therefore be physics based. For the analysis of the overall aircraft behavior, including the propulsion and flight control

system, a flight mechanics model is required. Flight mechanics is defined herein as the discipline which consists of both flight performance and flight dynamics [42]. Such a flight mechanics model should be straightforward to apply in the conceptual and preliminary design phase. The preliminary design phase in this context aims for the definition and selection of design concept on the level of each individual system [43].

The aim of this research study is twofold. First, the capabilities of an in-house developed flight mechanics toolbox and its application in the conceptual and preliminary design phase are demonstrated. Second, the propulsion system and flight control system design of a 300-passenger version of the PrandtlPlane is investigated.

The paper is structured as follows. First, the flight mechanics modeling environment and the baseline aircraft configuration are described in Sect. 2. Next, the propulsion system design is presented in Sect. 3. The inherent flying qualities, control surface sizing, and automatic flight control system design are discussed in Sect. 4. Finally, conclusions and recommendations are made.

2 Flight Mechanics Model

2.1 Modeling Environment

An in-house developed flight mechanics toolbox (FMT) is used as modeling environment. This toolbox enables the integration of submodels from various disciplines such as aerodynamics, structures, flight control, and propulsion, in a single full nonlinear aircraft model. The aircraft model can be used to analyze the performance of the complete system. The general application for which this toolbox has been designed is to be part of a design framework. The toolbox is therefore developed such that aircraft models can be created and analyzed in an automated fashion. This makes it possible to integrate the flight mechanics toolbox in a multidisciplinary design optimization framework. Some key features for which this modeling toolbox can be used are listed below:

- Basic aircraft performance analysis
- Mission analysis
- Handling qualities analysis
- Linearization
- Control law design
- Time domain simulation
- Loads prediction
- Aircraft response to atmospheric turbulence
- Automated model generation enabling multidisciplinary design optimization
- Simulation of in-flight dynamic transition of morphing aerostructures
- Real time simulation with a pilot in the loop
- Flexible aircraft dynamics

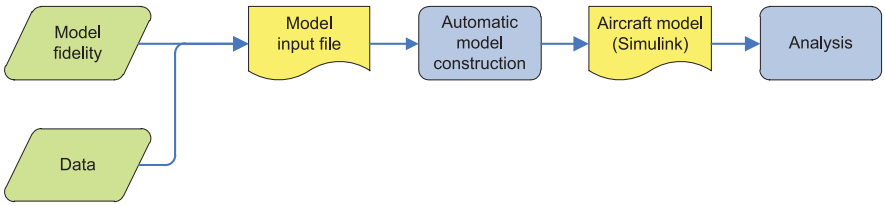

Fig. 1 Top-level overview of flight mechanics toolbox

The last feature (flexible aircraft dynamics), is currently still under development. The toolbox is set up in a modular structure which makes it straightforward to improve the fidelity of the various submodels and to extend the capabilities. It should be noted that the toolbox can be used both for aircraft and rotorcraft analysis. The FMT is created in the Matlab/Simulink environment and makes use of multibody dynamics (SimMechanics) when needed, e.g., for simulation of dynamic fuel transfer, landing gear motion and ground operations, flexible aircraft dynamics, slung loads under rotorcraft, and morphing aerostructures. A top-level overview of the complete model is presented in Fig. 1.

The user has to supply information about the model fidelity and corresponding data. For example, if the actuators of the flight control system are considered, then model fidelity contains information about the type of actuator model (transfer function, physics-based, user-defined etc.). The data contains all the relevant parameters for the actuator models such as rate limits, saturation limits but also the number and location of the actuators. Both the model fidelity and data are stored in a standardized input file. Automatic model construction commands are then used to create an aircraft model in Simulink. This model can be analyzed with a suite of analysis functions. All of these steps can be performed in an automated fashion or manually.

2.2 PrandtlPlane Aircraft Model

The basic aircraft configuration under investigation is a 300 passenger version of the PrandtlPlane. A number of PrandtlPlane designs with various sizes ranging from general aviation to very large aircraft capable of transporting up to 600 passengers were investigated by a consortium of Italian Universities [16] and by the University of Pisa [13–15]. An artist impression of a 250-passenger version of the PrandtlPlane during ground operations is presented in Fig. 2.

A basic flight mechanics model of this aircraft was developed with the flight mechanics toolbox. The aerodynamics is represented in the model with an aerodynamic dataset, which is a function of Mach number (M), angle of attack (α), sideslip angle (β), control deflections (δ), and angular rates (p, q, r). This dataset is created with the commercial software tool VSAERO [4], which is a first-order panel code with viscous boundary layer integration. The input to VSAERO is created with a parametric aircraft model, which contains all relevant design parameters of the aircraft.

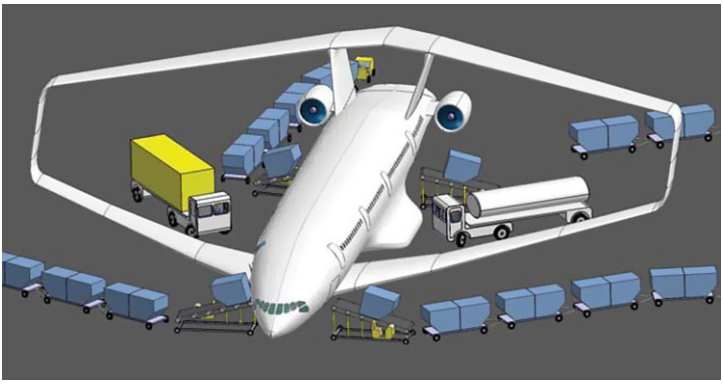

Fig. 2 Artist impression of the PrandtlPlane during ground operations [13]

The output is automatically transformed into the required format for the flight mechanics toolbox. In the current research, control surface deflections are modeled in VSAERO by changing the airfoil shape. Details on the fidelity of control derivatives obtained with VSAERO can be found in [35]. The engines are modeled with an inlet and exhaust velocity. The equations of motion are represented with multibody dynamics. Two separate bodies are present, one for the empty aircraft structure and one for the fuel. The fuel is in fact a body with variable mass and inertia, which can move relative to the airframe. The engines are modeled as static engines using lookup tables, which are functions of Mach number and altitude. The thrust, fuel consumption, and propulsion-related drags are all calculated. The propulsion tables are created using an in-house developed gas turbine simulation tool, of which more details are presented in the next section. Actuators are modeled as second-order systems with rate and saturation limits. An international standard atmosphere model is present [1], as well as two atmospheric turbulence models, the von Karman turbulence model and the Dryden wind turbulence model [2, 3]. Currently, the landing gear is not modeled.

3 Propulsion System Design

One particular aspect of the design of the 300-passenger version of the PrandtlPlane that has not been investigated is the propulsion system. The overall aircraft configuration allows some new possibilities in terms of the type of propulsion system, the number of engines, and their location. Engines can be placed on the front wing, the rear wing, on the rear of the fuselage, in between the two vertical tails, near the connections between the vertical tails and the rear wing, or at the connections of the vertical tails with the fuselage. Engines could even be placed in the vertical side wings, although this is most likely highly unfavorable with respect to engine out conditions. Conventional turbofan engines with a high bypass ratio can easily

be placed at the rear wing, without having to flatten the intake. This can be done because the rear wing has a large clearance from the ground. The rear wing could even be used to mount an open-rotor system. Engines placed on either the front or rear wing will have a significant impact on the center of gravity location, and this effect must be accounted for. The propulsion system design process used in this study is represented in Fig. 3.

The design process starts with the baseline aircraft design (without engines). The lift drag polar and weight are used to size the engines and to optimize the thermodynamic cycle. The lift drag polar is determined with empirical equations. The Oswald factor, which takes into account the improvements with respect to the induced drag compared to a conventional aircraft, is estimated with the method proposed by McMasters and Kroo [33]. The sizing and cycle optimization is done after the configuration is selected, in terms of number, location, and type of propulsion system. The shape of the propulsion system and the aircraft geometry are then taken as input for the aerodynamic analysis with VSAERO. Results of the aerodynamic analysis, the propulsion system tables, and the mass, centre of gravity, and inertia information of the aircraft including propulsion system are then fed as input to the flight mechanics model. This model is used to fly a complete mission. If desired, this process can be repeated until the best aircraft engine combination is found. In the next three sections, the configuration selection, engine sizing and cycle optimization, and aerodynamic and flight mechanics analysis is presented in more detail.

3.1 Configuration Selection

Several propulsion system types were considered for the 300-passenger version of the PrandtlPlane; the conventional turbofan, the geared turbofan, the intercooled recuperative engine, the more electric engine [38], the ducted propfan, the unducted propfan, boundary layer ingestion, distributed turbofans, and the hybrid turbofan. Some of these options are in fact complementary. For example, the intercooled recuperative engine makes use of the heat of the exhaust flow to preheat the flow between the high-pressure compressor and the combustion chamber through a recuperator [32]. This can be applied to all engine types. An extensive trade-off study was performed to select the most suitable option. The following criteria were evaluated in this trade-off: fuel burn, emissions, noise, compatibility with the PrandtlPlane configuration, development risk, acquisition cost, and maintenance costs. Based on this study, the more electric conventional turbofan was selected. In the more electric engine, the separate systems used to generate power for electric, pneumatic, and hydraulic systems are replaced by electrical generators, driven by the main shafts of the engine. According to NASA [22], this should result in a more efficient and reliable engine. The conventional turbofan outperformed the other propulsion types mainly due to the low risk, lower acquisition costs, and lower maintenance costs. The wing design of the PrandtlPlane is already a high-risk design, and therefore other systems should have a relatively low risk in order to keep the risk of the overall design acceptable.

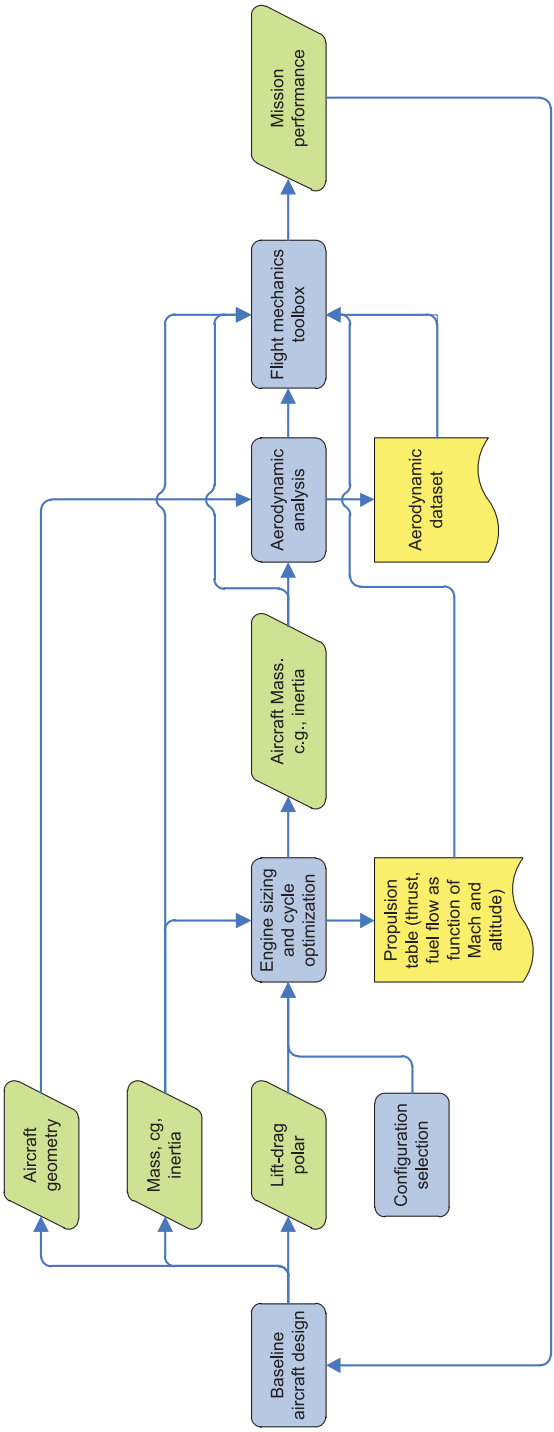

Fig. 3 Propulsion system design process

Two additional trade-offs were performed to determine (1) the number of engines and (2) their location. Selection criteria for the number of engines were: fuel efficiency, reliability/safety, acquisition costs, maintenance costs, construction weight, and finally the agreement between the take-off thrust requirements versus the cruise thrust requirement. It was decided to select a twin engine option mainly due to the high fuel efficiency. In the final trade-off (engine locations), several factors were taken into account: required landing gear length, aerodynamic interference, structural weight, cg location, one-engine out moment, structural stiffness, cabin noise and vibrations, accessibility, noise shielding from the ground, engine inlet, and the pitching moment of the thrust vector. Having two engines at the rear of the fuselage proved to be the most promising concept.

In summary, the propulsion system consists of two conventional turbofan engines located at the rear of the fuselage with electric power off-take only, known as the more electric engine.

3.2 Engine Sizing and Cycle Optimization

After the selection of the configuration, the engines have to be sized, and the thermodynamic cycle must be optimized. The process for engine sizing and cycle optimization is represented in Fig. 4.

The inputs to this process are basic aircraft parameters (mass, cg, inertia, lift-drag polar). As a starting point, a guess is made for the bypass ratio (BPR), the fan pressure ratio (FPR), the overall pressure ratio (OPR), and the burner outlet temperature (T_4). A first guess is then made for the mass flow through the engine and the total fuel weight. With all these parameters, a design point (cruise) analysis can be made. The design point analysis is done with an in-house developed gas turbine simulation tool [25]. It determines the cooling flows needed to keep the temperature of the turbines within the allowable limits. Subsequently, it calculates the condition of the gas at several stations throughout the engine. Finally, engine weight and drag are predicted with the weight prediction methods of Gerend [18] and Seddon [40] and the drag prediction methods of Mount [34] and Mattingly [31]. The aircraft mission analysis is performed simply with the Breguet range equation. A check is then made if the engines deliver the right amount of thrust and whether the design range is reached. If necessary, the mass flow through the engine and the total amount of fuel are adjusted, and the design point analysis is repeated until the results converge. After this process, an off-design point analysis is performed. A genetic algorithm is coupled to the process to find the best engine design in terms of BPR, FPR, OPR, and T_4. The genetic algorithm is based on the work of Whellens [44]. The objective of the optimization is to minimize direct operating cost, which in this case is formulated as a linear function of engine weight, MTOW, and mission fuel burn [30]. Once the optimum is found, a gradient-based optimization is employed to refine the results. Several constraints are placed on the design parameters to keep them within acceptable limits. The final design and an image of the engine location are presented in Table 1 and Fig. 5.

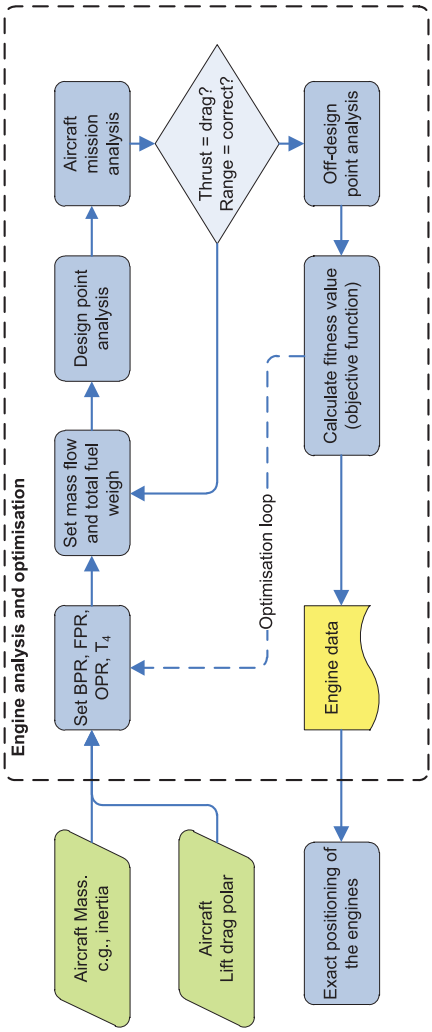

Fig. 4 Engine sizing and cycle optimization

Table 1 Basic engine parameters

Design parameter	Value
BPR	11 [–]
FPR	1.58 [–]
OPR	46 [–]
T_4 (cruise)	1610 [K]
T/W_{TO}	0.29 [–]
L_{nac}	5.1 [m]
D_{nac}	3.7 [m]

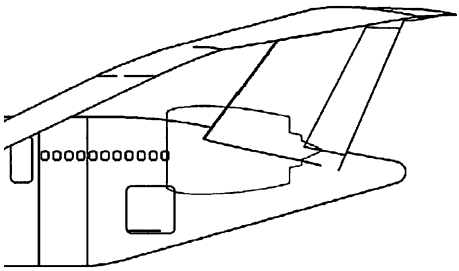

Fig. 5 Impression of the engine location

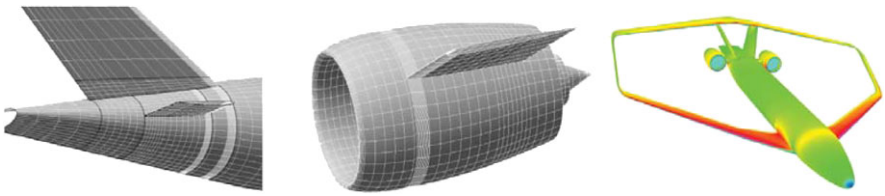

Fig. 6 Aerodynamic model of the airframe-engine integration

3.3 Aerodynamic Design and Flight Mechanics Analysis

The design presented in the previous section is analyzed with VSAERO at various flight conditions to generate an aerodynamic dataset for the flight mechanics toolbox. An impression of the aerodynamic model is presented below (Fig. 6). Note that the drag prediction is done separately with empirical methods [31, 33, 34]. VSAERO is used to calculate the lift distribution and the stability and control derivatives.

With the aerodynamic results, a virtual mission is flown with the flight mechanics toolbox. This mission is consists of: (1) take-off, (2) climb, (3) 11 000 km cruise flight at 11-km altitude and Mach 0.85, (4) descent, (5) 30-minute hold at 2-km altitude, (6) 370-km deviation to an alternate airport at 3-km altitude, and (7) approach and landing. The mission simulation is performed by trimming the full aircraft model at a large set of points throughout the mission (Fig. 7).

Halfway through the cruise phase, a step climb is performed to improve the cruise performance. The total amount of fuel required for the complete equals 97 500 kg.

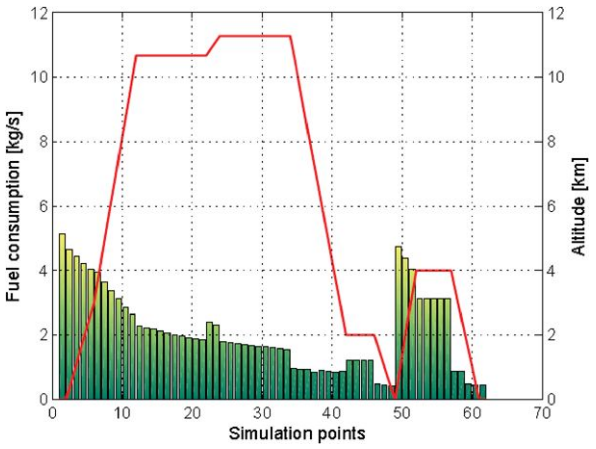

Fig. 7 Mission simulation

This number should only be used as reference when design changes are analyzed with the tools and methods presented in this paper. It should not be used for comparison with other aircraft of which data is available, either from calculations or flight tests, since a critical factor in the result is the drag prediction, which is not the focus of the current study. Drag predictions were made with empirical relations (see previous sections). For the current design, part of the fuel needs to be stored in the fuselage due to the fact that the wing volume is much lower than that of a conventional aircraft. If two aircrafts are considered, a PrandtlPlane and a conventional aircraft that have the same wing span, the same wing area, and that use similar airfoil with the same thickness over chord ratio, then the PrandtlPlane wing system has approximately half of the volume of the wing of a conventional aircraft (the thickness reduces, the chord reduces, and the number of wings increases). This is a disadvantage of the PrandtlPlane configuration. Additionally, when fuel is stored in the wing, it is located at a relatively large distance from the cg-position. The fuel system design should take this into account to make sure that there is no large cg-shift during flight. This concludes the propulsion system design. It is a recommendation for future work to analyze other engine configurations in combination with the baseline aircraft design.

4 Flight Control System Design

4.1 Control Surface Sizing

The general layout of the primary control surfaces of the PrandtlPlane, in terms of number, size, and location, was determined in a conceptual/preliminary design study [17]. In this study, use was made of VSAERO for the aerodynamic analysis. The aerodynamic results were implemented in the flight mechanics toolbox to analyze the overall behavior of the aircraft. An optimization study was done to minimize

Table 2 Handling qualities requirements for control surface sizing

Requirement	Take-off rotation speed (sea level)		Approach speed (sea level)		Cruise speed (10 500 m)	
	No cross wind	Cross wind	No cross wind	Cross wind	No cross wind	Cross wind
Aircraft trim	X	X	X	X	X	X
Take-off rotation (7 deg/s)	X	X				
Push pull manoeuvre (0.5 to 2.0 "g")			X	X	X	X
Minimum time to bank (2.3 s to 30 deg)			X		X	
One engine in-operative (trimmed flight)			X	X		
Steady turn			X	X		

the total control surface area, whilst keeping an adequate level of control power in all axes. The handling qualities requirements which had to be met are summarized in Table 2.

These requirements were taken from Coleman and Chuboda [9], MIL-F 8785C [2], and CS-25 [5]. The overall design process is presented in Fig. 8.

After performing the aerodynamic analysis, a control allocation scheme has to be derived, describing the relationship between the three pilot inputs and the deflection of the control surfaces. The direct allocation method [12, 19] was used during the sizing study. More details on the topic of control allocation are given in Sect. 4.3. The resulting architecture is presented in Fig. 9. It can be observed that control surfaces are present on both the front and rear wings. The inboard controls are mainly intended for longitudinal control and the outboard controls for lateral control. Each control however can have multiple functionalities.

4.2 Inherent Flying Qualities

The inherent flying qualities of the PrandtlPlane are analyzed at a single flight condition: 150 m/s, sea level conditions, the normal cg position, and maximum takeoff weight. In future work, the flying qualities should be analyzed throughout the flight envelope for all possible cg and weight combinations. First, the nonlinear aircraft model is trimmed in the specified flight condition, and subsequently, a linear aircraft model is obtained by numerical perturbation of the nonlinear aircraft model. This linear aircraft model is used for handling quality analysis. First, the longitudinal handling qualities are assessed. The phugoid mode has a natural frequency ω_{ph} of 0.095 rad/s, and a damping ratio ζ_{ph} of 0.034. The corresponding handling qualities are of level 2. The damping ratio should be increased to 0.04 to achieve level 1

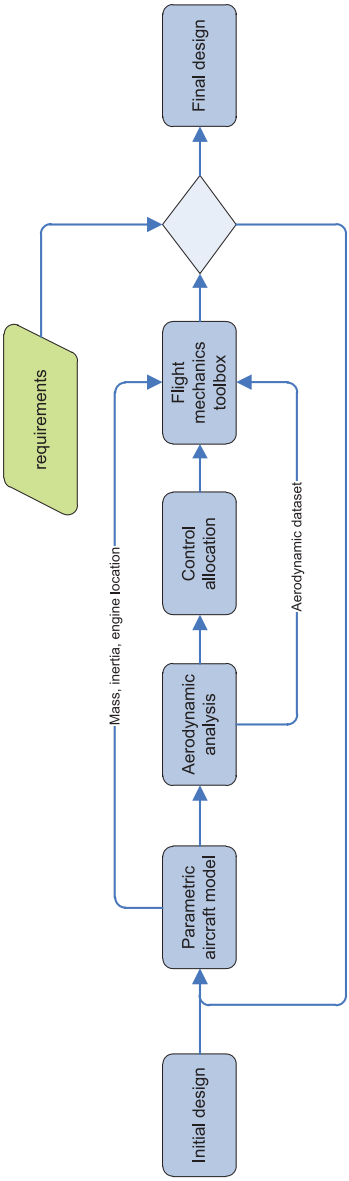

Fig. 8 Control surface design process

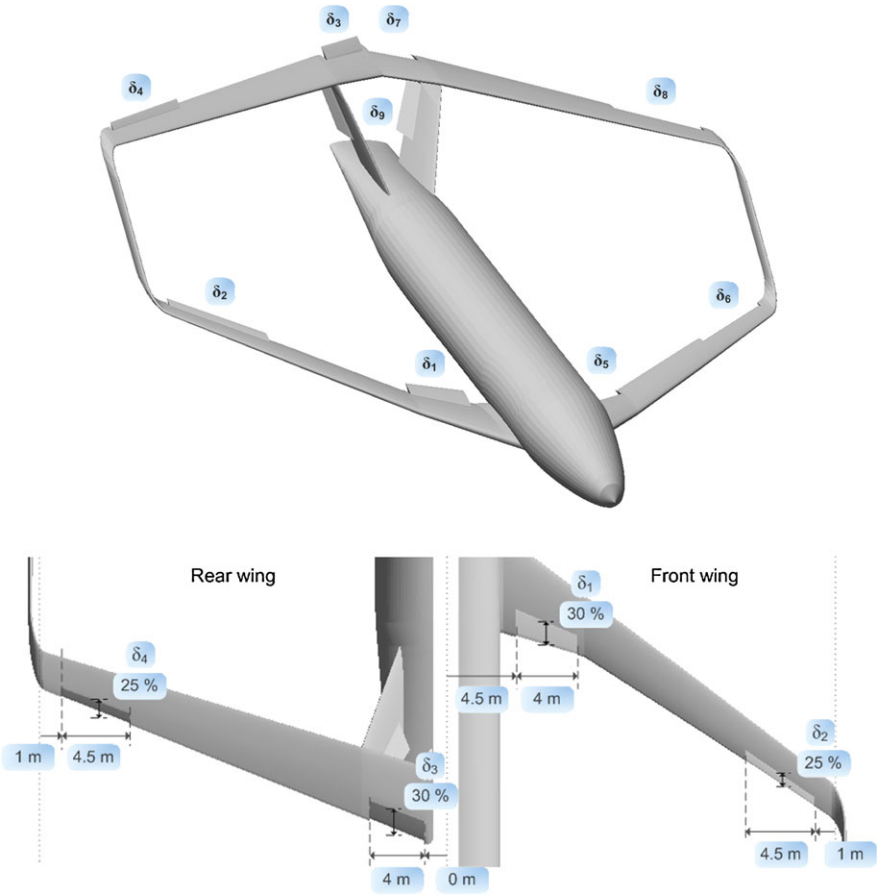

Fig. 9 Control surface architecture (*top*) and dimensions (*bottom*)

handling qualities. The short period handling qualities for category B flight phases, such as climb, cruise, loiter, and descent, are represented in Figs. 10 and 11. The frequency requirements are in the level 1 region and the damping requirements are in the level 2 region, close to level 1.

The lateral directional handling qualities are analyzed at the same flight condition. Three distinct modes are identified; the roll mode, the spiral, and the Dutch roll mode. The spiral mode has a time to double of 332 s, which is well into the level 1 region. The roll mode has a time constant of 3.7 s, which is of level 3. Finally, the Dutch roll mode has a frequency ω_d of 0.18 rad/s and a negative damping ratio ζ_d of -0.2352. So, in fact, the Dutch roll is unstable. In summary, the main issues with respect to the inherent flying qualities are the roll mode and the Dutch roll. In the future, a design study should be conducted to determine the optimal aircraft shape with respect to the inherent flying qualities.

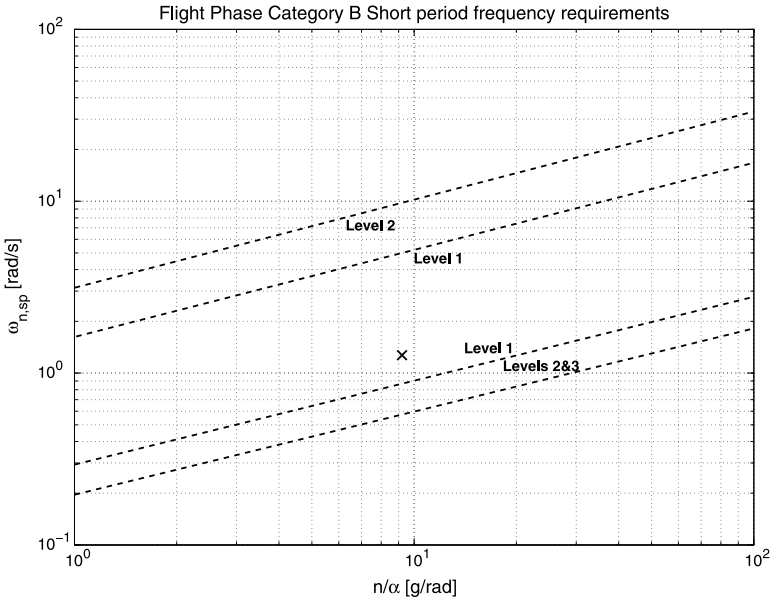

Fig. 10 Short-period frequency requirements; 150 m/s, normal cg position, sea level conditions

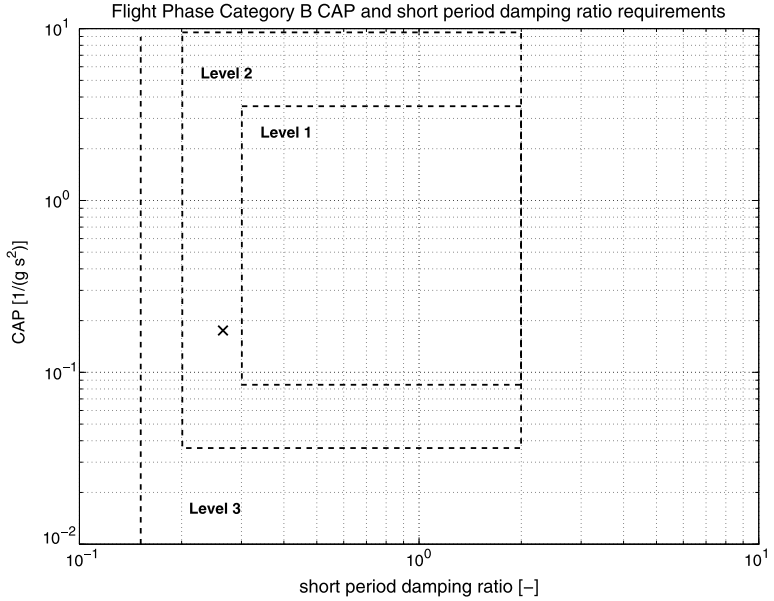

Fig. 11 Short-period damping requirements; 150 m/s, normal cg position, sea level conditions

4.3 Control Allocation

Many theories and allocation methods for managing multiple, redundant control effectors exist. The general control allocation problem can be defined with Eq. (1):

$$\mathbf{m}_d = \mathbf{B}\boldsymbol{\delta} \tag{1}$$

Here $\mathbf{m}_d$ is the desired moment vector, $\mathbf{B}$ is the aerodynamic effectiveness of the controls, and $\boldsymbol{\delta}$ is the control deflection vector. The control deflection limits are assumed to be 30 deg for all controls. So, in fact this is a constrained control allocation problem. For the current application, there is an infinite amount of solutions to this equation. In this study, it is merely the objective to create a simple and constant gearing ratio between the pilot inputs and the control deflections. Various objectives can be defined for the control allocation problem. Typically, the objective is to maximize control power. The control usage and remaining control power however can and should also be included in the problem. For example, if the pilot commands a very large pitch moment, and all control surfaces are deflected to their limits, then there is no control power left to generate a rolling moment. Another objective of a control allocation problem can be to minimize trim drag. For the PrandtlPlane, it could be useful to use different control allocation schemes throughout the flight envelope. In the cruise phase it is beneficial to minimize trim drag, whilst at lower velocities it is beneficial to maximize control power. During approach and landing, a direct lift control allocation scheme can be beneficial. More details on direct lift will be presented in the next section. A number of the most widely used control allocation techniques are listed below.

- Daisy chain
- Direct allocation [12, 19]
- Linear programming
- Fixed point iteration
- Weighted pseudo-inverse [7]
- Weighted least squares [21, 29]
- Cascaded generalized inverse [7]

Finally, it is possible to make the control allocation scheme an integral part of a multivariable control system, also known as multi-input multi-output control (MIMO). All these techniques are implemented in the flight mechanics toolbox and can be used when needed. For the current study, a simple daisy chain control allocation system has been selected. Finding the best control allocation system is not the objective of this research study. However, a control allocation scheme is required to perform simulations and for the flight control law design (Sect. 4.5). In the Daisy chain method, each control effecter is assigned to one or more control functions with a constant gearing. The Daisy chain method is chosen because it is very simple; it can even be implemented mechanically.

So, a differential deflection of the inboard controls on the front and rear wings is used for pitch control. The outboard controls of the left and right wings are deflected

differentially for roll control. Yaw control is achieved with the rudders in the vertical tails. Finally, direct lift control can be commanded by deflecting all the inboard control surfaces in the same direction.

4.4 Direct Lift Control

The control surface configuration of the PrandtlPlane with primary flight controls on both the front wing and rear wings makes it possible to use direct lift control in a straightforward manner. If both the front and rear wing controls are deflected in the same direction, then this results in a vertical force without a significant change in pitching moment. There should be a slight gearing ratio between the front and rear deflections to achieve a zero moment change since a deflection not only changes the lift coefficient but also the moment coefficient of the wing. The main advantages of using direct lift control are the following:

- Better precision in flight path control during approach and landing (improved handling qualities).
- Improved response to atmospheric turbulence (gust load alleviation).
- Precise flight path control for aerial refuelling (handling qualities).

Several research studies have shown that the precision of flight path control improves. Drake [10] reports altitude error improvements of 15%. Especially for large aircrafts that tend to have sluggish pitch control, direct lift control shows great benefits [10, 36]. A direct lift control system was implemented on the L-1011 Tristar, and this aircraft had "superior landing characteristics and touchdown accuracy" [41]. On conventional aircraft, direct lift control can be achieved by using the spoilers or flaps [20]. On the Tristar, four of the six spoilers on each wing were used. The downside of using flaps for example is that higher actuation rates and greater actuator power are required. Furthermore, part of the lift potential of the flap is sacrificed for the direct lift control function, and thus the approach speed may increase slightly. On the PrandtlPlane, a direct lift system can be easily implemented by making use of the mechanical control system.

4.5 Automatic Flight Control System Design

The control architecture described in the previous sections provides two clear opportunities: (1) a pure moment can be generated by deflecting the front- and rear-wing controls in a differential manner; (2) direct lift control can be applied by deflecting the surfaces on front- and rear-wing simultaneously in one direction. A mix of these two distinct control strategies can also be applied. These two opportunities are exploited in a novel automatic control law for the PrandtlPlane. The basic method used is model-based inversion flight control, as described by Yomchinda

and Horn [45], who successfully applied this technique to the design of a tilt rotor flight control system. There are several advantages to this technique [39]. First, it is possible to specify the desired response. Second, the controllers can be developed without having to tune gains. This is a clear advantage in the conceptual and preliminary design phase when typically many aircraft configurations are analyzed. To obtain the best handling and stability characteristics, tuning should be applied. However, this can be done in the detailed design phase. Third, gain scheduling is not a large task anymore. Altogether, this control technique can be applied in an automatic design environment, which makes it perfectly suitable for this research study. Model-based inversion flight control is used in this study to provide a rate command (RC) response type in the longitudinal, lateral, and directional axes. An additional outer loop is designed to provide direct lift control (DLC). This additional loop is designed using classical techniques. The overall schematic of the control system is presented in Figs. 12 and 13.

Two main control loops can be observed in the longitudinal control system. One is designed to create a pitch rate command response type by applying a differential deflection of the front and rear control surfaces. The other (vertical) control loop is used to control the height or height rate by applying a combined deflection. If this second control loop is active, then the commanded pitch rate is set equal to zero. The height control system consists of an inner loop, controlling the height rate, and an outer loop which controls the height and creates a height-rate command. The height-rate command signal is limited in the height control loop to prevent excessive control usage. Both loops (height and height-rate) are designed with classical techniques. The lateral directional control system consists of two control loops. The inputs to the lateral directional control system are a commanded roll rate and a commanded yaw rate. The roll and yaw rates are measured and used as feedback variables. Additionally, a turn coordination system is present. During a coordinated turn, the aircraft has a constant pitch rate and a constant yaw rate, which are functions of pitch attitude and roll attitude [26]. These rates are added to the pilot command such that the pilot does not have to apply longitudinal or directional inputs during a turn.

Automatic flight control system design is done for only one flight condition. A linear aircraft model was obtained by numerical perturbation of the full nonlinear aircraft model at 150 m/s and sea level. The linear aircraft model consists of nine rigid body states, 11 inputs, and one output. The inputs are the 10 control surface deflections and the throttle position. The altitude is included as output because it will be used as feedback for the direct lift control loop.

$$\dot{\mathbf{x}} = \mathbf{A}\mathbf{x} + \mathbf{B}\mathbf{u}, \tag{2}$$

$$\mathbf{y} = \mathbf{C}\mathbf{x} + \mathbf{D}\mathbf{u}, \tag{3}$$

$$\mathbf{x} = \left[\phi\ \theta\ \psi\ \ p\ q\ r\ u\ v\ w\right], \tag{4}$$

$$\mathbf{u} = \left[\delta_1\ \delta_2\ \delta_3\ \delta_4\ \delta_5\ \delta_6\ \delta_7\ \delta_8\ \delta_9\ \delta_{\text{throttle}}\right], \tag{5}$$

$$\mathbf{y} = [h]. \tag{6}$$

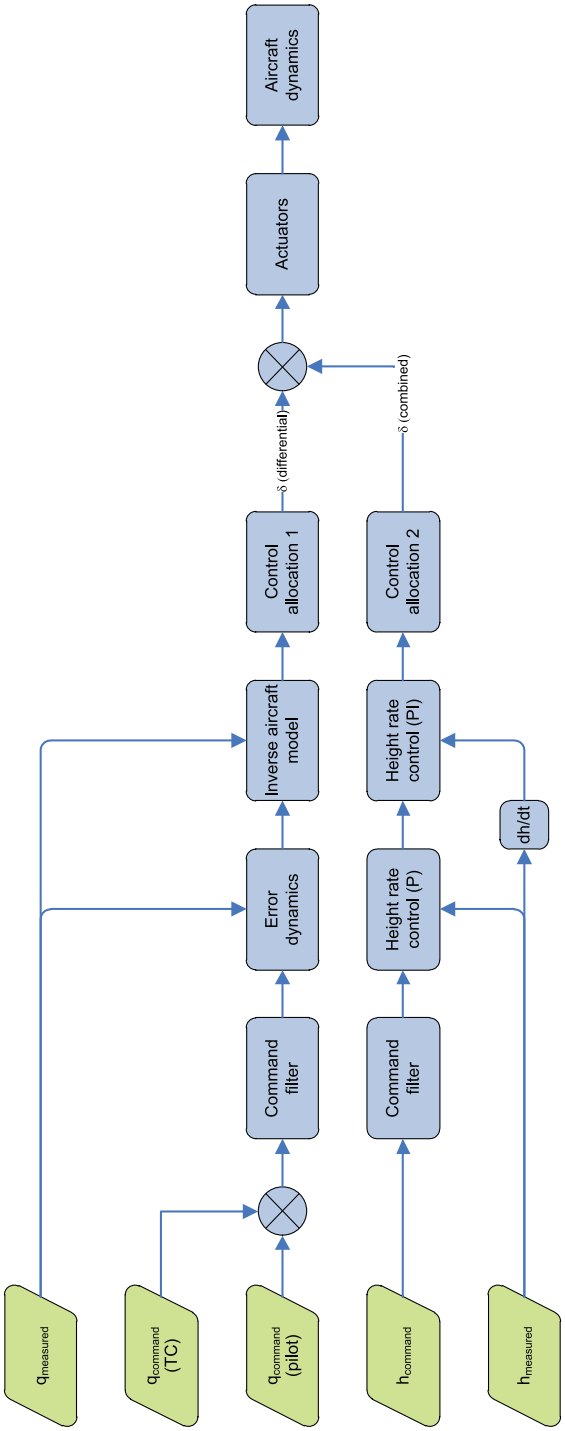

Fig. 12 Longitudinal control system

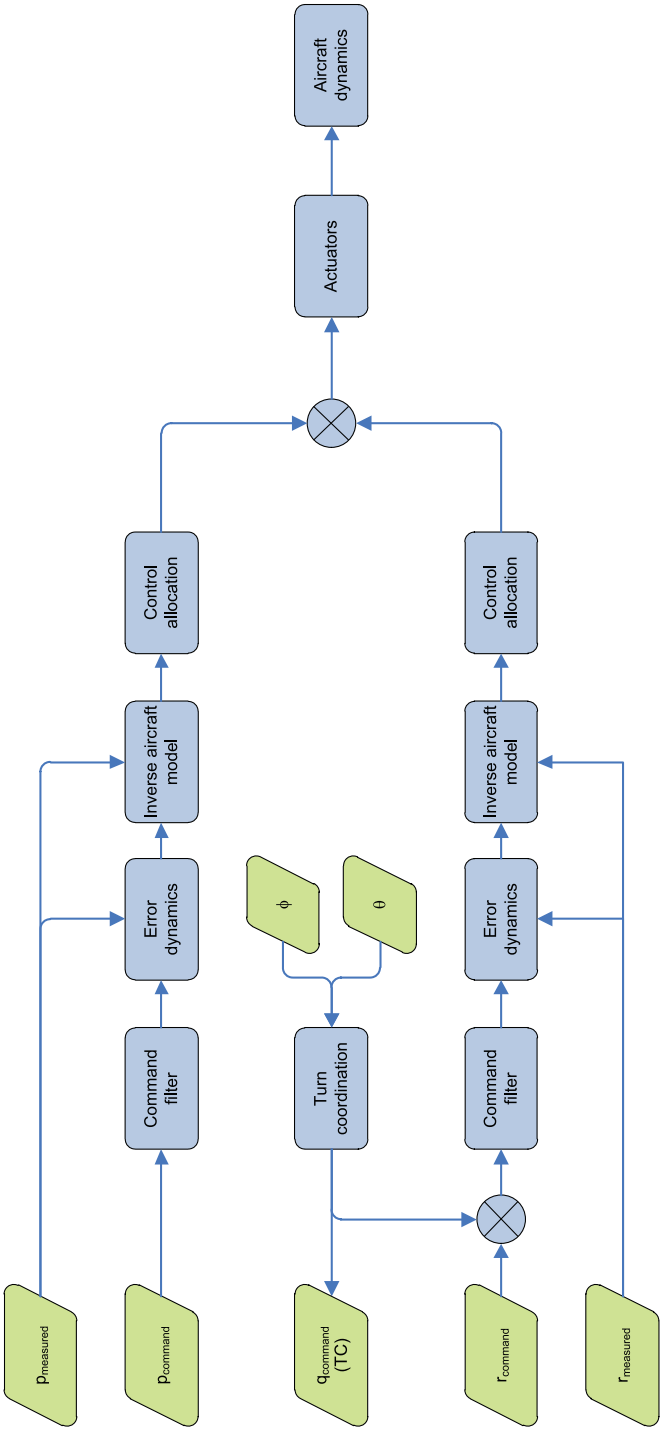

Fig. 13 Lateral directional control system

After the control system is designed with the methods described in detail by Yomchinda and Horn [45], it is implemented on the full nonlinear aircraft model. Aircraft responses and the control usage as a result of a pilot input are presented in Figs. 14, 15, and 16. Three different pilot commands are given; a pitch rate command, a roll rate command, and a height command with the direct lift system engaged. All simulations are performed with the full nonlinear aircraft model. Pilot inputs start at $t = 1$ s, and hence the trim condition can be observed from 0 to 1 s.

It can be observed that pitch rate tracking (Fig. 14) is accurate and fast. The rise time (to 90% of the desired value) is 1.53 s, settling time to within 5% of the final value is 2.34 s, and the overshoot is 0%. A maximum deflection change of approximately 3 deg is required from the pitch control surfaces to achieve this response. Similar observations can be made for the roll response to a lateral step input. The rise time is 0.49 s, settling time is 0.66 s, and the overshoot is 0%. The control activity required for this fast response is relatively large. Approximately 15 deg of control surface deflection is required. Finally, the direct lift capability is demonstrated. A height change of 1 m is commanded. A very precise tracking of the height can be observed. Rise time is 1.27 s, settling time is 1.44 s, and the overshoot is 0%. These time domain results show the potential of the control configuration of the PrandtlPlane. A future investigation should include detailed stability analysis, control law design for the complete flight envelope, and robustness analysis for cg and weight variations. Furthermore, piloted simulator trials should be conducted to investigate the flying qualities of both the control law and the bare airframe. The aim of the current study is merely to demonstrate the potential of the PrandtlPlane configuration, including the direct lift capabilities, and to show the advantage of using the model-based inversion control technique in the conceptual and preliminary design phase.

5 Conclusions and Recommendations

The propulsion system and flight control system design is conducted for a 300-passenger box-wing configuration, designated the PrandtlPlane. The best propulsion system configuration for this size aircraft consists of two more electric turbofans at the tail of the aircraft. A larger size PrandtlPlane might benefit from large open-rotor systems underneath the rear wing. The box-wing configuration places some constraints on the fuel system design due to the lower volume compared to a conventional wing system. Analysis of the inherent flying qualities demonstrates that the roll mode and the Dutch roll mode are inadequate. The aircraft shape and mass distribution should be redesigned in a future study to provide good flying qualities in the lateral directional axes. The longitudinal flying qualities are considered to be good, although small improvements could be obtained with respect to the short period damping ratio. A novel flight control law was developed using model-based inversion control techniques to prove the potential of the control configuration of the PrandtlPlane. The aircraft has primary control surfaces on the front and rear wing. Thus, a pure moment can be created by differential deflection of the controls, and a direct lift control can be applied by a combined deflection. This makes precision

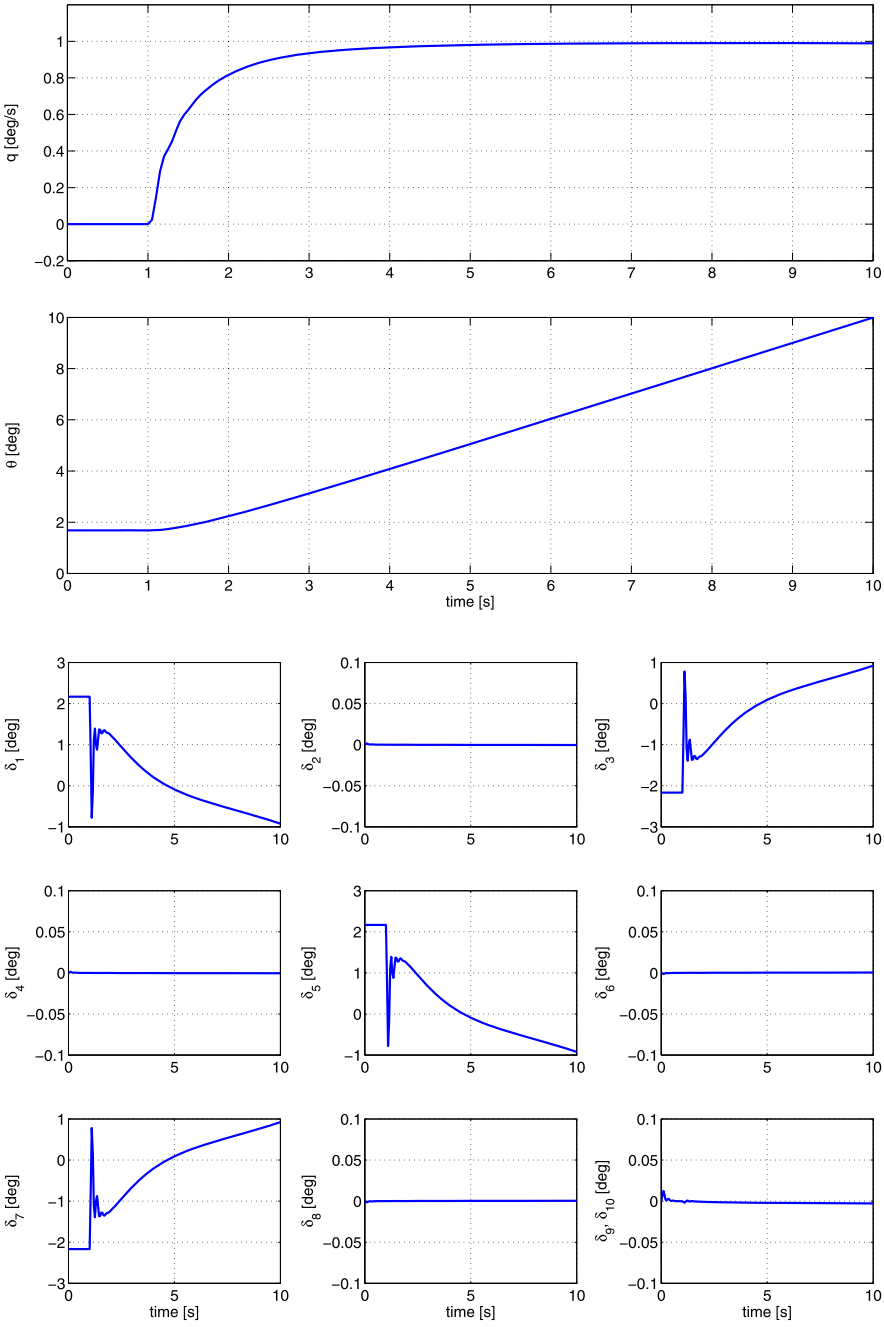

Fig. 14 Longitudinal aircraft response to a pitch rate command (*top*) and control activity (*bottom*)

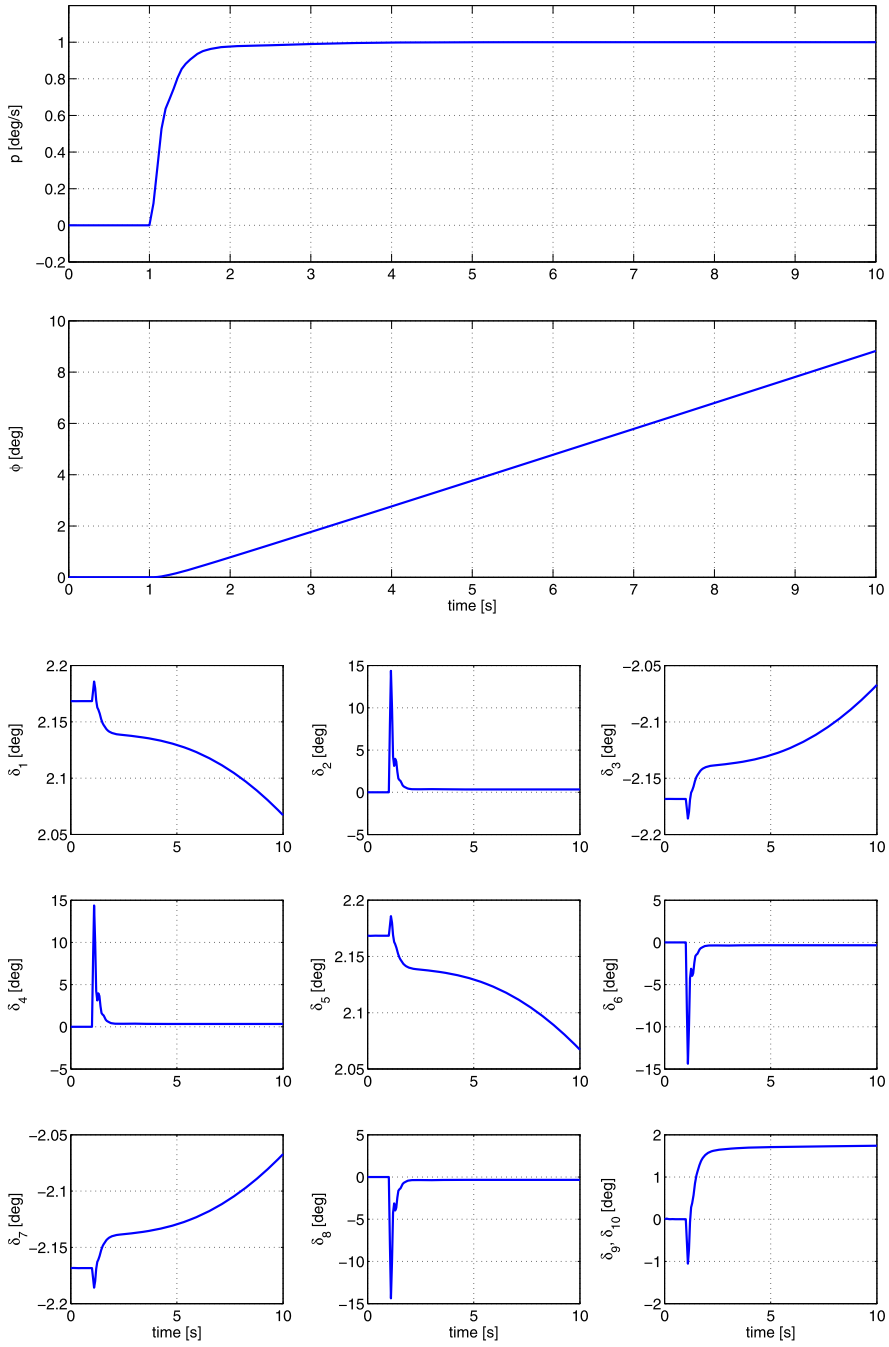

Fig. 15 Lateral aircraft response to a roll rate command (*top*) and control activity (*bottom*)

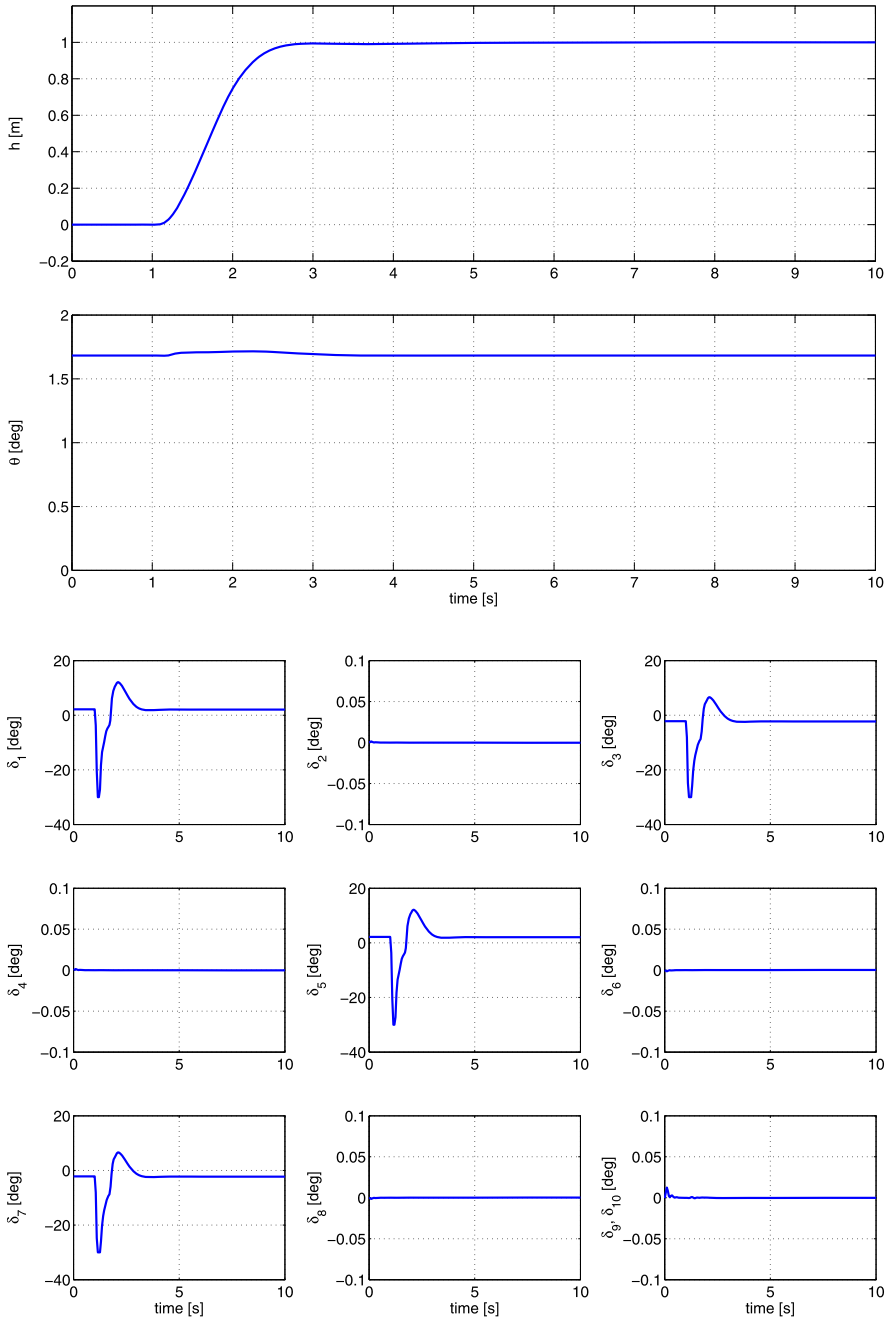

Fig. 16 Longitudinal aircraft response to a height command with direct lift (*top*) and control activity (*bottom*)

control of the flight path much easier than that of conventional aircraft. The model-based inversion control technique proves to be very useful in the conceptual and preliminary design phase because it does not require tuning of the gains. During all design efforts, the use is made of a flight mechanics toolbox. This Matlab-based toolbox can automatically construct flight mechanics models, which makes it highly suitable in a conceptual/preliminary design environment.

References

1. Anonymous: International Standard Atmosphere (ISA). International Organization for Standardization, ISO 2533 (1975)
2. Anonymous: U.S. Military Specification MIL-F-8785C Flying Qualities of Piloted AirPlanes (1980)
3. Anonymous: U.S. Military Handbook MIL-HDBK-1797 Flying Qualities of Piloted Aircraft (1997)
4. Anonymous: VSAERO a code for calculating the nonlinear aerodynamic characteristics of arbitrary configurations User's Manual Version 7.1. Analytical Methods Inc., Redmond, Washington, USA (2005)
5. Anonymous: Certification Specifications for Large AeroPlanes CS-25. European Aviation Safety Agency (2007)
6. Argeüelles, P., et al.: European Aeronautics: a Vision for 2020. European Commission (2001)
7. Bordignon, K.A.: Constrained control allocation for systems with redundant control effectors. Ph.D. Virginia Polytechnic Institute and State University (1996)
8. Butterworth-Hayes, P.: Better vibrations for turboprop technology. Aerosp. Am. **45**(7), 4–6 (2007)
9. Coleman, G., Chuboda, B.: A generic stability and control tool for conceptual design: prototype system overview. In: 45th AIAA Aerospace Sciences Meeting and Exhibit, Reno, Nevada, 8–11 January 2007
10. Drake, D.E.: Direct lift control during landing approaches. In: AIAA Second Annual Meeting, San Francisco, California, 26–29 July 1965
11. Demasi, L.: Investigation on conditions of minimum induced drag of closed wing systems and C-wings. J. Aircr. **44**(1), 81–99 (2007)
12. Durham, C.: Constrained Control Allocation. In: AIAA Guidance, Navigation and Control Conference, Hilton Head Island, South Carolina, 10–12 August 1992
13. Frediani, A.: A 250 Passenger PrandtlPlane transport aircraft preliminary design. In: XVIII Congresso Nazionale AIDAA, Volterra, Italy, 19–22 September 2005
14. Frediani, A.: The Prandtl Wing. V.K.I. Lecture series: Innovative Configurations and Advanced Concepts for Future Civil Transport Aircraft, 06–10 June 2005
15. Frediani, A., Montanari, G., Pappalardo, M.: Sul Problema di Prandtl della Minimia Resistenza Indotta di un Sistema Portante. In: XV Congresso Nazionale AIDAA 2, Torino, Italy, p. 267 (1999), (in Italian)
16. Frediani, A., Balis Crema, L., Chiocchia, G., Ghiringhelli, G.L., Morino, L.: Development of an innovative configuration for transport aircraft, a project of five Italian universities. In: XVII Congresso Nazionale AIDAA III, Roma, Italy, pp. 2089–2104 (2003)
17. Van Ginneken, D., Voskuijl, M., van Tooren, M.J.L., Frediani, A.: Automated control surface design and sizing for the PrandtlPlane. In: 6th AIAA Multidisciplinary Design Optimization Specialist Conference, Orlando, Florida, 12–15 April 2010
18. Gerend, R.P., Roundhill, J.P.: Correlation of gas turbine engine weights and dimensions. In: AIAA 6th Propulsion Joint Specialist Conference, San Diego, California, June 1970

19. Glaze, M., Durham, C.: Design and implementation of a control allocation toolbox for matlab V5.0. In: AIAA Guidance, Navigation and Control Conference and Exhibit, Boston, Massachusetts, 10–12 August 1998
20. Gorham: Means for controlling the vertical path of an aircraft. United States Patent 3,589,648 (1971)
21. Härkegård, O.: Backstepping and control allocation with applications to flight control. Ph.D. Linkoping University (2003)
22. Hoffman, A.C., et al.: Advanced secondary power system for transport aircraft. NASA Technical Paper 2463 (1985)
23. Iemma, U., Diez, M., Morino, L.: Community noise impact on the conceptual design of innovative aircraft configurations. In: 11th AIAA/CEAS Aeroacoustics Conference, Monterey California, 23–25 May 2005
24. Von Karman, T., Burgers, J.M.: General aerodynamic theory—perfect fluids. In: Durand, W.F. (ed.) Aerodynamic Theory, vol. II. Springer, Berlin (1935)
25. Kok, H.J.M., Voskuijl, M., van Tooren, M.J.L.: Distributed propulsion featuring boundary layer ingestion engines for the blended wing body subsonic transport. In: 6th AIAA Multidisciplinary Design Optimization Specialist Conference, Orlando, Florida, April 2010
26. Kothmann, B.D., Armbrust, J.: RAH-66 Comanche Core AFCS control law development DEMVAL to EMD. In: 58th Annual Forum of the American Helicopter Society, Montreal, Canada, 11–13 June 2002
27. Lange, R.H., et al.: Feasibility study of the transonic biPlane concept for transport aircraft application. NASA Contractor Report-132462, Lockheed (1974)
28. Liebeck, R.H.: Design of the blended wing body subsonic transport. J. Aircr. **41**(1), 10–25 (2004)
29. Luenberger, D.G.: Linear and Nonlinear Programming, 3rd edn. Springer, Berlin (2008)
30. Lundbladh, A., Grönstedt, T.: Distributed propulsion and turbofan scale effects. Technical report, Volvo Aero Corporation, 2005. ISABE-2005-1122 (2005)
31. Mattingly JD Heisser, W.H., Pratt, D.T.: Aircraft Engine Design. AIAA Education Series (1989)
32. McDonald, C.F., Massardo, A.F., Rodgers, C., Stone, A.: Recuperated gas turbine aeroengines. Part III: Engine concepts for reduced emissions, lower fuel consumption and noise abatement. Aircraft Eng. Aerospace Technol. **80**(4), 408–426 (2008)
33. McMasters, J.H., Kroo, M.I.: Advanced configurations for large subsonic transport airPlanes. NASA CR-198351, Boeing commercial airPlane group (1996)
34. Mount, J.S.: Effect of inlet additive drag in aircraft performance. J. Aircr. **2**, 5 (1965)
35. Nathman, J.K., McComas, A.: Comparison of stability and control calculations from vortex lattice and panel methods. In: 46th AIAA Aerospace Sciences Meeting and Exhibit, Reno, Nevada (2008)
36. Pinsker, W.J.G.: The control characteristics of aircraft employing direct lift control. Royal Aircraft Establishment Reports and Memoranda No. 3629 (1968)
37. Prandtl, L.: Induced drag of multiplanes. Technische Berichte, III(7) (1924)
38. Provost, M.J.: The more electric aero-engine; a general overview from an engine manufacturer. In: International Conference on Power Electronics, Machines and Drives, Bath, UK, June 2002
39. Rysdyk, R.T., Calise, A.J.: Adaptive model inversion flight control for tilt-rotor aircraft. J. Guid. Control Dyn. **22**(3), 402–407 (1999)
40. Seddon, J.J., Goldsmith, EL: Intake Aerodynamics, 2nd edn. AIAA Ed-ucation Series (1999)
41. Sim, G., Onspaugh, C.M.: Laboratory development of selected systems in the Lockheed L-1011 Tristar. In: AIAA 3rd Aircraft Design and Operations Meeting, Seattle, Washington, 12–14 July 1971
42. Torenbeek, E., Wittenberg, H.: Flight Physics, Essentials of Aeronautical Disciplines and Technology, with Historical Notes. Springer, Dordrecht (2009)
43. Van Toor: The role of advanced design in aircraft concept development and product definition. [Letter] (Personal communication, 12 July 2010) (2010)

44. Whellens, M.W., Singh, R., Pilidis, P., Taguchi, H.: Genetic algorithm based optimization of intercooled recuperated turbofan design. In: 41st Aerospace Sciences Meeting and Exhibit, Reno, Nevada, January 2003
45. Yomchinda, T., Horn, J.F.: Handling qualities assessment of a model inversion controller for a tiltrotor aircraft. In: Proceedings of the 3rd International Basic Research Conference on Rotorcraft Technology, Nanjing, China, October 2009